



HAL
open science

Mud generation from stratified sediments in a context of mud volcanism : the role of gas

Arthur Blouin

► To cite this version:

Arthur Blouin. Mud generation from stratified sediments in a context of mud volcanism : the role of gas. Earth Sciences. Université de Pau et des Pays de l'Adour, 2019. English. NNT : 2019PAUU3040 . tel-02881953

HAL Id: tel-02881953

<https://theses.hal.science/tel-02881953>

Submitted on 26 Jun 2020

HAL is a multi-disciplinary open access archive for the deposit and dissemination of scientific research documents, whether they are published or not. The documents may come from teaching and research institutions in France or abroad, or from public or private research centers.

L'archive ouverte pluridisciplinaire **HAL**, est destinée au dépôt et à la diffusion de documents scientifiques de niveau recherche, publiés ou non, émanant des établissements d'enseignement et de recherche français ou étrangers, des laboratoires publics ou privés.

THÈSE

UNIVERSITE DE PAU ET DES PAYS DE L'ADOUR
École doctorale des sciences exactes et leurs applications

Présentée et soutenue le 28 novembre 2019
par **Arthur BLOUIN**

pour obtenir le grade de docteur
de l'Université de Pau et des Pays de l'Adour
Spécialité : Sciences de la Terre

Formation de boue à partir de sédiments stratifiés dans un contexte de volcanisme de boue: le rôle du gaz

MEMBRES DU JURY

RAPPORTEURS

- Joe CARTWRIGHT
- Achim KOPF

Professeur / University of Oxford
Professeur / University of Bremen

EXAMINATEURS

- Lies LONCKE
- Régis MOURGUES
- Francis ODONNE

Maître de Conférence / Université Perpignan Via Domitia
Professeur / Le Mans Université
Professeur / Université de Toulouse 3

INVITE

- Patrice IMBERT

Chercheur / Total Pau

DIRECTEURS

- Jean-Paul CALLOT
- Nabil SULTAN

Professeur / Université de Pau et des Pays de l'Adour
Chercheur / Ifremer





Gaz bubble popping out from a gryphon (Sare Boga, Azerbaijan)

Acknowledgments/Remerciements

I would like to start by thanking all the jury members who accepted and did me the honor to read and examine my manuscript: Achim Kopf, Joe Cartwright, Lies Loncke, Régis Mourgues and Francis Odonne. I really hope that you will enjoy reading this work.

Je voudrais ensuite remercier la triforme de cette thèse, soit mes trois encadrants. Merci à Nabil pour ton efficacité, ta disponibilité malgré ton rôle de responsable d'unité et tes « dead lines ». Au début c'est un peu stressant, on se dit qu'on ne finira jamais les trois ans en restant sain d'esprit, mais in fine on s'y fait, on prend le rythme et c'est très efficace. Merci pour les conversations très ouvertes que nous avons pu avoir ensemble que ce soit sur de la science ou sur d'autres sujets. Encore désolé pour toutes les fois où tu as du corriger mes erreurs de calculs. Quoiqu'il en soit, grâce à toi, je peux dire que je maîtrise beaucoup mieux la géotechnique, en particulier dans le domaine marin ce qui était nouveau pour moi. Jean-Paul, merci énormément pour ta disponibilité. Tu as toujours répondu présent pour la moindre chose dont j'avais besoin. Merci pour avoir toujours proposé de nouvelles idées et d'avoir toujours su m'expliquer des concepts qui me paraissaient à première vue obscurs. Merci pour m'avoir souhaité la bienvenue à Pau avant même le début de mon contrat, et d'avoir su me mettre à l'aise dès le début en me spécifiant toute fois tes attentes sur cette thèse. Patrice, merci pour ta disponibilité, ta bonne humeur et de m'avoir appris toutes tes astuces de vieux pirate de l'interprétation sismique. Grâce à toi, j'arrive dans le monde du travail avec de solides compétences. Cela a été un réel honneur d'être ton dernier étudiant en thèse avant ton départ de Total. Merci de m'avoir guidé et pour les bons moments passés ensemble sur les trois grandes conférences où j'ai présenté mes travaux. Merci aussi pour m'avoir fait découvrir les cœurs de canard : je ne pense pas que j'aurais goûté cela un jour sans cette invitation à diner. Enfin, merci à vous trois pour avoir dirigé et encadré cette thèse dans des styles certes très différents (Patrice le poète et ses concepts, Nabil l'ingénieur et ses calculs et Jean-Paul l'encyclopédie humaine) mais toujours dans la bonne humeur. Je crois que je ne pouvais pas mieux tomber.

Cette thèse se fait dans le cadre d'un partenariat entre Ifremer et Total. Aussi merci à ces deux entreprises d'avoir cru en ce travail et de m'avoir fait confiance pour mener à bien cette recherche. Merci également pour les financements et les moyens matériels et humains déployés pour le bon déroulement de mon travail.

Merci à l'Université de Pau et des Pays de l'Adour de m'avoir accueilli comme étudiant et d'avoir fait des concessions afin de limiter mes déplacements Brest-Pau. Merci à toutes les personnes rencontrées là-bas pour l'intérêt porté sur mon travail et les discussions que j'ai pu avoir avec plusieurs d'entre vous à différentes occasions.

Merci à l'équipe de choc pour le terrain en Azerbaïdjan en 2017. Merci à Francis Odonne et Patrice Imbert de m'avoir proposé cette mission qui m'a permis de toucher du doigt (et du bras) mon sujet d'étude.

Merci à Matthieu Gertauda pour ces bons moments passés sur le terrain, et les balades dans Bakou. Merci pour le T-Shirt, je le porte fièrement au travail. *Special thanks to Orhan Abbasov and Elnur Baloglanov for their help and kindness. You were very friendly to us and I hope we will meet again soon.* Merci au moustique mutant qui m'a permis de connaître le système hospitalier de Hacıqabul, sans toi l'aventure n'aurait pas été la même.

Merci aux équipes et aux collègues de Total. En particulier merci à toute l'équipe R&D pour l'accueil et les nombreuses discussions. Remerciements stout particulier à Claude Gout qui a toujours cru dans le travail de Patrice (malgré les risques d'éboulements dans son bureau) et par extension dans mon travail. Toujours prêt à discuter, tu poses toujours la question qui permet d'aller plus loin. Merci à Jérémie Gaillot qui a pris du temps afin de m'expliquer les résultats de mes analyses biostratigraphiques, et à Claire Fialips pour sa participation dans les analyses minéralogiques et leur interprétation. Merci à toute l'équipe de la carothèque pour avoir déballé et remballé les carottes et cuttings je ne sais combien de fois. Merci à Cathy qui m'a souvent aidé avec mes démarches en interne à Total. Merci aussi à Fugro, sans qui, à deux mois près, je n'aurais pas eu accès aux sédiments d'Absheron.

Merci à toutes les personnes cotoyées à Ifremer. En particulier, merci beaucoup à Bruno Marsset toujours à l'écoute y compris des étudiants. Merci pour ton soutien et de m'avoir rappelé quelques fois que j'avais des congés pour une raison. Merci à Mickael Rovere pour m'avoir formé et passé du temps avec moi sur les oedomètres. Merci à Mickael Roudaut et à Ronan Apprioual pour la construction de la cellule d'essai et sa maintenance sans laquelle cette thèse n'aurait pas pu avoir lieu. Merci particulièrement à Mickael pour avoir passé une journée entière avec moi pour installer un système d'évacuation pour le CO₂. Merci à Livio, Vincent, Sébastien, Shane et Stephan pour les discussions et vos conseils qui m'ont permis d'améliorer mon travail. Merci à Pauline pour ton aide qui m'a permis de garder un ordinateur opérationnel durant ces trois ans (et c'était pas gagné). Merci à Alison, Sylvia et Babette pour m'avoir aidé plusieurs fois à m'en sortir avec mes ordres de mission (désolé pour les casses-têtes). *Thank you Alison for correcting my English.* Merci à Hélène et à Marie-Odile pour m'avoir permis de réaliser avec vous une vidéo sur les volcans de boue. La vidéo sur les hydrates n'a pas été rattrapée, je vais donc songer à m'inscrire à Twitter... Enfin un merci tout particulier à Frauke, Louis et Tania qui m'ont donné goût à la géologie marine dès le troisième.

Merci à tous les amis rencontrés pendant cette thèse, au gré de mes déplacements.

A Pau, je voudrais remercier tout particulièrement Salomé. Grâce à toi, j'ai intégré une super bande de potes, et même si nous venons tous d'endroits différents, vous resterez pour moi « les Palois ». Merci à Simon, Johann, Carl, Kasim, Amine et Veronica les expatriés du bâtiment EA. Merci à tous « les Palois » (désolé je ne vous cite pas tous) pour tous ces supers moments dans le Sud-Ouest pendant un an à base randonnées, de balade, de surf, de ski, de bonnes bouffes et de soirées. Merci à vous tous d'avoir été là dans les bons et les mauvais moments. Merci à Samy, mon moniteur de ski pour une journée : la prochaine fois je

ne tomberai pas dans le tapis roulant, c'est promis. Antoine, merci d'être aussi râleur que moi, je me sentais moins seul ! Merci à Alexandre (Dr. Pichat) et Etienne (Dr. Legeay) pour tous les bons conseils de vieux thésards ainsi que pour les pauses que vous vous accordiez lorsque j'étais de passage à l'UPPA.

A Brest mêm', merci à la bande de copains de toujours, pour m'avoir apporté des moments de décompression et de fun si précieux surtout rendu en fin de thèse. Big Up à Maud, Xavier et Julien qui m'ont fait reprendre le sport : ça m'a permis de souffler et de limiter ma prise de circonférence. Merci aussi à mes amis et collègues thésards et ex-stagiaires pour tous ces bons moments passés à Ifremer et en-dehors. Plus particulièrement une grosse pensée pour Farah et Déborah qui ont supporté ces deux dernières années mes grognements et sautes d'humeur à chaque fois que « Word a cessé de fonctionner » (ou pour toute autre raison d'ailleurs). Merci à Aurélien et Maude pour cette journée de pêche à pied mémorable ! Merci également à Alexandra Pierron, qui est ma première stagiaire. Tu as fait du super boulot, et ça m'a énormément aidé (Cf Chapitre 5).

A Nancy, merci à tous mes anciens amis de la promotion 2016 de l'ENSG. Je rêvais de faire cette école, mais en fait c'était encore mieux ! Merci à Briec et Mathieu, mes anciens colocataires, avec qui on a passé de supers moments, récemment ou non, et surtout avec qui j'ai appris à rédiger des rapports de terrain aux petits oignons. Je pense que cette compétence m'a été fort utile. Merci aussi à Yves Géraud et Jean-Marc Montel pour le soutien qu'ils m'ont apporté pendant l'école mais aussi depuis l'école.

Enfin, merci à ma famille et belle-famille ainsi qu'à tous les proches qui m'ont accompagné et soutenu pendant toutes mes études. Merci particulier à Françoise et Dominique qui m'ont donné le goût du voyage. *Gracias a la familia y amigos de Mexico que siempre estuvieron al pendiente de mis avances.* En particulier, merci à ma mère pour m'avoir toujours poussé à être curieux et pour m'avoir donné le virus de la recherche. Merci d'avoir toujours cru dans mes capacités et de m'avoir poussé (*i a chanclazos !*) à aller jusqu'au bout en faisant cette thèse. Merci à mon père sans qui ma vocation de « casseur de cailloux » ne serait pas apparue si tu ne m'avais pas fait visiter le musée de paléontologie à Paris. Merci à Axel, mon petit frère, pour le jeune homme intelligent, responsable et bon que tu es devenu. A toi maintenant d'aller au bout de tes rêves et de tes projets. Enfin, merci à Maud, toi qui plus que tous, a eu à supporter mon stress, mes humeurs et ma fatigue. Tu as su me canaliser et tu m'as accompagné depuis le tout début (en prépa), en passant par ces 4 années de distance (*we did it !*), jusqu'à Brest où tu as en plus dû apprendre à vivre tous les jours avec mon côté maniaque. Toi aussi tu as fait ton bonhomme de chemin ! Je ne suis définitivement plus un « petit étudiant » comme tu avais l'habitude de me dire.

Merci

Thanks

Gracias

Taşakkür



First contact with mud. I did not keep my hands clean very long (sorry Mum)

Table of contents

Acknowledgments/Remerciements.....	i
Table of contents	vii
List of Figures.....	xiii
List of tables.....	xxvii
List of equations	xxix
Chapter 1: Scientific Background.....	1
1. Introduction (English).....	5
1. Introduction (Français).....	9
2. Significance of mud volcanism	13
2.1. Mud volcano definition and lexicon	13
2.2. Occurrence and geological setting for mud volcanism	15
2.3. Mud composition and origin of the different constitutive elements.....	17
2.4. Morphology and architecture of a mud volcano system	19
2.4.1. Source domain.....	20
2.4.2. Intrusive domain.....	21
2.4.3. Extrusive domain	23
2.4.4. Roof domain	25
2.5. Triggers for mud genesis and drivers of sediment remobilization.....	26
2.5.1. Overpressure generation.....	26
2.5.2. The role of methane	31
2.5.3. Density inversion	32
3. Goal and scope of this research	35
3. But et cadre de ce travail de recherche	39
4. Thesis outline	43
4. Plan de la thèse	45

Chapter 2: Study Area, Data and Methodology	47
1. Study Area.....	51
1.1. South Caspian Basin.....	51
1.1.1. Geodynamics and present tectonic background.....	51
1.1.2. Paleogeography and regional stratigraphy	56
1.1.3. Oil & gas potential and mud volcanism.....	60
1.2. Absheron fold: gas-condensate field and geohazards	63
2. Data acquisition and location	64
2.1. 3D seismic survey.....	64
2.2. Geotechnical and geophysical survey.....	65
2.2.1. Geophysical dataset	65
2.2.2. Coring and in situ mechanical measurements	66
2.3. Exploration wells.....	66
2.3.1. Gamma-ray and caliper logs.....	67
2.3.2. Sonic logs	67
2.3.3. Density log	68
2.3.4. Neutron logs	68
2.3.5. Resistivity logs	68
2.3.6. Lithology	69
2.3.7. Formation pressure logs, rock strength, temperature and gas out	70
3. Methods.....	72
3.1. Seismic interpretation	72
3.2. Sediment analysis	72
3.2.1. Mineralogy.....	73
3.2.2. Biostratigraphy	74
3.2.3. Grain-size distribution	74
3.2.4. Mechanical properties of sediments.....	75
3.3. Well data interpretation	81
3.4. Numerical modeling.....	82
3.4.1. 1D sedimentation and pore pressure accumulation	82
3.4.2. Two-dimensional transient-diffusion process: Darcy's and Fick's laws	82
3.4.3. P-wave velocity with gas saturation	83
3.4.4. Fluid mud dynamics: modelling approach.....	84
4. Conclusion.....	85

Chapter 3: Evolution model for the Absheron mud volcano: from in situ observations to numerical modeling	87
1. Introduction	91
2. Regional Setting	92
3. Materials and methods	94
3.1. Seismic data	94
3.2. Sediment cores and geotechnical analysis	96
3.2.1. Sample collection.....	96
3.2.2. Mineralogical and biostratigraphic analysis of the mud	97
3.2.3. Geotechnical analysis of the mud	98
3.3. In situ well data and hydraulic conductivity calculations	99
3.4. Numerical modeling: sedimentation, transient pore pressure and gas diffusion	100
3.4.1. 1D sedimentation and pore pressure accumulation	100
3.4.2. Two-dimensional transient-diffusion process: Darcy's and Fick's laws	101
3.4.3. Hydrofracturing	102
4. Results.....	102
4.1. Geomorphological investigation of the Absheron mud volcano.....	102
4.2. Physical, sedimentological and geotechnical properties of the mud.....	115
4.3. In situ lithology, temperature and excess pore-pressure derived from in situ well data	119
4.4. Numerical calculations of transient pore pressure and methane diffusion.....	122
4.4.1. 1-D modeling	122
4.4.2. 2-D modeling	123
5. Discussion	126
5.1. What is the stratigraphic source of the mud?	126
5.2. How do the field pore pressure measurements compare to the model?.....	128
5.3. How does methane diffusion interact with excess pore pressure accumulation?	129
5.4. What is the most plausible sequence for the formation of the Absheron mud volcano..	130
5.5. Limits and perspectives of the study	133
6. Conclusions	134

Chapter 4: Sediment damage caused by gas exsolution: a key mechanism for mud volcano formation	137
1. Introduction	141
2. State of the art on gassy sediments	142
2.1. Definition of gassy sediments.....	142
2.2. Occurrence and relevance of gassy sediments	144
2.3. Creating gassy sediments during laboratory testing	146
2.4. Hydro-mechanical properties of gassy sediments	147
2.4.1. Gassy sediment acoustic response.....	147
2.4.2. Gassy sediment compressibility	148
2.4.3. Gassy sediment permeability	149
2.4.4. Sediment damage due to gas exsolution	150
2.4.5. Effect of gas bubbles on the sediment shear strength.....	151
3. Experimental testing	151
3.1. Properties of the tested soil and sample preparation	151
3.2. Experimental set-up and calibration	154
3.3. Testing program.....	158
4. Results.....	159
5. Synthesis of experimental results.....	167
5.1. Fractures, sediment damage and remolding.....	167
5.2. Effect of gas exsolution on P-wave velocity	169
5.3. Effect of degree of gas saturation on sediment compressibility.....	170
5.4. Hydraulic conductivity versus degree of gas saturation	171
5.5. Preconsolidation pressure evolution with degree of gas saturation	172
6. Discussion	173
6.1. Fracture size and number: main controlling factors	173
6.2. Gas exsolution/expansion: a permanent P-wave velocity attenuation?	174
6.3. Gas exsolution/expansion effects on sediment compressibility.....	175
6.4. Gas exsolution/expansion effects on sediment permeability.....	176
6.5. Gas exsolution/expansion effects on preconsolidation pressure and the consequence in terms of shear strength	177
7. Conclusions	178

Chapter 5: From stratified sediments to fluid mud generation.....	181
1. Introduction	185
2. Material and methods.....	186
2.1. Mud generation	186
2.2. Mud ascent	188
3. Results.....	190
3.1. Mud generation	190
3.1.1. One-dimensional sedimentation and pore pressure accumulation.....	190
3.1.2. Two-dimensional transient-diffusion processes, gas exsolution and damage.....	191
3.2. Mud ascent	199
3.2.1. Code1 v1	200
3.2.2. Code1 v2	203
3.2.3. Extrapolation to realistic viscosities: 1D calculations.....	206
4. Discussion	208
4.1. Synthesis of the main results.....	208
4.2. Overpressure, hydrofracturing and gas exsolution: from stratified sediments to fluid mud	209
4.3. Mud extrusion resulting from density-inversion driven by gas exsolution.....	211
4.4. Towards a quantitative formation model for the Absheron mud volcano	213
5. Conclusion.....	219
Chapter 6: Synthesis, conclusions and perspectives.....	221
1. Introduction	223
2. The formation of a mud volcano: a close relationship between gas and overpressure	223
2.1. The source of the Absheron Mud Volcano: intrinsic factors and external parameters....	223
2.2. Mud generation through gas exsolution	225
2.3. Integrated numerical models: mud generation and remobilization under geological conditions	226
3. Possible further improvements	228
3.1. Dataset.....	228
3.2. Experimental study	229

3.3. Numerical modeling.....	230
4. Scientific implications and perspectives	231
Chapitre 6 : Synthèse, conclusions et perspectives	233
1. Introduction	235
2. La formation d'un volcan de boue : une relation étroite entre le gaz et la surpression	235
2.1. La source du volcan de boue d'Absheron : facteurs intrinsèques et paramètres extérieurs	235
2.2. La génération de boue par exsolution de gaz.....	237
2.3. Modèles numériques intégrés : génération et remobilisation de la boue dans les conditions géologiques.....	239
3. Axes d'amélioration	241
3.1. Le jeu de données.....	241
3.2. Etude expérimentale	242
3.3. Modélisation numérique	243
4. Implications scientifiques et perspectives de cette étude	244
 References.....	 247
Appendix 1: Additional testing results.....	269
Appendix 2: Published journal articles.....	275

List of Figures

Chapter 1

Figure 1.1: a: Google Earth 2018 3D view of the Bozdag Guzdek mud volcano (Azerbaijan) with a vertical exaggeration of 3. This mud volcano has a basal diameter of 2 km, its crater being 500 m large and oval. Several km-long mudflows are visible on its northern flank. b: gryphon pictured in May 2017 at the top of the Sareboga seeping site (Azerbaijan). It shows the cm to m scale seeping sites that can be found at the top of active MVs during their dormant phase. It also displays the different phase composing the mud: fine-grained sediments, water and gas. c-d: mud expelled from onshore MVs in Azerbaijan. c: northern highly viscous and dry mudflow from the Koturdag MV (Azerbaijan, May 2017). It carries among its fine-grained matrix, m-scale to cm-scale rock clasts. Sinter structures (orange) correspond to points where gaseous methane was emitted and ignited spontaneously, heating the surrounding clay minerals. d: highly fluid mudflow emitted from the gryphon pictured in b. The mud is saturated with water and it behaves like a fluid. Mud flowed along the natural slope for 100 meters at least. 14

Figure 1.2: global distribution map of known mud volcanoes offshore and onshore (from Mazzini & Etiope, 2017). 15

Figure 1.3: Methane carbon and hydrogen isotope diagram for mud volcanoes (from Etiope et al., 2009). 18

Figure 1.4: schematic diagram of a mud volcano system, displaying its main structural domains. The features common for most of mud volcanoes are represented and only morphological and geometrical considerations are displayed (modified from Kirkham, 2015). 19

Figure 1.5: a- seismic section across a mud volcano system in the South Caspian Basin showing a thinning of the Maykop Formation interval interpreted as being the source layer of the mud volcano. b- Depth map of the top of the Maykop Formation underlining a thrust. c- Thickness map of the Maykop Formation showing a depleted zone inside the red dotted line (from Stewart & Davies, 2006). 20

Figure 1.6: interpreted seismic section showing the bowl-shaped features at the crest of an anticline in the South Caspian Basin, interpreted as former mud chambers (from Dupuis, 2017). Interval 2 is partially truncated by interval 3. Interval 1 is undisturbed. The interval 4 is interpreted as being mud extrusions initially sourced in the truncated interval 2. Sediment remobilization provoked a collapse of intervals younger than the source. 21

Figure 1.7: a: seismic section showing the subsiding column of intruded sediments named “downward tapering cone” by Stewart & Davies (2006). It is located below several biconical extrusive edifices (from Stewart & Davies (2006)). b: coherency time slice showing the chaotic structure inside the DTC (from Stewart & Davies, 2006). 22

Figure 1.8: example of a buried mud volcano offshore of Trinidad with the typical “Christmas tree” morphology. This architecture is the result of the cyclic development of the volcanic edifice, with short eruptive periods that contrast with the longer dormant periods when normal sedimentation dominates (from Deville, 2009). 24

Figure 1.9: Different morphologies of MVs due to different internal processes and external forces (from Mazzini & Etiope, 2017). (A) conical, (B) elongated, (C) pie-shaped, (D) multicroater, (E) growing diapir-like, (F) stiff neck, (G) swamp-like, (H) plateau-like, (I) impact craterlike, (J) subsiding structure, (K) Subsiding flanks, (L) sink-hole type. 25

Figure 1.10: pressure versus depth plot showing hydrostatic (P_{hydro}) and lithostatic (P_{litho}) pressures. The green line is the measured pressure. The difference between the measured pressure and hydrostatic pressure represents the overpressure and the difference between the lithostatic and measured pressure gives the effective stress (modified from Deming, 2002). 27

Figure 1.11: Conceptual mud volcano system model from Deville et al. (2010) showing a possible reaction chain and processes leading to sediment remobilization and mud volcano formation. 33

Chapter 2

Figure 2.1: Topographic/Bathymetric map around the South Caspian Sea using the GEBCO 2014 database. The -500 m contour line is represented and highlight the main depocenters in the Caspian Sea. The main fold and thrust belts and reliefs delimiting the South Caspian Basin are located as well as the main river systems linked to the SCB history. The study area is located by a purple rectangle. SCB: South Caspian Basin; CCB: Central Caspian Basin; NCB: North Caspian Basin. 51

Figure 2.2: Simplified tectonic map of the South Caspian area showing the main tectonic units (modified from Brunet et al., 2003). A: Aghdarband; Ap: Absheron; A Trialet: Achara-Trialet; EO: Erevan-Ordubad; E Pontides: Eastern Pontides; GB: Great Balkhan; Go: Gorgan; K: Karabakh; L Caucasus: Lesser Caucasus; Na: Nayband; R: Rasht; SP; Scythian platform; TC: Terek – Caspian basin; WT: Western Turkmenia. The present SCB is delimited by the red dotted line and is located partly onshore. 53

Figure 2.3: a: Simplified structural map of the Caspian area including GPS-derived estimations for plate velocities. ALBZ: Alborz block; AN; Anatolian Plate; CAUC: Caucasus Plate; SCB: SCB Block (modified from Santos Betancor, 2015). b: Map showing earthquakes of the CCB and SCB regions taken from the IRIS catalogue for the period between 1970 and 2010 and classified by depth of their hypocenters (modified from Santos Betancor, 2015). Blue dotted line marks the oceanic crust of the SCB and the purple rectangles show the approximate location of the study area. 55

Figure 2.4: Generalized lithostratigraphic column for the SCB. The Jurassic–Miocene sequence is known from outcrops in eastern Caucasus, while the Pliocene and younger section were drilled in the SCB. Ages are given in million years. The Lower PS are subdivided in Kala Suite (KAS), Under-Kirmaky Suite Sandstone (PK), Kirmaky Suite (KS), Above-Kirmaky-Sandstone (NKP) and Above-Kirmaky Shale (NKG). The transgressive and regressive trends are those given by Abreu & Nummedal (2007). Figure adapted and modified from Green et al., (2009) and Javanshir et al. (2015). 57

Figure 2.5: schematic map of the Paleo-drainage systems during the deposition of the Productive Series (Late Miocene–Pliocene). The possible sources of sediments are displayed as well as the location of the paleo-deltas. The purple box shows the approximate location of the study area (modified from Smith-Rouch, 2006). 58

Figure 2.6: HC generation and accumulation temporal chart for the Oligocene–Miocene Maykop/Diatom Total Petroleum System in the South Caspian Basin Province. Ak–Ap: Akchagyl and Absheron intervals. The critical moment correspond at the time when all the criteria for oil & gas generation, accumulation and preservation were present and correspond to the Akchagyl strata deposition (from Smith-Rouch, 2006). 62

Figure 2.7: Seafloor depth map extracted from the 3D seismic survey, showing the location of the other surveys and samples used during this research. The AMV is visible as a light blue patch where the dataset is denser. Seafloor depth is given in meters below mean sea level. The Purple rectangle shows the maximum extent of the 3D seismic survey, the black polygon shows the extent of the multibeam echo sounder survey, and the red rectangle, the area where backscattering image was processed. Samples are represented with different symbols depending on their type. Red circles with crosses: exploration wells; orange circles with dots: rotary drillings and CPT measurements; blue pentagons: piston cores from AUV survey, 2014; yellow square: box core from AUV survey, 2014; green triangles: samples for biostratigraphy from Chevron survey, 1999. 64

Figure 2.8: Log data from well ABX2 presented as an example of lithology interpretation. a: “quick-look” log plotted during drilling operations for monitoring purposes. The main data acquired with LWD tools are the gamma-ray (GR) signal (green) and the resistivity (shallow in blue, deep in red). These geophysical data are coupled with cuttings analysis in order to present a preliminary lithological section. b: final composite log, with all geophysical data obtained over a given section (GR; resistivity, shallow and deep field; sonic, DTP for P-waves and DTS for S-waves; density; neutron). Using data from resistivity coupled with sonic, and superimposed neutron and density, it is possible to refine the lithological log notably by precisely highlighting reservoir facies (yellow color, right column). 71

Figure 2.9: a: picture of the fall cone test apparatus, displaying the main elements. b: typical log-log diagram of the water content versus the penetration depth, displaying the reading methods for the Atterberg limits (from Feng, 2005). 75

Figure 2.10: a: picture showing one oedometer used during the study, displaying the main elements of the system. b: typical plot for an oedometer test result after increment load and unload, displaying the consolidation curve, the

swelling curve and the virgin consolidation curve. The method for calculating the preconsolidation pressure (σ'_{p0}) and for the reading of the compression index (C_c) and swelling index (C_s) is also displayed. A is the maximum inflexion point of the laboratory consolidation curve. From this point, the tangent to the curve and the horizontal line are drawn. The bisector between these two lines gives the point B at the intersection with the virgin consolidation curve. The horizontal coordinate of B gives σ'_{p0} 77

Figure 2.11: Picture showing the main modules of the special consolidation testing. Details are given in the Chapter 4, dedicated on the experimental testing program and results. 78

Figure 2.12: Adopted method to apply the effective medium theory of Helgerud et al. (1999) (modified from Taleb et al., 2018). 84

Chapter 3

Figure 3.1: A, structural map of the South Caspian region showing the main folds and faults, structural domains and depocenters (modified from Oppo et al., 2014). B, regional interpreted deep seismic section, showing the main subsurface structural elements with the folds above the Maykop detachment level associated in the northern part to deeply rooted thrusts. The location of the line is shown on the left map by a black line. The red box shows the approximate location of the Absheron structure (modified from Stewart & Davies, 2006). 92

Figure 3.2: Seismic amplitude map of the seafloor around the Absheron mud volcano. In orange, a high amplitude mudflow is imaged to the west of the volcano. The dark patch corresponds to the shield composing the mud volcano itself. On the same map, the location of the different coring and drilling sites are shown. Limits and location of the 3D seismic survey are presented on the regional map of the SCB (Figure 3.1A). Red lines indicate the location of the seismic lines presented in Figure 3.3, Figure 3.4 and Figure 3.5. The dotted black polygone is the limit of the zoom shown below, presenting a detailed image of the seafloor on and around the mud volcano acquired with a multi-beam echo sounder. Orange stands for the shallower areas, green is for the deeper parts. 96

Figure 3.3: Uninterpreted and interpreted seismic line crossing the anticline near the two exploration wells A and B; it was used as reference for horizon picking for this study. A deep thrust cores the Absheron anticline and another thrust, smaller is also visible at the NNE of the section. From the thickness differences between the flanks and the crest of the structure, we note that folding started during the Akchagyl deposition. The main growing phases are during deposition of the Absheron Suite (A3-A1) and later during the Post-Absheron times. See Figure 3.2 for location. 103

Figure 3.4: Uninterpreted and interpreted seismic line across the active mud volcano. The first 2 km are clearly imaged and show four seismically transparent wedges, corresponding to mudflows. A chaotic signal below can be

discriminated from the blind signal and is interpreted as reworked sediments. The rooting system is blind, maybe due to a masking effect from the low velocity mud deposits. Near the blind area, some normal faults are present between 1.5 and 3 km. A deep thrust is coring the main anticline. The activation of the mud volcano is contemporaneous to the main folding phase (see text and Figure 3.3 for details, Figure 3.2 for location).s directly be interpreted as mudflow deposits forming the mudvolcano edifice (green patch on Figure 3.4). Below 2 km at the center of the structure, a seismically transparent cone goes down to 7 km. This area could reveal the masking effect of the low velocity mass formed by the shallower mud deposits that may also be saturated with gas, preventing the acoustic signal from propagating below. Another seismic facies can be discriminated from the blind signal: the blue patch can be described as a chaotic signal. This area is located between the mudflows and host sediments. 105

Figure 3.5: Uninterpreted and interpreted seismic line south of the mud volcano center. The gas blanking effect reduces below the mudflows. The transparent and chaotic signals are still present. A bending of seismic horizons from 1.5 to 3 km is noted forming a bowl-like geometry. Horizons of the upper part of the Anhydritic Surakhany are truncated by younger intervals as well as a 400 m thick interval in the lower part of the Upper Productive Series. Horizons recovers their continuity and their flat geometry below 3800 m in the Productive Series. See Figure 3.2 for location..... 107

Figure 3.6: Applied method to channel recognition with the example of Layer 2 (Figure 3.7). A: the RMS of seismic amplitude is calculated on layers computed between two seismic horizons (here A3 and PS1). Elongated, curved and continuous bodies having the same RMS are potential channels. The surface location of the AMV is displayed with dotted lines. B: interpreted layer with confirmed channel bodies in green. The red line corresponds to the zoom of seismic section presented in C. The surface location of the AMV is displayed with dotted lines. C: zoom on a seismic section (location displayed in B, red line) perpendicular to a potential channel recognized on A. The seismic section is from the PSTM seismic block, and the vertical scale is given in ms TWTT (two-way travel time). At the exact location of the elongated body, a downward bending of two horizons is visible (red dotted rectangle). This bending is local and only affects two seismic horizons, thus, the body is interpreted as a channel. 108

Figure 3.7: A: interpreted section presented in Figure 3.3, displaying in green the stratigraphic interval where layers were computed. The black dotted line highlights the Layer 29. B: examples of channels found over several layers, in green. The surface location of the AMV is displayed. The black dotted rectangle highlights the area of crestal faulting that generated channel-like features. White dotted rectangles highlight the same NE-SW features south of the AMV corresponding to several pull-downs of the seismic signal due to the presence of low-velocity mudflows in the shallower intervals (see Figure 3.4). 109

Figure 3.8: A: map showing all the channels found over the interval A3-ASF. Each color correspond to a layer where channels are found. Surface location of the AMV is displayed and areas of data wipe-out are also displayed. B: Rose diagram showing the orientation of channels located in the interval A3-ASF. Channels are mainly oriented between N90° and N105°. C: map showing all the channels found over the interval ASF-PS1. Each color correspond to a layer where channels are found. Surface location of the AMV is displayed and areas of data wipe-out are also displayed. D:

Rose diagram showing the orientation of channels located in the interval ASF-PS1. Channels are mainly oriented N135° and N165° 110

Figure 3.9: A: thickness map computed between H33 and ASF horizons. B: thickness map computed between H3 and PS1 horizons. Minor contours represent 25 ms and major contours 200 ms. The surface location of the AMV is displayed with black dotted circles. Fault zones are represented as hatched areas. The spill point and the highest crestal point are detailed. 112

Figure 3.10: A: seafloor isochrone map showing the location of the zoom shown in B (black dotted rectangle) and of the section presented in C (red line) relatively to the surface expression of the AMV and of the two exploration wells. B: coherency map at 5496 msTWTT displaying one of the two subcircular buried mud cones, reaching 1km of diameter. C: uninterpreted (left) and interpreted (right) seismic section across the buried mud volcano, showing the entire mud volcano system, from its stratigraphic source with an area of truncated horizons located above a deeply rooted thrust, to the two buried bicones 1 sTWTT above the truncated horizons. Collapse of the horizon located between the truncations and the bicones are bended downwards and discontinuous. The black dotted line highlights the depth at which the coherency map in B was extracted. 114

Figure 3.11: Isopach map computed between the Top Maykop and the deepest horizon highlighted in Figure 3.10C. The black dotted area, corresponding to red to yellow colors, highlights an area thinner than the background corresponding to the area of truncated horizons in Figure 3.10C. The black dotted polygon correspond to the approximate limits of the youngest bicone imaged in Figure 3.10B. The hatched area correspond to the thrust throw. 115

Figure 3.12: A, whole rock mineralogical analysis for all the samples collected except the less than 5µm fraction of the MVF1E-RAW sample, for cuttings from the Anhydritic Surakhany interval and for cuttings from the unstable interval encountered during drilling operations. The main elements composing the mud are clearly clay minerals and quartz particles and mud samples have similar mineralogical signature than the unstable interval. B: mineralogical composition of clay for all the samples collected except the MVF1E-RAW>5µm and for cuttings from Anhydritic Surakhany and the drilled unstable interval. Globally, clay fraction is mainly composed by up to 50% of interstratified illite/smectite, 30% of Illite and/or micas, 15% of kaolinite and a minor part of chlorite and smectite, results different from the analysis of the Anhydritic Surakhany and its unstable interval. The less than 5 µm fraction of the MVF1E-RAW sample differs from the whole samples as they have less illite and/or micas, and more kaolinite and chlorite. See Figure 3.2 for location map, and Table 2-1 for details of samples. 116

Figure 3.13: A: oedometer tests with void ratio (e) versus vertical effective stress (σ'_v) for the different tested samples. For the natural samples, only the MECA-10 has a higher compressibility and a higher initial void ratio than the other samples. The input of coarser material reduce the initial void ratio and reduce the compressibility of the samples. B: hydraulic conductivity (k) versus void ratio (e) resulting from oedometer test and falling head method results for the

different samples analyzed. Again, MECA-10 has a lower permeability than other natural samples which fit the same trend. The input of coarser material reduces the hydraulic conductivity but the general trend stays parallel to natural samples. C: cumulative granulometry for the natural samples showing that MECA 10 is finer than the three other samples. See Figure 3.2 and Table 2-1 for more details on the samples. 118

Figure 3.14: A: overpressure logs for both exploration wells. Overpressures are in MPa. Continuous green line is the sonic-derived shale pressure and green crosses are the measured reservoir pressures. The orange dots are the LOT/FIT control points used in the construction of the fracture pressure plot (red line). The vertical line where overpressure is zero is the hydrostatic pressure. Seismic horizons are shown using the same color code as in Figure 3.3. Six different shale pressure peaks are highlighted in red B: 3D view of the two parallel seismic lines distant of 9.5 km. The right one is described in Figure 3.4. The left one in Figure 3.3. The pressure peaks are reported in front of the corresponding interval on seismic. 121

Figure 3.15: Results of the one-dimension sedimentation modeling. On the left, porosity vs. depth trend at the end of the 5 Ma of sedimentation with corrected sedimentation rates for each layer. On the right, overpressure vs. depth trend at the end of the 5 Ma of sedimentation. 122

Figure 3.16: Structural model based on Green et al. (2009) work and on the fault network observed in Figure 3.3. The line follows the same trend as the seismic section of Figure 3.1B. Eight layers extend along the section corresponding to different sedimentation rates, compaction laws and permeability trends (see Figure 3.15). The Layers NKG, Balakhany-Fasila, Sabunchy, Surakhany and Quaternary are named Layers 1 to 5 respectively in other figures. Numbers showed at the limits of the model correspond to limit conditions imposed for the diffusion of pore pressure and methane. 124

Figure 3.17: Results of overpressure and methane migration modeling after 5 Ma of calculation. A: overpressure (Δu) in kPa after 5 Ma of migration through the structural model presented on Figure 3.16. Overpressure migrated more rapidly through layer 4 which has a higher permeability. B: $\Delta u/\sigma'_v$ contours with values exceeding 0.75 and potentially reaching the level of hydro-fracturing. High values located in layer 5 are due to the low σ'_v near the seafloor. Black lines correspond to methane concentration contours. The top of the methane-saturated area corresponds to a zone where hydro-fracturing may occur if overpressure was slightly higher. Black dotted lines are for layer limits. 125

Figure 3.18: Formation model for the Absheron mud volcano based on in situ observations and measurements, laboratory tests and analysis and numerical modeling. 1- Rapid deposition of the Productive Series and maturation of the Maykop formation. Slow and extended methane migration. 2- Absheron fold creation. Focusing of the methane migration through fold-related fault network and $\Delta u/\sigma'_v$ increase at the anticline crest. 3- Rupture condition reached and hydrofracturing of the sedimentary column from the seafloor to the Anhydritic Surakhany. 4- Gas exsolution and expansion and remobilization of Anhydritic Surakhany sediments. First extrusion. 5- Propagation of gas exsolution and sediment remobilization. Depletion of the Anhydritic Surakhany and collapse of the overlying strata. 6- present geometry after alternation of several quiescent and active episodes for the mud volcano. More depletion of the source and collapse of the overlying strata is triggered at each active episodes. 132

Chapter 4

- Figure 4.1: Structure of unsaturated soils depending on the degree of gas saturation (S_g). (a) high S_g , the water phase is discontinuous and occluded around the solid particles when gas forms a continuous phase. (b) medium S_g , water and gaseous phases are continuous. (c) small S_g , the water phase is continuous and the gaseous phase is present in the form of discrete gas bubbles in the middle of the pore voids (from Wheeler, 1986). 143
- Figure 4.2: Extreme soil structure for unsaturated soils presenting discrete gas bubbles. (a) when gas bubbles are much smaller than the solid particles, (b) when gas bubbles are much larger than the solid particles (from Wheeler 1986). 143
- Figure 4.3: Experiments of gas injection into gelatin (proxy of sediment density and strength but not porosity) allowing illustrating the disk-shaped bubbles forming in cohesive sediments (from Boudreau, 2012). 144
- Figure 4.4: Map of the known occurrences of gassy sediments mentioned by Fleischer et al. (2001) (black areas) updated with enclosed seas occurrences (Caspian Sea), lakes (Baikal and Great Lakes) and places such as the Gulf of Guinea, Bay of Biscay, Ebro delta, Nile delta, and Levantine Basin (Red dots; modified from Fleischer et al., 2001). Numbers correspond to the listed occurrences in Fleischer et al. (2001). 145
- Figure 4.5: Experimental and theoretical decrease of P-wave velocity with increasing degree of gas saturation (from Sills et al., 1991). A decrease of 50% P-wave velocity is reached for less than 5% of gas saturation. 148
- Figure 4.6: Results of oedometer tests ran over several artificial gassy sediments with known degree of gas saturation. They display the clear decrease in sediment compressibility with decreasing degree of saturation, so increasing degree of gas saturation (from Nageswaran, 1983). 149
- Figure 4.7: Evolution of water relative permeability of sediments depending on the degree of gas saturation for different methods of gas recovery. It clearly shows that the stronger the degree of gas saturation is, the lower the water relative permeability is (from Egermann & Vizika, 2000). 150
- Figure 4.8: Section of a sediment core retrieved during ODP Leg 204 at southern Hydrate Ridge and displaying multiple cracks due to free gas expansion resulting from decompression during core ascent (from Riedel et al., 2006). 150
- Figure 4.9: Location of the study area. The Absheron mud volcano is located on the Absheron anticline (purple rectangle), 100 km to the SE of Baku, north of the South Caspian Basin. Details of the seafloor morphology of the area surrounding the mud volcano is given in the inset in the bottom left hand corner (read Chapter 2:2.1 and Chapter 3:4.1 for more details). The rotary drilling MVF1, located on the mudflow, is also displayed. 152
- Figure 4.10: Detailed experimental setup showing the consolidation cell, the saturation system and the main sensors emplacement. 154
- Figure 4.11: friction calibration during (a) loading and (b) unloading for different pore water pressures. The dotted black lines correspond to the envelop values of friction. The friction variation is within ± 2.5 kPa. 155

Figure 4.12: Results for test#8 with 4 load/unload cycles. Each color represents a load/unload cycle. a: void ratio (e) versus vertical effective stress (σ'_v) b: void ratio-versus P wave velocity (V_p); c: degree of gas saturation (S_g) versus σ'_v and d: S_g versus V_p . The grey line in (a) represents the reference consolidation test. 160

Figure 4.13: Pictures of the sample during test 8. a: before the second depressurization (cycle 4, Figure 4.12a) showing the sediment aspect before gas exsolution. b: after the second depressurization (Figure 4.12a). The sample swelled by 6 mm under the effect of gas exsolution, swelling partly due to the numerous cm-long and mm-thick fractures. 161

Figure 4.14: Results for test#11 with 4 load/unload cycles. Each color represents one load/unload cycle. a: void ratio (e) versus vertical effective stress (σ'_v) b: void ratio-versus P wave velocity (V_p); c: degree of gas saturation (S_g) versus σ'_v and d: S_g versus V_p . The grey line in (a) represents the reference consolidation test. 163

Figure 4.15: Pictures of the sample during test 11. a: before the second depressurization (cycle 3, Figure 4.14a) showing the sediment aspect before gas exsolution. b: after the second depressurization (Figure 4.14a). The sample swelled by 5 mm under the effect of gas exsolution and small and rare fractures appeared along a pre-existing weak zone (lighter color). c: before the second depressurization (cycle 3, Figure 4.14a) showing the sediment aspect before gas exsolution. d: after the second depressurization (Figure 4.14a). The sample swelled by 2.5 mm under the effect of gas exsolution with rare and very thin fractures at the base of the sample. e: before the third depressurization (cycle 4, Figure 4.14a) showing the sediment aspect before gas exsolution. f: after the third depressurization (Figure 4.14a). The sample swelled by 3.5 mm under the effect of gas exsolution, swelling partly due to the numerous cm-long and mm-thick fractures..... 164

Figure 4.16: Results for test#5 with 2 load/unload cycles. Each color represents one load/unload cycle. a: void ratio (e) versus vertical effective stress (σ'_v) b: void ratio-versus P wave velocity (V_p); c: degree of gas saturation (S_g) versus σ'_v and d: S_g versus V_p . The grey line in (a) represents the reference consolidation test. 166

Figure 4.17: Pictures of the sample during test 5. a: before complete depressurization (Figure 4.16a) showing the sediment aspect before gas exsolution. b: after complete depressurization (Figure 4.16). The sample swelled by 9.5 mm under the effect of gas exsolution. Numerous fractures generated and sediments took a slurry aspect. 166

Figure 4.18: P-wave velocity (V_p) versus void ratio (e). Colors stand for (a) S_g (%) and (b) S_{gmax} (%). Black lines correspond to the evolution of V_p with e for different values of S_g based on the effective medium theory modeling (Helgerud et al., 1999). (c) is the typical signal after gas exsolution, (d) is the typical signal after gas exsolution. Red line correspond to the source signal, green line is the received signal. 170

Figure 4.19: Compressibility versus S_{gmax} (%). Two type of compressibility are displayed. The grey vertical lines stand for the water-saturated sediments CC and CS, the dotted lines being the maximal and minimal values obtained during

the different tests. Values of CC_{frac} are annotated as labels, since values above 0.5 were plotted at 0.5 to condense the graph..... 171

Figure 4.20: a: hydraulic conductivity, K (m/s) versus void ratio. The blue dashed line is an exponential fit for hydraulic conductivities on water-saturated sediments obtained from oedometers (blue crosses). b: K (m/s) versus S_g (%). 172

Figure 4.21: Preconsolidation ratio versus S_{gmax} (%). a: ratio between preconsolidation pressures calculated before fracture closing, σ'_{p1} , and the initial preconsolidation pressure, σ'_{p0} . The labels correspond to the fracture classification given in Table 4-3. “s” stands for the fracture length, “d” for the fracture number. b: ratio between preconsolidation pressures calculated after fracture closing, σ'_{p2} , and the initial preconsolidation pressure, σ'_{p0} . Values from Sultan et al. (2012) are also plotted as comparison (red crosses). An exponential fit of the study results shows a strong determination coefficient (R^2)..... 172

Chapter 5

Figure 5.1: Updated geometry taking into account the ASF as a 300 meter thick incompressible and low-permeability layer (purple). The limit conditions are similar to the model presented in Chapter 3:4.4.2. However, condition 5 controlling the methane concentration injected at the base of the fault network is now considered as variable..... 187

Figure 5.2: Results of the one-dimensional sedimentation modeling at the southern edge of the 2D geometrical model in Figure 5.1. On the left, vertical hydraulic conductivity versus depth trend at the end of the 5 My of sedimentation. On the right, overpressure versus depth trend at the end of the 5 My of sedimentation with corrected sedimentation rates for each layer. The top of each simulated stratigraphic unit is represented as indication using the same colour code as in Figure 5.1 and the corresponding stratigraphic intervals are displayed inbetween. 191

Figure 5.3: Results of overpressure and methane diffusion modeling after 5 My of calculation considering the low permeability ASF interval. Black dotted lines are for layer limits. a: overpressure (Δu) in kPa after 5 My of migration through the structural model presented on Figure 5.1. Overpressure migrated more rapidly through layer 4 that has a higher permeability. b: $\Delta u/\sigma'_v$ contours with values exceeding hydrofracture condition below the ASF in the north of the model, where σ'_v is low. Black lines correspond to methane concentration contours. Lines are separated by 10 mM. c: Δu (kPa) vertical plot at the Absheron location (black arrow). 193

Figure 5.4: Results of overpressure and methane diffusion modeling after 5 My of calculation considering the low permeability ASF interval and faults as horizontal seals. Black dotted lines are for layer limits. a: overpressure (Δu) in kPa after 5 My of migration through the structural model presented on Figure 5.1. Overpressure builds up along the fault network. north of the fault network overpressure is only of 18 MPa. b: $\Delta u/\sigma'_v$ contours. The highest values are now distributed south of the fault network, along the ASF, at the crest of the Absheron fold. Methane distribution is

represented with black isolines, lines being separated by 10 mM. c: Δu (kPa) vertical plot at the Absheron location (black arrow)..... 195

Figure 5.5: Results of overpressure and methane diffusion modeling after 5 My of calculation considering the low permeability ASF interval, faults as horizontal seals and a fracture condition of 0.7. Black dotted lines are for layer limits. a: overpressure (Δu) in kPa after 5 My of migration through the structural model presented on Figure 5.1. b: $\Delta u/\sigma'_v$ contours. Fracture occurs along the bottom edge of the ASF, south of the fault network. Methane distribution is represented with black isolines, lines being separated by 10 mM. The dissolved methane distribution follows the fracture shape. c: Δu (kPa) vertical plot at the Absheron location (black arrow). 196

Figure 5.6: Results of the simulation considering the ASF, sealing faults, a fracture condition of 0.7 and an initial methane concentration of 5550 mM after 5 My. Black dotted lines are for layer limits. a: overpressure (Δu) in kPa after 2 My of migration through the structural model presented on Figure 5.1. b: $\Delta u/\sigma'_v$ contours. Fracture occurs along the bottom edge of the ASF, south of the fault network. Methane distribution is represented with black isolines. The dissolved methane distribution follows the fracture shape and is depleted around fractures due to gas exsolution. c: degree of gas saturation (S_g) calculated after fracture formation. Values as high as 1 are reached in the central part of the fracture, in an area close to the fault network. d: preconsolidation pressure (σ'_p). It increases linearly with depth, but it is disturbed in the same area where gas exsolution happened reaching zero in the center of the fracture. 198

Figure 5.7: Results of the simulation using code1 v1 for $\mu = 10^6$ kPa.s. The left column displays the evolution of mass-density with time (left color scale) as well as the velocity vectors (m/s). The right column displays the evolution of the degree of gas saturation with time (right color scale). 201

Figure 5.8: Results of the simulation using code1 v1 for $\mu = 10^5$ kPa.s and a 1000 m long vertical conduit. The left column displays the evolution of mass-density with time (left color scale) as well as the velocity vectors (m/s). The right column displays the evolution of the degree of gas saturation with time (right color scale). 202

Figure 5.9: Results of the simulation using code1 v2 for $\mu = 10^6$ kPa.s. The left column displays the evolution of mass-density with time (left color scale) as well as the velocity vectors (m/s). The right column displays the evolution of the degree of gas saturation with time (right color scale). 203

Figure 5.10: Results of the simulation using code1 v1 for $\mu = 10^5$ kPa.s and a 2000 m long vertical conduit. The left column displays the evolution of mass-density with time (left color scale) as well as the velocity vectors (m/s). The right column displays the evolution of the degree of gas saturation with time (right color scale). 204

Figure 5.11: Results of 1D calculations based on the case of a buoyant magma flow along a vertical dyke presented in Furbish (1997) considering a radius of 500 m corresponding to the mud source radius, compared to results obtained

with 2D simulations. a: maximum velocity versus viscosity, b: minimum time for extrusion versus viscosity. Black lines with crosses correspond to the case where the initial mud overpressure is not considered, red lines are for the case with mud overpressure. Grey dots correspond to the results of the 2D simulations using code1 v1 and white dots the results of 2D simulations with code1 v2. 207

Figure 5.12: Results of 1D calculations based on the case of a buoyant magma flow along a vertical dyke presented in Furbish (1997) considering a radius of 50 m corresponding to the conduit width, compared to results obtained with 2D simulations. a: maximum velocity versus viscosity, b: time for extrusion versus viscosity. Black lines with crosses correspond to the case where the initial mud overpressure is not considered, red lines are for the case with mud overpressure. Grey dots correspond to the results of the 2D simulations using code1 v1 and white dots the results of 2D simulations with code1 v2. 208

Figure 5.13: Formation model for the Absheron mud volcano based on in situ observations and measurements, sediment analysis, laboratory testing and mud generation and remobilization numerical modeling. Details of the different stages displayed in a, b, c, d, e, f and g are in the text. h: legend corresponding to a, b, c, e, f, g. 218

Appendix 1

Appendix 1 - Figure 1: Results for test#2 with 3 load/unload cycles. Each color represents a load/unload cycle. a: void ratio (e) versus vertical effective stress (σ'_v) b: void ratio-versus P wave velocity (V_p); c: degree of gas saturation (S_g) versus σ'_v and d: S_g versus V_p . The grey line in (a) represents the reference consolidation test. 269

Appendix 1 - Figure 2: Results for test#3 with 2 load/unload cycles. Each color represents a load/unload cycle. a: void ratio (e) versus vertical effective stress (σ'_v) b: void ratio-versus P wave velocity (V_p); c: degree of gas saturation (S_g) versus σ'_v and d: S_g versus V_p . The grey line in (a) represents the reference consolidation test. 270

Appendix 1 - Figure 3: Results for test#4 with 2 load/unload cycles. Each color represents a load/unload cycle. a: void ratio (e) versus vertical effective stress (σ'_v) b: void ratio-versus P wave velocity (V_p); c: degree of gas saturation (S_g) versus σ'_v and d: S_g versus V_p . The grey line in (a) represents the reference consolidation test. 271

Appendix 1 - Figure 4: Results for test#6 with 3 load/unload cycles. Each color represents a load/unload cycle. a: void ratio (e) versus vertical effective stress (σ'_v) b: void ratio-versus P wave velocity (V_p); c: degree of gas saturation (S_g) versus σ'_v and d: S_g versus V_p . The grey line in (a) represents the reference consolidation test. 272

Appendix 1 - Figure 5: Results for test#7 with 3 load/unload cycles. Each color represents a load/unload cycle. a: void ratio (e) versus vertical effective stress (σ'_v) b: void ratio-versus P wave velocity (V_p); c: degree of gas saturation (S_g) versus σ'_v and d: S_g versus V_p . The grey line in (a) represents the reference consolidation test. 273

Appendix 1 - Figure 6: Results for test#9 with 3 load/unload cycles. Each color represents a load/unload cycle. a: void ratio (e) versus vertical effective stress (σ'_v) b: void ratio-versus P wave velocity (V_p); c: degree of gas saturation (S_g) versus σ'_v and d: S_g versus V_p . The grey line in (a) represents the reference consolidation test. The fourth load/unload cycle is not displayed as exsolution was completed under a constant vertical stress and the results are not relevant in this study. As the sample broke into two separate parts during the first exsolution, the degree of gas saturation was calculated once the two halves were in contact again (black arrow). 274

List of tables

Chapter 2

Table 2-1: Sample details and type of analysis and measurements they underwent 73

Table 2-2: Sensors and important structural elements characteristics such as measure range and precision or limit pressure. 79

Chapter 3

Table 3-1: Details on sample preparation for oedometer tests and results. 98

Table 3-2: Results of hydraulic conductivity calculations based on sonic-log data and oedometer tests on natural mud. NTG is the net to gross, being the ratio between total sand thickness over total interval thickness. The mean void ratio is calculated from the sonic log (equation (3)) and K_h (horizontal hydraulic conductivity) and K_v (vertical hydraulic conductivity) result respectively from arithmetic and harmonic average of calculated hydraulic conductivities on individual sand or shale layers using equation (5). The 1D-sedimentation model gives a range of void ratio for each stratigraphic interval, corresponding to hydraulic conductivity ranges on oedometer test results obtained for different sand fraction content (Table 3-1). Measured and calculated K_s are in the same ranges of magnitude. 101

Chapter 4

Table 4-1: Synthesis of the main sample properties. Further details are given in Figure 3.13. 153

Table 4-2: Testing program with details on the number of loading/unloading cycles per test, the applied maximal effective stress at each stage, the initial gas pressure, the magnitude of depressurization for each exsolution. 158

Table 4-3: Summary of observations related to fracture networks created during gas exsolution. Each fracture network was classified into three size categories (1: length > 1 cm; 2: 0.5 cm < length < 1 cm; 3: length < 0.5 cm) and three fracture number groups (1: more than 10 fractures; 2: less than 10 fractures; 3: no fractures). Vertical scale is equivalent to the horizontal one on the pictures and their corresponding interpretations. 167

Chapter 5

Table 5-1: Parameters used for the different diffusion simulations presented in the chapter. Several parameters were modified to fit observations and regional background over the different simulations. 192

Table 5-2: Parameters used in the different simulations completed during the study. The varying parameters are the sole sediment viscosity and the fracture length. 200

Table 5-3: Synthesis of the main results obtained from the different simulations computed in this study. The initiation time of gassy-mud ascent, the time needed to reach the seafloor, the maximum velocity and the final diameter of the gassy-mud column are displayed for the two code versions. 205

List of equations

<i>Equation (1)</i>	76
<i>Equation (2)</i>	76
<i>Equation (3)</i>	76
<i>Equation (4)</i>	77
<i>Equation (5)</i>	77
<i>Equation (6)</i>	81
<i>Equation (7)</i>	81
<i>Equation (8)</i>	81
<i>Equation (9)</i>	81
<i>Equation (10)</i>	82
<i>Equation (11)</i>	84
<i>Equation (12)</i>	84
<i>Equation (13)</i>	85
<i>Equation (14)</i>	113
<i>Equation (15)</i>	119
<i>Equation (16)</i>	119
<i>Equation (17)</i>	189
<i>Equation (18)</i>	190

Chapter 1: Scientific Background

Abstract

Mud volcanoes (MVs) are the surface expression of sediment remobilization and focused fluid flow. They have been known for centuries and have been densely studied over the last five decades. The close relationship between hydrocarbon (HC) and MVs represents a great opportunity for Oil & Gas operators, as they consider MVs as indicators of HC accumulations and overpressured conditions. Moreover, MVs are active gas venting sites and therefore participate in the global budget of greenhouse gas emissions; their contribution needs to be quantified for us to understand the human impact on global warming. Another critical aspect of mud volcanism is geohazard assessment. MV eruptions are closely associated with tectonic activity and earthquakes and the Lusi catastrophe demonstrates the need to consider mud volcanism as a serious and potential geohazard for populations and infrastructures.

After introducing the main issues associated with MVs and proving the necessity to understand them, this chapter presents a state-of-the-art on MV scientific studies and research and related issues. The main notions and definitions of mud volcanoes are presented as well as their distribution and geological settings. The mud composition, the origin of the different constitutive elements and MV morphology, typical structures and geometrical elements are also developed. Finally, the possible mechanisms for mud generation and sediment remobilization are listed and described.

Chapitre 1: Contexte Scientifique

Résumé

Les volcans de boue sont une des expressions en surface possible d'une remobilisation des sédiments en profondeur ou d'une circulation de fluides. Ils sont connus depuis des siècles mais ont été surtout étudiés durant les cinquante dernières années. Leur lien étroit avec les hydrocarbures en fait un objet d'étude d'intérêt majeur pour les compagnies pétrolières qui voient les volcans de boues comme des indicateurs d'accumulations d'hydrocarbures et de zones en surpression. De plus, les volcans de boue étant des zones de dégazage naturel, ils participent donc au budget global d'émission de gaz à effets de serre. De ce fait, leur contribution doit être quantifiée si l'on veut comprendre l'impact anthropique sur le changement climatique. Enfin, les volcans de boue représentent un risque et un danger direct potentiel pour les hommes et les infrastructures (Cf catastrophe de Lusi, Indonésie), et doivent être pris en compte lors des études en gestion du risque. Par ailleurs, leur activité est étroitement liée aux séismes et à l'activité tectonique.

Ce chapitre, après avoir introduit les principaux problèmes liés aux volcans de boue et montrant la nécessité de la compréhension de ces objets, propose un état de l'art des recherches et des études scientifiques sur les volcans de boue et les sujets directement en lien. Les notions de base et les définitions essentielles liées aux volcans de boue sont présentées, et la distribution géographique de ces structures est détaillée. Le chapitre détaille également la composition de la boue, l'origine des différents éléments constitutifs ainsi que la morphologie des volcans de boue et les principales structures associées. Enfin, les mécanismes possibles pour la génération de la boue et la remobilisation des sédiments sont listés et détaillés.

1. Introduction (English)

Mud volcanoes (MVs) are the surface expression of sediment remobilization and focused fluid flow, and are one example of natural hydrocarbon seepage structures and natural gas venting systems (Kopf, 2002; Judd & Hovland, 2007; Deville, 2009; Mazzini & Etiope, 2017). MVs were first mentioned by Pliny the Elder in his “Naturalis Historia”, during the 1st century AD (Judd & Hovland, 2007; Niemann & Boetius, 2014). In the late 1800s and early 1900s, research focused on mud volcanoes due to their close connection to oil fields (Kopf, 2002; Judd & Hovland, 2007; Mazzini & Etiope, 2017). Research on MVs has regularly intensified over the last decades, notably due to the improvement of offshore imaging techniques, such as 3D-seismic or multi-beam bathymetry leading to an increased number of known structures, and the possibility to study offshore structures directly through submersible investigations (Kopf, 2002; Stewart & Davies, 2006; Judd & Hovland, 2007; Deville, 2009; Mazzini & Etiope, 2017). Moreover, the ongoing Lusi catastrophe (Sidorajo, Indonesia) shows the natural hazard that mud volcanism represents for populations and infrastructures (Tingay *et al.*, 2008, 2015, 2017; Mazzini *et al.*, 2012).

The close relationship between hydrocarbon (HC) and MVs represents a great opportunity for Oil & Gas operators, as they consider MVs as indicators of HC accumulations and overpressured conditions (Hedberg, 1974; Guliyev *et al.*, 2001; Dimitrov, 2002; Deville, 2009; Mazzini & Etiope, 2017). Natural HC seepages have long been used as indicators of economically interesting drilling areas (Hedberg, 1974; Judd & Hovland, 2007); additionally, MVs were proved to bring to the surface sediments, liquids and gases from several kilometers deep, thereby acting as a window toward deep intervals (Hedberg, 1974; Kopf, 2002; Deville, 2009). In frontier exploration areas, where no wells have already been drilled, MVs represent a precious exploration tool: they provide indications on the stratigraphic succession at depth (solid extruded material) and on the type of fluids trapped acting as a cost-free exploration well (Zitter, 2004; Deville, 2009). Moreover, understanding the relationship between MVs and overpressured intervals/areas (hydraulic connection with HC reservoirs or isolation) will reduce the operational and economical risks when drilling (Stewart & Davies, 2006; Javanshir *et al.*, 2015). Finally, MVs could help in assessing the maturation of a petroleum system. Indeed, the analysis of several wells in the South Caspian Basin has showed a correlation between HC accumulation and overpressure build-up and increasing MV activity (Yusifov & Rabinowitz, 2004).

Mud volcanoes are active hydrocarbon seeping and gas venting sites and therefore participate in the global budget of greenhouse gas emissions (Kopf, 2002; Etiope & Milkov, 2004; Deville, 2009; Etiope *et al.*, 2009; Mazzini & Etiope, 2017). To understand the human impact on global climate changes, it is paramount to quantify the natural sources of greenhouse gases in the atmosphere (Zitter, 2004). Several authors have attempted to estimate the volume of methane emitted at MVs (Dimitrov, 2002; Etiope & Milkov, 2004; Deville, 2009). Notably, Etiope & Milkov (2004) estimated that MV emissions accounted for 3-

5 % of natural methane sources, themselves representing only 32% of the global budget (68% being related to anthropogenic sources). MVs emit between 6 and 9 Mt/y of methane into the atmosphere (Etiope & Milkov, 2004; Deville, 2009; Etiope *et al.*, 2009). These numbers probably greatly underestimate the true methane budget of MVs in the atmosphere because they only consider terrestrial and shallow water MVs due to potential microbial processes affecting gases emitted in deep water (Etiope & Milkov, 2004; Etiope *et al.*, 2009). The short-lived nature of onshore MVs due to their tendency to erosion, the connection of offshore MVs to other systems like gas hydrate accumulations, the individual differences between MVs as well as their cyclic activity (regular seepage versus massive eruptions) make global volumetric estimations hard to tackle (Henry *et al.*, 1996; Milkov, 2000; Kopf, 2002; Zitter, 2004; Deville, 2009; Kopf *et al.*, 2010; Mazzini & Etiope, 2017). Moreover, with technical improvements and as deep offshore exploration and research evolve, more and more MVs are discovered every year and new estimates should be even higher (Kopf, 2002; Stewart & Davies, 2006; Judd & Hovland, 2007; Deville, 2009; Kirkham, 2015; Dupuis, 2017).

Another critical aspect of mud volcanism is whether mud volcano eruptions are indicators of high earthquake and tectonic activity. Many authors highlight the close relationship between mud volcanoes and tectonically active structures such as faults or anticlines (Fowler *et al.*, 2000; Yusifov & Rabinowitz, 2004; Zitter, 2004; Stewart & Davies, 2006; Bonini, 2009b; Roberts *et al.*, 2010; Menapace *et al.*, 2017). In particular, Fowler *et al.* (2000) related mud volcano emplacement through a fold in the South Caspian Basin to the main phase of fold growth. Zitter (2004) shows that distribution of MVs along the Eastern Mediterranean area is related to the presence of faults. Bonini (2009b) shows a structural control of mud volcano emplacement through the presence of faults in the Apennines (Italy) and demonstrates that their activity is controlled by fault reactivation. In another paper, he shows that mud volcano shape and organization of venting sites indicate stress orientation in the studied area (Bonini, 2012). Deville (2009) and Menapace *et al.* (2017) linked the pulses in mud volcano activity to earthquakes and seismicity in Trinidad and the Eastern Mediterranean. However, the presence of MVs was proposed as an explanation for the South Caspian Basin's lack of earthquakes, through regular tectonic stress relief (Guliev & Panahi, 2004). Finally, the triggering of the Lusi MV is explained by some authors as the consequence of a major earthquake, although this is still a matter of discussion (Mazzini *et al.*, 2007, 2012). Therefore, MVs could be either considered as a way to understand earthquake generation and tectonic processes or as a source of hazard and damage.

The Lusi catastrophe shows the need to consider mud volcanism as a serious and potential geohazard for populations and infrastructures. Its trigger is debated between the direct impact of an earthquake and human responsibility through drilling misconducts (Mazzini *et al.*, 2007, 2012; Davies *et al.*, 2008; Tingay *et al.*, 2008, 2015, 2017). The eruption started on 29 May 2006, when mud and gases began to flow at the surface near the Sidoarjo locality (East Java, Indonesia), 2833 m from an exploration well (BJP1) and two days after the Yogyakarta earthquake ($M_w = 6.3$) struck 254 km from the Lusi location (Mazzini *et al.*, 2007; Tingay *et al.*, 2008). The Lusi mud volcano has been continuously active for 13 years and nearly 40,000 people have

been displaced (Tingay *et al.*, 2015). Both potential triggers stress the importance of understanding the dynamics and initiation of MVs. Drilling operations need to assess the risks and geohazards caused by MVs (Yusifov & Rabinowitz, 2004; Roberts *et al.*, 2010; Unterseh & Contet, 2015). Drilling in overpressured areas near a MV may cause blowouts and sediment destabilization as in the case of Lusi (Yusifov & Rabinowitz, 2004; Deville, 2009; Tingay *et al.*, 2017). Moreover, the presence of a MV exposes offshore drilling infrastructures to potential giant mudflows and landslides and associated tsunamis (Judd & Hovland, 2007; Deville, 2009; Contet & Unterseh, 2015; Gautherot *et al.*, 2015; Unterseh & Contet, 2015).

Recent satellite images from Mars's surface have confirmed the presence of structures morphologically similar to terrestrial MVs (Skinner & Tanaka, 2007; Skinner & Mazzini, 2009; Oehler & Allen, 2010; Pondrelli *et al.*, 2011; Komar, 2019). If their MV nature is confirmed, the understanding of their dynamics, evolution and formation on Earth could help understanding the methane and water cycle on Mars. A variation in atmospheric methane concentration should imply the presence of active methane seepage on the planet (Mumma *et al.*, 2009). Besides, as MVs serve as windows to deep structures and processes, they could reveal precious information on methane occurrence and the possibility of life on Mars (Mazzini & Etiope, 2017).

All recent research studies dealing with MVs have attempted to assess one or more of the above listed issues. Before reaching the main subject of the present work, some general concepts and semantics about mud volcanism and related processes need to be introduced. Therefore, hereafter, a review of research on MVs is proposed, in order to explore the extent of present knowledge and the issues that remain to be addressed.

1. Introduction (Français)

Les volcans de boue (VB) sont l'expression de surface d'une remobilisation de sédiments et d'une circulation de fluides focalisée, et représente aussi un exemple de structures en lien avec les suintements d'hydrocarbures et les dégazages naturels (Kopf, 2002; Judd & Hovland, 2007; Deville, 2009; Mazzini & Etiope, 2017). Les VB sont pour la première fois mentionnés au 1er siècle après J.C. dans l'encyclopédie « Naturalis Historia » de Pline l'Ancien (Judd & Hovland, 2007; Niemann & Boetius, 2014). Entre la fin du XIX^{ème} siècle et le début du XX^{ème} siècle, la recherche s'est concentrée sur les VB pour leur étroite connexion avec les champs de pétrole (Kopf, 2002; Judd & Hovland, 2007; Mazzini & Etiope, 2017). Ces recherches se sont peu à peu intensifiées durant les dernières décennies, en partie grâce à l'amélioration des techniques d'imagerie offshore, comme la sismique 3D ou la bathymétrie multifaisceaux, qui a permis la découverte d'un grand nombre de nouveaux volcans, ainsi que la possibilité d'étudier directement les structures offshore par l'emploi d'engins submersibles (Kopf, 2002; Stewart & Davies, 2006; Judd & Hovland, 2007; Deville, 2009; Mazzini & Etiope, 2017). De plus, la catastrophe de Lusi (Sidoarjo, Indonésie), qui est encore en cours, a montré le risque naturel que représente le volcanisme de boue pour les populations et les infrastructures (Tingay *et al.*, 2008, 2015, 2017; Mazzini *et al.*, 2012).

Le lien étroit entre les hydrocarbures (HC) et les VB représente une réelle opportunité pour les compagnies pétrolières. Ils voient en effet les VB comme des indicateurs d'accumulations d'HC et de zones en surpression (Hedberg, 1974; Guliyev *et al.*, 2001; Dimitrov, 2002; Deville, 2009; Mazzini & Etiope, 2017). Les suintements naturels d'HC sont utilisés depuis longtemps comme des marqueurs d'accumulations d'HC à fort potentiel économique (Hedberg, 1974; Judd & Hovland, 2007); de plus, les VB ont montré leur efficacité à remonter des sédiments, des liquides et des gaz issus de plusieurs kilomètres de profondeur, et peuvent donc être vu comme une fenêtre vers les successions sédimentaires profondes (Hedberg, 1974; Kopf, 2002; Deville, 2009). Dans l'exploration de nouvelles zones, où aucun puits n'a encore été foré, les VB peuvent servir d'outils pour l'exploration : ils donnent des indications sur la succession stratigraphique sous-jacente (matériel solide expulsé en surface) ainsi que sur le type de fluides piégés, servant donc de puits d'exploration gratuit (Zitter, 2004; Deville, 2009). En outre, la compréhension des relations entre les VB et les zones en surpression (connexion ou isolation entre réservoirs d'HC) permet de réduire les risques opérationnels et économiques durant le forage (Stewart & Davies, 2006; Javanshir *et al.*, 2015). Enfin, les VB pourraient permettre d'évaluer la maturité d'un système pétrolier. En effet, l'analyse de plusieurs puits dans le Bassin sud caspien a montré une étroite corrélation des accumulations d'HC et des zones en surpression avec l'activité des VB (Yusifov & Rabinowitz, 2004).

Les volcans de boue sont des zones où les dégazages naturels sont fréquents et abondants et participent de ce fait au budget global des émissions de gaz à effet de serre (Kopf, 2002; Etiope & Milkov, 2004; Deville, 2009; Etiope *et al.*, 2009; Mazzini & Etiope, 2017). Afin de comprendre l'impact des

émission anthropiques sur les changements climatiques mondiaux, la quantification des émissions venant de sources naturelles de gaz à effet de serre dans l'atmosphère est indispensable (Zitter, 2004). Plusieurs auteurs ont déjà tenté des estimations du volume de méthane émis aux VB (Dimitrov, 2002; Etiope & Milkov, 2004; Deville, 2009). Etiope & Milkov (2004) ont notamment estimé que les émissions liées aux VB représentent 3 à 5% des sources naturelles de méthane, ces sources naturelles comptant elles-mêmes pour 32% du budget global (68% des émissions seraient d'origine anthropique). Les VB rejettent entre 6 et 9 Mt/an de méthane dans l'atmosphère (Etiope & Milkov, 2004; Deville, 2009; Etiope *et al.*, 2009). Cependant, ces chiffres sous-estiment certainement grandement la quantité de méthane réellement émise par ces structures, car ces études ne considèrent que les volcans terrestres et ceux situés en eau peu profonde à cause des processus microbiens qui peuvent affecter les gaz émis en milieu océanique profond (Etiope & Milkov, 2004; Etiope *et al.*, 2009). De plus, la nature éphémère des VB terrestres liée à leur sensibilité aux processus d'érosion, la connexion des structures sous-marines avec d'autres systèmes comme les accumulations d'hydrates de gaz, le fait que tous les volcans ne présentent pas la même activité cyclique (suintements réguliers opposés aux éruptions violentes) rendent une estimation des volumes des gaz émis à l'échelle globale ardue (Henry *et al.*, 1996; Milkov, 2000; Kopf, 2002; Zitter, 2004; Deville, 2009; Kopf *et al.*, 2010; Mazzini & Etiope, 2017). Enfin, avec les constantes améliorations techniques et technologiques, de plus en plus de VB sont découverts chaque année. De ce fait, de nouvelles estimations devraient être plus importantes que les anciennes (Kopf, 2002; Stewart & Davies, 2006; Judd & Hovland, 2007; Deville, 2009; Kirkham, 2015; Dupuis, 2017).

Un autre aspect important du volcanisme de boue est de comprendre si leurs éruptions peuvent être des indicateurs de forts séismes et d'une activité tectonique. Beaucoup d'auteurs ont souligné le lien étroit qui existe entre les VB et des structures tectoniquement actives comme des failles ou des anticlinaux (Fowler *et al.*, 2000; Yusifov & Rabinowitz, 2004; Zitter, 2004; Stewart & Davies, 2006; Bonini, 2009b; Roberts *et al.*, 2010; Menapace *et al.*, 2017). Fowler *et al.* (2000) a en particulier montré que l'apparition de différents VB situés sur un pli en Mer Caspienne est directement liée à la formation progressive du pli. Zitter (2004) a montré que la répartition des VB en Mer Méditerranée orientale peut s'expliquer par la présence de failles sous-jacentes. Bonini (2009b) a également montré que la mise en place des VB dans les Apennins (Italie) est contrôlée par la présence de failles, et montre que leur activité est contrôlée par la réactivation périodique de ces mêmes failles. Il montre dans un autre article que la forme des VB ainsi que la distribution des sites de dégazage à leur surface indiquent l'orientation des contraintes dans la zone du volcan (Bonini, 2012). Deville (2009) et Menapace *et al.* (2017) ont tous deux liés les pics d'activité de certaines structures avec la sismicité, respectivement à la Trinité et Tobago et en Méditerranée orientale. Néanmoins, la présence de VB dans le bassin sud Capsien est une raison possible pour l'absence de séisme dans la région : ils permettraient de relâcher régulièrement les contraintes tectoniques (Mazzini *et al.*, 2007, 2012). Par conséquent, les VB peuvent être à la fois considérés comme un moyen de mieux comprendre le déclenchement des séismes et les mécanismes tectoniques, ou comme un risque supplémentaire.

La catastrophe de Lusi montre la nécessité de considérer le volcanisme de boue comme un risque géologique potentiel et sérieux pour les populations et les infrastructures. Son déclenchement est encore débattu : un séisme déclenchant est avancé face à une responsabilité humaine au travers de mauvaises procédures de forage (Mazzini *et al.*, 2007, 2012; Davies *et al.*, 2008; Tingay *et al.*, 2008, 2015, 2017). L'éruption a commencé le 29 mai 2006, quand un mélange de boue et de gaz a commencé à être expulsé du sous-sol près de la ville de Sidoarjo (Java, Indonésie), à 2833 m d'un puits d'exploration (BJP1) en pleine activité de forage, et deux jours après le séisme de Yogyakarta ($M_w = 6.3$) dont l'épicentre se situe à 254 km du lieu de la catastrophe (Mazzini *et al.*, 2007; Tingay *et al.*, 2008). Le VB de Lusi est en activité depuis 13 ans et a nécessité l'évacuation de pas loin de 40 000 personnes (Tingay *et al.*, 2015). La controverse sur le déclencheur de la catastrophe montre la nécessité de comprendre la dynamique et l'initiation des VB. Les opérations de forage doivent prendre en compte les risques que représentent les VB (Yusifov & Rabinowitz, 2004; Roberts *et al.*, 2010; Unterseh & Contet, 2015). Les activités de forage dans des zones en surpression proche des VB peuvent provoquer des « blowouts » et des instabilités sédimentaires comme dans le cas de Lusi (Yusifov & Rabinowitz, 2004; Deville, 2009; Tingay *et al.*, 2017). De plus, la présence de VB à proximité d'opérations de forage offshore expose les infrastructures au risque de coulées de boue et de glissements de terrains sous-marins et aux potentiels tsunamis qui peuvent en découler (Judd & Hovland, 2007; Deville, 2009; Contet & Unterseh, 2015; Gautherot *et al.*, 2015; Unterseh & Contet, 2015).

Des images satellites récentes de la surface de Mars ont confirmé la présence de structures très similaires en terme de morphologie aux VB terrestres (Skinner & Tanaka, 2007; Skinner & Mazzini, 2009; Oehler & Allen, 2010; Pondrelli *et al.*, 2011; Komar, 2019). Si leur nature de volcan de boue est confirmée, la compréhension de leur dynamique, de leur évolution et de leur évolution sur Terre pourrait permettre de comprendre les cycles du méthane et de l'eau sur Mars. La variation de la concentration en méthane dans l'atmosphère martienne devrait normalement impliquer la présence de structures d'échappements de méthane sur la planète (Mumma *et al.*, 2009). De plus, comme les VB servent de fenêtre vers les structures et processus profonds, ils pourraient révéler de précieuses informations sur la présence de méthane et d'eau en profondeur, ainsi que sur la possibilité de vie sur Mars (Mazzini & Etiope, 2017).

Toutes les recherches récentes traitant des VB ont essayé de répondre à une ou plusieurs des questions et des problèmes listés plus haut. Avant d'entrer dans le cœur du sujet du travail présenté dans cette thèse, des concepts généraux et du vocabulaire sur le volcanisme de boue et les processus en lien doivent être introduits. Par conséquent, un état de l'art des recherches sur les VB est proposé par la suite, afin de visualiser l'étendue de l'état des connaissances actuelles sur le sujet et ce qui doit encore être traité.

2. Significance of mud volcanism

2.1. Mud volcano definition and lexicon

When sediments lose strength during burial through complex interplay of permeability, deformation and stress, their mobilization becomes possible through a variety of processes (Maltman & Bolton, 2003; Morley *et al.*, 2017). Processes differ with depth and pressure conditions, and loads responsible for the mobilization can be external, internal or hydraulic (Maltman & Bolton, 2003). Sediments may retain some residual strength and still reach large displacement through shearing under critical states conditions (detachment levels and mobile shales; Maltman & Bolton, 2003; Morley *et al.*, 2017) but they may also start behaving like fluids through liquefaction (load is sustained entirely by fluids) or through fluidization (grains become buoyant through the rapid input and circulation of external fluids) (Maltman & Bolton, 2003; Morley *et al.*, 2017).

A mud volcano (MV) is the surface or seafloor expression of a subsurface transfer of fluidized clayey sediments (Dimitrov, 2002; Kopf, 2002; Deville, 2009). It is expressed as a topographic structure, varying in size and shape, resulting from the natural seepage of a mix of liquids, gas and fine-grained sediments (Figure 1.1a,b; Dimitrov, 2002; Kopf, 2002; Judd & Hovland, 2007). This focused fluid flow crosses through the sedimentary column like any piercement structure (diapirs, dome, chimneys, pipes) and reaches the surface or the seafloor where the *mélange* is extruded (Dimitrov, 2002; Kopf, 2002; Kirkham, 2015; Mazzini & Etiope, 2017). A MV is a major venting site, and acts as a fluid outlet, allowing degassing and dewatering of deep stratigraphic units (Osborne & Swarbrick, 1997; Milkov, 2000; Deville, 2009; Kirkham, 2015).

MVs were named accordingly because of the important geometrical similarities they have with igneous volcanoes (Kopf, 2002; Judd & Hovland, 2007), but that is where the similarity stops. The processes related to igneous volcanoes (high temperature leading to rock fusion notably) are completely different from the cold geological and sedimentological processes controlling MVs (Kopf, 2002; Deville, 2009; Kirkham, 2015). Thus, the term MV is often used in a purely descriptive way, regardless of geological processes responsible for the observed structures (Dimitrov, 2002; Mazzini & Etiope, 2017). This could lead to confusions between mud volcanism and geothermal structures for instance (Mazzini & Etiope, 2017). Besides, similar features formed essentially by sand should not be confounded with MVs as they arise from sediment remobilization processes and are composed from materials having different properties (Ross *et al.*, 2011; Capaccioni *et al.*, 2017) but may be related to one another as described in Turkmenistan by Oppo & Capozzi (2016). Mud volcanism can be defined as the array of physical and sedimentological processes leading to this extrusion of clayey-material forming the mud volcano (Zitter, 2004; Deville, 2009). The complete three-dimensional architecture with all the features composing the plumbing system as well as the surface part of the MV is often related as the MV system (Figure 1.4; Stewart & Davies, 2006; Roberts *et al.*, 2010).

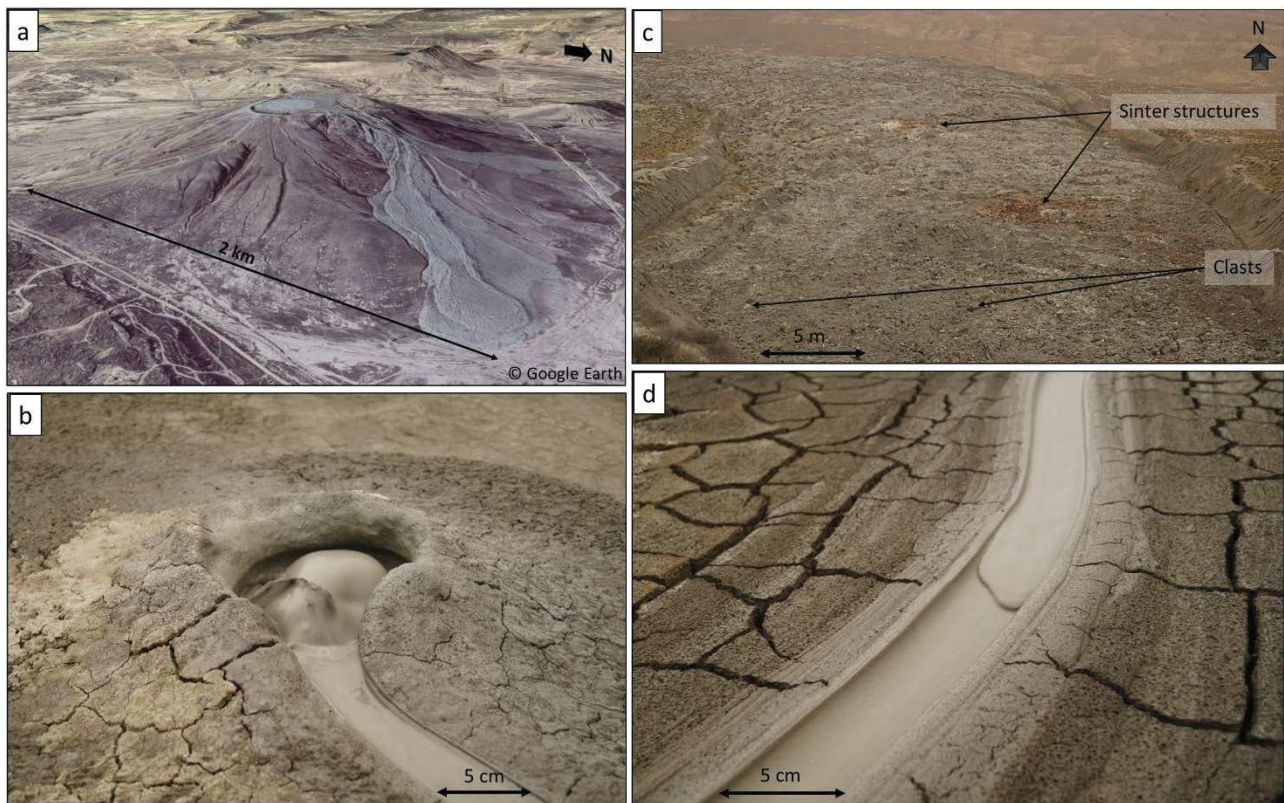


Figure 1.1: *a: Google Earth 2018 3D view of the Bozdag Guzdek mud volcano (Azerbaijan) with a vertical exaggeration of 3. This mud volcano has a basal diameter of 2 km, its crater being 500 m large and oval. Several km-long mudflows are visible on its northern flank. b: gryphon pictured in May 2017 at the top of the Sareboga seeping site (Azerbaijan). It shows the cm to m scale seeping sites that can be found at the top of active MVs during their dormant phase. It also displays the different phase composing the mud: fine-grained sediments, water and gas. c-d: mud expelled from onshore MVs in Azerbaijan. c: northern highly viscous and dry mudflow from the Koturdag MV (Azerbaijan, May 2017). It carries among its fine-grained matrix, m-scale to cm-scale rock clasts. Sinter structures (orange) correspond to points where gaseous methane was emitted and ignited spontaneously, heating the surrounding clay minerals. d: highly fluid mudflow emitted from the gryphon pictured in b. The mud is saturated with water and it behaves like a fluid. Mud flowed along the natural slope for 100 meters at least.*

The extruded mud is a mix of three or four different phases: gas, water, solid particles of various sizes (mainly clayey sediments) and in some cases oil (Figure 1.1c,d; Kopf, 2002; Zitter, 2004; Etiope *et al.*, 2009; Dupuis, 2017). This mélange is called mud breccia (Figure 1.1c; Cita, 1981; Kopf, 2002; Mazzini & Etiope, 2017). Etiope & Martinelli (2009) state that in order to consider such a structure as being a MV, it should expel gaseous methane. However, Bonini (2009) defends the possibility of forming MVs from mainly carbon dioxide emissions.

Moreover, a cyclicity of MV activity was observed on different places and at different time and space scales (Kopf, 2002; Deville & Guerlais, 2009; Antonielli *et al.*, 2014; Mazzini & Etiope, 2017; Menapace *et al.*, 2017). MVs alternate between long quiescent phases and short episodic violent eruptions (Zitter, 2004; Deville & Guerlais, 2009; Antonielli *et al.*, 2014). The eruptions are short and expel with a high flow rate a great volume of mud, angular rock clasts and gas that can sometimes ignite spontaneously forming sinter structures (Figure 1.1c; Kopf, 2002; Deville, 2009; Mazzini & Etiope, 2017). Kopf (2002) and Deville (2009) noted a medium frequency (years to tens of years) cyclic trend for main eruptions on several MVs in Trinidad and Azerbaijan. The cycle duration depends on the studied MV (Kopf, 2002; Deville & Guerlais, 2009). During quiescent phases, fluids are expelled continuously more or less vigorously at semi-permanent seeping sites

(gryphons, mud lakes; Deville, 2009; Antonielli *et al.*, 2014; Mazzini & Etiope, 2017), but Deville & Guerlais (2009) noted a high-frequency activity at these sites in Trinidad, with cold pulses separated by minutes. During these phases, representing up to 95% of a MV life, mainly water, gas and very fine and rounded particles are expelled (Figure 1.1d; Kopf, 2002). Offshore, thick carbonate crusts and biologic communities (bacterial mats, shell clusters) develop around venting sites (Zitter, 2004; Dupré *et al.*, 2008) as hemipelagic sediments covers the quiescent MV (Kopf, 2002; Deville, 2009). Therefore, offshore, the low frequency (thousands of years) cyclicity of the mud volcano activity can be recorded by measuring the thickness and dating the hemipelagic sediments deposited between each main active phase (Kopf, 2002; Zitter, 2004; Stewart & Davies, 2006; Deville, 2009). This is not possible onshore as no sediments are deposited during dormant phases of the MVs, but instead, they get eroded making difficult to differentiate and date the different active episodes (Kopf, 2002; Roberts, 2011). Besides, it has been demonstrated in several places that mud volcano activity may increase after earthquakes producing sufficient energy at the mud volcano location (Bonini, 2009b; Menapace *et al.*, 2017).

2.2. Occurrence and geological setting for mud volcanism

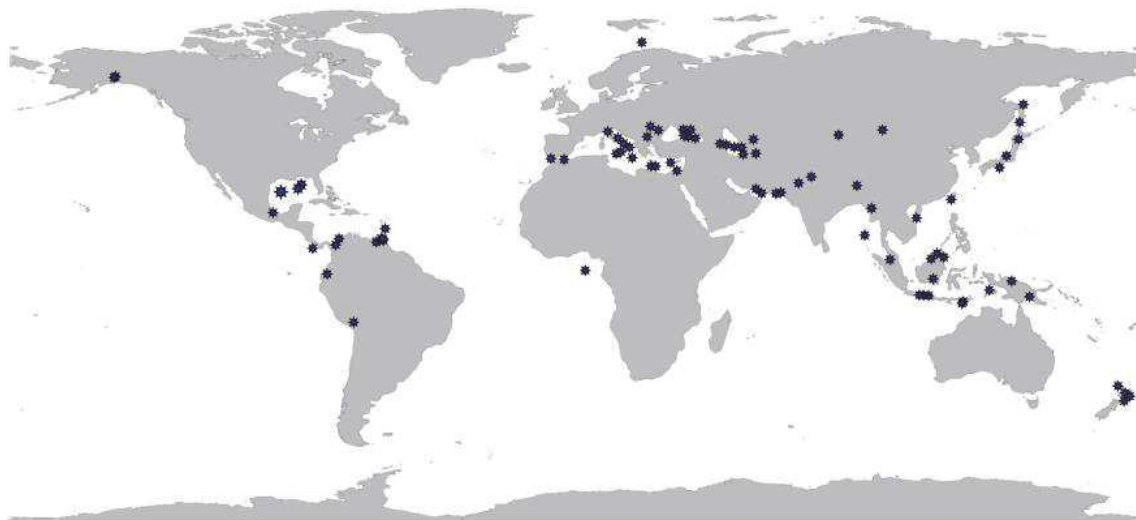


Figure 1.2: global distribution map of known mud volcanoes offshore and onshore (from Mazzini & Etiope, 2017).

Mud volcanism is a worldwide phenomenon, with several thousands of identified or inferred structures onshore and offshore (Figure 1.2; Milkov, 2000; Dimitrov, 2002; Kopf, 2002; Mazzini & Etiope, 2017). The most recent reviews list 652 onshore mud volcanoes in at least 26 countries and estimate the number of offshore structures between 1000-100000 (Milkov, 2000; Dimitrov, 2002; Mazzini & Etiope, 2017). One hundred and seventy-eight of the known mud volcanoes are onshore Azerbaijan (Javanshir *et al.*, 2015; Mazzini & Etiope, 2017). The number of offshore structures grows as more and more mud volcanoes are being discovered with the use of more advanced techniques for submarine exploration (Dimitrov, 2002; Zitter, 2004). No outcropping examples of onshore fossil mud volcanoes are known due to the poor consolidation of the structures exposed to meteoric phenomenon (Kopf, 2002). However, Clari *et al.* (2007) demonstrated the presence of an outcropping fossilized Miocene offshore MV, with the

presence of mud breccia, covered by hemipelagic sediments during quiescent stages. This highlights the difference between onshore conditions that does not allow the preservation of MV structures, while offshore environments allows burying MVs below hemipelagic sediments, thus preserving the structure. Other examples of buried and preserved offshore MVs are shown by Fowler *et al.* (2000) and Kirkham *et al.* (2017b). The area formed by the Mediterranean Sea and the Tethyan belt (from Southern Greece to Makran coast in Pakistan through the Black Sea and the Caspian Sea) has the denser mud volcano distribution (Dimitrov, 2002; Kopf, 2002).

Mud volcanoes are located in different geological contexts. Their density is higher in compressive areas as orogenic systems, foreland basins and accretionary prisms (Kopf, 2002; Zitter, 2004; Stewart & Davies, 2006; Deville, 2009; Praeg *et al.*, 2009; Roberts, 2011; Bonini, 2012; Antonielli *et al.*, 2014; Mazzini & Etiope, 2017). They can be found in passive margins, especially in deltaic contexts (Zitter, 2004; Deville, 2009; Roberts, 2011; Mazzini & Etiope, 2017). Deltas represents zones of active and rapid sedimentation, creating high overpressures (Dugan & Flemings, 2000) and compressive areas through gravity-driven tectonics (Sultan *et al.*, 2007) where their internal structure resemble accretionary prisms. Deltas may also be found on active margins, such as the Baram delta in Borneo, where interaction between gravity-driven tectonics and tectonic compression is possible (Tingay *et al.*, 2005). Some strike-slip provinces also display mud volcanoes (Davies *et al.*, 2008; Roberts, 2011; Dupré *et al.*, 2015) as well as areas with hydrothermal activity and active magmatic provinces (Kopf, 2002; Deville, 2009; Mazzini *et al.*, 2012; Mazzini & Etiope, 2017). Some MVs are closely related to underlying “mud diapirs” as they developed at the crest of such structures (Brown, 1990; Santos Betancor, 2015; Mazzini & Etiope, 2017), but most of them are not (Dimitrov, 2002; Kopf, 2002). The concept of mud diapirs was born from the interpretation of low-quality seismic data in the 80’s and 90’s that showed ascending column of deep shales (Barber *et al.*, 1986; Brown & Westbrook, 1988; Brown, 1990; Limonov *et al.*, 1996), but with the improvement of seismic imaging, many of the inferred mud diapirs were instead mud volcanoes creating imaging issues (Stewart & Davies, 2006). However, recent studies showed the occurrence of ascending clay-masses forming diapiric-like structures and canopies (Morley, 2003; Santos Betancor, 2015; Morley *et al.*, 2017).

Mud volcanoes are often associated with hydrocarbon producing provinces and traps (Dimitrov, 2002; Kopf, 2002; Loncke *et al.*, 2004; Roberts, 2011; Bonini, 2012). For instance, in the South Caspian Basin, mud volcanoes are found only in the area where the Maykop Formation, which is the regional active source rock, is present (Roberts, 2011). Mazzini & Etiope (2017), Loncke *et al.* (2004) as well as Dimitrov (2002) emphasize on the hydraulic connection between mud volcanoes and underlying hydrocarbon-rich fine-grained sediments. High sedimentation rate and rapidly subsiding basins are often associated with mud volcanoes (Kopf, 2002; Brunet *et al.*, 2003; Deville, 2009; Roberts, 2011). More locally, the structures are distributed along anticline axes, strike-slip and normal faults (Zitter, 2004; Bonini, 2009; Roberts, 2011; Bonini, 2012; Santos Betancor, 2015; Mazzini & Etiope, 2017).

2.3. Mud composition and origin of the different constitutive elements

Mud is composed of a mixing of liquids, gas (mainly methane), clayey particles and clasts of host rock with multiple origins (Figure 1.1b,c,d; Kopf, 2002; Deville, 2009; Antonielli *et al.*, 2014; Dupuis, 2017). More than three phases may coexist in the mud in cases where liquid hydrocarbons are present (Figure 1.1b,c,d; Kopf, 2002; Zitter, 2004; Etiope *et al.*, 2009; Mazzini & Etiope, 2017). Several interactions may take place between the different phases depending on the temperature and pressure of the system: notably gas dissolution in water, fluid or gas adsorption on clay or kerogen particles (Brown, 1990; Etiope *et al.*, 2009; Zhang *et al.*, 2013). The different phases composing the mud may have different stratigraphic sources (Deville, 2009; Mazzini & Etiope, 2017), and sources highly depends on the geological context of the volcano (tectonics, stratigraphy, maturity of source rocks; Mazzini & Etiope, 2017). Moreover, among a same sedimentary basin, the sources may differ between closeby MVs, as observed in the South Caspian Basin (SCB; Yusifov & Rabinowitz, 2004; Stewart & Davies, 2006; Dupuis, 2017; Blouin *et al.*, 2019). Depending on the proportion of each phase, the mud properties, in particular its viscosity and its capacity to carry larger solid particles and clasts, will be different (Figure 1.1c,d; Kopf, 2002; Deville, 2009; Mazzini & Etiope, 2017).

The solid phase is composed of a matrix of fine-grained, mainly clay-size to silts, particles (Dupuis, 2017; Blouin *et al.*, 2019). The grains are mainly clay minerals mixed with other minor mineral fractions such as quartz, micas, albite (Zitter, 2004; Deville, 2009; Dupuis, 2017; Blouin *et al.*, 2019). Kerogen maturity, diagenetic markers, or biogenic particles allow identifying the main source of the grains and defining a mud generation zone (Kopf, 2002; Zitter, 2004; Mazzini *et al.*, 2007; Deville, 2009; Dupuis, 2017; Blouin *et al.*, 2019). The mud particles source is most of the time related to a detachment level, like the Messinian salt interval in the Mediterranean Sea (Henry *et al.*, 1996; Kopf, 2002; Zitter, 2004; Kirkham *et al.*, 2017b; Morley *et al.*, 2017), or like a thick under-compacted shale interval (Dimitrov, 2002; Kopf, 2002; Tingay *et al.*, 2015; Morley *et al.*, 2017). The ascending mud is then combined with coarser particles and blocks from the different formations crossed on its way to the surface (Deville, 2009; Dupuis, 2017). Coarser solid particles, named clasts, can reach several meters in diameter (Figure 1.1c). The hydrofracturing on the conduit walls as well as stoping process generates those clasts, explaining the angular shapes that are observed on many clasts (Kopf, 2002; Zitter, 2004; Deville, 2009; Roberts, 2011).

The liquid phases can originate from various sources and may be generated by different mechanisms and reactions (Kopf, 2002; Dupuis, 2017; Mazzini & Etiope, 2017). Indeed, Mazzini & Etiope (2017) defined three main sources for water composing the mud: formation water, marine or fresh, trapped during burial, water resulting from clay dehydration and mineral diagenesis reactions, and meteoric waters. Moreover, sediment compaction, oil generation, clay dehydration and mineral diagenetic reactions can generate autochthonous liquids (Brown, 1990; Henry *et al.*, 1996; Kopf, 2002; Deville, 2009; Mazzini & Etiope, 2017). Exotic liquids can migrate from deeper fluid sources through different pathways such as permeable stratigraphic units, fracture networks or faults (Brown, 1990; Henry *et al.*, 1996; Deville, 2009; Etiope *et al.*, 2009).

al., 2009; Dupuis, 2017; Mazzini & Etiope, 2017), shallow water and oils may mix with deeper fluids when mud is driven upwards and crosses aquifers or HC reservoirs (Deville, 2009) and, at the surface, sea water or meteoric water may contribute in the final liquid phase composition (Henry *et al.*, 1996; Planke *et al.*, 2003; Dupuis, 2017). It is partly highlighted by the analysis of water expelled by mud volcanoes that show varying salinity and isotopic signatures depending on the location of the structure and represents a complex mixing of waters from different stratigraphic levels (Kopf, 2002; Dupuis, 2017; Mazzini & Etiope, 2017). However, many processes can modify the water geochemistry like subaerial oxidation and biological processes, interaction with rocks and other fluids, and also subsurface effects of the temperature and pressure variations (Kopf, 2002; Etiope *et al.*, 2009).

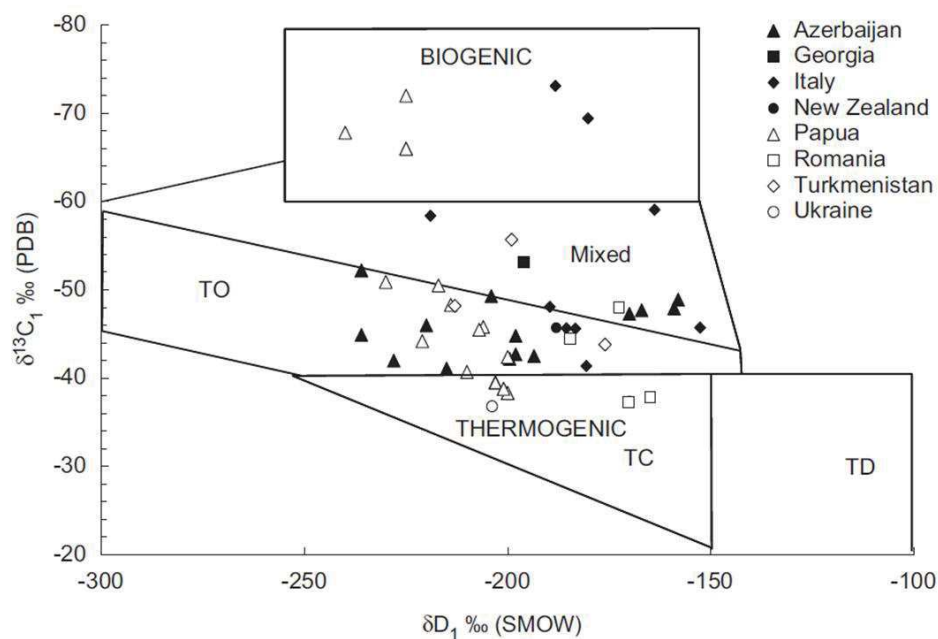


Figure 1.3: Methane carbon and hydrogen isotope diagram for mud volcanoes (from Etiope *et al.*, 2009).

The gaseous phase is mainly composed of methane and other alkanes, but fractions of carbon dioxide and nitrogen were noticed when analyzing the gases expelled at several MVs (Brown, 1990; Kopf, 2002; Deville, 2009; Mazzini & Etiope, 2017). Kopf (2002) estimated that 70-99% of the gas seeping from onshore mud volcanoes is methane. The gases expelled are mainly thermogenic, and more rarely biogenic or from a deep hydrothermal origin (Figure 1.3; Kopf, 2002; Etiope *et al.*, 2009; Mazzini *et al.*, 2012; Prinzhofer & Deville, 2013). Etiope *et al.* (2009) revealed that 76% of the mud volcanoes used in their study (worldwide) emits thermogenic methane only (Figure 1.3). However, methane from secondary sources such as hydrate dissociation or microbial activity may mix with the ascending mud (Henry *et al.*, 1996; Milkov, 2000; Mazzini & Etiope, 2017). Carbon dioxide is the principal gas expelled in a magmatic or hydrothermal context (Deville, 2009; Mazzini *et al.*, 2012) or can be related to shallower carbon dioxide reservoirs as shown by Bonini (2009). Besides, gases expelled at the surface are lighter than the gases produced from the reservoirs due to molecular fractionation (Deville *et al.*, 2003; Etiope *et al.*, 2009; Prinzhofer & Deville, 2013). During gas advection in MV feeder system driven by pressure gradients and contrast in density, a molecular

segregation may arise from differential adsorption on the clay particles of the mud and from differential solubility between the different gaseous molecules (Figure 1.3; Deville *et al.*, 2003; Etiope *et al.*, 2009; Prinzhofer & Deville, 2013). Therefore, during quiescent phase of the MV activity, advection is slow and the ratio of adsorbed gases is higher leading to expulsion of lighter gases, whereas it is often after eruptive phases that heavier gases (C₂ +, two carbons and more) are expelled (Deville *et al.*, 2003). In mud volcanoes from the Nile delta, Prinzhofer & Deville (2013) evidence that different source rocks may generate the gases present in the studied MVs, explaining the different chemical composition of the tested gases.

2.4. Morphology and architecture of a mud volcano system

Stewart & Davies (2006) and Kirkham (2015) define the 3D mud volcano system as being divided between the source domain, the intrusive domain, the extrusive domain and potentially the roof domain when the structure was buried offshore (Figure 1.4). Specific physical and sedimentological processes depending on pressure and temperature regimes as well as stress field, lithology and fluid nature and behavior may characterize each domain and will be developed for each zone in the following subsections (Deville, 2009).

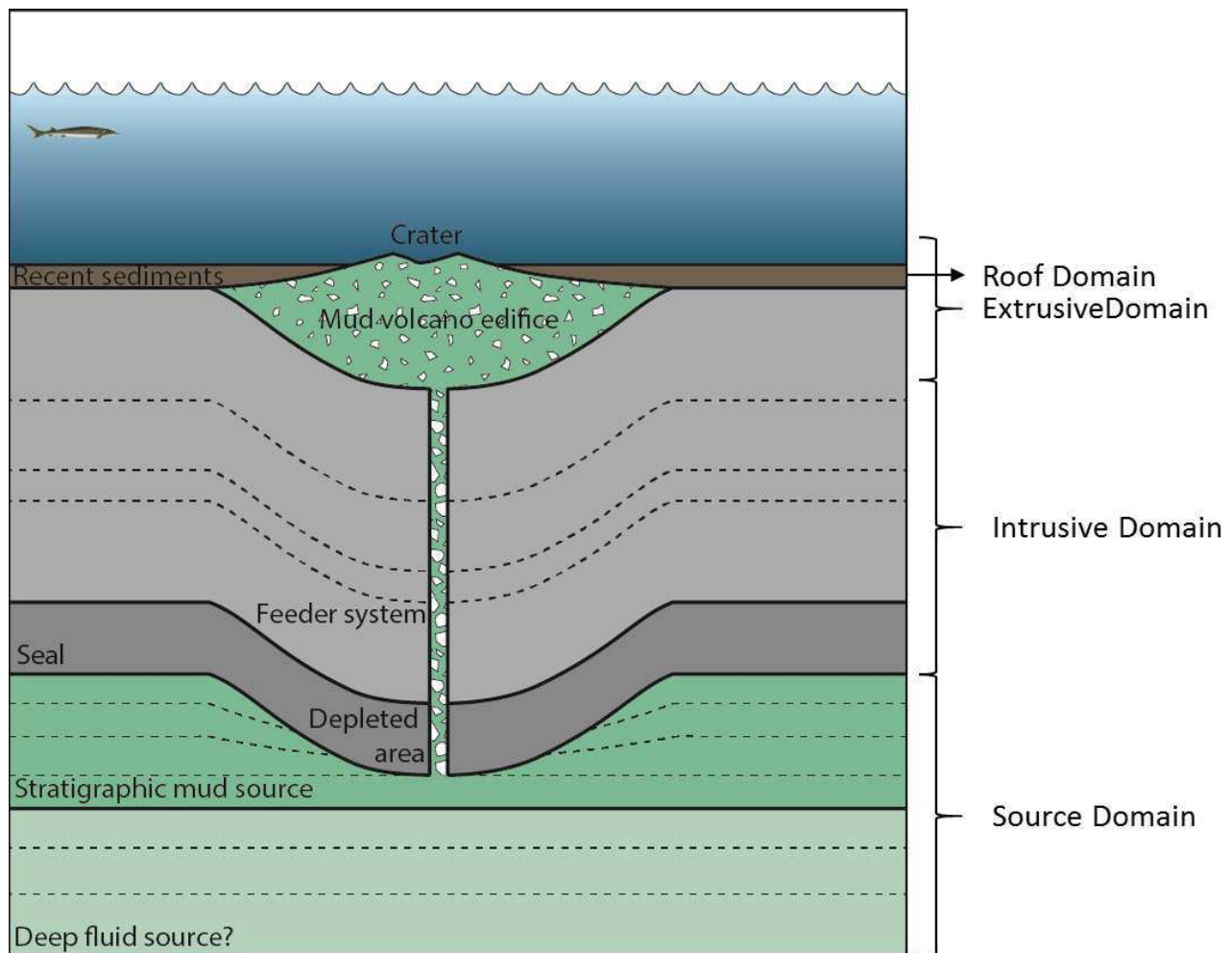


Figure 1.4: schematic diagram of a mud volcano system, displaying its main structural domains. The features common for most of mud volcanoes are represented and only morphological and geometrical considerations are displayed (modified from Kirkham, 2015).

2.4.1. Source domain

The source domain includes the stratigraphic levels from which sediments are remobilized as well as any deeper source of fluids and the structures connecting them to the mud source layers, like thrust sheets, faults, folds or diapirs (Figure 1.4; Brown, 1990; Kopf, 2002; Stewart & Davies, 2006; Deville, 2009; Roberts, 2011; Santos Betancor, 2015; Mazzini & Etiope, 2017). These deep structures may influence the location of the mud generation zone (Brown, 1990; Kopf, 2002; Stewart & Davies, 2006; Roberts, 2011). In some cases, a depleted area is present at the top of the source layer (Figure 1.4 and Figure 1.5). This depleted area is defined by a local thinning of the source layer due to the evacuation of remobilized sediments to the surface (Figure 1.5; Stewart & Davies, 2006; Roberts *et al.*, 2010; Dupuis, 2017; Kirkham *et al.*, 2017b), but may not be visible or imaged if the mud generation zone extends laterally or if the volcano is located in a highly compressive zone (Deville *et al.*, 2006). The roof of this domain is defined by the deepest stratigraphic layer intruded by allochthonous sediments coming from the source layer (Stewart & Davies, 2006; Roberts, 2011; Dupuis, 2017; Kirkham *et al.*, 2017b). Caldera margins are most of the time coincident with the area of the thinned source layer, the depleted zone, indicating that the collapse was initiated when sediments were remobilized to the surface (Figure 1.5; Stewart & Davies, 2006; Roberts, 2011).

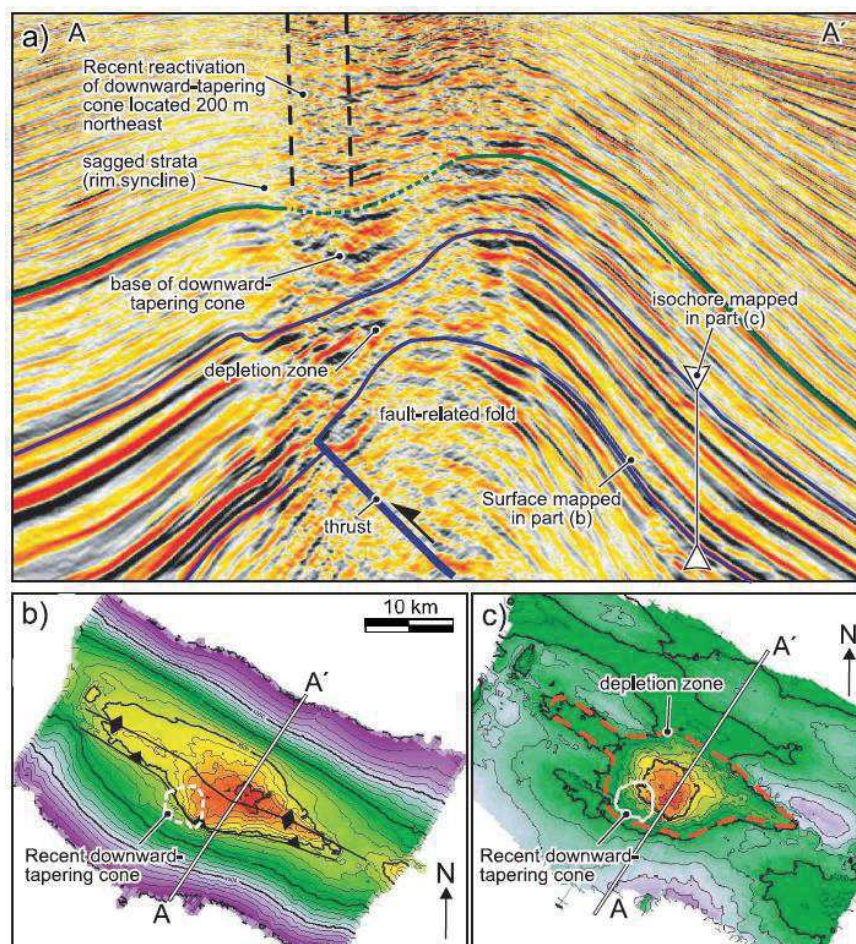


Figure 1.5: a- seismic section across a mud volcano system in the South Caspian Basin showing a thinning of the Maykop Formation interval interpreted as being the source layer of the mud volcano. b- Depth map of the top of the Maykop Formation underlining a thrust. c- Thickness map of the Maykop Formation showing a depleted zone inside the red dotted line (from Stewart & Davies, 2006).

Dupuis (2017) highlighted bowl shaped features located at the crest of anticlines in the South Caspian Basin (Figure 1.6), and at the top of faults in the Niger delta (Dupuis *et al.*, 2019). These geometries are the result of roof collapse into the mud generation zone, consequently to its progressive depletion to the surface (Dupuis, 2017; Dupuis *et al.*, 2019). The truncated interval forming the base of the structure is interpreted as being the former mud chamber (Dupuis, 2017). Kirkham *et al.* (2017b) describe similar architectures on mud volcanoes located on the western province of the Nile deep sea fan, with depletion zones located just below the Messinian Evaporites.

The term mud chamber can be ambiguous: whether it is an intrusive body located between the source domain and the surface, or it is the source itself (Planke *et al.*, 2003). Deville (2009) mentions a mud generation zone located where deep overpressure fluid flows are focused into an under-compacted shale interval. Many authors reports evidence for superficial secondary mud reservoirs or mud chambers between the deep mud source and the extrusive edifice that are periodically charged and the overpressure is released during eruptions (Planke *et al.*, 2003; Mazzini & Etiope, 2017; Odonne *et al.*, in press).

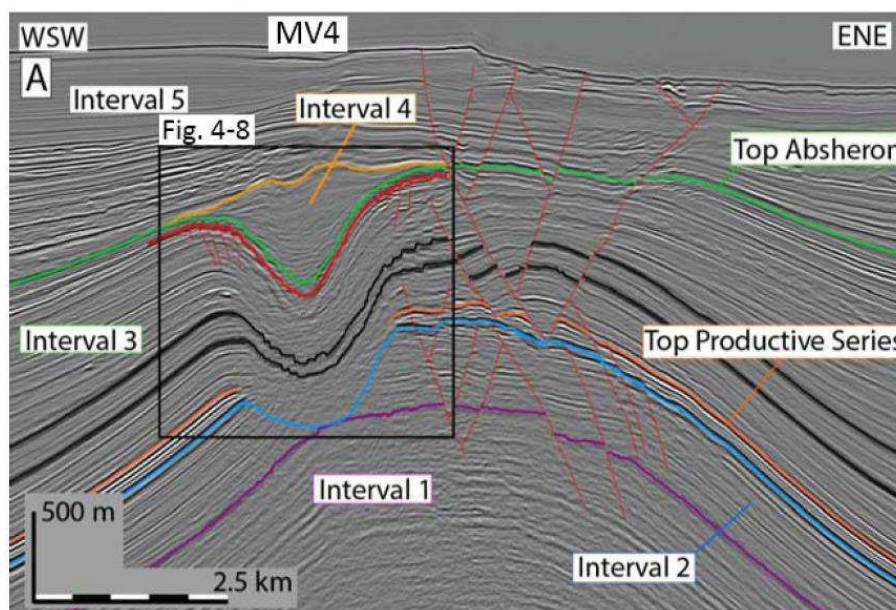


Figure 1.6: interpreted seismic section showing the bowl-shaped features at the crest of an anticline in the South Caspian Basin, interpreted as former mud chambers (from Dupuis, 2017). Interval 2 is partially truncated by interval 3. Interval 1 is undisturbed. The interval 4 is interpreted as being mud extrusions initially sourced in the truncated interval 2. Sediment remobilization provoked a collapse of intervals younger than the source.

2.4.2. Intrusive domain

The intrusive domain connects the extrusive edifice (the mud volcano) and the source domain. It is composed by the conduits for mud and fluids within the intruded host rock (Stewart & Davies, 2006; Roberts, 2011). It is limited by the source domain at the bottom and by the base of the last extrusive edifice (Stewart & Davies, 2006; Roberts, 2011). The precise anatomy and the fluid flow process inside the conduits are still poorly understood because of the very few known examples of outcropping MV feeder channels (Clari *et al.*, 2007; Roberts, 2011) due to their sensitivity to weathering processes (Roberts *et al.*, 2010).

However, estimations of the feeder channels diameter were made on several locations based on physical properties and flux measurements of mud breccia using fluid mechanics models (Kopf & Behrmann, 2000; Collignon *et al.*, 2018b). Results showed that feeder pipes do not exceed a few meters (Kopf & Behrmann, 2000; Collignon *et al.*, 2018b). The timing of the formation of the conduits are poorly constrained and seismic data quality does not allow to image vertical objects, which are moreover very often below seismic resolution, with gas blanking effects reducing data quality even more (Day-Stirrat *et al.*, 2010).

Different authors have suggested many architectures like bulbous diapirs, steep diatremes, network of mud dykes or sills or thin vertical pipes (Fowler *et al.*, 2000; Kopf, 2002; Stewart & Davies, 2006; Deville, 2009; Roberts, 2011; Kirkham *et al.*, 2017a). The size of these conduits varies from few centimeters to 100's meters on field examples, and can get as large as 3.5 km in seismic examples in the Black Sea (Brown, 1990; Kopf, 2002; Davies & Stewart, 2005; Roberts, 2011). The conduit may also be a pre-existing fault (Zitter, 2004; Bonini, 2009b). The intrusive domain in seismic sections often consists of seismic horizon discontinuities through large blanked-out columns with poor or no reflections or, sometimes, thin pipes: their geometry is circular in map view and pipe-like in 3D (Figure 1.5b,c and Figure 1.7; Stewart & Davies, 2006; Perez-García *et al.*, 2009; Kirkham *et al.*, 2017a).

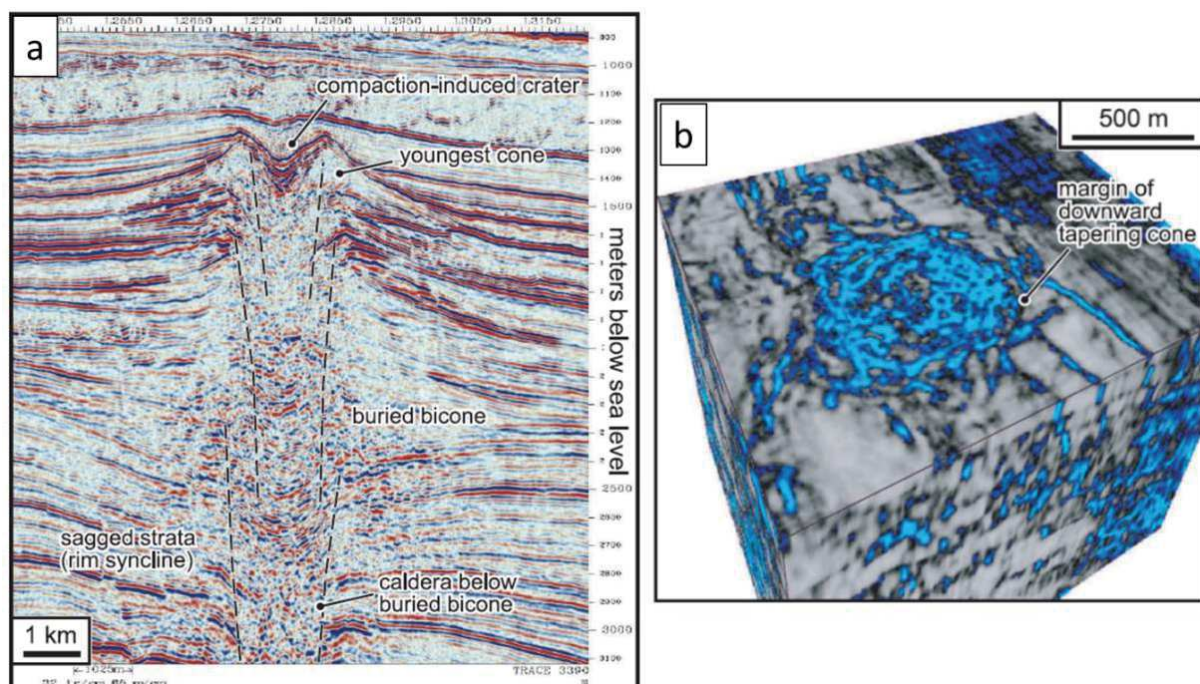


Figure 1.7: a: seismic section showing the subsiding column of intruded sediments named “downward tapering cone” by Stewart & Davies (2006). It is located below several biconical extrusive edifices (from Stewart & Davies (2006)). b: coherency time slice showing the chaotic structure inside the DTC (from Stewart & Davies, 2006).

Around the blanked area, some circular normal faults or a downward bending of the seismic reflectors (rim-syncline or bowl-shaped structure) may evidence the collapse due to depletion of the source domain (Figure 1.6 and Figure 1.7a; Fowler *et al.*, 2000; Davies & Stewart, 2005; Stewart & Davies, 2006; Perez-García *et al.*, 2009; Dupuis, 2017; Kirkham *et al.*, 2017a; Blouin *et al.*, 2019). Stewart & Davies (2006) describe what they call a “downward tapering cone” (DTC, Figure 1.7). It corresponds to the entire intruded column

that gets less resistant as the mud intrudes the host rock and hydrofractures and dykes get denser. By differential compaction, under the load of the extruded material and the normal sediment load, this column will start to subside (Stewart & Davies, 2006; Deville, 2009; Roberts, 2011). This effect amplifies the collapse of the structures into the depleted area. The DTC exhibit a low seismic coherency showing their complex internal geometry and the great heterogeneity (Figure 1.7a; Davies & Stewart, 2005; Stewart & Davies, 2006).

Some field examples of conduits exposed due to intense erosion of mud volcanoes were studied onshore Azerbaijan by Roberts *et al.* (2010). This study showed that the conduit was built by dense fracture propagation and stoping process, allowing pluri-metric country rock blocks to rotate and probably move with the ascending mud. The fractures are not pipe-like but tabular and present a brecciated aspect (Deville, 2009; Roberts, 2011).

2.4.3. Extrusive domain

The extrusive domain is constituted by the constructional edifice (outcropping or buried), with typically a conical to biconical shape and a summit crater (Figure 1.1a,b, Figure 1.4 and Figure 1.7a; Kopf, 2002; Stewart & Davies, 2006; Deville, 2009; Roberts, 2011). Nevertheless, morphologies vary greatly depending on mud composition and subsurface architecture (Kopf, 2002; Mazzini & Etiope, 2017). The constructional edifice may be composed of a stacking of several mud cones, forming a “Christmas tree” configuration resulting from the interplay between short periods of eruption and longer dormant periods, when normal sedimentation dominates and buries the youngest mudflows (Figure 1.7a and Figure 1.8; Deville, 2009; Roberts, 2011). The biconical shape observed on many MVs is due to the remobilization of the subsurface mud towards the surface, responsible for a collapse of the entire structure into the depleted area (Stewart & Davies, 2006).

The size and shapes of the extrusive edifice are highly variable, spanning from tens of meters to several hundreds of meters high for hundreds of meters to several km in diameter (Henry *et al.*, 1996; Kopf, 2002; Zitter, 2004; Deville, 2009; Antonielli *et al.*, 2014; Dupuis, 2017). Davies & Stewart (2005) described giant biconical structures 10 km in diameter and 1.4 km thick in the northern edge of the SCB. Composition of the mud is important and implies different size and morphologies for extrusive edifices (Kopf, 2002; Zitter, 2004; Roberts, 2011; Mazzini & Etiope, 2017). The fluid content as well as mud viscosity, density, grain size and width of the feeder conduit are key parameters controlling the height and slope of the mud volcano (Brown, 1990; Henry *et al.*, 1996; Kopf, 2002; Zitter, 2004; Deville, 2009; Roberts, 2011; Mazzini & Etiope, 2017).

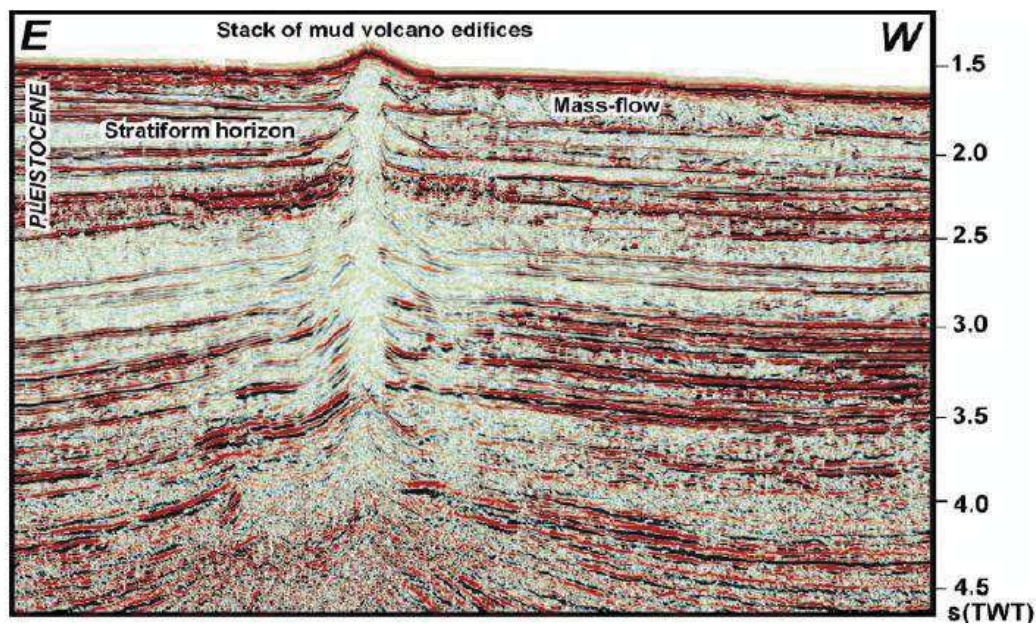


Figure 1.8: example of a buried mud volcano offshore of Trinidad with the typical “Christmas tree” morphology. This architecture is the result of the cyclic development of the volcanic edifice, with short eruptive periods that contrast with the longer dormant periods when normal sedimentation dominates (from Deville, 2009).

Different classifications exist. Some authors based their classification on shapes like Mazzini & Etiope (2017) in Figure 1.9 that reviewed and combined all the observed morphologies. These differences in morphology is mainly explained by mud composition and its fluid content that impacts its viscosity. Viscous mud (less water) will tend to create high morphologies with steep slopes, whereas fluid mud (high water content), tends to spread over large areas, thus creating flat morphologies (Kopf, 2002; Deville, 2009; Roberts, 2011; Mazzini & Etiope, 2017). The frequency and power of the eruptions (linked to overpressure and gas charging), the volume erupted each time, the width of the shallow conduits, pre-existing topography, erosion, basin subsidence and thickness and properties of the affected sedimentary sequence also controls the morphology of the MV (Roberts, 2011; Mazzini & Etiope, 2017). The most common morphologies at the extrusion are: regular bicone or cone (Kopf, 2002; Somoza *et al.*, 2003; Stewart & Davies, 2006; Deville, 2009; Mazzini & Etiope, 2017; Ceramicola *et al.*, 2018); “mud shield” with low height and smooth slopes and a plateau-like architecture (Kopf, 2002; Somoza *et al.*, 2003; Deville, 2009; Dupuis, 2017; Kirkham *et al.*, 2017; Mazzini & Etiope, 2017; Ceramicola *et al.*, 2018; Blouin *et al.*, 2019; Odonne *et al.*, in press); mud or brine lakes, which are flat (Kopf, 2002; Deville, 2009; Dupré *et al.*, 2014). Some structures are elongated in one direction; this elongation may indicate a feeder conduit elongation in one direction like faults or fractures (Zitter, 2004; Bonini, 2012) and also particular stress field, the external caldera being elongated in the direction of the minimum horizontal stress, and the extrusive edifice in the direction of the maximum horizontal stress (Bonini, 2012). Vent types can also be classified depending on their size, and mud composition (Roberts, 2011; Mazzini & Etiope, 2017). Gryphons are conical structures from 2 cm to 10 m with rather viscous mud. Mud pools are flat structures that emit only very fluid mud, having between 70-100 % of water.

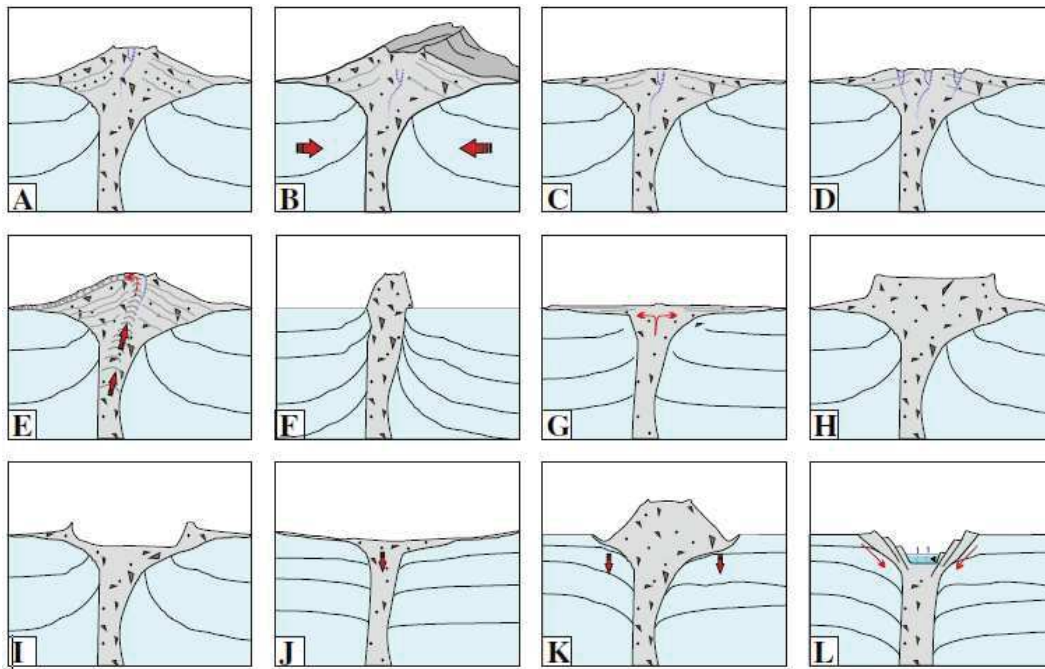


Figure 1.9: Different morphologies of MVs due to different internal processes and external forces (from Mazzini & Etiope, 2017). (A) conical, (B) elongated, (C) pie-shaped, (D) multicrater, (E) growing diapir-like, (F) stiff neck, (G) swamp-like, (H) plateau-like, (I) impact craterlike, (J) subsiding structure, (K) Subsiding flanks, (L) sink-hole type.

The summit crater is the surface expression of the feeder conduit, through which fluids and mud are dominantly expelled. This crater is sometimes delimited by normal faults (Kopf, 2002; Zitter, 2004; Deville, 2009; Mazzini & Etiope, 2017). The caldera consist of a conical normal fault zone that is circular in map view (Somoza *et al.*, 2003; Loncke *et al.*, 2004; Stewart & Davies, 2006; Deville, 2009; Dupré *et al.*, 2014; Kirkham *et al.*, 2017b) mainly due collapsing into the void generated by depletion of subsurface material, plus the effect of sediment loading due to extrusion of mud and local compaction effects due to overpressure release (Zitter, 2004; Deville, 2009; Roberts, 2011; Antonielli *et al.*, 2014). However, that causes a volumetric problem as highlighted by Odonne *et al.*, (1999) and Galland *et al.*, (2015) who show that caldera collapse is accommodated by normal faulting above the depleted area edges, accompanied by a central outward dipping cone-shaped reverse fault. Stewart & Davies (2006) differentiate DTC and caldera: caldera is filled with extruded material whereas DTC is composed of fractured and intruded host rock.

Smaller scale structures and objects affect the extrusive domain: gryphons, mud pools and salsas, which are the fluid seepage expression during the dormant phase of the volcano; mudflows and associated morphologies (for instance levees, ridges, channels); biological features like carbonate crusts, bacterial mats and shell colonies on offshore structures (Kopf, 2002; Zitter, 2004; Deville, 2009; Roberts, 2011; Dupuis, 2017; Mazzini & Etiope, 2017).

2.4.4. Roof domain

The roof domain tops the extrusive edifice when activity of offshore mud volcanoes is low enough compared to the background sedimentation to be buried (Figure 1.4; Fowler *et al.*, 2000; Stewart & Davies, 2006; Deville, 2009; Roberts, 2011; Dupuis, 2017). It is composed of the sediments covering the mud

volcano, and some late intrusive systems might crosscut the sedimentary column (Stewart & Davies, 2006). These intrusive features are, for instance, mud volcano re-activation, pockmarks, fluid escape features and connect the extrusive domain with the seafloor. Some faults and differential compaction related structures may be also present (Stewart & Davies, 2006; Roberts, 2011).

2.5. Triggers for mud genesis and drivers of sediment remobilization

The possibility to form a mud volcano depends on several preconditioning factors and parameters that may trigger mud generation and/or drive mud remobilization (Kopf, 2002; Deville, 2009; Mazzini & Etiope, 2017).

2.5.1. Overpressure generation

Overpressure is a global phenomenon that can be found in various geological contexts and lithologies (Carcione & Helle, 2002; Huffman & Bowers, 2002) and MVs are always associated with overpressured conditions (Dimitrov, 2002; Kopf, 2002; Deville, 2009; Mazzini & Etiope, 2017). The overpressure accumulation is one of the pre-requisites for mud generation and remobilization of sediments as it brings enough energy to fluidize sediments, fracture the sedimentary cover and bring the mud to the surface (Brown, 1990; Dimitrov, 2002; Kopf, 2002; Deville, 2009; Morley *et al.*, 2011; Mazzini & Etiope, 2017).

The overpressure is the pressure above the hydrostatic pressure. It is generated by numerous different mechanisms, and produces various effects on the rock properties such as preservation of an abnormally high porosity (Figure 1.10; Osborne & Swarbrick, 1997; Deming, 2002; Swarbrick *et al.*, 2002; Opara, 2011). The hydrostatic pressure results from the load of the overlying connected fluid column, whereas the lithostatic pressure is generated by the load of the complete overlying sedimentary column, fluids included (Figure 1.10; Deming, 2002). Overpressure cannot exceed the fracturing pressure of the rock, which is the pressure needed to initiate fractures (Nolen-hoeksema, 2013): beyond that limit, the rock may lose its fluid retention capacity (Swarbrick *et al.*, 2002; Judd & Hovland, 2007). Therefore, the maximum overpressure magnitude that is possible to reach, highly depends on the host rock mechanical properties (Swarbrick *et al.*, 2002).

Four main mechanisms can lead to overpressure (Osborne & Swarbrick, 1997; Deming, 2002; Swarbrick *et al.*, 2002).

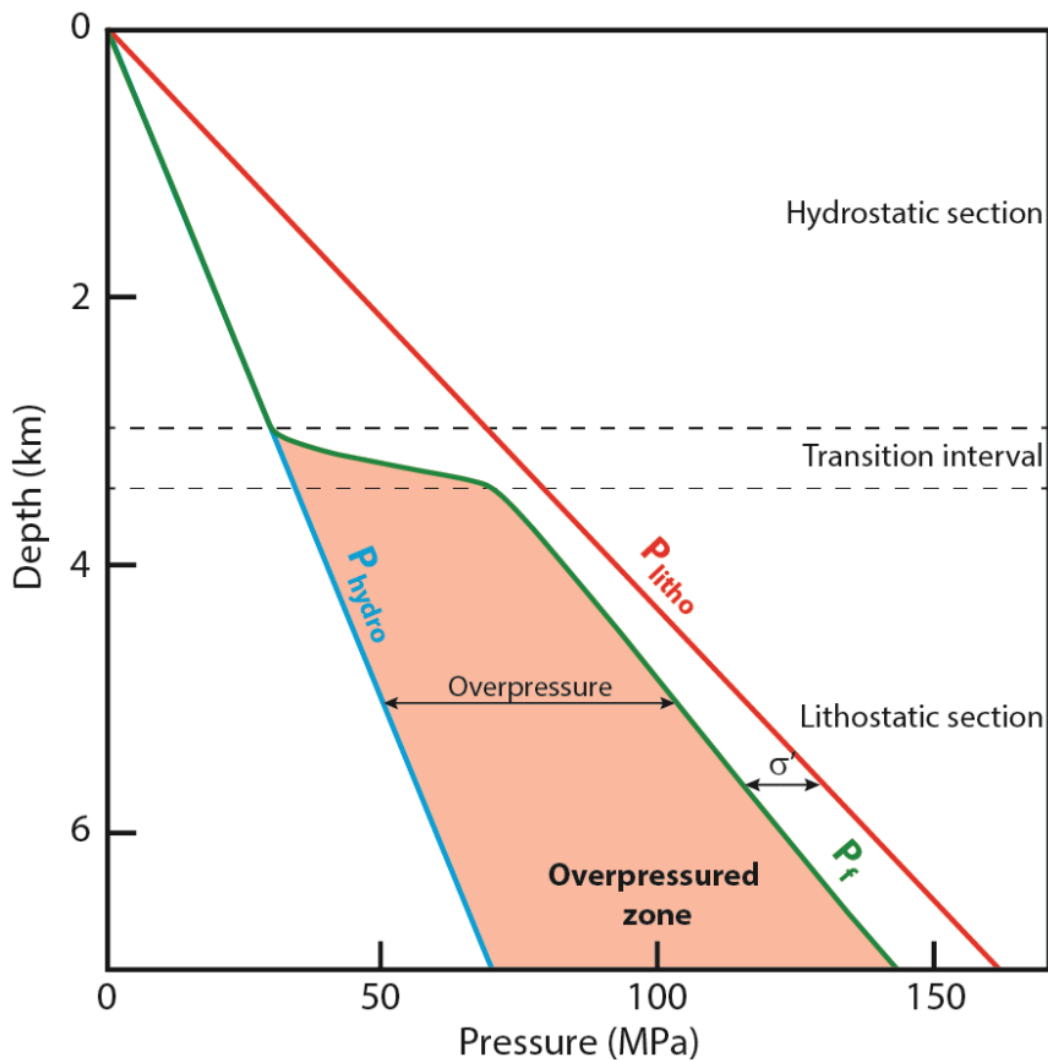


Figure 1.10: pressure versus depth plot showing hydrostatic (P_{hydro}) and lithostatic (P_{litho}) pressures. The green line is the measured pressure. The difference between the measured pressure and hydrostatic pressure represents the overpressure and the difference between the lithostatic and measured pressure gives the effective stress (modified from Deming, 2002).

i. Compaction disequilibrium

When low permeability sediments are rapidly buried, pore fluids might not be able to evacuate at a sufficient rate, so they will start to support part of the sediment load, generating overpressure (Osborne & Swarbrick, 1997; Gordon & Flemings, 1998; Revil *et al.*, 1999; Deming, 2002; Swarbrick *et al.*, 2002; Maltman & Bolton, 2003; Wanzhong, 2007; Opara, 2011). There is a depth called the fluid isolation depth where compaction disequilibrium starts and it varies with sediment permeability and burial rate (Osborne & Swarbrick, 1997; Swarbrick *et al.*, 2002; Tingay *et al.*, 2007). Another effect of this mechanism is that porosity departs from the normal compaction trend, so that sediment porosity keeps abnormally high values: they stay in an under-compacted state (Swarbrick *et al.*, 2002; Tingay *et al.*, 2007; Wanzhong, 2007; Day-Stirrat *et al.*, 2010). If high overpressure magnitudes are generated with this mechanism (Swarbrick *et al.*, 2002), the rock sealing capacity being limited, capillary leakage or seal fracturing may occur when combined to other overpressure generation processes (Finkbeiner *et al.*, 2001; Manzocchi & Childs, 2013; Hao *et al.*, 2015). The presence of seal bypass systems such as faults, intrusions or pipes may further compromise the sealing

(Cartwright *et al.*, 2007; Hao *et al.*, 2015; Kirkham, 2015). Moreover, this phenomenon is transient since the needed permeability in order to seal the overpressure for more than 1 Ma is lower than typical shale permeability values (Osborne & Swarbrick, 1997; Deming, 2002; Swarbrick *et al.*, 2002). Therefore, overpressure generated by compaction disequilibrium tends to dissipate with time (Osborne & Swarbrick, 1997). MVs are often associated to high sedimentation rates such as in Trinidad or in the South Caspian Basin, where their formation correlates with highest sedimentation rates (Kopf, 2002; Yusifov & Rabinowitz, 2004; Mazzini *et al.*, 2007). Moreover, under-compacted and overpressured shale-detachment levels are the main sources for MVs in several regions of the world (Yusifov & Rabinowitz, 2004; Stewart & Davies, 2006; Mazzini & Etiope, 2017; Morley *et al.*, 2017).

ii. Volumetric variations

Volume changes are also effective overpressure generating mechanisms (Osborne & Swarbrick, 1997; Swarbrick *et al.*, 2002; Opara, 2011). The pore fluid volume may rise either by generation of new fluids in the porous media, or by volumetric expansion of the pre-existing fluids dictated by thermal or pressure changes (Osborne & Swarbrick, 1997; Swarbrick *et al.*, 2002). Fluid generation mechanisms are mainly diagenetic reactions, dehydration of clay minerals and hydrocarbon generation which are pressure and temperature controlled reactions (Brown, 1990; Osborne & Swarbrick, 1997; Swarbrick *et al.*, 2002; Opara, 2011).

MVs are often associated to active HC provinces as stated in Chapter 1:2.2 and studies show the correlation between MV formation and source rock maturation (Yusifov & Rabinowitz, 2004). Swarbrick *et al.* (2002) estimate that kerogen transformation into oil (from 60°C to 120°C) will generate less overpressure than the gas generation (from 120°C to 180°C). This is due to volume changes: one volume of oil will crack into 500 volumes of methane in average and in standard pressure-temperature conditions (Osborne & Swarbrick, 1997). They calculated, for a source rock with type II kerogen, with vitrinite reflectance (% Ro) values ranging from 0.7-1.75 %, that up to 41 MPa of overpressure may be generated (Swarbrick *et al.*, 2002). The overpressure magnitude generated by secondary oil to gas cracking in in reservoir rocks would be much lower because of the higher permeability (Swarbrick *et al.*, 2002). However, hydrocarbon generation generates microporosity in the organic matter particles that may limit the overpressure generated by volume increase (Modica & Lapierre, 2012).

Mud generation zone often consists of clay-rich stratigraphic intervals (see Chapter 1:2.3). Clay-rich formations (in particular smectite-rich lithologies) produce water during burial with dehydration and smectite-illite and other clay transformation reactions (Swarbrick *et al.*, 2002; Zitter, 2004; Dubacq, 2008; Vidal & Dubacq, 2009). Smectite-Illite reactions generally start for temperature varying between 60-80 °C, and will stop for temperatures higher than 150°C (Osborne & Swarbrick, 1997; Vidal & Dubacq, 2009; Day-Stirrat *et al.*, 2010; Opara, 2011). Swarbrick *et al.* (2002) consider that clay dehydration and smectite/illite transformation as one of the main overpressure generation mechanism through volumetric expansion.

However, a quantification of the overpressure generated by this transformation is challenging because of the numerous different existing reactions (Opara, 2011) and because of the dependence of these reactions to other parameters than the sole temperature such as the nature of the interlayer cations and the water activity (Vidal & Dubacq, 2009). Furthermore, diagenetic reactions are responsible for fabric changes and porosity reduction referred as chemical compaction accompanied by water expulsion which can participate in the overpressure budget (Swarbrick *et al.*, 2002; Day-Stirrat *et al.*, 2010; Opara, 2011). Nevertheless, dissolution processes may also increase porosity causing overpressure decrease.

Nonetheless, volumetric expansion may be due to water expansion with temperature increase or to free methane expansion with decompression (Brown, 1990; Deville, 2009; Roberts, 2011; Antonielli *et al.*, 2014). Gas exsolution, gas desorption or gas hydrates dissociation for offshore deepwater MVs may also trigger a volume increase, and thus an overpressure generation (Brown, 1990; Osborne & Swarbrick, 1997; Kopf, 2002; Zitter, 2004; Deville, 2009; Zhang *et al.*, 2012; Antonielli *et al.*, 2014). Other diagenetic reactions such as gypsum-anhydrite transformation or cementation processes may generate overpressure by adding water into the system or reducing porosity and permeability (Osborne & Swarbrick, 1997).

iii. Lateral tectonic stress

Lateral tectonic stress has the same impact as the burial, increasing the total stress and exacerbating the compaction disequilibrium (Osborne & Swarbrick, 1997; Opara, 2011; Dupuis, 2017). Overpressure can increase rapidly with lateral stress but associated fault reactivation and fracturing may occur, releasing large volume of fluids and decreasing overpressure (Osborne & Swarbrick, 1997; Roberts, 2011; Dupuis, 2017). Therefore, tectonic related overpressure fluctuates rapidly (Osborne & Swarbrick, 1997). The cyclic activity of mud volcanoes can be related to this cyclic overpressure loading due to tectonic activity (Zitter, 2004; Deville & Guerlais, 2009; Bonini, 2009; Antonielli *et al.*, 2014; Dupré *et al.*, 2015). In addition, mud volcanoes are often related to compressive structures as anticline, and thrusts (Brown, 1990; Zitter, 2004; Roberts, 2011; Bonini, 2012; Santos Betancor, 2015; Mazzini & Etiope, 2017). For instance, mud volcanoes initiated synchronously with fold growth in the South Caspian Basin (Fowler *et al.*, 2000). Moreover, Bonini (2012) shows the close relationship between MV shape, orientation and location (elongation of cones or caldera, gryphons and salsas alignments) and the stress field surrounding it. The particular vertical distribution of stress in the core anticlines may control the development of fractures and therefore mud generation location (Bonini, 2012).

iv. Earthquakes

Earthquakes can trigger subsequent changes in the stress field and therefore in the pore pressure distribution by fault reactivation and fracture opening (Jónsson *et al.*, 2003; Miller *et al.*, 2004; Menapace *et al.* 2017). Fault reactivation and fracture opening may allow some deeper and overpressured fluids to circulate towards less overpressured areas, ultimately leading to rapid overpressure increase in shallower

strata (Osborne & Swarbrick, 1997). If enough overpressure accumulates below a seal and that this seal breaks, depending on the fluid compressibility, fluidization of sediments may happen, allowing to remobilize them towards the surface (Judd & Hovland, 2007). Miller *et al.* (2004) and Bonini (2009b) describe a pressure wave generated by earthquakes triggering changes in the surface venting style and causing aftershocks. Therefore ground shaking may provoke a rapid increase of overpressure near the initial rupture. The magnitude overpressure increases may be sufficient to generate mud at depth from already overpressured sediments, or at least to reactivate dormant structures depending on the distance and magnitude of the earthquake (Bonini, 2009b; Deville & Guerlais, 2009; Menapace *et al.*, 2017).

v. Pressure transmission

Pressure can be transmitted from overpressured areas, where overpressure is generated locally from other mechanisms, to less overpressured or normally pressured intervals through permeable drains (Corbet & Bethke, 1992; Dugan & Flemings, 2000; Deming, 2002; Javanshir *et al.*, 2015). A pressure equilibrium will happen between the two ends of the drain (Corbet & Bethke, 1992; Deming, 2002). Depending on the conditions and the magnitude of overpressure at each end of the drain, overpressure can be either transmitted to initially normally pressured areas, decreasing the overpressure magnitude in the overpressure source interval, or it can be entirely lost if the zone where pressure is transmitted is not sealed (Dugan & Flemings, 2000; Deming, 2002; Javanshir *et al.*, 2015). There are many possible permeable drains: continuous sandstone bodies with high permeabilities or undercompacted intervals (Corbet & Bethke, 1992; Gay *et al.*, 2003; Javanshir *et al.*, 2015; Chenrai & Huuse, 2017; Dupuis, 2017), faults depending on whether they are sealed or transmissive and fractured areas (Davies, 1999; Deming, 2002; Wibberley *et al.*, 2008). Faults capacity to act as pressure drains highly depends on the activity of the fault (faults more transmissive during or right after earthquakes; Jónsson *et al.*, 2003; Miller *et al.*, 2004) and on the type of material filling the fault plane (brecciated material versus cemented, clay versus sand or silt; Wibberley *et al.*, 2008, 2017; Haines *et al.*, 2009). Permeable layers can be more or less continuous and extensive, so more or less effective in transmitting overpressure. For instance, amalgamated braided channel deposits form in general rather extensive and continuous sandstone intervals (Javanshir *et al.*, 2015).

vi. Osmosis

Osmosis is another possible mechanism for overpressure generation (Corbet & Bethke, 1992; Swarbrick *et al.*, 2002; Opara, 2011). It is an exchange of fluids of different salinity through a semi-permeable layer such as some fault plains or clay-rich beds and may also take place in mud volcanism context to generate overpressured conditions (Hedberg, 1974; Kopf, 2002).

2.5.2. The role of methane

Methane seems to have a predominant role in mud formation and extrusion as it has been known for decades to be associated with MVs (Hedberg, 1974) and as it can decrease the source layer density and its mechanical resistance and generates high overpressure that can drive mud towards the surface (Kopf, 2002; Swarbrick *et al.*, 2002; Zitter, 2004; Deville, 2009; Etiope *et al.*, 2009; Sultan *et al.*, 2012; Antonielli *et al.*, 2014). Methane can be present in four forms in the subsurface: free gas, adsorbed on the surface of clay minerals or organic matter particles, dissolved in water and in solid form as gas hydrates (Brown, 1990; Zitter, 2004; Ross & Bustin, 2009; Zhang *et al.*, 2012; Riboulot *et al.*, 2016). Each of these forms are stable only on specific pressure-temperature interval and dissolution and adsorption processes are reversible (Brown, 1990; Zhang *et al.*, 2012; Tang *et al.*, 2016).

Dissolved gas contained in sediments can exsolve when the pressure decreases below the solubility pressure (Esrig & Kirby, 1977; Brown, 1990; Sultan *et al.*, 2012), for instance during mud ascent, or after hydrofracturing and subsequent decrease in pore pressure, or when a catastrophic event as a slump triggers unloading of a sedimentary interval (Kopf, 2002; Tingay *et al.*, 2008; Deville, 2009; Imbert *et al.*, 2014). Free methane has two particularities: it has a low density (in standard conditions, 1000 times lower than water), and a compressibility 100 to 1000 times higher than liquid water (Soave, 1972): therefore, free methane has a great expansion power and will rapidly reduce mud density and maintain pore pressure as it is transported upwards (Brown, 1990; Kopf, 2002). This methane exsolution and expansion due to sediment unloading was observed during sediment core retrieval offshore by Sultan *et al.* (2012). Besides, Lusi catastrophe monitoring showed that the connection of deep overpressured fluids with dissolved gas to shallower intervals through the exploration well triggered gas exsolution and subsequent hydrofracturing of the Kallibeng clays (Davies *et al.*, 2008; Tingay *et al.*, 2008, 2015, 2017).

Methane and carbon dioxide molecules can get adsorbed respectively on the surface of kerogen particles and clay minerals and their desorption will happen through pressure decrease or temperature increase (Zhang *et al.*, 2012; Tang *et al.*, 2016). Methane hydrates stability in the deep offshore also depends on the temperature and pressure conditions, so that any input of warm brines through ascending mud or change in effective stress may trigger their dissociation (Henry *et al.*, 1996; Milkov, 2000; Diaconescu *et al.*, 2001; Kopf, 2002; Riboulot *et al.*, 2016). A final kick and overpressure pulse may be brought by this shallow hydrate dissociation in order to trigger violent mud eruptions (Kopf, 2002; Mazzini & Etiope, 2017), but ascending free methane may also be captured through hydrate formation (Kopf, 2002).

The effect of gas generation on overpressure generation was already discussed in Chapter 1:2.5.1.ii. However, the direct effect of this gas generation on sediments was not described. At the source rock level, the maturation of kerogen and its cracking into oil and gas generate a micro-porosity (Modica & Lapierre, 2012) and the micro-fracturing of the source rock due to migration and expulsion of the generated

HC (Vernik, 1994) and this could impact the capacity of source rock to form and retain large overpressure magnitudes. The mechanical properties of sediments that underwent gas exsolution are completely changed, and several experimental studies noticed a sediment damage caused by gas exsolution (Lunne *et al.*, 2001; Hight & Leroueil, 2003; Sultan *et al.*, 2012). Free gas can also accumulate when there is alternation of fine-grained intervals with coarser lithologies (Revil *et al.*, 1998; Cathles, 2001). When gas saturates the finer intervals, the capillary entry pressure will be too high generating a capillary seal with an effective permeability lower than the lowest ones observed in natural deposits allowing to accumulate great overpressure magnitudes without leakage (Revil *et al.*, 1999; Cathles, 2001). Besides, a gas accumulation will generate overpressure depending on the accumulation height and due to density difference between gas and pore water (Swarbrick *et al.*, 2002).

The presence of dissolved gas is a parameter that is able to trigger a decrease in water chemical activity (Dubacq *et al.*, 2013). Clay dehydration increases with decreasing water activity as demonstrated by Dubacq (2008) and Vidal & Dubacq (2009). Therefore, the presence of dissolved methane in porous water may be able to enhance clay dehydration and increase the overpressure in clay-rich layers.

Therefore, methane in MV context may be present in four states and increases the overpressure magnitude through different processes (mainly through exsolution and expansion), it decreases the mud density and changes the mechanical properties of sediments through exsolution and thermal generation.

2.5.3. Density inversion

In order to be remobilized without compressive stress or external forces, the mud needs to have a lower density than the surrounding deposits (Kopf, 2002). This density inversion may come from intrinsic lithology properties or from secondary mechanisms like low density fluid input, hydrocarbon generation, diagenetic reactions or tectonic processes (Kopf, 2002; Roberts, 2011). This condition is necessary to initiate sediment remobilization, but this sole property can't explain the ascent of mud through the whole sedimentary column as other processes are needed in order to sustain the phenomenon (Kopf, 2002; Day-Stirrat *et al.*, 2010; Roberts, 2011; Morley *et al.*, 2017). This density contrast creates a buoyancy force that must be greater than the sediment load and cohesion in order to initiate the sediment remobilization. Roberts (2011) indicates that this density inversion will prepare and weaken the sediments for remobilization but will not be able to initiate any vertical motion.

This density inversion can be an inherent property of the remobilized formation (Kopf, 2002). Indeed, clay-rich intervals are prone for remobilization due to an important porosity lowering the formation density and their capacity to adsorb water (Bouchet *et al.*, 2000; Kopf, 2002; Zitter, 2004). The source-layer may be overpressured and under-compacted, which can cause the density inversion with overlying, normally compacted sediments (Swarbrick *et al.*, 2002; Tingay *et al.*, 2007; Wanzhong, 2007; Day-Stirrat *et al.*, 2010; Roberts, 2011). But most of the time, input of fluids, and particularly gas, will enhance the density inversion

(Brown, 1990; Kopf, 2002; Deville, 2009; Roberts, 2011). Moreover, during mud ascent, the effective stress decreases, therefore porosity increases, lowering its density (Brown, 1990). Conversely, if sediments get unloaded (uplift, slump, erosion, either climatic or tectonic), they will regain some porosity depending on their swelling index (Terzaghi & Peck, 1948) and the matrix elasticity, so density contrast may be improved between two distinct sedimentary intervals.

The different processes and mechanisms described before as being necessary conditions and/or potential drivers for mud generation applies at different depth and highly depends on the stratigraphic succession and the present structures (faults, folds, permeable units). It led Deville *et al.* (2010) to propose a conceptual model showing a potential chain of physical processes and mechanisms for sediment remobilization, each process or mechanism being tied to a specific part of the mud volcano system (Figure 1.11). They notably defined a mud generation zone related to the convergence of several parameters such as focused fluid flow, pressure transmission, gas generation and migration and sediments in compaction disequilibrium (Figure 1.11; Deville *et al.*, 2010).

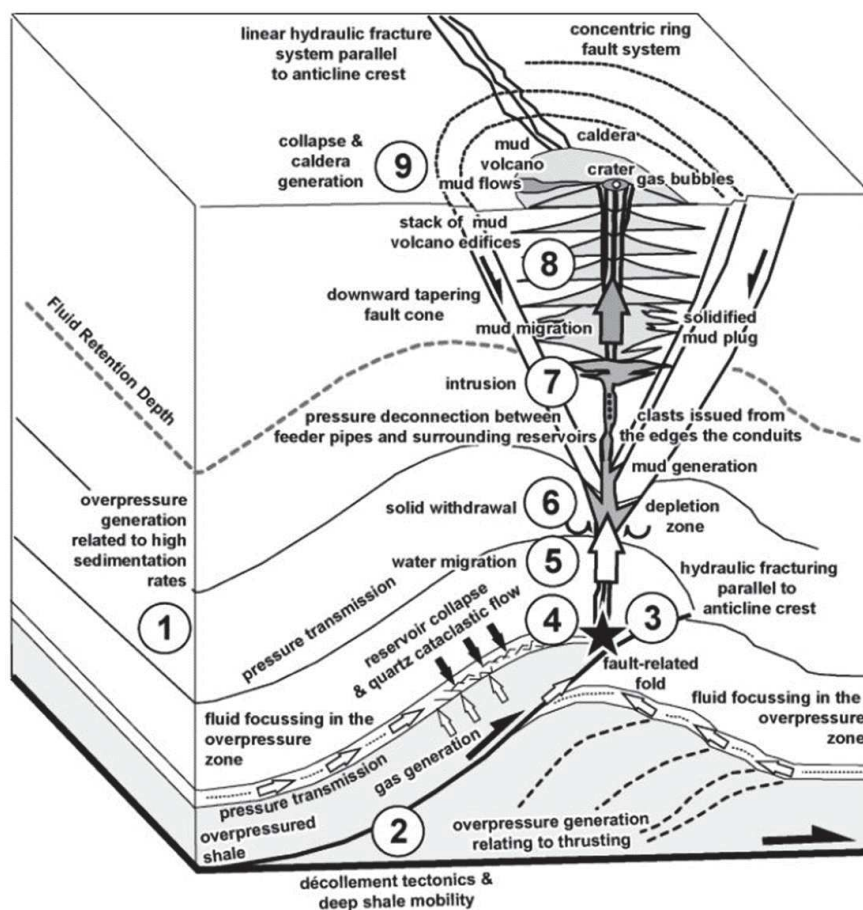


Figure 1.11: Conceptual mud volcano system model from Deville *et al.* (2010) showing a possible reaction chain and processes leading to sediment remobilization and mud volcano formation.

3. Goal and scope of this research

In the last several decades, a significant amount of studies focused on research problems related to mud volcanism using multidisciplinary approaches in different geological settings (Henry *et al.*, 1996; Kopf *et al.*, 2001, 2010; Dimitrov, 2002; Planke *et al.*, 2003; Zitter, 2004; Stewart & Davies, 2006; Deville & Guerlais, 2009; Etiope *et al.*, 2009; Antonielli *et al.*, 2014; Dupré *et al.*, 2015; Mazzini & Etiope, 2017; Menapace *et al.*, 2017; Dupuis, 2017; Gulmammadov *et al.*, 2017; Kirkham *et al.*, 2017b; Blouin *et al.*, 2019; Odonne *et al.*, in press). An effort was made in constraining the methane flux through mud volcanoes in a willingness to quantify natural greenhouse gas influx in the atmosphere caused by this natural phenomenon (Dimitrov, 2002; Kopf, 2002; Etiope *et al.*, 2009; Kopf *et al.*, 2010). Recent improvement of underground geophysical imaging allowed several authors to refine the architectural description of the underground structures of mud volcanoes (Fowler *et al.*, 2000; Stewart & Davies, 2006; Deville & Guerlais, 2009; Perez-García *et al.*, 2009; Kirkham, 2015; Dupuis, 2017; Blouin *et al.*, 2019). It allowed new considerations on the formation dynamics of mud volcanoes and on their sources (Deville, 2009; Perez-García *et al.*, 2009; Dupuis, 2017; Kirkham *et al.*, 2017a; Collignon *et al.*, 2018b; Blouin *et al.*, 2019). The relationship between mud volcano activity and their structural environment was also heavily studied thanks to technical improvement (Fowler *et al.*, 2000; Zitter, 2004; Bonini, 2009b; Kirkham *et al.*, 2017b). Besides, the recent Lusi catastrophe (Sidoarjo, Indonesia), started in 2006 and still going on, gave a unique opportunity of a monitoring of the complete formation process and evolution dynamics (Davies *et al.*, 2008; Tingay *et al.*, 2008, 2015, 2017; Mazzini *et al.*, 2012; Collignon *et al.*, 2018b). However, the mud generation processes are still poorly understood by many studies, and notably those on the Lusi monitoring, point out as necessary conditions the presence of a deep source of gas, and overpressured fine-grained and low density strata (Davies *et al.*, 2008; Deville, 2009; Mazzini *et al.*, 2012).

The impact of gas bubbles on the mechanical properties of sediments has also been widely addressed for geotechnical and geohazard assessment issues (Nageswaran, 1983; Thomas, 1987; Wheeler, 1988; Lunne *et al.*, 2001; Sills & Gonzalez, 2001; Hight & Leroueil, 2003; Boudreau, 2012; Rebata-Landa *et al.*, 2012; Sultan *et al.*, 2012; Nava Castro *et al.*, 2013; Jang & Santamarina, 2014). The presence of gas bubbles in marine sediments affects their elastic behavior and acoustic response, their compressibility, their permeability, their shear strength (Thomas, 1987; Wheeler, 1988; Helgerud *et al.*, 1999; Sultan *et al.*, 2012; Nava Castro *et al.*, 2013; Jang & Santamarina, 2014). Moreover, gas exsolution has also proved to be a factor controlling sediment damage and decrease in shear strength (Esrig & Kirby, 1977; Lunne *et al.*, 2001; Hight *et al.*, 2002; Sultan *et al.*, 2012; Sultan & Garziglia, 2014) through fracture creation due to bubble growth and expansion (Hight & Leroueil, 2003; Boudreau, 2012). Nevertheless, previous studies never demonstrated the possibility of generating mud from compacted sediments through the presence or the generation of gas bubbles.

The South Caspian Basin (SCB) and Greater Caucasus foothills onshore Azerbaijan are probably the most famous place for their numerous and highly active MVs (Dimitrov, 2002; Kopf, 2002; Mazzini & Etiope, 2017). The rate of subsidence and sediment infill is one of the highest known in the world, creating ideal overpressured and under-compacted conditions for MV emplacement (Stewart & Davies, 2006; Roberts, 2011; Javanshir *et al.*, 2015; Dupuis, 2017), and also ideal conditions for HC generation and accumulation (Tagiyev *et al.*, 1997; Inan *et al.*, 2002; Smith-Rouch, 2006; Guliyev *et al.*, 2011; Javanshir *et al.*, 2015). The region is intensely exploited for its rich HC resources, thus, it has been intensely studied by numerous surveys (seismic, geotechnics) and drillings (Contet & Unterseh, 2015; Gautherot *et al.*, 2015; Javanshir *et al.*, 2015; Alizadeh *et al.*, 2017). Notably, offshore MVs were studied and catalogued for safety reasons and geohazard assessment in potential drilling areas, but also to try to understand the potential impact of MVs on the pressure distribution at depth (Yusifov & Rabinowitz, 2004; Javanshir *et al.*, 2015; Unterseh & Contet, 2015). The SCB Pliocene to Quaternary units are impacted by high-amplitude folds, where HC are trapped and where MVs aligned along anticline crests (Fowler *et al.*, 2000; Roberts, 2011; Javanshir *et al.*, 2015; Dupuis, 2017).

Total has been operator of the Absheron gas condensate field, located 100 km SW of Baku, since 2009, with a first major discovery in 2011 (Gautherot *et al.*, 2015). The exploration phase between 1997 and 2011 started with a 650 km² 3D seismic survey acquired, followed by the drilling of a first well with no HC accumulation discovered (Gautherot *et al.*, 2015). Afterwards, geohazard assessment surveys (geotechnics, AUV surveys, Multi-beam bathymetry, sub-bottom profiler, sediment cores) were conducted in order to estimate the risks represented by the presence of a giant active MV at the crest of the Absheron anticline and its interaction with mass transport complexes (MTCs; Contet & Unterseh, 2015; Unterseh & Contet, 2015). Using these data, Imbert *et al.* (2014) studied the presence of a buried subcircular crater and filled with MTCs and the MV was notably assessed in terms of recent activity and shallow geometry and a comparison to onshore flat MVs by Dupuis (2017).

Therefore, the location of the Absheron mud volcano (AMV) on the Absheron gas condensate field, allowing studying a mud volcano with a dense and high-quality dataset acquired by Oil & Gas companies. Notably, it is composed of a 3D-seismic survey, well log data, sediment cores, cone penetration testing and multibeam bathymetry. This gives an opportunity to conduct an integrated study, with a possible comparison between in situ and geological conditions, and laboratory experiments on mud sampled directly on the mud volcano. The research presented in this thesis focuses on the role of gas in mud generation processes, using the well-imaged and well-documented AMV. The thesis proposes a formation model for the AMV, explores a mud generation process based on laboratory testing assessing the impact of gas exsolution on compacted sediments and estimates a volume of gas needed in order to remobilize sediments from the AMV source in the geological conditions. More precisely, this research work aims to investigate the following questions:

- Is it possible to locate the source of the AMV and define the physical mechanisms and geological conditions leading to its formation?
- Are gas exsolution and expansion alone able to generate a mud from compacted sediments?
- Can a numerical model integrating the behavior of gassy sediments under accurate geological conditions, simulate mud generation at depth and its remobilization towards the surface, and what is the needed critical degree of gas saturation?

3. But et cadre de ce travail de recherche

Durant les dernières décennies, un grand nombre d'études se sont intéressées à des thématiques de recherche liées au volcanisme de boue en utilisant des approches pluridisciplinaires dans des contextes géologiques différents settings (Henry *et al.*, 1996; Kopf *et al.*, 2001, 2010; Dimitrov, 2002; Planke *et al.*, 2003; Zitter, 2004; Stewart & Davies, 2006; Deville & Guerlais, 2009; Etiope *et al.*, 2009; Antonielli *et al.*, 2014; Dupré *et al.*, 2015; Mazzini & Etiope, 2017; Menapace *et al.*, 2017; Dupuis, 2017; Gulmammadov *et al.*, 2017; Kirkham *et al.*, 2017b; Blouin *et al.*, 2019; Odonne *et al.*, in press). Un effort particulier a été fait pour quantifier le flux de méthane émis aux volcans de boue dans une volonté d'estimation des émissions de gaz à effet de serre dans l'atmosphère par des sources naturelles (Dimitrov, 2002; Kopf, 2002; Etiope *et al.*, 2009; Kopf *et al.*, 2010). De récentes améliorations des techniques d'imagerie du sous-sol ont permis à plusieurs auteurs d'affiner notre connaissance de l'architecture et des structures formant la partie enfouie des volcans de boue (Fowler *et al.*, 2000; Stewart & Davies, 2006; Deville & Guerlais, 2009; Perez-García *et al.*, 2009; Kirkham, 2015; Blouin *et al.*, 2019; Dupuis *et al.*, 2019). Cela a ouvert la possibilité à de nouvelles considérations sur la dynamique de formation des volcans et sur leurs sources (Deville, 2009; Perez-García *et al.*, 2009; Dupuis, 2017; Kirkham *et al.*, 2017a; Collignon *et al.*, 2018b; Blouin *et al.*, 2019). La relation entre l'activité des volcans de boue et leur environnement structural a aussi été largement étudiée grâce aux améliorations des méthodes géophysiques (Fowler *et al.*, 2000; Zitter, 2004; Bonini, 2009b; Kirkham *et al.*, 2017b). De plus, la récente catastrophe de Lusi (Sidoarjo, Indonésie), qui a commencé en 2006 et est encore en cours actuellement, a permis pour la première fois de suivre le processus complet de formation d'un volcan de boue ainsi que son évolution (Davies *et al.*, 2008; Tingay *et al.*, 2008, 2015, 2017; Mazzini *et al.*, 2012; Collignon *et al.*, 2018b). Cependant, les processus de génération de la boue sont encore mal compris même si de nombreuses études, et notamment celles se concentrant sur Lusi, mettent l'accent sur la nécessité d'une source profonde de gaz et d'une couche de sédiments fins en surpression (Davies *et al.*, 2008; Deville, 2009; Mazzini *et al.*, 2012).

L'impact des bulles de gaz sur les propriétés mécaniques des sédiments est aussi une question qui a été vastement traité dans le cadre de problèmes géotechniques et d'évaluation des risques géologiques (Nageswaran, 1983; Thomas, 1987; Wheeler, 1988; Lunne *et al.*, 2001; Sills & Gonzalez, 2001; Hight & Leroueil, 2003; Boudreau, 2012; Rebata-Landa *et al.*, 2012; Sultan *et al.*, 2012; Nava Castro *et al.*, 2013; Jang & Santamarina, 2014). La présence de bulles de gaz dans les sédiments marins affecte directement leur comportement élastique, leur réponse aux ondes acoustiques, leur compressibilité, leur perméabilité et leur résistance au cisaillement (Thomas, 1987; Wheeler, 1988; Helgerud *et al.*, 1999; Sultan *et al.*, 2012; Nava Castro *et al.*, 2013; Jang & Santamarina, 2014). De plus, l'exsolution de gaz est un facteur reconnu d'endommagement des sédiments et de diminution de leur résistance au cisaillement (Esrig & Kirby, 1977; Lunne *et al.*, 2001; Hight *et al.*, 2002; Sultan *et al.*, 2012; Sultan & Garziglia, 2014) au travers de la formation de fractures causée par la croissance et l'expansion des bulles de gaz (Hight & Leroueil, 2003;

Boudreau, 2012). Cependant, les études précédentes n'ont jamais démontré la possibilité de générer de la boue à partir de sédiments compactés suite à la génération de bulles de gaz.

L'ensemble constitué par le Bassin sud caspien (BSC) et les contreforts du Grand Caucase en Azerbaïdjan est probablement la zone la plus reconnue pour son grand nombre de volcans de boue actifs (Dimitrov, 2002; Kopf, 2002; Mazzini & Etiope, 2017). Les taux de subsidence et de sédimentation sont parmi les plus élevés au monde, ce qui crée des conditions de surpression et de sous-compaction des sédiments idéales pour la mise en place de volcan de boue (Stewart & Davies, 2006; Roberts, 2011; Javanshir *et al.*, 2015; Dupuis, 2017), ainsi que les conditions idéales pour la génération et l'accumulation d'hydrocarbures (Tagiyev *et al.*, 1997; Inan *et al.*, 2002; Smith-Rouch, 2006; Guliyev *et al.*, 2011; Javanshir *et al.*, 2015). La région est donc intensément exploitée pour ses ressources et, de ce fait, elle a été étudiée au travers de nombreuses prospection et acquisition de données (sismique, géotechnique) et au travers de nombreux forages (Contet & Unterseh, 2015; Gautherot *et al.*, 2015; Javanshir *et al.*, 2015; Alizadeh *et al.*, 2017). En particulier, les volcans de boue sous-marins ont été étudiés et catalogués pour des raisons de sécurité et d'évaluation du risque géologique dans des zones de forage potentiel, mais aussi pour essayer de comprendre l'impact que pourrait avoir les volcans sur la distribution de pression en profondeur (Yusifov & Rabinowitz, 2004; Javanshir *et al.*, 2015; Unterseh & Contet, 2015). Les unités sédimentaires du Pliocène au Quaternaire du BSC sont affectées par de larges plis, où les hydrocarbures sont piégés et le long desquels les volcans de boue sont alignés (Fowler *et al.*, 2000; Roberts, 2011; Javanshir *et al.*, 2015; Dupuis, 2017).

Total est opérateur depuis 2009 du permis d'exploration d'Absheron, situé à 100 km au sud-ouest de Bakou. Le puits d'exploration foré en 2011 a mis en évidence une accumulation de gaz et condensats (Gautherot *et al.*, 2015). La phase d'exploration, qui s'est déroulée de 1997 à 2011, a débuté par une campagne d'acquisition d'un bloc sismique 3D de 650 km², suivi par le forage d'un premier puits qui s'est révélé être sec (Gautherot *et al.*, 2015). Ensuite, des campagnes d'estimation du risque géologique (acquisitions de données géotechniques, plongées de véhicules sous-marins autonomes, bathymétrie multifaisceaux, sondeurs de sédiments, carottes de sédiments) ont été conduites afin d'estimer le risque représenté par la présence d'un volcan de boue géant et actif à la crête de l'anticlinal d'Absheron et par l'interaction de celui-ci avec des instabilités sédimentaires (Contet & Unterseh, 2015; Unterseh & Contet, 2015). En utilisant ces données, Imbert *et al.* (2014) ont étudié la présence d'un cratère enfoui pseudo-circulaire rempli par des dépôts gravitaires et l'analyse de l'activité récente ainsi que la géométrie peu profonde du volcan de boue a été réalisée par Dupuis (2017) qui a comparé ce volcan à des volcans de boue terrestres plats.

Par conséquent, la localisation du volcan de boue d'Absheron (VBA) au-dessus du champ à condensats d'Absheron permet d'étudier un volcan de boue au travers d'un jeu de données dense et de bonne qualité acquis par des compagnies pétrolières. Ce jeu de données se compose d'un bloc sismique 3D, des données de deux forages (diagraphies), de carottes de sédiments, de tests de pénétrations au piezocône et de

bathymétrie multifaisceaux. Cela donne une opportunité unique de mener une étude complète, avec la possibilité de comparer les conditions géologiques in situ avec des expériences e laboratoire sur des sédiments prélevés directement sur le volcan de boue. L'étude présentée dans cette thèse se concentre sur le rôle joué par le gaz dans le processus de génération de la boue, en s'appuyant sur le VBA qui est bien imagé et bien documenté. La thèse propose un modèle de formation du VBA, explore un processus de formation de boue en s'appuyant sur des essais de laboratoire qui quantifient l'effet de l'exsolution du gaz sur des sédiments compactés et enfin estime un volume de gaz nécessaire afin de remobiliser des sédiments au niveau de la source du VBA dans les conditions géologiques. De façon plus précise, ce travail de recherche vise à répondre aux questions suivantes :

- Est-il possible de définir la source du VBA et de déterminer les mécanismes physiques et les conditions géologiques ayant mené à sa formation ?
- Est-ce que l'exsolution et l'expansion du gaz peuvent, à elles seules, générer de la boue à partir de sédiments compactés ?
- Un modèle numérique intégrant le comportement des sédiments gazeux dans les bonnes conditions géologiques peut-il simuler la génération de la boue en profondeur et sa remobilisation vers la surface, et quelle est le degré de saturation en gaz critique nécessaire ?

4. Thesis outline

Chapter 2 focuses on the detailed presentation of the study area, the dataset and their acquisition techniques as well as the methodologies and analysis methods that were necessary to carry out this research.

Chapter 3 focuses on a multidisciplinary analysis of the AMV. Its morphology is described using 3D-seismic data and multibeam bathymetry, and sediment analysis coupled with well log data interpretation assess the source of the mud. Preliminary numerical modeling is developed to consider the mud volcano source in its regional background and to understand the possible trigger mechanisms of the mud volcano formation. Part of this chapter is already published (Blouin *et al.*, 2019). The article is available in the Appendix 2.

Chapter 4 explores the effect of gas exsolution and expansion on the mechanical properties of compacted sediments. In this respect, a novel consolidation apparatus for gassy sediments was developed. The experimental testing program was defined to study the impact of gas exsolution on the hydro-mechanical properties of sediment acquired from the AMV. Part of this chapter is accepted in the *Engineering Geology* journal and awaits for the editor's decision after minor reviews.

Chapter 5 integrates the geological observations and results of the mechanical testing into an improved numerical model compared to the one introduced in Chapter 3 in order to simulate the conditions needed to generate mud at the Absheron location. Once a volume of mud is generated, modified Navier-Stokes equations taking into account the impact of gas expansion on mud properties are used in order to simulate the mud ascension through the sedimentary column. Results of the numerical models are used to transform the purely conceptual formation model proposed in Chapter 3 into a semi-quantitative model considering kinetics and magnitudes of the physical processes.

Chapter 6 summarizes all the important results of the thesis focusing on the role of gas in mud generation. It also concludes by answering as clearly as possible the initial questions. It discusses the limits of this research in terms of data, methods and models and explores potential perspectives regarding future research and models.

4. Plan de la thèse

Le chapitre 2 se concentre sur la présentation détaillée de la zone d'étude, du jeu de données et des techniques d'acquisition ainsi que sur les méthodes d'analyse qui ont été nécessaires afin de mener cette étude.

Le chapitre 3 s'articule autour d'une analyse pluridisciplinaire du VBA. Sa morphologie est décrite en utilisant les données de sismique 3D et la bathymétrie multifaisceaux. L'analyse des sédiments couplée à l'interprétation des données de puits permettent de déterminer la source de la boue. Un modèle numérique préliminaire est développé afin de replacer la source du volcan de boue dans son contexte régional, permettant ainsi de comprendre les possibles mécanismes ayant pu déclencher la formation du VBA. Une partie de ce chapitre est déjà publiée (Blouin *et al.*, 2019). L'article est disponible en annexe (Appendix 2).

Le chapitre 4 explore l'effet de l'exsolution du gaz et de son expansion sur les propriétés mécaniques de sédiments compactés. Un nouveau système de consolidation pour tester les sédiments gazeux a été développé dans ce but. Le programme d'essais a été défini pour étudier l'impact de l'exsolution du gaz sur les propriétés hydromécaniques des sédiments prélevés sur le VBA. Une partie du chapitre a été soumis sous forme d'article à *Engineering Geology*. L'article accepté avec des révisions mineures a été soumis de nouveau et est en attente de la décision finale de l'éditeur.

Le chapitre 5 intègre les observations géologiques et les résultats des essais mécaniques dans un modèle numérique amélioré par rapport à celui introduit dans le chapitre 3 dans le but de simuler les conditions nécessaires à la génération de boue au niveau du pli d'Absheron. Une fois le volume de boue créé, des équations de Navier-Stokes modifiées pour prendre en compte l'effet de l'expansion du gaz sur les propriétés de la boue sont utilisées afin de simuler la remontée de la boue au travers de la colonne sédimentaire. Les résultats de ces modèles numériques permettent de passer du modèle de formation purement conceptuel proposé au chapitre 3 à un modèle semi-quantitatif prenant en compte la dynamique et les processus physiques en jeu.

Le chapitre 6 résume les résultats principaux de la thèse en se concentrant sur le rôle du gaz dans la génération de la boue. Il conclut également en répondant le plus clairement possible aux questions posées initialement. Il discute des limites de cette étude en termes de données, de méthodes et de modèles et explore les perspectives de recherche ouvertes par ce travail, en particulier dans le domaine de la modélisation.

Chapter 2: Study Area, Data and Methodology

Abstract

Mud volcanoes and their genesis are closely associated to the geological setting as detailed in Chapter 1. Therefore, it is paramount to clearly understand the geological history and the current characteristics of the area surrounding the studied mud volcano.

This thesis focuses on an active mud volcano located in the South Caspian Basin (SCB), part of the Caspian Sea which is an intra-continental sea (or lake depending on the author) and a remnant of the Paratethys Ocean. This ocean disappeared during a complex compressive period, through the accretion and collision of several continental blocks and several subduction zones. This intense tectonic history led to intricate interplays between erosion, sedimentation, oceanic reconnections and climate and meteorological changes. Hence, SCB is one of the sedimentary basins having recorded in its recent history the highest sedimentation rates in the world, leading to the accumulation of a thick undercompacted sedimentary column, with high overpressure and deep mature source rocks. The basin holds the densest known distribution of active MVs. The studied structure is located on the Absheron gas condensate field, operated by Total. The mud volcano and its environment have already been studied, notably for geohazard assessment, and a dense dataset was acquired in the MV area.

This chapter presents a review of the regional and local (gas condensate field scale) geological settings. It details the type of data available and their method of acquisition and processing as well as their location relative to the mud volcano. Finally, this chapter presents and details the data interpretation methods, sediment analysis, laboratory measurements and numerical modeling conducted during the PhD.

Chapitre 2 : Zone d'étude, données et méthodologie

Résumé

Les volcans de boue et leur mise en place sont très clairement associés au contexte géologique comme montré dans le Chapitre 1. Il est donc essentiel de comprendre en détail l'histoire géologique de la zone d'étude ainsi que ses caractéristiques actuelles.

Ce travail de thèse se concentre sur un volcan de boue actif situé dans le Bassin sud caspien, qui fait partie de la mer Caspienne et est une mer intracontinentale. Cette mer est ce qu'il reste du paléo-océan Para-Téthys qui a disparu suite à une phase compressive complexe. Cette histoire tectonique intense a engendré une interaction complexe entre érosion, sédimentation, reconnections/isolations océanique et changements climatiques et météorologiques. De ce fait, le Bassin sud caspien est un des bassins sédimentaires ayant enregistré dans son histoire géologique récente les plus forts taux de sédimentation. Cela a permis l'accumulation d'une épaisse succession sédimentaire sous-compactée, avec génération de fortes surpressions et présence de roches mères matures profondément enfouies. Le bassin comporte également la plus forte concentration connue en volcans de boue actifs au monde. L'objet d'étude se situe sur le champ à condensats d'Absheron, opéré par Total. Le volcan et la zone ont déjà été étudiés afin d'évaluer les risques liés aux activités de forage dans une zone proche du volcan et un jeu de données dense a été acquis dans cette zone.

Ce chapitre propose donc une revue du contexte géologique à l'échelle régionale et à celle du champ pétrolier. Il détaille le type de données disponibles, ainsi que leur méthode d'acquisition, leur traitement et leur localisation par rapport au volcan de boue. Enfin, le chapitre présente en détail les méthodes d'interprétation des données, les méthodes d'analyse des sédiments, les méthodes de mesures en laboratoire et les méthodes de modélisation numérique qui ont été appliquées durant cette étude.

1. Study Area

1.1. South Caspian Basin

1.1.1. Geodynamics and present tectonic background

The study area is located in the South Caspian Basin (SCB), one of the three sedimentary basins composing the Caspian Sea along with the Central Caspian Basin and the North Caspian Basin. The Precaspian basin is also included by some authors as a 4th sedimentary basin in the studied region (Figure 2.1; Zonenshain & Pichon, 1986; Jackson *et al.*, 2002; Knapp, Knapp & Connor, 2004; Brunet *et al.*, 2007; Santos Betancor, 2015). The Caspian Sea covers a total area of 375,000 km² in central Eurasia, east of the Black Sea, and represents one of the greatest enclosed sea in the world, currently administered by Azerbaijan, Iran, Turkmenistan, Kazakhstan and Russia (Figure 2.1; Berberian, 1983; Forte & Cowgill, 2013; Santos Betancor, 2015; Abdullayev & Leroy, 2016). The present level of the Caspian Sea is 26.5 meters below the global sea level and it reaches a maximum depth of ca. 1000 m in the central SCB (Figure 2.1; Forte & Cowgill, 2013; Santos Betancor, 2015).

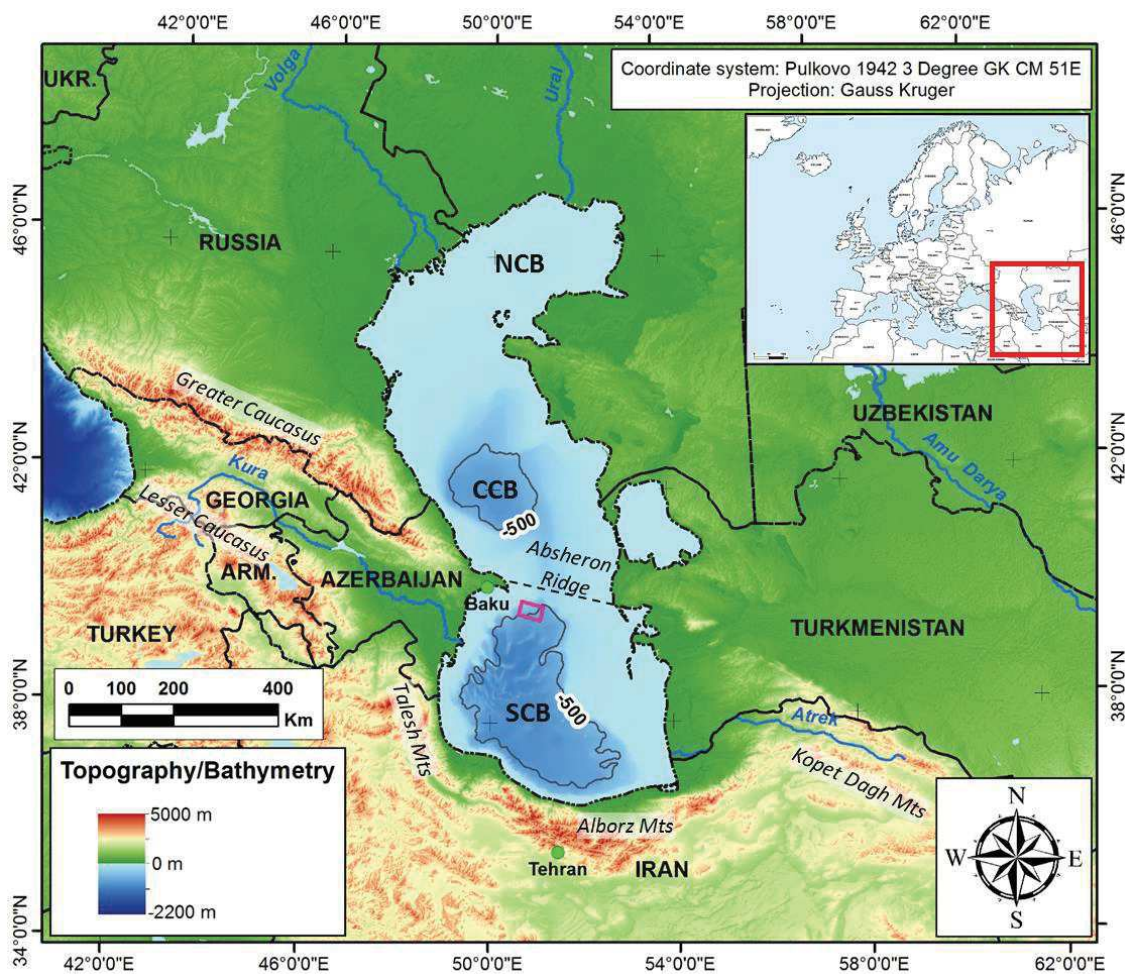


Figure 2.1: Topographic/Bathymetric map around the South Caspian Sea using the GEBCO 2014 database. The -500 m contour line is represented and highlight the main depocenters in the Caspian Sea. The main fold and thrust belts and reliefs delimiting the South Caspian Basin are located as well as the main river systems linked to the SCB history. The study area is located by a purple rectangle. SCB: South Caspian Basin; CCB: Central Caspian Basin; NCB: North Caspian Basin.

The origins of the South Caspian Basin trace back to a period spanning between Triassic and Eocene (Berberian, 1983; Popov *et al.*, 2004; Golonka, 2007; Bochud, 2011). Between Late Triassic and Early Jurassic, the accretion and collision of several microplates (South Caspian Block, Lut Plate, Central Iran Block, Caucasus Plate and Alborz Block) along the Eurasian margin, promoted the closing of the Tethys Ocean and the birth of the Paratethys (Berberian, 1983; Popov *et al.*, 2004; Golonka, 2007; Bochud, 2011). From Jurassic to Cretaceous, a north-dipping subduction developed along the new continental margin formed by suturing of the continental blocks (Golonka, 2007; Bochud, 2011). It resulted into a rifting phase due to trench-pulling effect of the subduction, therefore leading to the opening of a back-arc basin accompanied by active volcanism, the Greater Caucasus Basin (Berberian, 1983; Zonenshain & Pichon, 1986; Brunet *et al.*, 2007; Golonka, 2007; Bochud, 2011). This caused thinning of the continental crust and eventually formation of oceanic crust (Berberian, 1983; Brunet *et al.*, 2007; Golonka, 2007; Bochud, 2011). The Greater Caucasus Basin reached its maximum extent (900 km wide and 3,000 km long) during the closing of the Paratethys, in the Late Cretaceous and Early Paleogene (Zonenshain & Pichon, 1986; Golonka, 2007). During the Eocene, the Lesser Caucasus, Sanandaj Sirjan and Makran blocks were accreted to the Eurasian block, causing the subduction to jump further north (Golonka, 2007; Bochud, 2011). Since the Oligocene, the Arabian-Eurasian collision has been separating this basin into smaller ones including the South Caspian depression and the Black Sea (Zonenshain & Pichon, 1986; Popov *et al.*, 2004; Bochud, 2011), while the South Caspian microcontinent has been moving northward through rifting between South Caspian and the Alborz Block, opening the SCB from its SW (Golonka, 2007). The India-Eurasia collision caused deformation of Central Asia, accommodated through long NW-SE right-lateral transform faults (Golonka, 2007). During the Middle Miocene, the South Caspian depression separated the deeper eastern part, called the South Caspian Basin, from the western part, rapidly filled called Kura Basin (Dupuis, 2017). This is due to subsidence of the SCB through cooling of its oceanic crust and overthrusting on its borders (Berberian, 1983; Zonenshain & Pichon, 1986; Nadirov *et al.*, 1997), and to the presence of a fold and thrust belt in the Kura Basin that has been accommodating most of the Arabia-Eurasia collision since the Early Pliocene (Forte *et al.*, 2010). Subduction of the SCB oceanic crust below the Eurasian plate along the Absheron Ridge was also initiated during the Miocene (Figure 2.2; Allen *et al.*, 2002; Golonka, 2007; Hollingsworth *et al.*, 2008).

Two elements of the geodynamic history of the basin are still highly discussed. The basement of the SCB is abnormally thick (8-10 km) for an oceanic crust, but recorded P-wave velocities are about 6.6-7 km/s, corresponding to an oceanic crust signature (Knapp, Knapp & Connor, 2004; Brunet *et al.*, 2007; Egan *et al.*, 2009). Therefore, many authors refer to the SCB basement as a “modified” oceanic crust or sub-oceanic crust (Berberian, 1983; Knapp *et al.*, 2004; Brunet *et al.*, 2007). Nevertheless, some studies proposed another origin for the basement, arguing that the increasing subsidence of the SCB through its history is inconsistent with the normal subsidence behavior of an oceanic crust (Artyushkov, 2007). Artyushkov (2007) proposed the possibility of a deep phase change of gabbro to denser eclogite, process used by Brunet *et al.* (2007) to model the subsidence history of the NCB. The age of the initiation of the subduction of the SCB beneath

Eurasia is also a matter of debate. Allen *et al.* (2002) and Khain *et al.* (2007) calculate, from backstripping of sedimentary columns and structural analysis of the Absheron ridge, a subduction initiation at the end of Miocene (5.5 Ma) while Golonka (2007) and Hollingsworth *et al.* (2008) propose an older origin, spawning from Early to Middle Miocene (15-10 Ma). All the studies mentioned above agree in defining the SCB as a remnant of a marginal sea (Berberian, 1983; Zonenshain & Pichon, 1986; Brunet *et al.*, 2007; Golonka, 2007).

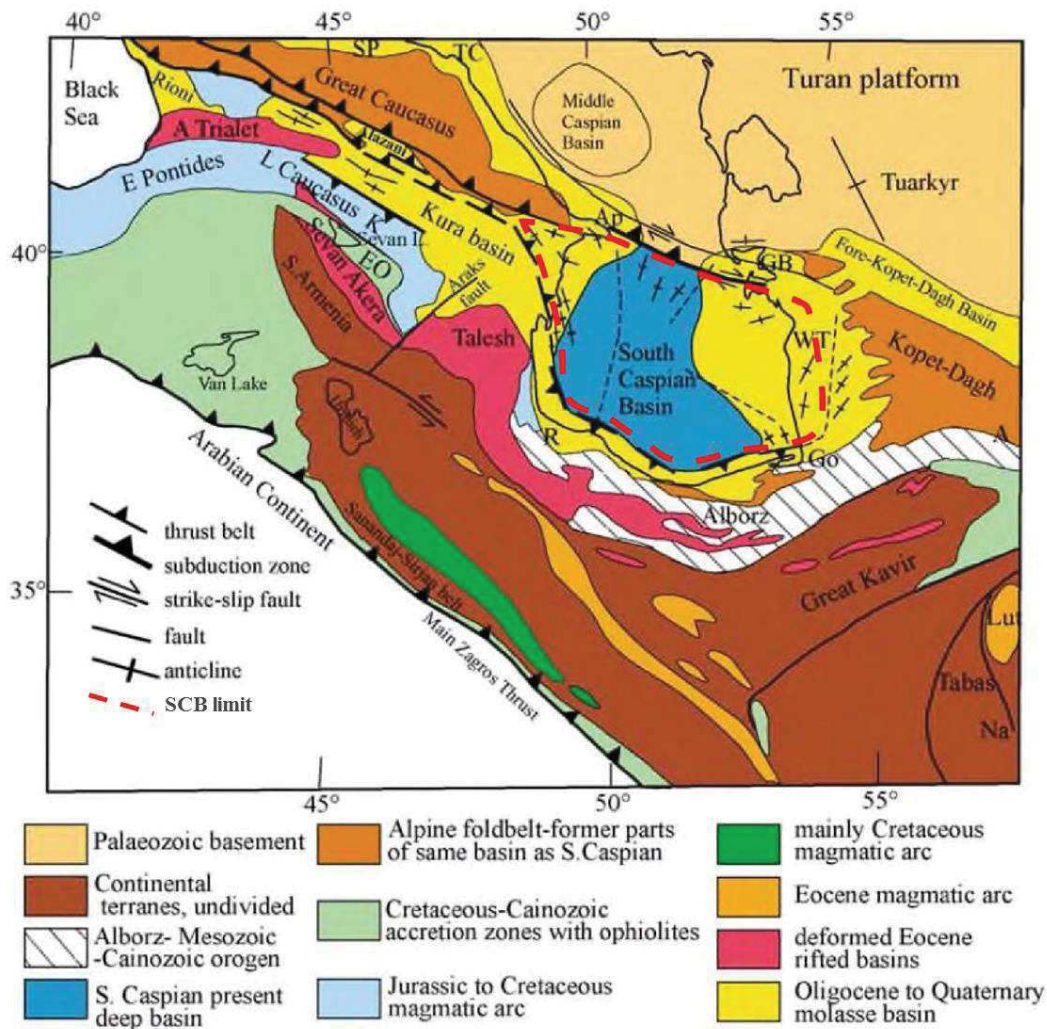


Figure 2.2: Simplified tectonic map of the South Caspian area showing the main tectonic units (modified from Brunet *et al.*, 2003). A: Aghdarband; Ap: Absheron; A Trialet: Achara-Trialet; EO: Erevan-Ordubad; E Pontides: Eastern Pontides; GB: Great Balkhan; Go: Gorgan; K: Karabakh; L Caucasus: Lesser Caucasus; Na: Nayband; R: Rasht; SP: Scythian platform; TC: Terek – Caspian basin; WT: Western Turkmenia. The present SCB is delimited by the red dotted line and is located partly onshore.

The South Caspian Basin is at present delimited to the north by the Absheron Peninsula (Baku) and the Absheron Ridge, to the south by the Alborz massif, to the west by the Greater and Lesser Caucasus and the Talesh Mountains, and to the east by the Kopet Dagh (Figure 2.1 and Figure 2.2; Berberian, 1983; Priestley *et al.*, 1994; Allen *et al.*, 2002; Jackson *et al.*, 2002; Vernant *et al.*, 2004; Engdahl *et al.*, 2006; Golonka, 2007). The Absheron Ridge and Peninsula separate the Central Caspian Basin from the SCB (Khain *et al.*, 2007). The SCB area is an active tectonic province, currently accommodating the convergence between the Arabian and Eurasian plates (Figure 2.2; Priestley *et al.*, 1994; Jackson *et al.*, 2002; Guliev & Panahi, 2004; Vernant *et al.*, 2004; Engdahl *et al.*, 2006; Hollingsworth *et al.*, 2008; Forte *et al.*, 2010).

Global Positioning System (GPS) measurements, distribution of earthquakes around the basin as well as motion on active fault systems allow understanding the present dynamics of the SCB (Figure 2.3; Priestley *et al.*, 1994; Jackson *et al.*, 2002; Guliev & Panahi, 2004; Vernant *et al.*, 2004; Engdahl *et al.*, 2006; Hollingsworth *et al.*, 2008; Forte *et al.*, 2010). Overall, the SCB has a motion to the north relative to Eurasia of 8-10 mm/yr, while the Iran plate has a northward motion relative to SCB of 13-17 mm/yr (Figure 2.3a; Reilinger *et al.*, 1997; Jackson *et al.*, 2002; Vernant *et al.*, 2004; Santos Betancor, 2015). In detail, there is differential motion between the east and the west of the basin, which is accommodated by a series of left-lateral and right-lateral fault systems across the Alborz, Lesser Caucasus and Kopet Dagh mountains (Reilinger *et al.*, 1997; Jackson *et al.*, 2002; Vernant *et al.*, 2004; Santos Betancor, 2015). Indeed, Forte *et al.* (2010) and Reilinger *et al.* (1997) show that the Kura fold and thrust belt (located along the Kura River Basin, see Figure 2.1) and the Greater Caucasus, have been accommodating 30 - 50 % of the total convergence between the Arabian and Eurasian plates since the Early Pliocene. Earthquake distribution and focal mechanisms around the SCB also evidence that the basin area is tectonically active (Figure 2.3b; Priestley *et al.*, 1994; Jackson *et al.*, 2002; Engdahl *et al.*, 2006).

Earthquakes mainly concentrate along the basin borders, while the SCB itself shows little tectonic activity, showing that it behaves as a stable block (Figure 2.3b; Berberian, 1983; Priestley *et al.*, 1994; Jackson *et al.*, 2002). Different focal mechanisms are detected around the SCB, not deeper than 30 km (Figure 2.3b; Jackson *et al.*, 2002). Near the basin edges to the south, west and east, focal mechanisms are mainly related to thrusting, showing the crustal shortening through overthrusting of the various continental blocks over the SCB (Figure 2.2 and Figure 2.3b; Priestley *et al.*, 1994; Engdahl *et al.*, 2006). The oblique shortening between Iran and SCB is partitioned between pure thrust and pure strike-slip at high elevation (Priestley *et al.*, 1994; Jackson *et al.*, 2002; Engdahl *et al.*, 2006). Along the Absheron ridge, earthquake foci are all comprised in a 200 km wide band, at depths varying between 30 and 80 km, showing thrust-related focal mechanisms (Figure 2.3b ; Priestley *et al.*, 1994; Jackson *et al.*, 2002; Knapp, Knapp & Connor, 2004; Engdahl *et al.*, 2006). This, along with the downward bending of the crust seismic horizons from south to north are interpreted as evidence for the northward subduction of the SCB below Eurasia along the Absheron ridge (Priestley *et al.*, 1994; Jackson *et al.*, 2002; Knapp *et al.*, 2004; Engdahl *et al.*, 2006). The low seismic activity recorded within the SCB itself (Priestley *et al.*, 1994; Jackson *et al.*, 2002) is explained by the presence of a thick sedimentary cover sliding over an overpressured detachment level forming high-amplitude folds, and by the presence of numerous mud volcanoes releasing tectonic stress through another process (Jackson *et al.*, 2002; Guliev & Panahi, 2004).

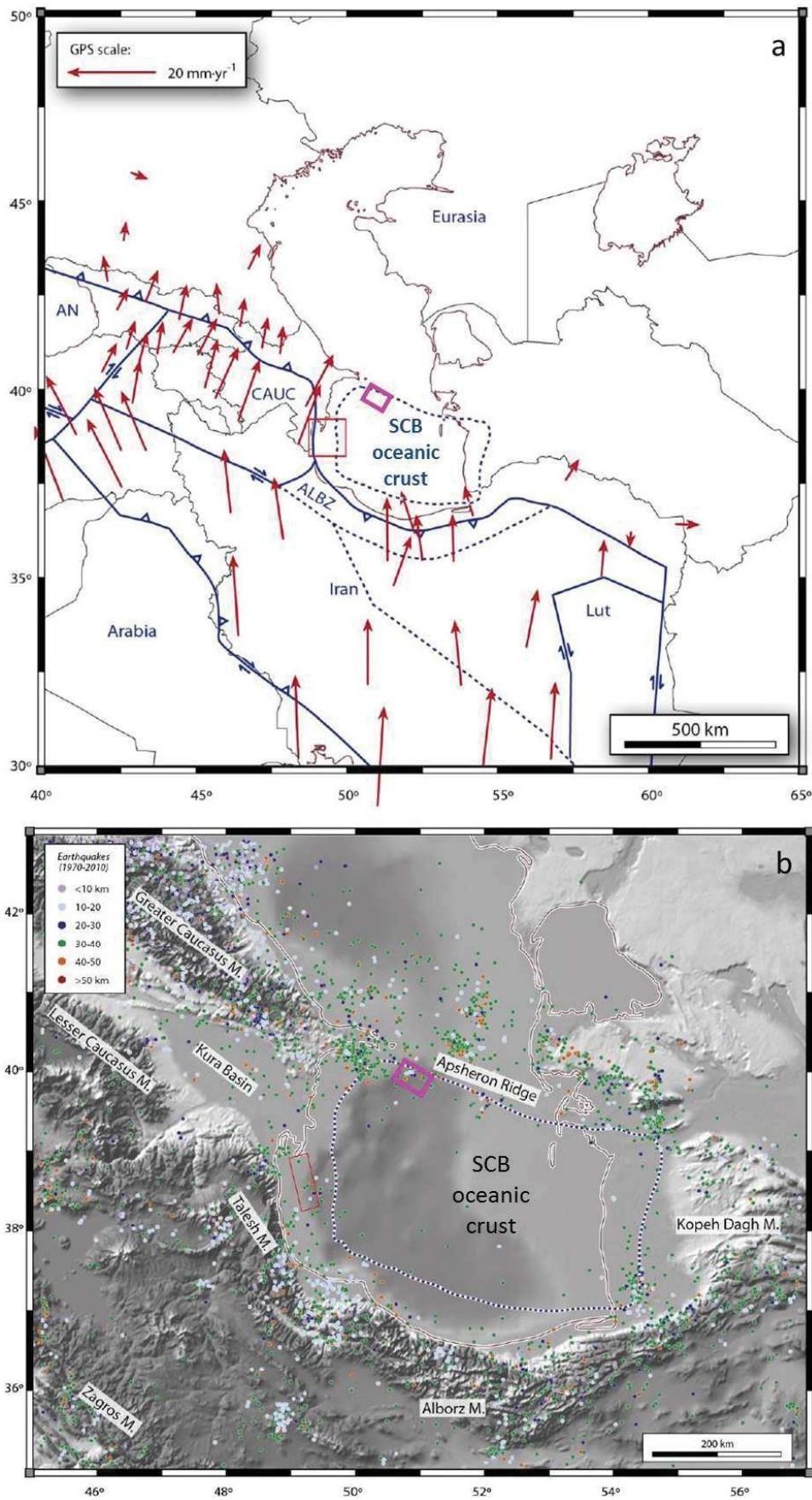


Figure 2.3: a: Simplified structural map of the Caspian area including GPS-derived estimations for plate velocities. ALBZ: Alborz block; AN; Anatolian Plate; CAUC: Caucasus Plate; SCB: SCB Block (modified from Santos Betancor, 2015). b: Map showing earthquakes of the CCB and SCB regions taken from the IRIS catalogue for the period between 1970 and 2010 and classified by depth of their hypocenters (modified from Santos Betancor, 2015). Blue dotted line marks the oceanic crust of the SCB and the purple rectangles show the approximate location of the study area.

Overall, this shortening resulted in an overall uplift of the the surrounding massifs and triggered strong subsidence of the SCB creating space for the thick sedimentary succession that fills the basin (Berberian, 1983; Nadirov *et al.*, 1997; Brunet *et al.*, 2003, 2007; Egan *et al.*, 2009; Guliyev *et al.*, 2011). The subduction created between 2.4 and 6 km of tectonic subsidence in the last 5.5 My which is faster than subsidence recorded in typical foreland basins; this subsidence accommodated the rapid sedimentation recorded in the basin during Pliocene and Quaternary times (Allen *et al.*, 2002; Brunet *et al.*, 2003, 2007; Egan *et al.*, 2009). The intense shortening resulting from SCB northward subduction generated high-amplitude folds, detached over a ductile and overpressured interval (Allen *et al.*, 2002; Jackson *et al.*, 2002; Brunet *et al.*, 2003; Egan *et al.*, 2009).

1.1.2. Paleogeography and regional stratigraphy

The intense and complex tectonic history of the SCB created the conditions to deposit one of the thickest sediment accumulation in the world (Allen *et al.*, 2002; Morton *et al.*, 2003; Knapp *et al.*, 2004; Smith-Rouch, 2006; Artyushkov, 2007; Brunet *et al.*, 2007; Guliyev *et al.*, 2011). Very high sedimentation rates are recorded in the SCB (up to 4.5 km/My), particularly since the Late Miocene, since which nearly 10 km of sediments were deposited subsequently to a rapid fall in the Caspian Sea level (Tagiyev *et al.*, 1997; Allen *et al.*, 2002; Inan *et al.*, 2002; Morton *et al.*, 2003; Smith-Rouch, 2006; Brunet *et al.*, 2007; Egan *et al.*, 2009; Green *et al.*, 2009).

Hereafter, the main regional Mesozoic and Cenozoic stratigraphic units are described in terms of lithology and deposition environment and the lithostratigraphic column synthesizing the main characteristics of each stratigraphic unit is given in Figure 2.4.

Jurassic deposits in the SCB area are widespread in the Greater Caucasus (location in Figure 2.1) where they can reach thicknesses greater than 7000 m (Bochud, 2011; Alizadeh *et al.*, 2017). The sediments were deposited in a back-arc basin environment and mainly consists of deep marine and slope deposits for the Lower and Middle Jurassic and consequently to a regression during the Upper Jurassic, deposits change to shallow marine and slope deposits (Figure 2.4; Golonka, 2007; Bochud, 2011; Alizadeh *et al.*, 2017). Some volcanic and volcano-clastic intervals are also observed in some areas, as well as black shale formations with high organic content (Figure 2.4; Green *et al.*, 2009; Bochud, 2011; Alizadeh *et al.*, 2017).

The thickness of Cretaceous sediments locally exceeds 5000 m in the Greater Caucasus and no depositional hiatus is observed (Bochud, 2011; Alizadeh *et al.*, 2017). They were deposited concordant to Upper Jurassic interval (Figure 2.4; Golonka, 2007; Bochud, 2011). Rapid transitions from siliciclastic turbidite facies to carbonate shelf facies are observed in the cretaceous succession of the Greater Caucasus (Bochud, 2011). Upper Cretaceous deposits are very rich in fossil marine fauna (ammonites, foraminifera, ostracodes) due to the connection to the Paratethys open sea environment (Golonka, 2007; Bochud, 2011).

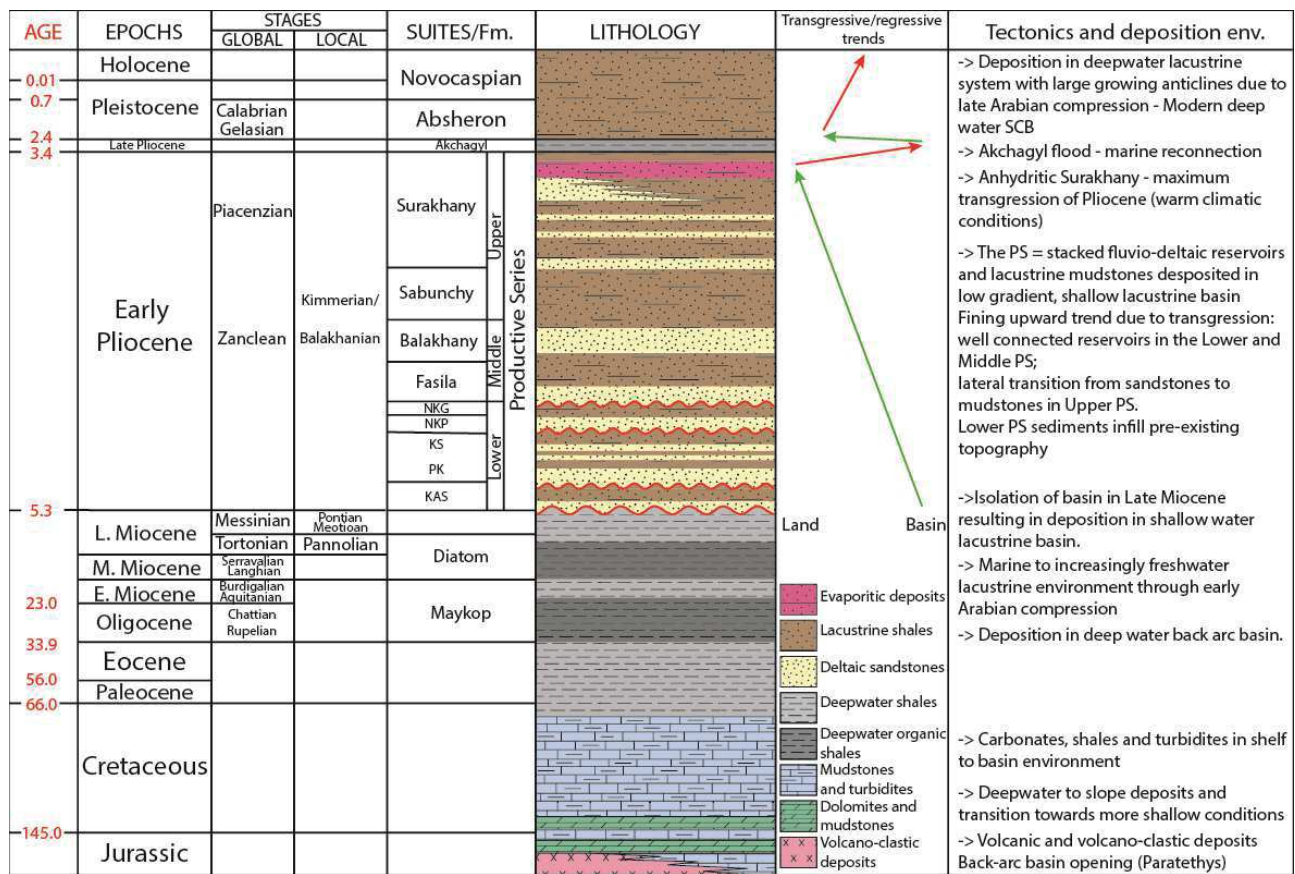


Figure 2.4: Generalized lithostratigraphic column for the SCB. The Jurassic–Miocene sequence is known from outcrops in eastern Caucasus, while the Pliocene and younger section were drilled in the SCB. Ages are given in million years. The Lower PS are subdivided in Kala Suite (KAS), Under-Kirmaky Suite Sandstone (PK), Kirmaky Suite (KS), Above- Kirmaky-Sandstone (NKP) and Above-Kirmaky Shale (NKG). The transgressive and regressive trends are those given by Abreu & Nummedal (2007). Figure adapted and modified from Green *et al.*, (2009) and Javanshir *et al.* (2015).

From Paleocene to Miocene, deep marine conditions prevailed in the area of the SCB leading to the deposition of a thick succession of marine shales (Figure 2.4; Golonka, 2007; Green *et al.*, 2009; Bochud, 2011). Sedimentation in the basin from Late Miocene to Quaternary highly depends on a complex interplay between tectonic and climatic forcing (Abreu & Nummedal, 2007; Krijgsman *et al.*, 2010; Vincent *et al.*, 2010; Choi *et al.*, 2011; Guliyev *et al.*, 2011; Forte & Cowgill, 2013). Tectonic processes, such as basin subsidence and uplift of the surrounding mountain belts, controlled several important factors: the source of sediments changed with the fold and thrust belt building throughout the basin history (Abdullayev, 2000; Morton *et al.*, 2003; Abdullayev & Leroy, 2016), and the location of the main depocenters that drifted with basin differential subsidence through overthrusting differences from west to east (Nadirov *et al.*, 1997; Santos Betancor, 2015). Uplift of the surrounding mountain ranges also controlled periods of basin isolation or reconnection to the global oceanic system (Krijgsman *et al.*, 2010; Forte & Cowgill, 2013), but also the fluvial input of fresh water and sediments (Morton *et al.*, 2003). Basin isolation and fluvial input are also controlled by climatic changes: glacial and interglacial periods influence basin isolation or reconnection through rising of the global oceanic level and more local meteorological variations change the sediment and water supply through rivers (Abdullayev, 2000; Abreu & Nummedal, 2007; Krijgsman *et al.*, 2010; Choi *et al.*, 2011; Forte & Cowgill, 2013).

Isolation and reconnection periods and the input of water through rivers generated high-amplitude sea-level variations that in turn controlled the basin stratigraphy and sedimentation style (Abdullayev, 2000; Abreu & Nummedal, 2007; Vincent *et al.*, 2010; Choi *et al.*, 2011; Guliyev *et al.*, 2011; Forte & Cowgill, 2013). Three main river systems have been supplying sediments to the SCB since the Late Miocene through their paleo-deltas: the Paleo-Kura delta from the west, the Paleo-Volga from the north, and the Paleo-Amu Darya from the east (Figure 2.5; Kroonenberg *et al.*, 2005; Smith-Rouch, 2006; Abreu & Nummedal, 2007; Abdullayev & Leroy, 2016). Depending on the location in the basin, the dominant influence evolve from one to another of the three deltas (Abdullayev, 2000; Abreu & Nummedal, 2007; Vincent *et al.*, 2010; Guliyev *et al.*, 2011; Abdullayev & Leroy, 2016).

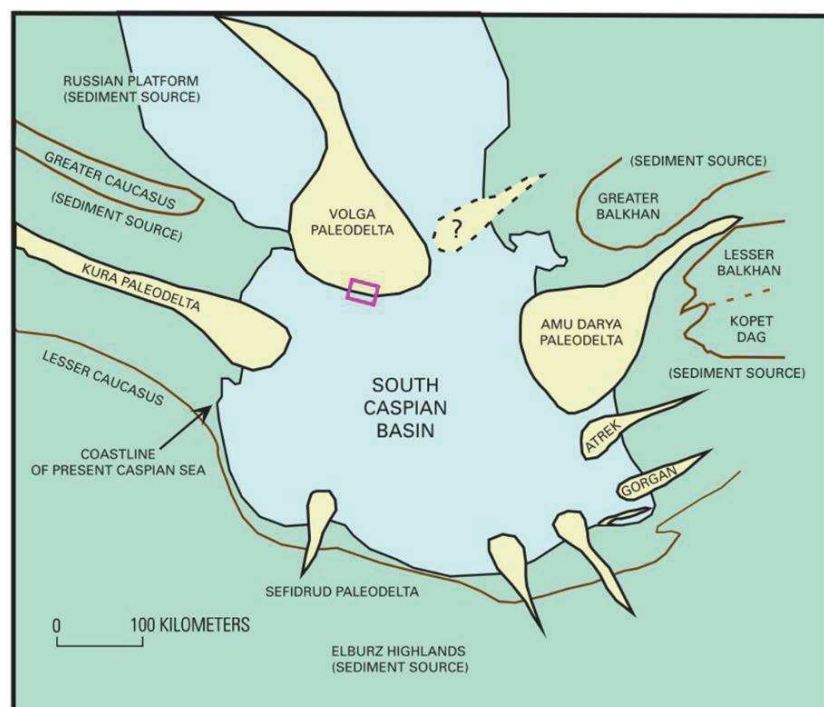


Figure 2.5: schematic map of the Paleo-drainage systems during the deposition of the Productive Series (Late Miocene-Pliocene). The possible sources of sediments are displayed as well as the location of the paleo-deltas. The purple box shows the approximate location of the study area (modified from Smith-Rouch, 2006).

The Maykop Formation, is known as being the main source rock of the Caspian and Black Seas area (Inan *et al.*, 2002; Smith-Rouch, 2006; Hudson *et al.*, 2008; Guliyev *et al.*, 2011) as well as the decollement levels for the high amplitude folds of the South Caspian Basin (Allen *et al.*, 2002; Smith-Rouch, 2006; Green *et al.*, 2009; Santos Betancor, 2015). It was deposited from the Oligocene to the Early Miocene (Figure 2.4; Hudson *et al.*, 2008; Green *et al.*, 2009; Guliyev *et al.*, 2011; Javanshir *et al.*, 2015) unconformably over Mesozoic successions (Knapp, Knapp & Connor, 2004; Javanshir *et al.*, 2015), in a anoxic to suboxic shallow marine environment, when the Parathetys Sea restriction increased and the basin was bordered by topographic highs (Inan *et al.*, 2002; Golonka, 2007; Hudson *et al.*, 2008; Bochud, 2011). The sediments composing this formation are mainly organic-rich and slightly calcareous marine shales with occasional thin interbeds of coarser detrital material brought by the paleo-Volga river from the north (Figure 2.4; Inan *et al.*, 2002; Hudson *et al.*, 2008; Green *et al.*, 2009). The organic matter contained in the Maykop formation is

mainly from marine sources with a low to moderate input of terrestrial organic matter (Inan *et al.*, 2002; Smith-Rouch, 2006; Guliyev *et al.*, 2011). Its thickness varies from north to south, ranging from 200 to 1200 m onshore and from 3000 to 1000 m offshore and is buried below a mean 8 km of more recent sediments in the deepest areas of the basin (Hudson *et al.*, 2008; Green *et al.*, 2009; Bochud, 2011). The Maykop Formation crops out onshore in the Kura sub-basin, but was never drilled offshore (Hudson *et al.*, 2008; Green *et al.*, 2009; Bochud, 2011).

The Middle and Late Miocene sediments were deposited in a context of global regression until the basin isolation after a rapid transgression during early Meotian (local equivalent of the Messinian), reconnecting the Paratethys and the Mediterranean Sea (Smith-Rouch, 2006; Krijgsman *et al.*, 2010; Forte & Cowgill, 2013). These sediments are thick clays and diatomic shales deposited in a shallow marine and lacustrine environment, and comprise another organic rich interval, the Diatom Formation (Figure 2.4; Hudson *et al.*, 2008; Bochud, 2011; Guliyev *et al.*, 2011; Javanshir *et al.*, 2015; Santos Betancor, 2015). Some evaporite deposits are found in the Pontian, which is the regional equivalent for the Messinian (Krijgsman *et al.*, 2010; Forte & Cowgill, 2013; Santos Betancor, 2015).

The Pliocene was dominated by deltaic and lacustrine environment during a regression phase (Figure 2.4), with sediment input coming from all the topographic highs surrounding the basin through the three main paleo-rivers (Figure 2.5; Morton *et al.*, 2003; Abreu & Nummedal, 2007; Vincent *et al.*, 2010; Choi *et al.*, 2011; Forte & Cowgill, 2013; Abdullayev & Leroy, 2016). These deposits, known as the Productive Series (PS) Formation, are mainly composed of an alternation of connected or isolated sandstone to siltstone bodies and continuous mudstone intervals (Hinds *et al.*, 2004; Vincent *et al.*, 2010; Choi *et al.*, 2011). The PS Formation is discordant over the Middle Miocene interval (Knapp *et al.*, 2004; Abreu & Nummedal, 2007). The sedimentation rate was at its highest magnitude, reaching occasionally 4.5 km/My, with up to 6 km of PS that were deposited (Tagiyev *et al.*, 1997; Smith-Rouch, 2006; Brunet *et al.*, 2007; Egan *et al.*, 2009; Green *et al.*, 2009). The subduction-related subsidence of the end of Miocene created enough space to accommodate such a thickness of deltaic deposits (Allen *et al.*, 2002).

Their lithology strongly varies depending on the location regarding the three main paleo-deltas (Figure 2.5; Morton *et al.*, 2003; Vincent *et al.*, 2010). The Fig. 8 in Green *et al.* (2009) shows the stratigraphy of the PS. It illustrates the complex geometry arising from the paleo-deltas input and their variation with space and time. However, in the SCB area the Lower PS mainly consist of channelized and sheet flood fluvial deposits alternating with lacustrine mudstones, and the Upper PS consists of amalgamated braided fluvial sandstones alternating with alluvial plain and lacustrine deposits (Hinds *et al.*, 2004; Abreu & Nummedal, 2007). The stratal succession correspond to high-frequencies climatic cycles, sandstone facies being deposited during lowstand periods and mudstone facies corresponding to transgression and highstand deposits (Abreu & Nummedal, 2007). The sandstone facies is more continuous in the Lower PS and in the Kura Basin forming hydraulic connection throughout the SCB, while the Upper PS sandstones are less

connected displaying an overall fining-up trend (Figure 2.4; Hinds *et al.*, 2004; Javanshir *et al.*, 2015). At the top of the Surakhany Formation, the final stage of PS deposition, the regression is maximal and evaporitic beds are deposited in the northern part of the basin (Javanshir *et al.*, 2015; Dupuis, 2017). Farther south, an erosional event is recorded without evaporitic deposition (Santos Betancor, 2015). This interval will be called Anhydritic Surakhany hereafter.

The Akchagyl Formation was deposited on a period extending over 700,000 years during the Late Pliocene (2.4-3.4 My) and was not deposited synchronously over the whole basin (Forte *et al.*, 2015). It was deposited during a major regional transgression, after a marine flooding event through a reconnection of the Caspian Sea with the Black Sea and potentially with the Mediterranean (Green *et al.*, 2009; Bochud, 2011; Forte & Cowgill, 2013). In several location of the Kura Basin, the Akchagyl Formation lies unconformably over older Miocene intervals due to this regional transgression (Bochud, 2011). The Akchagyl Formation is a condensed interval and its composition varies between shallow marine and fresh water facies (western part of Kura Basin), and deep water clayey facies interlayered with mud-rich turbidites in the SCB (Figure 2.4; Abdullayev, 2000; Green *et al.*, 2009; Bochud, 2011; Santos Betancor, 2015). The mud-rich turbidites were supplied by the Paleo-Amu Darya (Figure 2.5; Abdullayev, 2000).

The Absheron Formation was deposited from the Early Pleistocene (2.4 Ma) to present during a transgression and the subsequent regression (Green *et al.*, 2009; Forte & Cowgill, 2013; Santos Betancor, 2015). The Absheron deposits consist of prograding and deepwater fan systems and slumps (Abdullayev, 2000; Green *et al.*, 2009). Their lithology varies from clays to sandstones with some shell-rich limestone occurrences, volcanic ashes and conglomerates (Figure 2.4; Bochud, 2011; Santos Betancor, 2015). The depositional environment that prevailed was similar to the present situation: deep-water lake with brackish conditions (Abdullayev, 2000; Green *et al.*, 2009; Forte & Cowgill, 2013; Santos Betancor, 2015). The Novocaspian Formation is differentiated from the Absheron Suite on several studies (Abdullayev, 2000; Imbert *et al.*, 2014). This formation corresponds to deposits younger than 0.7 Ma and are mainly deep lacustrine shales (Figure 2.4; Green *et al.*, 2009; Imbert, Geiss & Fatjó de Martín, 2014).

1.1.3. Oil & gas potential and mud volcanism

The South Caspian Basin is one of the most prolific hydrocarbon (HC) provinces in the world and has been exploited for more than 150 years (Smith-Rouch, 2006; Abreu & Nummedal, 2007; Alizadeh *et al.*, 2017). Areas like the Absheron Peninsula, Absheron Ridge, the Kura basin and the Shelf margin of Azerbaijan have been intensively explored and produced (620 oil and gas fields discovered) while the deep water SCB and Turkmenistan shelf are areas less understood and remain frontier exploration areas (Smith-Rouch, 2006; Abreu & Nummedal, 2007; Alizadeh *et al.*, 2017).

The first favorable factor for the presence of such HC accumulations in the SCB region is the presence of several mature source rocks (Tagiyev *et al.*, 1997; Inan *et al.*, 2002; Smith-Rouch, 2006; Guliyev *et*

al., 2011). In particular, the Maykop Fm. (Figure 2.4) is known for its high HC generation potential as it is very rich in organic carbon with TOC (Total Organic Carbon) as high as 12.4 % (Smith-Rouch, 2006; Guliyev *et al.*, 2011). Moreover, this source rock (SR) has a Hydrogen Index (HI) of 588 mgHC/gC_{org} (Guliyev *et al.*, 2011), which correspond to the mass of HC generated by 1 gram of organic carbon, and in this case the HI value shows that the source rock has a very good to excellent HC generation potential (Peters & Cassa, 1994). The Maykop Fm. contains mainly type II kerogens, corresponding to marine organic matter in anoxic environments, with small input of type III kerogen corresponding to terrestrial organic matter (Smith-Rouch, 2006; Guliyev *et al.*, 2011). The Diatomaceous Formation (Figure 2.4) is also known to have good SR properties (Smith-Rouch, 2006; Guliyev *et al.*, 2011). Both SR formations are known from samples recovered from outcrops, onshore hydrocarbon wells or mud volcano ejecta. The first two sources of material yield samples that have not been deeply buried (Smith-Rouch, 2006; Guliyev *et al.*, 2011). Some older condensed intervals are also good SRs such as intervals in Middle Jurassic, Lower Cretaceous or Eocene (Inan *et al.*, 2002; Smith-Rouch, 2006; Guliyev *et al.*, 2011). High sedimentation rates during the Pliocene created low thermal gradient (13-18 °C/km) but also highly overpressured conditions in the Maykop (40 MPa at 10 km below seafloor) that stayed under-compacted, thus acting as a detachment level for the Pliocene and Quaternary folding (Tagiyev *et al.*, 1997; Inan *et al.*, 2002; Smith-Rouch, 2006; Brunet *et al.*, 2007; Guliyev *et al.*, 2011). From temperatures and vitrinite reflectance values, the oil generation window and gas generation window are presently respectively located between 5-7.5 km and 7.5-12 km on the shelf and continental slopes and between 8-11 km and 11-14 km in the deeper part of the basin (Tagiyev *et al.*, 1997; Guliyev *et al.*, 2011). The most intense oil generation period was reached during the last 5.2 My as shown in the chart in Figure 2.6 (Tagiyev *et al.*, 1997; Inan *et al.*, 2002; Smith-Rouch, 2006).

The other important element is the presence of the fluvio-deltaic PS succession which was deposited with very high sedimentation rates, therefore creating an under-compacted and overpressured strata with sandstones keeping very good reservoir properties (Figure 2.6; Smith-Rouch, 2006; Guliyev *et al.*, 2011; Javanshir *et al.*, 2015). Besides, the alternation of sandstones and mudstones created potential stratigraphic traps allowing HC to stay accumulated in laterally connected reservoirs (Figure 2.6; Smith-Rouch, 2006; Abreu & Nummedal, 2007; Guliyev *et al.*, 2011; Javanshir *et al.*, 2015). The reservoir quality of sandstone highly depends on the sediment source: Vincent *et al.* (2010) show that petrophysical properties of sandstones of the Kura Basin are better than those of the Absheron Peninsula due to the input of higher volume of coarser-grained bodies through the Paleo-Kura delta. The reservoir quality also depends on the age of the considered interval. Several authors showed that the most continuous and extensive sandstone bodies are those from the Fasila Suite in the Middle PS (Figure 2.4), those from the Lower PS being less connected and the Upper PS having a fining upward trend (Hinds *et al.*, 2004; Choi *et al.*, 2011; Guliyev *et al.*, 2011; Javanshir *et al.*, 2015). The stratigraphic observations and pressure obtained from several drilling sites throughout the SCB shows that there is a pressure gradient from the deeper central SCB towards the basin edges to the NW (Tagiyev *et al.*, 1997; Javanshir *et al.*, 2015). Therefore, oil and gas probably migrate in the same direction

(Tagiyev *et al.*, 1997; Guliyev *et al.*, 2011), but their migration is most of all impacted by tectonic structures such as folds and faults that trap HC (Imbert, pers. comm., 04-06-2019). Grosjean *et al.* (2009) and Javanshir *et al.* (2015) show that hydrodynamism results in tilting of the HC-water contacts, thereby shifting HC accumulations towards the N flanks of anticlines.

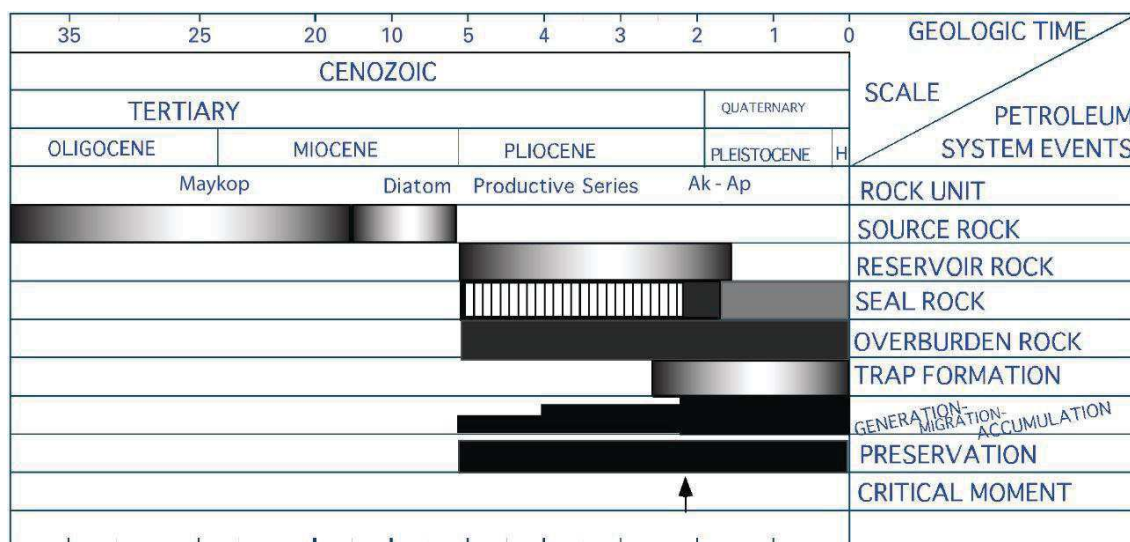


Figure 2.6: HC generation and accumulation temporal chart for the Oligocene–Miocene Maykop/Diatom Total Petroleum System in the South Caspian Basin Province. Ak-Ap: Akchagyl and Absheron intervals. The critical moment correspond at the time when all the criteria for oil & gas generation, accumulation and preservation were present and correspond to the Akchagyl strata deposition (from Smith-Rouch, 2006).

The deposition of thick deep water marine mudstones during the Quaternary period allowed the whole Oligocene-Pliocene interval to be deeply buried and trapped below an efficient thick seal (Figure 2.6; Abdullayev, 2000; Smith-Rouch, 2006; Green *et al.*, 2009; Bochud, 2011).

The intense compression caused by Arabic Plate convergence towards Eurasia coupled with the presence of a good detachment level allowed the creation of high-amplitude folds in all the SCB and Kura Basin from Pliocene to present (Allen *et al.*, 2002; Knapp *et al.*, 2004; Smith-Rouch, 2006; Forte *et al.*, 2010). They form topographic highs in reservoirs, creating excellent structural traps for HC (Figure 2.6; Smith-Rouch, 2006; Guliyev *et al.*, 2011; Javanshir *et al.*, 2015). Many anticlines are cored by deeply rooted thrusts and overpressured mobile Maykop creating potential vertical pathways for HC fluids (Smith-Rouch, 2006; Guliyev *et al.*, 2011; Santos Betancor & Soto, 2015).

The SCB is also known for the presence of numerous MVs onshore and offshore (Milkov, 2000; Dimitrov, 2002; Kopf, 2002; Yusifov & Rabinowitz, 2004). Most of the studied MVs are interpreted as being sourced from the Maykop from geochemical and biostratigraphic analysis of clasts onshore and from geometric considerations offshore (Dimitrov, 2002; Kopf, 2002; Yusifov & Rabinowitz, 2004; Stewart & Davies, 2006). However, some authors argue that other sources may be possible, in particular for recent or active structures where the Maykop is deeply buried (Yusifov & Rabinowitz, 2004; Dupuis, 2017; Blouin *et al.*, 2019). One general observation is that all the observed MVs are aligned along or near the anticline crests

(Fowler *et al.*, 2000; Yusifov & Rabinowitz, 2004; Stewart & Davies, 2006; Roberts *et al.*, 2010; Dupuis, 2017; Blouin *et al.*, 2019). Fowler *et al.* (2000) and Yusifov & Rabinowitz (2004) correlated the MV formation to the growing of folds, the timing of HC generation and accumulation and to high sedimentation rates during Pliocene.

1.2. Absheron fold: gas-condensate field and geohazards

Total has been operator of the Absheron gas condensate field (see location in Figure 2.1), located 100 km at the SW of Baku, since 2009, with a first major discovery in 2011 (Gautherot *et al.*, 2015). This gas field could represent reserves of 350 billion cubic metres (Bcm) of gas and 45 million tons of gas condensate and production may start in 2021 (*Wikipedia: Absheron gas field*, 2018).

The exploration phase between 1997 and 2006 started with a first well drilled with no HC discovered and a 650 km² 3D seismic survey acquired (Gautherot *et al.*, 2015; Unterseh & Contet, 2015). A first estimation of geohazards was conducted based on seismic data, evidencing the active AMV, regional scale MTCs and a large slope failure scar at seabed (Unterseh & Contet, 2015). Imbert, Geiss and Fatjó de Martín (2014) studied the presence of a buried, subcircular crater, filled with MTCs interpreted as being potentially the result of fluidification of sediments due to gas exsolution triggered by unloading of the strata by a massive slump. The MV was notably assessed in terms shallow geometry and a comparison to onshore flat MVs by Dupuis (2017). Up to three massive bevel-shaped thrust mudflows were described from the seismic data (Dupuis, 2017).

However, the resolution of the seismic data is not sufficient in order to assess with precision the geohazards over the Absheron field and notably to understand the recent activity of the AMV (Contet & Unterseh, 2015; Unterseh & Contet, 2015). The high-resolution geophysical and geotechnical data highlights the shallow complexity and geohazards at the Absheron site, mostly due to the interaction of several factors such as tectonics, mud volcanism, mass transport deposits and gaseous fluid upward migration (Unterseh & Contet, 2015). Gas migration generates several geohazards, such as shallow gas and the potential slope failure it may trigger, the presence of the active MV, seepages through faults and pockmarks (Unterseh & Contet, 2015). The high-resolution data also allows evidencing five recent mudflows as well as detail on the surface structure of the AMV with several gryphons and mud pies (Kieckhefer *et al.*, 2003; Contet & Unterseh, 2015; Dupuis, 2017). Contet & Unterseh (2015) dated these mudflows using palynological and biostratigraphic analysis of hemipelagites draping the mudflows and concluded that the AMV was active for the last 5000 years BP. They also evidenced that the last major recorded mudflow dated from 735 years BP, showing that the last major eruption is older than the mean time recurrence between mudflow (500 years), concluding that the area surrounding the AMV is not safe for drilling operations as the AMV may erupt in the near future (Contet & Unterseh, 2015). Dupuis (2017) calculated the volume of these five young events: each mudflow represent at least 0.5 km³ of mud.

MTCs are a major feature in recent stratigraphic intervals (Absheron suite, Figure 2.4), and Imbert, Geiss & Fatjó de Martín (2014) identified 4 MTCs in this interval. Dupuis (2017) shows that MTCs interact with the AMV: MTCs abut on the AMV, deform around the volcano and finally deviate from their initial direction.

2. Data acquisition and location

2.1. 3D seismic survey

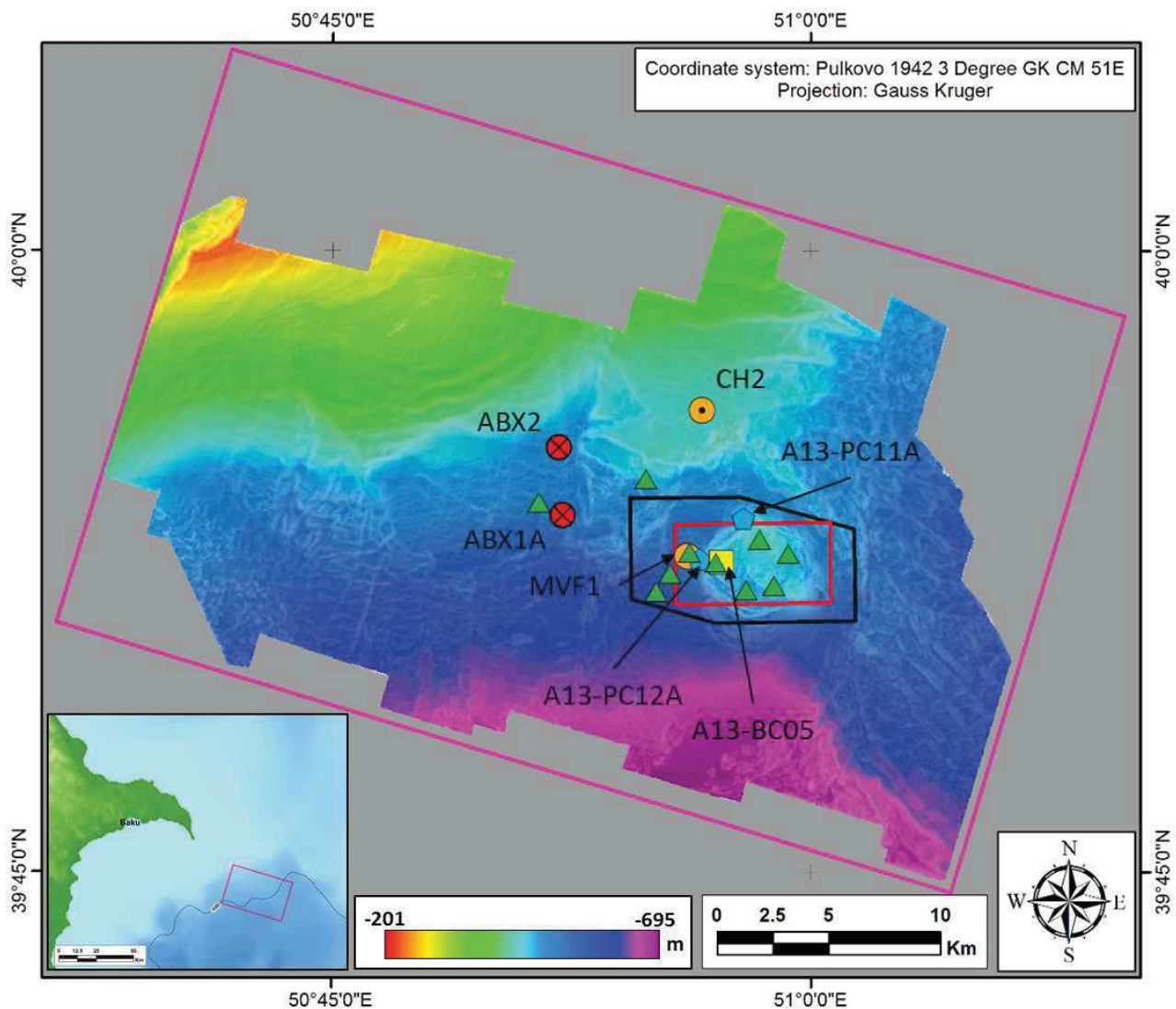


Figure 2.7: Seafloor depth map extracted from the 3D seismic survey, showing the location of the other surveys and samples used during this research. The AMV is visible as a light blue patch where the dataset is denser. Seafloor depth is given in meters below mean sea level. The Purple rectangle shows the maximum extent of the 3D seismic survey, the black polygon shows the extent of the multibeam echo sounder survey, and the red rectangle, the area where backscattering image was processed. Samples are represented with different symbols depending on their type. Red circles with crosses: exploration wells; orange circles with dots: rotary drillings and CPT measurements; blue pentagons: piston cores from AUV survey, 2014; yellow square: box core from AUV survey, 2014; green triangles: samples for biostratigraphy from Chevron survey, 1999.

The 3D seismic volume covers 650 km², in water depths ranging from 180 to 700 m (Figure 2.7). The seismic sections presented in this thesis are from Kirchhoff pre-stack time migration (PSTM) processing and pre-stack depth migration (PSDM) reprocessing (Robein, 2010), which was applied on 550 km² of the seismic

survey. The velocity model used in the reprocessing aimed to improve the imaging of the deep structures (thrust, dips), taking into account the lateral velocity variations across the thrust as well as the velocity heterogeneity in the shallow intervals due to the presence of the mud volcano and free gas (F. Adler, 12/12/2018, personal communication). The model parametrization is a vertical transverse isotropy (VTI) that considers the vertical anisotropy imposed by the sedimentary strata (Robein, 2010). The model was entirely built by tomographic inversion (Robein, 2010), and in the deep part, it was corrected using an interpretative method in order to preserve the structural coherency and to fit the well data (F. Adler, 12/12/2018, personal communication). The seismic volume is composed by 2203 inlines and 2120 crosslines with 12.5 m inline and 18.5 crossline spacing. The vertical resolution varies with depth as it depends on interval velocity. From visual observations of the sections, we estimate a resolution ca. 20 m in the strata above 2000 m, progressively decreasing to 150 m at 11 km.

2.2. Geotechnical and geophysical survey

A marine geological and geotechnical survey of the seabed above the Absheron gas discovery was carried out in 2014 in order to better constrain and delineate geological hazards associated with the mud volcano (Contet & Unterseh, 2015; Unterseh & Contet, 2015). The different data presented hereafter are extracted from several confidential Total proprietary reports written and produced by Fugro Survey Limited Caspian (G. Dan & S. Po, 12/09/2017, personal communication).

2.2.1. Geophysical dataset

An AUV-mounted multibeam echosounder (MBES Kongsberg EM 2040; Horvei & Nilsen, 2010) was used to acquire a high-resolution map to study the detailed surface morphology of the AMV (Figure 2.7; Contet & Unterseh, 2015; Unterseh & Contet, 2015). The AUV survey was carried out along 228 NNE-SSW directed inlines with 175 m of spacing and 88 crosslines oriented WNW-ESE with a spacing ranging from 500 m to 1 km. The AUV navigated at 60 m above seafloor on inlines to guarantee maximum coverage and 40 m above seafloor on crosslines. The bathymetry is obtained from the two-way travel time of the emitted signal (Zitter, 2004). The bathymetric map has been processed with a resolution of 3 m by 3m (Contet & Unterseh, 2015). The backscatter map was also acquired, allowing estimating seafloor roughness and differentiating mudflow deposits and clasts from the surrounding hemipelagic sediments (Zitter, 2004). Backscatter map results from the calculation of the energy of the incident signal dispersed at the contact of irregular surfaces (Zitter, 2004).

In parallel of MBES, a chirp Sub-bottom profiler mounted on the AUV allowed imaging the shallow succession of sediments over and around the AMV with a vertical resolution of 0.3 m and a penetration of 40 to 50 meters below seafloor (Contet & Unterseh, 2015). The velocity used in order to convert in depth the different time sections was 1500 m/s, which was measured from in situ on rotary drilling sites.

2.2.2. Coring and in situ mechanical measurements

The geotechnical/geological survey from 2014 includes rotary drilling, AUV (Autonomous Underwater Vehicle) sampling with a box corer and a 6 m long Kullenberg piston corer (Kullenberg, 1947) as well as in situ geotechnical testing (CPTu, Cone Penetration Testing; Lunne, 2010) in and around the AMV (Figure 2.7). Well logging and CPT were performed on two boreholes using the Seafloor Drill equipped with a penetration and coring system (Total proprietary report, G. Dan & S. Po, 12/09/2017, personal communication): CH2 was located outside the mud volcano area to provide a stratigraphic reference in continuous series, and MVF1 sampled on a mud volcano flow (Figure 2.7).

CPTu is an in situ penetration test procedure consisting in pushing vertically in sediments a steel rode and allowing measuring the soil resistance (Lunne *et al.*, 1997; Boggess & Robertson, 2011). Integrated probes allow a continuous recording of penetration depth, cone resistance, sleeve friction and in situ pore pressure which is measured through a differential pore pressure sensor (Lunne *et al.*, 1997; Boggess & Robertson, 2011). The well logging consisted notably in measuring the in situ acoustic properties of sediments (P-wave and S-waves) by emitting signals from a source and receiving them at several (Total proprietary report, G. Dan & S. Po, 12/09/2017, personal communication). Measurements were either made during penetration interruption (Seismic CPT) through downhole tests where the penetration rode includes geophones, either once the penetration tests reached their maximum depth after borehole casing. In the latter, geophones are placed at given depth for each measurements (Total proprietary report, G. Dan & S. Po, 12/09/2017, personal communication).

Along with CPT logging, rotary drilling allowed the sampling of 35 meters of sediment, notably coring through several mudflows (Total proprietary report, G. Dan & S. Po, 12/09/2017, personal communication). These samples allowed the dating of the drilled recent mudflows using pollen content and radiocarbon (^{14}C) (Contet & Unterseh, 2015). Another offshore survey was completed in 1999 by Chevron in order to date the mud emitted at the AMV using biostratigraphic content in the mud breccia clasts and the mud matrix. Several samples were collected at several locations, notably on the main mudflow (Figure 2.7).

2.3. Exploration wells

During exploration and appraisal stages of the Absheron field, two exploration wells were drilled. The first one, ABX-1A was drilled by Chevron in 2001 on the southern flank of the Absheron anticline and reached 6529 m TVD/MSL (True Vertical Depth below Mean Sea Level) and no commercially productive HC reservoirs was discovered. A second exploration well was drilled by Total in 2011 on the northern flank of the Absheron anticline and reached 6823.5 m TVD/MSL. The well discovered gas in several reservoirs of the Middle and Lower PS. Locations of both wells are given in Figure 2.7. During drilling, several measurements and analyses were carried out and two types of logging tools were used: LWD (Logging While Drilling) tools, which are attached to the drill string and allows logging without stopping drilling operations and WL (Wireline) tools

that are brought down in the borehole when the drilling bit is out. We used LWD recordings preferred for first stratigraphic correlations and wireline logs to get more detailed measurements over specific intervals.

The main source for the principles of log data acquisition and interpretation presented hereafter are the Crain's Petrophysical Handbook online (Crain, 2018), which is updated annually.

2.3.1. Gamma-ray and caliper logs

Three radioactive elements (Potassium, K, Thorium, Th, and Uranium, U) are widespread in nature, as main constituents of some common or accessory minerals (e.g. K in some feldspars and clay minerals derived from their alteration, or in K-evaporites; Th in monazite), or can be adsorbed like U on organic matter (Howell & Froscht, 1939; Marett *et al.*, 1976; Crain, 2018). As a result, rocks and sediments, depending on their mineral content naturally emit a certain amount of gamma radiation (Howell & Froscht, 1939; Marett *et al.*, 1976; Crain, 2018). Gamma ray (GR) logging tools measure the amount of GRs emitted by the formations surrounding them in an open or cased borehole, which is commonly correlated to the amount of clay minerals present among sediments, as they are rich in radioactive potassium and can charge in uranium and thorium through cationic exchange capacity (Howell & Froscht, 1939; Crain, 2018). Therefore, this tool allows differentiating between clay-rich lithologies (shales, claystones) and other lithologies (Marett *et al.*, 1976; Segesman, 1980; Crain, 2018). However, no distinction is possible through this tool between sandstones and carbonates for instance. The maximum GR value recorded in a formation containing shale is generally referred to as the shale base line. Any deflection to smaller GR values indicates the presence of non-radioactive minerals, typically quartz grains or carbonates formation is getting coarser (Abdelaziz, 2016).

The caliper log continuously records the diameter of the borehole, allowing to control its integrity (Segesman, 1980; Snyder & Fleming, 1985). The tool uses several articulated arms that are kept in contact with the wall of the drill hole, so it can record any variation of its diameter (Segesman, 1980). As the resistance of the wall highly depends on the constitutive sediment mechanical properties and cohesion, the variation of the size and shape of the borehole can be related to lithologies and correlates most of the time with GR log. For instance, shales have a tendency to swell or to form cavings during drilling operations, while permeable sandstones may absorb the filtrate of drilling fluids and leave the solid fraction as a "mud cake" on the borehole wall.

2.3.2. Sonic logs

Sonic tools consist of an acoustic source (with a typical frequency of 10-20 kHz) and at least 2 receivers mounted 2 feet apart on the logging tool and rely on Snell's law describing the propagation of acoustic waves at an interface of two different materials (Segesman, 1980; Crain, 2018). The acoustic velocity in fluid-saturated rocks is governed by physical properties synthesized in the Biot-Gassmann equations (Biot, 1956; Crain, 2018). Borehole wall sediments generally have a significantly higher acoustic velocity than the drilling

mud, so that the first signal received at the receivers is the signal refracted through the intact formation (while the direct wave propagating in the mud is received afterwards); the tool typically measures the time difference between first arrivals at two receivers mounted 2 feet apart, directly providing a slowness in $\mu\text{s}/\text{m}$ (the inverse of the velocity; Crain, 2018). Using at least two receivers allows compensating for the variations in drilling mud thickness (Segesman, 1980).

Empirical relationships are commonly used to estimate formation density and porosity from acoustic velocity (Wyllie *et al.*, 1958; Segesman, 1980). In addition, the presence of free gas in formation fluids decreases acoustic velocity, so that the presence of gas may be detected on sonic logs (Helgerud *et al.*, 1999).

2.3.3. Density log

This sidewall tool emits GR from an artificial radioactive source into an uncased drilled formations (Segesman, 1980; Snyder & Fleming, 1985). The GR interacts through Compton scattering process (Compton, 1923) with the electron cloud of the different elements present in the sediments (solids and fluids) and loses energy (Snyder & Fleming, 1985; Abdelaziz, 2016; Crain, 2018). The detector of the logging tool, a scintillation counter, measures the intensity of the back-scattered GR, which is inversely proportional to the electron density of the formation, itself relating directly to its bulk density (Snyder & Fleming, 1985; Abdelaziz, 2016; Crain, 2018). The density of the formation depends on its lithology, its porosity and the density and saturation of the pore fluids (Abdelaziz, 2016). Dense formations will absorb more GR than low-density formations as they are formed by heavier elements having a denser electronic cloud.

2.3.4. Neutron logs

The neutron logs allows quantifying the porosity of the drilled formations and can be used as a determining factor for lithology when coupled to a density log (Segesman, 1980; Abdelaziz, 2016; Crain, 2018). The logging tool is equipped with a neutron source that emits neutron with a high velocity into the sediments. Neutrons interact with hydrogen atoms contained in the tested formation through elastic scattering mechanism, slowing down until being captured by atoms (Snyder & Fleming, 1985; Abdelaziz, 2016; Crain, 2018). Therefore, the richest in hydrogen the formation will be, the faster neutrons will be slowed down. The neutron porosity measures altogether the drilling mud, the hydrocarbon portion (present in the pore space), the shale portion and the matrix portion each one of them containing hydrogens (Abdelaziz, 2016; Crain, 2018). The presence of HC fluids, and in particular methane, will generates a neutron porosity that is smaller, allowing to detect the presence of gas accumulations when combining the neutron log with other porosity logs (such as density logs).

2.3.5. Resistivity logs

This method consists in characterizing the sediments surrounding the borehole by measuring its electrical resistivity, namely the capacity that the material has to oppose the circulation of an electric current

(Crain, 2018). In boreholes, rocks and sediments acts as electric insulators, while the fluids they contain acts as conductors with the exception of HC fluids, which are even more resistive than sediments. Therefore, resistivity logs are a good tool for detecting HC during drilling operations (Geary, 2018). Classical resistivity logs have to be acquired in a borehole saturated with conductive mud or water (Geary, 2018). Oil-based drilling muds are very resistive so that electrical current is not able to circulate and to reach the tested formation (Doll, 1949; Snyder & Fleming, 1985). Therefore, in wells where oil-based drilling mud is used, resistivity is measured through induction tools (Doll, 1949; Snyder & Fleming, 1985). The electrical current is induced into the tested formation based on Maxwell's equations that gives the foundation of electromagnetism (Crain, 2018). Thus, the probe does not need to be in direct contact with the borehole wall (Doll, 1949).

Several source/receiver couples are used to measure resistivity, the distance between each source and each receiver being designed to measure resistivity at a certain distance from the borehole (Doll, 1949; Geary, 2018). Resistivity logs are used in the assessment of porosity, water saturation and presence of HC (Snyder & Fleming, 1985; Crain, 2018). Moreover, if permeability is low, drilling fluids will not be able to invade the pore space and will stay close to the borehole walls. Thus, resistivity measured in the close field and far field may be different as fluids allowing current to circulate are different. Conversely, if permeability is high, drilling fluids will be able to flow into the pore space, implying that close field and far field resistivity will be identical. Thus, resistivity logs allow to test the permeability of the drilled formations (Crain, 2018; Geary, 2018).

2.3.6. Lithology

Lithology at both wells is interpreted from the logs, calibrated by the analysis of ditch cuttings, which are fragments of solid material from the drilled stratigraphic intervals. They are produced from the rocks broken by the advance of the drilling bit and are moved to the surface along with the drilling mud that circulates in order to keep the borehole open by sustaining a pressure higher than the formation pressure. The cuttings are then separated from drilling fluids using shakers or centrifuges. They are sampled by the wellsite geologist at regular intervals, e.g. every 10 or 20 m in intervals with limited economic interest and every 5 m in intervals of specific interest. The mud logger or wellsite geologist then studies each interval. Visual observation and mineral recognition as well as X-ray diffractometric measurements allows defining the mineral composition and lithology on each studied interval. However, these analysis may be either polluted by drilling mud components (notably barite when high formation pressure are encountered) or samples are washed taking the risk to lose the finer fraction composing the interval lithology (clay minerals notably).

The GR, caliper and resistivity LWD logs along combined with cutting analysis allows reconstructing a preliminary lithological log describing the sediment succession drilled and presented in the "quick-look" log

which is plotted during drilling operations (Figure 2.8a). This log is then detailed, completed and corrected using the other type of acquired data like the sonic log, and coupled neutron and density plot that allows highlighting the presence of reservoir facies (yellow areas in the sonic column of Figure 2.8b). Moreover, the presence of HC can be highlighted by the resistivity signal.

2.3.7. Formation pressure logs, rock strength, temperature and gas out

Two types of formation pressures are provided in the Absheron exploration wells. The shale pressure is an estimate that results from Eaton's method applied to the sonic logs (Eaton, 1975). Eaton's method consists in comparing the sonic log with a linear trend based on the highest sonic values in completely shaly intervals and considered as reflecting the "normal compaction trend". Any negative deviation from this curve is considered to result from undercompaction due to pore overpressure and is therefore calculated along the entire borehole like the sonic log. In porous-permeable intervals, pressure in situ reservoir pore pressure was measured directly using Schlumberger's StethoScope pressure WL tool (Schlumberger, 2019). Only target reservoirs were tested, and some measurements failed due to tool issues.

Fracturing pressure log is calculated from shale and reservoir pressures, adjusted by calibration to leak-off tests or formation integrity tests (Lin *et al.*, 2008), as well as downhole mud losses.

Wireline tools measured temperatures at different points in either open hole or cased hole.

Additional information, such as the occurrence and composition of free gas is available. Free gas are emitted and recorded at the flow line in the shaker room within the drilling mud and cuttings recovered during drilling operations. These data gives information on the presence of gas reservoirs along the drilled stratigraphic column as well as the nature and composition of these gases, and potentially the maturity of source rocks.

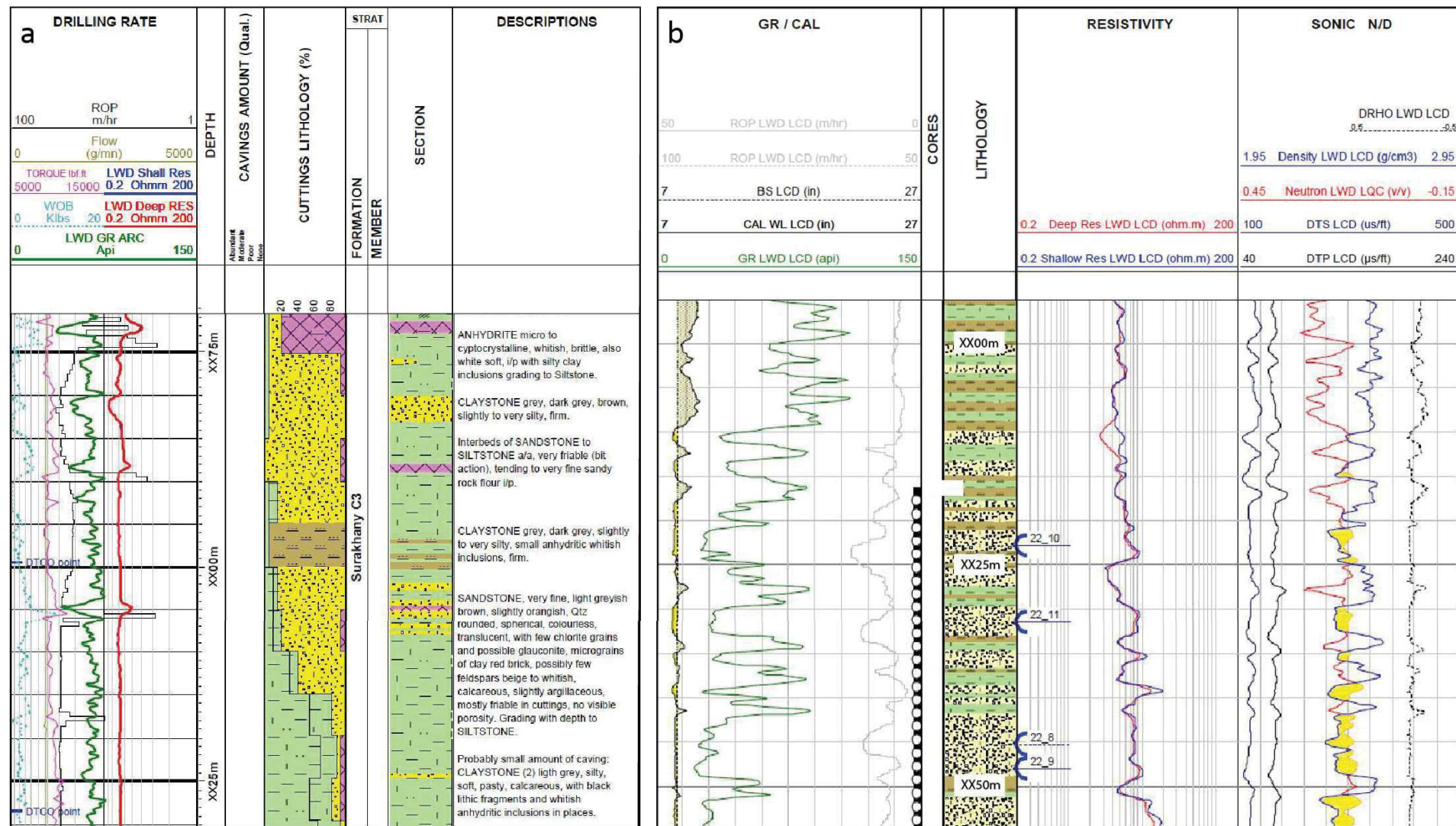


Figure 2.8: Log data from well ABX2 presented as an example of lithology interpretation. a: “quick-look” log plotted during drilling operations for monitoring purposes. The main data acquired with LWD tools are the gamma-ray (GR) signal (green) and the resistivity (shallow in blue, deep in red). These geophysical data are coupled with cuttings analysis in order to present a preliminary lithological section. b: final composite log, with all geophysical data obtained over a given section (GR; resistivity, shallow and deep field; sonic, DTP for P-waves and DTS for S-waves; density; neutron). Using data from resistivity coupled with sonic, and superimposed neutron and density, it is possible to refine the lithological log notably by precisely highlighting reservoir facies (yellow color, right column).

3. Methods

3.1. Seismic interpretation

Each medium has its own acoustic impedance. Therefore, when a seismic signal reaches a limit between two media with different impedances, part of the acoustic signal will be reflected (Nely, 1986). A seismic signal can be decomposed in wavelets which are characterized by their polarity, their amplitude (peak area), its period and its phase (Nely, 1986). Normal polarity is given by the seafloor polarity, which in the data presented hereafter is a wavelet with a strong central positive amplitude surrounded by two weak negative amplitudes. Thus, the normal polarity is a strong positive peak enclosed between two weak negative peaks indicating a step-wise increase in impedance. The opposite shows a step-wise decrease in impedance (Nely, 1986; Ricker, 1953).

Seismic interpretation was carried out using the Total in-house software Sismage (Guillon & Keskes, 2004). From the 3D seismic cube, we calculated the seismic coherency attribute, which can be projected on horizontal slices or seismic horizons. Seismic coherency allows to differentiate laterally continuous areas (undisturbed deposits) from low continuity zones (faults or mud volcano deposits for instance) (Bahorich & Farmer, 1995). Horizons were propagated and named according to stratigraphic limits encountered in the two exploration wells drilled on the Absheron anticline (Figure 2.7 for location). These stratigraphic limits are interpreted based on cuttings analysis and gamma-ray, sonic and resistivity logs (see Chapter 2:2.3). Between two horizons, it is possible to extract layers of regular thickness on which the Root Mean Square (RMS) of the seismic amplitude can be calculated. This allows visualizing in map view the spatial distribution of sediment bodies whose impedance contrasts with the background, thus imaging for instance channels, mudflows, and pipes.

Several imaging artifacts may arise from the recording and processing of seismic data. The presence of free gas is a well-documented cause of signal attenuation, causing what is known as wipe-out (Graue, 2000; Benjamin & Huuse, 2017). Several studies showed a strong seismic signal attenuation below active mud volcanoes (Graue, 2000; Benjamin & Huuse, 2017). Mud volcanoes are known to be accompanied by large emissions of free gas (Kopf, 2002; A. Mazzini & Etiope, 2017), so seismic masking is expected to occur below large structures such as the Absheron mud volcano. Steeply dipping intervals reflect incident signal away from the receivers, wherever they are located above the seabed, so that the resulting imaging issues cannot be settled by migration algorithms (Day-Stirrat *et al.*, 2010).

3.2. Sediment analysis

Several analyses and measurements were made on sediments sampled during the AUV and geotechnical surveys in order to determine and characterize their mineralogy, ages, grain-size distribution, as well as their mechanical properties.

To improve the characterization of mud volcano deposits, we selected thirteen samples from different sediment cores, thus sampling several mudflows having different ages and location. This allowed to verify the spatial and temporal variability of the mud properties. Moreover, eight other samples were used in a newly developed geotechnical laboratory test in order to test the impact of gas exsolution on sediment mechanical properties. Table 2-1 lists these samples and the analyses they went through, and Figure 2.7 shows their location with respect to the mud volcano.

Table 2-1: Sample details and type of analysis and measurements they underwent.

Core Name	Sample Name	Type of sample	Type of analysis	Water depth (m)	Depth Below Seafloor (m)	
					Top	Bottom
MVF1C	MECA-1	Core Sample	Consolidation cell	521	0.25	0.32
	MECA-2	Core Sample	Consolidation cell		1.00	1.07
	MECA-3	Core Sample	Consolidation cell		2.00	2.08
	MECA-4	Core Sample	Consolidation cell		2.19	2.26
	MECA-5	Core Sample	Consolidation cell		3.00	3.11
	DRX1	Core Sample	Mineralogy		3.53	3.55
	MECA-6	Core Sample	Grain size distribution, oedometer and mineralogy		3.71	3.80
	MECA-7	Core Sample	Consolidation cell		4.00	4.08
	MECA-8	Core Sample	Consolidation cell		4.75	4.82
	MECA-10	Core Sample	Grain size distribution, oedometer and mineralogy		5.14	5.22
MVF1D	MECA-15	Core Sample	Grain size distribution, oedometer and mineralogy	522	10.00	10.08
	MECA-16	Core Sample	Oedometer		10.41	10.48
	MECA-17	Core Sample	Oedometer		10.68	10.75
	DRX2	Core Sample	Mineralogy		19.00	19.06
MVF1E	DRX3	Core Sample	Mineralogy	522	33.04	33.06
	MECA-22	Core Sample	Grain size distribution, oedometer and mineralogy		33.08	33.15
	RAW>5 μ m	fraction >5 μ m	Mineralogy		34.00	34.61
	RAW<5 μ m	fraction <5 μ m	Mineralogy		34.00	34.61
	MECA-23	Core Sample	Consolidation cell		33.70	33.77
A13-PC11A	DRX4	Core Sample	Mineralogy	467	0.91	1.00
A13-PC12A	DRX5	Core Sample	Mineralogy	505	0.11	0.17
A13-BC05	DRX6	Core Sample	Mineralogy	453	0.32	0.36

3.2.1. Mineralogy

The MVF1E RAW sample was separated into two different grain size classes, with a limit at 5 μ m, in order to compare the composition of the clay-size fraction and the coarser fraction. The >5 μ m of the raw sample was extracted by suspension of fine fractions in water followed by centrifugation.

The eight samples were analyzed using a reference quantitative mineralogy method called MinEval QM (Fialips *et al.*, 2018). This method is based on the integration of results from various measurements performed on crushed samples, including X-Ray diffraction on bulk powders and extracted fine fractions, Loss On Ignition, X-Ray Fluorescence, Insoluble Residue upon HCl 15% treatment, bulk solid density and Cationic Exchange Capacity (see Fialips *et al.* (2018) for more details). This method performs an initial semi-quantitative mineralogy analysis by Rietveld refinement of the XRD patterns (Rietveld, 1969) and quantification is completed applying a dedicated software that uses an iterative approach. The <5 μ m fraction of MVF1E-RAW only obtained a semi-quantitative mineralogical analysis of clay minerals. The quantity of fine material obtained after separation was insufficient to perform the complete quantitative study.

3.2.2. Biostratigraphy

A biostratigraphic study was carried out by Chevron in 2000 with the aim of dating the oldest material present the mudflows. A series of samples were recovered in and around the mud volcano location (green triangles in Figure 2.7). The samples around the structure were used as age control points. The elements picked and counted on the samples are diatoms, pollens, foraminifera, nannofossils and ostracods.

Moreover, another analysis of nannofossils was carried out by the Biostratigraphy Dpt. in Total during the PhD on clasts sampled along sediment cores MVF1 and PC-11A (location in Figure 2.7). The goal was to verify the age of these cm-sized clasts present within the mud breccia. Foraminifera fauna was also looked into.

3.2.3. Grain-size distribution

Grain size distribution for the natural mud was determined using the Mastersizer 3000 device for laser diffraction granulometry (Ryzak & Bieganowski, 2011). This device is a laser diffractometer that measures the diffraction of a laser beam through water in which solid particles of the mud are suspended. The diffraction angle and the diffracted beam intensity highly depend on the grain size. The bigger the particle, the smaller is the diffraction angle and the stronger is the diffracted beam (Ryzak & Bieganowski, 2011). This diffracted beams are directly analyzed by a dedicated software, which directly gives the results in terms of grain-size distribution using the Mie solution to Maxwell's equations that describes the scattering of an electromagnetic wave by a sphere, whatever the nature of the sphere (Stratton, 1941).

The procedure consists in sampling 1 g of sediment and is mixing it with water and 1 g of sodium hexametophosphate which helps to deflocculate clay particles (Landrou, Brumaud & Habert, 2016). Samples are put for 10 minutes into an ultrasound tube in order to break more rapidly potential clay floccules and then they are mixed into a mechanical stirrer. Afterwards, the content of each bottle is poured into the diffractometer container that measures the grain-size distribution, and eventually proceeds to auto-cleaning of its tanks.

3.2.4. Mechanical properties of sediments

i. Atterberg Limits

Atterberg limits are the water contents which define transition between different mechanical states and behaviors of a given sediments (from solid to liquid). The water content corresponds to the ratio between the mass of water and the mass of the dry sample. The mass of water is obtained by subtracting from the (wet) sample mass the mass of the same sample after drying during 24 hours in an oven at 105°C. The liquid limit (w_L) is the water content above which sediments stop deforming as a plastic material but start behaving as fluid (Skempton, 1944; Terzaghi & Peck, 1948). The plastic limit (w_p) is the water content below which a sediment stops deforming as a plastic material and starts to deform as a friable material (Skempton, 1944; Terzaghi & Peck, 1948). The plasticity index (PI) is obtained by subtracting w_p from w_L ($PI = w_L - w_p$) and indicates the range of water content where the soil behaves as a plastic material.

In this work, the Atterberg limits were determined using the fall cone method (Figure 2.9; Feng, 2000, 2005) which consists in dropping vertically a calibrated steel cone (Figure 2.9a) from a position where the tip is just in contact with the sample surface (Figure 2.9a; Feng, 2005). Feng and co-authors (2005) showed that the penetration of the cone depends on the water content w and corresponds to 2 mm when w is equal to the plastic limit and to 20 mm when w is equal to the liquid limit (Figure 2.9b).

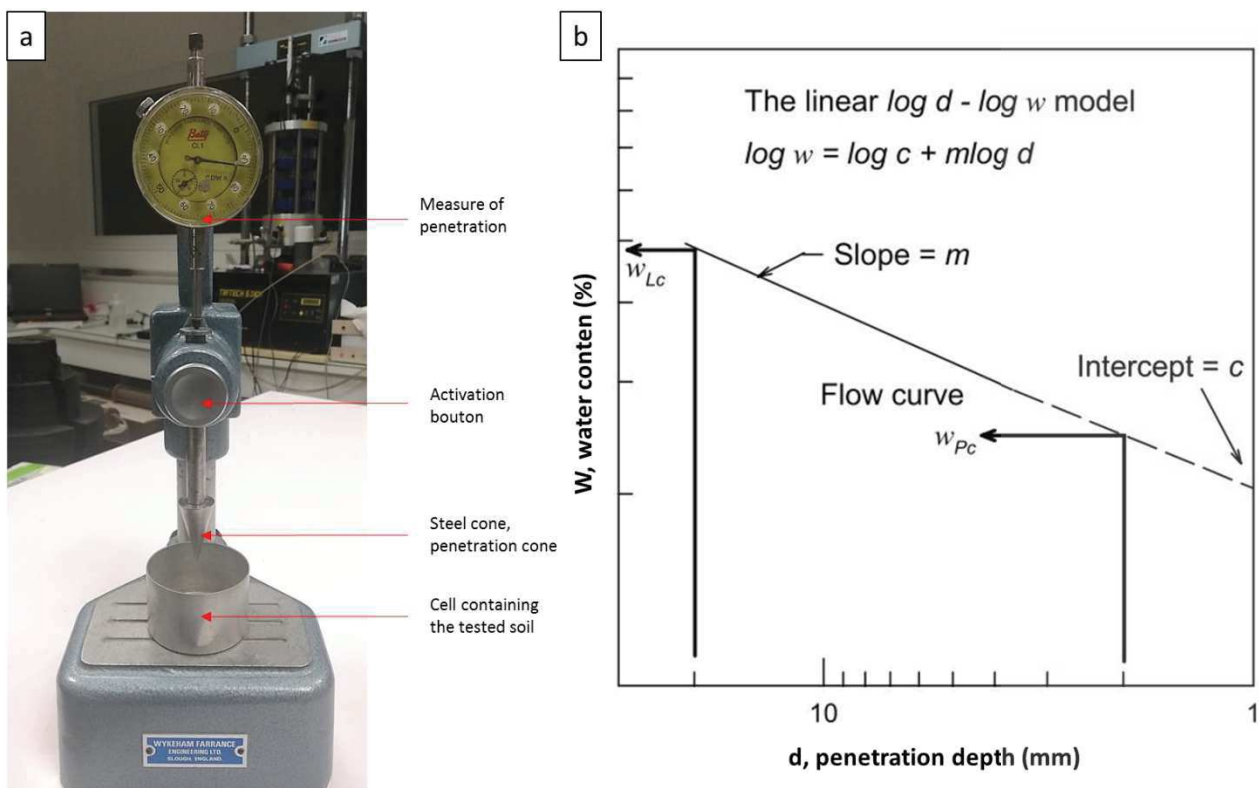


Figure 2.9: a: picture of the fall cone test apparatus, displaying the main elements. b: typical log-log diagram of the water content versus the penetration depth, displaying the reading methods for the Atterberg limits (from Feng, 2005).

ii. Oedometer and permeameter tests

Oedometer tests were carried out along with permeability measurements on four samples taken from the GT1-MVF1 core (MECA 6-10-15-22 in Table 2-1). Tests were duplicated in order to check for potential trial mistakes. The samples were selected based on Cone Penetration Testing (CPT, location in Figure 2.7; Lunne 2010) data showing at least four mechanically distinct intervals (Total proprietary report, G. Dan & S. Po, 12/09/2017, personal communication). The aim of these oedometer tests was to define compressibility characteristics (void ratio versus effective stress; ASTM International, 1996).

The void ratio e changes are tied to the vertical effective stress σ'_v by the following compressibility relation:

$$e = e_0 - C_C \log\left(\frac{\sigma'_v}{\sigma'_{v0}}\right) \quad (1)$$

where e_0 is the initial void ratio for a reference vertical effective stress σ'_{v0} and C_C is the compression index depending on the sediments.

The samples were all reconstituted with an artificial initial water content of around $1.5 w_L$. Oedometer tests were conducted using incremental loading (Figure 2.10a) according to the ASTM D-2435 method (ASTM International, 1996). The remolded sediments are placed into a cell and between two porous stone plates (Figure 2.10a). The load is applied at the top of the sample through a lever arm (Figure 2.10a). At the other end of the lever arm, masses are doubled every 24 hours until reaching 32 kg corresponding to a maximum vertical stress of 1765 kPa. During unloading, the applied mass is divided in half every hour. The variation in height of the sample is measured using a displacement sensor precise at 0.01 mm (Figure 2.10a).

The initial void ratio e_0 of the remolded sample is obtained from the initial water content (w_0) using the following equation:

$$e_0 = w_0 \cdot G_s \quad (2)$$

Where G_s is specific gravity of soil solids.

Final results of the oedometer test are displayed as variations of e as a function of σ'_v (Figure 2.10b), e being obtained at each increment step calculating the sample height variation, ΔH , and normalizing it with the initial height, H_0 , and with e_0 :

$$e = e_0 - \frac{\Delta H}{H_0} (1 + e_0) \quad (3)$$

From this plot, several sediment mechanical properties can be obtained through graphical methods (Figure 2.10b). Notably, the compression index, C_C , is read directly as the slope of the virgin consolidation curve (Figure 2.10b) and corresponds to the slope of Eq. (1). The swelling index, C_s , is the slope of the swelling

curve (Figure 2.10b). Finally, the preconsolidation pressure of sediments is obtained following the graphical method described by Das (2013) and displayed in Figure 2.10b.

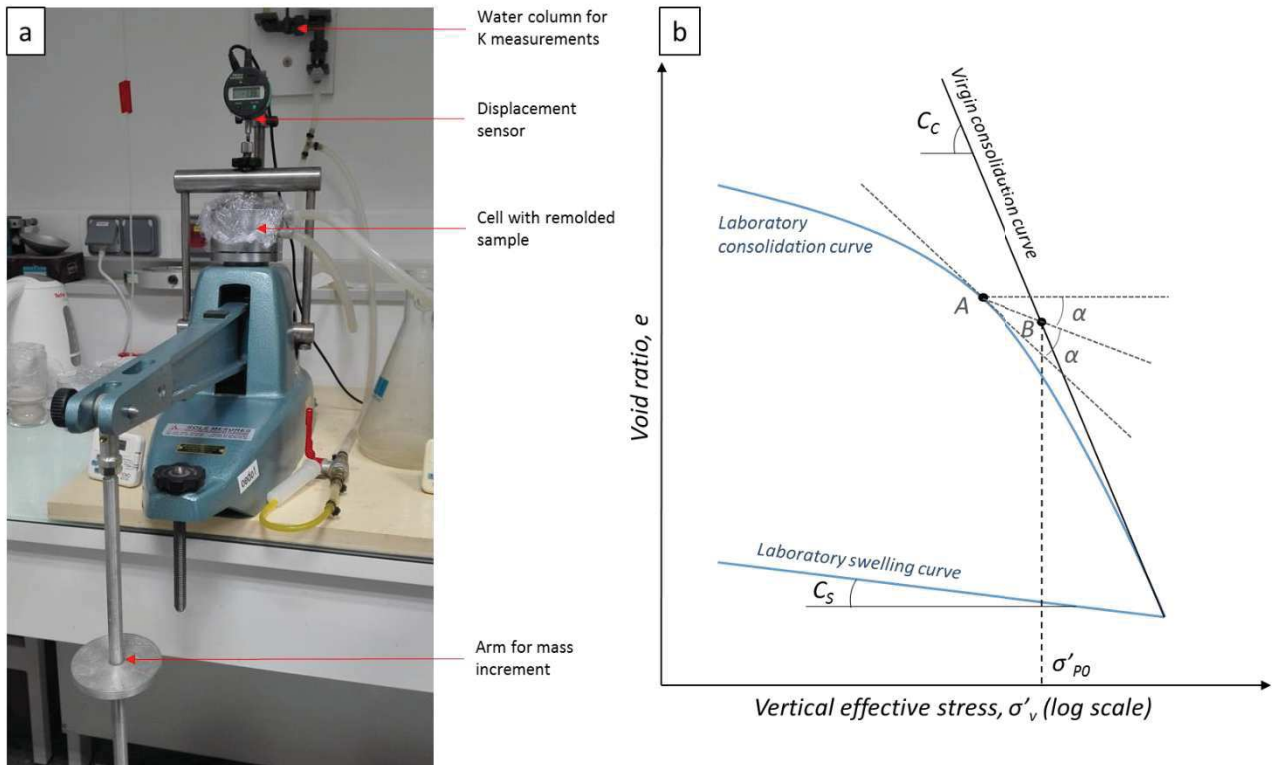


Figure 2.10: a: picture showing one oedometer used during the study, displaying the main elements of the system. b: typical plot for an oedometer test result after increment load and unload, displaying the consolidation curve, the swelling curve and the virgin consolidation curve. The method for calculating the preconsolidation pressure (σ'_{PO}) and for the reading of the compression index (C_c) and swelling index (C_s) is also displayed. A is the maximum inflexion point of the laboratory consolidation curve. From this point, the tangent to the curve and the horizontal line are drawn. The bisector between these two lines gives the point B at the intersection with the virgin consolidation curve. The horizontal coordinate of B gives σ'_{PO} .

The hydraulic conductivity relation to void ratio is assumed to be:

$$\ln(K) = ae + b \quad (4)$$

with K the Darcy permeability (Das, 2013) or hydraulic conductivity (m/s), a and b are constants characteristic of the tested sediments.

The determination of hydraulic conductivities is possible using the falling head method. It consists in imposing one meter of water head above the oedometer sample and recording the decrease of the water level over time (Das, 2013). The water head is imposed through infill of capillary (see Figure 2.10a). From the water head variation we can calculate a hydraulic conductivity (Das, 2013):

$$K = \frac{sL}{S.t} \log \frac{h_1}{h_2} \quad (5)$$

where s is the surface area of the cross section of the capillary tube (m^2), S is the surface area of the tested sample (m^2), L is the length of the tested sample (m), t is the time elapsed since the beginning of the

falling head test (s), h_1 is the initial level of the water head (m) and h_2 is the level of the water head at the time of the measurement (m).

The calculation of K is repeated at each measurement, and a mean value of K is calculated for each loading stage, therefore relating a value of K to a given value of e .

In order to artificially characterize the impact of coarse material on mechanical properties, additional oedometer tests were carried out on grouped MECA-16 and MECA-17 samples (Table 2-1) mixed with a known mass of fine sand (80-125 μm); the goal was to obtain their compressibility and permeability in order to integrate these results in numerical diffusion models. The fractions of coarse material added to the samples were selected based on the “sand / shale ratio” (ratio between sand layer cumulated thicknesses over total interval thickness) values calculated from well data on different stratigraphic intervals.

iii. Consolidation test with gas exsolution

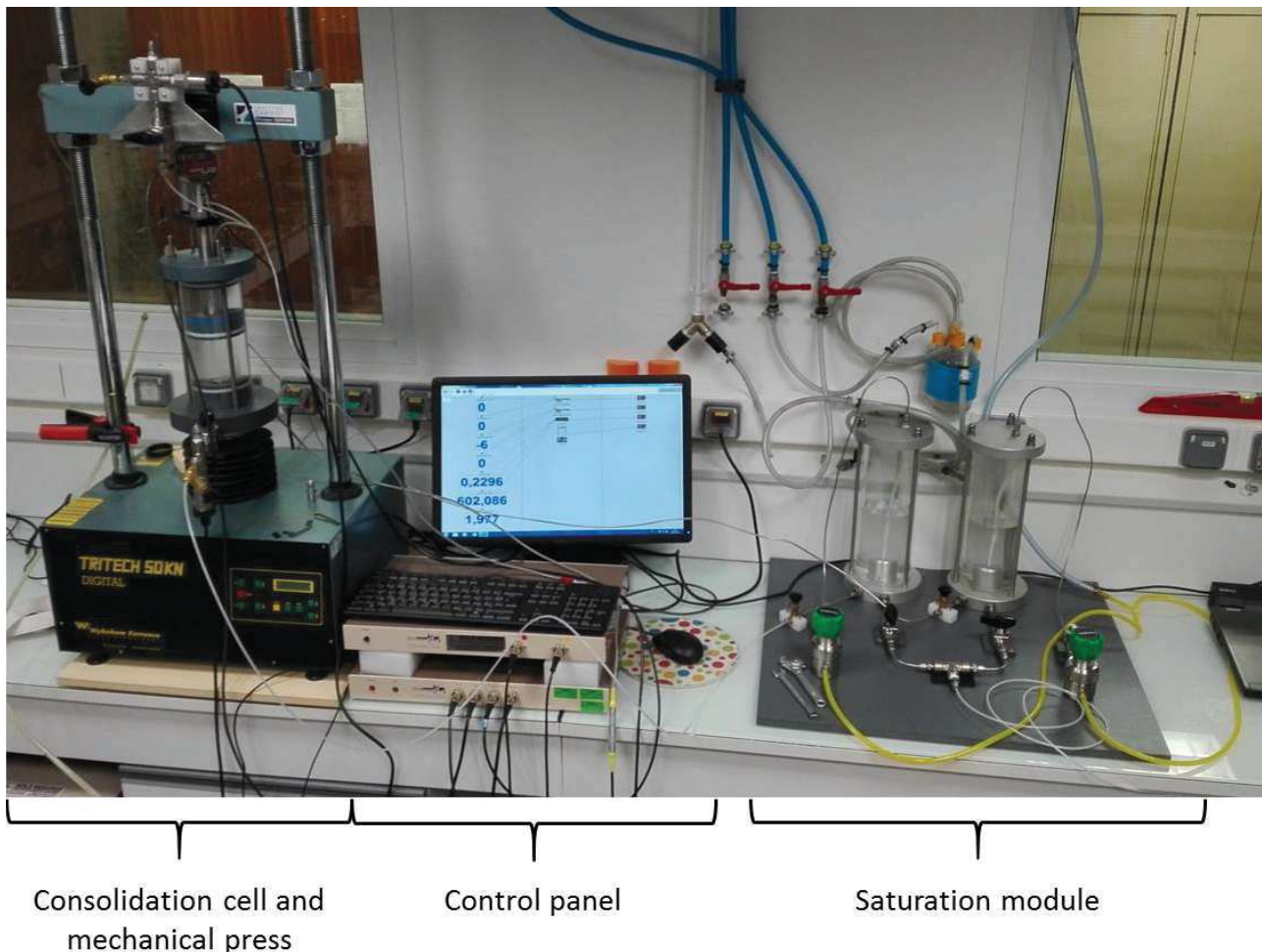


Figure 2.11: Picture showing the main modules of the special consolidation testing. Details are given in the Chapter 4, dedicated on the experimental testing program and results.

A novel experimental set-up composed of three main modules was developed to analyze the gassy sediments and the effects of gas exsolution on the mechanical behavior of compacted sediments (Figure 2.11). The three modules are: a consolidation cell with a mechanical press designed to apply vertical

loads, a saturation module where water is carbonated under a given CO₂ gas pressure and the control panel that connects all the experimental set-up sensors with a computer in order to constrain and record the different parameters.

The consolidation cell is composed of a Plexiglas cylinder that forms, along with its two end covers, the fixed part of the system (Figure 2.11). The piston is composed of a steel rod fixed into a pierced plastic cylinder (Figure 2.11). Two porous stones placed at the top and the bottom of the sample ensure the consolidation of the sediment during loading by letting water percolate out of the tested sediments. A load cell and a vertical displacement sensor allow controlling the rate of displacement and the axial force applied to the sample (Figure 2.11). A lip seal circles the piston and avoids sediments flowing above the piston, with the adverse effect that it generates a non-negligible friction on the inner surface of the Plexiglas cylinder. Force balance at the sediment-piston contact shows that the measured force is a composition of the friction, a vertical upload force due to the different piston surfaces on which fluid pressure is applied (Figure 2.11), and the net applied load. Friction is always opposed to piston movement. Calibration testing was necessary in order to constrain the friction related to the asymmetrical lip seal, therefore several tests were made in water with different gas pressures; the results show that the friction depends on gas pressure and is different during loading and unloading. Further details on calibration are given in Chapter 4. Details on the different sensors and structural elements such as Plexiglas cylinder and lip seals are displayed in Table 2-2.

Table 2-2: Sensors and important structural elements characteristics such as measure range and precision or limit pressure.

Sensors and gauges		Structural components	
Load cell		Consolidation Cell Cylinder	
Maximum load	5 kN	Material	Plexiglas
Maximum vertical stress	1300 kPa	Type	PMMA XT
Precision	± 0.005 kN	Elastic Modulus	3.3 Gpa
Displacement sensor		Yield Stress	70-80 Mpa
Maximum displacement	50 mm	Thickness	15 mm
Precision	± 0.125 mm	Saturation tanks	
Pressure gauges		Material	Plexiglas
Limit pressure	3 Mpa	Type	PMMA XT
precision	± 0.75 kPa	Limit pressure	1 MPa
CO2 bottle pressure gauge		Lip seals	
max pressure delivery	2.5 Mpa	Friction Error	± 0.01 kN
Bender elements			
Type	GDS Bender System		
Limit pressure	3.5 MPa		
wave-type	S-waves, P-waves		
wave shape	Sinusoidal, square		
Frequency ranges	0.01-100 kHz		
Working frequency	100 kHz		

The saturation system is composed of two Plexiglas tanks, the same type as the consolidation cell (Figure 2.11). Both tanks are connected at the top to a CO₂ bottle equipped with an adjustable pressure gauge. Tanks are half-filled with water, the other half being occupied by gas. Adjustable security valves are connected at the top of the two tanks and allow to expel gas if a pressure threshold is reached (green buttons in Figure 2.11). Each tank connects to the top or the bottom of the consolidation cell by their bottom end. Differential pressures at the top and bottom of the sample can be applied through the two tanks allowing the carbonated water to circulate through the sample, allowing saturating easily the sediments with dissolved CO₂. Pressure gauges control the pore pressure of the system (top and bottom of the consolidation cell in Figure 2.11). Further technical details on the pressure gauges are displayed in Table 2-2. All the sensors used (load cell, vertical displacement sensor and pressure gauges) are connected to a control panel (Figure 2.11). The computer monitors, records and controls the different test parameters.

A pressure generator is connected at the bottom end of the consolidation cell for water permeability measurements. The pressure generator creates a pressure gradient while measuring water volume change. Using Darcy's law, it is possible to calculate the hydraulic conductivity of the sediment. A falling head method can also be applied using the differential pressure between the two saturation tanks. P-wave velocities are measured using GDS bender element system. To obtain repeatable and comparable measurements, the received signal is picked on the last relative minimum before the first received peak. Technical information on the GDS bender system is given in Table 2-2.

The main purpose of this experimental study is to evaluate the impact of gas exsolution and accumulation on the mechanical behavior of the tested sediments (e.g. compressibility, preconsolidation pressure, permeability, P-wave velocity). To do so, several loading/unloading cycles are applied during each test on water-saturated sediments and gassy sediments. Each test can be described with the following basic scheme and stages:

- Water saturation with CO₂.
- Sample saturation with carbonated water.
- Consolidation/unloading cycle(s) of water-saturated sediments.
- Gas exsolution.
- Consolidation of gassy sediments.

In the case of partial degassing, the last two stages can be repeated to obtain different gas saturations during the same test. Further details on testing execution can be read in Chapter 4. Gas saturation is calculated from the volume of gas exsolved, measured by the sample swelling during the exsolution phase.

3.3. Well data interpretation

The sand / shale ratio (cumulated sand thickness divided by total interval thickness) was calculated for each drilled formation based on the lithological, GR and caliper logs (see Chapter 2:2.3.1 and Chapter 2:2.3.6).

Moreover, the ratio between the fracturing pressure and the lithostatic pressure in wells gives a pressure condition for hydrofracture generation.

In the absence of direct measurements, we estimated interval hydraulic conductivity from the sonic log using the sonic vs. porosity relationship of Wyllie *et al.* (1958) and the Kozeny-Carman equation to derive permeability from porosity (Kozeny, 1927; Carman, 1937).

Wyllie *et al.* (1958) gave a relationship between measured P wave velocity of a porous media and its porosity ϕ :

$$\frac{1}{V_m} = \frac{\phi}{V_f} + \frac{(1-\phi)}{V_s} \quad (6)$$

with V_m the measured acoustic velocity, V_f the acoustic velocity in pore fluid and V_s the acoustic velocity in the rock matrix.

As void ratio and porosity are linked through the relation

$$e = \frac{\phi}{1-\phi} \quad (7)$$

it is possible to calculate hydraulic conductivities K for reservoir layers using the Kozeny-Carman relationship (Ren *et al.*, 2016):

$$K = C_F \frac{1}{S_s^2} \frac{\gamma_f}{\mu \rho_s^2} \frac{e^3}{(1+e)} \quad (8)$$

where C_F is a shape constant around 0.2, S_s is the specific surface area of particles (m^2/g) taken here as equal to $0.5 \text{ m}^2/\text{g}$, γ_f is the unit weight of pore fluid (N/m^3), ρ_s (kg/m^3) is the particle mass-density and μ is fluid viscosity ($\text{N}\cdot\text{s}/\text{m}^2$).

Oedometer test results on natural mud were used as a proxy to estimate shale permeability. From the lithological log, the column was split into reservoirs and shale intervals. Using Eq. (4), (6), (7) and (8), we calculate for each individual sand and shale strata their hydraulic conductivity K . The arithmetic average of hydraulic conductivities gives the horizontal hydraulic conductivity (K_h) for the considered stratigraphic interval while the harmonic average gives its vertical hydraulic conductivity (K_v , Das, 2013). Finally, the ratio between K_h and K_v was calculated in order to estimate the permeability anisotropy on each interval.

3.4. Numerical modeling

3.4.1. 1D sedimentation and pore pressure accumulation

Excess pore pressure can be related to high sedimentation rates, the mechanism of overpressure generation being called compaction disequilibrium (see Chapter 1:2.5.1.i; Osborne & Swarbrick, 1997; Sultan et al., 2004; Swarbrick et al., 2002). The sedimentation rates observed in the basin are among the highest recorded worldwide (see Chapter 2:1.1). Therefore, the modeling work focuses on this sedimentation effect as a first approach. The SeCoV3 proprietary software of IFREMER (Sultan *et al.*, 2004) allows quantifying the evolution of pore pressure using a back analysis based on sedimentation rates, compressibility properties (Eq. (1)) and permeability evolution with void ratio (Eq. (4)). In addition to the equations solved by SeCoV3, in the present work we use a mesh-update method considering the compressibility of sediments and the mobile position of the upper boundary (seawater-sediment interface) at each calculation step. For further details on the methods, used parameters and results of the 1D simulations please read Chapter 3:3.4.1.

3.4.2. Two-dimensional transient-diffusion process: Darcy's and Fick's laws

The excess pore pressure generated by sedimentation and calculated using SeCoV3 was considered as a boundary condition for the 2D Darcy transient flow calculation. The two-dimensional dissipation and transmission of overpressure is calculated using the 2D diffusion equation given by:

$$\frac{\partial \Delta u}{\partial t} = \left(\frac{\partial(D_{hx}\partial\Delta u)}{\partial x^2} + \frac{\partial(D_{hy}\partial\Delta u)}{\partial y^2} \right) \quad (9)$$

with $\Delta u(x,y,t)$ being the overpressure and D_{hx} and D_{hy} respectively the horizontal and vertical hydraulic diffusivities that are calculated directly from the horizontal and vertical hydraulic conductivities Kx and Ky .

In addition to the transmission/diffusion of pore pressure, we considered in the present work the molecular diffusion of dissolved methane through Fick's law. Methane diffusion is calculated using a two-dimensional diffusion equation referred to as Fick's law (Eq. (10)), which allows for the description of diffusion of dissolved molecules into a solvent (Crank, 1975):

$$\frac{\partial C}{\partial t} = D_C \left(\frac{\partial(D_C\partial C)}{\partial x^2} + \frac{\partial(D_C\partial C)}{\partial y^2} \right) \quad (10)$$

with C being the dissolved methane concentration, and D_C the methane molecular diffusivity of the porous water. The effect of tortuosity of pores on molecular diffusivity is considered through the porosity of the sediment as described by Boudreau (1996).

To solve numerically the 2D diffusion equations (Eq. (9) and (10)), a centered explicit finite difference discretization scheme is used by considering the initial and boundary conditions for pore pressure and methane concentration.

Faults are characterized by their own methane molecular diffusivities creating preferential pathways or diffusive barriers. As the modeled stratigraphic column is formed by a succession of metric-scale sand layers and plurimetric shale intervals, a ratio between horizontal and vertical hydraulic conductivities was integrated based on the results of the hydraulic conductivity calculations at wells (Chapter 2:3.3). This ratio allows modeling the natural anisotropy of the sedimentary column due to sand-shale successions. A hydrofracturing condition based on well data interpretation (Chapter 2:2.3.7) is also used: once the ratio $\Delta u/\sigma'_v$ reaches these conditions, fractures are created and propagate in the critical area. The fracture permeability properties are calculated from the hydraulic conductivity variation with void ratio, defined on the stratigraphic layer where the fracture creates and from a fracture void ratio defined by the user.

If fractures open in a dissolved-methane saturated area, decrease in Δu due to fracture generation may be sufficient to trigger methane exsolution. Therefore, depending on methane solubility (Brown, 1990; Duan & Mao, 2006), and depending on the magnitude of the pressure decrease, the software calculates gas saturation (S_g), and the consequent decrease in preconsolidation pressure of sediments (σ'_{p0}) based on the constitutive law obtained in Chapter 4 from experimental testing.

The software used in order to compute the simulations of this study was developed internally at Ifremer for this PhD.

3.4.3. P-wave velocity with gas saturation

Helgerud *et al.* (1999), based on the Biot-Gassman theory and on previous works by Dvorkin *et al.* (1999) on elasticity of marine sediments, proposed an effective medium model to predict P-wave and S-wave velocities in sediments containing free gas and/or gas hydrates based on mineralogy, compressibility and initial void ratio.

We used this model to draw a chart for predicted P-wave velocity variation with void ratio for different values of S_g (Chapter 4) in order to compare our P-wave velocity laboratory measurements during consolidation testing with gas exsolution (Chapter 2:3.2.4.iii). Compressibility of sediments are obtained from oedometer testing (Chapter 2:3.2.4.ii) and are detailed in Chapter 3:4.2 and in Chapter 4. The average number of contacts per grain in a bulk unit (called n in the Helgerud *et al.* (1999) model) was taken as equal to 4. The mineralogy from XRD measurements (Chapter 2:3.2.1) was simplified into three poles (clays, quartz and carbonates) as detailed in Chapter 4. The adopted method and the utilization made from Helgerud *et al.* (1999) effective medium theory is summarized in Figure 2.12.

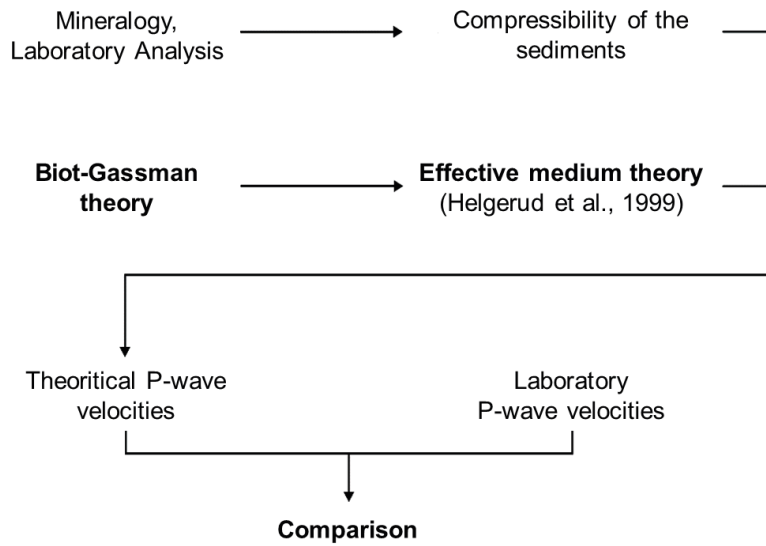


Figure 2.12: Adopted method to apply the effective medium theory of Helgerud et al. (1999) (modified from Taleb et al., 2018).

3.4.4. Fluid mud dynamics: modelling approach

In order to model the mud flowing towards the surface, a fluid mechanics approach is often adopted using simplified Navier-Stokes equations (Gisler, 2009; Zoporowski & Miller, 2009; Collignon *et al.*, 2018a).

Navier-Stokes equations are governed by two basic equations. First, for neglected surface tension, gravity as sole body force and constant viscosity, the momentum equation is given by:

$$\rho \frac{\partial u}{\partial t} + \rho \nabla \cdot uu = -\nabla p + \rho g + \mu_0 \nabla^2 u \quad (11)$$

where ρ is the mass-density of the mud (kg/m^3), u is the fluid velocity (m/s), g is the the gravity (m/s^2), μ_0 is the viscosity considered as constant (Pa.s) and p is the fluid pressure (Pa) (Tryggvason *et al.*, 2006).

Secondly, the mass conservation for incompressible fluids is given by:

$$\nabla \cdot u = 0 \quad (12)$$

as stated in Tryggvason *et al.* (2006).

One method for the resolution of this system of equations (Eq. (11) and Eq. (12)) is given by Tryggvason (2012). The momentum equation is integrated with time by splitting Eq. (11) into a velocity term and a pressure term, integrated separately. Then, each term of Eq. (11) is discretized using a Finite-Volume approach where both equations are applied over a small control volume. More details concerning the basic Navier-Stokes equations and the numerical methods are shown in Tryggvason (2012).

In the present work, we introduce the effect of gas on the mud mass-density through the following equation:

$$\rho = \phi(1 - S_g)\rho_w + (1 - \phi)\rho_s \quad (13)$$

Where ϕ is the porosity and ρ , ρ_w and ρ_s are respectively the mass-density of mud, water and solid particles. The density of free gas is considered as being negligible compared to the water-mass density and the mass-density of the solid particles. The gas solubility and compressibility are also calculated at each time calculation step using the Boyle's law and Henry's law.

4. Conclusion

The Absheron Mud Volcano is located in the South Caspian Basin, a complex area that has recorded intense tectonic activity since the Cretaceous and which is one of the sedimentary basins having recorded the largest subsidence and sedimentation rates worldwide, notably through the interaction of three paleo-river deltas. It is also a province of intense O&G activity due to the presence of several mature source rocks and numerous high-quality regional reservoirs and structural traps in the anticline crests. The SCB is also known to hold the densest distribution of MVs worldwide. They are related to anticline crests where gas accumulations are found and their formation seems intimately linked to fold growth.

The Absheron anticline is a gas condensate field with a high strategical and economical interest for Total, and production may start as soon as 2021. Therefore, a dense and varied dataset was accumulated over the exploration phase, with notably high resolution industrial geophysical data (3D seismic, 2D seismic, HR multibeam bathymetry, Sub Bottom Profiler), geotechnical in situ measurements (CPTu), sediment cores and two exploration wells together with industrial logs. The dataset is very complete, and multidisciplinary, thus the AMV can be apprehended through different approaches. Its morphology through geophysical methods can be understood in detail and compared with in situ data and sediment analysis in order to get a comprehensive model of its formation. The sediments can be laboratory tested through innovative techniques to understand the mechanical behavior of the mud. Finally, the comprehensive formation model and the laboratory results can be confronted through numerical models computing several physical and geological processes. All in all, the AMV is located in an area that gives a unique opportunity to study an active MV, its morphology, its dynamic and its formation.

Chapter 3: Evolution model for the Absheron mud volcano: from in situ observations to numerical modeling

Abstract

The morphology of mud volcanoes (MV) has been extensively studied over the last few decades. Although recent research has begun to focus on deep processes and structures, little is known about mud generation mechanisms. This study aims to investigate the feeder system and formation of an active kilometer-scale MV by relying on a 3-D seismic survey and an in situ dataset on the Absheron anticline (South Caspian Basin). Seismic data show a depleted area in the Anhydritic Surakhany Formation (ASF), whose mineralogical composition fits with surface mud. Well data show that the ASF is a succession of evaporitic beds and low temperature shales near its fracture pressure. Biostratigraphic analysis confirms a Pliocene origin for the mud, suggesting that the ASF may be the source. Numerical modeling of sedimentation coupled with laboratory test results and well sonic logs fairly reproduces the observed in situ overpressure trend. Two-dimensional methane diffusion coupled with overpressure caused by rapid sedimentation highlights the superposition of critical fracturing conditions with methane-saturated sediments at the base of the studied MV. This demonstrates the predominant role of fluid overpressure due to sedimentation and gas saturation in the formation of the Absheron MV, and this is shown to occur as follows: (1) methane migration through the thrust-related faults reaching the ASF, accompanied by (2) lateral overpressure, caused by rapid sedimentation, diffusing along the ASF leading to (3) hydro-fracturing of overpressured and methane-saturated sediments resulting in an important decrease in overpressure, causing (4) gas exsolution and expansion triggering sediment remobilization.

Chapitre 3 : Modèle de formation du volcan de boue d'Absheron : des observations in situ au modèle numérique

Résumé

La morphologie des volcans de boue a été étudiée de façon approfondie depuis quelques dizaines d'années. Bien que les recherches récentes commencent à se concentrer sur les processus et les structures profondes des volcans de boue, la compréhension des mécanismes de génération de la boue reste partielle. Cette étude vise à étudier le système profond et la formation d'un volcan de boue actif de quatre kilomètres de diamètre en se basant sur un bloc de sismique 3D et sur des données in situ couvrant l'anticlinal d'Absheron (Bassin sud caspien). La sismique permet de mettre en évidence une zone déplétée dans la Formation du Surakhany Anhydritique (ASF) dont la composition minéralogique s'approche de celle de la boue du volcan. De plus les données de forage montrent que l'ASF est formé d'une succession de lits évaporitiques et de bancs argileux, est actuellement proche de sa pression de fracturation et est à une température bien inférieure à la limite de remobilisation des argiles. L'analyse biostratigraphique de la boue permet de confirmer son origine Pliocène. La modélisation numérique de la sédimentation, couplé aux propriétés mécaniques de la boue et aux diagraphies soniques dans les puits permet de reproduire de façon assez précise le champ de pression mesuré in situ. La modélisation de la diffusion de pression en deux dimensions couplé à la diffusion de méthane dissous montre la superposition de surpressions proches des conditions de fracture et de la zone saturée en méthane dissous sous le volcan actuel. Ce chapitre démontre l'importance de la surpression générée par une sédimentation rapide ainsi que la présence de gaz dissous dans la formation du volcan de boue d'Absheron. Le chapitre conclut par le modèle de formation pour ce volcan le plus probable au vue de l'analyse des données : (1) migration de méthane dissous le long du réseau de failles se terminant dans l'ASF ; (2) en parallèle, formation d'une zone à forte surpression au niveau de l'ASF due à la sédimentation rapide dans la partie profonde du bassin ; (3) hydrofracturation des sédiments en surpression et saturés en méthane dissous induisant une chute rapide de la surpression ; (4) déclenchement de l'exsolution et expansion du gaz dissous permettant la remobilisation de sédiments.

1. Introduction

Although mud volcano (MV) surface morphologies have been described in detail and worldwide, both onshore and offshore, little is known about their evolution and formation processes (e.g. Kopf, 2002; Deville, 2009; Mazzini & Etiope, 2017). On the other hand, earlier extensive work on fluid emissions at the surface has improved understanding of subsurface processes and the multiple sourcing of the different elements forming the material ejected by mud volcanoes (Deville, 2009; Kopf, 2002; Mazzini & Etiope, 2017).

Nevertheless, recent technical improvement of geophysical tools, such as high-resolution 3D seismic imaging, allows for detailed analysis of the MV rooting system and has opened the way for studying mud generation processes (Stewart & Davies, 2006; Dupuis, 2017; Kirkham *et al.*, 2017a). Understanding these generation mechanisms is a key issue for geohazard assessment (e.g. the Lusi catastrophe near Sidoarjo, Indonesia since 2006, Tingay *et al.*, (2015)), for environmental impacts on seabed ecosystems (Zitter, 2004; Foucher *et al.*, 2009), targeting drilling areas and anchoring zones for offshore infrastructures (Tingay *et al.*, 2008; Contet & Unterseh, 2015). Furthermore, one characteristic shared by all MVs around the world is the presence of gas in the ejected material (Hedberg, 1974; Etiope *et al.*, 2009). Yet it is not clear at present if the gas is a driver of mud extrusion or a passive actor, captured in the mud during its ascent. If gas has a driving role in mud extrusion, the understanding of mud generation mechanisms could provide elements to quantify the volume of expelled methane and therefore evaluate the natural contribution of MVs to the atmospheric carbon budget (Kopf, 2002).

The South Caspian Basin (SCB), along with its onshore continuation, the Lower Kura Basin, is a prolific hydrocarbon basin and is also known to hold the highest density of MVs (Guliyev *et al.*, 2011; Mazzini & Etiope, 2017). The Absheron gas field is a challenging exploration and production area due to the presence of a giant active MV. A high-resolution 3D seismic block was acquired in 1996, two exploration wells were drilled in 1999 and 2011, and a geotechnical marine survey with sediment core sampling and in situ measurements was operated in 2014 for geohazard assessment.

Altogether, the dataset provides a rare opportunity to study a mud volcano with a complete set of surface and subsurface data. Several issues are assessed in this chapter regarding the stratigraphic source of the mud, the stratigraphic and lateral location of the mud generation zone and the physical mechanisms responsible for the mud volcano formation.

We provide within this study a detailed geomorphological description of the structure as well as the extrusion timing based on seismic imaging and other data. Well data and sediment analysis results were integrated into numerical 1D and 2D models in order to quantify the lateral pressure transmission and the gas migration effect. Finally, a conceptual evolution model based on these results is proposed.

2. Regional Setting

The South Caspian Basin is a remnant of the Paratethys Sea that became isolated from the world ocean during the Late Miocene, Early Pliocene, at the end of the compressive phase of the Alpine tectonic cycle (Popov *et al.*, 2004; Golonka, 2007; Bochud, 2011). It is now delimited to the north by the Absheron peninsula and ridge, to the south by the Alborz massif, to the west by the Greater and Lesser Caucasus separated by the Kura depression, and to the east by the Kopet Dagh (Figure 3.1; Allen *et al.*, 2002; Brunet *et al.*, 2003; Popov *et al.*, 2004; Morley *et al.*, 2011).

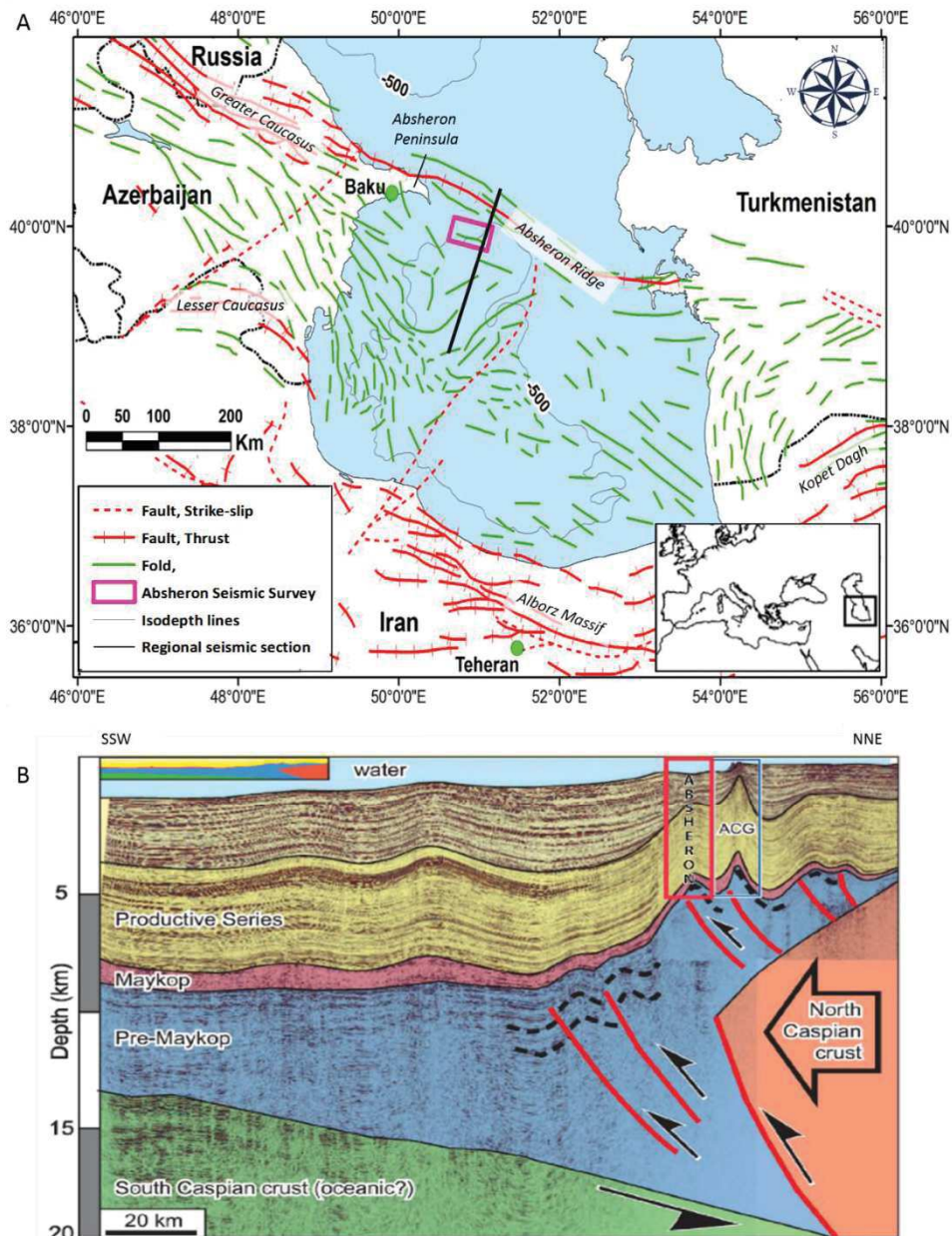


Figure 3.1: A, structural map of the South Caspian region showing the main folds and faults, structural domains and depocenters (modified from Oppo *et al.*, 2014). B, regional interpreted deep seismic section, showing the main subsurface structural elements with the folds above the Maykop detachment level associated in the northern part to deeply rooted thrusts. The location of the line is shown on the left map by a black line. The red box shows the approximate location of the Absheron structure (modified from Stewart & Davies, 2006).

Since the Middle Miocene, compression uplifted all these massifs and triggered the high amplitude folding of the South Caspian sedimentary series (Allen *et al.*, 2002; Popov *et al.*, 2004; Egan *et al.*, 2009; Javanshir *et al.*, 2015). This compression initiated the subduction of the South Caspian basement below the basement of the North Caspian domain, creating the Absheron ridge in-between (Figure 3.1; Allen *et al.*, 2002; Stewart & Davies, 2006). The subduction allowed the deposition of more than 8 km of sediments over the last 5.5 Ma based on a representative stratigraphic column of the northwestern part of the basin, which is faster than sedimentation rates recorded in typical foreland basins (Allen *et al.*, 2002; Stewart & Davies, 2006; Morley *et al.*, 2011).

The Maykop Formation was deposited from the Late Oligocene to the Early Miocene in a shallow marine anoxic environment (Popov *et al.*, 2004; Golonka, 2007; Hudson *et al.*, 2008). It is the main hydrocarbon source rock for the Caspian and Black Sea areas (Allen *et al.*, 2002; Hudson *et al.*, 2008) and acts as the main decollement level for the high amplitude folds of the South Caspian Basin (Allen *et al.*, 2002; Stewart & Davies, 2006). The Maykop sediments are mainly organic-rich clays with a minor fraction of coarser detrital material (Hudson *et al.*, 2008).

Post-Maykop Miocene sediments were deposited in a context of global regression until basin isolation occurred in the Late Miocene. These sediments are shallow marine and lacustrine thick clayey deposits (Allen *et al.*, 2002; Javanshir *et al.*, 2015).

The Pliocene was dominated by deltaic and lacustrine environments during a regression phase, fed from the ancestral Kura, Volga and Amu-Darya rivers that drained sediments from all the topographic highs surrounding the basin (Allen *et al.*, 2002; Abdullayev & Leroy, 2016). The subduction-related subsidence at the end of the Miocene accommodated the deposition of thick deltaic deposits forming the regional hydrocarbon reservoirs (Allen *et al.*, 2002; Javanshir *et al.*, 2015). The sedimentation rate was very high, reaching 2.4 km/Ma, with up to 6 km of the Productive Series (PS) (Allen *et al.*, 2002; Brunet *et al.*, 2003; Stewart & Davies, 2006). At the top of the Surakhany Formation (Upper PS), the regression was maximal and evaporitic beds are found in the northern part of the basin (Javanshir *et al.*, 2015). This interval will hereafter be called Anhydritic Surakhany.

Above the Productive Series, the Akchagyl Suite consists of open marine mudstones. This transgressive interval records the temporary reconnection of the SCB to the world ocean from 2.4 to 1.6 Ma (Allen *et al.*, 2002; Javanshir *et al.*, 2015; Dupuis, 2017). From 1.6 Ma to present, deep-water lacustrine and brackish conditions have dominated, forming the Absheron Suite and younger units.

More detailed information on the stratigraphy of the South Caspian Basin is given in Chapter 2:1.1.2 and is synthesized in Figure 2.4.

The presence of the high TOC (Total Organic Carbon) Maykop Formation and of the well-connected PS reservoirs make the SCB a prolific hydrocarbon basin (Hudson *et al.*, 2008; Javanshir *et al.*, 2015; Alizadeh *et al.*, 2017). The Maykop Formation generates gas in the deeper part of the basin and is still generating oil onshore and in the northern margin of the basin (Figure 2.6; Javanshir *et al.*, 2015). Large-scale anticlines (50-150 km long), detached over the overpressured and under compacted Maykop formation (Morley *et al.*, 2011) form excellent oil and gas traps as hydrocarbons migrate from the deep basin into the onshore heights along the regionally continuous reservoirs (Javanshir *et al.*, 2015). The large-scale anticlines main growth stage occurred at the end of Pliocene. However, fold-growth is ongoing although slower (Mosar *et al.*, 2010).

One hundred and eighty active MV's are listed onshore, and at least the same amount is estimated in the offshore part of the SCB (Milkov, 2000; Guliyev *et al.*, 2001; Kopf, 2002; Mazzini & Etiope, 2017). These structures are mainly located along the crests of anticlines where oil and gas have accumulated in reservoirs (Deville, 2009; Javanshir *et al.*, 2015; Mazzini & Etiope, 2017). They are generally considered to be sourced by the Maykop Formation (Kopf, 2002; Stewart & Davies, 2006; Roberts *et al.*, 2010). Additionally, Fowler *et al.* (2000) noticed on the offshore Shah Deniz anticline a close relationship between the development of folds and mud volcano activity as mud volcanoes activated during or after fold initiation and the authors correlate structural growth with mud volcano activity phases.

The Absheron anticline is a NW-SE oriented, 40 km-long fold, located at the northwestern edge of the SCB, 100 km to the south-west of Baku and 50 km south of the ACG gas-field (Figure 3.1A). Methane was recently discovered in the Absheron field and a giant active mud volcano pierces the crest of the structure at the southwestern limit creating potential hazards for drilling operations. Previous studies on the Absheron anticline evidenced the presence of four mass transport deposits (MTDs) in the Post-Absheron interval (Imbert *et al.*, 2014). The most recent MTD covers the whole anticline with the exception of the mud volcano location where it stumbles on the northern flank of the volcano. Morphology of the mud volcano in the upper 500 m of the sediment pile is described in Dupuis (2017). The poorly imaged central part is surrounded by three stacked wedges affected by multiple thrusts. Recent activity of the mud volcano is confirmed by four mudflows imaged in the first 100 m below seafloor (mBSF).

3. Materials and methods

3.1. Seismic data

This study focuses on the Absheron anticline, where an active mud volcano is imaged by a 3D seismic survey (limits and location on Figure 3.1). The seismic survey covers 650 km², in water depths ranging from 180 to 700 m. The seismic sections presented here are from Kirchhoff pre-stack time migration (PSTM) processing and from Kirchhoff pre-stack depth migration (PSDM) reprocessing (Robein, 2010), which was

applied on 550 km² of the seismic survey. The velocity model used in the reprocessing aimed to improve the imaging of the deep structures (thrust, dips), taking into account the lateral velocity variations across the thrust as well as the velocity heterogeneity in the shallow intervals due to the presence of the mud volcano and free gas (Adler, 2018, pers. com.). The model parametrization is a vertical transverse isotropy (VTI) that considers the vertical anisotropy imposed by the sedimentary strata (Robein, 2010). The model was entirely built by tomography inversion (Robein, 2010), and in the deep part, it was corrected using an interpretative method in order to preserve the structural coherency and to fit the well data (Adler, 2018, pers. com.). The seismic volume is composed by 2203 inlines and 2120 crosslines with 12.5 m spacing inline and 18.5 crossline. The vertical resolution varies with depth as it depends on interval velocity. From visual observations of the sections, we estimate a resolution ca. 20 m in the strata above 2000 m, progressively decreasing to 150 m at 11 km.

Each medium has its own acoustic impedance. Therefore, when a seismic signal reaches a limit between two media with different impedances, part of the acoustic signal will be reflected (Nely, 1986). A seismic signal can be decomposed in wavelets which are characterized by their polarity, their amplitude (peak area), its period and its phase (Nely, 1986). Normal polarity is given by the seafloor polarity, which in the data presented hereafter is a wavelet with a strong central positive amplitude surrounded by two weak negative amplitudes. Thus, the normal polarity is a strong positive peak enclosed between two weak negative peaks indicating a step-wise increase in impedance. The opposite shows a step-wise decrease in impedance (Nely, 1986; Ricker, 1953).

Seismic interpretation was carried out using the Total in-house software Sismage (Guillon & Keskes, 2004). From the 3D seismic cube, we calculated the seismic coherency attribute, which can be projected on horizontal slices or seismic horizons. Seismic coherency allows to laterally differentiate continuous areas (undisturbed deposits) from low continuity zones (faults or mud volcano deposits for instance) (Bahorich & Farmer, 1995). Horizons were propagated and named according to stratigraphic limits encountered in the two exploration wells drilled on the Absheron anticline (Figure 3.2 for location). These stratigraphic limits are interpreted based on cuttings analysis and gamma-ray, sonic and resistivity logs (see Chapter 2:2.3). Between two horizons, it is possible to extract layers of regular thickness on which the Root Mean Square (RMS) of the seismic amplitude can be calculated. This allows visualizing in map view the spatial distribution of sediment bodies whose impedance contrasts with the background, thus imaging for instance channels, mudflows, and pipes.

The presence of free gas is a well-documented cause of attenuation or data wipe-out (Graue, 2000; Benjamin & Huuse, 2017). Mud volcanoes are known to be accompanied by large emissions of gas (Kopf, 2002; Mazzini & Etiope, 2017). Therefore, seismic masking is expected to occur below large structures such as the Absheron mud volcano (Graue, 2000; Benjamin & Huuse, 2017). Imaging issues that cannot be settled by migration algorithms may arise from steep dips (Day-Stirrat *et al.*, 2010).

In parallel of the seismic imaging, high-resolution bathymetric maps (Figure 3.2) were acquired using a multi-beam echosounder.

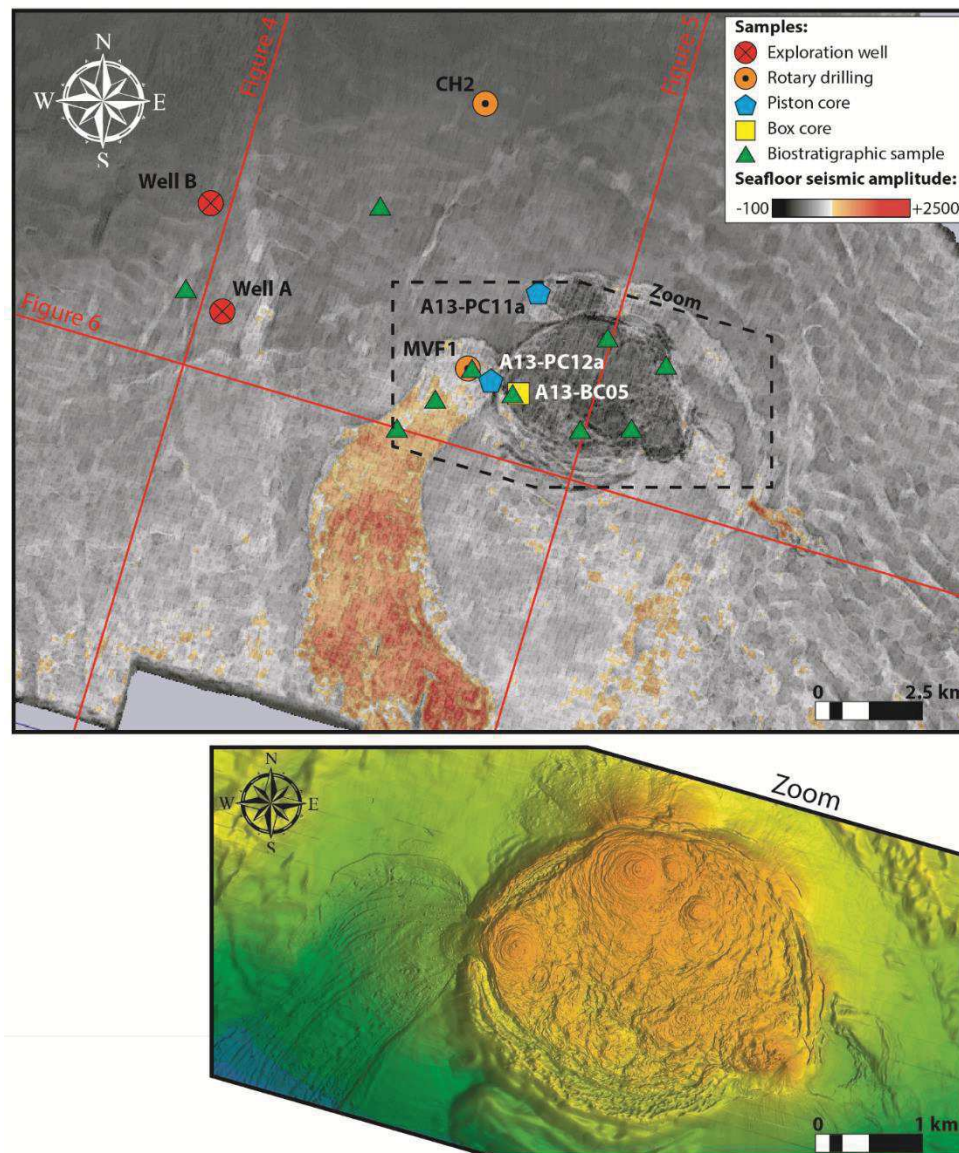


Figure 3.2: Seismic amplitude map of the seafloor around the Absheron mud volcano. In orange, a high amplitude mudflow is imaged to the west of the volcano. The dark patch corresponds to the shield composing the mud volcano itself. On the same map, the location of the different coring and drilling sites are shown. Limits and location of the 3D seismic survey are presented on the regional map of the SCB (Figure 3.1A). Red lines indicate the location of the seismic lines presented in Figure 3.3, Figure 3.4 and Figure 3.5. The dotted black polygon is the limit of the zoom shown below, presenting a detailed image of the seafloor on and around the mud volcano acquired with a multi-beam echo sounder. Orange stands for the shallower areas, green is for the deeper parts.

3.2. Sediment cores and geotechnical analysis

3.2.1. Sample collection

A marine geological and geotechnical survey of the seabed above the Absheron gas discovery was carried out in 2014 in order to better constrain and delineate geological hazards associated with the mud volcano (Total proprietary report, Dan & Po, 2017, pers. com.). The geotechnical/geological survey used rotary drilling, AUV (Autonomous Underwater Vehicle) sampling with box corer and piston corer as well as in situ geotechnical testing (Cone Penetration Testing). Well logging and CPT were performed on two boreholes:

CH2 was located outside the mud volcano area to provide a stratigraphic reference in continuous series, and MVF1 sampled on a mud volcano flow (for location see Figure 3.2).

To improve the characterization of mud volcano deposits, we selected thirteen samples from different sediment cores. Table 2-1 lists the coordinates and depth below seabed of these samples (all samples mentioned in Table 2-1, except samples that underwent consolidation testing) and Figure 3.2 shows their location with respect to the mud volcano. The samples were selected to provide information on the spatial and temporal variability of the mud volcano deposit (Total proprietary report, Dan & Po, 2017, pers. com.). Five samples were selected at three different depths from the same rotary drilling cores MVF1, thus potentially on different mud eruption episodes. One sample from A13-PC12a core was taken from the same mudflow as the one drilled by MVF1 but at a different location. A different mudflow was sampled on the A13-PC11a core at the northern edge of the mud volcano. Finally, a sample was taken from the A13-BC05 core directly on the top of the mud shield (see Table 2-1 for further details and Figure 3.2 for location).

3.2.2. Mineralogical and biostratigraphic analysis of the mud

The MVF1E RAW sample was separated into two different grain size classes, with a limit at 5 μm , in order to compare the composition of the clay-size fraction and the coarser fraction. The $>5\mu\text{m}$ of the raw sample was extracted by suspension of fine fractions in water followed by centrifugation.

The eight samples were analyzed using a reference quantitative mineralogy method called MinEval QM (Fialips *et al.*, 2018). This method is based on the integration of results from various measurements performed on crushed samples, including X-Ray diffraction on bulk powders and extracted fine fractions, Loss On Ignition, X-Ray Fluorescence, Insoluble Residue upon HCl 15% treatment, bulk solid density and Cationic Exchange Capacity (see Fialips *et al.* (2018) for more details). This method performs an initial semi-quantitative mineralogy analysis by Rietveld refinement of the XRD patterns (Rietveld, 1969) and quantification is completed applying a dedicated software that uses an iterative approach. The $<5\mu\text{m}$ fraction of MVF1E-RAW only obtained a semi-quantitative mineralogical analysis of clay minerals. The quantity of fine material obtained after separation was insufficient to perform the complete quantitative study.

Furthermore, a biostratigraphic study by Chevron in 2000 was carried out with the aim of dating the oldest material composing the mudflows. A series of samples were recovered in and around the volcano location (green triangles in Figure 3.2). The samples around the structure were used as age control points. The elements picked and counted on the different samples are diatoms, pollens, foraminifera, nannofossils and ostracods.

Initial grain size distribution for the natural mud was determined using the Mastersizer 3000 device for laser diffraction granulometry (Ryzak & Bieganowski, 2011).

3.2.3. Geotechnical analysis of the mud

Oedometer tests with permeability measurements were carried out on four samples taken from the GT1-MVF1 core (MECA 6-10-15-22 in Table 2-1 and tests from 1 to 8 in Table 3-1). Tests were duplicated in order to check for potential trial mistakes. The samples were selected based on Cone Penetration Testing (CPT, Das (2013)) data showing at least four mechanically distinct intervals (Total proprietary report, Dan & Po, 2017, pers. com.). The aim of these oedometer tests was to define compressibility characteristics (void ratio versus effective stress) and to determine the relationship between hydraulic conductivity and void ratio of the considered sediment intervals (ASTM International, 1996).

Table 3-1: Details on sample preparation for oedometer tests and results.

Test number	Sample	σ'_{vmax} (kPa)	w_L	e_0	C_c	Sample Preparation
1	MECA-6	1765.12	0.42	1.95	0.35	1.5 wL water input
2	MECA-22	1765.12	0.43	1.7	0.34	1.5 wL water input
3	MECA-10	1765.12	0.56	2.11	0.42	1.5 wL water input
4	MECA-15	1765.12	0.44	1.79	0.32	1.5 wL water input
5	MECA-6	1765.12	0.42	2.23	0.36	1.5 wL water input
6	MECA-22	1765.12	0.43	1.9	0.33	1.5 wL water input
7	MECA-10	1765.12	0.56	2.58	0.46	1.5 wL water input
8	MECA-15	1765.12	0.44	2.18	0.34	1.5 wL water input
9	MECA-16+17 + 5% sand	1765.12	0.44	1.38	0.25	1.5 wL water input, mixed samples
10	MECA-16+17 + 10% sand	1765.12	0.44	1.23	0.23	1.5 wL water input, mixed samples
11	MECA-16+17 + 25% sand	1765.12	0.44	1.14	0.20	1.5 wL water input, mixed samples

The void ratio e changes is tied to the vertical effective stress σ'_v by Eq. (1) (Chapter 2:3.2.4.ii). e_0 and C_c for the tested samples are shown in Table 3-1. The permeability is linked to void ratio following Eq. (4) (Chapter 2:3.2.4.ii).

The samples were all reconstituted with an artificial initial water content of around 1.5 w_L (w_L being the liquid limit). The w_L (Table 3-1) was determined using the fall cone method (Feng, 2005). Oedometer tests were conducted using incremental loading according to the ASTM D-2435 method (ASTM International, 1996). The determination of hydraulic conductivities and permeability coefficients was also

possible using the falling head method. Using an exponential regression on the obtained measurements is necessary to obtain a law of the form of Eq. (4).

In order to artificially characterize the impact of coarse material on mechanical properties, additional oedometer tests were carried out on grouped MECA-16 and MECA-17 samples (Table 2-1 and Table 3-1) mixed with a known mass of fine sand (80-125 μm); the goal was to obtain their compressibility and permeability in order to integrate these results in the numerical diffusion model. The fractions of coarse material added to the samples were selected based on the net to gross (ratio between sand layer cumulated thickness over total interval thickness) values calculated from well data.

Further details on the measurements and analysis methods are given in Chapter 2:3.2.4.

3.3. In situ well data and hydraulic conductivity calculations

Stratigraphic information was obtained from the two exploration wells drilled on the Absheron anticline (Figure 3.2). Well A reached 6506 m TVD/MSL (true vertical depth below mean sea level) whilst Well B reached 6823 TVD/MSL.

Lithology is obtained from cuttings analysis. Pore pressures in shales were estimated from sonic data using Eaton's method (Eaton, 1975). Sonic logs were acquired either with wireline or logging while drilling (LWD) tools depending on the interval. The StethoScope pressure-while-drilling tool (Schlumberger, 2019) was used to measure in situ reservoir pore pressure. Fracturing pressure log is evaluated from leak-off tests (LOT) or formation integrity tests (FIT) (Lin *et al.*, 2008), as well as down hole mud losses. Wireline tools measured temperatures at different points either in open hole or cased hole.

The sonic measurements are given as slowness of the acoustic waves, e.g. the inverse of acoustic velocity, which is linked to the porosity of the logged sedimentary interval using Wyllie *et al.*, (1958) relationship given in Eq. (6) (Chapter 2:3.3). The void ratio and porosity are linked by Eq. (7) (Chapter 2:3.3), thus allowing calculating hydraulic conductivities K for reservoir layers using the Kozeny-Carman relationship given in Eq. (8) (Chapter 2:3.3).

Therefore, it is possible to estimate the hydraulic conductivity of reservoirs directly from acoustic log data. Oedometer test results on natural mud allowed calculation of permeability in the shales. From the lithological log, the column was split into reservoirs and shale intervals. Using Eq. (4), (6), (7) and (8), we calculate for each defined interval the hydraulic conductivity K . The net to gross ratio (cumulated sand thickness divided by total interval thickness) was calculated for each drilled formation. The arithmetic average of hydraulic conductivities gives the horizontal hydraulic conductivity for the considered formation while the harmonic average gives its vertical hydraulic conductivity (Das, 2013).

Further details are given in Chapter 2:3.3.

3.4. Numerical modeling: sedimentation, transient pore pressure and gas diffusion

3.4.1. 1D sedimentation and pore pressure accumulation

Geological formations remain at hydrostatic pressure after deposition and burial as long as pore fluids are able to escape up through the overburden or laterally towards the seabed or surface. High permeabilities or low sedimentation rates help pore water escaping during consolidation. In contrast, when permeability is low or sedimentation rate is high enough, fluids cannot escape fast enough to keep hydrostatic conditions. As loading increases through sedimentation, pore water starts to support part of the overburden pressure, which prevents pores from closing. Thus, normal consolidation is delayed, sediments become under-compacted and pore pressure increases above hydrostatic conditions. This excess pore pressure is called overpressure and this mechanism of overpressure buildup is called compaction disequilibrium (Osborne & Swarbrick, 1997; Swarbrick *et al.*, 2002; Sultan *et al.*, 2004).

In this work, we calculate in one dimension the overpressure generated (Δu) only by sedimentation effect in the southern part of the considered section where the sedimentary column is the thickest. The high sedimentation rates observed in the basin are within the strongest recorded worldwide (Allen *et al.*, 2002; Brunet *et al.*, 2003; Stewart & Davies, 2006). Moreover, high sedimentation rates are considered to be one of the main overpressure generation mechanism (Osborne & Swarbrick, 1997; Swarbrick *et al.*, 2002). Therefore, the modeling work focuses on this sedimentation effect as a first approach. The SeCoV3 proprietary software of IFREMER (Sultan *et al.*, 2004) allows quantification of the evolution of pore pressure using a back analysis based on sedimentation rates, compressibility properties (Eq. (1), Chapter 2:3.2.4.ii) and permeability evolution with void ratio (Eq. (4), Chapter 2:3.2.4.ii). In addition to the equations solved by SeCoV3, in the present work we use a mesh-update method considering the compressibility of sediments and the mobile position of the upper boundary (seawater-sediment interface) at each calculation step.

Sedimentation rates and the model geometry used in this study were calculated using present thicknesses and ages from Green *et al.* (2009). These sedimentation rates have been corrected (decompression) for compaction using Terzaghi compaction equations (Terzaghi, 1943). At the end of sedimentation and compaction modeling, we applied a trial and error method until the model matched present-day observed thicknesses.

Compressibility and permeability properties characterizing each of the defined layers were determined based on oedometer and permeability tests (Table 3-1) carried out on natural mud mixed with known fractions of very fine sand (ASTM International, 1996). The fractions of added sand were selected thanks to net to gross values calculated from well data (Table 3-2). The purpose was to model the behavior of layers having different amounts of coarser material.

Table 3-2: Results of hydraulic conductivity calculations based on sonic-log data and oedometer tests on natural mud. NTG is the net to gross, being the ratio between total sand thickness over total interval thickness. The mean void ratio is calculated from the sonic log (equation (3)) and K_h (horizontal hydraulic conductivity) and K_v (vertical hydraulic conductivity) result respectively from arithmetic and harmonic average of calculated hydraulic conductivities on individual sand or shale layers using equation (5). The 1D-sedimentation model gives a range of void ratio for each stratigraphic interval, corresponding to hydraulic conductivity ranges on oedometer test results obtained for different sand fraction content (Table 3-1). Measured and calculated K_s are in the same ranges of magnitude.

Layer Name	Layer number in model	NTG (%)	Mean void ratio from logs	K_h (m/s)	K_v (m/s)	K_h/K_v	Void ratio ranges from 1D-model	K ranges from oedometer tests (m/s)	model k_x/k_y
Novocaspian - Absheron	Layer 5	5	0.33	5.03E-07	2.27E-10	2212	2.73 - 0.36	5.01E-07 - 3.53E-10	2200
Surakhany	Layer 4	8	0.18	3.18E-09	2.13E-10	15	0.43 - 0.24	7.50E-10 - 4.17E-10	15
Sabunchy	Layer 3	12	0.14	1.27E-09	1.95E-10	6	0.22 - 0.21	4.70E-10 - 4.56E-10	6
Balakhany - Fasila	Layer 2	24	0.17	5.16E-10	2.57E-10	2	0.27 - 0.24	7.78E-10 - 7.05E-10	2
NKG	Layer 1	8	0.17	2.18E-10	2.10E-10	1	0.24 - 0.22	4.17E-10 - 3.92E-10	1

3.4.2. Two-dimensional transient-diffusion process: Darcy's and Fick's laws

The two-dimensional transient dissipation of excess pore pressure generated by the sedimentation process is considered along a 63-km-long and 10-km-thick block of the section presented in Figure 11 of Green *et al.* (2009). We defined the geometrical model with 300 horizontal and 50 vertical nodes by considering six stratigraphic layers, the fault network around the Absheron fold and normal faults at the extrados of the fold.

The excess pore pressure generated by sedimentation and calculated using SeCoV3 was considered as a boundary condition for the 2D Darcy transient flow calculation. The two-dimensional dissipation and transmission of overpressure is calculated using the 2D diffusion equation given in Eq. (9) (Chapter 2:3.4.2). D_{hx} and D_{hy} , respectively the horizontal and vertical hydraulic diffusivities are calculated directly from the horizontal and vertical hydraulic conductivities K_x and K_y (Table 3-2).

In addition to the transmission/diffusion of pore pressure, we considered in the present work the molecular diffusion of dissolved methane. Methane diffusion is calculated using a two-dimensional diffusion equation referred to as Fick's law (Eq. (10), Chapter 2:3.4.2), which allows for the description of diffusion of dissolved molecules into a solvent (Crank, 1975).

To solve numerically the 2D diffusion equations (Eq. (9) and (10), Chapter 2:3.4.2), a centered explicit finite difference discretization scheme is used by considering the initial and boundary conditions for pore pressure and methane concentration.

Faults are characterized by their own methane molecular diffusivities creating preferential pathways for methane. Moreover, as the modeled stratigraphic column is formed by a succession of metric-scale sand layers and plurimetric shale intervals, a ratio between horizontal and vertical hydraulic conductivities was

integrated based on the results of the hydraulic conductivity calculations at wells (Table 3-2). This ratio allows modeling of the natural anisotropy of the sedimentary column due to sand-shale successions.

3.4.3. Hydrofracturing

In some cases, excess pore pressure can exceed the effective least principal stress plus the tensile strength of the medium allowing hydrofracturing to occur (Alfaro & Wong, 2001). When sediments are only submitted to the load of the overlying sedimentary cover, the greatest effective stress is vertical (σ'_v) whereas the least effective stress is horizontal (σ'_h) (Sibson, 2003). Fractures then open in the direction of the least principal stress and propagate in the direction of the plane perpendicular to the least principal stress (Hubbert & Willis, 1957). Therefore, in the case of sole loading effects, hydrofractures will propagate vertically.

The vertical effective stress and excess pore pressure are an output of 2D Darcy's diffusion equation. The ratio between fracturing pressure and overburden pressure (lithostatic stress) observed in the well ranges between 0.83 and 0.99, with an average of 0.9. Consequently, we consider in the present work that hydrofracturing will occur whenever the ratio between excess pore pressure and vertical effective stress ($\Delta u / \sigma'_v$) exceeds 0.9.

4. Results

4.1. Geomorphological investigation of the Absheron mud volcano

Figure 3.3 and Figure 3.4 present two parallel SSW-NNE sections. Figure 3.3 runs across the axis of the Absheron fold in the vicinity of the two exploration wells drilled on the anticline and Figure 3.4 cuts through the center of the Absheron mud volcano as located on Figure 3.2. The ages of five of the seismic horizons that are presented in this study were calibrated from the stratigraphic results of the well (Total proprietary data). We were able to map the top of Absheron Suite, the top of the Akchagyl Suite, the top of the Productive Series, the top of the Anhydritic Surakhany Formation, the Top Diatom Suite and the top of the Maykop Suite (see Figure 2.4 for the stratigraphic column). Seven other seismic horizons were interpreted in order to highlight particular structures such as normal faults or the morphology of the fold.

The deep part of the Absheron fold is cut by a deep E-W trending thrust that dies out in the Diatom Suite. This thrust has more than 2 km of throw and the northern block overrides the southern block. The thickening of the interval between Top Diatom and Top Maykop is interpreted as the result of a backthrust system that would have been inverted later during its history. Another thrust 5 km to the NNW has a throw of less than 1 km (Figure 3.3). The main thrust is responsible for the formation of the Absheron fold and several folding phases can be distinguished. The Productive Series interval has a rather uniform thickness of 5 km

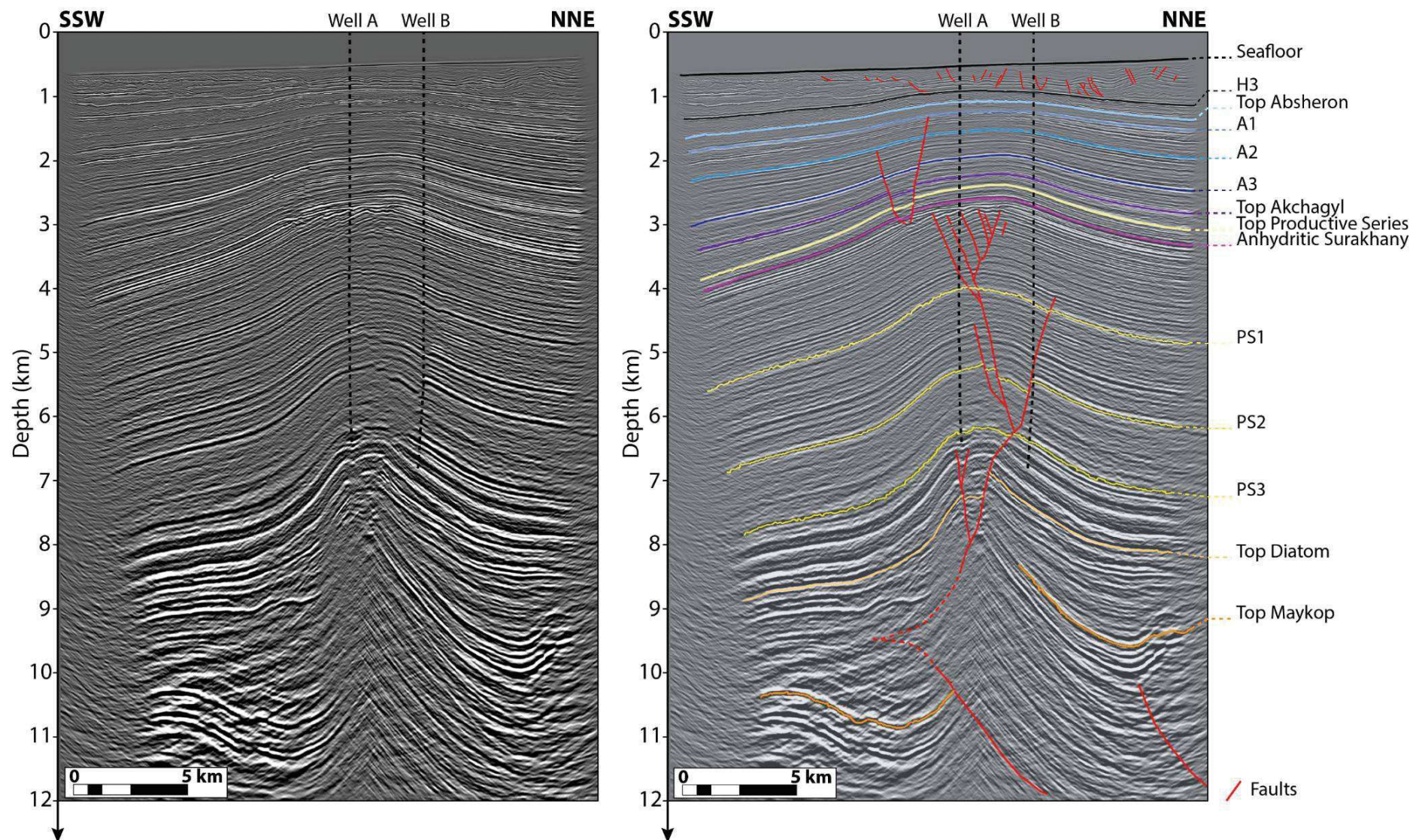


Figure 3.3: Uninterpreted and interpreted seismic line crossing the anticline near the two exploration wells A and B; it was used as reference for horizon picking for this study. A deep thrust cores the Absheron anticline and another thrust, smaller is also visible at the NNE of the section. From the thickness differences between the flanks and the crest of the structure, we note that folding started during the Akchagyl deposition. The main growing phases are during deposition of the Absheron Suite (A3-A1) and later during the Post-Absheron times. See Figure 3.2 for location.

across the anticline with only 10% of total thinning from the flanks to the crest of the anticline, indicating a rapid deposition during a phase of low-activity for the fold (Figure 3.3). The Akchagyl Suite above presents a thickening towards the southern flank of the fold of 300 m, corresponding to 60% of its maximum thickness (Figure 3.3), thus indicating that growth of the anticline was accelerated during deposition of this interval. Fold activity was still strong during deposition of the Absheron Suite as the thinning at the crest reaches 650 m for this interval, 35% of its maximum thickness. More precisely, the interval between horizons A3 and A2 recorded a thinning of 330 m (45% of maximum thickness), and between A1 and A2, 190 m (40% of maximum thickness, Figure 3.3). More recently, during Post-Absheron times, the fold re-activated and another 450 m of thinning (45% of maximum thickness) is visible from Top Absheron horizon to the seafloor (Figure 3.3). Therefore, sediment thinning at the crest of the anticline indicates that fold activity really started at the Akchagyl times, when it reached its climax. During the Absheron Suite deposition, the fold activity was intense for a longer time interval, and recent intense fold activity was also recorded in the Post Absheron interval.

Besides, normal faults on the extrados of the fold form a complex network from the thrust up to the Upper Productive Series (Figure 3.3). The back thrust was then inverted to form the main observed normal fault.

The Absheron mud volcano (AMV) is located in the SE part of the 3D seismic survey. Figure 3.2 shows the seismic amplitude of the seafloor horizon, with a color-scale set to outline high and low amplitude zones. Orange stands for the highest amplitude and darker areas correspond to lower amplitude zones. The high-resolution bathymetric map (Figure 3.2) reveals present seafloor morphology related to recent mud volcano activity. Near surface morphology of the mud volcano was already detailed by Dupuis (2017), with the presence of three main wedges (“Transparent Facies” and “Chaotic Facies” on Figure 3.4) and at least four recent mud flows evidenced on seismic data.

This mud volcano is a subcircular mud shield, 4 to 5 km in diameter (Figure 3.3). It is surrounded by a gently-dipping apron (average outward slope from 4° to 6°), the relief above the surrounding seafloor does not exceed 70 meters (Figure 3.2). The highest area is a relatively flat plateau, but at a closer look reveals at least four gently mounded circular structures, 0.5 to 1 km diameter (Figure 3.2); we interpret these as the loci of most recent mud emission. At the western edge of the mud shield, a 12-km-long, 1.5 to 3-km wide high-amplitude patch extends from the volcano to the west before following the natural slope towards the south of the Absheron seismic survey (Figure 3.2). This high-amplitude patch was already described as a giant mudflow by Dupuis (2017). This mudflow shows up strongly on seabed amplitude maps, indicating that is closer to seabed than the resolution of the dataset.

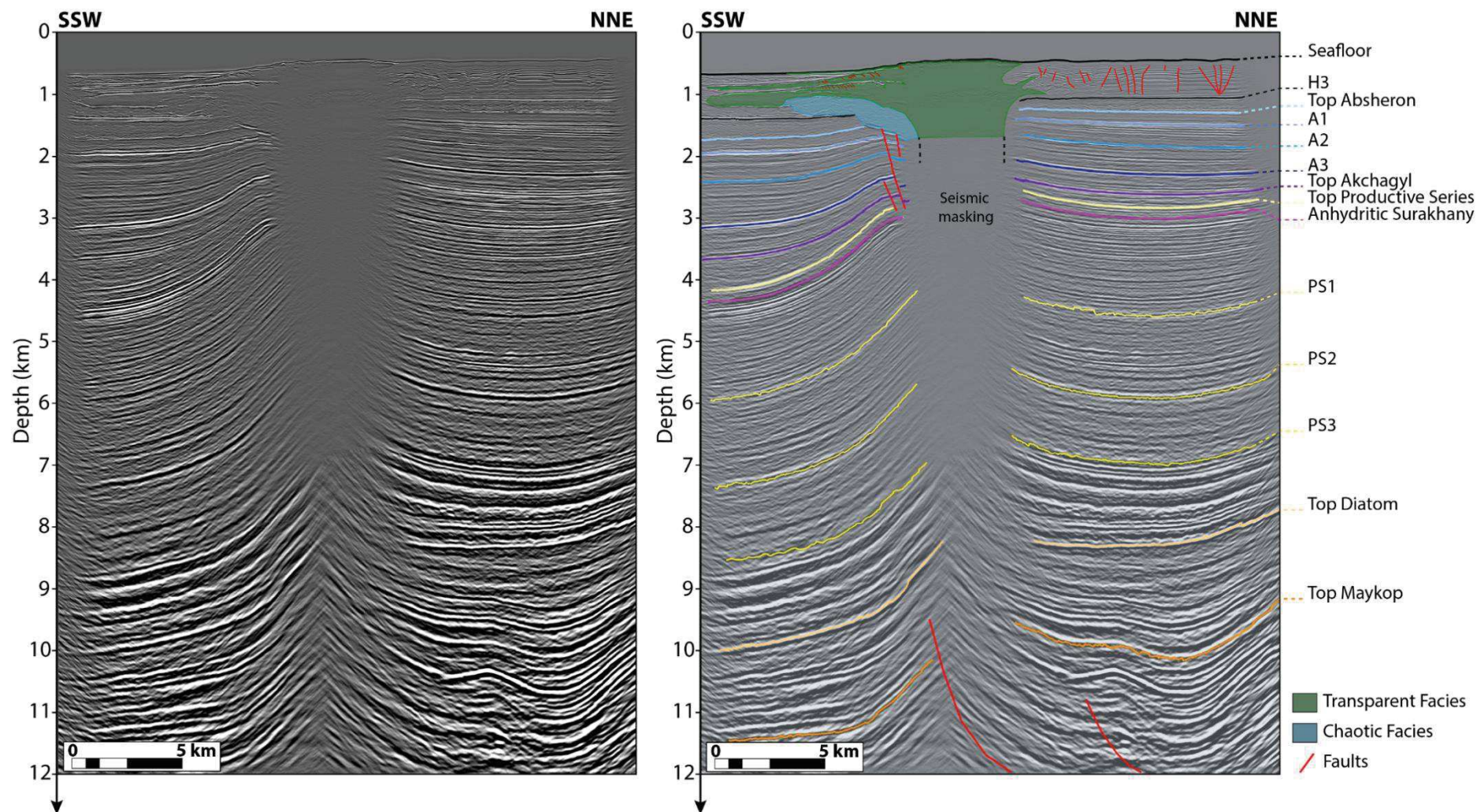


Figure 3.4: Uninterpreted and interpreted seismic line across the active mud volcano. The first 2 km are clearly imaged and show four seismically transparent wedges, corresponding to mudflows. A chaotic signal below can be discriminated from the blind signal and is interpreted as reworked sediments. The rooting system is blind, maybe due to a masking effect from the low velocity mud deposits. Near the blind area, some normal faults are present between 1.5 and 3 km. A deep thrust is coring the main anticline. The activation of the mud volcano is contemporaneous to the main folding phase (see text and Figure 3.3 for details, Figure 3.2 for location).s directly be interpreted as mudflow deposits forming the mudvolcano edifice (green patch on Figure 3.4). Below 2 km at the center of the structure, a seismically transparent cone goes down to 7 km. This area could reveal the masking effect of the low velocity mass formed by the shallower mud deposits that may also be saturated with gas, preventing the acoustic signal from propagating below. Another seismic facies can be discriminated from the blind signal: the blue patch can be described as a chaotic signal. This area is located between the mudflows and host sediments.

Interpretation of the section running through the center of the AMV (Figure 3.2 for location) is given in Figure 3.4. The first obvious observation is the presence of a large seismically transparent body spreading horizontally in the first 500 m below seafloor (BSF). Four wedges of this feature are imaged at the SSW from the center of the volcano. These interdigitations reunite at the center of the structure and form one large seismically transparent zone from the seafloor down to 1 km BSF. The shallowest digitation follows exactly the seafloor seismic horizon and is less than 50 m thick. As it was sampled notably with the box core A13-BC05 (Figure 3.2), this transparent area can directly be interpreted as mudflow deposits forming the mudvolcano edifice (green patch on Figure 3.4). Below 2 km at the center of the structure, a seismically transparent cone goes down to 7 km. This area could reveal the masking effect of the low velocity mass formed by the shallower mud deposits that may also be saturated with gas, preventing the acoustic signal from propagating below. Another seismic facies can be discriminated from the blind signal: the blue patch can be described as a chaotic signal. This area is located between the mudflows and host sediments.

Moreover, the deeply rooted thrusts described on Figure 3.3, are still imaged, yet not as clearly because of the seismic masking. Nevertheless, the Absheron mud volcano is centered above the exact vertical of the main thrust (Figure 3.4). The first mud flows imaged were deposited during the post-Absheron interval, between seismic horizons H3 and the Seafloor. No activity is recorded before H3. Consequently, the Absheron mud volcano seems to have been initiated after the end of the Absheron folding phase, during the post-Absheron folding phase.

Normal faults are imaged near the blind cone (Figure 3.4). They cross the Absheron Suite and end in the Upper Productive Series, near the Anhydritic Surakhany interval.

After the time of extrusion, we addressed the issue of the primary source of the mud by identifying a possible depletion zone (Stewart & Davies, 2006; Kirkham *et al.*, 2017b). In order to alleviate the seismic masking, we looked at lines crossing the volcano away from its center. Figure 3.5 presents a WNW-ESE seismic section, perpendicular to the section shown in Figure 3.4 and crossing the volcano 2 km away from its center. The section crosses the distal part of both transparent facies bodies and of the chaotic facies body from 0.5 to 2 km. The mudflow deposits appears 200 m above the H3 seismic horizon. The Top Absheron horizon is truncated by the chaotic mass. Deeper seismic horizons, from Absheron to Top Productive Series, bend downwards, forming a bowl shape particularly visible on tracked horizons A1 and A3. The Anhydritic Surakhany horizon and the 200 m thick interval below are truncated by downlapping younger intervals. Another truncated interval, 400 m thick, is imaged between 3400 and 3800 m, contained approximately the lower interval of the Upper Productive Series, below the Anhydritic Surakhany Formation. From 3800 m to deeper, horizons become continuous and flat again.

Two main eruptive events can be distinguished (one seismic phase between the two green blocks in Figure 3.5). This can be due either to a quiescent phase of the mud volcano activity when normal

sedimentation was recorded or to very high sedimentation events, such as mass-flows, that can drap mud volcanoes (Deville et al., 2006). The continuity of the seismic horizon separating the two mud masses is in favour of a normal sedimentation and doesn't seem related to any sediment instability present during the Post-Absheron interval (Imbert *et al.*, 2014). Normal faults flank the bowl-shaped area from 1500 m to 2000 m and show the motion towards the center of the bowl-shaped geometry.

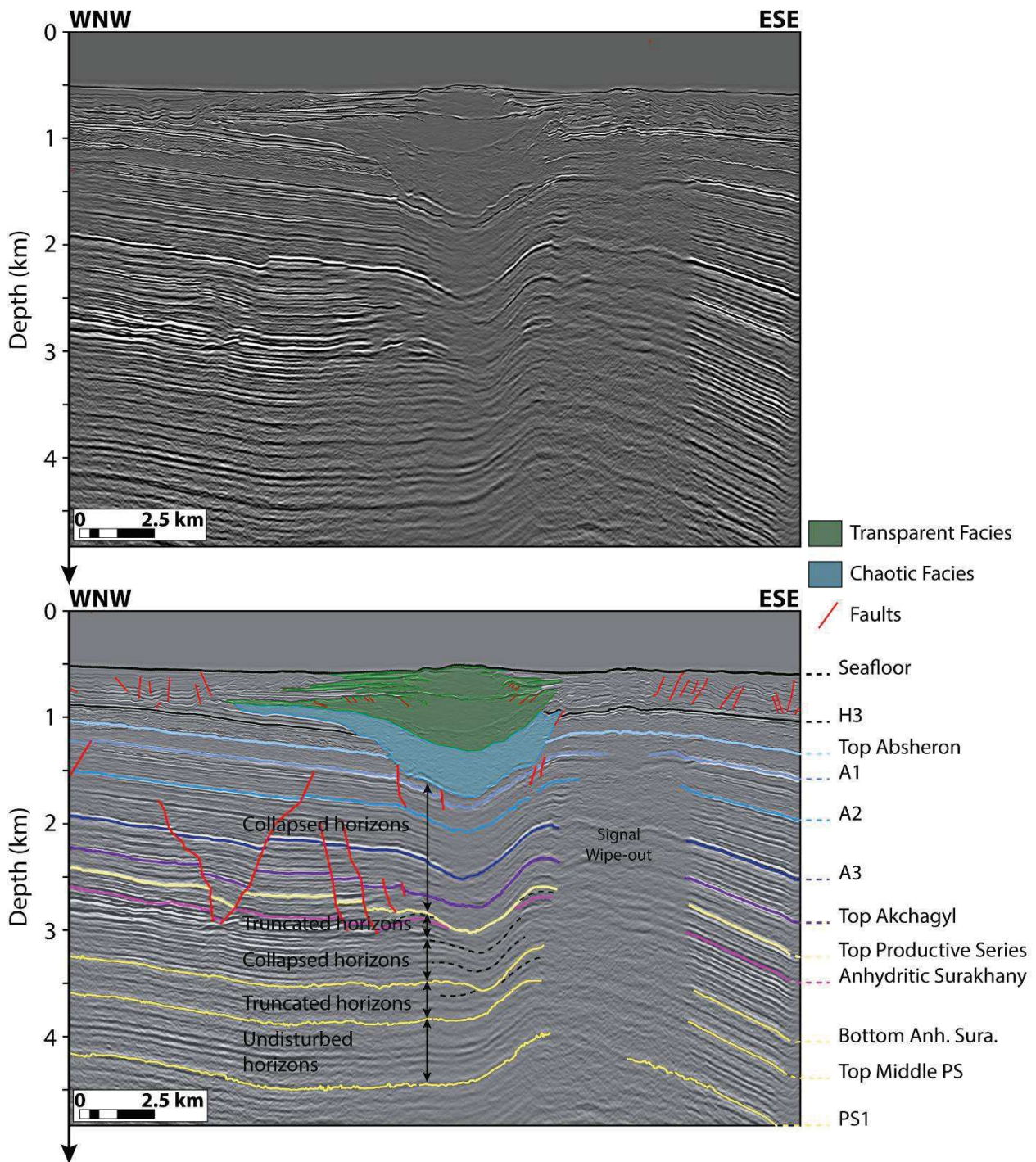


Figure 3.5: Uninterpreted and interpreted seismic line south of the mud volcano center. The gas blanking effect reduces below the mudflows. The transparent and chaotic signals are still present. A bending of seismic horizons from 1.5 to 3 km is noted forming a bowl-like geometry. Horizons of the upper part of the Anhydritic Surakhany are truncated by younger intervals as well as a 400 m thick interval in the lower part of the Upper Productive Series. Horizons recovers their continuity and their flat geometry below 3800 m in the Productive Series. See Figure 3.2 for location.

Thus, the main feature is the presence of a bowl-shaped geometry in the Absheron interval, truncating the upper part Anhydritic Surakhany as well as the lower part of the Upper Productive Series where some of the horizons are discontinuous and downlap on the younger intervals. Seismic continuity then extends into the Middle Productive Series and some normal faults are imaged around the edges of the bowl-shaped area.

In order to assess the possible ways of feeding the AMV in fluids and charging it in overpressure, the presence of channels related to the AMV and the stratigraphic intervals surrounding the ASF was explored using the RMS of the seismic amplitude projected on fine layers. 50 layers were computed between horizons A3 and PS1 (Figure 3.3 and Figure 3.7A), therefore creating layers 55 meters thick. Figure 3.6 shows the method used in order to recognize channel bodies. Any continuous and elongated body with roughly constant RMS values is first recognized in map view (Figure 3.6A). In order to confirm that it is a channel, we look at seismic sections perpendicular to each body (Figure 3.6A,C). If a downward bending of the horizon aligned to the studied layer is visible at the location of the body observed in map view (Figure 3.6C), the body is therefore interpreted as a channel and the trace of each channel is reported in map view (Figure 3.6B).

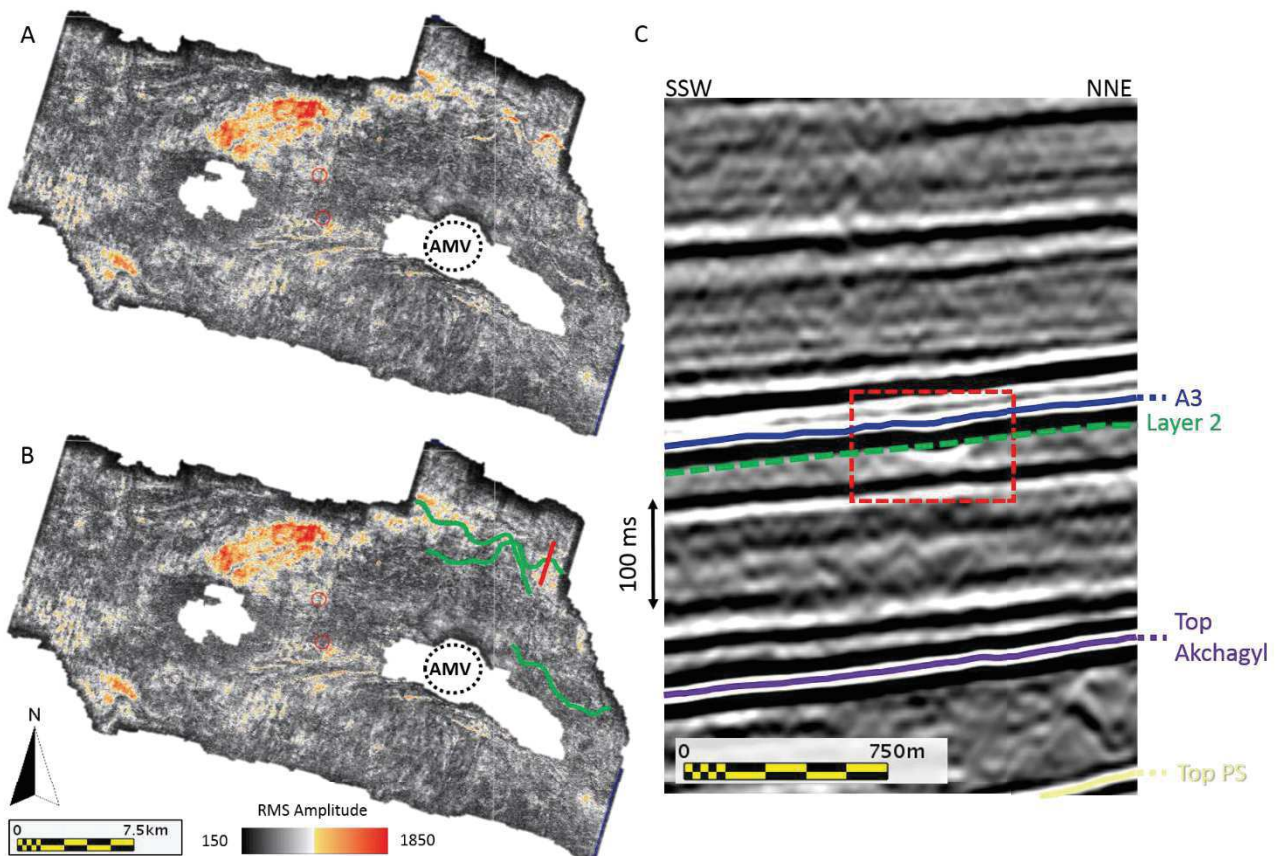


Figure 3.6: Applied method to channel recognition with the example of Layer 2 (Figure 3.7). A: the RMS of seismic amplitude is calculated on layers computed between two seismic horizons (here A3 and PS1). Elongated, curved and continuous bodies having the same RMS are potential channels. The surface location of the AMV is displayed with dotted lines. B: interpreted layer with confirmed channel bodies in green. The red line corresponds to the zoom of seismic section presented in C. The surface location of the AMV is displayed with dotted lines. C: zoom on a seismic section (location displayed in B, red line) perpendicular to a potential channel recognized on A. The seismic section is from the PSTM seismic block, and the vertical scale is given in ms TWTT (two-way travel time). At the exact location of the elongated body, a downward bending of two horizons is visible (red dotted rectangle). This bending is local and only affects two seismic horizons, thus, the body is interpreted as a channel.

The same method was applied over the 50 computed layers and some other examples are displayed in Figure 3.7B showing the variety of channel location and morphology. Layer 29 shows two areas where channels were initially interpreted (Figure 3.7, black and white dotted rectangles). At the crest of the anticline, crestral normal faults are present below the ASF horizon (Figure 3.7A). This affect the quality of the layering as layers cut through seismic horizons creating similar features in RMS maps as channels (Figure 3.7A, black dotted line). Moreover, as the interval between A3 and the Top PS is not isopach, the layers are not perfectly parallel to seismic horizons and they may cut each other on the anticline flanks. The features observed in the white rectangle south of the AMV on Layer 29 are observed on most of the other layers above and below and is due to a pull-down effect due to the presence of low-velocity mudflows in the shallower intervals (Figure 3.4).

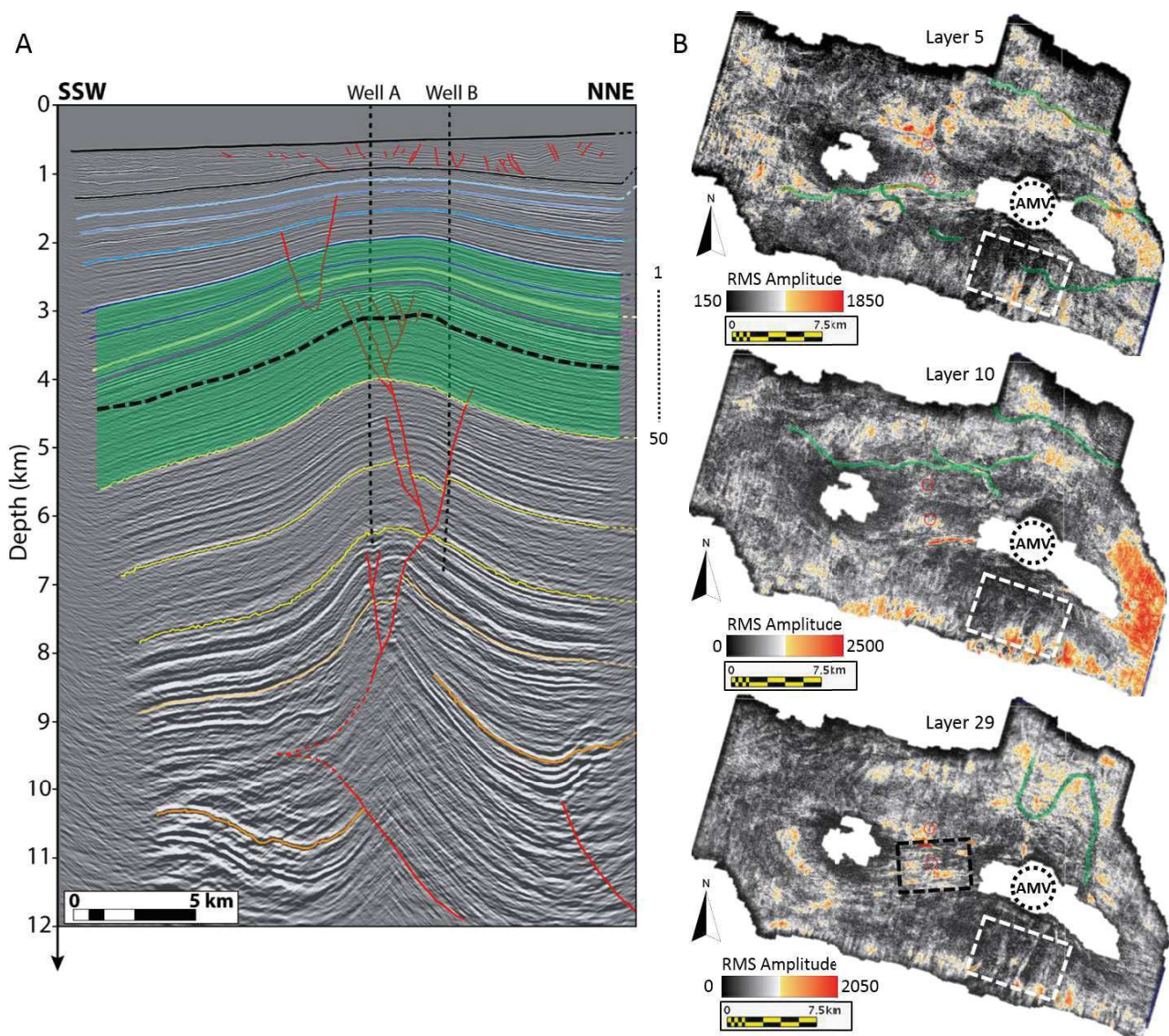


Figure 3.7: A: interpreted section presented in Figure 3.3, displaying in green the stratigraphic interval where layers were computed. The black dotted line highlights the Layer 29. B: examples of channels found over several layers, in green. The surface location of the AMV is displayed. The black dotted rectangle highlights the area of crestral faulting that generated channel-like features. White dotted rectangles highlight the same NE-SW features south of the AMV corresponding to several pull-downs of the seismic signal due to the presence of low-velocity mudflows in the shallower intervals (see Figure 3.4).

The complete results of the layer analysis are presented in Figure 3.8. All the channels are represented on two maps with colors corresponding to the layer on which they were observed (Figure 3.8A,C). Figure 3.8A regroup all the channels observed over the interval A3-ASF, therefore above the top of the ASF. Figure 3.8C displays the channels observed over the interval ASF-PS1, thus below the top of the ASF. A large number of channels are observed on A3-ASF compared to the ASF-PS1 interval (Figure 3.8A,C). Above the ASF, nearly all layers present channels (Figure 3.8A) while only 3 layers below the top ASF present channels (Figure 3.8C).

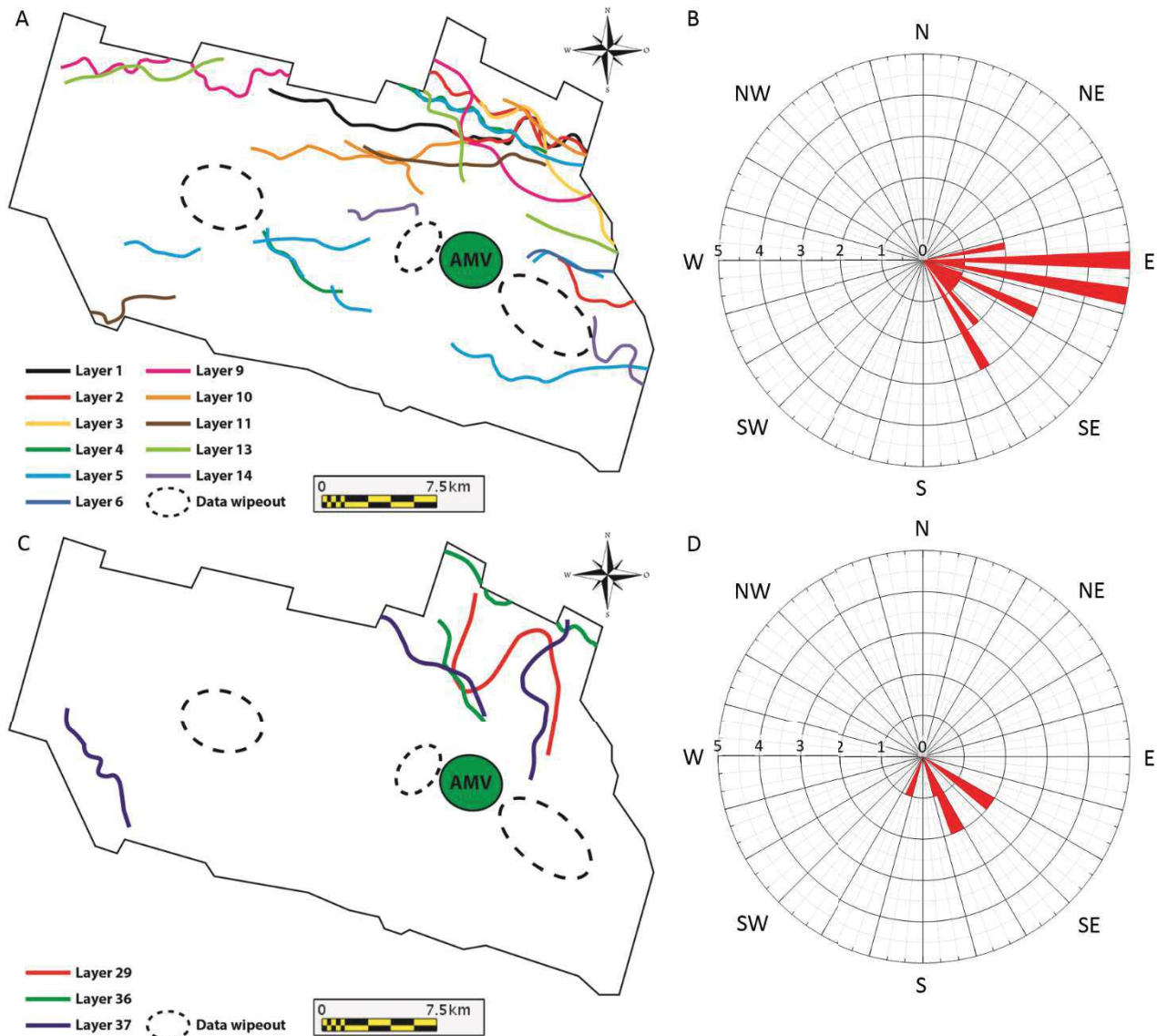


Figure 3.8: A: map showing all the channels found over the interval A3-ASF. Each color correspond to a layer where channels are found. Surface location of the AMV is displayed and areas of data wipe-out are also displayed. B: Rose diagram showing the orientation of channels located in the interval A3-ASF. Channels are mainly oriented between $N90^{\circ}$ and $N105^{\circ}$. C: map showing all the channels found over the interval ASF-PS1. Each color correspond to a layer where channels are found. Surface location of the AMV is displayed and areas of data wipe-out are also displayed. D: Rose diagram showing the orientation of channels located in the interval ASF-PS1. Channels are mainly oriented $N135^{\circ}$ and $N165^{\circ}$.

In Figure 3.8A, channels concentrate on the northern flank of the Absheron anticline and align along the syncline axis between Absheron and the ACG field (NNE of Absheron). Comparatively, very few channels are observed on the southern flank of the anticline (Figure 3.8A). Besides, some channels cross the anticline crest and roughly align with the AMV. A rose diagram showing the orientation of all the channels relatively

to the north (Figure 3.8B) shows a main trend for most of the channels with a direction varying between N90° and N105°. Minor pics are observed at N115° and N160° and orientations vary between N80 and N160°.

Figure 3.8C displays the rare channels that were observed below the top ASF. Except for one, all of them group between Absheron and ACG. The last one is roughly parallel to the others but flowed along the southern flank of the present anticline. The two main directions for these channels are N135° and N165° (Figure 3.8D) and two of them seem to align with the AMV surface location (Figure 3.8C).

Therefore, channels were observed, but mainly above the top ASF. These channels cannot be related to the bowl-shape geometry observed in the ASF and on the intervals below (Figure 3.5). Below the top ASF, the channels imaged at the seismic resolution are rarer. However, the Upper PS in the northern SCB were deposited in a fluvio-deltaic setting which was fluvial dominated during the Upper PS which is a period of low stand (Figure 2.4; Hinds *et al.*, 2004; Abreu & Nummedal, 2007). In a fluvio-deltaic context, the model of Posamentier & Allen (1999) shows that the reservoir facies composed by numerous channels are well connected and forms a multi-layer geometry with alternating reservoir and shale para-sequences. This observation was made in the northern SCB region by Grosjean *et al.* (2009) showing that well-connected reservoir facies are probably present in the Upper PS even if they do not represent economically interesting intervals compared to the Middle and Lower PS. Rare channels are imaged due to the fact that most of them may be under seismic resolution, and that the channels in fluvio-deltaic environments tend to migrate laterally in a short period of time and that does not allow thick accumulations or deep erosion. Thus, only deep and stable channels are expressed in seismic data.

In order to understand what impact such a reservoir would have on the formation of the AMV, it is paramount to study the anticline structuration at the time of the AMV formation. This will allow to quantify the gas column that potentially existed below the AMV. Free gas was indeed identified in the gas-out data of exploration wells over the Upper Productive Series. A reservoir will trap gas as long as it does not overflow into another topographic high. The point where fluids can overflow is called spill point. Therefore the maximum gas column thickness will be the difference between the highest point and the spill point.

Two cases are studied: a gas column starting at the Top ASF and gas column starting in the Upper PS (PS1). Therefore two thickness maps were computed: one between H3 and ASF, the second between H3 and PS1 (Figure 3.9).

Figure 3.9A displays the thickness map between the horizon H3 and the Top ASF. The spill point correspond to a thickness of 1650 ms (\approx 1300 m) and the crestal point correspond to a thickness of 1265 ms (\approx 980 m). Therefore, at the time of the AMV formation (H3), a gas column of 320 m could have existed.

Cathles *et al.* (2010) state that sediments becomes quick in a chimney when the buoyancy of a gas accumulation equals the overburden, which is equivalent to this equation:

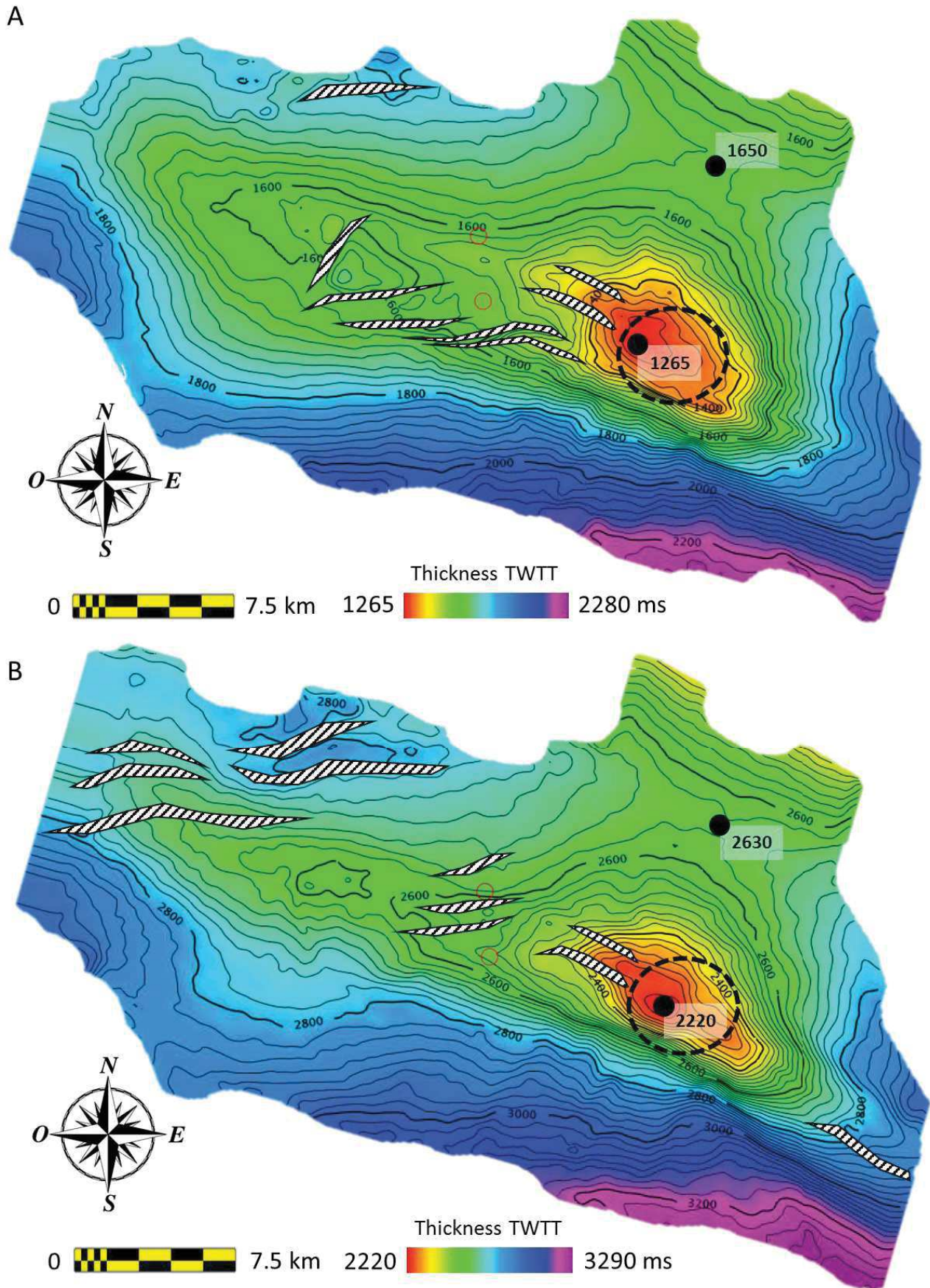


Figure 3.9: A: thickness map computed between H33 and ASF horizons. B: thickness map computed between H3 and PS1 horizons. Minor contours represent 25 ms and major contours 200 ms. The surface location of the AMV is displayed with black dotted circles. Fault zones are represented as hatched areas. The spill point and the highest crestal point are detailed.

$$(\rho_w - \rho_g)gh_g = (\rho_{sed} - \rho_w)gh_{sed} \quad (14)$$

with $\rho_w = 1000 \text{ kg/m}^3$ the water mass-density, $\rho_{sed} = 1800 \text{ kg/m}^3$ the sediment mass-density, ρ_g the methane mass-density that strongly depends on the pressure and temperature conditions, h_g the maximum height of the gas column (m) and h_{sed} the height of the overlying sediments (m).

From Egan *et al.* (2009) subsidence model, the water depth at the time of H3 is estimated to be roughly the same as now, around 500 m (± 50 m of sea level fluctuation from Forte *et al.* (2015)). Thus, at the time of the AMV formation, the ASF was located at 1500 m below sea level, and at 980 below seafloor. Therefore, the potential gas column was trapped under 15 MPa of pressure and at a temperature of 21.5 °C (using a thermal gradient of 16°C/km and a seafloor temperature of 5.85°C (Diaconescu *et al.*, 2001)). Using a free calculator from Courtois Energies (Courtois Energies Conseil, 2010), the gas mass-density value under these conditions is 97 kg/m³. Therefore applying Eq. (14) with $h_g = 320$ m and $h_{sed} = 980$ m (at the crest), it was found that the buoyancy of the gas column would have reached 2.8 MPa when the overburden pressure would have been as high as 7.7 MPa.

Figure 3.9B shows the thickness map between H3 and PS1. Using the same methodology, the gas column below PS1 at the time of the AMV formation would have been 540 m thick. The gas would have been trapped below 1920 m of sediments in 500 m of water depth. Therefore, $\rho_g = 151 \text{ kg/m}^3$ under 24,2 MPa and 37°C (Courtois Energies Conseil, 2010). Applying Eq. (14) with $h_g = 540$ m and $h_{sed} = 1920$ m (at the crest), the buoyancy of this gas column would have reached 4.5 MPa for 15.1 MPa of overburden.

Therefore, none of these possible gas accumulations would have been sufficient in order to break their sealing and trigger the AMV formation. Other physical phenomena had to participate in its formation. In this study, we assess the possibility for regional scale lateral pressure transmission through high sedimentation rates through numerical modeling (read Chapter 3:3.4 and Chapter 3:4.4).

8 km at the NW of the AMV, a buried mud volcano is imaged on the 3D seismic block (Figure 3.10A for location). The paleo-surface morphology of the MV is visible using the seismic coherency attribute at 5496 msTWT below sea level (Figure 3.10B). The coherency map displays a subcircular shape, 1 km in diameter corresponding to a buried bicone of this MV. The seismic section in Figure 3.10C allows noticing that the MV is actually formed by a superposition of two separate buried bicones separated by 100 msTWT. Below the first bicone, all horizons are bended downwards and are discontinuous at the lowest part of the bending. The discontinuities are aligned vertically forming a pipe like feature of roughly 100 m of diameter. The two bicones are also bended downward. From 6 sTWT to 6.5 sTWT, there is an area where no continuous horizons are imaged. However, from 6.5 sTWT to 6.8 sTWT, horizons are visible but are truncated, notably the Top Maykop horizon, forming a bowl-shaped area as for the AMV where horizons disappear. Below, horizons regain continuity and the deeply rooted thrust that was already described at the

NNE of Figure 3.4 and Figure 3.5 is imaged. The NNE block forms the hanging wall of the thrust that presents a throw of 100 msTWTT. The truncated area is centered above the highest point of the hanging wall of the thrust.

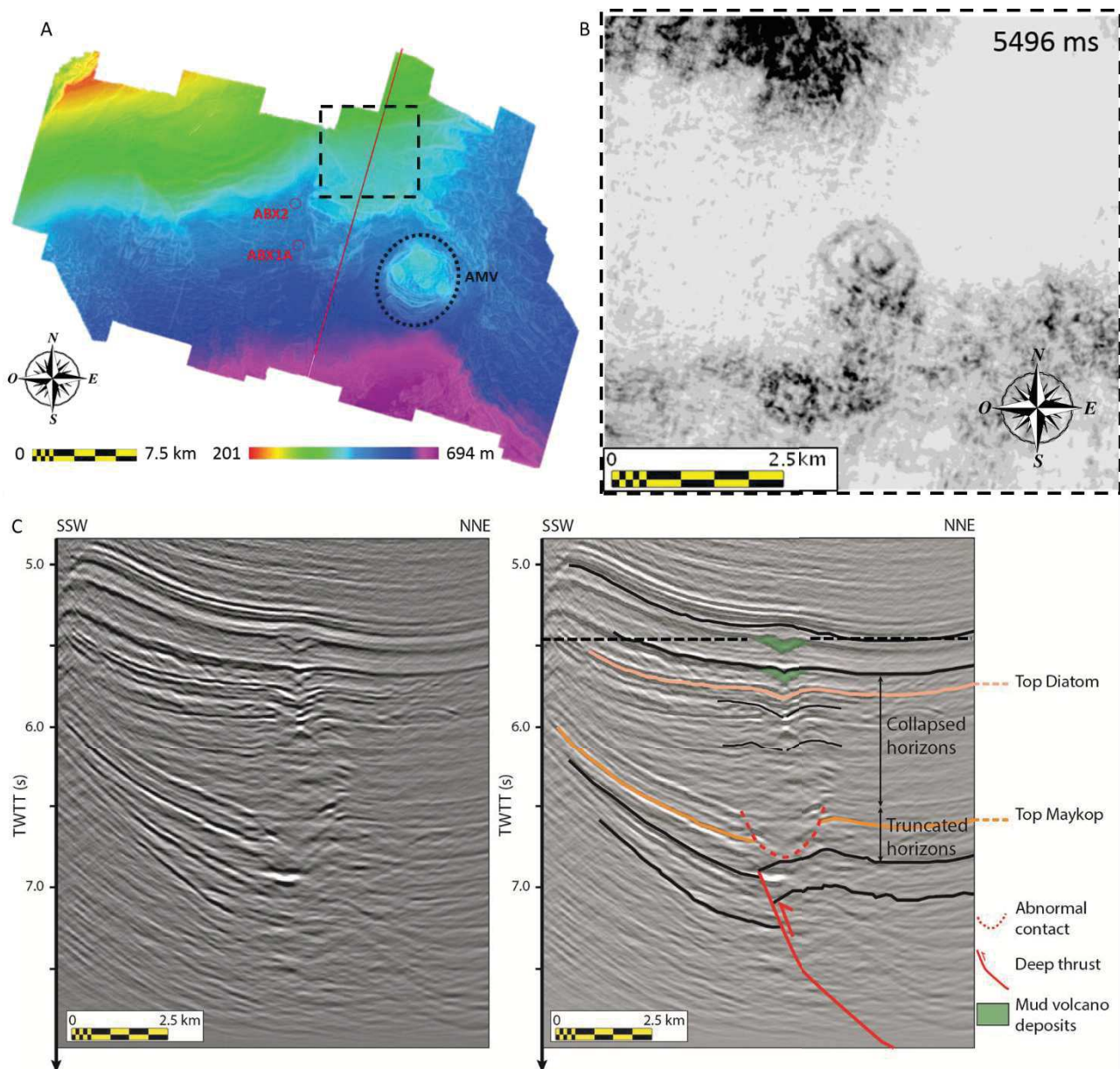


Figure 3.10: A: seafloor isochrone map showing the location of the zoom shown in B (black dotted rectangle) and of the section presented in C (red line) relative to the surface expression of the AMV and of the two exploration wells. B: coherency map at 5496 msTWTT displaying one of the two subcircular buried mud cones, reaching 1 km of diameter. C: uninterpreted (left) and interpreted (right) seismic section across the buried mud volcano, showing the entire mud volcano system, from its stratigraphic source with an area of truncated horizons located above a deeply rooted thrust, to the two buried bicones 1 sTWTT above the truncated horizons. Collapse of the horizon located between the truncations and the bicones are bended downwards and discontinuous. The black dotted line highlights the depth at which the coherency map in B was extracted.

In order to evaluate the volume corresponding to the truncated area, a thickness map was computed between the Top Maykop horizon and the deepest horizon highlighted in Figure 3.10C. The Top Maykop horizon was considered continuous and as following the abnormal contact. The result shows a thinned area corresponding to the area where horizons are truncated Figure 3.11. The thinned area represents roughly the same surface than the youngest bicone of Figure 3.10B. The two features are not perfectly superimposed

as the thinned area is elongated in the thrust direction and the bicone is subcircular and is shifted of 200 m towards the SW compared to the center of the thinned zone. The thinned area is not located at the direct apex of the fault but rather at the topographic high formed by the hanging wall strata as shown in Figure 3.10C. This is also evidenced in Figure 3.11, the thinned area being located not over the thrust but rather to its NNE, on the hanging wall side.

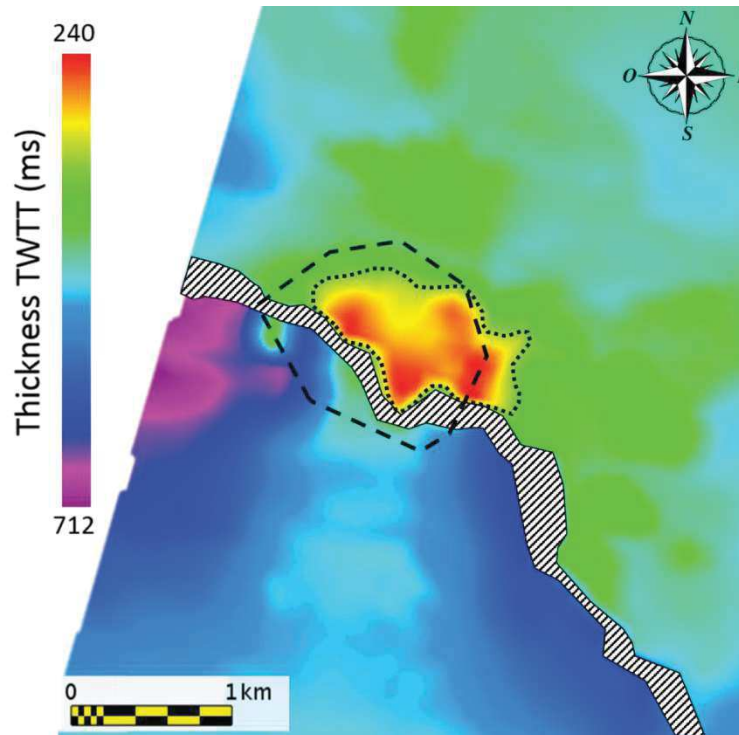


Figure 3.11: Isopach map computed between the Top Maykop and the deepest horizon highlighted in Figure 3.10C. The black dotted area, corresponding to red to yellow colors, highlights an area thinner than the background corresponding to the area of truncated horizons in Figure 3.10C. The black dotted polygon correspond to the approximate limits of the youngest bicone imaged in Figure 3.10B. The hatched area correspond to the thrust throw.

Therefore, the AMV was preceded by a more little MV that is now buried below 7 km of sediments. This other MV is not related to the same thrust as the AMV and is rather linked to a smaller one to the NNW. Similar features as in the AMV are highlighted such as a bowl-shape truncated area below the actual MV bicones. However, the truncated area is located in the uppermost strata of the Maykop Formation and is no longer related to the AMV. This smaller MV allows a more precise interpretation of the rooting system of the MV, eventually displaying the feeder pipe and evidencing that the bowl-shape truncated area is elongated along the thrust and aligned with the topographic high formed in the hanging wall of the thrust.

4.2. Physical, sedimentological and geotechnical properties of the mud

DRX analysis (Figure 3.12A) reveals that all the samples contain 42.3 to 53.6 mass% of clays and micas, between 19.8 and 24.9 mass% of quartz, around 8 mass% of albite. Calcite is also a major mineral of the tested mud of which it represents 6.1 to 14.4 mass%. Pyrite is relatively constant for all the samples with around 1.5 mass%. The clay fraction was analyzed in detail (Figure 3.12B) and is composed of 38 to 49%

interstratified illite/smectite, 29 to 38% Illite and/or micas and around 15% kaolinite. The rest is composed of around 5% Chlorite and less than 2% smectite.

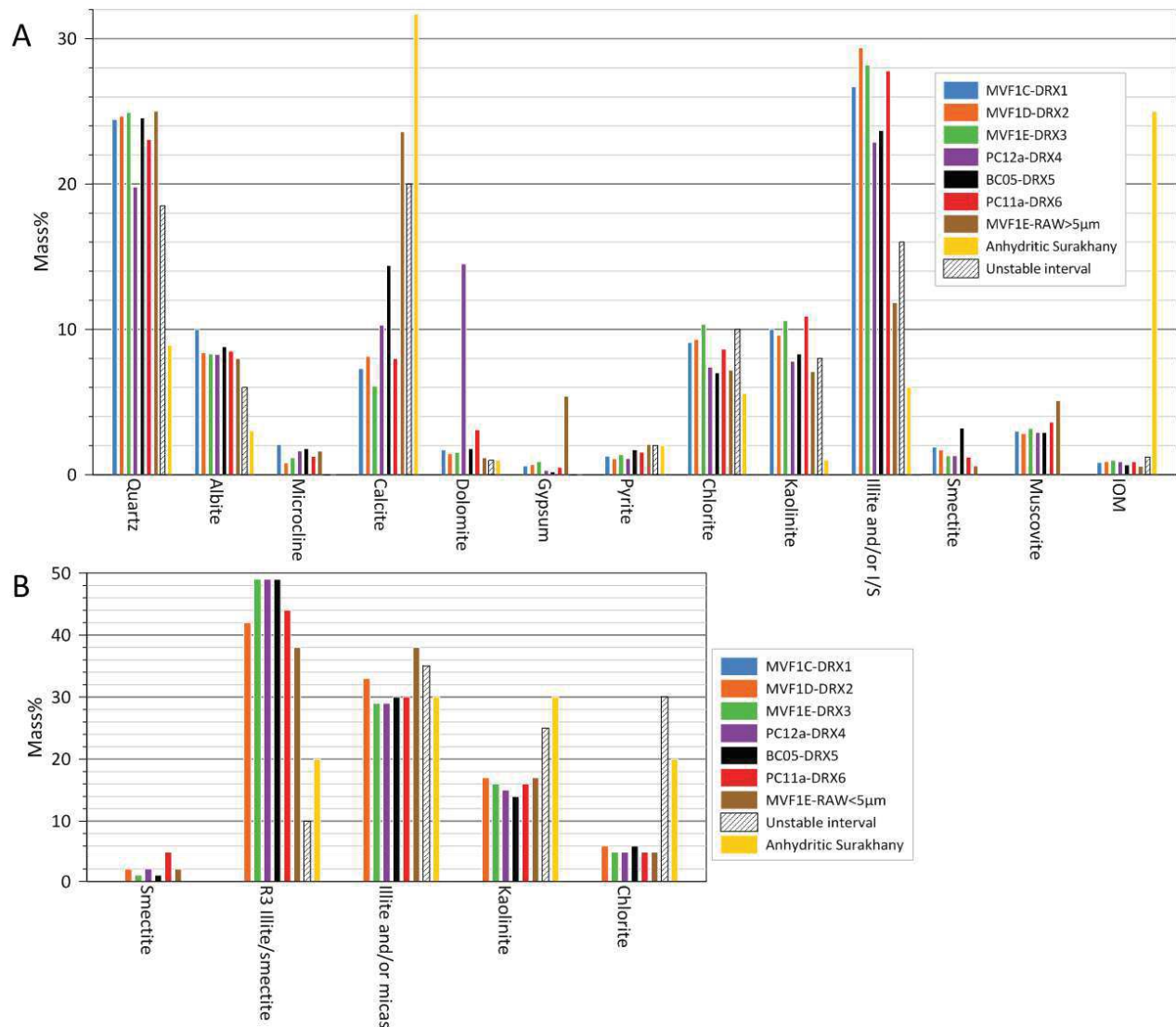


Figure 3.12: A, whole rock mineralogical analysis for all the samples collected except the less than 5µm fraction of the MVF1E-RAW sample, for cuttings from the Anhydritic Surakhany interval and for cuttings from the unstable interval encountered during drilling operations. The main elements composing the mud are clearly clay minerals and quartz particles and mud samples have similar mineralogical signature than the unstable interval. B: mineralogical composition of clay for all the samples collected except the MVF1E-RAW>5µm and for cuttings from Anhydritic Surakhany and the drilled unstable interval. Globally, clay fraction is mainly composed by up to 50% of interstratified illite/smectite, 30% of illite and/or micas, 15% of kaolinite and a minor part of chlorite and smectite, results different from the analysis of the Anhydritic Surakhany and its unstable interval. The less than 5 µm fraction of the MVF1E-RAW sample differs from the whole samples as they have less illite and/or micas, and more kaolinite and chlorite. See Figure 3.2 for location map, and Table 2-1 for details of samples.

More details are provided by the results of the two fractions of the same samples (Raw>5µm; Raw<5µm, see Table 2-1). Even when separating the clay-size particles from the rest, the coarser fraction is still composed of 31.8 mass% of clay minerals (Figure 3.12) showing the presence of clay aggregates or claystone clasts larger than 5µm that were not separated during suspension and centrifugation processes (Figure 3.12). The maximum amount of calcite and the only significant gypsum content are reached on this fraction with respectively 23.6 and 5.4 mass%. Comparatively with the <5µm fraction, it also contains a greater part of chlorite with 23% of the clay fraction. Further analysis on the chlorite fraction would be

necessary to conclude on its origin and the reasons for this variability as acid treatment destroys chlorite minerals.

In the fraction of particles less than 5 μ m in diameter (Figure 3.12B), there is only 20% illite and/or micas but also more kaolinite and chlorite (23% and 13% respectively). Illite is known to form at a higher temperature than interstratified illite/smectite (Pollastro, 1993), which means that the finer fraction is composed of a smaller portion of high temperature clay minerals than the unseparated samples but is also composed of more kaolinite and chlorite.

Peaks of carbonates have been observed in the coarser fraction of MVF1E as well as the BC05-DRX5 and the PC12a-DRX4. Sample BC05 was recovered from the top of the mud shield whilst PC12a comes from the top of the mud flow (Figure 3.2 and Table 2-1. This peak could be the result of the formation of authigenic carbonate crusts due to methane bubbling through fresh mud after an eruptive phase or at the top of the structure during a dormant phase (Kopf, 2002; Zitter, 2004).

Thus, the Absheron mud is essentially composed of clay minerals and quartz particles (Figure 3.12). Clay minerals are not only contained in the matrix as fractions of particles larger than 5 μ m also contain more than 30% of clays.

Biostratigraphic results on pollens and ostracods show a clear difference between samples collected on the mud volcano or on mudflows and background samples (Figure 3.2 for location). Samples from the mud volcano shield and the mudflow contain pollens from Miocene to Recent and ostracods from Late Miocene (Productive Series). Conversely, background sediments when not barren contain pollens from the Pleistocene and Holocene ostracods (Post-Absheron). Diatoms were only found in shallow background sediments and mudflows, with Pleistocene to Holocene taxa. The presence of diatoms identical to those of the background in mudflows and their absence from shield samples may indicate that the flows remobilized surface sediments on their way downslope and mixed with them. Nannofossil results are not considered reliable due to the poorness of elements present in the samples. Put together, these biostratigraphic results seem to indicate that the mud expelled at the Absheron MV only comes from the Productive Series.

Samples for oedometer tests were initially selected based on MVF1 CPT data from the Absheron mudflow (Figure 3.2 for location, Total proprietary report, Dan & Po, 2017, pers. com.). CPT curves (cone resistance, pore pressure and friction) present four intervals with distinct evolution of the three measured parameters. We suppose that these distinct tendencies are related to different intrinsic mechanical behavior of the mud intervals and oedometer tests were run on one selected reconstituted sample per interval at water content of around 1.5 wL in order to test this hypothesis (Table 2-1 and Table 3-1). Details on preparation and results of these oedometer tests are presented in Table 3-1. Oedometer tests presented in Figure 3.13A show no distinct behavior except for the MECA 10 sample, which also has a slightly different granulometric curve than the other three selected samples (Figure 3.13C). Indeed, the MECA 10 sample has

a greater fraction of fine material (from 2 to 10 μm) and less coarse fraction (from 30 to 300 μm) than the three other samples. This also matches with the high initial void ratio and the high compressibility of the MECA 10 sample with respect to the other samples (Figure 3.13A). Likewise, natural sediments show similar hydraulic conductivity with void ratio results except for MECA-10 that has a slightly lower permeability trend in accordance with the lower granulometry of this sample (Figure 3.13B-C).

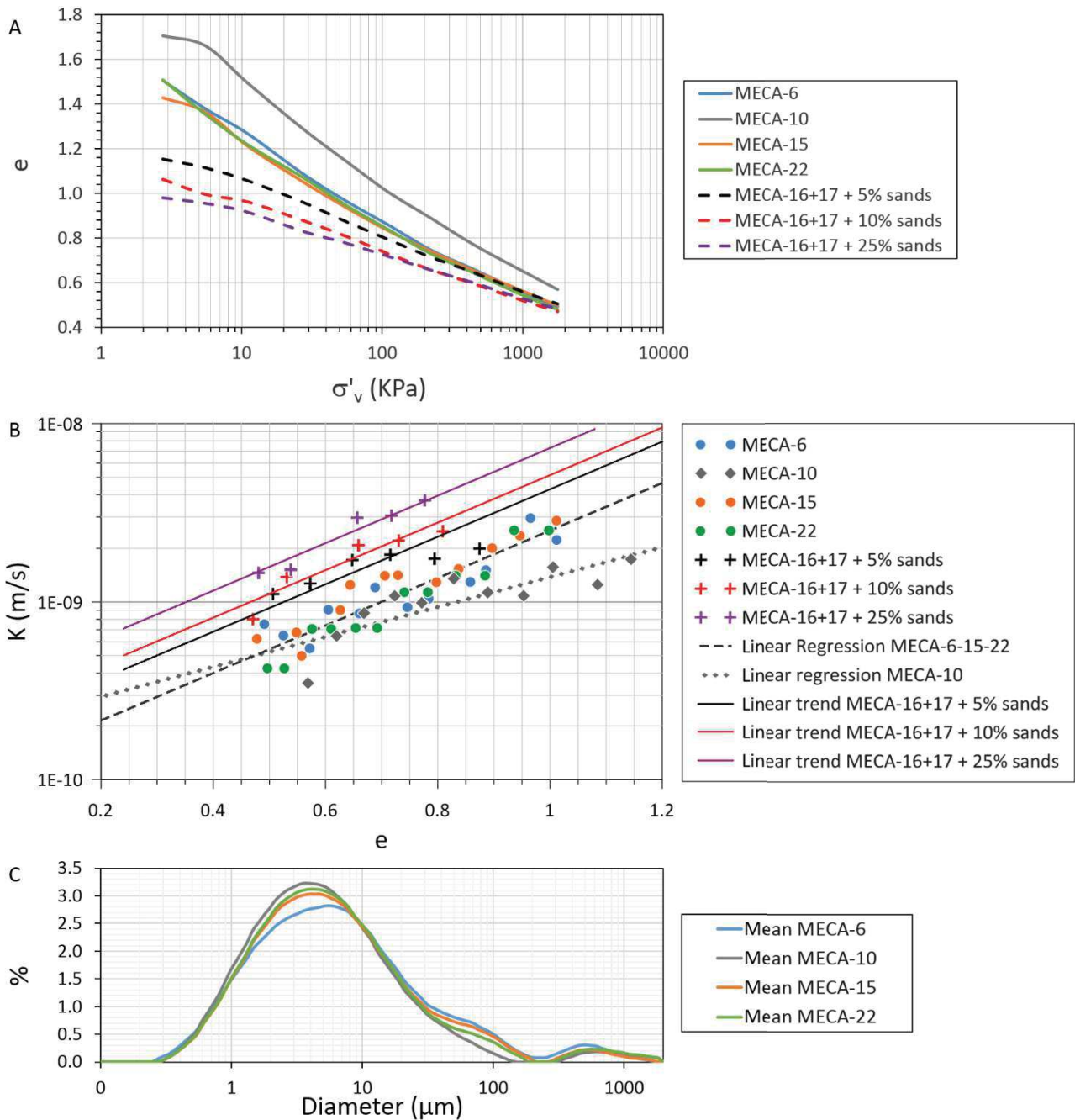


Figure 3.13: A: oedometer tests with void ratio (e) versus vertical effective stress (σ'_v) for the different tested samples. For the natural samples, only the MECA-10 has a higher compressibility and a higher initial void ratio than the other samples. The input of coarser material reduce the initial void ratio and reduce the compressibility of the samples. B: hydraulic conductivity (k) versus void ratio (e) resulting from oedometer test and falling head method results for the different samples analyzed. Again, MECA-10 has a lower permeability than other natural samples which fit the same trend. The input of coarser material reduces the hydraulic conductivity but the general trend stays parallel to natural samples. C: cumulative granulometry for the natural samples showing that MECA 10 is finer than the three other samples. See Figure 3.2 and Table 2-1 for more details on the samples.

MECA 6-15-22 compressibility curve (Eq. (15)) was considered as representative of all the other natural mud samples given the very low variability between the three different samples (Figure 3.13A) taken from different depths of the MVF1 core (Table 2-1).

$$e = 1.64 - 0.37 * \log\left(\frac{\sigma'_v}{\sigma'_{v0}}\right) \quad (15)$$

Permeability results showed no real differences between the different natural samples except for MECA-10 (Figure 3.13B), and a global linear regression for the other natural samples between $\ln(K)$ and the void ratio was adopted:

$$\ln(K) = 3.06e - 22.48 \quad (16)$$

Figure 3.13A shows that oedometer tests carried out on natural mud with a coarser fraction are characterized by a relatively low compressibility with a low initial void ratio (Table 3-1). At around 1000 kPa of vertical effective stress, the different compressibility curves converge at the same void ratio (Figure 3.13A). The permeability globally increases with the fraction of coarser material with the same parallel trend as natural sediments (Figure 3.13B).

4.3. In situ lithology, temperature and excess pore-pressure derived from in situ well data

The Post-Absheron interval and the Upper part of the Absheron Suite are composed of claystone. Interstratified claystones and siltstones form the rest of the Absheron Suite and the Akchagyl Suite. The Anhydritic Surakhany Formation extends from 2501 to 2887 meters TVD/MSL in well B and 2522 to 2905 meters TVD/MSL in well A. It is composed of claystone and evaporitic beds (mainly anhydrite and halite) and a minor part of siltstone. Over the 400 meters of drilled Anhydritic Surakhany, 30% of evaporitic beds were encountered with individual thicknesses ranging from less than one meter to eight meters. Finally, the rest of the Productive Series varies from claystone with rare pluri-decimetric to metric beds of siltstone to sandstone in the Surakhany (Upper Productive Series) to interstratified claystones, siltstones and sandstones in the Lower Productive Series. Some of the sandstone beds reach 15 meters in thickness.

Table 3-2 shows the results of NTG calculations based on well B data. The maximum NTG is reached for the Balakhany-Fasila interval (layer 2 in the numerical model), with a 24% NTG. The Surakhany interval has only 8% of NTG, and the Novocaspian-Absheron interval has the smallest NTG with 5%. As the well ends in the NKG interval, the NTG calculation for this particular layer may be inaccurate. From Eq. (3) and (5), vertical and horizontal hydraulic conductivities were calculated based on sonic logging. The calculated values fall within the measured ranges of oedometer tests on samples having a coarse content selected on the base of the NTG value of each interval.

Moreover, an unstable interval was crossed during the drilling of the Anhydritic Surakhany Formation in well B. This interval, described as a swelling claystone and is interstratified between two 5-meter thick evaporite layers. A high acoustic velocity and abnormally low electric resistivity characterize the interval. Cuttings from the interval present a rather similar mineralogical composition to the mud analyzed in this study (Figure 3.12) with 18.5 mass% of quartz, 34 mass% of clays and micas in which there is 35% illite and/or micas, 25% kaolinite and no smectite. However, some fractions vary from the mud analyzed: 12.8% of anhydrite were measured in the unstable interval; none was detected in the mud. Similarly, chlorite is present at 30% of the total clay fraction when in the mud, less than 10% was measured as well as calcite which was present at 20 mass% at the considered interval, when around 10 mass% was measured in the mud.

During drilling, temperatures were also measured at different points of the well allowing to approach a geothermal gradient of 16 °C/km.

Both wells, which are located 9.5 km west of the mud volcano (Figure 3.14), are overpressured at only 200 to 300 meters below seafloor (BSF) and remain in an overpressured state down to the well bottom. Overall, shale overpressure increases more or less linearly down to the top Productive Series with a gradient of 3 MPa/km. Deeper down, the increase is linear again, with a higher gradient. In addition, six pressure peaks, that are located all along the Productive Series Interval, can be observed in both wells (Figure 3.14). On these intervals, shale pressure values nearly reach the fracturing pressure, making the concerned intervals easier to fracture if pressure buildup happens. The concerned formations are the Anhydritic Surakhany (peak 1 in Figure 3.14) as well as five other intervals of the Productive Series.

We noted potential links between structural features and pressure peaks (Figure 3.14). For instance, the pressure peak 4 in well A, is split into two minor peaks in well B. There is a normal fault cut by well B that matches the pore pressure decrease observed at well B. Moreover, pressure peaks can be transposed below the mud volcano to visualize which intervals are more prone to overpressure below the structure.

Pressures were also recorded in the reservoirs. In well A, reservoirs tested above 5000 meters BSF are in equilibrium with surrounding shales. Below 5000 meters, in wells A and B, reservoirs are at least 20 MPa below the surrounding shales. In well A, some of these deep reservoirs are as overpressured as the shales. These results show that shallower reservoirs are not able to dissipate overpressure whereas deeper ones appear drained and their pressure is much lower than surrounding shales. The deeper reservoir intervals are known to be regionally continuous and some even outcrop onshore in Azerbaijan (Javanshir *et al.*, 2015). They act as regional drains for overpressured fluids with a northward hydraulic gradient as shown by the work of (Bredehoeft *et al.*, 1988; Javanshir *et al.*, 2015). The sands in the northern area of the SCB are at hydrostatic pressure while an excess hydraulic head creates deeper in the center of the basin.

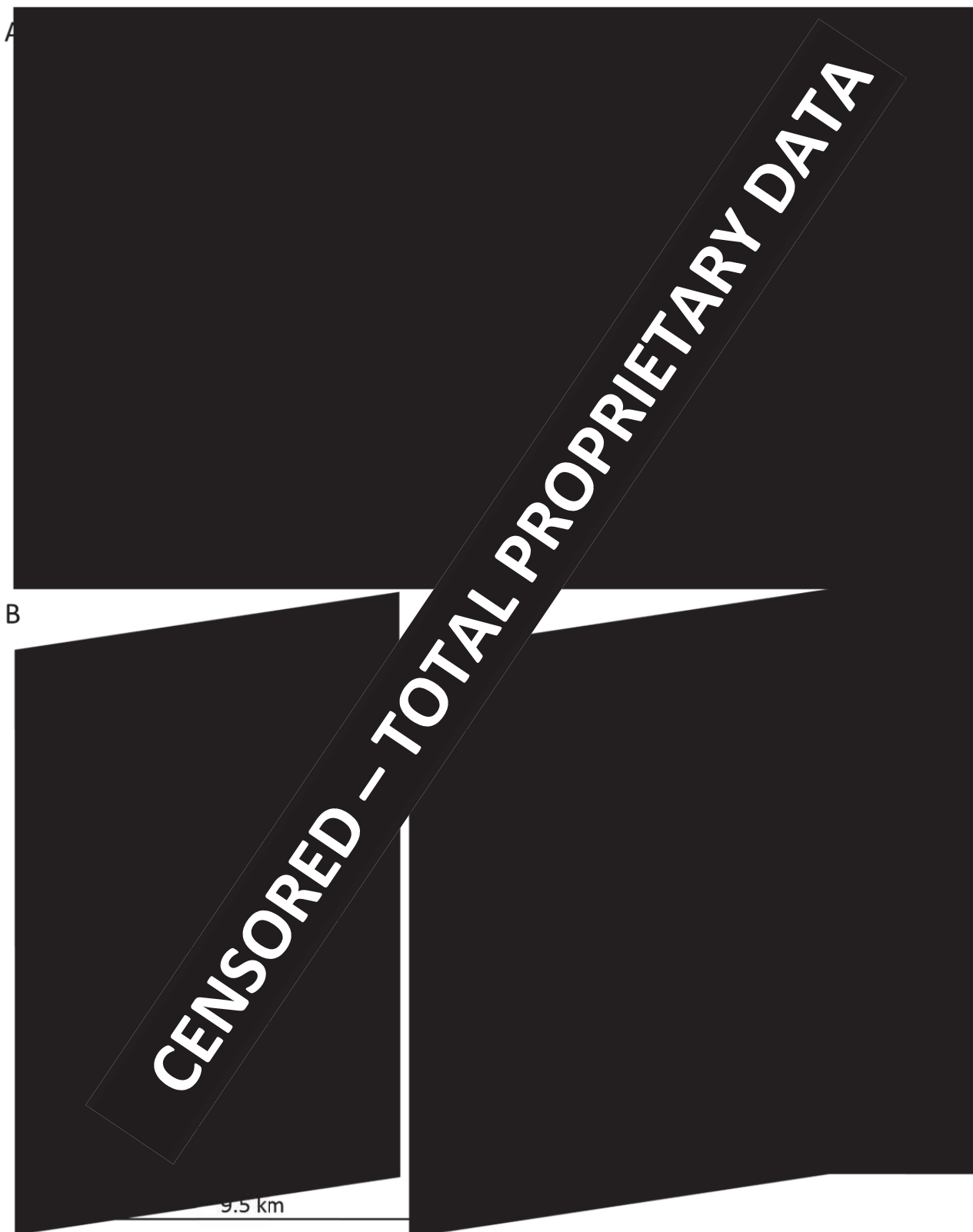


Figure 3.14: A: overpressure logs for both exploration wells. Overpressures are in MPa. Continuous green line is the sonic-derived shale pressure and green crosses are the measured reservoir pressures. The orange dots are the LOT/FIT control points used in the construction of the fracture pressure plot (red line). The vertical line where overpressure is zero is the hydrostatic pressure. Seismic horizons are shown using the same color code as in Figure 3.3. Six different shale pressure peaks are highlighted in red B: 3D view of the two parallel seismic lines distant of 9.5 km. The right one is described in Figure 3.4. The left one in Figure 3.3. The pressure peaks are reported in front of the corresponding interval on seismic.

4.4. Numerical calculations of transient pore pressure and methane diffusion

4.4.1. 1-D modeling

The first step of the numerical modeling was a one-dimension calculation of sedimentation-generated overpressure in the deep part of the basin, 25 km south of Absheron. For this purpose, each layer was characterized by a compaction-corrected sedimentation rate based on Green *et al.* (2009) sediment ages and present thicknesses, compressibility and permeability laws (Figure 3.15). Nadirov *et al.* (1997) gave average sedimentation rates for the South Caspian Basin also based on present seismic thicknesses. Their estimated rate values span from 1 to 3 km/Ma for the Quaternary and around 0.5 km/Ma for the Productive Series interval. These values are too low considering the results of our compaction-corrected 1D modeling (Figure 3.15). However, our sedimentation rates depend on the compressibility laws integrated in the model. In the present paper, we present compressibility behavior of samples artificially created from natural mud and a known fraction of sand. Compressibility laws for natural sediments of each modeled stratigraphic interval might be different from the laws used in this study.

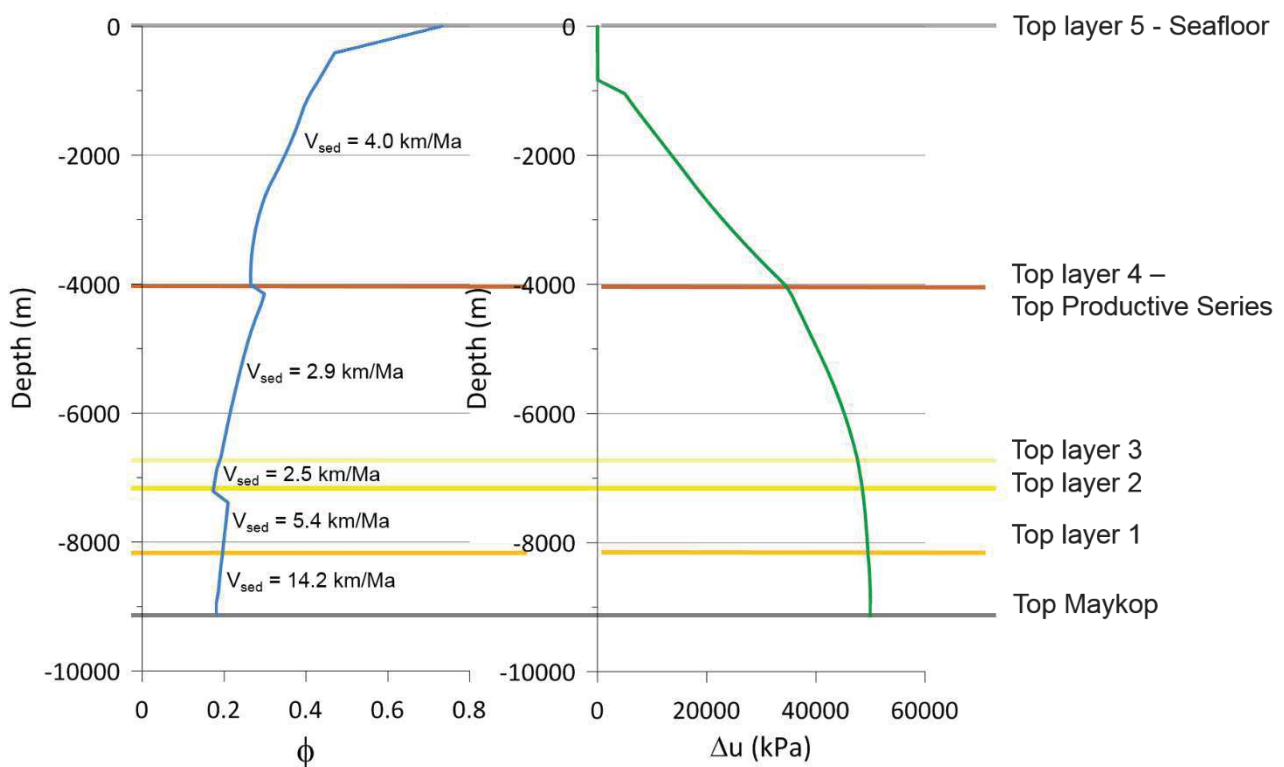


Figure 3.15: Results of the one-dimension sedimentation modeling. On the left, porosity vs. depth trend at the end of the 5 Ma of sedimentation with corrected sedimentation rates for each layer. On the right, overpressure vs. depth trend at the end of the 5 Ma of sedimentation.

The calculation runs over 5 Ma, during which 9600 m of compacted sediments have been deposited. As compression laws for mixed mud and very fine sands were measured for the first 1800 kPa of vertical effective stress, at higher effective stress, the void ratio may reach negative values in some layers. In order to avoid this type of problem, we set a minimum limit for the void ratio at 0.1 in the software to obtain a

compressibility trend similar to the ones presented by Chong & Santamarina (2016). Permeability laws for natural mud and mud mixed with very fine sands obtained from oedometer test results were integrated to characterize each stratigraphic interval (Figure 3.13A-B). The validity of the permeability laws was confirmed by the calculations on sonic logging (Table 3-2).

Figure 3.15 shows the porosity profile vs. depth at the end of the sedimentation history. It gives a good representation of how sediments have compacted during the sedimentation history. The overpressure plot shown in Figure 3.15 corresponds to the overpressure generated by high sedimentation rates in the deepest part of the basin. Overpressure rises rapidly with depth in the low permeability layer 5 as overpressure cannot be evacuated and transmitted rapidly to the whole interval. The increase is slower from Layer 4 down because of higher permeability. Finally, overpressure increases with a very low gradient from Layer 2 below, Layer 2 having the highest permeability.

4.4.2. 2-D modeling

The second part of the modeling consisted of creating a structural model for two-dimensional diffusion of overpressure and methane. The structural model presented in Figure 3.16 is based on the work of Green *et al.* (2009) and on the fault network observed on the reference section in Figure 3.3. The initial section presented by Green *et al.* (2009) was only reproduced from the deeper part of the basin to the Absheron Ridge, where the seafloor is shallowest. The direction is the same as the section presented in Figure 3.1B. The total length of the section is 55 km, and its maximum depth 9.6 km. Faults shown in Figure 3.16 are meant to represent not only the fault surfaces (localized thin shear zone), but also to the damage zone surrounding them. We estimated the thickness of the damage zone based on the work of Savage & Brodsky (2011), who relate the damaged thickness around a fault to the throw of the fault. With a total throw about 1 sec TWTT for the main, a damage zone of a few hundred meters is expected. In the present work, a damage zone of 300 meters is considered as representative of the fault zones.

Figure 3.16 shows the boundary conditions used for the numerical calculation of methane and pore pressure diffusions. No lateral or vertical exchange of pore pressure and methane with the outside of the model is permitted through the laterally impermeable southern and northern borders and the vertically impermeable upper and lower borders. The sea water has a fixed pore pressure of 0 kPa and a methane concentration of 1.0×10^{-5} mM (milli-molar, 1 molar corresponding to a solution of 1 mol/L of concentration) which is a mean oceanic value (Lamontagne *et al.*, 1973). The pore pressure calculated in one dimension from sedimentation with SeCoV3 (Figure 3.15), is imposed at the southern border of the model, where the sedimentary column is the thickest. Finally, a methane concentration of 1.0×10^{-3} mM is fixed at the bottom of the fault network, methane being generated in the Maykop Formation, the regional source rock, the deeper layer represented in the model.

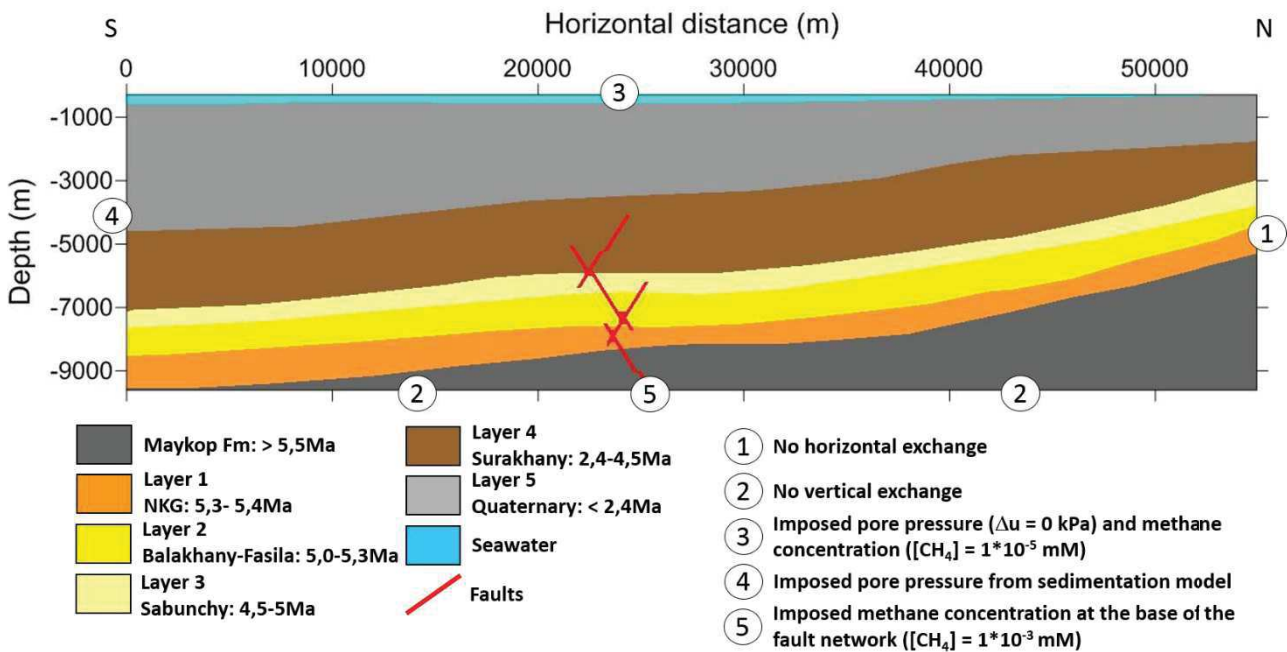


Figure 3.16: Structural model based on Green et al. (2009) work and on the fault network observed in Figure 3.3. The line follows the same trend as the seismic section of Figure 3.1B. Eight layers extend along the section corresponding to different sedimentation rates, compaction laws and permeability trends (see Figure 3.15). The Layers NKG, Balakhany-Fasila, Sabunchy, Surakhany and Quaternary are named Layers 1 to 5 respectively in other figures. Numbers showed at the limits of the model correspond to limit conditions imposed for the diffusion of pore pressure and methane.

Pressure and methane migration calculation were run over 5 Ma. Results of the diffusion equation resolution (Eq. (9) and (10), Chapter 2:3.4.2), in terms of overpressure migration, are shown in Figure 3.17A. Methane concentration and ratio between overpressure and vertical effective stress are shown together in Figure 3.17B in order to compare possible hydrofractured zones with high dissolved methane saturated areas.

Overpressure (Δu) propagated from south to north of the model at different diffusion rates. Indeed, depending mainly on permeability laws, overpressure will propagate more or less quickly and in different directions. For instance, in layer 5 overpressure did not accumulate (Figure 3.17A). This layer being the youngest, it maintained a high void ratio and so a higher permeability. The effect is amplified by the ratio between horizontal and vertical permeabilities. Layer 5 having a ratio of 2200 (Table 3-2), the horizontal permeability in the model is 2200 times larger than the permeability defined by oedometer test results. Therefore, in layer 5, pressure diffusion is mainly horizontal and the seawater condition (no overpressure) has significant impact on the overpressure values of this interval. From layer 4 below, the pressure is mainly diffused laterally creating a pressure front. At a given distance from the south of the model, where overpressure was injected from one-dimension sedimentation modeling (Figure 3.16), overpressure is larger in layer 4 than in other layers reproducing the pressure peaks observed at the wells (Figure 3.14).

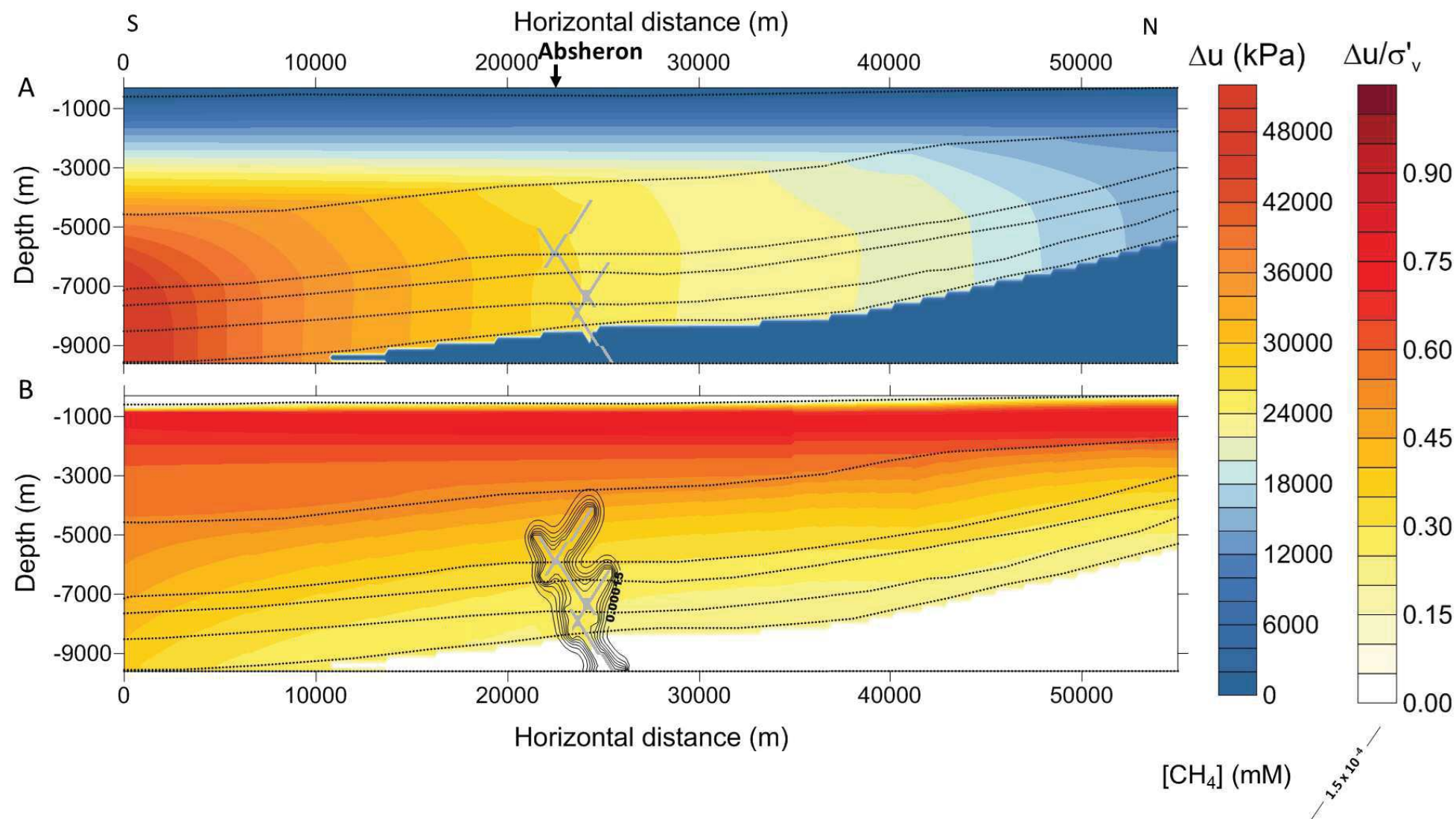


Figure 3.17: Results of overpressure and methane migration modeling after 5 Ma of calculation. A: overpressure (Δu) in kPa after 5 Ma of migration through the structural model presented on Figure 3.16. Overpressure migrated more rapidly through layer 4 which has a higher permeability. B: $\Delta u/\sigma'_v$ contours with values exceeding 0.75 and potentially reaching the level of hydro-fracturing. High values located in layer 5 are due to the low σ'_v near the seafloor. Black lines correspond to methane concentration contours. The top of the methane-saturated area corresponds to a zone where hydro-fracturing may occur if overpressure was slightly higher. Black dotted lines are for layer limits.

Faults and associated damage zones were designed to rapidly diffuse methane therefore artificially reproducing methane advection through fractured zones. Methane was injected at the base of the fault network with a concentration of 1.0×10^{-3} mM (Figure 3.16). Methane molecular diffusivity in the rest of the model is three orders of magnitude lower than in faults. As a result, methane rapidly saturated the area adjoining the faults, and then diffused slowly through the sedimentary column until saturating an area nearly 2 km wide around the fault network (Figure 3.17B). The ratio of overpressure over vertical effective stress ($\Delta u / \sigma'_v$) is higher in layer 5, particularly in the north of the model. As it is the shallowest interval, σ'_v is the lowest of the model. Besides, little overpressure accumulation was possible in layer 5. Nevertheless, values are high at the top of the layer 4, where the ratio varies between 0.5 and 0.6. So we expect critical values in the area of high methane saturation at the Absheron crest.

5. Discussion

5.1. What is the stratigraphic source of the mud?

The geomorphological description of the Absheron mud volcano evidenced a bowl-shaped geometry below the mass extruded through the Absheron interval (Figure 3.5). This feature is formed by the Anhydritic Surakhany horizons that terminate as truncations (Catuneanu *et al.*, 2009) below the younger seismic horizons of the Upper Productive Series. Truncations are also observed 500 m below, in the lower part of the Upper Productive Series. Horizon continuity resumes in the Middle Productive Series. This particular geometry was already described and corresponds to a depleted area forming a potential former mud generation zone (Stewart & Davies, 2006; Dupuis, 2017; Kirkham *et al.*, 2017b; Dupuis *et al.*, 2019). The presence of two truncated intervals (Figure 3.5) indicates that there may have been several mud generation stages.

The unstable interval drilled in the Anhydritic Surakhany has a mineralogical composition similar to the mud analyzed in this study (Figure 3.12), with nearly 50% of clay minerals. Mud sampled at the seafloor is poorer in Anhydrite, chlorite and calcite than the unstable interval analyzed in the Anhydritic Surakhany Formation. The mineralogical differences may be explained by the different paths and histories of the samples. Mud was driven upwards and deposited at the seafloor after a catastrophic event leading to remobilization of deep sediments. Thus, it potentially interacted with seawater but also with deeper fluids and gases forming for instance carbonate crusts at some methane seeping points or during diffuse degassing after a mud eruption (Kopf, 2002; Zitter, 2004). Conversely, the unstable interval cuttings were extracted directly from the formation through the drilling process and was in contact with the drilling mud.

From the biostratigraphic analysis of the mud and recent background sediments deposited at the seafloor, we can infer a Late Miocene to Pliocene (Productive series) origin for the mud.

Mineralogical analysis showed that fine fraction is poorer in illite and micas than unseparated samples (Figure 3.12B). These minerals are high temperature minerals compared to smectite or interstratified illite/smectite (Pollastro, 1993). Unseparated samples are composed of a non-negligible fraction of diverse clasts when the fine fraction extraction is constituted of mud matrix particles. Therefore, clasts and coarse particles may find their source deeper than the mud matrix. However, the presence of a larger percentage of chlorite in the fine fraction (Figure 3.12B) tends to show a degradation of micas and illite in the mud matrix. The contact of deep fluids and seawater with the mud matrix particles may be responsible for this reaction while coarser particles and clasts may preserve better illite and micas. Thus, mineral reactions with deep fluids and seawater could explain the different mineralogical compositions of mud matrix and they might come from the same depth magnitudes.

The Anhydritic Surakhany interval has several particularities. First, it is composed of 30% of evaporitic beds that can reach up to 8 meters in thickness. The rest is mainly composed of claystones. An unstable interval was noticed during drilling but others may exist in the Anhydritic Surakhany. Therefore, this interval may have a specific mechanical behavior. Moreover, the thermal gradient approximated from the temperatures measured at the wells is 16 °C/km which is in accordance with mean thermal gradients measured at other SCB locations (Ginsburg *et al.*, 1992). Considering that the mud volcano activated after deposition of H3 (Figure 3.5), and considering that the thermal gradient remained constant during the Quaternary, the Anhydritic Surakhany temperature was around 30°C when the first eruption occurred. Day-Stirrat *et al.* (2010) state that above 80°C, chemical compaction (cementation processes, precipitations) will strengthen the mudstone fabric and this process is irreversible i.e. the mudstone can no longer behave in a ductile way. Thus, the Anhydritic Surakhany Formation would have been well within the temperature range where ductile deformation is conceivable.

Finally, overpressure logs show that the Anhydritic Surakhany forms a pressure peak at both wells (Figure 3.14). Rupture in this interval would happen earlier than in other formations for a given pressure increase or stress decrease. The fact that highly overpressured mudstones are blocked between meter-thick layers of evaporites may explain the weak behavior of some layers. As compaction water cannot be expelled vertically because of evaporites, these layers are likely to stay under-compacted and overpressured.

From these observations and measurements it seems plausible to conclude that Upper Productive Series, and more precisely the Anhydritic Surakhany Formation, is the source of the solid fraction of the mud expelled at the Absheron mud volcano.

5.2. How do the field pore pressure measurements compare to the model?

It is quite clear on pressure logs that pressure regimes are completely different in shales and in reservoirs. Indeed, shales are highly overpressured all along the well, following a trend nearly parallel to the lithostatic pressure from the Top Akchagyl to the Bottom Productive Series. In the bottom part of the wells (from the PS2 seismic horizon downwards), overpressure level in shales remains rather constant while reservoir pressures are nearly hydrostatic. Javanshir *et al.* (2015) describe similar pressure regime and magnitudes in the neighboring Shah Deniz fold. The Upper Productive Series there have equal sandstone and shale overpressures and as the reservoir facies become more abundant and continuous in the Bottom Productive Series, they become less overpressured. Therefore, in Shah Deniz and Absheron, the deep reservoirs seem to act as permeable drains as they allow overpressure to dissipate. The fact that shale pressure is also affected shows that dewatering might occur in the thinner shale intervals contained in the Bottom Productive Series. Indeed, the abundance of permeable reservoirs would allow compaction water to be drained away from the shales, reducing their pressure. There is lateral pressure transmission from the deep part of the basin to the edges through regional-scale reservoirs (Javanshir *et al.*, 2015), from the south to the north of the sections presented in Figure 3.14.

However, pressure horns in Absheron shales are not recorded in the data of Javanshir *et al.* (2015). Some intervals of the Productive Series of Absheron wells are more overpressured than the rest of the stratigraphic interval. These peaks bring the corresponding intervals to pressure values between 5 and 10 MPa below hydrofracturing pressure in wells located 9.5 km from the mud volcano center. The difference between hydrofracturing pressure and shale pressure may be even smaller near the mud volcano, or it may have been smaller in the past, before mud volcano activation. Therefore, they represent weak areas where a local rise in overpressure through clay dehydration or tectonic overpressuring for instance (Osborne & Swarbrick, 1997), or a drop in effective stress (erosion or fold growth and crestal uplift) could generate hydrofractures.

Pressures recorded in the two wells are not exactly the same (Figure 3.14): in the southern well (Well A), shale pressure decrease more gently within the Bottom Productive Series and reservoir pressures are higher. Moreover, pressure horns are stronger in well B (to the north). Differential sedimentation between the deep basin located at the south of the Absheron anticline and the northern edge of the basin where less sediments accumulate could explain this phenomenon (Grosjean *et al.*, 2009; Javanshir *et al.*, 2015). As pressure transmission is oriented roughly from the south to the north of the anticline, the northern side of the anticline would accumulate more overpressure in the shales whereas reservoirs would be more drained than in the southern flank. This phenomenon was also noted at the neighboring Shah Deniz anticline (Javanshir *et al.*, 2015).

2D model sections reproducing the main features of the pressure plots are shown on Figure 3.17. The overpressure rises down to 2000 and 5000 meters deep depending on the location. Then overpressure remains constant at 30 MPa at the Absheron location and even decreases to 25 MPa when reaching the bottom part of the Productive Series where highly continuous and abundant reservoir facies are present. Moreover, the numerical modeling results emulate the Top Surakhany pressure horn. Yet, the modeling results underestimate the overpressure at the Absheron location (Figure 3.17A) as they are not in accordance with overpressure values recorded at the wells. Indeed, from Top Surakhany down, overpressure reaches values between 20 MPa and 50 MPa. The discrepancy between measured and calculated overpressures may be related to the compressibility and permeability laws applied to the model which were obtained from artificial (reconstituted) sandy-clayey samples and not from natural samples from the different stratigraphic layers. Besides, the considered source of overpressure is related to fast sedimentation and might not be sufficient to model the natural pressure conditions of the Absheron anticline. Indeed, additional sources of pore pressure may play an important role and are yet to be considered in the modeling work.

However, and as a first approach, the present calculation was able to reproduce the main overpressure trends visible at the wells.

5.3. How does methane diffusion interact with excess pore pressure accumulation?

From results of the pressure generated by potential gas columns that could have been trapped in the ASF at the time of the AMV activation, it is clear that external parameters are needed in order to explain the AMV formation. The effect of high sedimentation rates and basin wide lateral pressure transmission on the overpressure at the Absheron location was therefore studied through numerical modeling. The significant lateral fluid migrations through the SCB was already shown by Bredehoeft *et al.* (1988), Javanshir *et al.* (2015) and Gautherot *et al.* (2015).

Modeling results shows that high values of $\Delta u / \sigma'_v$ fit with high dissolved methane concentrations and occur around the fault network below the Absheron mud volcano (Figure 3.17B). The consequence of high $\Delta u / \sigma'_v$ causing hydrofracturing may be an important decrease in pore pressure leading to methane exsolution and expansion (Duan & Mao, 2006) and generation of overpressured mud. Gas exsolution in sediments has proved to be a critical factor controlling sediment damage. Indeed, experience on gassy sediment core recovery in deep water shows important damage and loss of structure during the core ascent to the surface and associated hydrostatic pore reduction (Sultan *et al.*, 2012). Loss of acoustic signal corresponding to the presence of free gas correlates with dramatic decrease of the yield stress ratio illustrating the damage made to the sediments.

Moreover, the presence of normal faults at the anticline crest between the Upper Productive Series and the Top Absheron (Figure 3.3) shows that the state of stress where the primary source of mud was

identified was extensive at the time when the Absheron mud volcano formed. If compressive state was dominating at these time and location, the observed faults must have been thrusts. Therefore, σ_1 (the maximum principal stress) was certainly vertical, so the least principal stress was horizontal. Fractures opens in the direction of the least principal stress and then propagates in a plane perpendicular to this direction (Hubbert & Willis, 1957). Thus, hydrofractures generated at the time of the mud volcano formation above the mud generation zone are expected to be vertical.

A present-day studied example of clastic extrusion triggering displays similar results. Indeed, the Lusi disaster, whose 2006 triggering cause is still a matter of debate between an earthquake and drilling issues (Mazzini *et al.*, 2007; Tingay *et al.*, 2008, 2017), was initiated by the combination of under-compaction / overpressure in the source layer and the presence of dissolved and free gas. According to Davies *et al.*, (2008), fractures generated by drilling activities have caused an important decrease in pore pressure and the consequence was gas exsolution and expansion, overpressured mud generation and the extrusion of mud to the surface (Davies *et al.*, 2008). However, Mazzini *et al.* (2012) proposed an hydrothermal source for the gas, yet Lusi triggering is already explained by gas flowing in under-compacted and overpressured sediments.

Thus, we suggest that the theoretical mechanism we propose for mud generation and extrusion with a combination potential fracture zones and gas-saturated areas would also be applicable to the Absheron fold, where the studied mud volcano is located.

5.4. What is the most plausible sequence for the formation of the Absheron mud volcano

Based on previous observations and conclusions, a qualitative formation model for the Absheron mud volcano is proposed. This model is developed in six main phases:

Phase 1: rapid deposition of the Productive Series (over 3.5 km in 2 Ma) above the gas-mature Maykop Formation that would generate hydrocarbons migrating slowly through the sedimentary column (Figure 3.18-1). Maykop Formation started generating gas during the Late Miocene in the Shah Deniz region located less than 50 km from Absheron gas discovery (Figure 2.9 in Alizadeh *et al.*, 2017). Moreover, the deposition of the Anhydritic Surakhany Formation proves that the sea level must have been lower than nowadays at the end of the Productive Series deposition.

Phase 2: folding started during deposition of the Akchagyl Suite. It is linked to the propagation of a deep thrust terminating in the Maykop formation and linked to normal faults related to the fold formation. Methane migration is then focused into the faulted core of the anticline (Figure 3.18-2). The folding also has the effect of generating preferential rupture zones at its crest (Figure 3.18-2). Indeed, at the anticline crest, σ'_v is lower than on the flanks. Besides, as more space is available for sediment deposition in the surrounding synclines and in the deeper part of the basin, overpressure is generated and transmitted towards the

Absheron location. Overpressure generation and transmission as well as lower σ'_v at the crest increases the $\Delta u / \sigma'_v$ ratio thereby increasing pore gas solubility.

Phase 3: $\Delta u / \sigma'_v$ ratio reaches the hydro-fracturing threshold (Figure 3.18-3), leading to a significant decrease in pore pressure.

Phase 4: hydrofracturing triggers gas exsolution and expansion in gas-saturated and mechanically weak layers such as Anhydritic Surakhany Formation (Figure 3.18-4). Exsolution remobilizes the weak interval, generating mud. Overpressured and low-density mud is then transported to the seafloor provoking the first mud extrusion. As gas, mixed with sediments and water, migrates up the hydrofracture network, methane expands amplifying the process and potentially eroding fracture walls (Figure 3.18-4).

Phase 5: the process goes on with gas exsolution propagating in the Anhydritic Surakhany, depleting this layer continuously. Collapse of the upper strata into the depleted area creates the rather flat and low topography volcano (Figure 3.18-5). The extruded mud slowly degasses at the seafloor.

Phase 6: quiescent and active phases of the mud volcano alternates, creating a complex interdigitation geometry where normal sedimentation predominates during quiescent phases of the volcano. Further depletion happens in the source, triggering more collapse, while more mud is extruded at the seafloor (Figure 3.18-6).

The initial trigger of this mud volcano is not related to gas, as hydrofracturing due to overpressure build-up and weakness of the fold-crest initiates the succession of events. However, in this conceptual model, methane would have three essential effects:

- Gas needs to saturate the porous network in its dissolved state before hydrofracturing in order to provoke remobilization of sediments. Exsolution of methane weakens and disaggregates host sediments (Sultan *et al.*, 2012; Tingay *et al.*, 2015).
- As free gas has very low density (typically about 1/1000 of that of water in normal conditions), it will flow towards the surface (Brown, 1990), carrying the mud away (solid particles and formation water).
- Finally, as gas goes up into the pipe, it expands (Brown, 1990), accelerating the mud ascent, sustaining mud pressure and eroding fracture walls, creating clasts, to end-up with mud breccia extrusion at the surface.

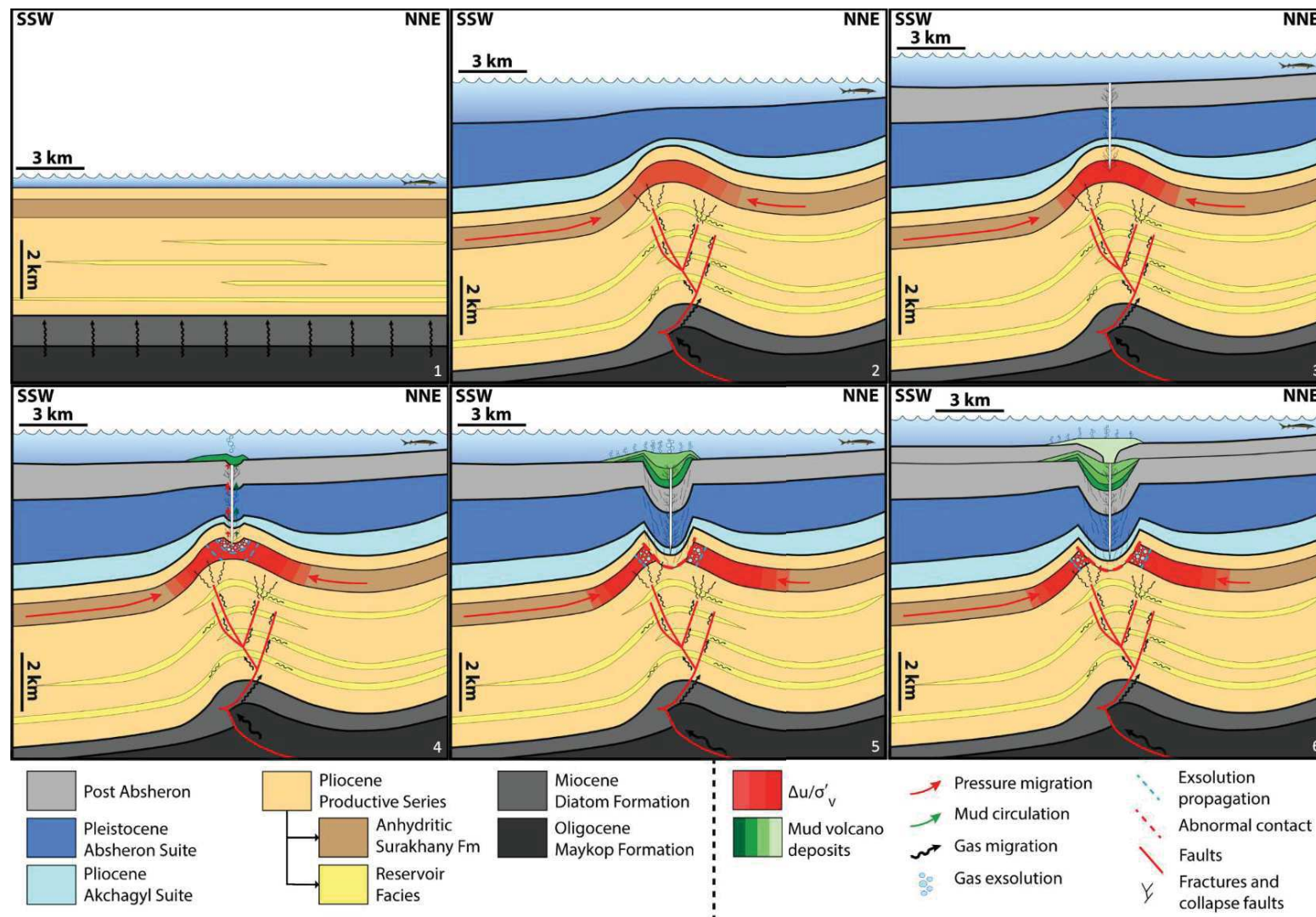


Figure 3.18: Formation model for the Absheron mud volcano based on in situ observations and measurements, laboratory tests and analysis and numerical modeling. 1- Rapid deposition of the Productive Series and maturation of the Maykop formation. Slow and extended methane migration. 2- Absheron fold creation. Focusing of the methane migration through fold-related fault network and $\Delta u/\sigma'_v$ increase at the anticline crest. 3- Rupture condition reached and hydrofracturing of the sedimentary column from the seafloor to the Anhydritic Surakhany. 4- Gas exsolution and expansion and remobilization of Anhydritic Surakhany sediments. First extrusion. 5- Propagation of gas exsolution and sediment remobilization. Depletion of the Anhydritic Surakhany and collapse of the overlying strata. 6- present geometry after alternation of several quiescent and active episodes for the mud volcano. More depletion of the source and collapse of the overlying strata is triggered at each active episodes.

Thus, methane exsolution is the key to mud formation but also the main driver for mud remobilization towards the surface due to its low density and expansion capacity. Initial rupture is essential in order to start the chain reaction and methane expansion and exsolution will maintain the pipes open and even enlarge them.

5.5. Limits and perspectives of the study

This conceptual formation model of the AMV closely fits with observations and analysis of the available dataset and is partly based on the numerical modeling results presented earlier.

However, improvements may be made at several levels:

Dataset: For instance, the seismic masking prevents direct observation of the center of the volcano's plumbing system. Re-processing of the data was attempted several times and with different methods and approaches, but it remains challenging due to the presence of gas-charged mud and free gas. The available biostratigraphic analyses are not quantitative and for further precision on the mud origin quantitative analyses of the fauna and flora in mud will be necessary. Analysis of the clasts will also help to refine the mud origin.

Numerical modeling: The compressibility laws used in the current model could be improved to consider soil compressibility for the highest stress range (Chong & Santamarina, 2016). In the present work and in order to avoid negative void ratio values, the software limits the minimum void ratio to 0.1. In the present model, pore pressures generated by sedimentation and pressure transmission are not calculated simultaneously. Overpressure due to sedimentation is calculated over 5 Ma of sedimentation history and is integrated as a boundary condition into the 2D Darcy's and Fick's diffusion equations. The next step would be to integrate both sedimentation and diffusion processes into one unique 2D model. Finally, the model does not simulate the post-hydrofracturing process causing gas exsolution and overpressured mud expulsion. Gas exsolution and expansion processes will have to be integrated into this model in order to reproduce mud volcano initiation.

Overpressure generation mechanisms: the mud volcano is located at the crest of an active anticline and triggered after one of the main folding phases. Thus lateral tectonic overpressuring is expected to have happened before the mud volcano formation (Osborne & Swarbrick, 1997; Swarbrick *et al.*, 2002). This tectonic overpressuring has proved to increase the global overpressure up to 16 MPa at 3.5 km deep partly due to porosity decrease (Couzens-Schultz & Azbel, 2014; Obradors-Prats *et al.*, 2017). Moreover, internal sources have not been considered such as clay dehydration and smectite-illite reactions that generate a large volume of water in the pore space, thus generating overpressure (Osborne & Swarbrick, 1997; Swarbrick *et al.*, 2002). Gas generation is also considered as an overpressure generation mechanism and may have implications for this numerical model as gas is generated and diffused through the sedimentary column

(Osborne & Swarbrick, 1997; Swarbrick *et al.*, 2002). Considering these new pore pressure input, the $\Delta u / \sigma'_v$ ratio may increase drastically and the model may be able to reproduce the observed in situ pore pressure measurements.

Moreover, the presence of the buried MV gives the possibility to enrich our model of MV formation with other important elements. When comparing the AMV with the small MV, several common characteristics appear. Both MVs are directly related to deep thrusts and the setting of anticline crests (the hanging wall topographic high in the case of the small MV, Figure 3.4 and Figure 3.10C). Similar architectural elements were observed such as a bowl-shaped depleted area corresponding to the mud generation zone (Figure 3.5 and Figure 3.10C). The small MV brings further details on what could be the precise 3D architecture of the AMV rooting system. The depleted area of the small MV is elongated along the thrust direction and thus, it is not a perfect bowl-shaped area (Figure 3.11). Moreover, centered into the collapsed strata, what could be the feeding pipe is imaged. The extruded structures and the depletion zone are not perfectly aligned and have not the same shape (Figure 3.11). Therefore, the AMV may present similar features that are masked by the imaging issues due to gas and the presence of low-velocity mud.

However, despite the similarities, both structures are different. First, the timing of formation is not the same. The small MV is much older than the AMV as its extruded structures are now buried 7 km below seafloor. The presence of the small MV above the northern thrust confirms that the northern thrust is older than the thrust coring the Absheron fold. Moreover, the mud generation zones are not in the same stratigraphic intervals. The AMV is related to the ASF while the small MV is related to the Maykop Formation. This shows, as highlighted by other authors (Yusifov & Rabinowitz, 2004; Dupuis, 2017), that all MVs in the SCB may be different and are not all related to the Maykop Formation, even in the same area. Besides, the small MV was formed before the Maykop Fm becomes mature to gas. Therefore, all these differences could relate to different formation mechanisms.

This comparison shows the possibility to compare MV structures to better understand their morphology but also the necessity to study each structure separately when dealing with formation processes, each MV being related to specific conditions.

6. Conclusions

Based on 3D seismic data, mineralogical, geotechnical and biostratigraphic analyses of the sampled mud together with well data, we conclude that the Anhydritic Surakhany Formation is a plausible source for the Absheron mud volcano. Pressures recorded at the wells show, as in Shah Deniz, that deep reservoirs act as drains for pressure provoking a decrease in overall shale pressure logs. Pressure horns were also recorded at specific intervals, as for the ASF, where shale pressure is close to the fracture limit.

Based on these observations, a numerical model with 2D-diffusion equations was applied on a basin scale section. Sedimentation-related overpressures underestimate by 50% the pressures measured in the wells but reproduce fairly well the observed trends. Additional sources of in situ overpressure generation (i.e. clay dehydration and transformation), which are not included in the current model, may explain the discrepancy between the model prediction and the pore-pressure values of wells. The main observation made through the numerical model is the superposition of methane-saturated areas with potential hydrofracturation zones. Indeed, hydrofracturing may produce a drastic decrease in pore pressure, allowing gas exsolution and expansion. Based on the present model results, on experimental results of gassy-sediment behavior in which the gas exsolution damages the sediment and reduces its mechanical strength and on the Lusi disaster studies, we conclude that the superposition of potential hydrofracturing areas and gas-saturated zones can explain that the Absheron mud volcano activated at the crest of the anticline.

As a result, we propose a conceptual evolutionary model for the Absheron mud volcano as follows: initial stages of folding focus methane migration into the anticline crest bringing methane to the upper geological layers and mainly to the Anhydritic Surakhany Formation. Pore pressure accumulation and its lateral migration through the Anhydritic Surakhany Fm. promote hydrofracturing at the location of the Absheron mud volcano causing a decrease in pore pressure. These conditions lead to methane exsolution and expansion and to the upward remobilization of the already weak Anhydritic Surakhany interval, generating low density and overpressured mud. During mud ascent, gas bubbles expand, splintering fracture walls and incorporating clasts into the mud. Finally, extrusion at the seafloor happens where the mud slowly expels methane. As extrusion continues, a collapse of the overlying strata into the depleted mud generation zone forms.

Therefore, even though the trigger point for the whole MV formation process in our model is hydrofracturing, clay-rich sediments have to be initially saturated with methane in order to generate mud. The methane is essential and has three main roles: exsolution allows creating mud from weak layers, its low density decreases that of the mud and accelerates its upward flow to the surface, and gas expansion decreases mud density, which causes splintering of gas-saturated fracture walls creating clasts.

With the available dense dataset, we highlight that, in order to form the Absheron mud volcano, a combination of three factors is required: high pore pressure, gas saturation and clay-rich sediments. Recent work on the Lusi eruption also demonstrated the importance of the same factors in a different geological environment. Therefore, detecting the presence of these three factors may help understand the preconditioning factors of MV formation.

Chapter 4: Sediment damage caused by gas exsolution: a key mechanism for mud volcano formation

Abstract

Gassy sediments are common in marine environments and are characterized by a specific mechanical behavior significantly different from that of water-saturated sediments. It is shown that gas causes damage and initiates fractures in sediments. To define the controlling parameters dominating the damage process during gas exsolution and its consequences in terms of hydro-mechanical behavior, we developed a specific consolidation apparatus to test sediments from the active Absheron mud volcano (South Caspian Basin). Indeed, mud volcano formation is initiated by gas exsolution and expansion and subsequent mud formation as demonstrated in Chapter 3.

Gas was generated in the studied samples by circulating carbonated water through the sediment and then decreasing the total pressure. Particular attention was given to the impact of gas saturation and associated damage and fractures on P-wave velocity, sediment compressibility, permeability and preconsolidation pressure. Results show that fracture geometry is mainly controlled by the degree of gas saturation and preconsolidation pressure. The damage level increases with the degree of gas saturation while the elastic modulus of sediments is degraded. Experimental data show that sediments do not entirely recover their original mechanical behavior when gas disappears. Finally, the experimental data confirm that gas exsolution and expansion in the host sediment can lead to mud formation.

Chapitre 4 : Endommagement des sédiments par exsolution de gaz : un mécanisme clé pour la formation des volcans de boue

Résumé

Les sédiments gazeux sont fréquents dans les environnements marins et ils sont caractérisés par un comportement mécanique qui diffère de celui d'un sédiment saturé en eau. La présence de gaz dans les sédiments marins est un facteur d'endommagement et de fracturation. Afin de définir les paramètres qui contrôlent l'endommagement des sédiments lors de l'exsolution de gaz ainsi que les conséquences causées sur leur comportement hydromécanique, une cellule de consolidation spéciale a été développée afin de tester des sédiments prélevés sur le volcan de boue actif d'Absheron (Bassin sud caspien). En effet, la formation d'un volcan de boue est initiée par l'exsolution et l'expansion du gaz dans les sédiments, générant la boue en profondeur comme montré dans le Chapitre 3.

Du gaz a été libéré dans les échantillons sédimentaires en y faisant d'abord circuler sous pression de l'eau saturée en dioxyde de carbone, puis en faisant chuter la pression totale à la suite de la consolidation. Les effets de la saturation en gaz et ses conséquences sur l'endommagement et la fracturation ont été observés en mesurant et en analysant la vitesse des ondes P, la compressibilité du sédiment, sa perméabilité et sa pression de préconsolidation. Les résultats montrent que la géométrie des fractures est principalement contrôlée par le degré de saturation en gaz et la pression de préconsolidation. Le niveau d'endommagement augmente avec le degré de saturation en gaz, et en parallèle, le module élastique du sédiment est dégradé. Les résultats expérimentaux montrent que le sédiment ne recouvre pas complètement son comportement mécanique initial lorsque le gaz disparaît. Enfin, les essais confirment que l'exsolution et l'expansion du gaz dans les sédiments peuvent mener à la formation de boue.

1. Introduction

Sediments partially saturated with free gas are a widespread occurrence and are found in varying marine environments (Grozic *et al.*, 2000). Nageswaran (1983) discriminates between two free-gas distributions: continuous gas phase and discrete separated gas bubbles. The latter is defined as gassy sediments and Nageswaran (1983) gives a maximum limit in terms of the degree of gas saturation ($S_g < 15\%$). Gassy sediments are a well-known issue in marine geotechnics that have been studied for decades as the detection and quantification of free-gas content is essential for geohazard assessment (Esrig & Kirby, 1977; Sobkowicz & Morgenstern, 1984; Thomas, 1987; Sultan *et al.*, 2004, 2012; Judd & Hovland, 2007; Riboulot *et al.*, 2013).

The main difficulty when studying gassy sediments in the laboratory is to obtain a discrete distribution of gas bubbles. Several techniques exist including the generation of free gas through the zeolite molecular sieve technique (Nageswaran, 1983; Thomas, 1987; Wheeler, 1988; Sills *et al.*, 1991; Nava Castro *et al.*, 2013), the generation of biogenic gas through bacteria (Sills & Gonzalez, 2001; Rebata-Landa *et al.*, 2012) and finally the generation of gas bubbles through the circulation of overpressured carbonated water followed by decompression (Grozic *et al.*, 2000; Sultan *et al.*, 2012). Each method is detailed in Chapter 4:2.3.

The mechanical behavior of gassy sediments has been extensively studied over the last few decades and all the studies demonstrate that it differs completely from saturated sediment behavior (Thomas, 1987; Wheeler, 1988; Sills *et al.*, 1991; Helgerud *et al.*, 1999; Grozic *et al.*, 2005; Sultan *et al.*, 2012; Nava Castro *et al.*, 2013; Jang & Santamarina, 2014). Details on the hydro-mechanical properties of gassy sediments are provided in Chapter 4:2.4.

Mud volcanoes are one of the most spectacular geological features related to gas venting. Gas, mostly methane and carbon dioxide, is expelled at the seafloor along with a fluid melange, varying in proportion, of water, fine-grained sediments and larger rock fragments (Kopf, 2002; Mazzini & Etiope, 2017). Mud is commonly sourced from depths of several kilometers (Stewart & Davies, 2006; Kirkham, 2015; Blouin *et al.*, 2019). The Lusi catastrophe, ongoing since 2006, allowed to monitor mud volcano generation from its initiation (Tingay *et al.*, 2008, 2017; Mazzini *et al.*, 2012). Tingay *et al.* (2017) demonstrated that the key parameters of the Lusi triggering were the high overpressure and the gas influx into weak layers. Moreover, Capaccioni *et al.* (2017) show that the emplacement of sand volcanoes during Cone Penetration Testing in Italy was caused by gas exsolution and expansion in loose deposits. Therefore, Tingay *et al.* (2015) and Blouin *et al.* (2019) proposed gas exsolution and expansion triggered by hydrofracturing and the subsequent drop in pore fluid pressure as mud generation mechanisms.

The aim of this present study is to identify the impact of gas expansion and exsolution on the mechanical behavior of sediment sampled directly from an active mud volcano (Absheron mud volcano AMV,

South Caspian Basin; Blouin *et al.*, 2019). Particular attention was given to the gas impact on sediment structure, acoustic properties (P-wave velocity), compressibility and preconsolidation pressure by carrying out a series of consolidation/compressibility tests using a novel experimental set-up. The main questions motivating this work are summarized below:

- If gas exsolution within sediment is already proven to cause damage (Sultan *et al.*, 2012), what are the controlling parameters dominating the process and what are the consequences in terms of hydro-mechanical behavior?
- Do the mechanical properties of the sediment recover from gas exsolution/expansion after mechanical reloading?
- What are the conditions that allow gas exsolution and expansion in the host sediment to generate mud?

2. State of the art on gassy sediments

2.1. Definition of gassy sediments

Natural soils are not always saturated with water; instead, their voids can be filled partly with water and with free gas/air and the soil are therefore called unsaturated soils (Nageswaran, 1983; Wheeler, 1986; Thomas, 1987). Depending on the degree of gas saturation (S_g), the structure of unsaturated soils may vary greatly (Wheeler, 1986). Figure 4.1 shows three possible structures for unsaturated soils depending on the S_g . For high S_g , the water phase will be discontinuous and occluded between grain contacts and the gaseous phase is continuous (Figure 4.1a; Wheeler (1986)). For intermediate S_g , the two phases are continuous (Figure 4.1b; Wheeler (1986)). For small S_g , the water phase is continuous and free gas is present in the form of discrete gas bubbles in the middle of pore voids (Figure 4.1c; Wheeler (1986)). These different structures imply a different mechanical behavior (Wheeler, 1986).

When gas is present in the form of discrete bubbles, soil structure varies greatly depending on the relative size of bubbles and solid particles (Wheeler, 1986; Thomas, 1987). Two extreme models were presented by Wheeler, (1986). When the bubbles are small enough to be contained in the pore space without deforming the soil structure, so much smaller than the soil particles, the structure will resemble the illustration of Figure 4.2a. At the opposite, when bubbles are much larger than the particle size, the soil structure will be disturbed by the presence of the bubble (Figure 4.2b). Anderson *et al.* (1998) give a classification with three types of discrete gas bubbles: interstitial bubbles that are small enough to be contained in the pore space without deforming the solid matrix; reservoir bubbles that are larger than the pore space but is contained into an area of undeformed solid matrix; gas voids (Wheeler, 1986) that are much larger than the normal pore space and therefore disturb the solid particle structure due to bubble expansion.

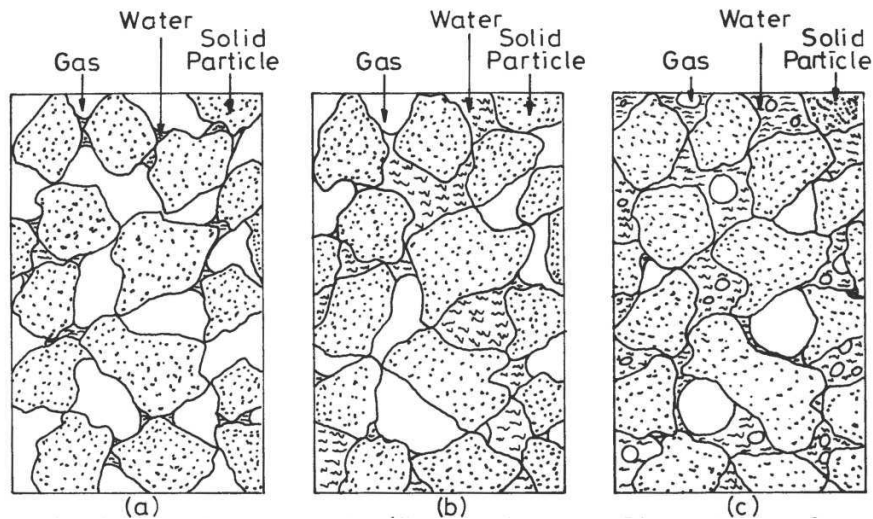


Figure 4.1: Structure of unsaturated soils depending on the degree of gas saturation (S_g). (a) high S_g , the water phase is discontinuous and occluded around the solid particles when gas forms a continuous phase. (b) medium S_g , water and gaseous phases are continuous. (c) small S_g , the water phase is continuous and the gaseous phase is present in the form of discrete gas bubbles in the middle of the pore voids (from Wheeler, 1986).

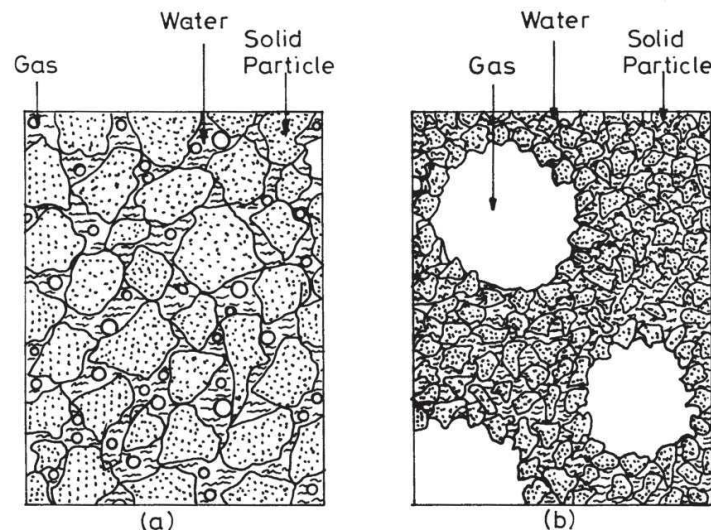


Figure 4.2: Extreme soil structure for unsaturated soils presenting discrete gas bubbles. (a) when gas bubbles are much smaller than the solid particles, (b) when gas bubbles are much larger than the solid particles (from Wheeler 1986).

In order for the gaseous phase to exist within the form of discrete gas bubbles, the degree of gas saturation should be smaller than 15% (Nageswaran, 1983; Wheeler, 1986; Thomas, 1987). Nageswaran (1983) names this type of unsaturated soils gassy soil. Therefore, illustrations in Figure 4.2 represent gassy soil possible structures. Nageswaran (1983) states “the bubbles may be spherical or irregular in shape” (Nageswaran, 1983, p.15). However, recent studies show that the shape of bubbles highly depends on the mechanical properties of sediments (Boudreau *et al.*, 2005; Barry & Boudreau, 2010; Katsman, 2015). In particular, Katsman (2015) concludes that bubbles generating in weak sediments are small with higher surface-to-volume ratio (thin bubbles) while bubbles forming in stronger sediments tend to be larger and more spherical (larger). Nevertheless, bubbles forming into gelatin considered as a proxy of sediments density and shear strength tend to be rather disk-shaped than spherical (Figure 4.3; Boudreau, 2012; Katsman, 2015).

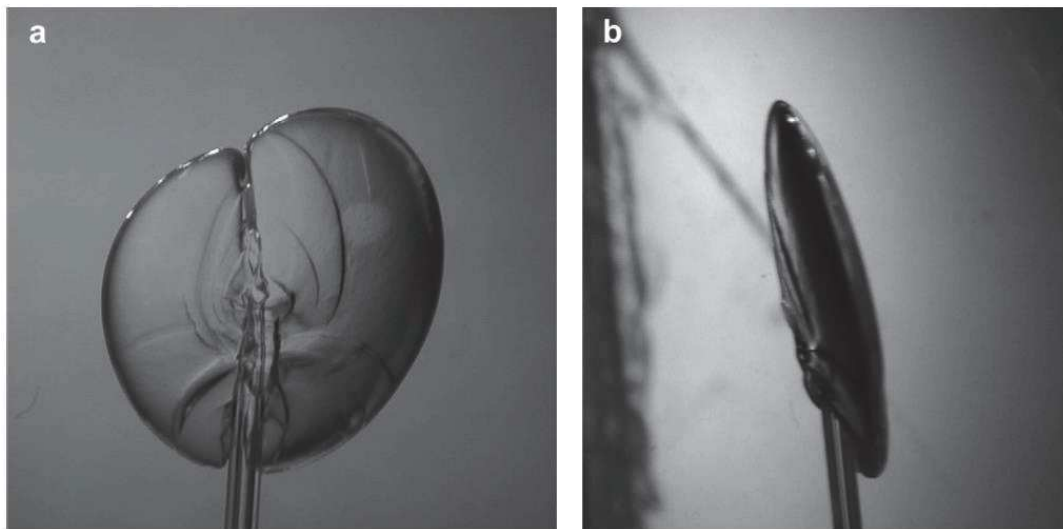


Figure 4.3: Experiments of gas injection into gelatin (proxy of sediment density and strength but not porosity) allowing illustrating the disk-shaped bubbles forming in cohesive sediments (from Boudreau, 2012).

Onshore, unsaturated soils are either due to evaporation in the first few meters of soil or to a water table lower than the soil surface (Nageswaran, 1983). Most of the time, the gas/air is present as a continuous phase up to the atmosphere (Nageswaran, 1983; Thomas, 1987). However, offshore, gas, most of the time methane, nitrogen or carbon dioxide, is generated within the sediment or comes from deeper geological intervals (Wheeler, 1986; Thomas, 1987). A variety of different processes may be responsible for gas generation in marine sediments (Wheeler, 1986; Thomas, 1987; Judd & Hovland, 2007). The most frequent origin of gases are: microbial gas generated by biogenic and anaerobic degradation of organic matter (Nageswaran, 1983; Judd & Hovland, 2007); thermogenic gas generated from the thermal cracking of kerogen particles (Nageswaran, 1983; Judd & Hovland, 2007); hot gases produced by magmatic, volcanic and geothermal submarine processes (Nageswaran, 1983; Judd & Hovland, 2007). These gases either can form directly into the considered sediment, or may be transported by several processes towards shallower intervals (buoyancy, overpressure, permeable drains, and hydrofractures).

2.2. Occurrence and relevance of gassy sediments

Gassy sediments are a widespread occurrence around the globe onshore, but mainly in a variety of marine environments, from coastal environments to deep sea, and in very different tectonic and geological settings such as passive margins or subduction zones (Esrig & Kirby, 1977; Nageswaran, 1983; Fader, 1997; Grozic *et al.*, 2000; Fleischer *et al.*, 2001; Judd, 2003). Figure 4.4 is a map showing the known occurrences of gassy sediments in 2001 (Fleischer *et al.*, 2001). This map was updated as gassy sediments were observed in the Gulf of Guinea (Sultan *et al.*, 2012), in the Caspian Sea (Evans *et al.*, 2007), in the bay of Biscay (Michel, 2017) or in lakes such as Baikal or Great Lakes (Naudts *et al.*, 2012). Moreover, features related to free gas seepage (pockmarks, mud volcanoes, methane-seep carbonates) are found in all the seas, oceans and even lakes (Baikal, Great Lakes) showing the global distribution of gassy sediments (Judd & Hovland, 2007). Many buried or fossil structures have been described showing that gassy sediments is not a modern

feature but may be as ancient as life on Earth (Fowler *et al.*, 2000; Stewart & Davies, 2006; Agirrezabala *et al.*, 2013; Riboulot *et al.*, 2013; Dupuis, 2017; Kirkham *et al.*, 2017a).



Figure 4.4: Map of the known occurrences of gassy sediments mentioned by Fleischer *et al.* (2001) (black areas) updated with enclosed seas occurrences (Caspian Sea), lakes (Baikal and Great Lakes) and places such as the Gulf of Guinea, Bay of Biscay, Ebro delta, Nile delta, and Levantine Basin (Red dots; modified from Fleischer *et al.*, 2001). Numbers correspond to the listed occurrences in Fleischer *et al.* (2001).

The presence of gassy sediments could result in various engineering issues and creates potential natural hazards that jeopardize offshore infrastructures. Free gas can cause several problems when characterizing the sediments. First, the presence of free-gas in sediments causes imaging issues, mainly due to acoustic wave attenuation across free gas (Sills *et al.*, 1991; Fader, 1997; Helgerud *et al.*, 1999; Graue, 2000; Evans *et al.*, 2007; Benjamin & Huuse, 2017). Indeed, seismic evidence for gassy sediments are varied: acoustic masking, gas brightening (bright spots), pull-down, reflection doming, flat spots, acoustic blanking (Fader, 1997; Wilkens & Richardson, 1998; Judd & Hovland, 2007). Besides, the recovery of gassy sediment cores is very challenging due to gas expansion that destroys part of the sediment structure (Esrig & Kirby, 1977; Sultan *et al.*, 2012). More importantly, gassy sediments can cause major issues when dealing with anchoring of offshore platforms (Colliat *et al.*, 2011). Finally, the presence of free gas can also trigger natural hazards such as submarine landslides (Esrig & Kirby, 1977; Field & Barber, 1993; Sultan *et al.*, 2004; Riboulot *et al.*, 2013; Imbert *et al.*, 2014) and pockmark generation (subcircular crater-like features at the seafloor; Riboulot *et al.*, 2013).

2.3. Creating gassy sediments during laboratory testing

Due to the difficulty to sample gassy sediments without damaging sediments and losing gas (Esrig & Kirby, 1977; Sultan *et al.*, 2012), gassy sediments have to be created artificially in order to study their mechanical behavior. Several methods exist and have proven to be effective.

Many laboratory experiments used a method called zeolite molecular sieve technique (Nageswaran, 1983; Wheeler, 1986; Thomas, 1987; Sills *et al.*, 1991; Nava Castro *et al.*, 2013). This method relies on the properties of a natural mineral, the zeolite. They have a strong affinity for polar molecules such as water, but in absence of which they can also accept other small molecules into their crystalline network such as methane or nitrogen (Breck, 1974; Sills *et al.*, 1991; Hong *et al.*, 2017). The used experimental procedure is to dry zeolite minerals and to allow those minerals to store gas molecules under a relatively high pressure (Wheeler, 1986; Sills *et al.*, 1991). Then, zeolites are mixed with the tested sediments (Wheeler, 1986; Sills *et al.*, 1991). When put in contact of a water-saturated environment such as saturated clays, zeolites will free the gas molecules and uptake water, creating an uniform and repeatable distribution of discrete gas bubbles in the sample that can undergo testing such as consolidation afterwards (Thomas, 1987; Sills *et al.*, 1991; Nava Castro *et al.*, 2013). This technique is designed in order to recreate gas generation process as it occurs in marine sediments, with bubble initiation around a specific site: a bacteria nucleus in natural environment, a zeolite in laboratory (Sills *et al.*, 1991; Boudreau, 2012). However, a drawback of this technique is that gas forms on the early stage of the testing, faster than the self-weight consolidation processes: the timing of gas generation is not controlled (Sills & Gonzalez, 2001).

The second method consists on using methanogen bacteria (Sills & Gonzalez, 2001) or nitrogen reduction and denitrification of soils through bacterial respiration (Rebata-Landa *et al.*, 2012). This technique presents the benefit of having the control on the production rate and timing (Sills & Gonzalez, 2001). Indeed, the bacterial activity can be accelerated or moderated by modulating the temperature or by increasing or decreasing the nutrients provided to the samples (Sills & Gonzalez, 2001). Moreover, many different bacteria, with different properties (nutrients needed, type of gas generated, optimal temperatures) exist, allowing flexibility and adaptability of the experimental conditions (Rebata-Landa *et al.*, 2012). Nevertheless, the method presents two drawbacks: bacteria may die under compression tests, through pore space and pore connection reduction (Rebata-Landa & Santamarina, 2006), and the modification of pore fluid viscosity due to the presence of bacteria that impacts directly on time-dependent behavior of the sediments (Sills & Gonzalez, 2001).

Finally, there is the possibility of directly circulating gas through samples (Sobkowicz, 1982; Amaratunga & Grozic, 2001; Lunne *et al.*, 2001; Sultan *et al.*, 2012; Cuss *et al.*, 2014). The experiments of Cuss *et al.* (2014) show that several months are needed in order to circulate free gas through 8 cm samples of low porosity claystones. Therefore, in order to reduce the testing time, the gas is circulated through the

sample in a dissolved state (Sobkowicz & Morgenstern, 1984; Amaratunga & Grozic, 2001; Lunne *et al.*, 2001; Sultan *et al.*, 2012). De-aired distilled water is saturated in separate tanks by increasing the gas pressure and circulating free gas through the water (Sobkowicz, 1982; Amaratunga & Grozic, 2001; Sultan *et al.*, 2012). Then a differential pressure is generated between both tanks to initiate circulation and replace fresh water by carbonated water (Amaratunga & Grozic, 2001; Sultan *et al.*, 2012). This method reduces the time needed to saturate the sample with gas, but yet between 5 and 15 days are needed for clayey samples (Sultan *et al.*, 2012). However, the advantage of this method is the possibility to create gassy sediments but through violent degassing; thus it allows measuring and observing the impact of gas exsolution and expansion on the host sediments (Amaratunga & Grozic, 2001; Sultan *et al.*, 2012). This method was proved to be efficient to study sediment damaging through gas exsolution processes due to gas-hydrate destabilization, gas expansion in sediment cores or mud generation at depth (Sultan *et al.*, 2012).

2.4. Hydro-mechanical properties of gassy sediments

2.4.1. Gassy sediment acoustic response

The presence of free gas causes several issues when dealing with acoustic signals (Sills *et al.*, 1991; Wilkens & Richardson, 1998; Helgerud *et al.*, 1999; Judd & Hovland, 2007; Sultan *et al.*, 2012). It provokes strong attenuation, velocity reduction and scattering of the signal, ultimately preventing any signal propagation as highlighted in Figure 4.5 (Sills *et al.*, 1991; Wilkens & Richardson, 1998; Judd & Hovland, 2007). Therefore, P-wave velocity attenuation is effective to detect the presence of free gas in sediments (Rebata-Landa *et al.*, 2012; Sultan *et al.*, 2012) and for degree of gas saturation estimation (Helgerud *et al.*, 1999; Lee & Collett, 2006; Morgan *et al.*, 2012).

Bubbles have an impact on the acoustic and mechanical properties of the medium, by increasing signal attenuation, by scattering the acoustic energy, by reducing acoustic-wave velocity and by changing the tensile strength of sediments (Judd & Hovland, 2007). Depending on the bubble size relatively to grain size, so depending on gassy soil structure (Figure 4.2; Wheeler, 1986), the bubbles will not have the same effect on the acoustic response (Wilkens & Richardson, 1998). In the case of bubbles smaller than the solid particles (Figure 4.2a), the acoustic response is mainly affected by changes in the pore-fluid compressibility due to the presence of gas bubbles in the pore space (Wilkens & Richardson, 1998; Judd & Hovland, 2007). In the case of bubbles larger than solid particles (Figure 4.2b), the sediment skeleton is deformed by the presence of bubbles, so the acoustic response of the sediments is mainly due to bubble compressibility and resonance as well as the change in the sediment frame (Wilkens & Richardson, 1998; Judd & Hovland, 2007). Moreover, the size of bubbles compared to the signal wavelength also affects the acoustic response: small bubbles compared to wavelength scatter the signal, when large bubbles attenuate the signal and reduce the acoustic wave velocity (Wilkens & Richardson, 1998; Judd & Hovland, 2007). The sediment shear strength is also a

parameter that will influence the bubble impact on acoustic response: low shear strength sediments such as soft clays will increase bubble resonance (Judd & Hovland, 2007).

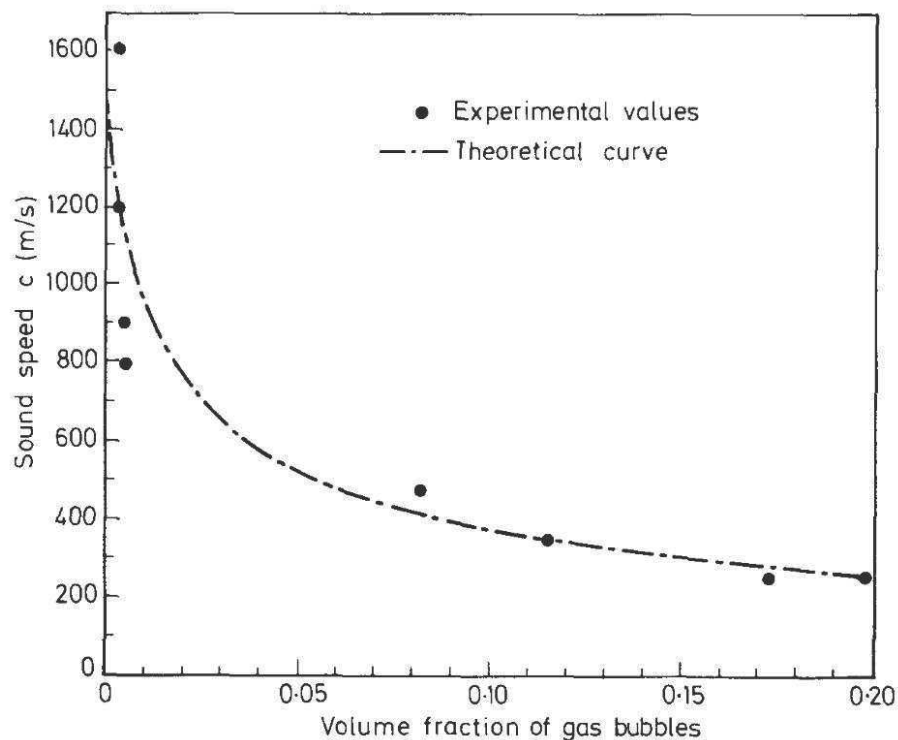


Figure 4.5: Experimental and theoretical decrease of P-wave velocity with increasing degree of gas saturation (from Sills *et al.*, 1991). A decrease of 50% P-wave velocity is reached for less than 5% of gas saturation.

2.4.2. Gassy sediment compressibility

The presence of gas bubbles in the pore space also affects the way sediments are compacted by modifying their compressibility as displayed in Figure 4.6 (Nageswaran, 1983; Thomas, 1987; Sills *et al.*, 1991; Nava Castro *et al.*, 2013).

Thomas (1987) shows that gassy sediments under consolidation compact as a water-saturated soil containing discrete compressible solid inclusions representing the gas bubbles. Several other experiments also determined an increase in marine sediment compressibility with the presence of gas bubbles (Sills *et al.*, 1991; Nava Castro *et al.*, 2013). Gas bubbles sustain part of the load applied on the sample. Therefore, soil compressibility measured on gassy sediment is primarily due to bubble compression and deformation, and secondarily due to normal sediment compression, implying water expulsion (Thomas, 1987; Sills *et al.*, 1991; Nava Castro, 2010). The presence of free gas in sediments is also responsible for a delay in consolidation: until gas dissolves or is expelled from the sediments, normal compaction through water expulsion cannot happen (Sills *et al.*, 1991; Nava Castro *et al.*, 2013).

Gas exsolution has a double impact on compressibility through sediment damaging and formation of gas bubbles in the pore space (Sultan *et al.*, 2012). Sultan *et al.* (2012) clearly identified this impact of gas exsolution on the compressibility of clayey sediments. Their results showed that after gas exsolution, the

compressibility lies between the swelling index and the compression index of the initial saturated sediments. This compressibility degradation was interpreted as being the result of sediment damaging during free gas generation (Sultan *et al.*, 2012).

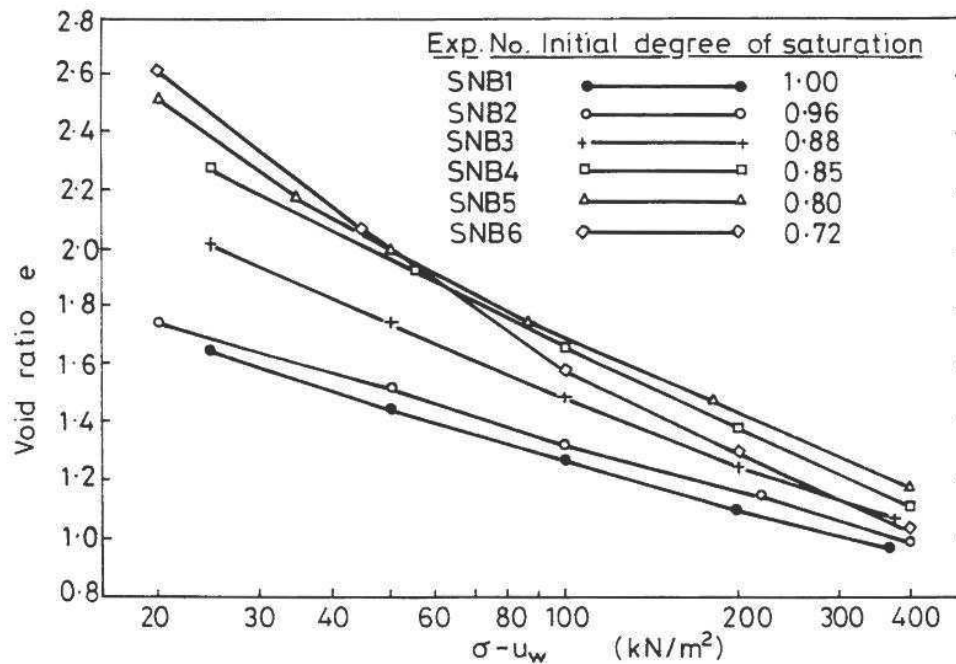


Figure 4.6: Results of oedometer tests ran over several artificial gassy sediments with known degree of gas saturation. They display the clear decrease in sediment compressibility with decreasing degree of saturation, so increasing degree of gas saturation (from Nageswaran, 1983).

2.4.3. Gassy sediment permeability

Several mechanisms may affect the sediment permeability, such as consolidation of sediments that provokes a decrease in hydraulic conductivity (Olsen, 1960; Chu *et al.*, 2002). The formation of free gas in fine-grained sediments can either increase or decrease the permeability as illustrated in Figure 4.7 (Egermann & Vizika, 2000; Naylor *et al.*, 2000; Hight & Leroueil, 2003; Jang & Santamarina, 2014). Indeed, depending on the degree of gas saturation and on the distribution of gas bubbles the impact will be different: a continuous gaseous phase may locally increase the gas permeability when discrete gas bubbles reduces the permeability (Zuo *et al.*, 2012; Jang & Santamarina, 2014). It partly depends on the mode of generation of gas bubbles: gas bubbles generated by internal processes, for instance by methanogens, reduce permeability as a discrete gas distribution will be created (Jang & Santamarina, 2014). This could be related to the presence of interstratification of fine and coarser lithologies and heterogeneities (fractures): at the interface, a capillary seal may form (a gas cap), generating an effective permeability even lower than the intrinsic permeability of the fine-grained layers (Revil *et al.*, 1998; Cathles, 2001).

Fractures may form during gas exsolution and bubble formation (Boudreau, 2012) especially in fine-grained sediments (Jain & Juanes, 2009; Shin & Santamarina, 2011). Fractures can improve the permeability depending on their orientation relative to the hydraulic gradient (Frank & Barkley, 1995; Alfaro & Wong, 2001), and depending on the infilling fluids and connectivity between fractures (continuous versus

discrete gas distribution; Long & Witherspoon, 1985; Jang & Santamarina, 2014). Moreover, violent gas exsolution may trigger a grain reorganization leading to further permeability reduction (Luhmann *et al.*, 2013)

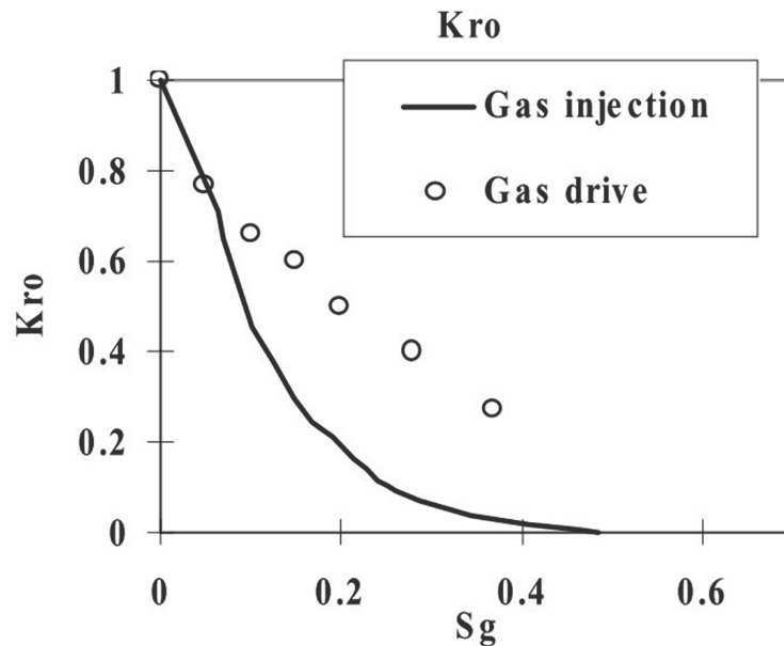


Figure 4.7: Evolution of water relative permeability of sediments depending on the degree of gas saturation for different methods of gas recovery. It clearly shows that the stronger the degree of gas saturation is, the lower the water relative permeability is (from Egermann & Vizika, 2000).

2.4.4. Sediment damage due to gas exsolution

Several studies noted that during marine sediment sampling, the structure and mechanical properties of sediments are impacted by gas exsolution and expansion (Esrig & Kirby, 1977; DeGroot *et al.*, 2010; Sultan, Savoye *et al.*, 2010; Sultan *et al.*, 2012; Priest *et al.*, 2014) like during ODP Leg 204 at southern Hydrate Ridge where several sediment cores display cracks (Figure 4.8; Riedel *et al.*, 2006).

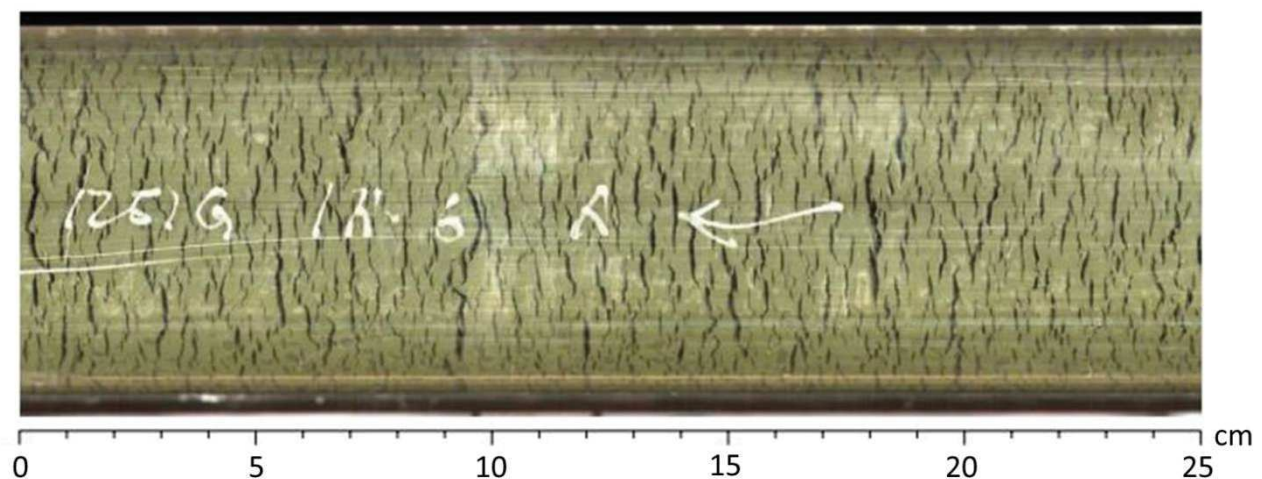


Figure 4.8: Section of a sediment core retrieved during ODP Leg 204 at southern Hydrate Ridge and displaying multiple cracks due to free gas expansion resulting from decompression during core ascent (from Riedel *et al.*, 2006).

Sultan, De Gennaro & Puech (2012) determined that damage of sediments from Gulf of Guinea through a decrease in preconsolidation pressure were directly linked to the degree of gas saturation. This decrease in

preconsolidation pressure with increasing degree of gas saturation was already highlighted on other sediments by several studies (Lunne *et al.*, 2001; Hight *et al.*, 2002). For Hight and Leroueil (2003), the loss of preconsolidation pressure results from sediment damage due to gas exsolution and expansion (bubble-growth) in the sediments. The degree of damage for equivalent degree of gas saturation may differ depending on the sediments, because it mainly depends on the level of structure of the sediments before exsolution (Hight & Leroueil, 2003; DeGroot *et al.*, 2010).

2.4.5. Effect of gas bubbles on the sediment shear strength

Wheeler (1988) showed with triaxial tests that the presence of methane bubbles in reconstituted clayey samples whether increases or decrease the undrained shear strength of the sample depending on the total and effective stresses. Low values of effective stress and high values of total stress (shallow depth below seafloor with important water column) promote the strength reduction due to gas bubbles (Wheeler, 1988). Moreover, Wheeler (1988) also demonstrated that during undrained shear strength testing, the degree of gas saturation decreases (samples potentially getting fully saturated before the peak shear strength is measured) but sediment structure stays permanently affected by the former presence of bubbles. More recent triaxial testing from Lunne *et al.* (2001), Hight, Hamza & El Sayed (2002) and Sultan, De Gennaro & Puech (2012) all point out that the peak shear strength is considerably decreased in gassy sediments compared to saturated sediments.

3. Experimental testing

3.1. Properties of the tested soil and sample preparation

To identify the potential geohazard of the AMV, Fugro conducted an offshore geotechnical survey in 2014 (Dan & Po, 12/09/2017, pers. com.) including rotary drilling with sediment coring up to 34 meters deep (Figure 4.9 for location) and in situ CPTu measurements (Cone Penetration Testing, with piezocone; Lunne, 2010; Boggess and Robertson, 2011). These data and cores are used in the present work to characterize the geotechnical properties of the natural and remolded sediments.

CPTu profiling and sediment type classification acquired at the MVF1 drilling site, on the western mudflow of the AMV (Dan & Po, 12/09/2017, pers. com.) show the presence of three different mechanical intervals. For this study, and in order to carry out basic geotechnical analyses, we selected three samples from the three different intervals (MECA-6, MECA-15 and MECA-22; Table 2-1).

Grain size distribution was determined with a laser diffraction apparatus (Mastersizer 3000, Ryzak and Bieganowski, 2011). Results show that the three reference samples have roughly the same grain size distribution with peak values between 4 and 6 μm and a minor signature around 400 μm (Figure 3.13C). However, the MECA-6 sample is slightly poorer in the fine fraction and richer in the coarser fraction. The d_x

is the grain size where $X\%$ of the grains are finer. The three samples differentiate on the coarser fraction as their d_{10} and d_{50} are roughly the same (Table 4-1). Nevertheless, all the samples have a d_{90} greater than $35\ \mu\text{m}$, meaning that 90% of the particles are smaller than $35\ \mu\text{m}$. 50% of the mud particles are smaller than $5\ \mu\text{m}$. Therefore, the studied samples are essentially composed of silts and clay-size particles with a minor fraction of very fine to medium sand.

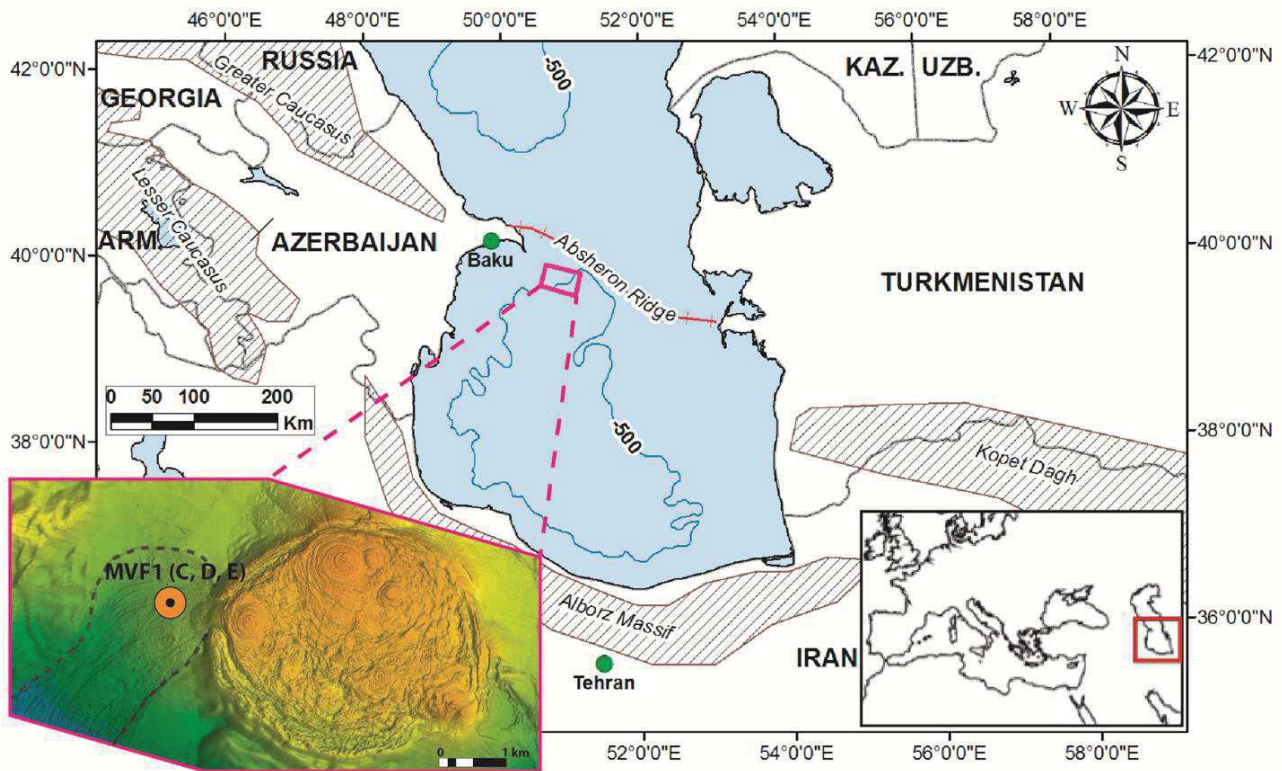


Figure 4.9: Location of the study area. The Absheron mud volcano is located on the Absheron anticline (purple rectangle), 100 km to the SE of Baku, north of the South Caspian Basin. Details of the seafloor morphology of the area surrounding the mud volcano is given in the inset in the bottom left hand corner (read Chapter 2:2.1 and Chapter 3:4.1 for more details). The rotary drilling MVF1, located on the mudflow, is also displayed.

A mineralogical analysis was performed on two of the samples used in this study (MECA-6 and MECA-22, see Table 2-1). Table 4-1 displays the main mineralogical fractions for the two tested samples (see Figure 3.12A) grouped into three poles: quartz, clay and calcite. Other minerals type were distributed between the pole according to their density or their mineral group. For instance, the dolomite percentage was added to the calcite pole, and apatite to the clay pole.

The Atterberg limits were determined using the fall cone method (Feng, 2000). Results are presented in Table 4-1. Sediment from the three samples has a mean plastic limit value of (w_p) 20.3%, a mean liquid limit (w_L) of 43% and a mean plasticity index (PI) of 22.7%.

Oedometer tests were carried out on the same reference samples using incremental loading according to the ASTM D-2435 method (ASTM International, 1996). Three oedometer reference samples were prepared from three mud samples (MECA-6, MECA-15, MECA-22; Table 4-1) with a water content of approximately 1.5 the liquid limit (w_L). Compressibility curves during loading and unloading tests are plotted in Figure 3.13A.

The three samples have almost the same virgin consolidation curve with a compression index C_c of 0.3 and a swelling index C_s of 0.08 (Table 4-1).

During consolidation tests, hydraulic conductivity measurements were carried out using the falling-head test method. Figure 3.13B summarizes the results as a cross-plot of hydraulic conductivity versus void ratio. The three samples have a similar trend and hydraulic conductivity K stands between $8 \cdot 10^{-8}$ and $7 \cdot 10^{-9}$ m/s for void ratios between 1 and 0.4. Skempton (1944) gives an empirical expression linking the compression index and the liquid limit of remolded clays. Using the mean liquid limit of the tested sediment, the calculated C_c is 0.32, which is in agreement with values obtained using oedometer tests (Table 4-1).

Table 4-1: Synthesis of the main sample properties. Further details are given in Figure 3.13.

	MECA-6	MECA-15	MECA-22
d_{10} (μm)	1.17	1.22	1.21
d_{50} (μm)	5.91	5.41	5.23
d_{90} (μm)	53.7	42.9	36.8
w_p (%)	21.0	23.0	17.0
w_L (%)	42.0	43.0	44.0
PI	21.0	20.0	27.0
C_c	0.32	0.29	0.31
C_s	0.08	0.07	0.07
mass% Quartz	38.5		36
mass% Clays	51.5		55.5
mass% Calcite	10		8.5

Due to the insignificant variability of the basic properties of the three tested samples, eight other samples were selected from the same three intervals of the MVF1 core in order to test the impact of gas exsolution using the new experimental apparatus developed in the present study (samples with the mention "consolidation cell" in the column "type of analysis" of Table 2-1). To obtain homogeneous samples, the eight samples were mixed and remolded with a water content of approximately twice the liquid limit (Table 4-1). Remolding was carried out using a mechanical stirrer. The same slurry was used in all the tests presented in the paper. At the end of each test, a small part of the tested sample served to measure the final water content.

3.2. Experimental set-up and calibration

A novel experimental set-up composed of three main modules was developed to analyze the gassy sediments (Figure 4.10): the consolidation cell and the mechanical press designed to apply vertical loads and the saturation module where water is carbonated under a given CO₂ gas pressure. The last module is the control panel that connects all the experimental set-up sensors with a computer in order to constrain and record the different parameters.

The consolidation cell is composed of a Plexiglas cylinder that forms, along the two end covers, the fixed part of the system (Figure 4.10). The type of Plexiglas used for the consolidation cell is PMMA XT, which has an elastic modulus of 3.3 GPa and a yield stress of 70-80 MPa. The Plexiglas cylinder is 15 mm thick. The piston is composed of a steel rod fixed into a pierced plastic cylinder (Figure 4.10). Two porous stones placed on the top and the bottom of the sample ensure the consolidation of the sediment during loading. A load cell and a vertical displacement sensor allow controlling the rate of displacement and the axial force applied to the sample (Figure 4.10). The load cell is limited to 5 kN (≈ 1300 kPa considering the sample section) with a precision of ± 0.005 kN. A bender element system (supplied by GDS Ltd, UK; Hasan and Wheeler (2015)) is integrated into the piston and the bottom pedestal to measure P-wave velocity (Figure 4.10).

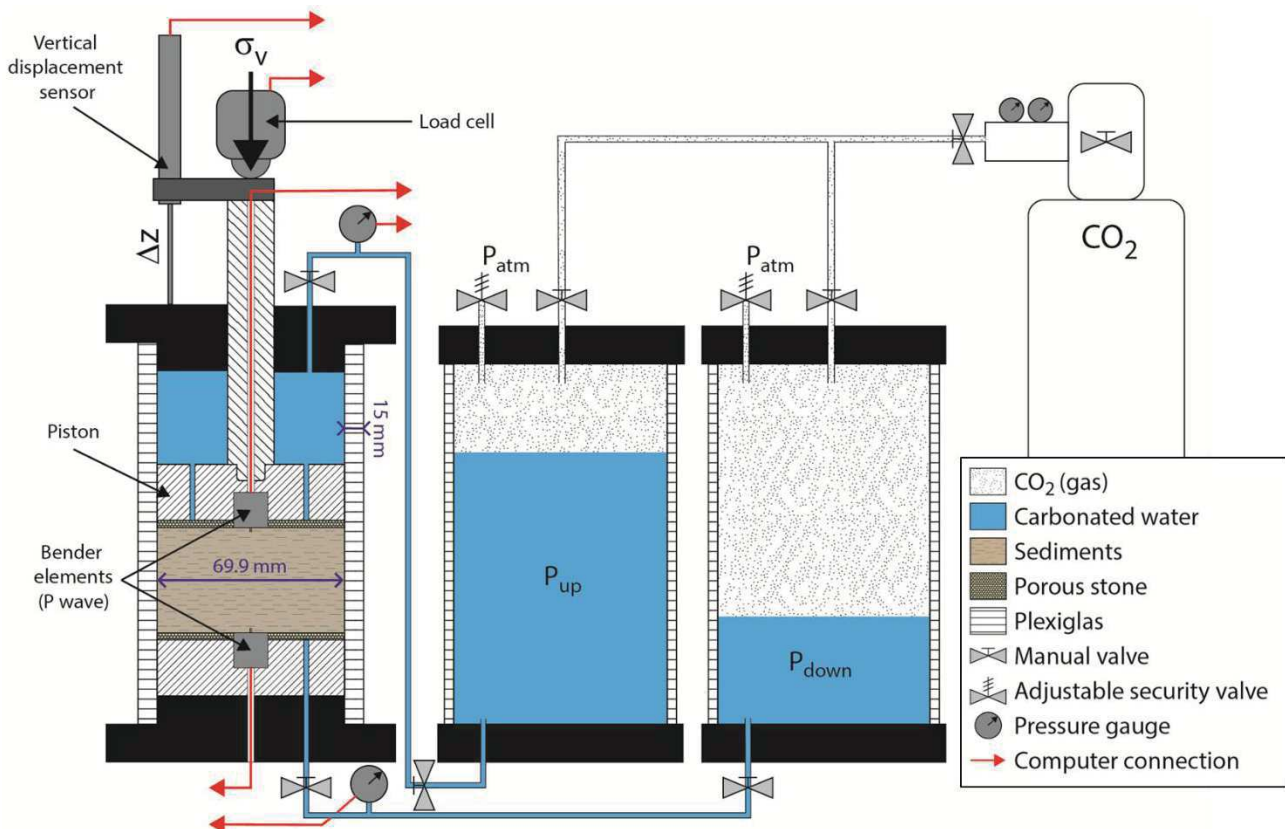


Figure 4.10: Detailed experimental setup showing the consolidation cell, the saturation system and the main sensors emplacement.

A lip seal circles the piston and avoids sediments flowing above the piston but generates a non-negligible friction on the inner surface of the Plexiglas cylinder. This friction is measured by the load cell and

is calibrated to properly calculate the net applied vertical effective stress. Force balance at the sediment-piston contact shows that the measured force is a composition of the friction, a vertical upload force due to the different piston surfaces on which fluid pressure is applied (Figure 4.10), and the net applied load. Friction is always opposed to piston movement.

The lip seal is asymmetrical. Therefore, calibration of friction must be made during loading and unloading (Figure 4.11). To do so, the consolidation cell was filled with water and underwent different load and unload cycles at different pore water pressures. The piston velocity used in the different calibration tests is the same in the rest of our testing program: 0.12 mm/h during loading, 0.5 mm/h during unloading. The load velocity was determined by comparing the oedometer compressibility curve (Figure 3.13A) to the compressibility one using the present advanced consolidation cell.

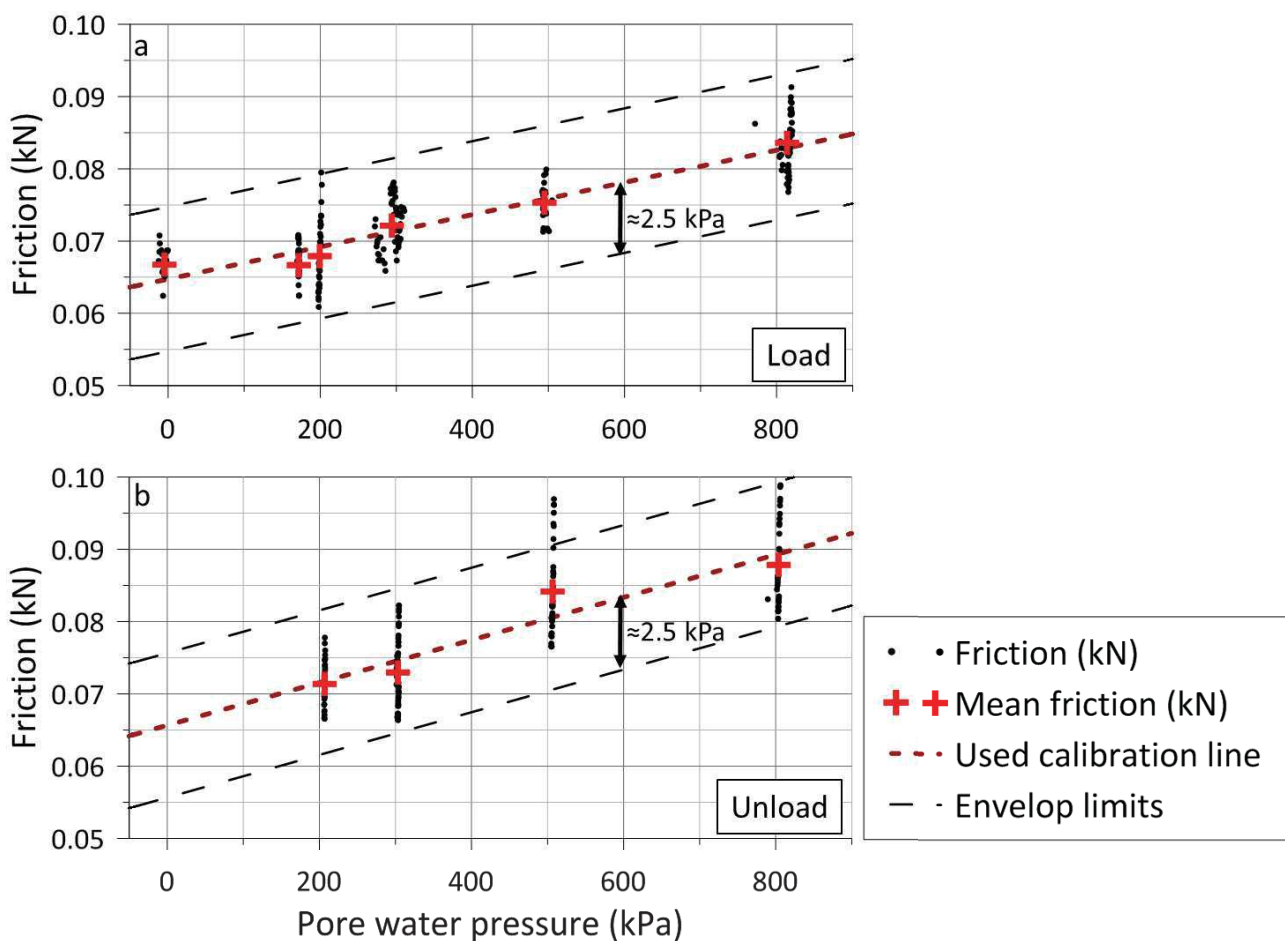


Figure 4.11: friction calibration during (a) loading and (b) unloading for different pore water pressures. The dotted black lines correspond to the envelop values of friction. The friction variation is within ± 2.5 kPa.

The results show that the friction is a linear function of pressure and differs during loading and unloading (Figure 4.11). For each pore water pressure, the friction variation is, for the corresponding diameter, within ± 2.5 kPa. The two friction laws obtained were then added to the vertical effective stress calculations. The effective stress corresponds to the net load force applied to the sediment. During loading stages, this force is calculated by subtracting friction force and the vertical upload (force resulting from the

area difference between the piston top and bottom, see Figure 4.10) from the total measured load. During unloading stages, friction is added, as it is always oriented in the direction opposed to piston movement.

The saturation system is composed of two Plexiglas tanks, the same type as the consolidation cell, designed to support 1 MPa of water/gas pressure (Figure 4.10). Both tanks are connected at the top to a CO₂ bottle equipped with an adjustable pressure gauge that can deliver up to 2.5 MPa of gas pressure (Figure 4.10). Tanks are half-filled with water, the other half being occupied by gas. Adjustable security valves are connected at the top of the two tanks and allow to expel gas if a pressure threshold is reached (Figure 4.10). Each tank connects to the top or the bottom of the consolidation cell by their bottom end. Differential pressures at the top and bottom of the sample can be applied through the two tanks allowing the carbonated water to circulate through the sample.

Pressure gauges control the pore pressure and are limited to 3 MPa with a precision of ± 0.75 kPa. Pressure gauges can be either isolated from the consolidation cell or isolated from the tanks thanks to valves present between the two parts of the system (Figure 4.10). All the sensors used (load cell, vertical displacement sensor and pressure gauges) are connected to a control panel (Figure 4.10). The computer monitors, records and controls the different test parameters.

A pressure generator is connected at the bottom end of the consolidation cell for water permeability measurements. The pressure generator creates a pressure gradient while measuring water volume change. Using Darcy's law, it is possible to calculate the hydraulic conductivity of the sediment. A falling head method can also be applied using the differential pressure between the two saturation tanks. Due to the large internal diameter of the saturation tanks (91.9 mm), only hydraulic conductivities obtained from water head variations greater than 10 mm are considered as accurate.

P-wave velocities are measured using GDS bender element system. Due to sample dimensions (diameter: 69.9 mm; initial height around 65 mm), it was necessary to calibrate the signal frequency to avoid a waveguide effect of the Plexiglas cell and lateral rebounds (Chan, 2012). After several tests, a frequency of 100 kHz appeared to record the clearest received signal. To obtain repeatable and comparable measurements, the received signal is picked on the last relative minimum before the first received peak.

The different characteristics of the system mentioned above are listed and synthesized in Table 2-2.

The main purpose of this experimental study is to evaluate the impact of gas exsolution and accumulation on the mechanical behavior of the tested sediments (e.g. compressibility, preconsolidation pressure, permeability, P-wave velocity). To do so, several loading/unloading cycles are applied during each test on water-saturated sediments and gassy sediments. Each test can be described with the following basic scheme and phases:

- **Phase 1 - carbonated water:** Water in the two saturation tanks is saturated with CO₂ for at least two days with gas pressure between 300 and 800 kPa. During this first phase, carbonated water is isolated from the consolidation cell (valves closed at the base of the tanks, Figure 4.10).
- **Phase 2 - saturation using carbonated water:** Remolded sediments are poured into the consolidation cell and connected to the saturation cells. Differential water pressure is applied between the two saturation tanks, creating a hydraulic gradient and a carbonated water flow through the sediment. The aim is to replace the pure pore water initially present by carbonated water. Circulation is imposed until the carbonated water volume flow reaches the initial total sample volume. During this stage, some gravity settling of sediments can be observed.
- **Phase 3 - consolidation of water-saturated sediments:** The piston is manually moved until contact with sediments is established. The first loading/unloading cycle starts with a loading velocity of 0.12 mm/h and an unloading velocity of 0.5 mm/h. A maximal total load is configured based on the target value of effective stress ($\sigma'_v = 100, 200$ or 400 kPa). Another loading/unloading cycle can be applied to record the swelling index of the sediments. During these cycles, P-wave velocity and hydraulic conductivity are regularly measured.
- **Phase 4 - degassing and gas exsolution process:** After unloading, the piston is manually raised to allow gas expansion/exsolution and sediment swelling. Complete or partial depressurization is applied using the two valves connected to the saturation cells (Figure 4.10). Both valves are opened simultaneously so that the depressurization applies on both side of the sample. The partial gas exsolution is not always visible. Therefore, free gas presence is detected by comparing P-wave velocity before and after depressurization. To ensure full degassing, this phase is maintained for around 15 hours.

Phase 5 - consolidation of gassy sediments: After degassing, contact between the piston and the sample is made manually and generally, a swelling of the sample is noted. The change in the sample height is used to calculate S_g . Another loading/unloading cycle is then applied to the gassy sediments with a σ'_v values exceeding the one applied at phase 4. As loading increases, gas saturation is expected to decrease. During this phase, P-wave velocity and permeability are measured to determine the influence of gas saturation on both parameters.

In the case of partial degassing, the two last phases can be repeated to obtain different gas saturations during the same test. Void ratio, e , and gas volume V_{gas} are calculated at each time step using the initial void ratio value (e_0) and the change in sample height. Gas saturation S_g is calculated from pore water volume V_w before degassing and the measured V_{gas} :

$$S_g = \frac{V_{gas}}{V_{gas} + V_w} \quad (13)$$

3.3. Testing program

In the scope of this study, eleven tests were performed, one being a normal consolidation test (no gas and under atmospheric pressure) which is the reference test for compressibility (Table 4-2). The good agreement between a loading/unloading curve obtained during an oedometer test (ASTM D-2435, ASTM International, 1996) and the present reference test has allowed to validate the used loading velocity. During the ten other tests, fifteen degassing were triggered under different conditions (e.g. preconsolidation pressure, initial gas pressure, u_i , magnitude of depressurization, Δu ; Table 4-2). Sediment mechanical compressibility as well as P-wave velocity and hydraulic conductivity were measured before and after each degassing stage. This study contains 270 P-wave measurements and 26 hydraulic conductivity measurements (Table 4-2). Details of the testing program are provided in Table 4-2:

Table 4-2: Testing program with details on the number of loading/unloading cycles per test, the applied maximal effective stress at each stage, the initial gas pressure, the magnitude of depressurization for each exsolution.

Test number	Cycle (load/unload)	σ'_{vmax} (kPa)	u_i (kPa)	Δu (kPa)	Number of measured V_p	number of measured K	Comments
2	1	100	350	0	13	0	
	2	1000	350	-350	9	0	
	3	1000	350	-350	3	0	
3	1	400	800	0	13	0	
	2	1000	800	-800	6	0	
4	1	200	500	0	19	5	
	2	1000	500	-500	10	0	
	3	1200	0	0	10	0	
5	1	100	800	0	13	2	
	2	1000	800	-800	19	0	
6	1	100	500	0	9	1	
	2	400	500	0	16	1	
	3	1000	500	-500	18	3	
7	1	100	800	0	9	3	

	2	400	800	0	7	0	
	3	1000	800	-400	10	0	
8	1	100	800	0	4	1	
	2	400	800	0	3	0	
	3	1000	800	-300	8	0	
	4	1200	500	-500	3	3	
9	1	400	800	0	7	1	
	2	1000	800	-100	2	0	
	3	1200	700	-250	7	0	
	4	1200	450	-450	4	1	Degassing under $\sigma'_v = 100$ kPa
10	1	1200	0	0	9	3	drained consolidation test (reference)
11	1	400	800	0	8	1	
	2	800	800	-200	12	0	
	3	1100	600	-200	11	0	
	4	1400	400	-400	8	1	

4. Results

In the following, we have provided the details of three tests only as, of the eleven tests, these three show the main behavioral features observed. Results of the other test are displayed in Appendix 1, in the same fashion as the plots presented hereafter .

During test#8, 4 load/unload cycles were applied on the remolded sediment sample (Figure 4.12a). The first two cycles were completed on the water-saturated sample under constant carbonated water pressure (u_i) of 800 kPa. They showed a normal loading-unloading compressibility curve (Figure 4.12a). However, the beginning of loading 1 (σ'_v lower than 20 kPa) differs from the reference test. The difference between the two stages is related to the applied carbonated water pressure. A reference test was applied under atmospheric pressure where normal sediment settling took place. For the other ten tests, initial loading (cycle 1) took place under a carbonated water pressure gradient. This affected the normal settling velocity and accelerated sedimentation. After the first unloading in cycle 1, the loading in cycle 2 followed the swelling trend of the sediment until reaching preconsolidation pressure ($\sigma'_{p0} = 100$ kPa, σ'_{p0} will be used in the rest of paper to refer to the preconsolidation pressure that the sediment underwent over the last loading phase). From this stage, the sample recovers a normal consolidation trend following the virgin consolidation curve to a vertical effective stress of 400 kPa. The C_c and C_s values are comparable to those obtained from oedometer tests (Figure 3.13 and Table 4-1).

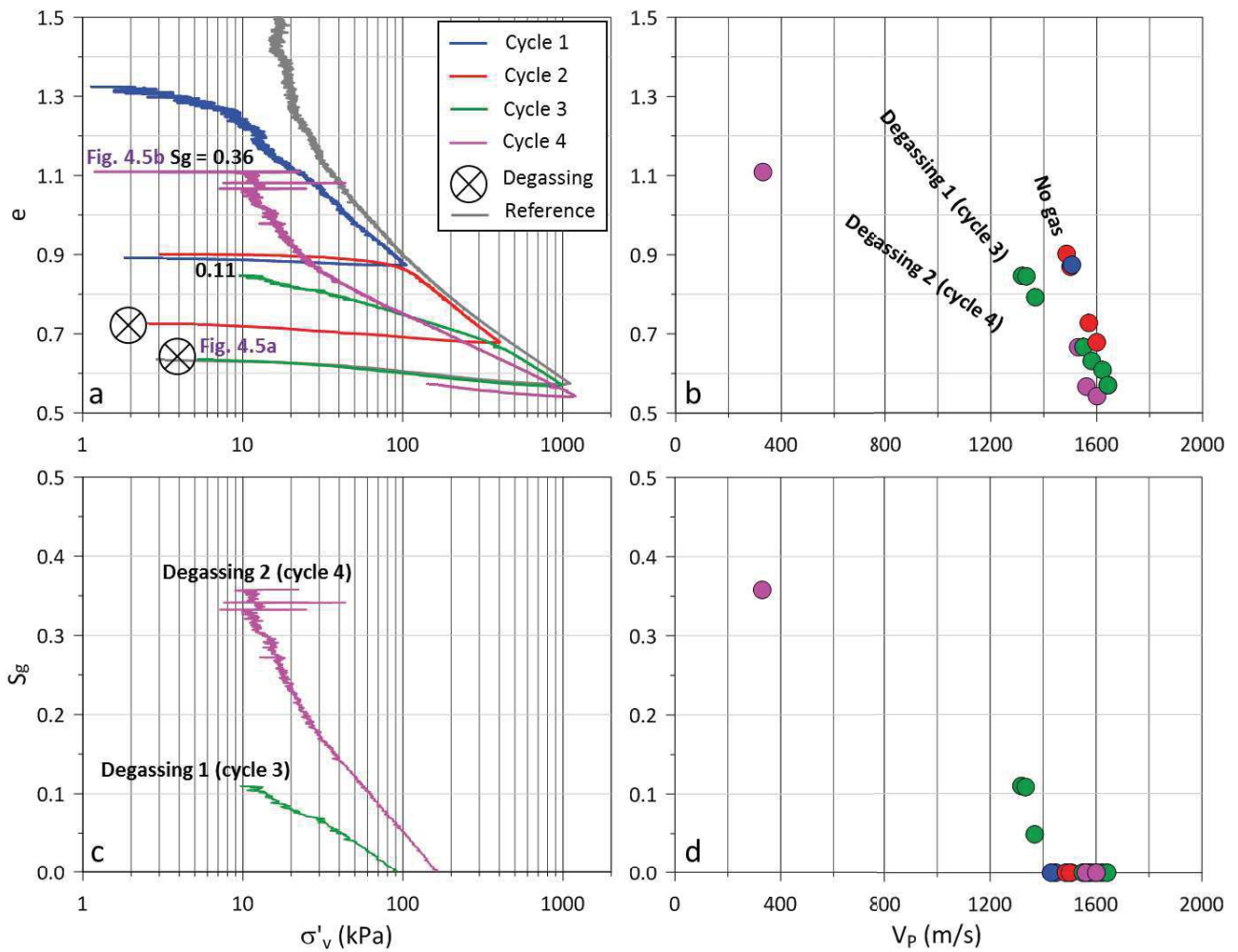


Figure 4.12: Results for test#8 with 4 load/unload cycles. Each color represents a load/unload cycle. a: void ratio (e) versus vertical effective stress (σ'_v); b: void ratio-versus P wave velocity (V_p); c: degree of gas saturation (S_g) versus σ'_v and d: S_g versus V_p . The grey line in (a) represents the reference consolidation test.

After unloading 2, partial depressurization (Δu) of -300 kPa was applied. No fractures or discontinuities were noticed during this phase. However, the sample swelled by 1.5 mm, corresponding to S_g of 11%. The mechanical behavior after this first degassing stage changed drastically. The sample did not display an elastic trend during reloading showing a compressibility characterized by a slope varying between the swelling index and the compression index (Figure 4.12a). This intermediate compressibility lasted until reaching an effective stress of 400 kPa corresponding to σ'_{p0} , well after gas saturation reached zero (Figure 4.12a,c). Then, the compressibility followed the normal compaction trend. P-wave velocities show a constant trend for cycles 1 and 2 (blue and red dots in Figure 4.12b,d) while the presence of free gas in cycle 3 causes an important decrease in P-wave velocities (green dots in Figure 4.12b,d). During the loading in cycle 3, S_g decreases and the P-wave velocity increases and reaches normal values only when sediment behaves as a normally consolidated material.

The intermediate compressibility slope (cycle 3 between 20 kPa and 400 kPa in Figure 4.12a) was calculated and is named C_{Cgas} in all the following tests carried out in this study. For test#8, C_{Cgas} is equal to 0.09. The preconsolidation pressure was also calculated using the normal elastic curve and the virgin

compression curve. The intersection between the two curves gives a preconsolidation pressure that we called σ'_{p2} equal to 130 kPa which is significantly less than the applied 400 kPa in cycle 2 (Figure 4.12a).

Cycle 4 began with complete depressurization ($\Delta u = -500$ kPa) which immediately affected the structure of the sample (Figure 4.13). Fractures formed during the first minutes following depressurization, ultimately showing a complete remolding of the upper part of the sample (Figure 4.13). Fractures are horizontally oriented in accordance with the maximum principal stress orientation. This degassing provoked a swelling of 6 mm of the sample partly adapted by the cm-long and mm-thick horizontal fractures (Figure 4.13). S_g at this stage was found equal to 36% (Figure 4.12a,c).

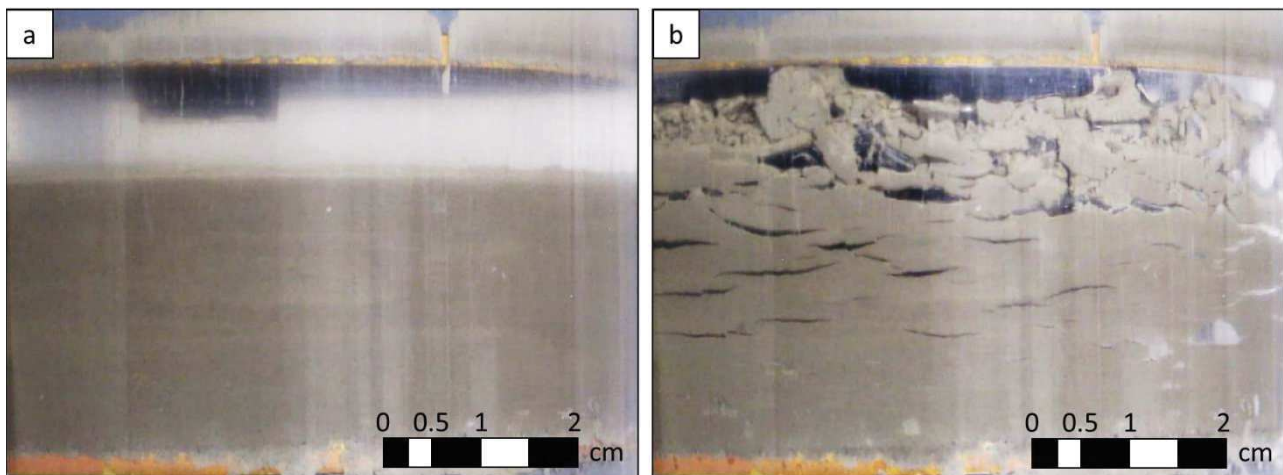


Figure 4.13: Pictures of the sample during test 8. a: before the second depressurization (cycle 4, Figure 4.12a) showing the sediment aspect before gas exsolution. b: after the second depressurization (Figure 4.12a). The sample swelled by 6 mm under the effect of gas exsolution, swelling partly due to the numerous cm-long and mm-thick fractures.

Nageswaran (1983) gives an upper limit for gassy sediments in terms of degree of gas saturation. In this definition, sediments having S_{gmax} higher than 15% should not be regarded as gassy sediments but as unsaturated soil. However, the gaseous phase is not homogeneously distributed and is not continuous as gas invades the sample through fracture generation (Jain & Juanes, 2009). Moreover, once fracture opens, gas exsolution and bubble growth occur predominantly at fracture sites that act as preferential nucleation and bubble growth sites (Jang and Santamarina, 2014; Katsman, 2015). Given the short duration of exsolution (12 hours on average), free gas does not have time to diffuse through the complete sample. Experiments by Cuss *et al.*, (2014) demonstrated that months are needed to saturate a low-porosity sample. Therefore, free gas mainly concentrates in fracture spaces and is not present as separated spherical bubbles as in the Nageswaran (1983) definition.

The loading of cycle 4 can be divided into two stages. The first stage corresponds to the part having a compressibility slope larger than the virgin compression line. This stage corresponds to the fracture closing. Once all the fractures closed, an intermediate compressibility state, similar to that described for cycle 3, is observed. The normal compression trend began at around 900 kPa but is not well expressed since the test was stopped at σ'_v around 1000 kPa. S_g reached zero around 180 kPa during the intermediate stage

(Figure 4.12a,c). Again, a drop in P-wave velocities highlights the presence of free gas after gas exsolution (Figure 4.12b,d). This decrease is greater than during cycle 3 due to greater gas saturation. P-wave velocities shift from the water-saturated values even after S_g reaches zero.

The slopes of the two compressibility states during reloading in cycle 4 were also measured. $C_{C_{gas}}$ equals 0.17. The slope for the state corresponding to fracture closing is named $C_{C_{frac}}$ in the following analyses. For cycle 4, $C_{C_{frac}}$ reaches 0.7. In this cycle, two preconsolidation pressures can be calculated. σ'_{p2} using the method already described after fracture closing and σ'_{p1} which is calculated using the intersection of the two slopes $C_{C_{gas}}$ and $C_{C_{frac}}$. σ'_{p1} was found equal to 25 kPa while σ'_{p2} was not calculated because, as mentioned above, the normal compression trend is not well expressed in cycle 4.

P-wave velocities display different evolutions with void ratio depending on the cycle (Figure 4.12b). Cycles 1 and 2, where the measurements were made on water-saturated sample, show the same trend while the two other cycles indicate specific trends. P-wave velocities decrease with the presence of free gas (Helgerud *et al.*, 1999; Sultan *et al.*, 2012). The impact of free gas on acoustic velocities is well illustrated with test#8 as P-wave velocity trend with void ratio have gentler slope with increasing initial gas saturation (Figure 4.12b). Decreased values of P-wave velocities were measured even after free gas disappeared ($S_g = 0$), and normal values were reached once sediments followed the normal compression trend (Figure 4.12a,b,c).

During test#11, only one water-saturated cycle was completed, revealing that the sediments have a normal loading/unloading compressibility curve (Figure 4.14a). Indeed, the virgin compaction curve and the swelling trend of test#11 perfectly fits with the drained consolidation test used as reference (Figure 4.14a).

After unloading 1, partial depressurization (Δu) of -200 kPa is applied. Small and thin fractures appeared along a pre-existing weak zone that expended during gas exsolution (light color strip Figure 4.15a,b). At the beginning of the loading stage of cycle 2, a swelling of 5 mm was recorded (visible on Figure 4.15a,b), corresponding to a S_g of 24% (Figure 4.14a). The compressibility of the gassy sediments during loading 2 is characterized by a slope comprised between C_c and C_s . Here again, it shows an intermediate compressibility before reaching the virgin compression curve once the σ'_{p0} (400 kPa) was exceeded (Figure 4.14a). S_g reached zero before 200 kPa, therefore, the intermediate compressibility lasted longer than the presence of free gas in the sediments (Figure 4.14a,c). P-wave velocities decrease after degassing, compared to the trend obtained on the water-saturated sample during cycle 1 (Figure 4.14b). Even after the moment S_g reaches zero, P-wave velocities are attenuated, showing that gas exsolution affects them even after free gas entirely disappeared from the sample (Figure 4.14b,c). Finally, cycle 2 loading reached 800 kPa before unloading the sample once again.

The intermediate compressibility slope $C_{C_{gas}}$ equals 0.12. Using the swelling and virgin compaction curves, σ'_{p2} was found equal to 100 kPa (cycle 1 reached a $\sigma'_{p0} = 400$ kPa).

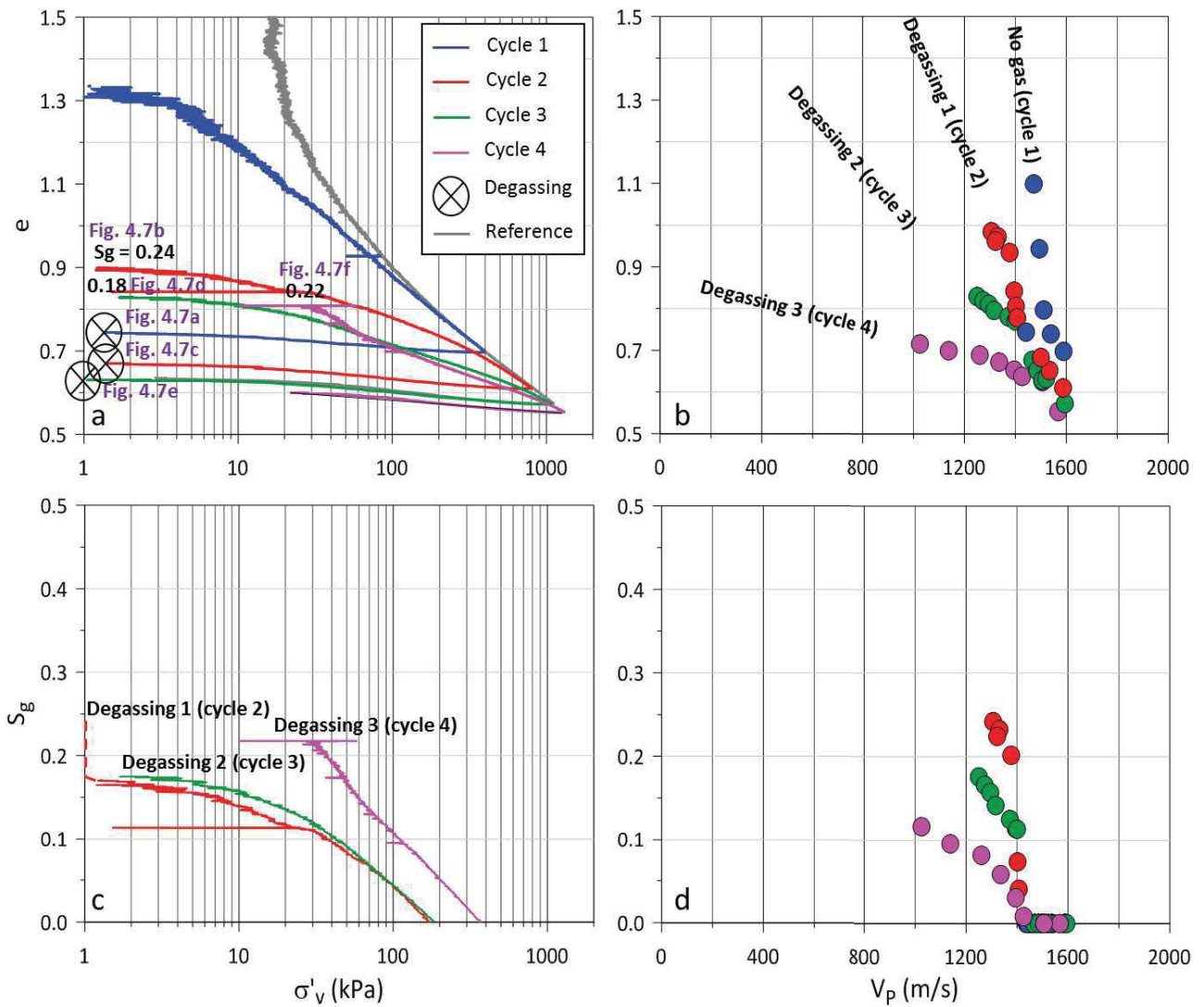


Figure 4.14: Results for test#11 with 4 load/unload cycles. Each color represents one load/unload cycle. a: void ratio (e) versus vertical effective stress (σ'_v); b: void ratio-versus P wave velocity (V_p); c: degree of gas saturation (S_g) versus σ'_v and d: S_g versus V_p . The grey line in (a) represents the reference consolidation test.

Cycle 3 started after another partial depressurization of -200 kPa was applied. Rare and localized very thin fractures formed at the base of the sample (Figure 4.15c,d). No trace of the former weak strip was noticed at this stage. Additionally, 2.7 mm of swelling shows that free gas exsolved in the sample, resulting in a S_g of 18%. An intermediate compressibility is observed until the end of the loading phase. The normal compression trend began at around 900 kPa but is not well expressed since the test was stopped at σ'_v around 1100 kPa. The gas saturation reached zero at only 200 kPa, thus most of the intermediate compressibility was measured on water-saturated sediments (Figure 4.14a,c). P-wave velocities are reduced compared to the water-saturated sediment (Figure 4.14b,d). The depressurization of cycle 3 generated a smaller volume of free gas compared to cycle 2. Nevertheless, P-wave velocities measured during cycle 3 also decreased compared to those of cycle 2 (Figure 4.14b,d), showing that even after a complete cycle, sediments did not entirely recover their normal acoustic properties.

The intermediate compaction slope measurement resulted in a $C_{C_{gas}}$ of 0.12 and the σ'_{p2} of 180 kPa when σ'_{p0} was 900 kPa (cycle 2).

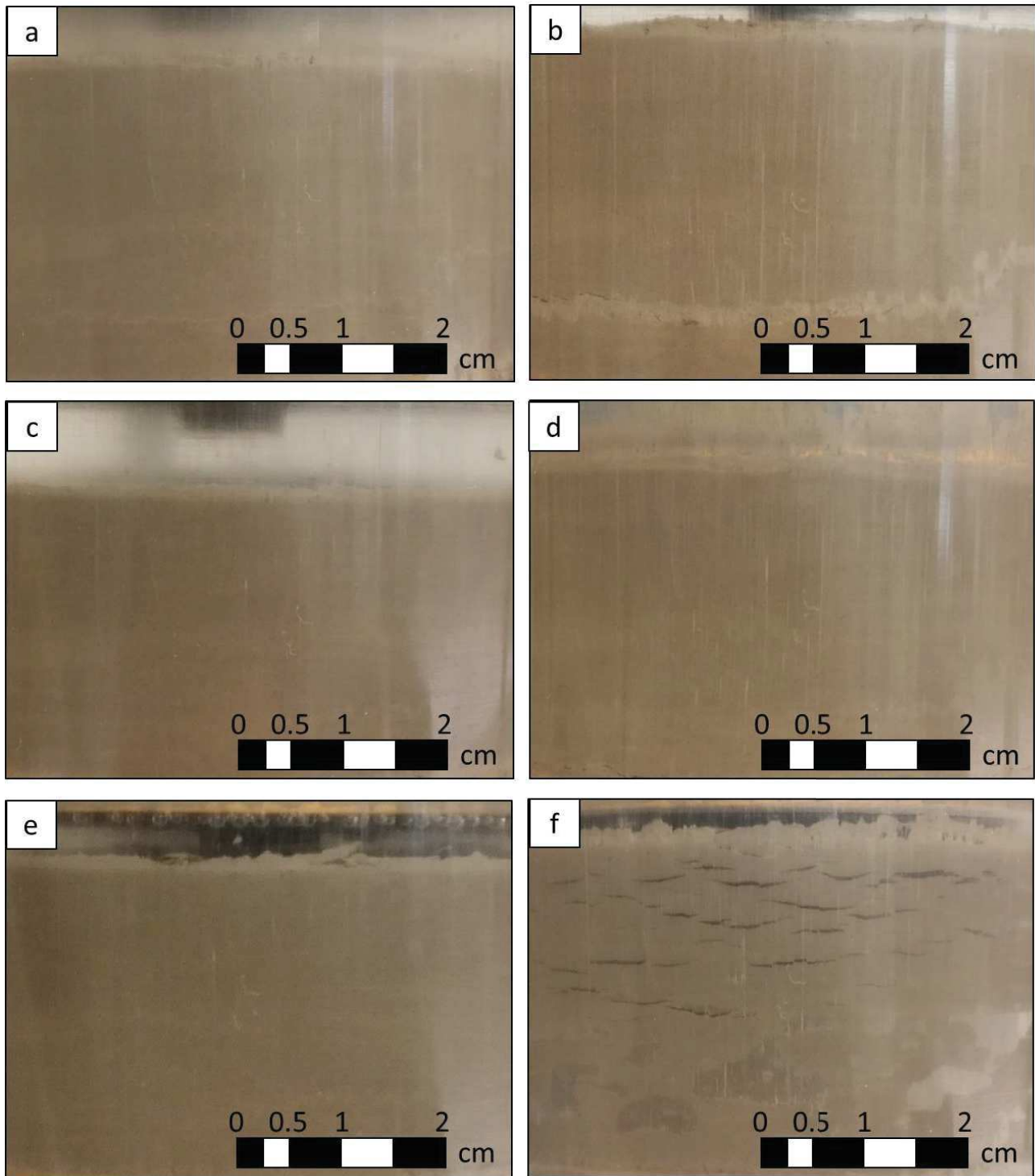


Figure 4.15: Pictures of the sample during test 11. a: before the second depressurization (cycle 3, Figure 4.14a) showing the sediment aspect before gas exsolution. b: after the second depressurization (Figure 4.14a). The sample swelled by 5 mm under the effect of gas exsolution and small and rare fractures appeared along a pre-existing weak zone (lighter color). c: before the second depressurization (cycle 3, Figure 4.14a) showing the sediment aspect before gas exsolution. d: after the second depressurization (Figure 4.14a). The sample swelled by 2.5 mm under the effect of gas exsolution with rare and very thin fractures at the base of the sample. e: before the third depressurization (cycle 4, Figure 4.14a) showing the sediment aspect before gas exsolution. f: after the third depressurization (Figure 4.14a). The sample swelled by 3.5 mm under the effect of gas exsolution, swelling partly due to the numerous cm-long and mm-thick fractures.

P-wave velocities have different trends with void ratio depending on the cycle (Figure 4.14b). Cycle 1, where P-wave velocities were measured on water-saturated sediments, differs from the other cycles. The impact of free gas on acoustic velocities is again displayed in this test as P-wave velocity trend with void ratio

have a gentler slope when sediments contain free-gas (Figure 4.14b). Once S_g equals zero, P-wave velocities are attenuated until reaching the normal compression trend (Figure 4.14a,b,c). Moreover, the cycle having the biggest gas saturation is not the one displaying the smallest values of V_p . Instead, P-wave velocities decrease after each gas exsolution showing that sediments did not recover their normal acoustic response after free gas disappeared and reloading.

Only two cycles were completed during test#5. The first cycle is not displayed in Figure 4.16a as the pressure difference between the two ends of the sample was maintained during the whole cycle for carbonated water circulation. Therefore, the calculated σ'_v for this cycle is not representative. However, total depressurization completed on the sample ($\Delta u = -800$ kPa), triggered a complete remolding of sediments as shown in Figure 4.17. The sample fractured completely and so intensely that it resembled slurry. The total swelling recorded was 9.5 mm, corresponding to gas saturation of 38%, which is the maximum value obtained in this study. For this reason, test#5 is regarded as the extreme scenario. Two intermediate compressibilities were measured. The first one corresponds to the fracture closing and has a sub-vertical slope (Figure 4.16a). The second one has a slope greater than the virgin compaction curve. Finally, from $\sigma'_v = 150$ kPa to the end of the loading, sediments follow the normal compression trend (grey line in Figure 4.16a). The normal compressibility was recovered when S_g was already equal to zero for 50 kPa (Figure 4.16a,c). However, normal compression trends on other tests were recovered with a larger delay from free gas disappearance even though they displayed a lower gas saturation.

P-wave velocities were recorded throughout the two cycles. Figure 4.16c,d clearly shows the difference in velocity magnitudes before and after exsolution. P-wave velocities recorded after exsolution decreased by more than 50% for high void ratios ($e > 1$). After gas disappearance ($\sigma'_v > 100$ kPa, Figure 4.16c), P-wave velocity for cycle 2 quickly increases with decreasing void ratio and recovers a trend parallel to the water-saturated reference when the minimum void ratio for cycle 1 is exceeded (Figure 4.16b). Therefore, gas exsolution seems to disturb P-wave velocities even after all the free gas has disappeared.

The slopes for the two intermediate compressibilities were measured. The closing of fractures corresponds to a slope C_{frac} of 1.6. The intermediate compressibility slope, C_{gas} , was measured at 0.5. Therefore, a σ'_{p1} of 42 kPa was calculated, the initial preconsolidation pressure, σ'_{p0} , being around 60 kPa. σ'_{p2} was not calculated as the classical method for its determination is not applicable in this case. However, due to the slurry aspect of the sample after gas exsolution (which led to the maximum measured S_g of this study) and based on how the compaction curve fits the reference, this test is considered as representative of a critical remolded state where the sediment has entirely lost its preconsolidation pressure. We consider, for this test, $\sigma'_{p2} = 0$.

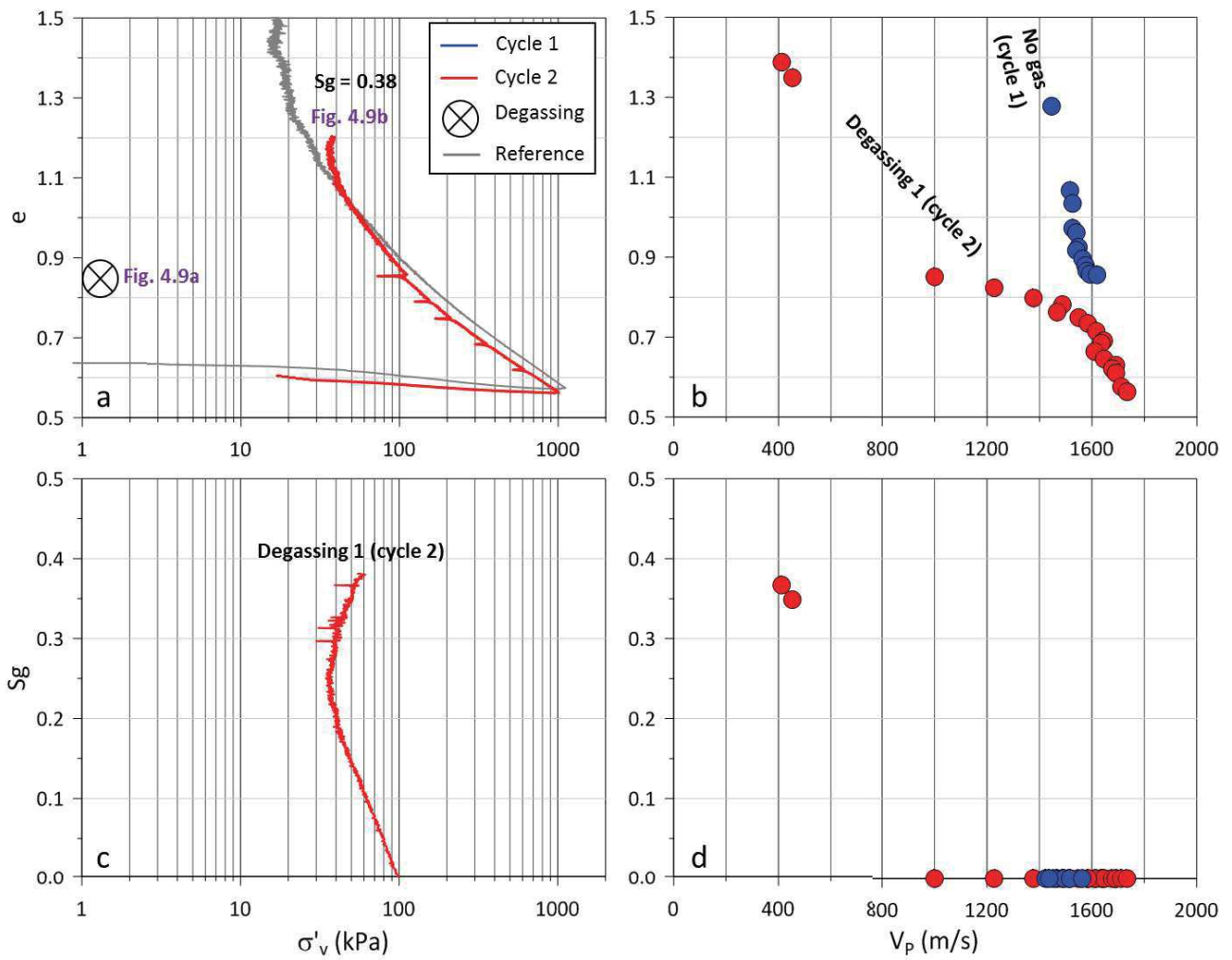


Figure 4.16: Results for test#5 with 2 load/unload cycles. Each color represents one load/unload cycle. a: void ratio (e) versus vertical effective stress (σ'_v) b: void ratio-versus P wave velocity (V_p); c: degree of gas saturation (S_g) versus σ'_v and d: S_g versus V_p . The grey line in (a) represents the reference consolidation test.

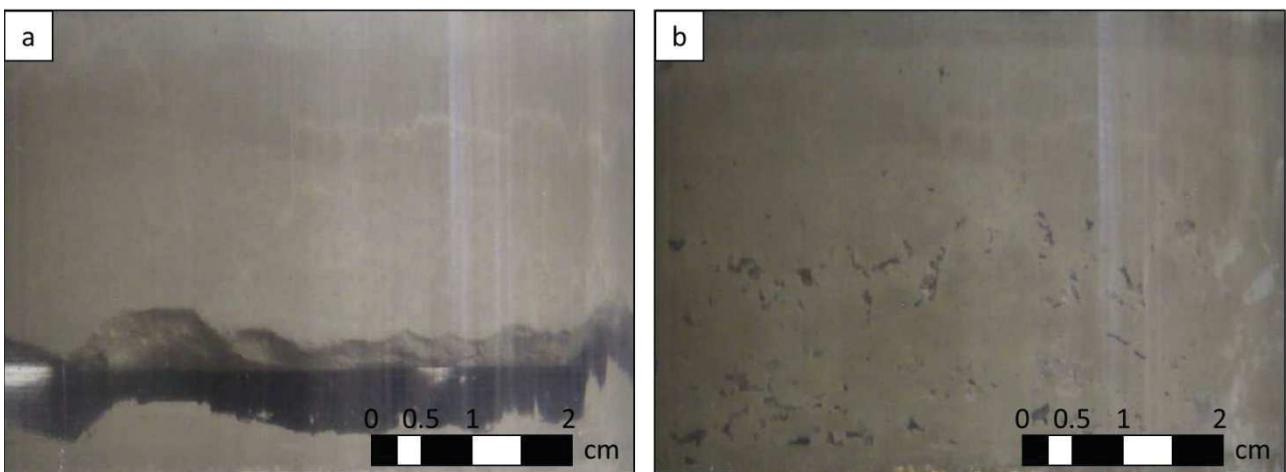



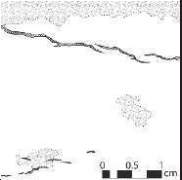
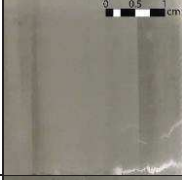
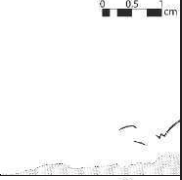

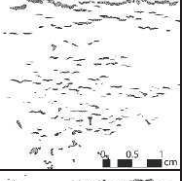

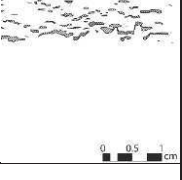

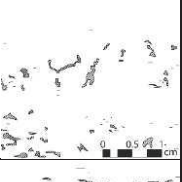

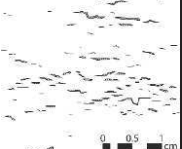
Figure 4.17: Pictures of the sample during test 5. a: before complete depressurization (Figure 4.16a) showing the sediment aspect before gas exsolution. b: after complete depressurization (Figure 4.16). The sample swelled by 9.5 mm under the effect of gas exsolution. Numerous fractures generated and sediments took a slurry aspect.

5. Synthesis of experimental results


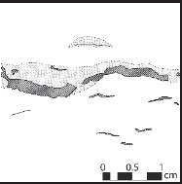


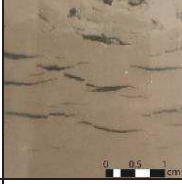
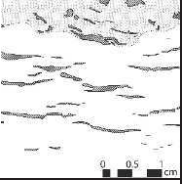



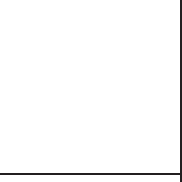

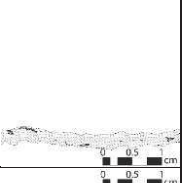


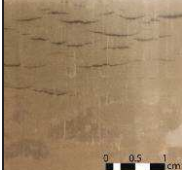
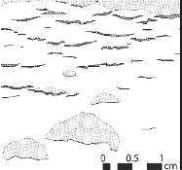
5.1. Fractures, sediment damage and remolding

On the eleven conducted tests, fifteen exsolution events triggered under different conditions (e.g. different σ'_{p0} , different initial gas saturation corresponding to different gas pressure u_g , and different decompression Δu) created diverse fracture distributions, with varying size, shapes and numbers. The observations made on each experiment along with pre-existing conditions are summarized in Table 4-3.

Table 4-3: Summary of observations related to fracture networks created during gas exsolution. Each fracture network was classified into three size categories (1: length > 1 cm; 2: 0.5 cm < length < 1 cm; 3: length < 0.5 cm) and three fracture number groups (1: more than 10 fractures; 2: less than 10 fractures; 3: no fractures). Vertical scale is equivalent to the horizontal one on the pictures and their corresponding interpretations.

Test	σ'_{p0} (kPa)	u_g (kPa)	Δu (kPa)	S_{gmax} (%)	fracture type	Photo	Interpretation	Fracture length	Fracture number
2	118	350	-350	10	cm-scale connected horizontal fractures. Not numerous. Mainly at the top of the sample.			1	2
2	970	350	-350	5	cm-scale and very thin rare fractures.			2	2
3	446	800	-800	32	mm-scale horizontal fractures. Numerous. Homogeneously distributed.			2	1
4	195	500	-500	17	mm-scale horizontal fractures. Numerous. Mainly on the top third of the sample.			2	1
5	65	800	-800	38	Numerous mm-scale horizontal fractures. Slurry aspect. Completely remolded sediment.			2	1
6	367	500	-500	23	Numerous mm-scale horizontal fractures. Homogeneously distributed.			2	1

End of Table 4-3 on next page

Test	σ'_{p0} (kPa)	u_g (kPa)	Δu (kPa)	S_{gmax} (%)	fracture type	Photo	Interpretation	Fracture length	Fracture number
7	398	800	-400	20	cm-scale horizontal fractures. Not numerous. Sample is cut into two parts.			1	2
8	405	800	-300	11	No visible fractures.			3	3
8	995	500	-500	36	Numerous cm-scale horizontal fractures.			1	1
9	408	800	-100	5	No visible fractures.			3	3
9	895	700	-250	17	No visible fractures.			3	3
11	398	800	-200	24	Few mm-scale fractures distributed along a pre-existing light color horizontal layer. Light area thickens during exsolution.			3	2
11	806	600	-200	18	Few mm-scale to cm-scale fractures, mm-thick in the bottom edge of the sample.			2	2
11	1071	400	-400	22	Numerous cm-scale fractures. Higher fracture number and thicker fractures on the top half of the sample.			1	1

An empirical classification of fractures was defined based on the sample visible surface after exsolution. Based on the observations in Table 4-3, fractures generated by gas exsolution are classified in three different length categories:

- 1- Fractures longer than 1 cm
- 2- Fractures between 1 cm and 0.5 cm long
- 3- Fractures shorter than 0.5 cm.

Conversely, number of visible fracture are arbitrarily classified as:

- 1- More than 10 visible fractures
- 2- Less than 10 fractures
- 3- No visible fractures.

This classification is empirical and the number of fractures is underestimated as only the sample surface is visible. Nevertheless, as the same classification was applied to all fracture networks, comparison between tests is considered as representative of the actual volume density.

5.2. Effect of gas exsolution on P-wave velocity

The effect of free gas on the acoustic properties of marine sediments has been already widely studied (Helgerud *et al.*, 1999; Rebata-Landa *et al.*, 2012; Sultan *et al.*, 2012). Helgerud *et al.* (1999), based on previous works by Dvorkin *et al.* (1999) on elasticity of marine sediments, proposed an effective medium model to predict P-wave and S-wave velocities in sediments containing free gas and/or gas hydrates based on mineralogy, compressibility and initial void ratio.

We used this model to draw a chart for predicted P-wave velocity variation with void ratio for different values of S_g (black lines in Figure 4.18a,b). The properties of sediments used in the modeling are summarized in Table 4-1 (mass% of minerals, C_c). The average number of contacts per grain in a bulk unit (called n in the Helgerud *et al.* (1999) model) was taken as equal to 4. The mineralogy was simplified into three poles (clays, quartz and carbonates) and is indicated in Table 4-1.

The P-wave velocities obtained from this study were plotted on the theoretical chart (Figure 4.18a,b). Two variables are considered in Figure 4.18: the degree of gas saturation (Figure 4.18a) and the maximum degree of gas saturation for each cycle (Figure 4.18b). Figure 4.18 also displays two examples of signals that are considered reliable for the V_p determination: one with a high degree of gas saturation, after gas exsolution (Figure 4.18c), the other on a water-saturated and undisturbed sample, before gas exsolution (Figure 4.18d).

The first observation is the good agreement between the curve corresponding to $S_g = 0\%$ on the chart and the P-wave velocity measurements obtained before exsolution (Figure 4.18a). Once exsolution occurs, P-wave velocities decrease drastically even for low values of S_{gmax} (red and blue crosses on Figure 4.18b). For the highest values of S_{gmax} , this decrease reaches 75% of the water-saturated value for a given void ratio. During the loading stage following exsolution, free gas is dissolved or expelled from the sample and S_g decreases. Accordingly, P-wave velocities increase once again (Figure 4.18a). Once S_g reaches zero, P-wave velocities remain below the reference values and follow a trend between the curve corresponding to $S_g = 0\%$ and $S_g = 2.5\%$ (Figure 4.18a).

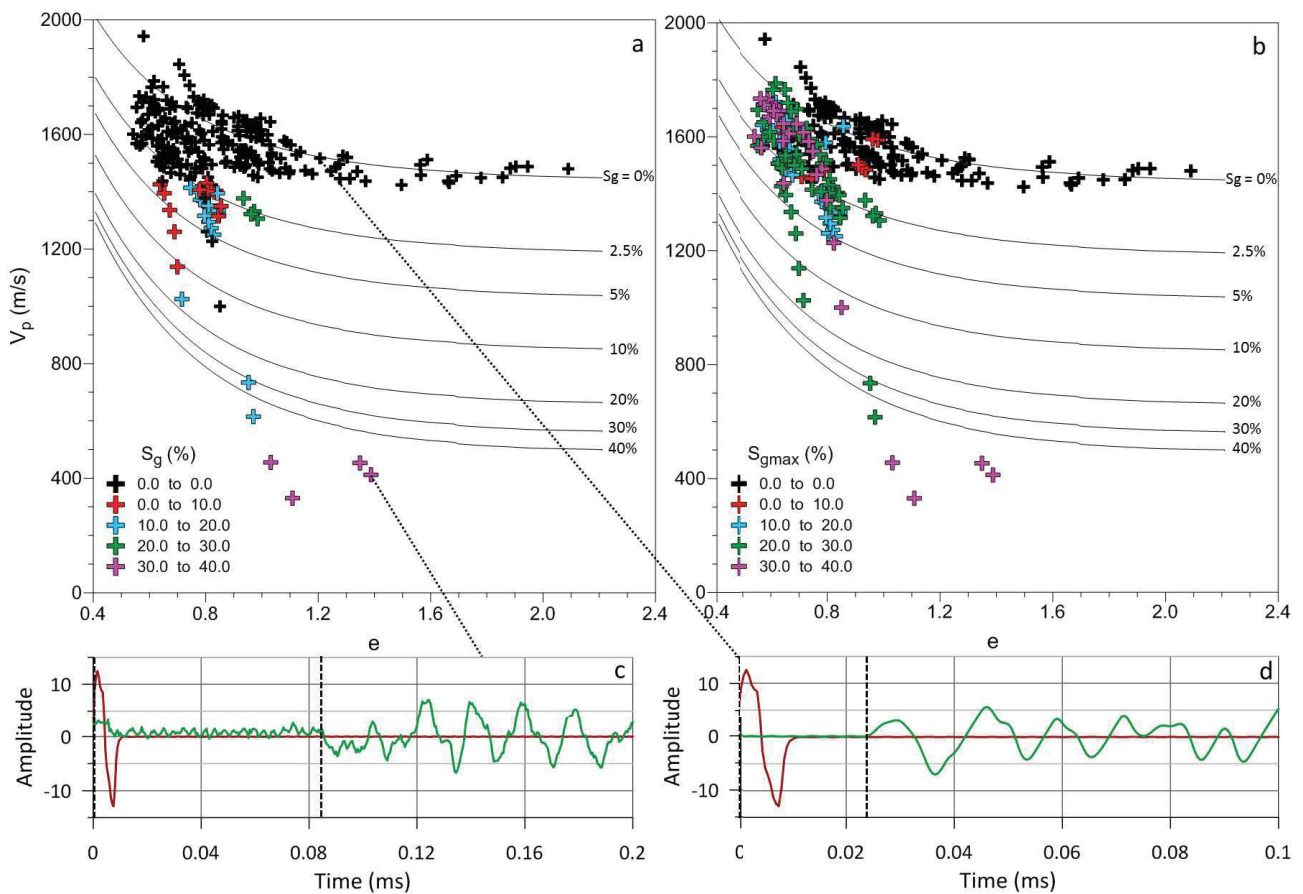


Figure 4.18: P-wave velocity (V_p) versus void ratio (e). Colors stand for (a) S_g (%) and (b) S_{gmax} (%). Black lines correspond to the evolution of V_p with e for different values of S_g based on the effective medium theory modeling (Helgerud et al., 1999). (c) is the typical signal after gas exsolution, (d) is the typical signal after gas exsolution. Red line correspond to the source signal, green line is the received signal.

5.3. Effect of degree of gas saturation on sediment compressibility

During the tests completed during this study, a clear difference in sediment compressibility was observed when comparing the state before and after gas exsolution. The compressibility after gas exsolution has a slope comprised between C_C and C_S called C_{Cgas} . When fractures were abundant and/or large enough, a first compressibility state was observed with slopes generally larger than C_C and called C_{Cfrac} .

For a comparative analysis, values of C_{Cgas} and C_{Cfrac} obtained from the different tests were plotted against the maximum degree of gas saturation determined during each loading/unloading cycle (S_{gmax}) and were then compared to C_C and C_S of water-saturated sediments (Figure 4.19). C_{Cgas} are all comprised between the C_C and the C_S of water-saturated sediments.

C_{Cfrac} values, except for two cases, are much larger than the C_C of water-saturated sediments. This compressibility slope, observed after fracture initiation, corresponds to fracture closing. C_{Cfrac} obtained from tests 7 and 11 are lower than C_C . Test 7 fracture network is unique as a large fracture split the sample in half (Table 4-3), and contact between the two halves occurred when the fracture closed. For test 11, the fracture network is one of the densest, with centimeter-scale fractures. Before reloading (cycle 4), a permeability

measurement under an imposed vertical hydraulic gradient partially closed the thinner fractures. This could be an explanation for the lower values of C_{Cfrac} obtained on both tests.

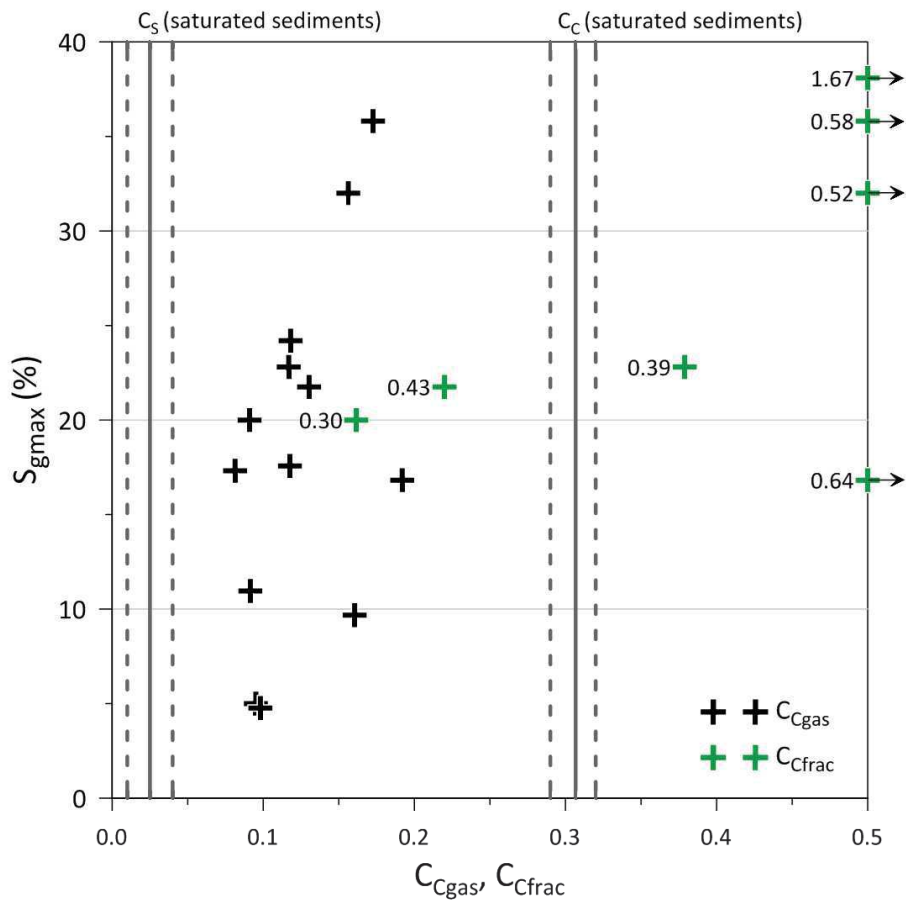


Figure 4.19: Compressibility versus S_{gmax} (%). Two type of compressibility are displayed. The grey vertical lines stand for the water-saturated sediments C_C and C_S , the dotted lines being the maximal and minimal values obtained during the different tests. Values of C_{Cfrac} are annotated as labels, since values above 0.5 were plotted at 0.5 to condense the graph.

5.4. Hydraulic conductivity versus degree of gas saturation

Hydraulic conductivity (K) data versus void ratio are shown in Figure 4.20a. K values obtained on the same sediment using the classical falling head method are plotted for comparison.

K measurements made before exsolution on water-saturated samples fit well with odometer measurements (Figure 4.20a). After gas exsolution, K increases above the water-saturated sample trend. Thereafter, K decreases rapidly during the beginning of reloading and reaches values below the trend of water-saturated samples. This decrease happened during a short time interval compared to the decrease of K during consolidation of the water-saturated sample. However, some of the K values acquired on water-saturated sediments seem to spread relatively to the trend curve in the same way. Nevertheless, Figure 4.20b clearly shows that K increases with the S_g .

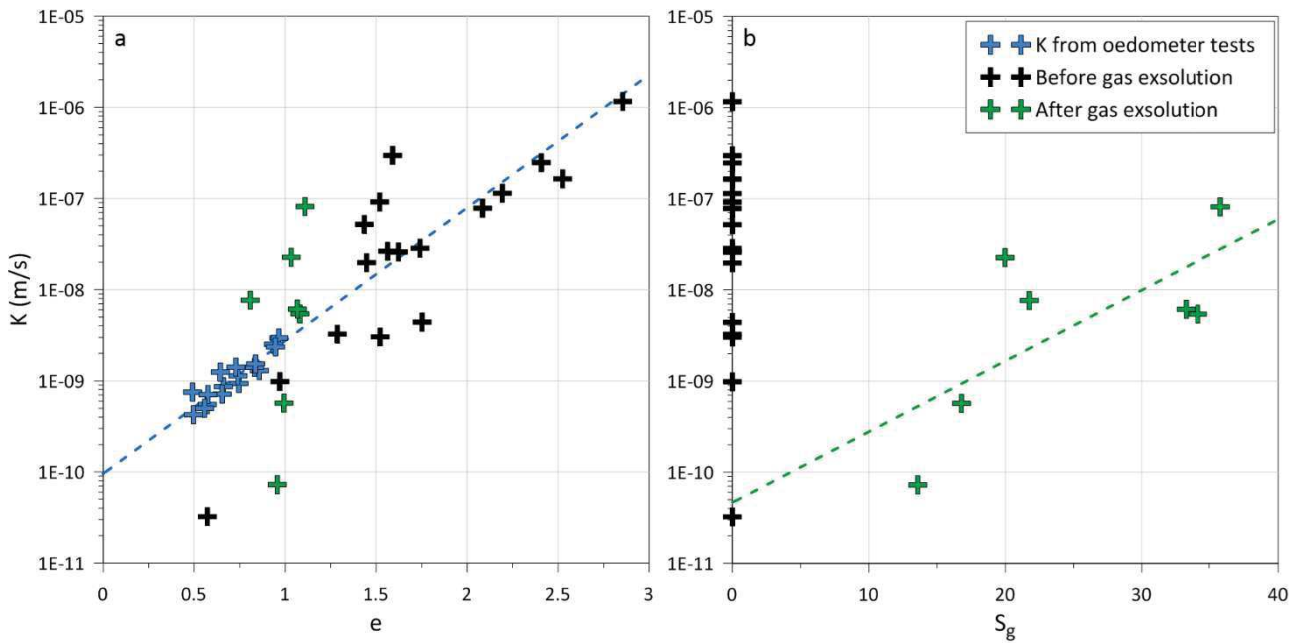


Figure 4.20: a: hydraulic conductivity, K (m/s) versus void ratio. The blue dashed line is an exponential fit for hydraulic conductivities on water-saturated sediments obtained from oedometers (blue crosses). b: K (m/s) versus S_g (%).

5.5. Preconsolidation pressure evolution with degree of gas saturation

In this paper, two preconsolidation pressures were determined. Before fracture closing, the intersection between the two slopes corresponding to C_{frac} and C_{Cgas} gives the σ'_{p1} . After fracture closing, σ'_{p2} was determined by the intersection of the swelling curve and the virgin compaction curve.

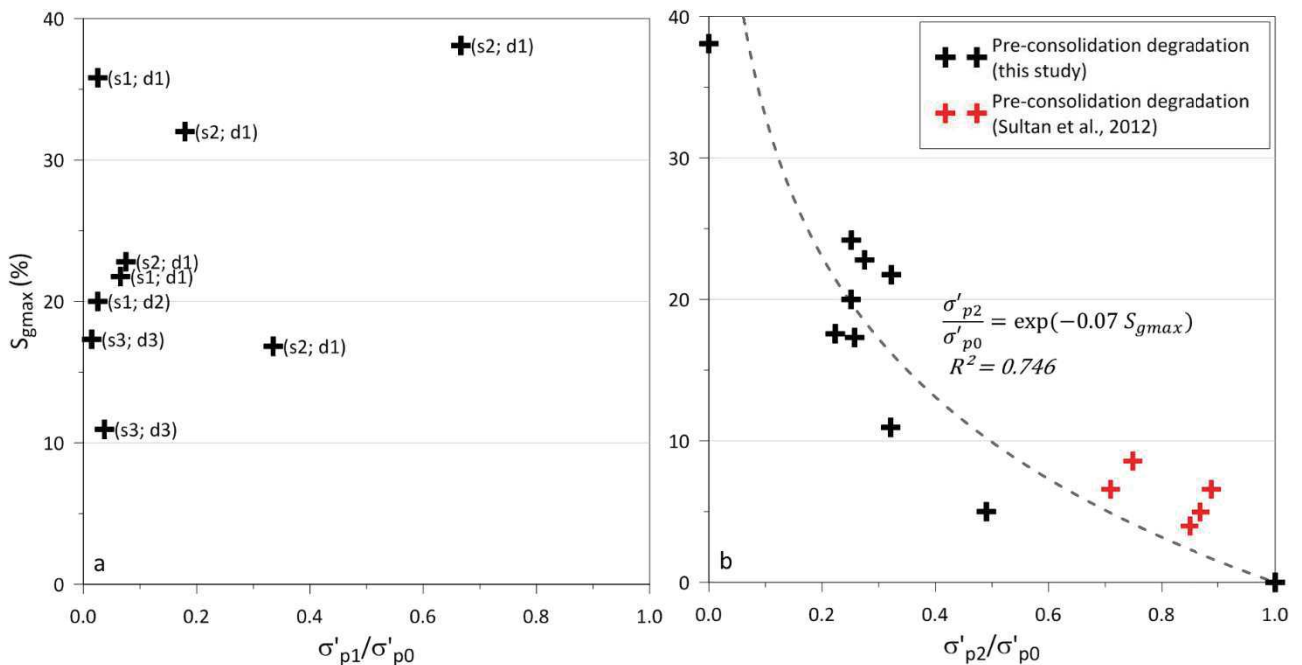


Figure 4.21: Preconsolidation ratio versus S_{gmax} (%). a: ratio between preconsolidation pressures calculated before fracture closing, σ'_{p1} , and the initial preconsolidation pressure, σ'_{p0} . The labels correspond to the fracture classification given in Table 4-3. “s” stands for the fracture length, “d” for the fracture number. b: ratio between preconsolidation pressures calculated after fracture closing, σ'_{p2} , and the initial preconsolidation pressure, σ'_{p0} . Values from Sultan et al. (2012) are also plotted as comparison (red crosses). An exponential fit of the study results shows a strong determination coefficient (R^2).

To compare the two parameters over the entire set of test results, we normalized them with respect to σ'_{p0} (Figure 4.21). The $\sigma'_{p1}/\sigma'_{p0}$ increases generally with increasing S_{gmax} but without a clear tendency (Figure 4.21a). Moreover, comparing these values to fractures in Table 4-3 shows that there is no clear relationship between fracture size and number and $\sigma'_{p1}/\sigma'_{p0}$.

Regarding the ratio between σ'_{p2} and σ'_{p0} , results show that it decreases with increasing S_{gmax} , evidencing a preconsolidation pressure degradation with S_{gmax} (Figure 4.21b). As a comparison, values from the study by Sultan *et al.* (2012) on gassy sediments from the Gulf of Guinea were also added to Figure 4.21b. The results show a clear logarithmic trend with a strong determination coefficient of 0.75 and starting with a ratio equal to 1 when S_g is zero. Values from the Gulf of Guinea are not exactly on the proposed trend. They were obtained on sediments having a completely different behavior in a water-saturated state, with a C_c as high as 2 (Colliat *et al.*, 2011).

6. Discussion

6.1. Fracture size and number: main controlling factors

The classification of fractures depending on their size and number was compared to the other parameters used or obtained during the testing program (e.g. σ'_{p0} , Δu or S_{gmax} ; Table 4-3). The aim is to identify the main parameters controlling fracture size and number.

First, the length of fractures formed during this study range from one mm to few cm. Their observable thicker part corresponds to the center of the crack. Boudreau (2012) shows that growth and rise of gas bubbles in sediments is possible through fracture generation and that bubbles will be disk-shaped (also demonstrated by Katsman (2015)). Shin and Santamarina (2011) as well as Jain and Juanes (2009) show that gas-driven fractures are favored in fine-grained sediments. Therefore, gas exsolution and subsequent bubble generation and growth explains the shape of fractures. The observed cracks are not pre-existing discontinuities.

It clearly appeared during our study that the S_{gmax} controls the fracture number. The larger the volume of free-gas generated, the bigger the number of fractures. However, some exceptions, like with test#11, show that this is not the unique controlling factor for fracture number. A secondary parameter, the magnitude of depressurization (Δu), seems to participate in controlling fracture number. The higher Δu , the more numerous the fractures. The two parameters are closely related as the S_g , corresponding to a volume of free gas generated during exsolution, is a direct consequence of the magnitude of depressurization.

From visual observations, three main fracture distributions can be discriminated (Table 4-3): dense and small fractures (tests 3, 4, 5 and 6), dense and large fractures (tests 8 and 11), and rare or inexistent fractures (tests 2, 8, 9, and 11).

The two denser distributions correspond to high S_{gmax} values (more than 20%) reached by complete depressurization. Test#4 is an exception. It presents a very dense fracture network but only at the top of the sample. The sample was clearly not entirely saturated with carbonated water hence explaining fracture distribution. Besides, S_{gmax} is calculated for the complete sample. Thus, applied to the fractured volume, S_{gmax} is much higher than calculated. Smaller S_{gmax} or partial depressurization lead to fracture networks with few or no fractures at all.

Preconsolidation pressure (σ'_{p0}) is the controlling factor of fracture size. Observation of the two groups with dense fracture networks (high S_{gmax}) shows that when σ'_{p0} is small (below 500 kPa) fractures are small. For higher σ'_{p0} (above 500 kPa), these fractures get longer and thicker. Various studies on bubble growth and shape in marine sediments yielded the same results. Boudreau *et al.*, (2005), Barry and Boudreau (2010) and Katsman, (2015) demonstrate that bubble shape and size is mainly controlled by the mechanical properties of sediments. In particular, Katsman (2015) concludes that bubbles generating in weak sediments are small with higher surface-to-volume ratio (thin bubbles) while bubbles forming in stronger sediments tend to be larger and more spherical (larger).

Therefore, the controlling factors for fracture network architectures are S_{gmax} and Δu both controlling the number of fractures while σ'_{p0} controls the size of the fractures.

6.2. Gas exsolution/expansion: a permanent P-wave velocity attenuation?

The presence of free gas has been always an issue when dealing with P-wave velocities (Sills *et al.*, 1991; Helgerud *et al.*, 1999; Sultan *et al.*, 2012). It provokes strong attenuation of the signal, ultimately preventing any signal propagation. Therefore, P-wave velocities are often used as a tool to detect free gas formation (Rebata-Landa *et al.*, 2012; Sultan *et al.*, 2012) as well as for estimating a degree of gas saturation (Lee & Collett, 2006; Morgan *et al.*, 2012). The acoustic response of gassy sediments is theoretically supposed to join the trend of saturated sediments whenever S_g becomes equal to zero.

The present study confirms this attenuating effect of free gas on P-wave velocities (Figure 4.18). The higher the S_g , the stronger the P-wave velocity attenuation. Besides, as free gas is dissolved and compressed during reloading, P-wave velocities increase once again. It shows the strong correlation between P-wave velocities and the S_g . Nevertheless, during reloading, when S_g reaches zero, P-wave velocities remain attenuated compared to the normal trend for water-saturated sediments (Figure 4.18a). Therefore, the damage generated by gas exsolution seems to delay the normal acoustic response of the sample.

The presence of fractures is a known factor for attenuating P-wave velocities in the perpendicular direction, independently of its filling material (Anderson *et al.*, 1974; Kahraman, 2002; Leucci & Giorgi, 2006; Popp & Salzer, 2007). Fracture generation may have triggered local changes in the shear modulus and/or the

bulk modulus of the sediment (Huang *et al.*, 1995). Therefore, even after mechanical reloading and water saturation, long-term impact of fractures on the acoustic response is expected.

Moreover, Helgerud's model, predicting P-wave velocities for given S_g 's (Helgerud *et al.*, 1999), does not fit with most of the P-wave velocities recorded after gas exsolution (Figure 4.18a). P-wave velocities are greatly overestimated (up to 300 m/s) for samples where dense fracture networks appeared during gas exsolution (Table 4-3) and they are underestimated (less than 100 m/s) for samples presenting rare or no fractures after gas exsolution (Table 4-3). P-wave velocities measured on samples with a higher degree of gas saturation present a signal that can be misleading. This may lead to errors in measurement that partly explain the differences observed with the model (≈ 100 m/s). Considering the potential errors in measuring P-wave velocities for gassy samples, the Helgerud model is in adequacy with the measurements made on samples without or with rare fractures. The impact of fractures and discontinuities in the sample over P-wave velocities is responsible for the rest of the discrepancy, as modeled values are calculated for a homogeneous medium.

Thus, sediment damage caused by gas exsolution (through fractures, or with no visible markers), seems to have a durable impact on acoustic properties of sediments.

6.3. Gas exsolution/expansion effects on sediment compressibility

Sultan *et al.* (2012) have clearly identified the impact of gas exsolution on the compressibility of clayey sediments. Experimental data of Sultan *et al.* (2012) showed that after gas exsolution, the compressibility of the sediments decreased significantly and is between the swelling index and the compression index of the initial intact sediments. This compressibility degradation was interpreted as being the result of sediment damaging during free gas generation. Previous experiments also highlighted a decay of compressibility with the presence of gas bubbles in soft marine clays (Sills *et al.*, 1991; Nava Castro *et al.*, 2013; Liu *et al.*, 2016). They concluded that gas bubbles bear part of the load applied on the sample and that soil compressibility measured on gassy sediment is primarily due to bubble compression and secondarily due to normal sediment compression, implying water expulsion. The presence of free gas in sediments was also proved to be responsible for a delay in consolidation. As gas escapes or dissolves, consolidation happens faster (Sills *et al.*, 1991; Nava Castro *et al.*, 2013).

This study showed that gas exsolution creates two intermediate compressibilities after fracture generation (C_{frac} and C_{Cgas}) and only one when no fractures appeared (C_{Cgas}) (Figure 4.12a, Figure 4.14a and Figure 4.16a). The formation of fractures strongly impacted the compressibility of sediments. C_{frac} were only measured for dense fracture networks and were generally higher than C_c (Figure 4.19). Conversely, fracture number affected the compressibility after fracture closure (C_{Cgas}). For equivalent S_{gmax} , higher C_{Cgas} were recorded for higher number of fractures (Table 4-3 and Figure 4.19). C_{Cgas} was always comprised between C_c and C_s (Figure 4.19).

Nevertheless, C_{Cgas} were also measured when no fractures were generated in the sediments. This shows that if fractures have an impact on the compressibility of sediments, the main controlling factor is the presence of gas. Indeed, this study shows that when S_{gmax} increases, C_{Cgas} increases (Figure 4.19). For low S_{gmax} , C_{Cgas} is closer to the swelling index of water-saturated sediments. This correlation was also noted by Hight and Leroueil (2003) during loading of a sample with occluded gas bubbles. Therefore, gas exsolution tends to destroy the elastic behavior of sediments.

Test#5 displayed an extreme behavior with a slurry aspect after gas exsolution and a C_{Cgas} higher than C_c . The virgin compaction curve was reached very fast compared to other tests (Figure 4.16a) showing that, after gas exsolution in test#5, the sediments behaved as the initial remolded sediment.

Moreover, compressibility recovers a normal trend once σ'_{p0} is reached, long after S_g reached zero. Hight and Leroueil (2003) demonstrated that once gas bubbles collapsed during reloading of a sample containing occluded gas bubbles, it recovers its normal C_c . The difference in this study is that free gas is concentrated along fracture planes and is not in the form of occluded gas bubbles. Therefore, as for P-wave velocity attenuation, the delay in compressibility recovery may be due to a permanent impact of fractures and damage caused by gas exsolution.

6.4. Gas exsolution/expansion effects on sediment permeability

Permeability of sediments can be affected by several mechanisms. Normal consolidation of sediments provokes a decrease in hydraulic conductivity (Olsen, 1960; Chu *et al.*, 2002). The presence of fractures may enhance this permeability depending on the fracture orientation relative to hydraulic gradient (Alfaro & Wong, 2001). Besides, free gas in fine-grained sediments were proved to be a factor for permeability reduction (Egermann & Vizika, 2000; Naylor *et al.*, 2000; Hight & Leroueil, 2003; Jang & Santamarina, 2014). If free gas accumulates in clayey layers, a capillary seal may form (a gas cap), generating an effective permeability even lower than the intrinsic permeability of the clayey layer (Revil *et al.*, 1998; Cathles, 2001).

Gas exsolution triggered the formation of horizontal millimeter to centimeter-scale fractures. Their orientation corresponds to a direction orthogonal to the possible fluid expulsion, which is not favorable to an increase in permeability. However, as observation of the fracture network was only possible at the sample surface, it is possible that fluid pathways created through connections between fractures, thus explaining the observed increase in permeability right after gas exsolution (Figure 4.20). These fractures were filled with free gas after gas exsolution, which may rather be a parameter in favor of a decrease in permeability. However, we do observe an increase in sample permeability just after fracture creation showing that gas filling the fractures may be in a continuous phase through an interconnected fracture network (Jang & Santamarina, 2014).

During reloading, the rapid decrease in permeability (Figure 4.20) is probably related to the closing of fractures, and the consequent reduction of fluid pathways. Consequently to fracture closing, trapping of free gas in reduced areas changes free-gas distribution from a continuous phase to a more discrete distribution, a factor that was proved by Jang and Santamarina (2014) to reduce sample permeability. The creation of potential capillary seals along the former fracture planes could explain the hydraulic conductivity values that are below the normal trend (Cathles, 2001).

Therefore, gas exsolution provokes an increase in permeability through fracture creation, creating preferential pathways. Then, reloading quickly reduces permeability due to fracture closure and capillary sealing as a consequence of free gas being captured in a discrete distribution.

6.5. Gas exsolution/expansion effects on preconsolidation pressure and the consequence in terms of shear strength

Besides the fracture formation that has already been discussed, gas exsolution has an impact on the preconsolidation pressure of sediments, showing the degree of sediment damage caused.

Before fracture closing, the degradation of sediment preconsolidation pressure is significant but seems to decrease with S_{gmax} (Figure 4.21a). However, no clear trend appears. Except for one value, corresponding to test#5, all the ratios are below 0.35. It tends to indicate that at 35% of the σ'_{p0} fractures are closed as σ'_{p1} indicates a degradation connected to fracture closing. The sample of test#5 was completely fractured during gas exsolution explaining the high value for the $\sigma'_{p1}/\sigma'_{p0}$ ratio: fractures took more time to close.

σ'_{p2} was measured after fracture closing, therefore it evaluates the part of sediment damage that is visually imperceptible. The ratio between σ'_{p2} and σ'_{p0} correlates with S_{gmax} through a logarithmic law (Figure 4.21b): the bigger S_{gmax} , the more the sediment was remolded, recording a decrease in preconsolidation pressure. This type of relation was already noted on sediments from the Gulf of Guinea (Sultan *et al.*, 2012) but at lower S_{gmax} (below 10%). Besides, several other studies demonstrated this decrease in preconsolidation pressure with an increasing degree of gas saturation (Lunne *et al.*, 2001; Hight *et al.*, 2002). For Hight and Leroueil (2003), it is mainly the result of damage due to bubble-growth in the sediments, the degree of damage being related to the initial level of structure. The initial level of structure may be the explanation for the differences observed between the measurements made during this study and the results obtained by Sultan *et al.* (2012) on a different sediment.

This study showed, for different sediments and at a higher S_{gmax} that a complete loss of preconsolidation pressure is feasible. For 38% of S_{gmax} , preconsolidation pressure was completely lost, showing that sediments were entirely remolded by gas exsolution. The corresponding sample (test#5) had a slurry aspect right after gas exsolution and displays extreme behavior in terms of compressibility and sediment damage.

Therefore, the experimental results confirm that gas exsolution causes sediment damage and remolding. For strong gas exsolution, leading to high S_{gmax} , sediments can even reach a state where they entirely lose their preconsolidation pressure.

Wheeler (1988) showed that methane bubbles might decrease or increase the undrained shear strength of reconstituted silty-clay samples. This was shown to depend on the level of total and effective stress. In the Wheeler (1988) experiments, gas bubbles were formed artificially by using the zeolite molecular sieve technique. Gas naturally formed in sediments or was generated by circulation of carbonated water. Subsequent decompression was shown to negatively affect the undrained shear strength. Lunne *et al.* (2001), Hight, Hamza and El Sayed (2002) and Sultan *et al.* (2012) all point out that the degree of gas saturation significantly reduces preconsolidation pressure and shear strength.

Sultan and Garziglia (2014) proposed a constitutive model to simulate the mechanical behavior of gassy sediments where preconsolidation pressure is the main parameter controlling yield surface and therefore shear strength of the sediment. By introducing to a conventional Cam Clay type model the “preconsolidation pressure - degree of gas saturation” logarithmic relationship equivalent to the one shown in Figure 4.21b, they were able to reproduce the observed data published by Lunne *et al.* (2001), Hight, Hamza and El Sayed (2002) and Sultan *et al.* (2012). Data shown in Figure 4.21b highlight the important consequence of gas formation on the shear strength of the sediment from the AMV where the damage due to bubble growth may strongly decrease its shear strength. A S_{gmax} of 38 % seems to be the upper limit for complete destruction of the structure and therefore the shear strength of AMV sediments and favoring mud formation.

7. Conclusions

This chapter investigates the impact of gas exsolution on the mechanical behavior of mud samples recovered on mudflows expelled from the Absheron Mud Volcano. The goal was to understand the factors that control sediment damaging and to quantify and determine the criteria by which we may determine that sediments are completely remolded, and considered as changed into mud. Eleven consolidation tests using a novel experimental apparatus allowed to generate free gas under different consolidation conditions. Results show that:

- 1- The number of fracture generated through exsolution is controlled by the degree of gas saturation while preconsolidation pressure mainly controls their length.
- 2- Gas exsolution provokes sediment damage (through fracture emplacement and loss of preconsolidation pressure) and it increases with the degree of gas saturation while the elastic modulus of sediments is partly lost. Shear strength is also expected to decrease as a consequence of sediment damage.

- 3- Acoustic response remains degraded long after free gas has entirely disappeared from the sample. Compressibility is also durably modified, reaching normal trends only when initial preconsolidation is exceeded. Permeability first increases through fracture creation, but quickly deteriorates due to the presence of gas leading to capillary sealing during reloading. Therefore, sediments do not recover entirely from gas exsolution damage during reloading.
- 4- During testing, critical behavior was observed for a degree of gas saturation of 38%. Gas exsolution triggered complete remolding of sediments (entire loss of preconsolidation pressure and therefore its shear strength) that took a slurry aspect. The same test displayed the highest compressibility at the beginning of reloading. Its compressibility trend was close to the initial compaction behavior while sediments had not yet compacted. Therefore, gas exsolution alone was able to generate mud from compacted sediments.

Our experimental results show that gassy sediments with a discontinuous gas phase may take place for S_g greater than 15 %. We show that such an experimental study can help determine the criteria for mud formation under laboratory conditions and on a particular sediment sample: mud expelled from the Absheron Mud Volcano. These criteria can be implemented into numerical models, integrating mechanical behavior under the geological conditions observed and determined in the field. Ultimately, this experimental study offers a unique opportunity to quantify the volume of gas required to generate the volume of mud at depth that was extruded to form the observed Absheron Mud Volcano.

Chapter 5: From stratified sediments to fluid mud generation

Abstract

The Absheron Mud Volcano area in the South Caspian Basin offers a unique multidisciplinary dataset that led to develop a conceptual formation model. This model mainly relies on hydrofracturing of overpressured strata saturated with dissolved gas, leading to gas exsolution in under-compacted and evaporite-rich layers, generating overpressured mud driven to the seafloor through density inversion and gas expansion. Through laboratory testing, gas exsolution in compacted marine sediments leads to significant sediment damage (loss of preconsolidation pressure and decrease of shear strength), eventually forming completely reworked material like the mud expelled at the volcanoes. The integration of geological observations, in situ physical parameters, sediment properties and empirical behavior of sediments with gas exsolution into 2D diffusion models allowed to simulate the geological and physical conditions required to generate mud at depth at the Absheron location. The integration of the Anhydritic Surakhany Formation acting as a regional seal and of faults with sealing capacities are important parameters in order to trigger hydrofracturing. Moreover, the mud remobilization towards the surface was also modeled through modified Navier-Stokes equations considering gas expansion impact on mud density. From simulations it transpires that mud would be extruded after 100 years when considering only density inversion.

Chapitre 5 : Génération de boue fluide à partir de sédiments stratifiés

Résumé

La zone du volcan de boue d'Absheron, dans le Bassin sud caspien, offre un jeu de données multidisciplinaire unique ayant déjà permis d'en proposer un modèle de mise en place. Dans ce modèle, l'hydrofracturation de strates en forte surpression et saturées en gaz dissous déclenche l'exsolution du gaz contenu dans des couches sous-compactées et riches en évaporites, ce qui génère de la boue en surpression qui remonte jusqu'au fond marin par inversion de densité et expansion des bulles de gaz. Par ailleurs, des essais en laboratoire ont démontré que l'exsolution du gaz dans des sédiments marins compactés provoque un endommagement considérable de ces sédiments (perte de leur pression de préconsolidation et diminution de la résistance au cisaillement) menant potentiellement à un matériel complètement remanié comme la boue des volcans. L'intégration des observations géologiques, des propriétés physiques in situ, des propriétés des sédiments et des lois de comportement empiriques des sédiments après exsolution du gaz dans un modèle régional de diffusion 2D a permis de définir les conditions nécessaires pour la génération de boue en profondeur dans la zone d'Absheron. L'intégration de la Formation du Surakhany Anhydritique agissant comme une couverture régionale ainsi que la prise en compte de failles jouant le rôle de barrières de perméabilité horizontale sont des paramètres nécessaires afin de déclencher l'hydrofracturation. La remontée de la boue vers la surface a également été modélisée par le biais d'équations de Navier-Stokes modifiées afin de prendre en compte l'effet de l'expansion du gaz sur la densité. Ces simulations montrent qu'en ne considérant que l'inversion de densité, la boue prendrait une centaine d'années pour atteindre la surface.

1. Introduction

While extensive work has been focused for decades on mud volcano (MV) architecture and on gassy sediments, few studies have numerically explored MV formation and evolution. Several authors have attempted to reproduce visible structures and the morphological evolution of MVs through analogue models (Woolsey *et al.*, 1975; Nermoen *et al.*, 2010; Mourgues *et al.*, 2012; Dupuis, 2017; Odonne *et al.*, in press). The results provide understanding of the evolution of surface structures and morphology as well as exploring possible subsurface mechanisms able to reproduce surface and subsurface features as observed in the field. However, most of these models used non-cohesive materials to simulate fine-grained cohesive sediments (Woolsey *et al.*, 1975; Nermoen *et al.*, 2010; Dupuis, 2017) following the theory on scaled models (Hubbert, 1937) and therefore, the processes used to remobilize material in the models may be different from those applying to natural MVs. Other authors developed numerical models to explain remobilization and the subsurface mechanism for mud transport (Brown, 1990; Gisler, 2009; Zoporowski & Miller, 2009; Collignon *et al.*, 2018a). These models are based on physical, chemical and mechanical laws applied to natural conditions, therefore approaching processes more accurately. However, these numerical models only assess the fluid mud flow or the mechanical evolution of mud during its ascent. Deville *et al.* (2010) computed regional fluid flow models in the Barbados prism and showed that MVs are located above overpressured zones. Therefore, modeling of mud volcanoes focused on reproducing the observed structures or the mud flow dynamics, while other studies looked into the regional background to explain MV location. None of the models integrated both the regional and local processes into a unique model. Moreover, the impact of gas exsolution and expansion on the behavior of the mud flow is often ignored or simplified.

The AMV has been densely surveyed for hydrocarbon exploration purposes and for geohazard assessment (Contet & Unterseh, 2015; Gautherot *et al.*, 2015; Unterseh & Contet, 2015; Dupuis, 2017) giving a dense and high-quality multidisciplinary dataset. The SCB is also densely studied, and several subsidence, thermal and fluid-flow models provide understanding of regional scale phenomena. Overall, existing data present a unique opportunity to model and simulate the formation of a mud volcano within its geological background. Preliminary modeling work was conducted in order to explain the location of the AMV at the crest of the Absheron anticline, coupling sedimentation-related overpressure generation and 2D-diffusion equations for fluid flow and methane accumulation (Chapter 3:4.4; Blouin *et al.*, 2019). It showed that the AMV was formed at the location where critical overpressure (near-fracture conditions) affected methane-saturated areas. However, hydrofracturing conditions were not reached solely through sedimentation and with the geological structure modeled in Chapter 3:4.4.

The present chapter assesses the following main two questions:

- Is it possible to simulate mud generation conditions at depth by considering mechanical properties of sediments, sedimentation rates, structural elements and the impact of gas exsolution?
- Is the sole impact of gas expansion on the mud properties able to drive mud up to the seafloor?

Hereafter, we present the improvements brought to the 2D-diffusion model by considering a low-permeability interval corresponding to the Anhydritic Surakhany Formation and by integrating fracture generation conditions, gas exsolution and sediment damage (Chapter 4:5.5); these make it possible to propose a possible geological and physical setting and a chain of processes leading to mud generation. Modified Navier-Stokes equations accounting for gas bubble expansion and changes in mud properties (density and pressure) were used in order to simulate mud ascension through the sedimentary strata.

2. Material and methods

2.1. Mud generation

The method used to characterize sediment properties (including compressibility and hydraulic conductivities) of the modelled stratigraphic layers was already discussed in Chapter 2:3.2.4. The software used to calculate the sedimentation-related overpressure (SeCoV3 Ifremer in-house software) was described in Chapter 2:3.4.1 and Chapter 3:3.4.1 and no further developments were done in the following modeling work.

The geometrical model, based on work by Green *et al.* (2009), was slightly modified (Figure 5.1) to take into account the Anhydritic Surakhany Formation (ASF, see Chapter 2:1.1.2 and Chapter 3:4.3). The fault network geometry is based on seismic interpretation (Chapter 3:4.1). In order to decrease the calculation time, the resolution was reduced by considering a vertical increment equal to 192 m with a total of 50 vertical nodes, and a horizontal increment equal to 244 m with a total of 225 horizontal nodes (Figure 5.1).

The 2D-diffusion software was modified in order to consider two additional phenomena: hydrofracturing and gas compressibility and exsolution (Boyle's and Henry's laws). In a context where the maximum principal stress is vertical ($\sigma_1 = \sigma_v$), hydrofracturing is vertical and occurs when and where the fluid pressure is exceeding the sum of the tensile strength of the host sediment and the minimum horizontal stress (σ_3). For the purpose of modeling, a realistic approximation is to consider that hydrofracturing occurs for a given ratio between overpressure and vertical effective stress ($\Delta u / \sigma'_v$), generally obtained from pressure logs (see Figure 1.10, Chapter 1:2.5.1 for details). When the ratio $\Delta u / \sigma'_v$ reaches the critical condition, hydrofractures are generated in the concerned area. As a working hypothesis, the hydrofractured area permeability is calculated from the hydraulic conductivity laws (Eq. (4)) using a void ratio of 1. The methane diffusivity (D_c) of hydrofractured area is considered as being the same as faults. Fracture may trigger a

decrease in overpressure in the fractured zone leading to a decrease in the saturation concentration and consequently to gas exsolution. Hence, a degree of gas saturation (S_g) after exsolution is calculated in the fractured area. This calculation is made following the gas compressibility (Boyle's law) and the dissolution/exsolution capacity of methane (Henry's law), both being pressure and temperature dependent. Therefore, temperature distribution was calculated through the modeled sedimentary column. We estimated a thermal gradient from temperature measurements in the two exploration wells (16°C/km, see Chapter 3:4.3) and seafloor temperature from Diaconescu et al., (2001) at 5.85°C. The degree of gas saturation is subsequently used to calculate the impact of gas exsolution on sediment damage through preconsolidation pressure decrease (equation in Figure 4.21, Chapter 4:5.5).

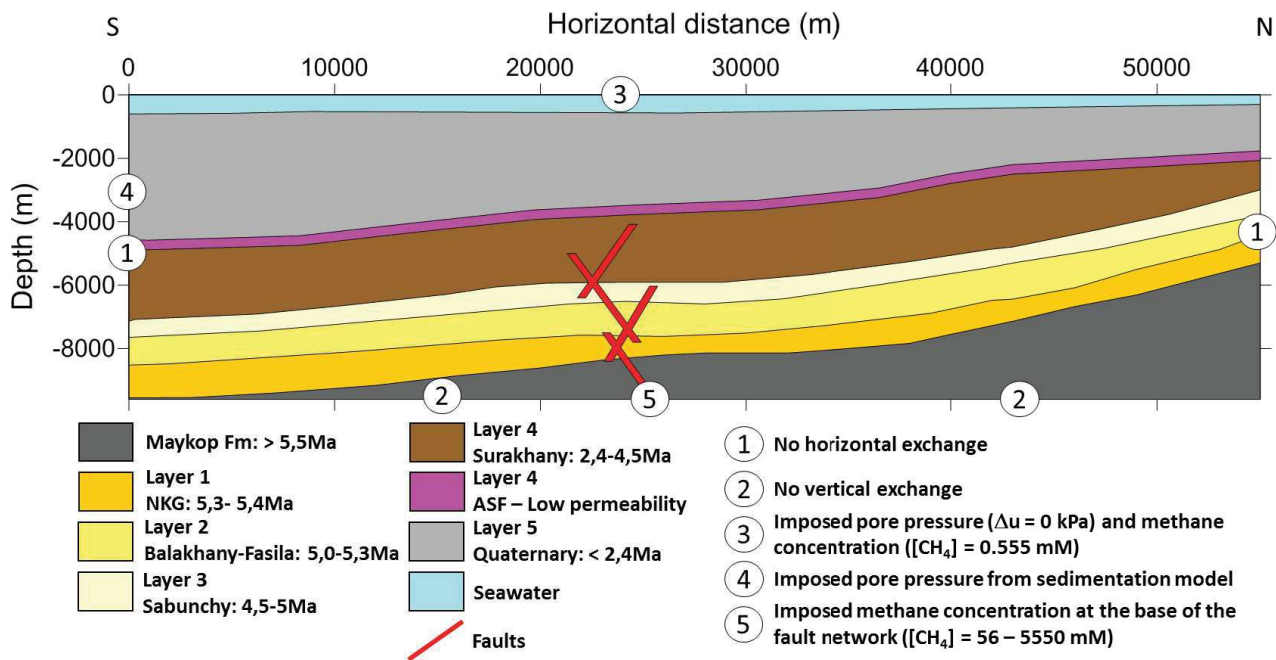


Figure 5.1: Updated geometry taking into account the ASF as a 300 meter thick incompressible and low-permeability layer (purple). The limit conditions are similar to the model presented in Chapter 3:4.4.2. However, condition 5 controlling the methane concentration injected at the base of the fault network is now considered as variable.

Methane and pore-pressure diffusion calculations may be initiated at different periods accounting for the HC production from mature rocks since the beginning of Pliocene times, at the very beginning of the modeled sedimentation process. Boundary conditions are the same as those described and used in Chapter 3:4.4.2 except for condition 5: the methane concentration imposed at the base of the fault network was considered between 56 and 5550 mM (Figure 5.1). Several tests were made on the hydraulic diffusivity (D_h) of the fault network, considering faults as either transmissive or sealing for lateral fluid flow based on regional studies and previous models (Bredehoeft *et al.*, 1988; Gordon & Flemings, 1998; Battani *et al.*, 2010; Gautherot *et al.*, 2015; Javanshir *et al.*, 2015; Wibberley *et al.*, 2017).

2.2. Mud ascent

The modeling of mud generation is complemented by the modeling of the ascent of the fluid mud. The purpose of this model is to determine whether the mud mass is able to rise up to the seafloor through gas expansion processes only.

To model the ascent of low-density mud, we combined two approaches: one solving the problem in two dimensions at low viscosities (Tryggvason, 2012) and one for extrapolating the results to realistic higher viscosities using one-dimensional calculations (Furbish, 1997). The 2D calculations were completed using the Datarmor Ifremer supercomputer (PCDM, 2018) allowing to reduce significantly the time of calculation by parallel processing. Simulations that would need a week on a PC, are completed on less than 24 hours using Datarmor supercomputer.

The 2D approach models the mud as a one-phase fluid flow using simplified Navier-Stokes equations (Eq. (11) and Eq. (12), see Chapter 2:3.4.4), taking into account gas compressibility through Boyles's law. Methane modifies the mass-density of the mud following Eq. (13) (Chapter 2:3.4.4) leading to mass-density inversion between the mud generation zone and the host rock (Brown, 1990; Kopf, 2002; Deville, 2009; Collignon *et al.*, 2018a). Mud and host rocks are modelled as having the same viscosity, constant over time and that does not vary with the presence of free gas. The methods of resolution using discretization of the different terms of the simplified Navier-Stokes equations was adapted from Tryggvason *et al.* (2011). The Navier-Stokes (NS) software used in this chapter is based on code1 of Tryggvason (2012).

Two modified versions of code1 were tested. The modifications were made at the Ifremer, for the purpose of the study. The first version (code1 v1) applies directly the numerical resolution method of Tryggvason (2012) by considering the gas exsolution and expansion phenomenon and by including the impact of free gas in the computation on the mass-density evolution. The second version (code1 v2) considers an initial mud overpressure due to the presence of free gas which varies with the gas expansion during mud ascent.

The 2D simulation of mud ascent was completed over structural models with 100 nodes per 100 nodes representing an area of 10 km in length and 4 km in depth corresponding to the approximate length of the Absheron anticline in a SSW-NNE direction and to the depth below sea level of the mud generation zone. The water column is considered and serves as an upper boundary limit where no exchange with the mud and sediment zones is allowed. Therefore, the extrusion of mud and its behavior after reaching the surface is not considered in the present work as it implies complex chemical and physical interactions between sea water and formation water (Kopf, 2002; Etiope *et al.*, 2009). The two lateral boundaries are considered as no exchange boundaries. The sediment column presents a mass-density ranging from 2100 kg/m³ for the deepest sediments to 1900 kg/m³ for the shallowest sediments. These values are calculated from porosities at wells, derived from sonic data (see Chapter 2:3.3) and using a grain solid mass-density of 2650 kg/m³. An

initial mud body is considered at the initial state as a convex-up half-disk corresponding to the volume of damaged sediments calculated from the regional diffusion simulation and having the same mass-density as unconsolidated marine sediments (1900 kg/m³). In code1 v2, this initial volume of mud has also an initial overpressure which was obtained from diffusion simulations.

The mud generation process implies the formation of hydrofractures. This hydrofractures should propagate vertically in the context of the extrados of the Absheron anticline where normal faulting was observed. Therefore, vertical conduits having the same mass-density as the mud source can be introduced in the initial geometry in order to simulate the potential presence of vertical fractures.

Viscosities measured for surface marine sediments highly depends on the type of sediments, but are clearly below 10⁵ kPa.s (Locat & Demers, 2008; Torrance, 2010; Jeong, 2013). However, this range of values is not representative of highly consolidated and stratified sediments, whose typical values of viscosity exceed 10¹⁴ kPa.s, value corresponding to evaporitic sediments (Mukherjee *et al.*, 2010; Collignon *et al.*, 2018b). With the depth range and type of host sediment encountered here, taking realistic values leads to exceedingly long computation times. The Lusi catastrophe provided the first direct monitoring of a mud volcano initiation (Mazzini *et al.*, 2012; Tingay *et al.*, 2015, 2017). Tingay *et al.* (2017) proved using the BJP-1 well data and reports that the mud generation and its ascent from a depth of 1000 m happened within two days. Following these observations (Tingay *et al.*, 2017), the simulations were limited to the first 24 hours after the mud generation, leading to calculations time on the supercomputer Datarmor of more than 30 days for a viscosity of 10⁷ kPa.s. This directly arises from the resolution method: the time increment depends on the mesh resolution and on the viscosity. For instance, for a viscosity of 10⁷ kPa.s and for the used mesh of 100 nodes per 100 nodes (mesh resolution of 100 m horizontally and 39 m vertically), a time increment dt of 10⁻⁵ s was needed in order to reach numerical convergence. This implies 1.7 x 10⁹ calculations to simulate the 24 hours of mud ascent. We therefore ran models based on Tryggvason (2012) over three orders of magnitudes for viscosity (10⁵, 10⁶ and 10⁷ kPa.s) and observed that the main change was with the timing, other parameters of interest being insensitive to viscosity changes.

The extrapolation to more realistic viscosity values was completed by a simple 1D calculation following a simple example of Furbish (1997) modeling a buoyant magma flow within a vertical dyke. It was possible to calculate the velocity of the ascending mud using the equation:

$$v(x) = \frac{1}{2\mu} (\rho_c - \rho) g (r^2 - x^2) \quad (17)$$

with v the velocity of the ascending mud (m/s), μ the viscosity of the mud (kPa.s), ρ and ρ_c the mass-densities of the mud and of the surrounding rock (reference) respectively (kg/m³), g the gravity (m/s²) and r is the radius of the mud chamber (m) and x the lateral position relatively to the center of the mud chamber (m). The mass-density of the reference rock was calculated just above the mud generation zone using the porosity

obtained through the 2D sedimentation models and a mass-density for solid grains of 2650 kg/m^3 . The degree of gas saturation was taken at 0.38, i.e. the limit for mud generation based on the laboratory testing presented in Chapter 4. It allowed the calculation of the mud mass-density using Eq. (13) (see Chapter 2:3.4.4). Therefore, applying Eq. (17), a maximum mud velocity was calculated for different sediment viscosities.

3. Results

3.1. Mud generation

3.1.1. One-dimensional sedimentation and pore pressure accumulation

The presence of the low permeability ASF has prevented fluids from being expelled during burial of the Productive Series. The increase in the overpressure gradient below the ASF displayed in Figure 3.14A clearly shows that fluids are trapped below the ASF, building-up the overpressure in the underlying strata. Therefore, the Upper PS might have kept an abnormally high porosity through compaction disequilibrium (Osborne & Swarbrick, 1997). Javanshir *et al.* (2015) as well as the reservoir overpressure values displayed in Figure 3.14A show that the Middle Productive Series and Lower Productive Series are drained through laterally continuous and connected reservoirs, and that should have limited the under-compaction of these intervals. Thus, in the following simulations Layer 4 permeability was artificially kept higher than underlying and overlying intervals using a modified permeability law (Eq (18)) reproducing the under-compaction caused by the ASF as displayed in Figure 5.2.

$$\ln(K) = 3.06e - 17.66 \quad (18)$$

with K the hydraulic conductivity in m/s, and e the void ratio.

Using the permeabilities obtained from oedometer tests and well data analysis (Table 3-2 and Figure 3.13A, B), initial 1D properties were obtained from the deeper part of the section presented in Figure 5.1. After 13 iterations, allowing to correct from compaction the initial sedimentation rates that are derived from present thicknesses, the present observed thicknesses were obtained by SeCoV3. The corrected sedimentation rates are summarized in Figure 5.2 and are quite similar to those obtained in the previous modeling work presented in Chapter 3:4.4.1 (Figure 3.15).

The ASF is a 300 meters thick interval forming the uppermost interval of the Productive Series that is composed by a succession of evaporitic beds and low resistivity shale intervals, some of which presented swelling behavior during drilling operations. It acts as an efficient seal, as overpressure rapidly builds up below this interval (see Chapter 3:4.3, Figure 3.14A). The layer is therefore modeled as being incompressible ($C_c = 0$) and with a permeability reduced by one to two orders of magnitudes compared to other layers, and

three orders of magnitude lower than the most permeable layer (Layer 4). Its sedimentation rate was taken equal to the one used for Layer 4, as being part of the same large stratigraphic interval.

Figure 5.2 displays the main results of the 1D modeling that are taken as boundary condition 4 (Figure 5.1) in the 2D-diffusion models presented below. The results show the impact of the low-permeability ASF on overpressure that rises sharply when crossing this interval, accounting for the observed pressure build-up in well pressure logs (Figure 3.14A). The low-permeability zone is well expressed in Figure 5.2 and contrasts with the high-permeability Layer 4. The overpressure slowly builds up over Layer 1, stays constant over Layer 4 and slightly increases over Layer 3, 2 and 1. The highest overpressure reached 40 MPa, which is in accordance with the pore pressure measured in the wells (Figure 3.14A).

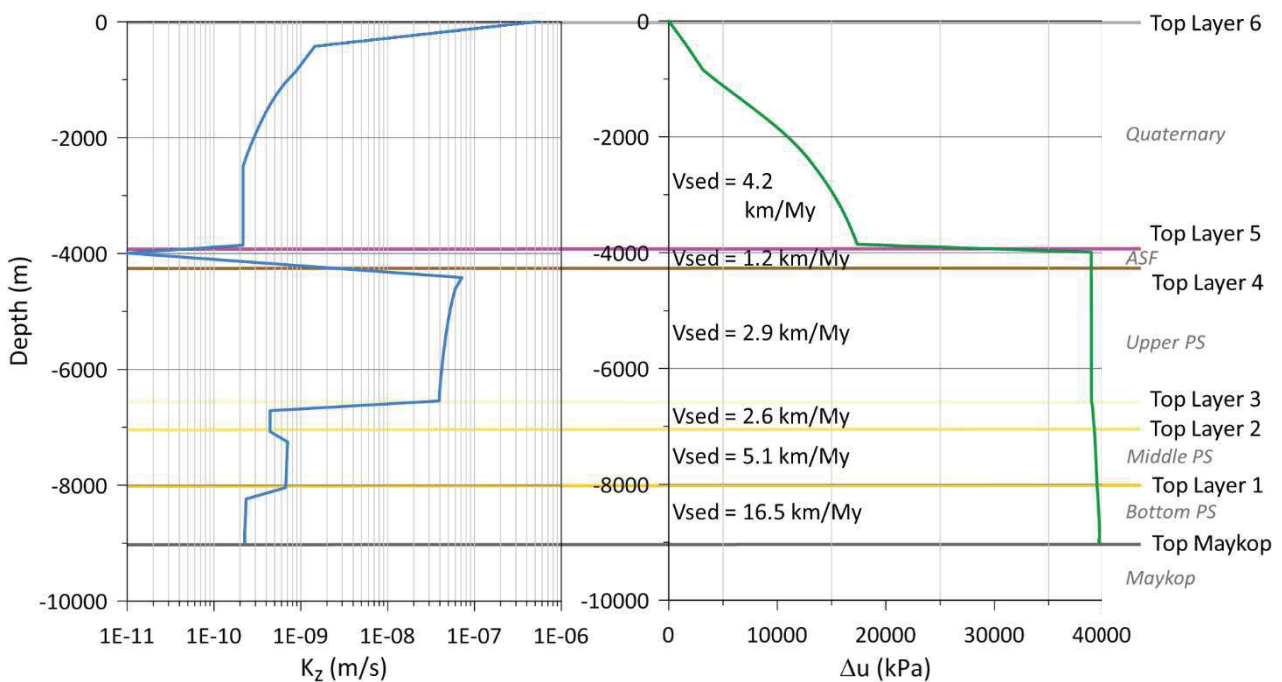


Figure 5.2: Results of the one-dimensional sedimentation modeling at the southern edge of the 2D geometrical model in Figure 5.1. On the left, vertical hydraulic conductivity versus depth trend at the end of the 5 My of sedimentation. On the right, overpressure versus depth trend at the end of the 5 My of sedimentation with corrected sedimentation rates for each layer. The top of each simulated stratigraphic unit is represented as indication using the same colour code as in Figure 5.1 and the corresponding stratigraphic intervals are displayed inbetween.

3.1.2. Two-dimensional transient-diffusion processes, gas exsolution and damage

Four numerical simulations were conducted with different input parameters. The parameters used during the simulations are synthetized in Table 5-1. Most of the parameters are common for all the simulations and were obtained from literature and industrial reports (seafloor temperature, Henry methane constant) or from laboratory testing and well log interpretation (temperature gradient, sediment petrophysical properties). Four parameters were modified in order to fit observations and regional geology: fault hydraulic diffusivity, fracture condition, starting date for overpressure transmission, initial methane concentration.

Table 5-1: Parameters used for the different diffusion simulations presented in the chapter. Several parameters were modified to fit observations and regional background over the different simulations.

		Simulation 1	Simulation 2	Simulation 3	Simulation 4
nodes number	vertically	50			
	horizontally	225			
Seafloor temperature		5.85°C			
grad(T)		16°C/km			
Henry methane constant		$1.5 \times 10^{-3} \text{ M.atm}^{-1}$			
fluid viscosity		$1.15 \times 10^{-6} \text{ kPa.s}$			
methane diffusivity		$1.49 \times 10^{-7} \text{ m}^2/\text{s}$			
e_0, C_c	Layer 6	2.734; 0.159			
	Layer 5, ASF	0.500; 0.000			
	Layer 4	2.014; 0.105			
	Layer 3	1.821; 0.094			
	Layer 2	1.643; 0.080			
	Layer 1	1.659; 0.081			
$a, b, K_h/K_v$ $K=\exp(ae+b) \text{ (m/s)}$	Layer 6	3.064; -22.866; 2200.0			
	Layer 5, ASF	0.000; -25.328; 15.0			
	Layer 4	3.064; -17.666; 15.0			
	Layer 3	3.064; -22.150; 5.0			
	Layer 2	3.064; -21.803; 2.0			
	Layer 1	3.064; -22.333; 1.0			
e_0, C_c	faults	3.5; 0.0			
$D_h \text{ (m}^2/\text{s)}$		5.5×10^{-6}	5.5×10^{-8}	5.5×10^{-8}	5.5×10^{-8}
$D_c \text{ (m}^2/\text{s)}$		$5.5 \times 10^{-6} \text{ m}^2/\text{s}$			
fracture condition: $\Delta u/\sigma'_v$		0.9	0.9	0.7	0.7
e_{frac}		1.0			
Start of overpressure diffusion (Ma)		1 My	1 My	1 My	3 My
Initial methane concentration (mM)		55.5	55.5	55.5	5550

i. Case 1: integration of the ASF layer properties

The 2D geometrical model, based on the work presented in Green et al., (2009), was modified in order to consider the impact of the ASF low permeability. The modeled geometry is displayed in Figure 5.1. The fracture condition $\Delta u/\sigma'_v$ was initially set at 0.9 given the mean fracture condition obtained from well data (Chapter 3:4.3). Lateral overpressure transmission started 1 My after methane diffusion in fault networks. Results of this simulation after 5 My are displayed in Figure 5.3. Methane diffusivity was set at $1.49 \times 10^{-7} \text{ m}^2/\text{s}$ in sediments, and the faults have a hydraulic diffusivity of $5.5 \times 10^{-6} \text{ m}^2/\text{s}$ and a relatively high methane diffusivity coefficient of $5 \times 10^{-4} \text{ m}^2/\text{s}$ in order to include artificially gas advection impact and create a preferential advective pathway for fluids.

Figure 5.3a shows overpressure diffusion across the structural model. Overpressure strongly increases below the ASF reaching 38 MPa in the south of the model, and stays lower than 18 MPa above the ASF. Moreover, as Layer 4 is more permeable than the others, overpressure propagates more rapidly along this stratigraphic layer. Figure 5.3c shows the overpressure build-up below the ASF at the Absheron location that reaches 35 MPa over less than 1000 m. The main difference with results obtained in Chapter 3:4.4.2 without

the ASF (Figure 3.17) is this clear and strong pressure build-up in Layer 4. The previous simulation calculated higher overpressure in Layer 5 (corresponding to present Layer 6), and overpressure build-up with depth was more progressive.

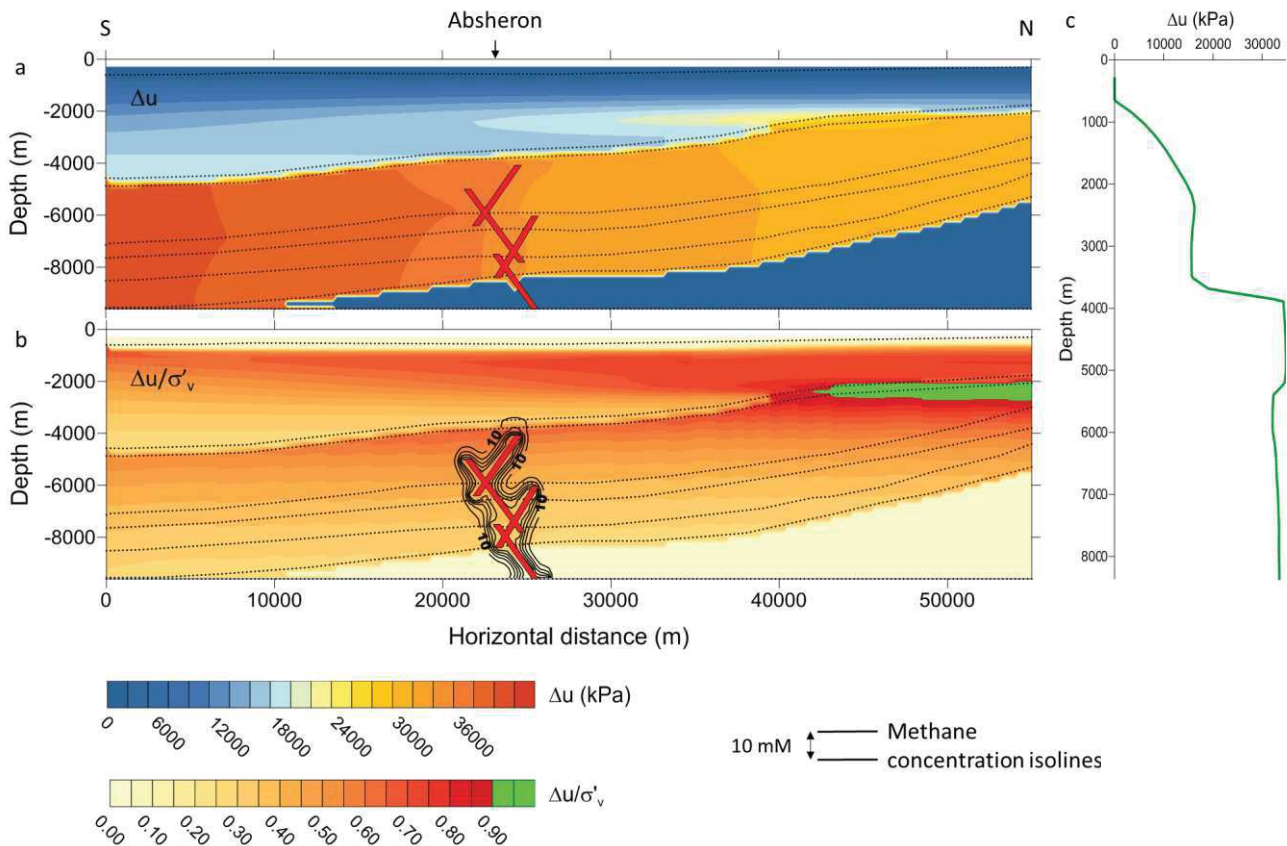


Figure 5.3: Results of overpressure and methane diffusion modeling after 5 My of calculation considering the low permeability ASF interval. Black dotted lines are for layer limits. a: overpressure (Δu) in kPa after 5 My of migration through the structural model presented on Figure 5.1. Overpressure migrated more rapidly through layer 4 that has a higher permeability. b: $\Delta u/\sigma'_v$ contours with values exceeding hydrofracture condition below the ASF in the north of the model, where σ'_v is low. Black lines correspond to methane concentration contours. Lines are separated by 10 mM. c: Δu (kPa) vertical plot at the Absheron location (black arrow).

However, in terms of $\Delta u/\sigma'_v$ distribution, Figure 5.3b clearly shows that the maximum is reached just below the ASF, in the northern edge of the model where σ'_v is low due to thin overburden and probably to the boundary condition (Figure 5.1), preventing lateral exchange between the model and the outside, therefore allowing overpressure build-up along the northern edge of the model. Hydrofracturing conditions are reached as $\Delta u/\sigma'_v$ is above 0.9 (green area in Figure 5.3b). No fracture conditions are reached at the Absheron location where calculated values do not exceed 0.7. Methane circulation is effective around the fault network showing that over 5 My, sediments get saturated with dissolved methane through the simulated transmissive fault network. The values of $\Delta u/\sigma'_v$ calculated here are higher than in the simulations described in Chapter 3:4.4.2 (Figure 3.17). The highest values are now localized below the ASF (Figure 5.3) when they were distributed along the interval immediately above in the former version of the simulation (Figure 3.17). Methane distribution is similar to that of the former simulation (Figure 3.17) as the parameters for methane diffusivity were not modified.

Thus, the presence of the low permeability ASF allows reproducing pressure transmission and build-up mainly below this interval as well as reaching hydrofracturing conditions along the bottom end of the ASF. However, fracture opens at the north of the structural model where low σ'_v are present and where overpressure accumulates due to the model boundary limits. Besides, no free gas, and consequently no sediment damage was observed due to the fracture formation in an area where no dissolved gas was present.

ii. Case 2: sealing faults

The previous simulation shows that overpressure does not accumulate at the Absheron location but at the northern boundary of the model. Therefore, another simulation was conducted with modified boundary condition. The pore-pressure was drained at several depths below the ASF in order to dissipate overpressures in the north by setting Δu to zero. Hinds *et al.* (2004) and Javanshir *et al.* (2015) show that several sandstone intervals of the Productive Series are continuous and crop out onshore, especially in the lower PS. Therefore, the modeled hydraulic connection between the deeper part of the SCB and the surface, where atmospheric pressure prevails, does exist and was directly inferred from pressure logs at different well sites (Figure 3.14A; Javanshir *et al.*, 2015). However, the results of the simulation were inconclusive as overpressure was entirely dissipated at the north border of the model without any hydrofracturing in the calculation zone. Besides, the $\Delta u/\sigma'_v$ at the Absheron location did not change.

Thus, another working hypothesis was tested. Faults were initially set to create preferential pathways for fluids. Nevertheless, faults could be vertical pathways but horizontal seals for fluid circulation due to permeability anisotropy (Caine *et al.*, 1996; Evans *et al.*, 1997; Wibberley *et al.*, 2008). Indeed, different authors noted in several regions around the world that faults may be sealing in the perpendicular direction but transmissive in the fault direction and that their permeability may vary depending on external parameters such as pore pressure, deformation style and the lithologies put in contact through the fault (Morley *et al.*, 2017; Wibberley *et al.*, 2017; Henry *et al.*, 2019). This feature was also already highlighted over the SCB and particularly at the Absheron location where gas was found in the north of the anticline, and 3 km south no economically interesting gas accumulation was found (Gautherot *et al.*, 2015; Javanshir *et al.*, 2015). Several regional fluid flow numerical models already integrated the fault anisotropy (Gordon & Flemings, 1998; Schneider *et al.*, 2004; Deville *et al.*, 2010). Besides, now that the ASF is modeled, slight corrections in the fault geometry are needed to fit the observations of Figure 3.3 where the fault network ends in the ASF.

To simulate the horizontal sealing effect of the fault, the hydraulic diffusivity of the fault was taken equal to $5.5 \times 10^{-8} \text{ m}^2/\text{s}$. The vertical transmissivity was simulated by keeping a methane diffusivity of $5 \times 10^{-4} \text{ m}^2/\text{s}$. Results of this simulation are displayed in Figure 5.4.

Figure 5.4a displays the 2D distribution of overpressure after 5 My of calculation. The main feature is that with the sealing faults, overpressure builds up south of the faults, reaching 40 MPa, while in the northern

part, the overpressure stays limited (around 18 MPa). The effect of the high permeability layer 4 contrasting with the low permeability ASF is still displayed with overpressure transmitting more rapidly along the Layer 4 than in above intervals and with limited overpressure in Layer 1. Figure 5.4c shows the overpressure profile with depth at the Absheron location. The rapid overpressure increase once the ASF is crossed is well illustrated as well as the weak overpressure gradient along Layer 1. Besides, an overpressure contrast is visible between Layer 4 and Layer 3 due to the effect of sealing faults, creating a trend similar to that observed in pressure logs at wells, with pressure horns and peaks (Figure 3.14A, Chapter 3:4.3).

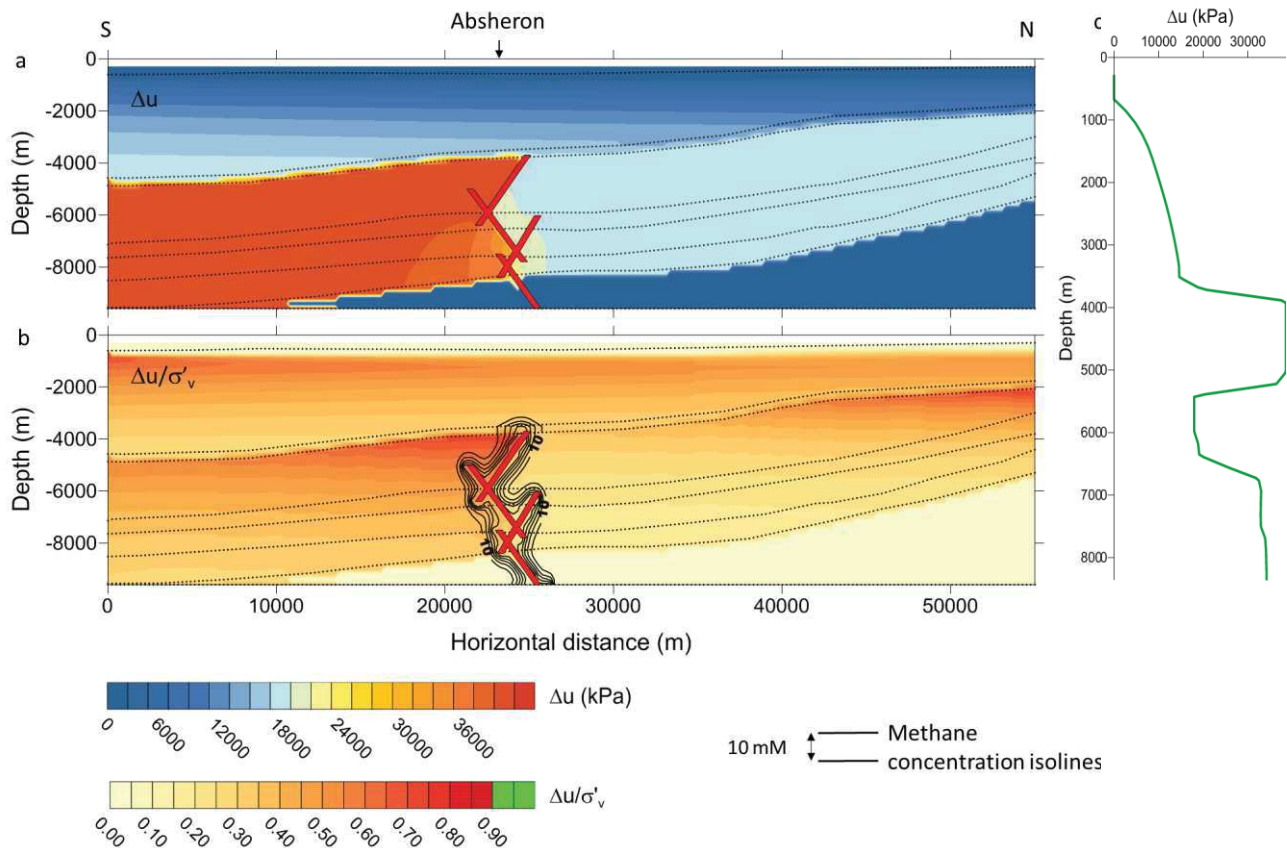


Figure 5.4: Results of overpressure and methane diffusion modeling after 5 My of calculation considering the low permeability ASF interval and faults as horizontal seals. Black dotted lines are for layer limits. a: overpressure (Δu) in kPa after 5 My of migration through the structural model presented on Figure 5.1. Overpressure builds up along the fault network. north of the fault network overpressure is only of 18 MPa. b: $\Delta u/\sigma'_v$ contours. The highest values are now distributed south of the fault network, along the ASF, at the crest of the Absheron fold. Methane distribution is represented with black isolines, lines being separated by 10 mM. c: Δu (kPa) vertical plot at the Absheron location (black arrow).

High values of $\Delta u/\sigma'_v$ are now distributed in two main areas. To the north of the structural model where σ'_v is low and where some overpressure accumulated below the ASF, but most of all just south of the sealed fault network and along the ASF at the crest and along the southern flank of the Absheron anticline (Figure 5.4b). However, the fracture condition 0.9 is not reached, thus no fractures were created. The highest $\Delta u/\sigma'_v$ values reached are comprised between 0.70 and 0.75 (Figure 5.4b). Methane diffusion is similar to what was observed in the previous simulations as methane diffusivity of faults and sediments were not modified (Figure 5.4b). Methane concentrations are also the same.

Therefore, the fault network now acts as a seal for lateral pressure transmission and as a vertical pathway for fluids, allowing to approach critical conditions at the Absheron location.

iii. Case3: new assessment of fracture conditions

The fracture condition was previously set at 0.9 because of the mean value obtained on well data of the ratio between fracture pressure and overburden pressure. However, this value may be as low as 0.8 depending on the considered depth. Besides, at the time when the AMV started being active, sediments may have been less consolidated than at present which led to lower tensile strength hence lower hydrofracturing conditions. Therefore, a fracture condition of 0.7 was considered as plausible and is now considered in the following calculations. This value $\Delta u/\sigma'_v$ was already given as a minimum value for brittle failure of sedimentary rocks in several studies (Grauls & Baleix, 1994; Sibson, 2003).

A new calculation only changing the fracture from 0.9 to 0.7 was carried out. Figure 5.5 synthesizes the results after 5 My of calculation.

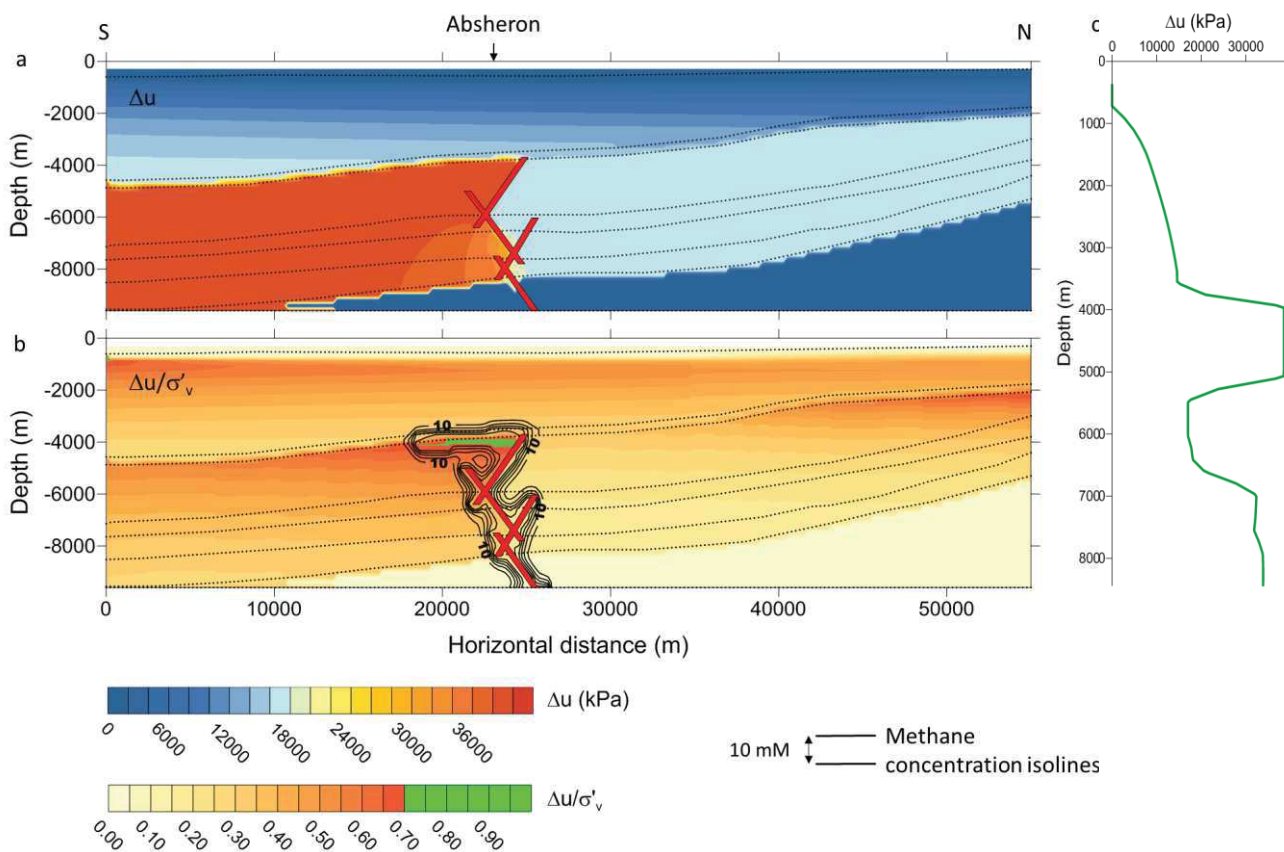


Figure 5.5: Results of overpressure and methane diffusion modeling after 5 My of calculation considering the low permeability ASF interval, faults as horizontal seals and a fracture condition of 0.7. Black dotted lines are for layer limits. a: overpressure (Δu) in kPa after 5 My of migration through the structural model presented on Figure 5.1. b: $\Delta u/\sigma'_v$ contours. Fracture occurs along the bottom edge of the ASF, south of the fault network. Methane distribution is represented with black isolines, lines being separated by 10 mM. The dissolved methane distribution follows the fracture shape. c: Δu (kPa) vertical plot at the Absheron location (black arrow).

Figure 5.5a and Figure 5.5c are roughly the same as in Figure 5.4, as no changes were made that could affect directly the pressure field. Figure 5.5b shows that fracture condition was reached and that a fracture

opened in the area of the Absheron anticline, south of the fault network, where $\Delta u/\sigma'_v$ is the strongest. As fractures have a methane diffusivity of $5 \times 10^{-4} \text{ m}^2/\text{s}$, pore fluids migrated through the fractures along a horizontal plane, changing the dissolved methane (Figure 5.5b). However, no gas exsolution occurred in this model since the degree of gas saturation stayed at zero. This could be either due to the fact that pressure decrease through fracture was not high enough, or that the dissolved methane concentration is not sufficient, two parameters that controls gas exsolution processes (Brown, 1990; Duan & Mao, 2006). Figure 5.5a and Figure 5.5c do not display any pressure decrease at fracture depth. As fracture generated in an area where overpressure is constant, no drainage of fluids was possible, preventing pore pressure from a significant decrease. A vertical fracture that would have connected Layer 4 and Layer 6 through the ASF would have permitted a strong pressure decrease. Nevertheless, this was not possible since the ASF layer is characterized by a low-permeability coefficient impeding vertical pore pressure diffusion and therefore hydrofracturing.

Another important point is that hydrofracturing happened only 500,000 years after the beginning of pressure diffusion calculation, so 1.5 My after the beginning of the simulation. This shows that there is no need for calculating diffusion for a period as long as 5 My and that diffusion calculation could start at 3 Ma, date when all the PS were already deposited (Figure 2.4). This could account for the deposition time of the main reservoirs, when HC generation was already active (Figure 2.6).

As a conclusion of this calculation, fractures were generated at the Absheron anticline crest, south of the fault network, and dissolved gas diffused into the fracture network. However, no free gas was formed because of either unsubstantial pressure decrease or low dissolved methane concentration.

iv. Case 4: high gas concentration at the base of the fault network

In order to test the impact of the free gas at the fracture location (Figure 5.5b), the dissolved methane concentration of the fluid source at the bottom of the fault network (coming from a deeper source such as the Maykop source rock) was increased to 555 mM and to 5550 mM. The latter high methane concentrations (two times higher than methane solubility at source temperature and pressure conditions) suppose the presence of free gas in addition to dissolved molecules. However, this initial free gas volume which accumulates during several thousands of years is not supposed to cause any damage to the sediment. Indeed, damaging is considered to occur only during short-term exsolution process. The simulations start calculating pressure diffusion after 3 My of methane diffusion through the faults and the stratified sediment layers.

The simulation considering an initial methane concentration of 555 mM was not conclusive as the results obtained are the same in Figure 5.5. However, this showed that pore-pressure diffusion starting at 3 My does not impact the previous results.

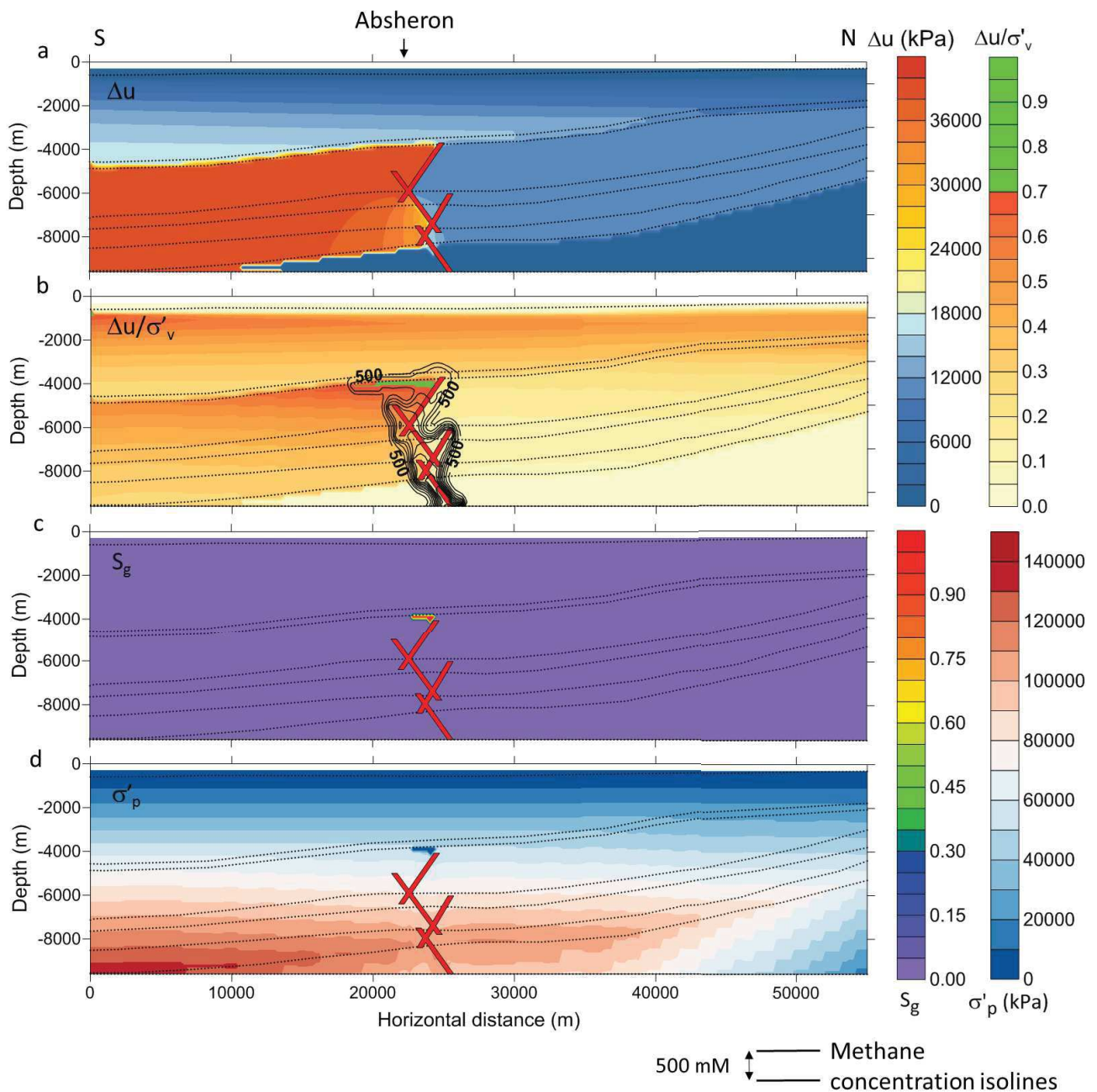


Figure 5.6: Results of the simulation considering the ASF, sealing faults, a fracture condition of 0.7 and an initial methane concentration of 5550 mM after 5 My. Black dotted lines are for layer limits. a: overpressure (Δu) in kPa after 2 My of migration through the structural model presented on Figure 5.1. b: $\Delta u/\sigma'_v$ contours. Fracture occurs along the bottom edge of the ASF, south of the fault network. Methane distribution is represented with black isolines. The dissolved methane distribution follows the fracture shape and is depleted around fractures due to gas exsolution. c: degree of gas saturation (S_g) calculated after fracture formation. Values as high as 1 are reached in the central part of the fracture, in an area close to the fault network. d: preconsolidation pressure (σ'_p). It increases linearly with depth, but it is disturbed in the same area where gas exsolution happened reaching zero in the center of the fracture.

Figure 5.6 shows the results of the simulation with an initial methane concentration of 5550 mM. Figure 5.6a shows that the overpressure field does not change compared to previous simulations. Figure 5.6b shows a similar $\Delta u/\sigma'_v$ distribution than in Figure 5.6b with a fracture generation below the ASF, south of the fault networks. The dissolved methane concentration follows the faults and fractures but with higher concentrations, the lower value plotted being 500 mM (Figure 5.6b). Figure 5.6c displays the degree of free gas saturation (S_g) calculated across the structural model. S_g is above zero in an area corresponding to the

fractured area close to the fault network and just below the ASF limit. Maximum values of 1 are reached in the center of the fractures. The model triggers gas exsolution locally after fracture generation for sufficient dissolved methane concentration.

Gas exsolution has a twofold effect. First, dissolved methane distribution is disturbed and partly depleted around the faults compared to the simulation proposed in Figure 5.5 (see Figure 5.6b) due to the fact that, locally, a part of the initially dissolved methane exsolved to form free gas. Moreover, as the simulation calculates the preconsolidation pressure (σ'_p), based on the equation in Figure 4.21 (Chapter 4:5.5) linking S_g with a preconsolidation ratio, we observe a local decrease in preconsolidation pressure in response to the presence of free methane (Figure 5.6d). This decrease in σ'_p is observed in the area where S_g is non-zero. σ'_p reaches almost 0 kPa where S_g is greater than 0.38, in areas where it was around 50 MPa before gas exsolution (Figure 5.6d).

Thus, this simulation taking into account 1- the presence of ASF; 2- sealing faults; 3- a fracture condition of 0.7; and 4- an initial methane concentration of 5550 mM, was able to model the sediment damage in an area just below the ASF and at the Absheron anticline crest, through fracture opening and the subsequent gas exsolution.

The integration of a low permeability layer corresponding to the ASF allowed transmitting overpressure in the Upper Productive Series and reaching critical overpressure conditions. The modification of fault hydraulic diffusivity in order to create horizontal seals resulted in critical conditions at the crest of the Absheron Anticline. These critical conditions created fractures that, coupled with sufficiently high dissolved methane concentration, allowed gas exsolution. Gas exsolution locally decreased the preconsolidation pressure of sediments sufficiently for them to lose all their initial structure. The observations made during the laboratory testing presented in Chapter 4 allow concluding that with the used parameters, conditions for mud generation are reached in the Upper PS, at the AMV location.

3.2. Mud ascent

The approximate volume of mud and the initial geometrical conditions for the mud ascent modeling were estimated from the previous calculations of the mud generation (Figure 5.6). The initial (2D) mud body for all simulations was set as a convex-up half-disc with a radius of 500 m, its base (diameter of the half-disc) being located 3400 meters below the seafloor with 500 meters of water column above and centered on the horizontal direction (Table 5-2). For code1 v2, the initial mud overpressure was set at 35 MPa, which is the pressure obtained in the mud generation zone at the end of the simulation presented in Figure 5.6. Mass-densities used for all simulations are indicated in Table 5-2.

Three values of the common viscosity of the ascending mud and host sediments were tested using both codes (with and without pressurized mud) as well as the impact of the presence of vertical conduits and of their length (Table 5-2).

Table 5-2: Parameters used in the different simulations completed during the study. The varying parameters are the sole sediment viscosity and the fracture length.

code version	viscosity (kPa.s)	conduit length (m)	dimensions		mud source			Mass-densities (kg/m ³)			
			length	depth	dimension	position	overpressure	bottom	top	mud	Solid grains
code1 v1	10 ⁵	0	10 km	3900 m	radius 500 m	x = 5000 m z = 3900 m	No mud overpressure	2100	1900	1900	2650
		1000									
		2000									
	10 ⁶	0									
		1000									
		2000									
	10 ⁷	0									
		1000									
		2000									
code1 v2	10 ⁵	0	100 nodes	100 nodes	radius 500 m	x = 5000 m z = 3900 m	35 MPa	2100	1900	1900	2650
		1000									
		2000									
	10 ⁶	0									
		1000									
		2000									
	10 ⁷	0									
		1000									
		2000									

3.2.1. Code1 v1

Figure 5.7 displays the results of the simulation for the median case, $\mu = 10^6$ kPa.s, using code1 v1. The initial state shows the initial geometry of the mud generation zone modeled as a 500 meters radius half-disc. The imposed mass-density is displayed, varying linearly from 1900 kg/m³ at the seafloor to 2100 kg/m³ at 3900 m. The mud mass-density is initially at 1900 kg/m³. The degree of gas saturation (S_g) is initially 0 everywhere except in the mud generation zone where it is set at 0.38. The gassy-mud column starts rising after 3500 s. The changes in mass-density are mainly localized around the gassy-mud column and the velocity vectors are mainly disturbed in the immediate vicinity of the mud source reaching 0.04 m/s at 3750 s. The surrounding stratified sediments stay undisturbed, apart from the lateral edges where boundary conditions create some artifacts. As the degree of gas saturation increases due to methane expansion, the mass-density in the mud decreases (orange and green colors in Figure 5.8), triggering an acceleration of the process at 4500 s, when the gassy-mud column reaches 2200 m. The surrounding sediments are also impacted as the gassy-mud column rises, as non-negligible displacements are computed 2000 m away from the column with velocities reaching 0.1 m/s at 4500 s. The final stage (6000 s) shows that the gassy-mud column reaches the

seafloor, with a width of 500 m. The corresponding mass-density of the gassy-mud column has values of 1450 kg/m^3 just below the seafloor. The gassy mud displays velocities of 0.25 m/s and surrounding sediments are disturbed significantly up to 3000 m away from the center of the model. The mass-density of the host sediment remains stable except near the model lateral boundaries due to computation artifacts. However, the initial stratification is preserved.

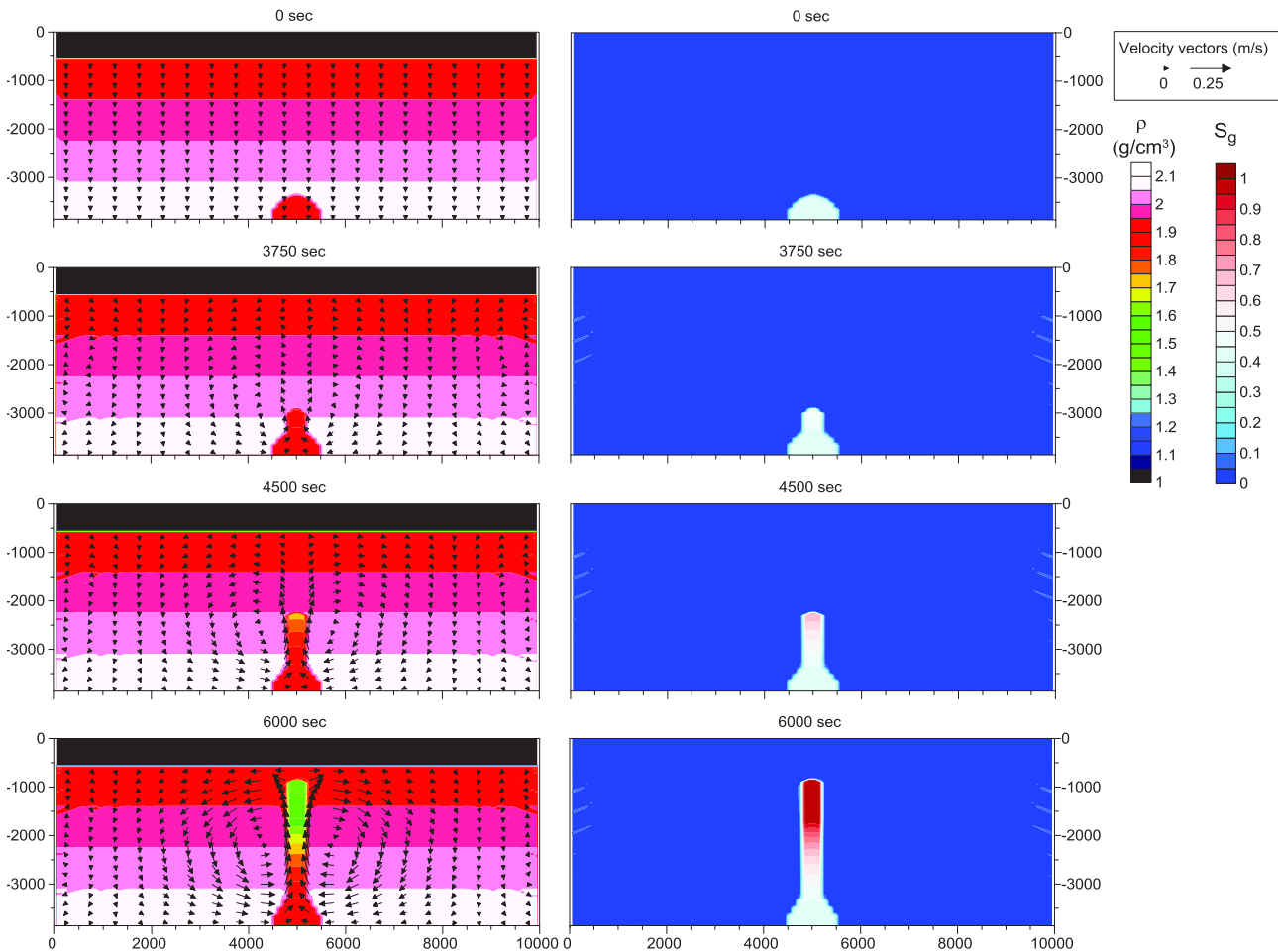


Figure 5.7: Results of the simulation using code1 v1 for $\mu = 10^6 \text{ kPa.s}$. The left column displays the evolution of mass-density with time (left color scale) as well as the velocity vectors (m/s). The right column displays the evolution of the degree of gas saturation with time (right color scale).

For $\mu = 10^5 \text{ kPa.s}$ (minimum case), the same observations are made but events occur 10 times faster. The initiation of mud ascent is observed after 350 s , and the final stage is reached after only 600 s . The velocity reaches 3.2 m/s in the ascending column and displacements are also visible in a radius of 3000 m around the center of the model. The stratification is also preserved and the ascending column is nearly 1 km wide. The mass-density is not disturbed around the gassy-mud column.

For $\mu = 10^7 \text{ kPa.s}$ (maximum case), after $100,000 \text{ s}$, the gassy sediment column does not rise. We therefore tested the response of the simulation when a pre-existing conduit was added to the model (Table 5-2). As there are 100 nodes horizontally, it was not possible to center the vertical conduit, hence creating some dissymmetry in the results of simulations presented hereafter.

Two conduit lengths were tested: 1000 m and 2000 m from the base of the model (Table 5-2). The result of the simulation with $\mu = 10^5$ kPa.s and a 1000 m long vertical conduit is presented in Figure 5.8, where the conduit is displayed at the initial stage, with the same mass-density and the same degree of gas saturation as the mud generation zone. The initiation of gassy-mud ascent starts at 300 s. The gassy-mud ascent is mainly focused along the conduit, but it is superimposed with the normal gassy-mud ascent due to the presence of the mud source (as was observed without conduit). It is particularly visible as the conduit is not perfectly centered over the mud generation zone. The final stage is reached at 750 s. The final width of the gassy-mud column is 250 m. The velocity of the host sediments reaches 1.2 m/s at the direct proximity of the conduit and decreases to nil over a distance of 3 km. The timing of ascent conduit of 2-km conduit is very similar to the previous one, but the velocity only reaches 0.5 m/s, and the gassy-mud ascent is only focused above the vertical discontinuity, hence the final gassy-mud column is only 100 m wide.

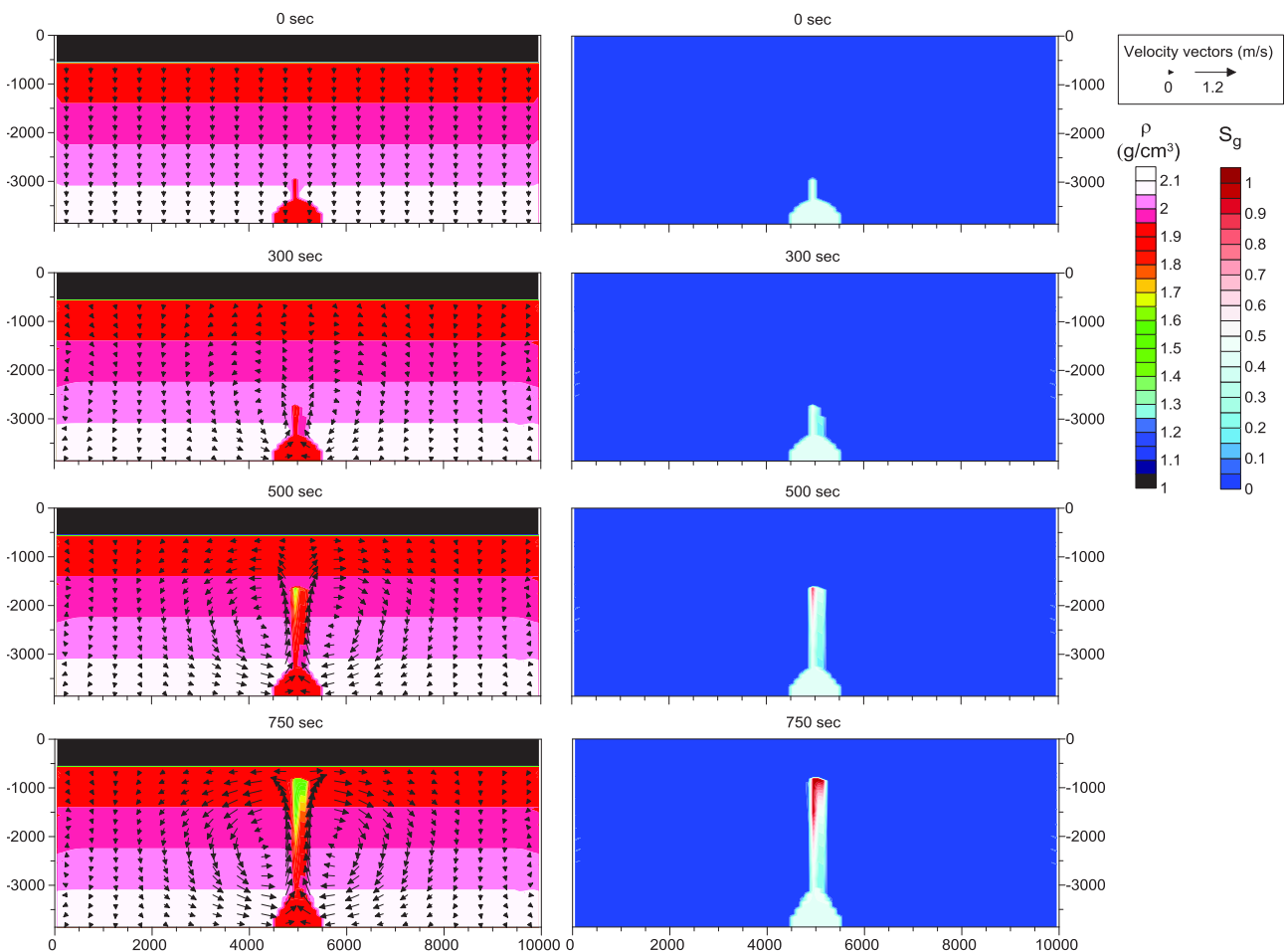


Figure 5.8: Results of the simulation using code1 v1 for $\mu = 10^5$ kPa.s and a 1000 m long vertical conduit. The left column displays the evolution of mass-density with time (left color scale) as well as the velocity vectors (m/s). The right column displays the evolution of the degree of gas saturation with time (right color scale).

We also tested the impact of conduits for $\mu = 10^6$ kPa.s. The results are overall similar to what has been described above with $\mu = 10^5$ kPa.s, apart from the timing: initiation of gassy-mud ascent happens after 3000 s for both conduit lengths, and mud reaches the seafloor after 7000-7500 s. The maximum velocity is

0.12 m/s for a 1-km conduit and 0.05 m/s for a 2-km conduit. The width of the gassy-mud column remains unchanged.

With $\mu = 10^7$ kPa.s, even with 2 km-long conduits, no gassy-mud column was observed, even after 100,000 s, corresponding to over 3 weeks of computation time, exceeding the time limitation imposed on the Datarmor supercomputer.

3.2.2. Code1 v2

Code1 v2 considers the initial mud overpressure and its evolution with gas expansion. Fluid pressure in Eq. (11) (Chapter 2:3.4.4) is calculated separately through Boyle's law when free gas is present.

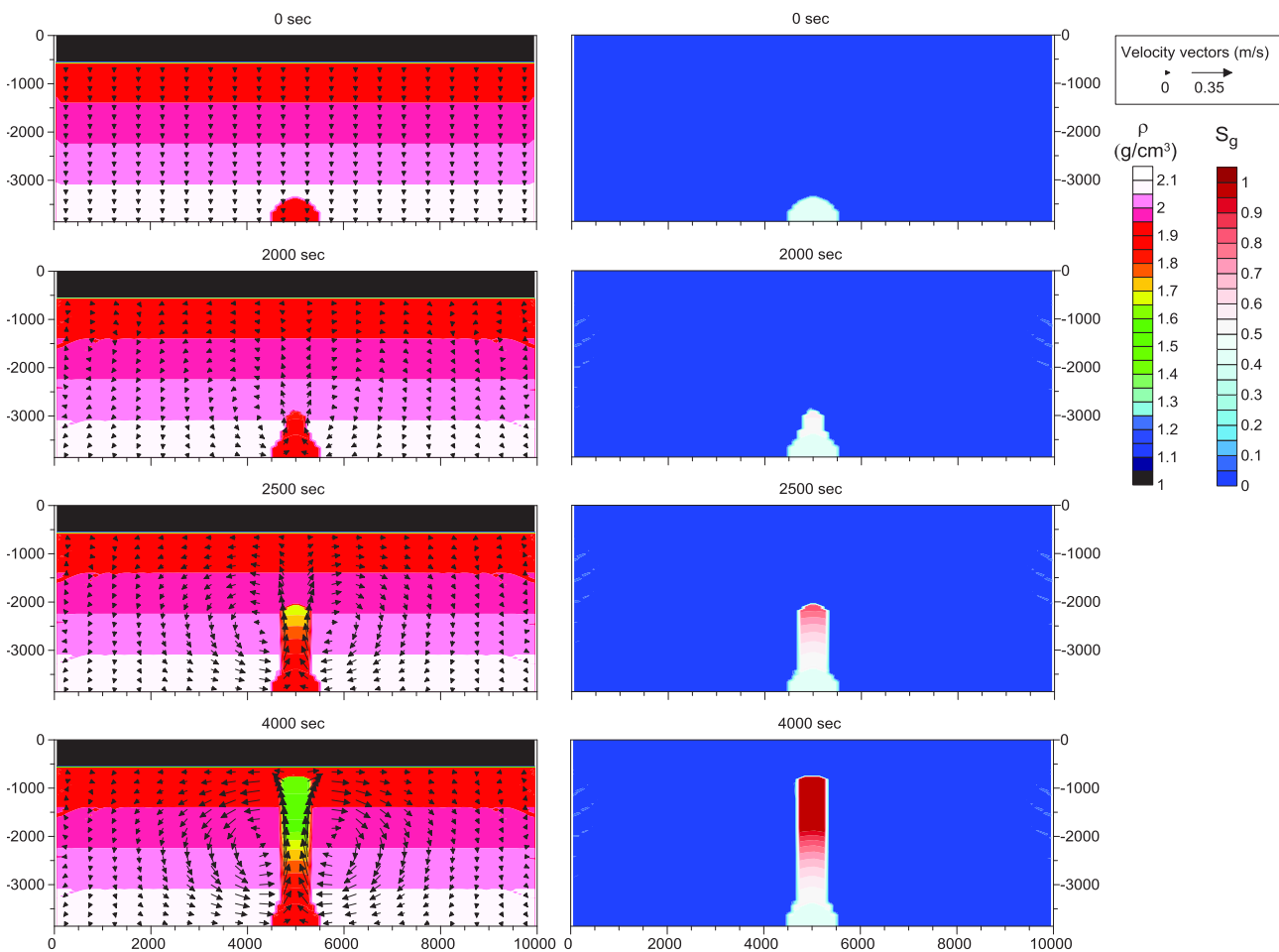


Figure 5.9: Results of the simulation using code1 v2 for $\mu = 10^6$ kPa.s. The left column displays the evolution of mass-density with time (left color scale) as well as the velocity vectors (m/s). The right column displays the evolution of the degree of gas saturation with time (right color scale).

Figure 5.9 displays the results of the simulation for $\mu = 10^6$ kPa.s using code1 v2. The initial state is the same as in Figure 5.7. The different stages described for code1 v1 are the same with this version, but they occur earlier in the simulation. The ascending column initiates at 1750 s, and it is accompanied by a slight disruption in velocity vectors as shown in Figure 5.9 at 2000 s. This disruption increases as the ascending gassy-mud column rises, reaching 0.35 m/s in the ascending column at the final stage of the simulation and affecting a radius of 3000 m around the center of the model. The ascending column reaches the seafloor

after 4000 s. A minimum mass-density of 1450 kg/m^3 is obtained at the top of the ascending column near the seafloor, 1000 m above the depth where the degree of gas saturation reaches 1. The ascending column is nearly 750 m wide at the final stage. The initial mass-density stratification is preserved as in Figure 5.7. Some computation artifacts due to the limit conditions of the model are still present.

Again, for $\mu = 10^5 \text{ kPa}\cdot\text{s}$ the same observations are made but 10 times earlier in the simulation than in Figure 5.9. The initiation of gassy-mud ascent is observed after 200 s, and the final stage is reached after only 400 s. The velocity reaches 3.5 m/s in the ascending column and displacements are also visible in a radius of 3000 m around the center of the model. The stratification is also preserved and the ascending column is also 750 m wide. The density is not disturbed near the column.

As observed earlier in code1 v1, for $\mu = 10^7 \text{ kPa}\cdot\text{s}$, after more than 10 days of computations, the simulation only reached 5000 s, and no initiation of an ascending column was visible. Further simulations with vertical discontinuities were made to understand the impact of conduits above the mud source (Table 5-2).

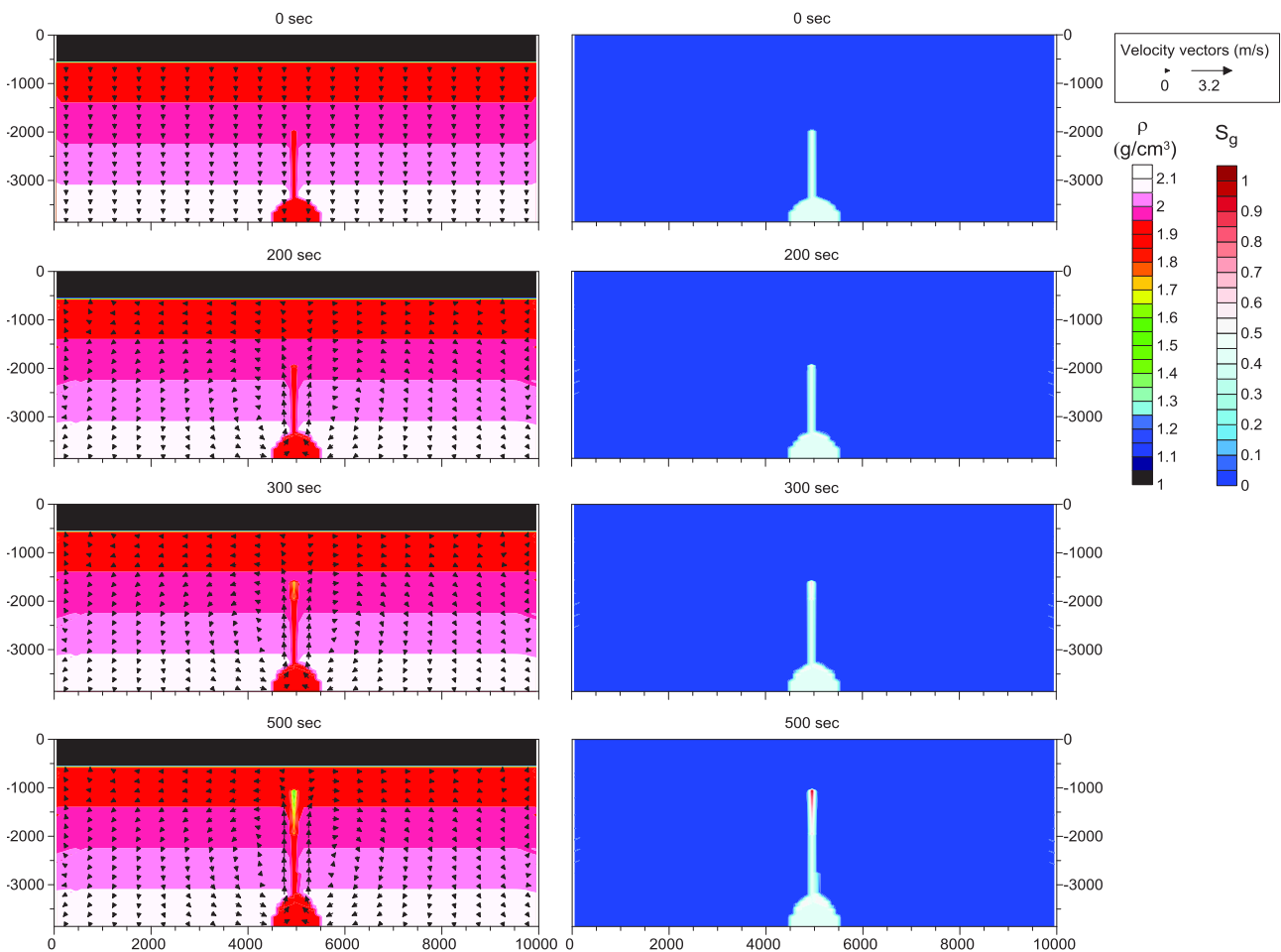


Figure 5.10: Results of the simulation using code1 v1 for $\mu = 10^5 \text{ kPa}\cdot\text{s}$ and a 2000 m long vertical conduit. The left column displays the evolution of mass-density with time (left color scale) as well as the velocity vectors (m/s). The right column displays the evolution of the degree of gas saturation with time (right color scale).

At $\mu = 10^5$ kPa.s, the presence of a 1 km long vertical discontinuity generates similar effects to those obtained with code1 v1 and displayed in Figure 5.8. The gassy-mud column initiates at 200 s, mainly focusing along the conduit, but the direct impact of the mud generation zone is also visible (same as Figure 5.8). The column reaches the seafloor after 400 s, reaching 750 m in diameter and velocities of 4.2 m/s above the mud chamber. The velocity field is disturbed in a radius of 3 km around the conduit. The case of a 2-km conduit is displayed in Figure 5.10. An ascending gassy-mud column starts forming at 200 s just at the termination of the vertical conduit. The mud column gets larger at 300 s, forming a drop-shaped low density area. The gassy mud reaches the surface between 500 and 600 s with velocities reaching locally 3.2 m/s at the intersection between the conduit and the mud chamber. The gassy-mud column is 100 m wide at the end of the simulation.

This version of the code leads to computation times even longer than the v1, so no process initiation was observed for $\mu = 10^7$ kPa.s, even with 2 km-long conduits.

Table 5-3: Synthesis of the main results obtained from the different simulations computed in this study. The initiation time of gassy-mud ascent, the time needed to reach the seafloor, the maximum velocity and the final diameter of the gassy-mud column are displayed for the two code versions.

code	μ (kPa.s)	Conduit length (m)	Initiation (s)	Extrusion (s)	Max. velocity (m/s)	Final diameter of gassy-mud column (m)
1 v1	10^5	0	350	600	3.2	1000
		1000	300	750	1.2	250
		2000	300	750	0.5	100
	10^6	0	3500	6000	0.25	500
		1000	3000	7000	0.12	250
		2000	3000	7500	0.05	100
	10^7	0	Computation too time consuming			
		1000				
		2000				
1 v2	10^5	0	200	400	3.5	750
		1000	200	500	4.2	400
		2000	200	500	3.2	100
	10^6	0	1750	4000	0.35	750
		1000	1500	4500	0.36	400
		2000	2000	4750	0.32	100
	10^7	0	Computation too time consuming			
		1000				
		2000				

All the results obtained with the different 2D simulations discussed above are synthesized in Table 5-3. These results highly depend on the spatial and temporal resolution of the simulations, hence small variations are not considered to be relevant. It clearly shows that when viscosity increases by one order of magnitude, velocity decreases by one order of magnitude while the timing of initiation and extrusion increases by one order of magnitude (Table 5-3). When mud overpressure is considered in the simulations, it decreases the

time for initiation and extrusion by a ratio of 0.65 to 0.5 (Table 5-3). The presence of vertical conduits above the mud chamber mainly influences the V_{\max} which seems to decrease as the length of the conduit increases in the case of code1 v1 (Table 5-3). For code1 v2, V_{\max} seems to remain roughly constant. The presence of a conduit also influences the final diameter of the gassy-mud column that decreases as the length of the conduit increases (Table 5-3).

3.2.3. Extrapolation to realistic viscosities: 1D calculations

In order to extrapolate the 2D simulation results obtained through the code modified from Tryggvason (2012), we tested simple 1D calculations based on the case of a buoyant magma flow along a vertical dyke (Furbish, 1997) in order to compare the velocities and timing obtained. Using Eq. (17) with r the radius of the mud chamber ($r = 500$ m) and taking $x = 0$ (maximum velocity above the center of the mud chamber) it was possible to obtain the maximum velocity above the mud chamber for varying viscosities. Figure 5.11a shows the results of 1D calculations of maximum velocities (V_{\max}) for viscosities comprised between 10^5 and 10^{12} kPa.s, considered as a valid approximation range for mud viscosities that are typically below the viscosity of sedimentary rocks. Two sets of models were run: the first one without initial mud overpressure (black), corresponding to the mud mass-density calculated through Eq. (13); the second (red line) considers an initial mud overpressure. Overpressure is limited to 78% of the effective stress (value of $\Delta u/\sigma'_v$ near the mud source at the end of 2D diffusion models, see Chapter 5:3.1.2.iv), thus, the mass-density of mud was multiplied by 0.78 to take the mud overpressure into account. The maximum velocities obtained above the mud chambers for the 2D simulations without conduit are also plotted in Figure 5.11a. Figure 5.11b displays the same results in terms of minimum time for extrusion that was calculated considering that the velocity is V_{\max} all along the conduit. The results in Figure 5.11b clearly show that the minimum time needed for the buoyant mud to reach the seafloor and form a mud volcano depends on mud viscosity.

The 1D calculations shows that the maximum velocity is inversely proportional to the viscosity (Figure 5.11a). Considering the initial mud overpressure, without modifying the viscosity, increases V_{\max} by a factor 4.5, so that the two trends are parallel. For higher viscosities (10^{12} kPa.s), the maximum velocity is comprised between 10^{-6} and 10^{-7} m/s. Logically, the time for extrusion increases by an order of magnitude for each order of magnitude of μ (Figure 5.11b), results directly arising from the form of Eq. (17). The consideration of the mud overpressure allows reducing this time for extrusion. Therefore, for $\mu = 10^{12}$ kPa.s, it would take a minimum of 500 years for the buoyant mud to reach the surface if the mud overpressure is not considered, while it would take only 100 years if the mud overpressure is integrated in the calculation.

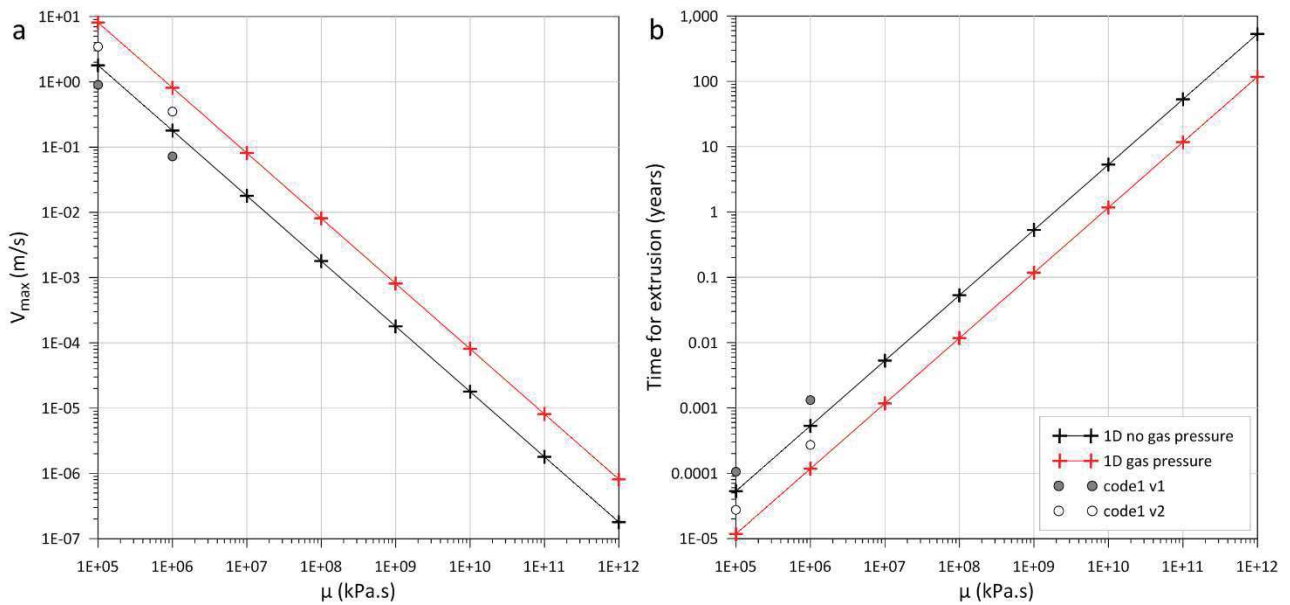


Figure 5.11: Results of 1D calculations based on the case of a buoyant magma flow along a vertical dyke presented in Furbish (1997) considering a radius of 500 m corresponding to the mud source radius, compared to results obtained with 2D simulations. a: maximum velocity versus viscosity, b: minimum time for extrusion versus viscosity. Black lines with crosses correspond to the case where the initial mud overpressure is not considered, red lines are for the case with mud overpressure. Grey dots correspond to the results of the 2D simulations using code1 v1 and white dots the results of 2D simulations with code1 v2.

The 2D simulations results display the same relationship. μ and V_{\max} are inversely proportional (Figure 5.11a). Taking into account the initial mud overpressure in code1 v2 leads to a 4-fold increase of V_{\max} compared with code1 v1 (Figure 5.11a). Moreover, the values obtained with code1 v1 stands close to the black line (1D calculations without mud overpressure), and the values of code1 v2 are closer to the red line compared to code1 v1 results (1D calculations considering mud overpressure).

The same calculation was applied but in the case of a 50 m wide conduit corresponding to the size of the conduits in the 2D simulations (Figure 5.12). The same relationship between μ and V_{\max} and μ and the time for extrusion are displayed in Figure 5.12. The impact of mud overpressure seems to be limited as the difference between the V_{\max} and the time for extrusion obtained considering mud overpressure and without mud overpressure is reduced compared to Figure 5.11. Moreover, the V_{\max} extracted from 2D simulations are larger by nearly one order of magnitude than those obtained from 1D calculations (Figure 5.12a). Therefore, the time for extrusion are smaller by one order of magnitude (Figure 5.12b). Besides, the conduit width corresponds to the minimum that could be computed considering the model resolution, 1 node corresponding to 100 m and the conduit being computed over a unique node. Hence, the results displayed are not relevant of the circulation that would occur in natural fractures whose width is much smaller.

From this 1D calculation, it arises that the time required for achieving extrusion, considering a viscosity of 10^{12} kPa.s, is significantly increased. Considering mud overpressure, it would take more than 10,000 years for the mud to reach the surface through thin fractures when it was 100 years for the calculation considering the mud chamber radius.

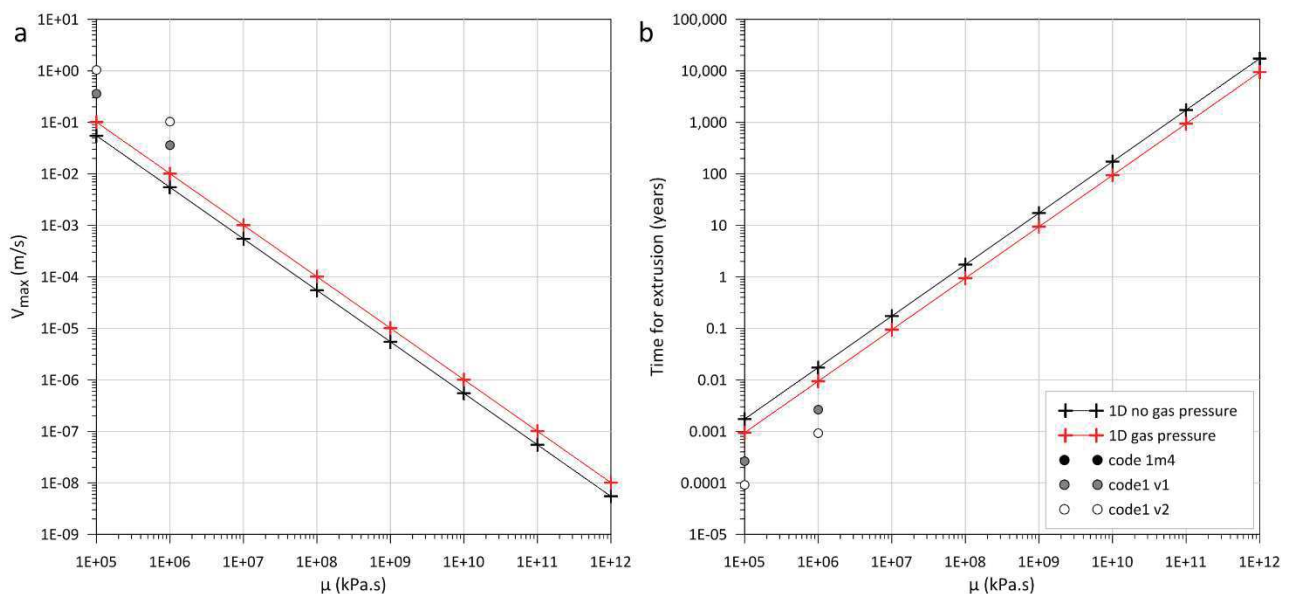


Figure 5.12: Results of 1D calculations based on the case of a buoyant magma flow along a vertical dyke presented in Furbish (1997) considering a radius of 50 m corresponding to the conduit width, compared to results obtained with 2D simulations. a: maximum velocity versus viscosity, b: time for extrusion versus viscosity. Black lines with crosses correspond to the case where the initial mud overpressure is not considered, red lines are for the case with mud overpressure. Grey dots correspond to the results of the 2D simulations using code1 v1 and white dots the results of 2D simulations with code1 v2.

4. Discussion

4.1. Synthesis of the main results

The consideration of the low-permeability Anhydritic Surakhany Formation (ASF) allowed to simulate in 1D the generation of a sedimentation-related overpressure contrast between layer 6 and deeper layers reproducing the overpressure sharp increase observed in well-log data (Figure 3.14A). Moreover, the model simulates maximum overpressure values of 40 MPa corresponding to the values measured in situ at the Absheron exploration wells (Figure 3.14A). It also improved the 2D diffusion model presented in Chapter 3:4.4.2 (Figure 3.17) with overpressure now occurring essentially below the ASF and transmitted through Layer 4 (Figure 5.3). Overpressure diffusion started after 3 My of simulation, a date corresponding to the deposition of the entire Productive Series interval. Lateral compartmentalization of the 2D model through the presence of faults having low horizontal permeability (Gautherot *et al.*, 2015; Javanshir *et al.*, 2015) was necessary to create overpressured conditions at the location of the AMV (Figure 5.4). Faults are often regarded as presenting permeability anisotropy depending on their internal structure and material and depending on external parameters such as pore pressure (Caine *et al.*, 1996; Evans *et al.*, 1997; Schneider *et al.*, 2004; Wibberley *et al.*, 2008; Deville *et al.*, 2010; Morley *et al.*, 2017; Henry *et al.*, 2019), thus methane-saturated water migration from the Maykop Fm. was provided by high methane diffusivity in faults, artificially simulating high vertical permeability accounting for advection processes. A new fracture condition of 0.7 was adopted, based on pressure logs at well sites, allowing to create a fractured area at the Absheron crest, just below the ASF (Figure 5.5). For an initial methane concentration of 5550 mM, gas exsolution was triggered in the fractured area resulting in a strong sediment damage in the fracture zone, with preconsolidation

pressure locally approaching zero (Figure 5.6). From the results of the laboratory testing discussed in Chapter 4, the improved 2D diffusion model simulated the mud generation zone formation below the Absheron MV.

To understand a possible ascent mechanism of the mud from its source to the seafloor, we based our approach on fluid mechanics using modified 2D Navier-Stokes equations considering the impact of gas expansion (Boyle's law) on the mass-density of the mud. Mud viscosities were limited to values between 10^5 kPa.s and 10^7 kPa.s because higher viscosities resulted in exceedingly long simulations and results were extrapolated with a simple 1D calculation to viscosities up to 10^{12} kPa.s. Results of the 2D simulations show that ascent velocity is inversely proportional to mud viscosity, while the times needed for mud ascent initiation and for mud extrusion is proportional to viscosity (Table 5-3). When mud overpressure is considered in the simulations, it decreases the time for initiation and extrusion by a ratio of 0.5-0.65 (Table 5-3). The presence of conduits mainly influences the final width of the gassy-mud column, which decreases with an increasing conduit length (Table 5-3). Through one-dimensional extrapolation it would take a minimum of 500 years for a buoyant high-viscosity mud to reach the surface if mud overpressure is not considered, while it would take only 100 years if the mud overpressure is integrated in the calculation (Figure 5.11b). Considering the radius of a conduit (Figure 5.12b), it arises that the timing for extrusion is significantly increased as it would take more than 10,000 years for the same overpressured mud to reach the surface. Combining 1D and 2D simulations, adapting the Navier-Stokes equations to consider the impact of gas expansion on sediment mass-density through Boyle's law and the influence of mud overpressure over the ascension velocity allowed estimating the time needed for mud generated at depth to reach the seafloor and to form a mud volcano through density-inversion.

In the following, the results of the calculations carried out in this chapter will be discussed and confronted to previous research to assess the two main questions of the introduction:

- Is it possible to simulate mud generation conditions at depth by considering the mechanical properties of sediments, the sedimentation rates, structural elements and the impact of gas exsolution?
- Is the sole impact of gas expansion on the mud properties able to drive mud up to the seafloor?

4.2. Overpressure, hydrofracturing and gas exsolution: from stratified sediments to fluid mud

Calculations of pressure related to the maximum gas column that could have been trapped within the ASF in Chapter 3 showed that the sole effect of the presence of a gas reservoir at the crestal location of the Absheron fold cannot explain the formation of the Absheron mud volcano, as the fracture pressure was not reached. Hydrofracturing is believed to be necessary to initiate a MV formation as demonstrated through the monitoring of the Lusi initiation (Tingay *et al.*, 2017) and through the analysis of the Absheron Mud Volcano

dataset (Chapter 3). Therefore, additional parameters are required to explain the AMV formation. The sedimentation rates recorded in the SCB are among the highest in foreland basins (Tagiyev *et al.*, 1997; Allen *et al.*, 2002; Smith-Rouch, 2006; Egan *et al.*, 2009; Green *et al.*, 2009). High sedimentation generates overpressure in low-permeability strata (Osborne & Swarbrick, 1997; Dugan & Flemings, 2000; Opara, 2011) and overpressure is one of the key triggers and drivers for MV formation (Dimitrov, 2002; Kopf, 2002; Deville, 2009; Mazzini & Etiope, 2017).

The 2-D diffusion model presented in this chapter is based on regional data extracted from literature (Diaconescu *et al.*, 2001; Green *et al.*, 2009), on observations and in situ measurements made on the Absheron gas condensate field, as well as on the laboratory experiments presented in Chapter 4. The regional-scale pressure gradient and northward fluid circulation from the deep SCB was already observed and discussed by several studies (Bredehoeft *et al.*, 1988; Gautherot *et al.*, 2015; Javanshir *et al.*, 2015), and this type of modeling, studying the influence of regional physical parameters such as sedimentation rate and pressure gradient on local structures such as landslides or venting sites, was already applied to other sedimentary basins (Dugan & Flemings, 2000; Schneider *et al.*, 2004; Kvalstad *et al.*, 2005; Hustoft *et al.*, 2009). Deville *et al.* (2010) applied a similar fluid flow numerical model to show that MVs in Trinidad are located above overpressured areas. However, it is the first time, in our knowledge, that a 2D-diffusion model is applied to simulate sediment remobilization into mud at depth.

More precise measurements and estimations of layer permeability and fracture pressure would now be needed to improve this simulation. Laboratory testing on rock fragments from the different modeled layers would be necessary to improve their hydro-mechanical properties. Most of the modeled stratigraphic intervals are known to outcrop onshore, along the Kura Basin, the Absheron Peninsula or in the Greater Caucasus where such rock samples would be easily accessible (Morton *et al.*, 2003; Hinds *et al.*, 2004; Vincent *et al.*, 2010; Bochud, 2011; Choi *et al.*, 2011; Forte *et al.*, 2015; Abdullayev & Leroy, 2016). Fracturing pressure was only estimated from pressure logs. However, LOT/FIT data shown in Figure 3.14A indicate that hydrofracturing may occur for an overpressure of 25 MPa. Therefore, less than 2 My of overpressure diffusion may be necessary in our simulation in order to obtain the needed 25 MPa to trigger fracture generation as the fracture in Figure 5.6 generated for over 35 MPa of overpressure.

The simulation generated a horizontal fractured area where gas was able to exsolve, reaching S_g greater than 0.38 locally and therefore damaging sediments that entirely lost their preconsolidation pressure. This area represents the mud generation zone and is 1300 m long and locally 220 m thick (Figure 5.6). The presence of the low-permeability ASF prevented pore pressure and therefore fractures to propagate vertically even if the maximum principal stress is vertical, the simulation ignoring the impact of compressive tectonics that are observed over the basin.

The 2D modeling presented in this study allows drawing a coupled process for mud generation below the AMV. Due to high sedimentation rates, overpressure is generated in the deeper part of the SCB and is transmitted northwards along under-compacted layers that kept an abnormally high permeability. The fault system at the core of the Absheron anticline leads to local overpressure build-up above the crest of the anticline, eventually initiating hydrofracturing and saturating the pore waters of the Upper Productive Series with methane. Hydrofracturing may trigger a local decrease in overpressure, allowing exsolution of the dissolved methane and triggering sediment damage when S_g exceeds 0.38 (see Chapter 4). Thus, the 2D diffusion model integrating the mechanical properties of sediments, sedimentation rates, compartmentalization effect of faults and regional seal and the impact of gas exsolution is able to reproduce the mud generation conditions at depth below the AMV.

4.3. Mud extrusion resulting from density-inversion driven by gas exsolution

Once the mud is generated at depth, it is necessary to understand how it is transported to the surface. The modeling work shows that mud ascent time is proportional to mud viscosity. Taking mud overpressure into account improve the convergence of 1D and 2D results (Figure 5.11). Similar values of velocity were obtained by Collignon *et al.* (2018b) who calculated flow rates depending on pipe radius, particle size and density and the type of gas for equivalent viscosities. One-dimensional extrapolation allows to test viscosities closer to those of sedimentary rocks, which was not possible on the 2D simulations due to time limitations. It would take approximately 100 years for the mud generated at the AMV location to rise to the surface if mud was only transported through density inversion and mud overpressure. The link between 2D results and the extrapolation in 1D may not be straight forward. The extrapolation in 1D is made over 6 orders of magnitude of viscosities and compared to only two 2D control points. The relationship between mud remobilization and the host sediment viscosity may not be a linear process when dealing with high values of μ . Therefore, the results have to be addressed with precautions. Nevertheless, some MVs display very small extrusion rates, such as the Koturdag (onshore Azerbaijan), that extrudes high viscosity and slightly wet mud with an estimated rate of 0.02 m/day (Dupuis, 2017), in other words 2.3×10^{-7} m/s, which is the order of magnitude obtained from our modeling.

The presence of a preexisting conduit in our simulations does modify the extrusion time, but it reduces the extrusion rate as a smaller volume of mud is able to rise through the sedimentary column. One-dimensional calculations considering fracture radius show that for $\mu = 10^{12}$ kPa.s, the extrusion time is close to 10,000 years. The simulations shown here do not address multi-phase flow, gas being only considered in the mass-density calculation. If free-gas was able to flow directly through the fracture, it may be able to fracture and/or damage shallower sediments, forming a secondary mud generation zone. This was observed at Lusi location, where the BJP-1 well allowed overpressured fluids charged with gas to flow to shallower and more fragile strata, triggering hydrofractures and mud generation (Tingay *et al.*, 2008, 2015).

In contrast to our numerical model in which mud ascent occurs along a unique wide fracture, field work reported by Roberts *et al.* (2010) has shown that mud volcano conduits rather consist of an intricate and complex fractured volume with detached and rotated blocks that was observed on field by Roberts *et al.* (2010). They explain their observations by the rising of overpressured and low-density mud that generates and propagates fractures as it rises, slowly opening its way up to the surface. Thus, the 2D simulations should rather compute the progressive opening of fractures as mud overpressure increases due to gas expansion. This would imply a combination of solid-rock mechanics and fluid mechanics that represents a complete field of research in modeling and computation, notably applied to hydrofracturing issues in well bores (Mainguy & Longuemare, 2002; Wu & Olson, 2015). The Lusi catastrophe allowed to monitor the initiation of a mud volcano formation. From the analysis of drilling reports, and notably records on the expelled gas, drilling mud losses and drilling mud pressure, Tingay *et al.* (2017) show that 24-48 hours separate the moment when free-gas was detected at the bottom of the well, and the moment when the mud extruded at the surface. Therefore, gas-driven mud generation and transport seem to occur very fast. Our model points to a transport duration of 100 years to cross the 3000 meters of strata separating the mud source from the surface but through the sole density inversion driven by gas expansion. The impact of gas expansion on overpressure and on rock failure is not explored but is expected to reduce significantly the time for extrusion. Besides, this combination of processes would imply a similar plumbing system as the one described by Roberts *et al.* (2010).

Another limitation of the current model is that the influence of gas exsolution on mud rheology was not accounted for. The presence of gas and liquids in the mud are known to strongly affect its viscosity (Kopf, 2002; Mazzini & Etiope, 2017). Collignon *et al.* (2018b) and Zoporowski & Miller (2009) have both considered a dynamic viscosity in their simulations and shows that the contrast between mud viscosity and the viscosity of the surrounding rock increases flow rates. Modeling results of Collignon *et al.* (2018b) demonstrated that the feeding pipe of the Lusi MV has to be smaller than 1.5 m radius in order to match its maximal mud discharge, when our model displays very long extrusion time for small fractures. Thus, the integration of a dynamic viscosity depending on gas content, would certainly increase the velocity of the extrusion process in our model. It will also allow to study the effect of low-viscosity layers, for instance containing evaporites like the ASF. Besides, the gas mass-density was considered negligible in the calculation of the mud mass-density. However, gas mass-density highly depends on the pressure and temperature conditions, and represents 1/5 of the water mass-density at 35 MPa and 50 °C.

Finally, the code of Tryggvason (2012) was developed to answer fluid mechanics issues. Working with values corresponding to a geological background leads to very long calculation time due to computing limitations arising from the resolution method. Therefore, the code should be improved or another resolution method should be explored in order to be able to run 2D simulations with parameters fitting the geological reality over shorter period of time.

The sole effect of gas expansion on the mud mass-density is thus able to drive mud ascent up to the seafloor. The process may be accelerated if the influence of gas exsolution and expansion on mud viscosity and on fracture propagation ahead of the rising mud. This modeling work resulted in extrusion rates of the same order of magnitude that what is measured on MVs extruding high viscosity mud.

4.4. Towards a quantitative formation model for the Absheron mud volcano

The conceptual formation model developed in Chapter 3 for the AMV was improved by integrating the main findings of Chapter 4 and of the numerical models. This allows to move from a purely qualitative model, to a semi-quantitative one including the formation dynamics as a function of the main physical parameters controlling the mud volcano formation: ratio of overpressure to vertical effective stress, dissolved methane concentration and degree of gas saturation. The updated formation model is composed of 7 different phases shown in the different panels of Figure 5.13:

Stage 1 - At 3.4 Ma, end of the rapid deposition of the Productive Series (over 3.5 km in 2 Ma) above the gas-mature Maykop Formation that generated hydrocarbons diffusing slowly through the sedimentary column (Figure 5.13a). The Maykop Formation started generating gas during the Late Miocene in the Shah Deniz region located less than 50 km away from the Absheron gas discovery (Figure 2.9 in Alizadeh *et al.*, 2017). Moreover, the deposition of the Anhydritic Surakhany Formation provided an efficient seal allowing a slow and uniform overpressure build-up in the Productive Series generated by high sedimentation rates.

Phase 2 – At 0.7 Ma, the growth of the rate of deformation at the Absheron fold increased significantly. Methane circulation was therefore focused into the faulted core of the anticline (Figure 5.13b). The difference of overburden between the anticline and adjacent syncline generated an overpressure gradient allowing overpressure build-up against the sealing faults (Figure 5.13b). Besides, at the anticline crest, the vertical effective stress σ'_v is lower than on the flanks due to reduced overburden thickness. Thus, overpressure generation and transmission as well as low σ'_v at the crest increased the $\Delta u / \sigma'_v$ ratio.

Phase 3 – At ≈ 0.6 Ma, $\Delta u / \sigma'_v$ ratio reached the hydro-fracturing threshold of 0.7 (Figure 5.13c), allowing hydrofracturing. These led to a local decrease of overpressure through fluid dissipation and triggered methane exsolution where the dissolved-methane concentration reached the methane solubility (Henry's law; Figure 5.13c). For a degree of gas saturation higher than 0.38, the sediment lost its preconsolidation pressure leading to mud generation (Figure 5.13c).

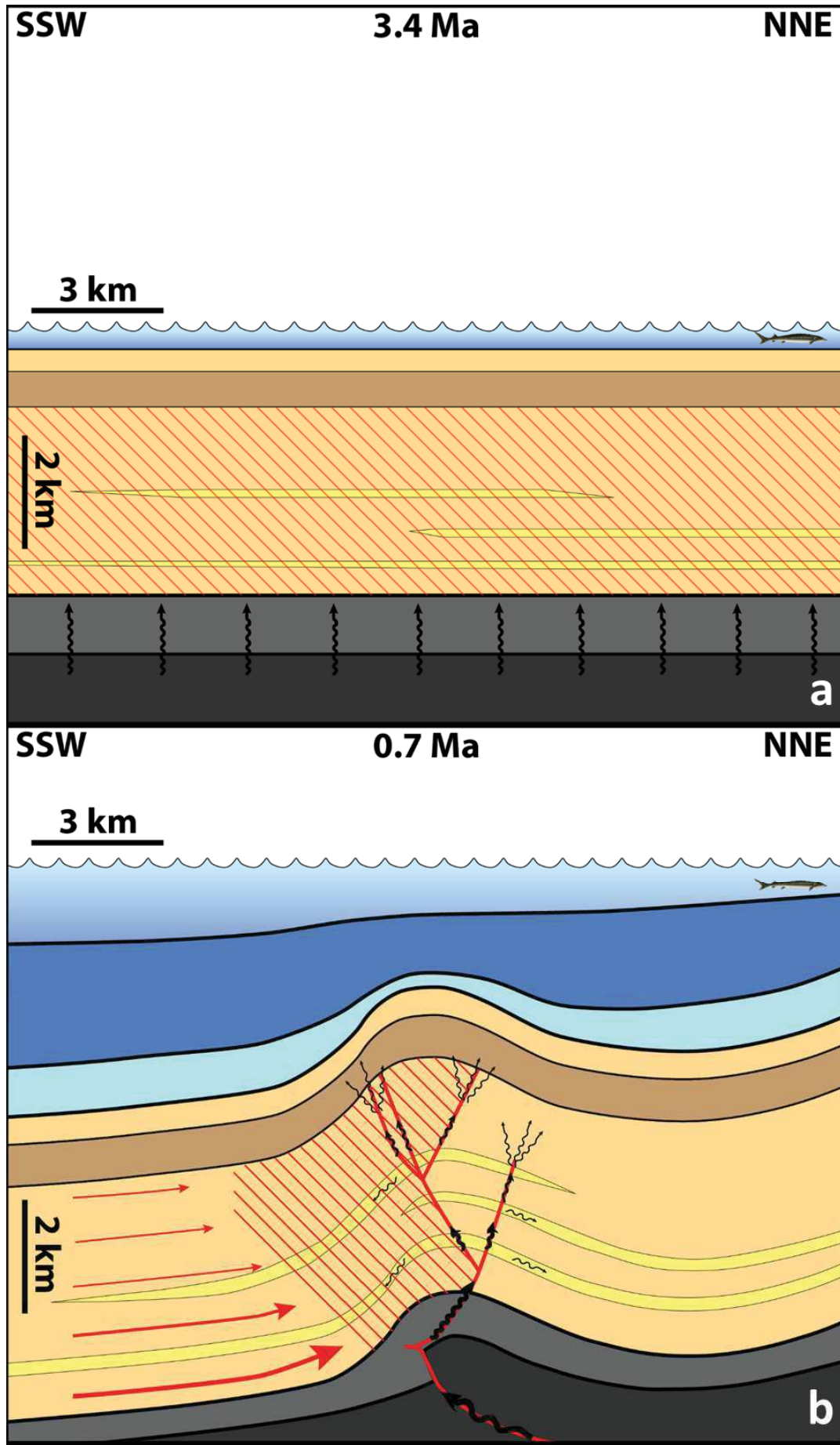
Phase 4 – The presence of gas bubbles in the mud significantly reduced its mass-density and its viscosity (Figure 5.13d). Therefore, the gassy mud started to rise along the open fractures. As the gas bubbles moved up, they expanded (following Boyle's law), hence increasing the degree of gas saturation and decreasing the

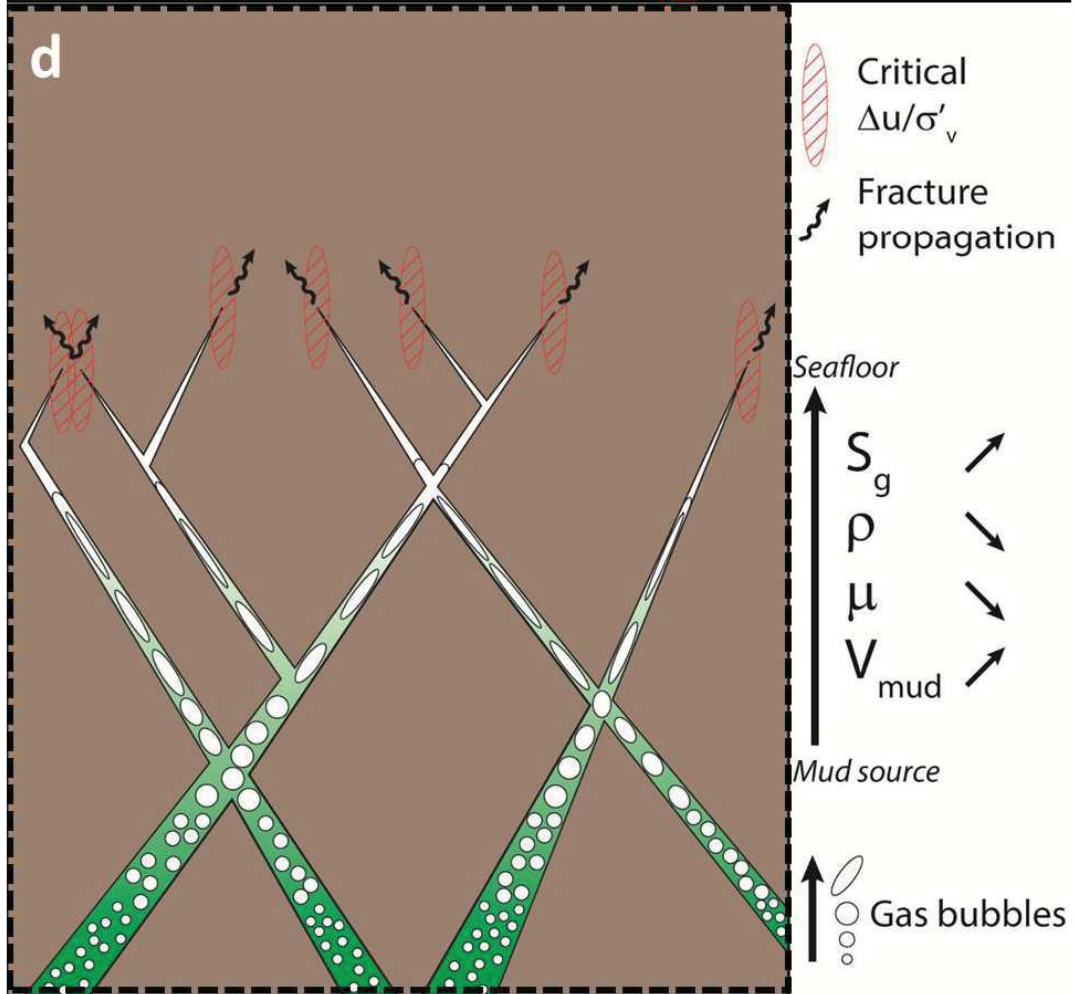
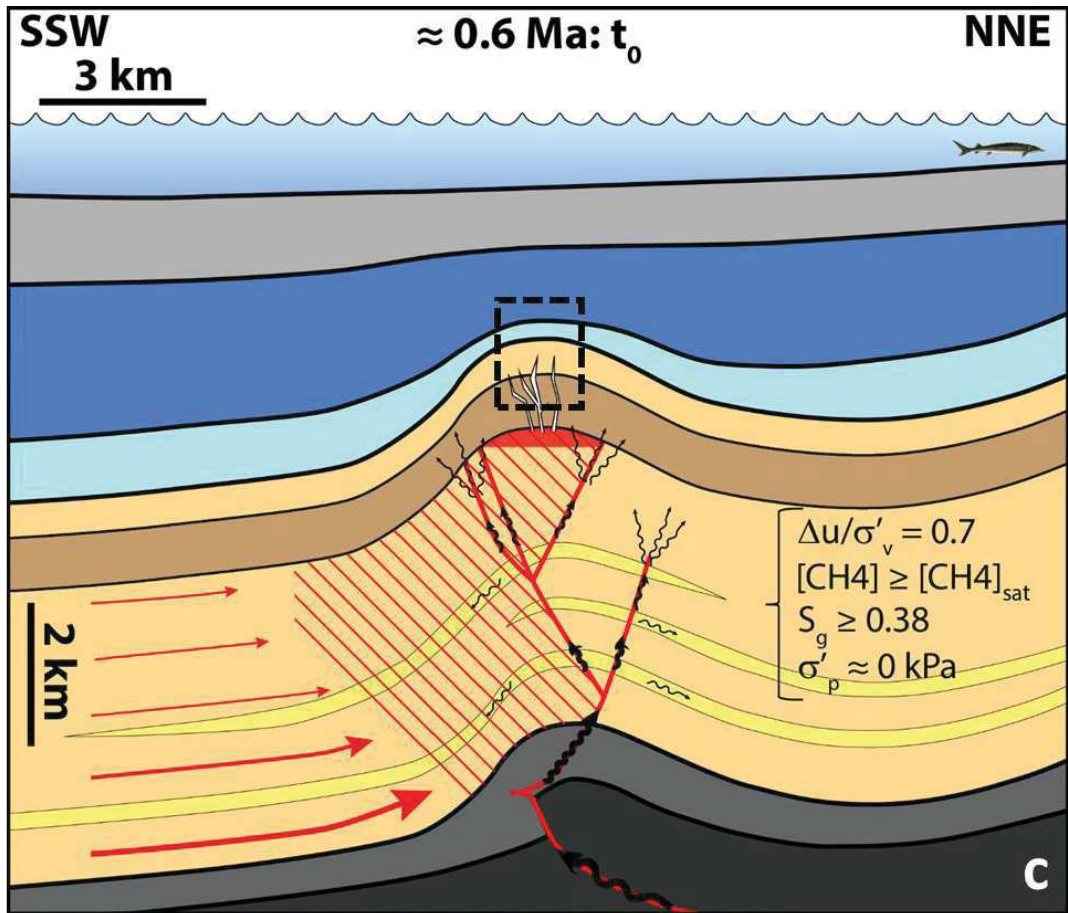
mud mass-density and viscosity (Figure 5.13d). Thus, mud velocity increased as bubbles expanded. The gas expansion maintained the overpressure as mud rose along fractures, leading to a critical value of $\Delta u / \sigma'_v$ and to fracture propagation towards the surface (Figure 5.13d). This stage should have happened over a short period of time, ranging from hours to days.

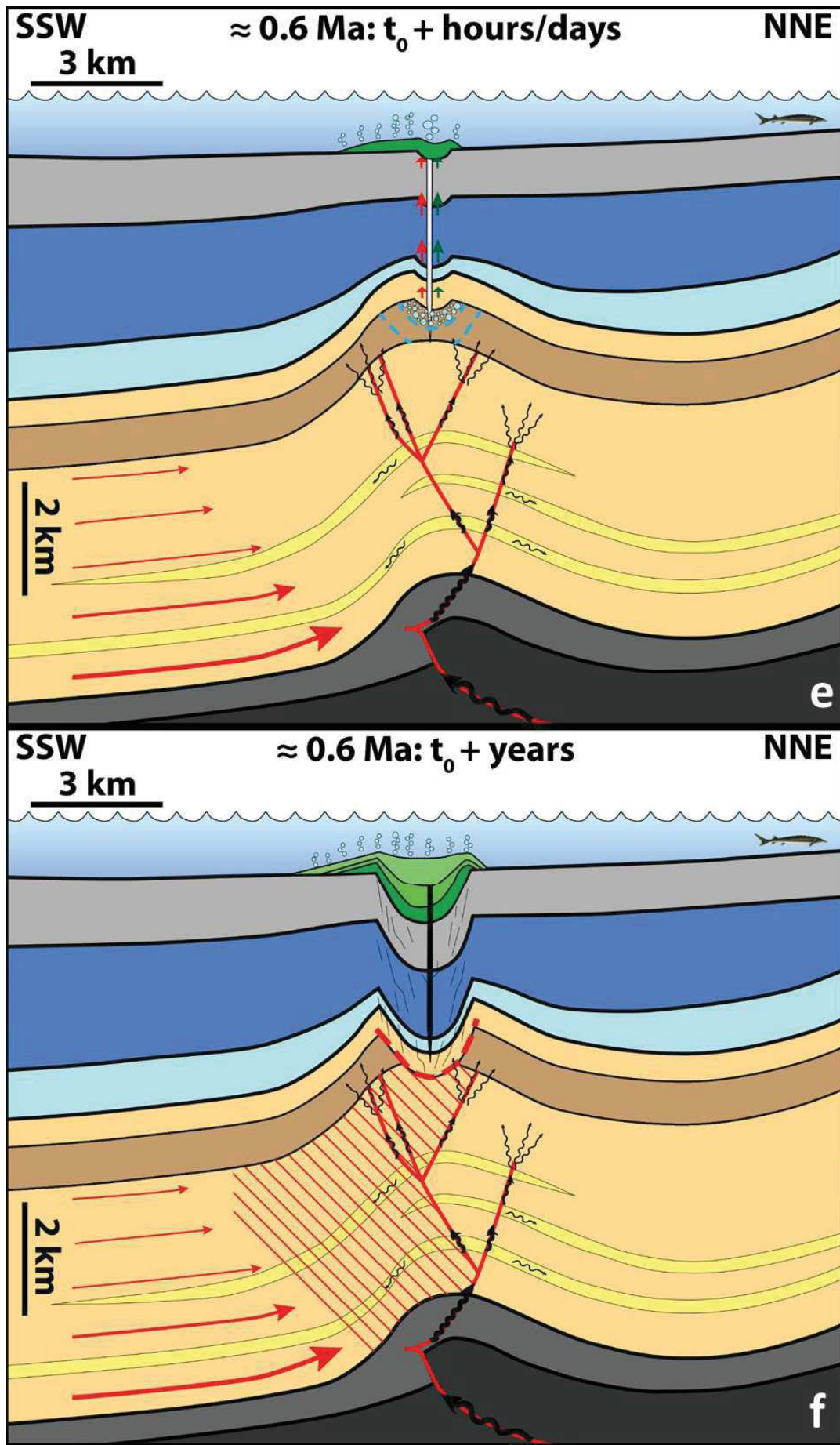
Phase 5 – After several days, the fractured “pipe” connected the mud generation zone, where gas exsolution is still damaging sediments, with the seafloor (Figure 5.13e). First mud extrusion happened at the seafloor leading to the progressive formation of the extrusive edifice, while mud slowly degassed in the water column (Figure 5.13e). This direct hydraulic connection prevented overpressure from building up again at depth as it is directly transmitted to the surface (Figure 5.13e), thus preventing gas exsolution from stopping. At depth, the extrusion of remobilized mud slowly led to roof collapse, forming what is known as a “depletion zone” (Stewart & Davies, 2006; Kirkham *et al.*, 2017a; Dupuis *et al.*, 2019).

Phase 6 – After several years, multiple mud extrusion episodes reached the surface as the depletion zone became bigger along with the collapse of the overlying strata, forming a giant mud shield at the seafloor (Figure 5.13f). The AMV then entered a quiescent phase. The overpressure was not maintained high enough to keep fractures open and overpressure builds up again along the sealing faults, preventing further gas exsolution (Figure 5.13f).

Phase 7 – Present day geometry, after a succession of multiple phases of quiescence and activity, creating a complex interdigitated geometry where normal sedimentation predominates during quiescent phases of the volcano. When $\Delta u / \sigma'_v$ reaches the fracture opening threshold, further depletion happens in the source, triggering more collapse, while more mud is extruded at the seafloor during the active phases (Figure 5.13g).







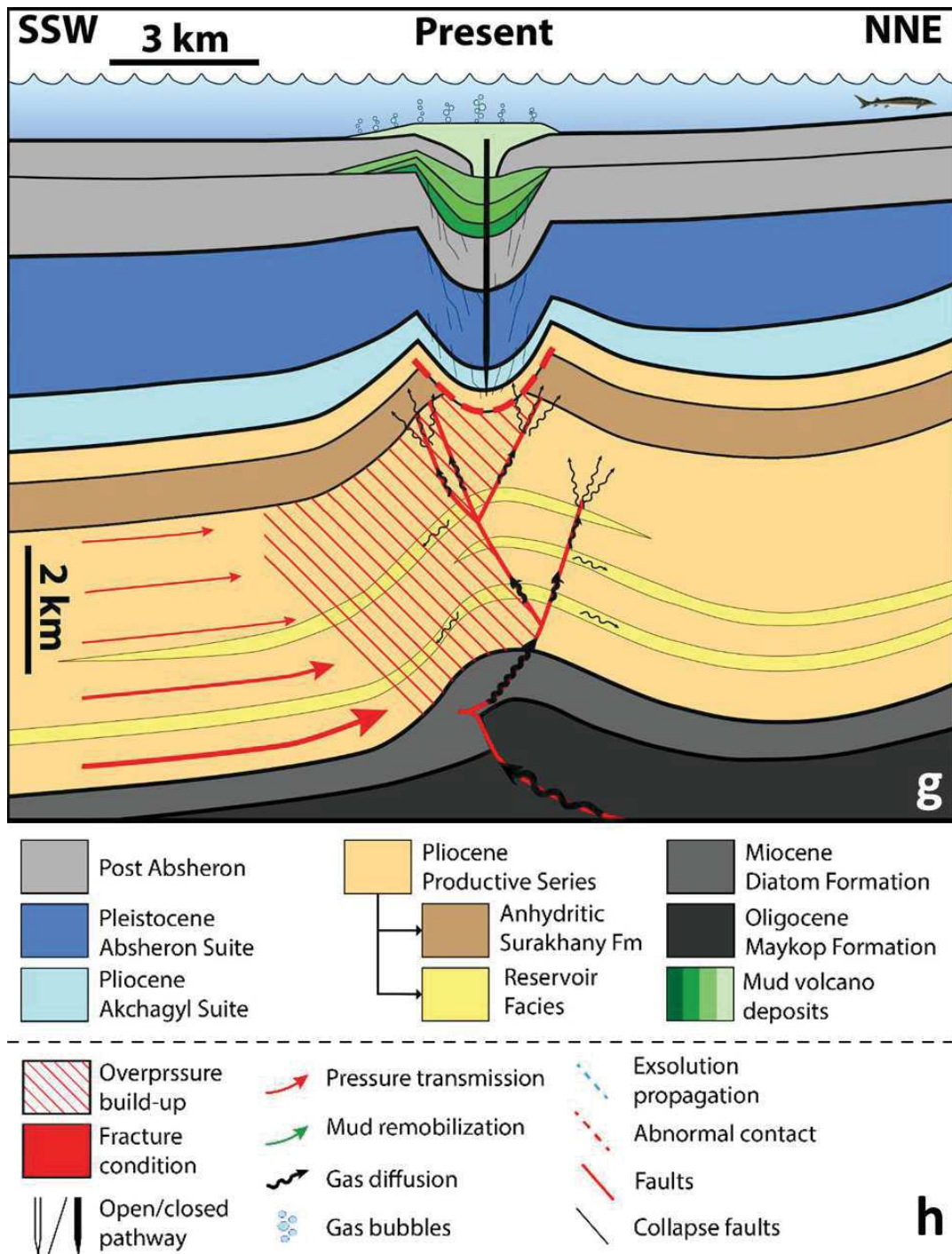


Figure 5.13: Formation model for the Absheron mud volcano based on in situ observations and measurements, sediment analysis, laboratory testing and mud generation and remobilization numerical modeling. Details of the different stages displayed in a, b, c, d, e, f and g are in the text. h: legend corresponding to a, b, c, e, f, g.

5. Conclusion

This chapter explored the possibility of simulating mud generation and extrusion processes through numerical modeling based on simple physical principles. The ultimate goal is to simulate the complete formation of the Absheron Mud Volcano (AMV) and to quantify the overpressure conditions and methane concentration that led to the present structure. A first model, considering 2D-diffusion laws (Darcy's law and Fick's law) was used to explain the location of the AMV as well as the conditions required to generate fluid mud from stratified solid sediments. The second model applies a fluid mechanics approach to test whether the sole impact of gas expansion on the mud density can lead to mud extrusion. The main results are:

- 1- The 2D-diffusion model showed that using sedimentation rates corrected from compaction to calculate overpressure in the deep basin and considering the low-permeability Anhydritic Surakhany Formation and sealing faults as flow baffles, critical fracture conditions are obtained at the crest of the Absheron anticline, below the ASF, where the depleted area was observed in Chapter 3.
- 2- A methane concentration of 5550 mM, injected at the base of the fault network considered as permeable in the vertical direction creates the conditions for triggering gas exsolution and subsequent loss in preconsolidation pressure showing that liquid mud is generated at depth.
- 3- Mud ascent up to the seafloor through the sole density-inversion provoked by gas expansion is possible over a period of 100 years minimum. This period of time for extrusion corresponds to extrusion rates measured at particular MVs.
- 4- To accelerate the process, additional parameters such as dynamic viscosity and the upward propagation of fracture as consequences of gas expansion have to be considered.

We show that simple physical models integrating realistic geological and hydro-mechanical parameters and behavior of sediments are able to reproduce the conditions that initiated the formation of the Absheron Mud Volcano. We simulated the key processes inferred from the available dense dataset and from the present geometry that were described in the conceptual model in Chapter 3. A dense and high-quality dataset is paramount to complete such models using the same methodology on other mud volcanoes located in similar contexts.

Chapter 6: Synthesis, conclusions and perspectives

Abstract

The dataset composed of geophysical data (seismic, bathymetry), in situ measurements and sediment cores, allowed to show that the Anhydritic Surakhany Formation and some other Upper Productive Series intervals are the source for the Absheron Mud Volcano. The study of pressure data and a preliminary numerical model proved that overpressure initiated by the regional high sedimentation rates associated to gas circulating along the fault system coring Absheron, would explain its formation. Experimental testing study using a new consolidation apparatus to saturate samples with carbonated water and to create free gas by decompression demonstrated the capacity of gas exsolution to transform compacted sediments into mud for a critical degree of gas saturation. Numerical models using simple physical diffusion equations and integrating results from observations, in situ measurements and laboratory testing results were able to reproduce the mud generation process at the Absheron location. Finally, fluid mechanics models show that mud extrusion through density inversion is possible.

Possible improvements to the developed methods have been identified. The dataset that could be improved through new processing and further analysis. The consolidation apparatus could be upgraded to support higher pressures and better simulate real geological stress conditions. Numerical models, notably the fluid mechanics approach, could be made more realistic, for instance by integrating a dynamic viscosity varying with gas expansion, and considering vertical fracture propagation due to mud overpressure which would significantly improve the mud extrusion simulation.

This study identified key parameters for mud volcano formation that are believed to be common to most of these structures and allowed developing a modeling approach that may be adapted and improved to describe mud volcanoes formation in other geological context.

1. Introduction

This chapter aims to synthesize the main conclusions of this study in order to directly answer the following initial questions posed in Chapter 1:

- Is it possible to locate the source of the Absheron mud volcano and define the physical mechanisms and geological conditions leading to its formation?
- Are gas exsolution and expansion alone able to generate mud from compacted sediments?
- Can a numerical model, integrating the behavior of gassy sediments under accurate geological conditions, simulate mud generation at depth and its remobilization towards the surface, and what is the critical degree of gas saturation required?

Moreover, this section insists on the limitations arising directly from the dataset, from the experimental study and from the numerical models. Further potential improvements are proposed and discussed. Finally, we examine the implications of this work in terms of future research on mud volcanoes, but also on the significance of mud volcanism for O&G exploration. Future perspectives for this study are also presented.

2. The formation of a mud volcano: a close relationship between gas and overpressure

2.1. The source of the Absheron Mud Volcano: intrinsic factors and external parameters

The subsurface geometry of the Absheron Mud Volcano (AMV) was studied using the 3D seismic volume covering the Absheron anticline. The main feature was the observation of the collapse of the stratigraphic layers into several truncated intervals, leading to a bowl-shaped geometry (Figure 3.5). Several normal faults flank the collapsed strata, with a V-shape oriented towards the truncated interval. This type of geometry has been already observed in other areas, under other mud volcanoes, such as in the Nile delta (Kirkham *et al.*, 2017b, 2017a), and offshore Nigeria (Dupuis *et al.*, 2019), but also at a neighboring anticline of Absheron, Shah Deniz, where there are several buried MVs (Dupuis, 2017). These authors interpreted this geometry as being the result of the collapse of strata into a “depletion zone” corresponding to the mud generation zone (Deville, 2009; Dupuis, 2017; Kirkham *et al.*, 2017b; Dupuis *et al.*, 2019). Therefore, the mud generation zone, i.e. the stratigraphic source of the VBA, correspond to the sediments that were initially comprised between the truncated surface and the base of the collapsed strata, currently reunited into a weld surface (Dupuis *et al.*, 2019).

This geometrical observation was confirmed by sediment analysis. The extruded mud recovered from surface coring and sediments from cutting samples from the Anhydritic Surakhany Formation (ASF) recovered during exploration drilling have similar mineralogy (Figure 3.12); biostratigraphic analysis of the extruded

mud confirmed its Pliocene origin, i.e. from the Productive Series. Thus, the AMV along with the examples from Dupuis (2017) confirm that the Maykop Formation is not the unique source for all the MVs present in the Caspian area as already discussed by Yusifov & Rabinowitz (2004). The source of the AMV therefore includes the ASF and some deeper intervals of the Upper Productive Series.

The ASF has several particularities that may explain why it is able to feed large MVs. This interval is composed by an interstratification of evaporite (anhydrite and halite) and clay-rich beds. Moreover, resistivity logs show that some of the clay-rich strata trapped between evaporites have very low resistivity, strongly suggesting high porosity and low density, themselves resulting from undercompaction. These intervals proved very difficult to drill due to swelling. Besides, pressure logs (Figure 3.14) make it clear that the ASF acts as a good seal for fluids, as overpressure develops along the interval, nearly reaching the fracture pressure and stays abnormally high below. Finally, temperature gradients estimated from measurements in the two exploration wells indicate that the ASF would have been at around 30°C at the time of the AMV formation, which is clearly below the limit for irreversible chemical compaction processes (Day-Stirrat *et al.*, 2010). Thus, the ASF is composed of evaporitic layers and under-compacted low-density and overpressured clay-rich strata. Besides, as the ASF is a good seal, the intervals directly below may be under-compacted as high sedimentation rates were recorded in the South Caspian Basin (SCB; Brunet *et al.*, 2007; Egan *et al.*, 2009; Green *et al.*, 2009) and the ASF would have prevented fluids to be expelled generating compaction disequilibrium (Osborne & Swarbrick, 1997; Wanzhong, 2007; Opara, 2011).

The seismic observation of fluvio-deltaic channels around the ASF (Figure 3.8) (Hinds *et al.*, 2004; Abreu & Nummedal, 2007) led to the conclusion that well-connected reservoirs exist and would have permitted gas migration towards the anticline crest over geological times. Structural restoration of the Absheron fold (Figure 3.9) indicates that overpressure due to the buoyancy of the maximum gas column that could be trapped at the initiation of the AMV was well below the fracturing pressure at the time. Therefore, external forcing phenomena were required to trigger the AMV formation.

From the monitoring of Lusi catastrophe (Tingay *et al.*, 2017), the combined effects of the damaging caused by gas exsolution and expansion and overpressure build-up seem to be key parameters for the formation of a MV. Javanshir *et al.* (2015) and Gautherot *et al.* (2015) identified a basin-scale pressure gradient oriented from the deep SCB where the Productive series are thick and dominantly fine-grained towards the northern edge of the basin where reservoirs crop out. This pressure gradient directly impacts the pressure recorded at the crest of anticlines and the resulting hydrodynamism (Hubbert, 1953) tilts gas-water contacts towards the northern flanks of the anticlines (Grosjean *et al.*, 2009; Gautherot *et al.*, 2015; Javanshir *et al.*, 2015). Moreover, the AMV is located at the crest of the Absheron anticline, above a normal-fault network connecting a deep thrusting system rooted in the overpressured Maykop Formation (the mature source rock of the SCB petroleum system; Smith-Rouch, 2006; Guliyev *et al.*, 2011) with the ASF. Faults, in particular normal faults are often regarded as vertical pathways for fluids (Gordon &

Flemings, 1998; Deville *et al.*, 2010; Wibberley *et al.*, 2017). The fault system rooting the Absheron crest can thus be regarded as pathways for methane migration. Therefore, along with the ASF intrinsic properties, overpressure and the presence of gas seems to be essential to explain the location of the AMV.

Consequently, the ASF and some other Upper Productive Series intervals are the source for the AMV. The location of the source is determined by intrinsic properties of the source stratigraphic interval but also by external parameters such as overpressure and gas migration.

2.2. Mud generation through gas exsolution

To understand the impact of gas exsolution on the hydro-mechanical properties of compacted sediments, we developed a novel consolidation system in order to replace sediment pore water by carbonated water before consolidation and to generate free gas by decompression. We tested several exsolution and preconsolidation conditions on mud samples reconstituted from surface sediments recovered from AMV mudflows. Results led to several conclusions.

First, fractures appeared during gas exsolution and their number correlates at first order with the degree of gas saturation, while preconsolidation pressure seems to control their length (Table 4-3). Therefore the damage of compacted sediments during gas exsolution depends both on its consolidation states and on the volume of gas that is exsolved. Various studies on bubble growth and shape in marine sediments yielded the same results. Boudreau *et al.*, (2005), Barry and Boudreau (2010) and Katsman (2015) demonstrate that bubble shape and size are mainly controlled by the mechanical properties of sediments. In particular, Katsman (2015) concludes that bubbles generating in weak sediments are small with higher surface-to-volume ratio (thin bubbles) while bubbles forming in stronger sediments tend to be larger and more spherical (larger).

Gas exsolution leads to sediment damage (fracture creation and loss of preconsolidation pressure). This sediment damage increases with the degree of gas saturation through an exponential relationship linking the degree of gas saturation to the normalized preconsolidation pressure (Figure 4.21). The same relationship was observed by Sultan *et al.* (2012) on sediments from the Gulf of Guinea. Other studies already showed the decrease in preconsolidation pressure with the degree of water saturation (Lunne *et al.*, 2001; Hight *et al.*, 2002). For Hight and Leroueil (2003), the loss of preconsolidation pressure is related to bubble growth in sediments. Sediment damage is in turn expected to reduce the shear strength of sediments as was observed from several experiments (Wheeler, 1988; Lunne *et al.*, 2001; Hight *et al.*, 2002; Sultan *et al.*, 2012). From the constitutive model proposed by Sultan & Garziglia (2014), where they show that preconsolidation pressure is the main controlling parameter for shear strength of the sediments, it is possible to infer that the damage caused to sediments from the AMV with gas exsolution will cause a subsequent decrease of their shear strength.

The acoustic response of damaged sediments remains degraded long after free gas has been compressed and dissolved during reloading (Figure 4.18). The presence of free gas is known to strongly affect acoustic signal propagation in sediments (Sills *et al.*, 1991; Helgerud *et al.*, 1999). However, the acoustic response of gassy sediments is theoretically supposed to link the trend of saturated sediments whenever S_g becomes equal to zero (Helgerud *et al.*, 1999). The presence of fractures is a known factor for attenuating P-wave velocities in the perpendicular direction (Anderson *et al.*, 1974; Kahraman, 2002; Leucci & Giorgi, 2006; Popp & Salzer, 2007). Fracture generation may trigger local changes in the shear modulus and/or the bulk modulus of the sediment (Huang *et al.*, 1995). Therefore, even after mechanical reloading and water saturation, long-term impact of fractures on the acoustic response is expected. Similarly, compressibility only recovers its normal trend when the initial preconsolidation pressure is exceeded (Figure 4.18). Previous experiments also highlighted a change of compressibility with the presence of gas bubbles in soft marine clays (Sills *et al.*, 1991; Nava Castro *et al.*, 2013; Liu *et al.*, 2016). They concluded that gas bubbles bear part of the load applied on the sample delaying consolidation. Hight and Leroueil (2003) demonstrated that once gas bubbles collapsed during reloading of a sample containing occluded gas bubbles, it recovers its normal compressibility. The difference in this study is that free gas is concentrated along fracture planes and is not in the form of occluded gas bubbles. The same observation can be made over permeability that starts to increase through fracture creation and deteriorates quickly due to the presence of gas bubbles forming capillary seals during reloading (Figure 4.20). These observations are in adequacy with past studies. The presence of fractures may enhance this permeability (Alfaro & Wong, 2001), but free gas in fine-grained sediments is a factor for permeability reduction (Egermann & Vizika, 2000; Naylor *et al.*, 2000; Hight & Leroueil, 2003; Jang & Santamarina, 2014). Besides, when free gas accumulates in clayey layers, a capillary seal may form (a gas cap) with an effective permeability even lower than the intrinsic permeability of the clayey layer (Revil *et al.*, 1998; Cathles, 2001).

For a degree of gas saturation higher than 38% sediments were entirely remolded after gas exsolution (entire loss of preconsolidation pressure, thus of shear strength; Figure 4.21), taking a slurry aspect (Figure 4.17). Their compressibility during reloading follows the virgin compaction curve of remolded sediments. This critical behavior after gas exsolution is interpreted as the result of mud generation from compacted sediments.

2.3. Integrated numerical models: mud generation and remobilization under geological conditions

In order to check the conceptual formation model proposed in Figure 3.18, the hypothesis of a regional-scale pressure gradient generated by high sedimentation rates in the deep basin (Egan *et al.*, 2009; Javanshir *et al.*, 2015) combined with methane circulation along fault systems was tested through integrated numerical model. To do so, we used simple 2D diffusion equations (Darcy's law and Fick's law) integrating 1D sedimentation-related overpressure generation, in situ physical parameters, geological observations and

mechanical properties of sediments from laboratory analysis. The corresponding model computes the 2D overpressure (Δu) distribution and evolution over time, as well as the $\Delta u/\sigma'_v$ allowing to compute hydrofracturing when it reaches a threshold defined from well data. The model also integrates Henry's law to simulate gas exsolution depending of pressure and the empirical relationship between the degree of gas saturation and the loss of preconsolidation obtained from laboratory testing. This type of diffusion modeling has already been applied to other sedimentary basins with the aim to explain the location of landslides or venting sites such as MVs (Dugan & Flemings, 2000; Kvalstad *et al.*, 2005; Hustoft *et al.*, 2009; Deville *et al.*, 2010).

Calculation results show that using accurate sedimentation rates and a structural compartmentation, through the low-permeability ASF and sealing faults, our model is able to reach critical fracture conditions at the Absheron crest, below the ASF, where the depleted area was observed in Chapter 3. The faults in the SCB were already described as having sealing capacities (Gautherot *et al.*, 2015; Javanshir *et al.*, 2015) while faults are often regarded as complex areas where permeability is anisotropic (Caine *et al.*, 1996; Evans *et al.*, 1997; Wibberley *et al.*, 2008). Hence, faults were considered as a medium with high vertical permeability, accounting for the advection of dissolved methane along the fault system, and low horizontal permeability. Previous fluid flow models already simulated faults as having anisotropic permeability (Dugan & Flemings, 2000; Schneider *et al.*, 2004; Deville *et al.*, 2010). An imposed high dissolved-methane concentration (5550 mM) at the base of the fault system was necessary to trigger gas exsolution and subsequent mud generation through loss in preconsolidation pressure at the anticline crest, below the ASF.

Therefore, numerical modeling using simple physical equations and integrating results from observations, in situ measurements and laboratory testing was able to reproduce the mud generation process at the Absheron location.

The process of remobilization of the mud to the surface was simulated using a fluid mechanics model, considering the impact of gas expansion, through the Boyle's law, on the density of the ascending mud. Thus, density inversion is regarded as the main driver for mud ascent towards the seafloor. The model solves modified Navier-Stokes equations (Tryggvason, 2012) to simulate in 2D the velocity of mud from its source up through the sedimentary column. The Navier-Stokes equations have already been used in several studies to model the mud flowing along a pipe, and to quantify mud discharge at the surface (Gisler, 2009; Zoporowski & Miller, 2009; Collignon *et al.*, 2018b). The method of resolution being very time consuming, 2D simulations were only applied to low mud viscosities, as the calculation time is proportional to the viscosity. In order to extrapolate the 2D simulations to values of viscosities corresponding to sedimentary rocks, simple 1D calculations were performed (Furbish, 1997).

Results of the study show that, considering the overpressure of the mud, it would take 100 years to the mud to reach the seafloor through density inversion. However, the example of Lusi catastrophe shows

that from the initial pressure kick recorded at the well to the initiation of the eruption at the surface, less than two days elapsed, implying a very fast mud remobilization process (Tingay *et al.*, 2017). Kopf & Behrmann (2000) estimated similar timing using examples from Mediterranean MVs. Moreover, field observations on eroded mud volcanoes onshore Azerbaijan showed that the feeding pipe of a mud volcano is composed of many dykes over a highly fractured area (Roberts *et al.*, 2010). Roberts *et al.* (2010) interpret these observations as being the result of hydrofracture opening through the ascension of the overpressured mud. The model we used does not explore the impact of gas expansion over the mud viscosity. Viscosity is often regarded as being highly dependent on the fluid content of the mud (Henry *et al.*, 1996; Kopf, 2002; Mazzini & Etiope, 2017), and mud viscosity at the extrusion can reach values as low as 10^3 kPa.s, which is significantly lower than the values used in our modeling. Besides, Collignon *et al.* (2018b) used a dynamic viscosity and showed the importance of this parameter over the mud discharge and flow rate in a pipe.

Therefore, our modeling shows that mud extrusion through density inversion is possible although after a time significantly longer than what was observed at Lusi. Considering extrusion rates at MV such as the Koturdag (onshore Azerbaijan) that expels high viscosity mud, our timing estimate is therefore valid for this type of MVs. The integration of a dynamic viscosity varying with gas expansion and the considerations of the impact of vertical fracture propagation through mud overpressure would significantly reduce this extrusion timing.

These numerical modeling results allowed to slide from a purely conceptual formation model for the AMV, towards a semi-quantitative model presenting kinetic considerations and magnitudes of the controlling physical parameters.

3. Possible further improvements

The current state of this research represents a compromise between physical realism and constraints due to the time frame of a PhD work. In the future, several improvements could be made to overcome the residual limitations of the current approach.

3.1. Dataset

Although the dataset used in this study is dense and quite complete and multidisciplinary, it has nonetheless limitations.

First, the mineralogy of the extruded mud was compared to the mineralogy of cuttings from the ASF that might have been polluted by the drilling mud, or have suffered from the cleaning process. As no cores were sampled over the Upper Productive Series interval, it is difficult to compare with a good degree of confidence the two mineralogies. Moreover, the mud samples at the AMV location may have been polluted by clasts from shallower intervals. Therefore, the comparison of two potentially polluted materials were

made. However, comparison were made over relative proportions of the main minerals, so this limitations does not impact our conclusion about the mud source, which relies mainly on other considerations, such as internal geometry. A possible improvement would be to carefully sieve mud samples in order to extract the coarse material and only keep the finer fraction and to compare with the lateral equivalent of the ASF located onshore (Azerbaijan) where the Productive Series outcrop.

Second, the biostratigraphy analysis could be improved to obtain a more precise age dating for the mud source. Age dating using biostratigraphy is complex in the Caspian Sea, as it was isolated from the world ocean during Pliocene (Krijgsman *et al.*, 2010; Forte & Cowgill, 2013). Charts for the Caspian Sea fauna exist but are not as complete as in other areas (Jones & Simmons, 1998). Moreover, very few specimens were found in the mud samples analyzed, showing the need for a more extensive biostratigraphic study of the mud.

Finally, the 3D seismic data was processed with the aim of imaging the deep geometry corresponding to the reservoirs that represent economic targets. The velocity model was improved to diminish the effects of shallow gas accumulations and low-velocity mud. However, the volume and surface represented by the mud volcano is too large, so masking occurred at the mud volcano location, preventing a good imaging of the MV plumbing system. Several reprocessing attempts were made by geophysicists from Total in order to settle this issue, but no real improvements were possible. Therefore, it might be necessary to acquire new seismic data over the AMV in order to get a more precise image of the center of the AMV plumbing system. As the Absheron field is about to start its production phase, it is not impossible that such acquisition may be done in a near future.

3.2. Experimental study

The following improvements to the consolidation apparatus used in the study could be considered.

In order to control visually the impacts of gas exsolution on the tested sediments, a Plexiglas cell was preferred to a more resistant material such as steel. Therefore, the conducted tests could not exceed 1300 kPa of vertical effective stress which correspond roughly to 50 meters of burial. Mud generation below the AMV happened at 2000 m below seafloor. This might be the strongest limitation of this study as the damage of sediments observed under experimental conditions was extrapolated to the geological conditions. Therefore, now that fracture geometry resulting from gas exsolution was observed, a new apparatus with more resistant material could be conceived to test gas exsolution at effective stress corresponding to greater depth. Sultan *et al.* (2010), for instance, led consolidation test on a triaxial reaching 60 MPa, the equivalent of 2600 m of burial. However, the high sedimentation rates in the SCB (Brunet *et al.*, 2007; Egan *et al.*, 2009) generated overpressured conditions even in shallow intervals as displayed in the pressure logs in Figure 3.14. Sedimentation-related overpressure in clay-rich intervals is related to compaction disequilibrium (Osborne & Swarbrick, 1997; Swarbrick *et al.*, 2002) leading to under-compacted intervals. The whole Miocene to

Quaternary interval in the SCB is known to be undercompacted (Smith-Rouch, 2006). At the Absheron location, normal compaction should happen over the first 500 m below seafloor, where no overpressure build-up has been recorded, while below, the consolidation is delayed due to compaction disequilibrium. Therefore, the new apparatus may be limited to an effective stress of 35-40 MPa corresponding to a burial ranging from 1500 to 1800 m.

The fracture geometry was analyzed from the visible external surface of the sample and may be more complex than what is described in Chapter 4. X-ray scanning would allow visualizing the internal fracture distribution and geometry. Besides, such a system would allow a precise quantification of the degree of gas saturation through a precise fracture volume quantification. Normal X-ray apparatus are not adapted as it would imply disassembling the consolidation cell before the end of testing. Hence, a special X-ray device has to be developed in order to be adapted to our consolidation apparatus. If a more resistant consolidation cell is developed, the material chosen should be able to transmit X-rays. Steel is therefore proscribed.

3.3. Numerical modeling

Numerical modeling developed for this study could now be improved in the following ways.

First, the 2D diffusion model only considers diffusive processes and ignores potential advection mechanisms through reservoirs or along the faults. Advection along faults was artificially reproduced by increasing their methane diffusivity, with ad hoc values of fracture porosity resulting in a local increase in permeability. It would be better to consider that local advective flow may arise from fracture creation. Due to the presence of the low-permeability ASF, simulated fractures could not propagate vertically with the current fracture simulation method. Moreover, the computation of sediment damage through gas exsolution is based on the laboratory testing results and should be updated with testing reaching higher effective stress values. The geometry used in the simulations correspond to the current geometry and has not been restored to the time of the AMV formation when the overburden was at least 1000 m thinner. The geometrical model could be improved by interpreting on regional seismic data the horizon corresponding to the base of the first mud volcano deposits.

The simulation of mud remobilization towards the surface has several major limitations that were partly discussed in Chapter 5. For instance, gas expansion does not only affect the sediment mass-density but also its viscosity. The mud viscosity would be able to change from 10^{12} to 10^3 kPa.s through gas expansion considering the estimations of Kopf & Behrmann (2000), increasing the mud flow rate. Nevertheless, this improvement would imply even greater calculation times. Thus, the numerical resolution method needs to be optimized in order to reduce the time needed to run a simulation. Moreover, the mud remobilization process is believed to occur as a combination between density inversion and fracture propagation (Kopf, 2002; Roberts *et al.*, 2010). Therefore, an improved version of the model needs to consider the impact of fracture propagation. As the combination of fluid mechanic models and rock failure models is still an active

field of research, an artificial approach of fractures may be a simpler solution. For instance, imposing a very low mass-density and viscosity in the fractured areas, a pattern implying that when a fracture is created it is instantly filled by mud.

4. Scientific implications and perspectives

This study of the AMV answered several scientific questions specific to this research. Broader implications and perspectives may arise from our conclusions.

Chapter 1 highlighted the specificities of each mud volcano that may form in very different geological context: their morphology, their mud source and their activity highly depends on their geological and physical background. Even two volcanoes over the same area could differ. For instance, on Absheron, the buried mud volcano differs slightly in its morphology, and has a different source from the AMV although they are located over similar structures. Similarly, Fowler *et al.* (2000) and Dupuis (2017) have shown that the ca. 10 buried MVs on the Shah Deniz anticline, have different morphologies and sources. Therefore, our study confirms the observations of Yusifov & Rabinowitz (2004) and the model of Deville (2009) that state that MVs are not necessary identical over a same area as a MV formation depends on a variety of factors such as the properties the underlying strata, the overpressure conditions, the structure development (fold and faults) and the presence of a mature source rock and of pathways to drive gas towards the stratigraphic source.

However, similarities are noted between these structures. For instance the overpressure and the presence of gas seem to be essential features accompanying the presence of MVs (Chapter 1). The monitoring of the Lusi eruption confirmed that the triggering mechanism of a MV may be the superimposition of overpressure and sediment damage through gas expansion resulting in hydrofracturing (Tingay *et al.*, 2017). Our observations, measurements and numerical modeling lead to the same conclusions. Instead of an overpressure building up vertically and over a very short period of time through an open borehole, overpressure builds up laterally over thousands to millions of years through under-compacted sedimentary layers, due to high sedimentation rates.

Thus, through this study of the AMV, we suggest that the formation of most of MVs should be directly linked to overpressure build-up over the fracture pressure and to the presence of gas at depth, which are necessary conditions in order to initiate sediment remobilization. The methodology that was developed for the AMV may be useful in the study of other MVs. This methodology mainly relies on the definition of the mud source and its connections to regional structures, the determination of the hydro-mechanical properties of the mud source and surrounding strata and the integration of these elements into their geological conditions through numerical modeling. Hence, some data are paramount to lead such a study. Notably a good-quality seismic dataset, information about the pressure field (through well data or regional models), a good knowledge of the regional background and sediments. Regarding sediments, to avoid the limitations

we had over our data, we would recommend to use accessible lateral equivalents of the modelled layers instead of mud from the volcano. These lateral equivalents could be found in the case of the SCB onshore for instance. It would allow to measure directly the hydro-mechanical parameters of each modeled layers.

In terms of industrial implications, the AMV model shows that the gas it expels does not come from the economic reservoirs. Thus, the presence of the AMV does not represent a potential economic risk for the production of the Lower Productive Series reservoirs. Besides Javanshir *et al.* (2015) did not observe any perturbation of the pressure field due to the presence of a MV at the neighboring ACG and Shah Deniz fields. It confirms that even MVs connected to targeted reservoirs should not represent an actual exploration risk. However, precautions need to be taken when drilling through the stratigraphic mud source of a mud volcano as it may be under-compacted, overpressured and saturated with gas, and represent therefore a potential source for pressure kicks and blowouts. Our study quantifies the criteria for the Absheron mud volcano formation notably in terms of hydrofracturing conditions. These criteria are dependent on the considered area and should be estimated and considered before drilling operations in sensitive strata (overpressured and undercompacted strata) in order to avoid catastrophes such as Lusi.

To our knowledge, this was the first time that 2D regional pressure models were used to explain the mud generation at depth. The present work considered only a basic source of overpressure related to sedimentation while other sources of overpressure generation may be involved. For instance, the regional tectonic activities may be an important source of pore fluid pressure as well as the clay-dehydration.

Mud volcanoes represent a complex field of research due to the complexity and diversity of these structures and their geological background. The formation of the AMV was interpreted from a dense dataset that is quite rarely available over mud volcanoes, but improvements are yet to be made in the applied methods and in data processing. This study defines and quantifies the physical processes leading to mud volcano formation and develops a numerical modeling approach that may be adapted and improved for other mud volcanoes.

Chapitre 6 : Synthèse, conclusions et perspectives

Résumé

L'étude pluri-disciplinaire du volcan de boue d'Absheron a permis de montrer que sa source correspond à la Formation du Surakhany Anhydritique et d'autres intervalles des *Upper Productive Series*. De plus, cette étude a permis de démontrer que la formation du volcan de boue s'expliquerait par l'association en crête de l'anticlinal d'Absheron de fortes surpressions, dues aux forts taux de sédimentation dans le bassin, et de la migration verticale de gaz le long des failles. Une étude expérimentale, se basant sur un nouveau système de consolidation de sédiments permettant de les saturer avec de l'eau saturée en CO₂ et ainsi de générer du gaz libre par dépressurisation, a démontré que l'exsolution de gaz peut transformer des sédiments compactés en boue pour un degré de saturation en gaz critique. En intégrant les observations, les mesures in situ, et les résultats de l'étude expérimentale dans un modèle numérique simple basé sur des équations de diffusion classiques, le processus de génération de la boue en profondeur a pu être simulé dans les conditions géologiques. Enfin, il a été démontré que l'extrusion de la boue par inversion de densité est possible grâce à un modèle de mécanique des fluides.

Des voies d'amélioration des méthodes développées dans cette étude ont été identifiées. Le jeu de données pourrait être amélioré grâce à de nouveaux traitements et au travers de nouvelles analyses. Des matériaux plus résistants pourraient être utilisés pour que l'appareil de consolidation puisse supporter des pressions plus élevées et ainsi approcher l'état de contrainte en condition géologique. Les modèles numériques, notamment l'approche en mécanique des fluides, pourraient être plus réalistes en prenant par exemple en compte une viscosité qui varie avec l'expansion du gaz et en considérant la propagation verticale de fractures due à la surpression dans la boue. Cela améliorerait de façon significative la simulation d'extrusion de la boue.

Cette étude a permis d'identifier les paramètres clés contrôlant la formation d'un volcan de boue, qui seraient commun à la plupart de ces structures. Une méthode de modélisation a été développée et elle peut être adaptée et améliorée afin de simuler la formation de volcans de boue dans des contextes différents.

1. Introduction

Ce chapitre vise à synthétiser les conclusions principales de cette étude afin de directement répondre aux trois questions initialement posées dans le chapitre 1 :

- Est-il possible de définir la source du volcan de boue d'Absheron et de déterminer les mécanismes physiques et les conditions géologiques ayant mené à sa formation ?
- Est-ce que l'exsolution et l'expansion du gaz peuvent, à elles seules, générer de la boue à partir de sédiments compactés ?
- Un modèle numérique intégrant le comportement des sédiments gazeux dans les bonnes conditions géologiques peut-il simuler la génération de la boue en profondeur et sa remobilisation vers la surface, et quelle est le degré de saturation en gaz critique nécessaire ?

De plus, cette section met l'accent sur les limitations découlant directement du jeu de données, de l'étude expérimentale ou de la modélisation numérique. Des voies d'amélioration potentielles sont proposées et discutées. Enfin, les implications de ce travail en termes de future recherche sur les volcans de boue mais aussi en termes de l'importance des volcans de boue dans l'exploration d'hydrocarbures sont détaillées. Les perspectives directes de cette étude sont aussi présentées.

2. La formation d'un volcan de boue : une relation étroite entre le gaz et la surpression

2.1. La source du volcan de boue d'Absheron : facteurs intrinsèques et paramètres extérieurs

La géométrie souterraine du volcan de boue d'Absheron (VBA) a été décrite en utilisant la sismique 3D qui couvre l'anticlinal d'Absheron. L'observation principale est l'effondrement d'une partie de la colonne sédimentaire dans certains intervalles stratigraphiques tronqués, formant une géométrie en forme de bol (Figure 3.5). Plusieurs failles normales entourent la zone d'effondrement, formant une géométrie en « V » orientée vers la zone tronquée. Ce type de géométrie a été observée sous d'autres volcans de boue (VB), dans d'autres zones comme dans le delta du Nil (Kirkham *et al.*, 2017b, 2017a) et au large du Nigeria (Dupuis *et al.*, 2019), mais aussi sur un anticlinal voisin d'Absheron, Shah Deniz, où plusieurs volcans enfouis ont été étudiés (Dupuis, 2017). Ces auteurs ont interprété cette géométrie comme étant le résultat d'un effondrement des strates sédimentaires dans une zone de déplétion correspondant à la zone de génération de la boue (Deville, 2009; Dupuis, 2017; Kirkham *et al.*, 2017b; Dupuis *et al.*, 2019). Par conséquent, la zone de génération de la boue, c'est-à-dire la source stratigraphique du VBA correspondrait aux sédiments initialement compris entre la surface de troncature et la base de la série effondrée, actuellement réunies un une surface de soudure (Dupuis *et al.*, 2019).

Cette observation géométrique est confirmée par l'analyse des sédiments. La boue récupérée par des carottages de sédiments à la surface du VBA et les sédiments extraits des déblais des forages d'exploration provenant de la Formation du Surakhany Anhydritique (ASF) présentent une minéralogie similaire (Figure 3.12) ; l'analyse du contenu biostratigraphique de la boue confirme son origine Pliocène, c'est-à-dire des Séries Productives. Le VBA et les exemples de volcans enfouis de Shah Deniz présentés par Dupuis (2017) confirment donc que la Formation Maykop n'est pas la seule source possible pour les volcans de boue présents dans le Bassin sud caspien comme cela avait déjà été discuté par Yusifov & Rabinowitz (2004). La source du VBA inclut par conséquent l'ASF et certains intervalles plus profonds des Séries Productives Supérieures.

L'ASF présente plusieurs particularités qui pourraient expliquer pourquoi elle alimente de grands VB. Cet intervalle est formé par une interstratification de couches évaporitiques (anhydrite et halite) et de lits argileux. De plus, les logs de résistivité montrent que certains des lits argileux pris au piège entre des couches évaporitiques présentent une très faible résistivité, suggérant une forte porosité et une faible densité, résultant directement d'un processus de sous-compaction. Le gonflement de ces argiles a induit des difficultés de forage. De plus, les enregistrements de pression aux puits (Figure 3.14) montrent clairement que l'ASF agit comme une excellente couverture pour les fluides, la surpression augmentant nettement le long de l'ASF, atteignant presque la pression de fracturation et restant anormalement haute en-dessous. Enfin, une estimation du gradient de température lors de la formation du VBA, extrapolé à partir des mesures faites aux puits indique une température de l'ASF proche de 30°C, nettement en-dessous du seuil à partir duquel les processus irréversibles de compaction chimiques s'appliquent (Day-Stirrat *et al.*, 2010). Donc, l'ASF est formé de couches d'évaporites et de lits argileux sous-compactés, à faible densité et en surpression. De plus, cette formation étant une bonne couverture, les intervalles sous-jacents pourraient être sous-compactés du fait du fort taux de sédimentation enregistré dans le Bassin sud caspien (SCB ; Brunet *et al.*, 2007; Egan *et al.*, 2009; Green *et al.*, 2009). La présence de l'ASF aurait empêché les fluides d'être expulsés suffisamment rapidement, conduisant à un déséquilibre de compaction (Osborne & Swarbrick, 1997; Wanzhong, 2007; Opara, 2011).

L'observation en sismique de chenaux fluvio-deltaïques autour de l'ASF (Figure 3.8) (Hinds *et al.*, 2004; Abreu & Nummedal, 2007) a permis de conclure à la présence de réservoirs bien connectés qui auraient permis la migration de gaz vers la crête de l'anticlinal au cours du Quaternaire. La restauration de la structure du pli d'Absheron au moment de l'activation du VBA (Figure 3.9) indique que la poussée engendrée par la colonne de gaz maximale qui aurait pu être stockée dans ce réservoir aurait été bien en dessous de la valeur de la pression de fracturation. De ce fait, un forçage extérieur est nécessaire pour expliquer la mise en place du VBA.

A partir des enregistrements réalisés pendant la catastrophe de Lusi (Tingay *et al.*, 2017), l'effet combiné de l'endommagement causé par l'exsolution du gaz et son expansion sur les sédiments et de l'augmentation de la surpression semble avoir été déterminant dans la formation du VB. Javanshir *et al.*

(2015) et Gautherot *et al.* (2015) ont identifié un gradient de pression à l'échelle du bassin orienté de la partie profonde du SCB où les Séries Productives sont les plus épaisses et constitués essentiellement de sédiments fins vers les bords du bassin où cet intervalle affleure. Ce gradient de pression affecte directement les pressions enregistrées en crête des anticlinaux et l'hydrodynamisme qui en résulte (Hubbert, 1953) décale le contact entre les accumulations de gaz et l'eau vers le nord de ces structures (Grosjean *et al.*, 2009; Gautherot *et al.*, 2015; Javanshir *et al.*, 2015). Le VBA est localisé à la crête de l'anticlinal d'Absheron, au-dessus du réseau de failles normales qui relie le système chevauchant profond ancré dans la Formation Maykop en surpression (la roche mère mature du système pétrolier du SCB ; Smith-Rouch, 2006; Guliyev *et al.*, 2011) avec l'ASF. Les failles, et en particulier les failles normales sont souvent considérées comme des conduits permettant la migration verticale des fluides (Gordon & Flemings, 1998; Deville *et al.*, 2010; Wibberley *et al.*, 2017). Le réseau de failles au cœur de l'anticlinal d'Absheron peut donc être considéré comme un chemin de migration pour le méthane générée dans le Maykop. Par conséquent, la surpression et la présence de gaz semblent être des facteurs déterminants pour expliquer la localisation du VBA.

En conclusion, l'ASF ainsi que d'autres intervalles des Séries Productives Supérieures sont la source du VBA. La localisation de la source est contrôlée par des caractéristiques propres à l'intervalle stratigraphique source mais aussi par des paramètres externes comme la surpression et la migration du gaz.

2.2. La génération de boue par exsolution de gaz

Pour comprendre l'effet de l'exsolution du gaz sur les propriétés hydromécaniques des sédiments compactés, un nouveau système de consolidation a été mis au point afin de remplacer l'eau de pore par de l'eau saturée en CO₂ avant consolidation et ainsi pouvoir générer du gaz libre par dépressurisation. Plusieurs conditions d'exsolution et de préconsolidation ont été testées sur des échantillons de boue reconstitués à partir des sédiments de surface prélevés sur les coulées du VBA. Les résultats de l'étude mènent aux conclusions suivantes :

Premièrement, l'exsolution du gaz induit une fracturation des échantillons. Leur nombre est directement lié au degré de saturation en gaz atteint dans l'échantillon, alors que leur longueur semble contrôlée par la préconsolidation atteinte avant exsolution (Table 4-3). L'endommagement des sédiments compactés lors d'une exsolution de gaz dépend donc de l'état de consolidation des sédiments et du volume de gaz généré. Plusieurs études sur la croissance et la forme des bulles de gaz dans les sédiments marins ont mené aux mêmes conclusions. Boudreau *et al.*, (2005), Barry and Boudreau (2010) et Katsman (2015) démontrent que la forme et la taille des bulles de gaz sont essentiellement contrôlées par les propriétés mécaniques du sédiment. Katsman (2015) conclut que les bulles générées dans des sédiments peu résistants sont petites et allongées, alors que celles générées dans un sédiment plus résistant sont plus larges et arrondies.

L'exsolution du gaz provoque un endommagement des sédiments (création de fractures et perte de la pression de préconsolidation). Cet endommagement augmente exponentiellement avec le degré de saturation en gaz (loi exponentielle liant le degré de saturation en gaz à la pression de préconsolidation normalisée ; Figure 4.21). Une relation similaire avait été observée par Sultan *et al.* (2012) sur des sédiments provenant du Golfe de Guinée. D'autres études ont déjà montré cette baisse de la pression de préconsolidation avec le degré de saturation (Lunne *et al.*, 2001; Hight *et al.*, 2002). Pour Hight & Leroueil (2003) cette baisse est directement liée à la croissance des bulles de gaz dans les sédiments. Cet endommagement provoquerait à son tour une diminution de la résistance au cisaillement des sédiments comme démontré lors de plusieurs études (Wheeler, 1988; Lunne *et al.*, 2001; Hight *et al.*, 2002; Sultan *et al.*, 2012). A partir du modèle de Sultan & Garziglia (2014) qui montre que la résistance au cisaillement des sédiments est principalement fonction de leur pression de préconsolidation, on peut déduire que l'endommagement causé sur les sédiments du VBA par l'exsolution du gaz provoque une réduction de leur résistance au cisaillement.

La réponse acoustique des sédiments endommagés demeure perturbée longtemps après la disparition du gaz libre par compression et dissolution lors de la recharge de l'échantillon (Figure 4.18). La présence de gaz libre est un facteur connu d'atténuation des ondes acoustiques dans les sédiments (Sills *et al.*, 1991; Helgerud *et al.*, 1999). Cependant, la réponse acoustique des sédiments gazeux est censée rejoindre celle des sédiments saturés lorsque le degré de saturation en gaz devient nul (Helgerud *et al.*, 1999). La présence de fractures est également un facteur connu d'atténuation et de dispersion des ondes acoustiques dans la direction perpendiculaire à l'allongement des fractures (Anderson *et al.*, 1974; Kahraman, 2002; Leucci & Giorgi, 2006; Popp & Salzer, 2007). La création de fractures peut provoquer des modifications localisées du module de cisaillement et/ou du module de compression des sédiments (Huang *et al.*, 1995). Par conséquent, un impact durable des fractures sur la réponse acoustique est possible, même après compaction de l'échantillon et disparition du gaz libre. De même, la compressibilité des sédiments ne retrouve sa valeur initiale que lorsque la pression préconsolidation initialement atteinte avant exsolution est dépassée (Figure 4.18). D'autres expériences ont également mis en évidence ce changement de compressibilité dû à la présence de gaz libre dans des sédiments marins argileux (Sills *et al.*, 1991; Nava Castro *et al.*, 2013; Liu *et al.*, 2016). Elles concluent que les bulles de gaz supportent en partie la charge appliquée sur l'échantillon, retardant sa consolidation. Hight & Leroueil (2003) ont démontré qu'une fois que les bulles de gaz isolées dans la matrice sédimentaire disparaissent, l'échantillon retrouve sa compressibilité normale. La différence dans notre étude est que le gaz libre n'est pas présent sous forme de bulles isolées mais se concentre le long des plans de fractures. La même observation a été faite sur la perméabilité des sédiments qui commence par augmenter de façon significative lors de l'ouverture des fractures pour diminuer rapidement à cause de l'accumulation de gaz libre formant des barrières capillaires lors de la consolidation (Figure 4.20). Ces observations sont en accord avec les résultats de précédentes études. La présence de fracture peut en effet augmenter la perméabilité d'un sédiment (Alfaro & Wong, 2001), mais la présence de gaz libre dans des

sédiments fins est un facteur de réduction de cette perméabilité (Egermann & Vizika, 2000; Naylor *et al.*, 2000; Hight & Leroueil, 2003; Jang & Santamarina, 2014). De plus, quand du gaz libre s'accumule le long de couches argileuses, une barrière capillaire peut se former générant une perméabilité effective plus basse que la perméabilité propre au sédiment. (Revil *et al.*, 1998; Cathles, 2001).

Pour un degré de saturation en gaz supérieur à 38%, les sédiments sont entièrement remaniés par l'exsolution du gaz (perte complète de leur pression de préconsolidation et donc de leur résistance au cisaillement ; Figure 4.21) et prennent l'apparence de boue (Figure 4.17). Leur compressibilité durant la recompaction suit la courbe de compaction initiale obtenue initialement à partir des échantillons reconstitués et remaniés. Ce comportement critique est interprété comme le résultat de la génération de boue à partir de sédiments compactés.

2.3. Modèles numériques intégrés : génération et remobilisation de la boue dans les conditions géologiques

Afin de vérifier la validité du modèle conceptuel de formation du VBA proposé en Figure 3.18, nous avons testé l'hypothèse d'un gradient de pression régional généré par les forts taux de sédimentation dans le bassin profond (Egan *et al.*, 2009; Javanshir *et al.*, 2015) combiné avec la circulation de méthane au travers du réseau de failles à l'aide de modèles numériques intégrés. Des équations de diffusion en deux dimensions (loi de Darcy et de Fick), intégrant la génération de surpression liée à la sédimentation en 1D, les mesures physiques in situ, les observations géologiques ainsi que les propriétés mécaniques des sédiments obtenues en laboratoire, ont été utilisées à cet effet. Ce modèle numérique calcule en 2D la distribution et l'évolution au cours du temps de la surpression (Δu) ainsi que du rapport $\Delta u/\sigma'_v$ permettant de simuler la création d'hydrofractures lorsque ce rapport atteint un seuil défini à partir des données de puits. Le modèle intègre également la loi de Henry pour simuler l'exsolution du gaz en fonction de la pression et de la température ainsi que la relation empirique entre le degré de saturation en gaz et la baisse pression de préconsolidation obtenue grâce aux essais en laboratoire. Ce type de modèle de diffusion a déjà été appliqué à d'autres bassins sédimentaires afin d'expliquer la localisation de glissements sous-marins ou de zone de dégazage comme les volcans de boue (Dugan & Flemings, 2000; Kvalstad *et al.*, 2005; Hustoft *et al.*, 2009; Deville *et al.*, 2010).

Les résultats des simulations montrent qu'en utilisant les bons taux de sédimentation et en compartimentant la géométrie au travers d'une couche à faible perméabilité comme l'ASF et au travers de failles bloquantes, notre modèle permet d'atteindre les conditions de fracturation à la crête de l'anticlinal d'Absheron, sous l'ASF, là où la zone de déplétion a été observée au chapitre 3. Les failles dans le SCB ont déjà été décrites comme étant bloquantes (Gautherot *et al.*, 2015; Javanshir *et al.*, 2015), et les failles sont souvent décrites comme étant des zones complexes où la perméabilité est anisotrope (Caine *et al.*, 1996; Evans *et al.*, 1997; Wibberley *et al.*, 2008). De ce fait, les failles ont été modélisés comme un milieu avec une perméabilité verticale importante, permettant de prendre en compte les phénomènes d'advection le long

des failles, et une perméabilité horizontale faible. De précédents modèles d'écoulements dans les bassins avaient déjà modélisés les failles avec une anisotropie de perméabilité (Dugan & Flemings, 2000; Schneider *et al.*, 2004; Deville *et al.*, 2010). Une forte concentration initiale en méthane dissous au niveau de la source (5550 mM) est nécessaire afin de déclencher une exsolution et ainsi la génération de la boue à la crête de l'anticlinal, sous l'ASF, lors de l'ouverture des fractures.

Par conséquent, un modèle numérique fondé sur des principes physiques simples et intégrant les résultats des observations, des mesures in situ et des essais et analyses en laboratoire a permis de simuler la génération de boue au niveau du VBA.

Le processus de remobilisation de la boue vers la surface a été simulé en utilisant un modèle de mécanique des fluides qui considère l'impact de l'expansion du gaz (au travers de la loi de Boyle-Mariotte) sur la densité de la boue lors de sa remontée. L'inversion de densité est donc considérée dans cette étude comme étant le moteur principal de la remontée de la boue vers la surface. Le modèle (Tryggvason, 2012) résout les équations de Navier-Stokes modifiées pour prendre en compte l'effet du gaz sur la densité de la boue et calcule la vitesse de remontée de la boue de sa source jusqu'à la surface. Ces équations ont déjà été utilisées dans plusieurs études afin de modéliser la circulation de la boue le long de conduits et pour quantifier la quantité de boue rejeté en surface (Gisler, 2009; Zoporowski & Miller, 2009; Collignon *et al.*, 2018b). Dans la méthode de résolution choisie, le temps de calcul est proportionnel à la viscosité. En conséquence, les simulations en 2D n'ont été réalisées que pour des viscosités faibles, les résultats ont été extrapolés à des valeurs correspondant à la viscosité des roches sédimentaires à partir de calculs simples en 1D utilisant la méthode de Furbish (1997).

Les résultats de cette analyse démontrent qu'en considérant la surpression de la boue il faut 100 ans pour que la boue atteigne le fond de mer par simple inversion de densité. Cependant, l'exemple de Lusi a montré que moins de deux jours s'étaient passés entre le pic de pression enregistré au puits et le début de l'éruption en surface, ce qui implique un processus de remobilisation très rapide (Tingay *et al.*, 2017). Kopf & Behrmann (2000) ont obtenu des ordres de grandeur similaires pour des VB situés en Méditerranée. De plus, des observations de terrain sur des volcans à terre érodés en Azerbaïdjan ont montré que le conduit d'alimentation des volcans est en fait constitué de plusieurs dykes sur une zone intensément fracturée (Roberts *et al.*, 2010). Roberts *et al.* (2010) interprètent ces observations comme le résultat de l'hydrofracturation déclenchée par la remontée de la boue en surpression. Le modèle actuel ne prend pas en compte l'effet de l'expansion du gaz sur la viscosité de la boue. Or la viscosité dépend largement de la quantité de fluides présents dans la boue (Henry *et al.*, 1996; Kopf, 2002; Mazzini & Etiope, 2017), la viscosité de la boue en surface ayant été mesurée à 10^3 kPa.s ce qui est bien plus bas que les valeurs utilisées dans cette étude. De plus, Collignon *et al.* (2018b) ont utilisé dans leur modèle une viscosité dynamique et ils montrent l'importance de ce paramètre sur le débit de la boue dans les conduits.

En conclusion, notre modèle montre que la seule inversion de densité suffit à remonter la boue jusqu'en surface en une durée significativement supérieure à ce qui a été observée à Lusi. Cependant, des VB comme le Koturdag (Azerbaïdjan) présentent un débit de sortie très faible avec une boue très visqueuse. En considérant ce débit de sortie comme étant la vitesse de la boue dans les conduits, notre estimation de 100 ans est dans le bon ordre de grandeur pour ce type de volcans. En prenant en compte une viscosité qui dépend de l'expansion du gaz et en considérant la possibilité de former des réseaux de fractures verticales au fur et à mesure de la remontée de la boue en surpression, la durée pour que la boue atteigne le fond marin devrait être réduite de façon significative.

Ces résultats permettent de passer d'un modèle purement conceptuel de formation du VBA à un modèle semi-quantitatif prenant en compte la dynamique des processus et les ordres de grandeurs des paramètres physiques contrôlant la formation du volcan.

3. Axes d'amélioration

L'état actuel de ce travail de recherche représente un compromis entre réalisme physique et les contraintes liées à la durée limitée d'un travail de thèse de doctorat. A l'avenir, plusieurs améliorations pourraient être faites afin de dépasser les limitations restantes de cette étude.

3.1. Le jeu de données

Le jeu de données, bien que dense, assez complet et multidisciplinaire, présente néanmoins des limites.

Premièrement, la minéralogie de la boue du VBA a été comparée à la minéralogie de l'ASF observée sur les déblais de forage des puits d'exploration. On sait que ces déblais ont été pollués par la boue de forage et/ou dégradés lors du processus de nettoyage. Comme aucune carotte n'a été prélevée dans les Séries Productives Supérieures au niveau des puits, la comparaison précise entre les deux minéralogies reste difficile. De plus, la boue du volcan a pu être contaminée par des clastes arrachés à des niveaux stratigraphiques moins profonds lors de la remontée de la boue. La comparaison a donc été réalisée à partir d'échantillons probablement en partie pollués par des éléments extérieurs. Néanmoins, la comparaison a été faite sur les proportions relatives des différents types de minéraux et non sur des valeurs absolues. Donc ce biais ne doit pas influencer nos conclusions sur l'origine stratigraphique de la boue qui est déduite d'autres éléments comme l'observation de la zone de déplétion. Une amélioration faisable serait de tamiser avec précaution la boue afin de ne garder que la fraction fine et de comparer cela à la minéralogie d'équivalents latéraux de l'ASF, les Séries Productives étant à l'affleurement à terre (Azerbaïdjan).

Deuxièmement, l'analyse biostratigraphique pourrait être améliorée afin d'obtenir une datation plus précise de la source de la boue. La datation biostratigraphique dans la région de la Mer Caspienne est

complexe car la Mer Caspienne a été isolée du reste des masses océaniques durant le Pliocène (Krijgsman *et al.*, 2010; Forte & Cowgill, 2013). Des chartes biostratigraphiques pour cette région existent mais sont moins complètes que dans d'autres zones (Jones & Simmons, 1998). De plus, peu de spécimens ont été retrouvés dans les échantillons de boue analysés ce qui montre la nécessité de mener une étude biostratigraphique de la boue plus poussée, par exemple avec une approche quantitative.

Enfin, le traitement de la sismique 3D a été réalisé dans le but d'imager les structures profondes où les réservoirs économiquement intéressants se situent. Le modèle de vitesse a été amélioré pour diminuer les effets de la présence d'accumulations de gaz peu profondes et de l'effet de masquage lié à la présence de la boue. Cependant, le volume de boue est si important que cet effet de masquage n'a pas pu être réglé, empêchant d'imager correctement la partie souterraine du VBA. Plusieurs traitements différents ont été testés par les géophysiciens de Total afin de résoudre ce problème sans succès. Dans l'hypothèse qu'une nouvelle acquisition soit faite sur zone, je recommanderais de reprendre l'interprétation sismique du VBA afin d'affiner la géométrie de la source, d'en estimer son volume et d'observer les éventuels conduits et ainsi résoudre un certain nombre d'incertitudes liées à la mauvaise transmission du signal sismique sous le volcan.

3.2. Etude expérimentale

Les améliorations suivantes sur le système de consolidation utilisé lors de cette étude peuvent être considérées.

Afin de contrôler visuellement l'impact de l'exsolution du gaz sur les sédiments, une cellule en Plexiglas a été utilisée plutôt qu'une cellule plus résistante. C'est pourquoi les essais ne pouvaient pas dépasser les 1300 kPa de contrainte effective, ce qui correspond aux conditions subies par un sédiment enfoui sous 50 mètres. La zone de génération de la boue se situe à environ 2000 m sous le VBA. Cette limite est sans doute la plus importante de cette étude car l'endommagement observés dans les conditions expérimentales a été extrapolée aux conditions géologiques. Maintenant que la géométrie des fractures générés lors de l'exsolution a été observée, une nouvelle cellule de consolidation pourrait être construite avec des matériaux plus résistants afin de tester l'effet de l'exsolution dans des conditions de contrainte correspondant à des profondeurs proches des conditions géologiques. Sultan *et al.* (2010) a par exemple mené des tests de consolidations sur une cellule triaxiale permettant d'atteindre 60 MPa, l'équivalent de 2600 m d'enfouissement. Néanmoins, les forts taux de sédimentation observés dans le SCB (Brunet *et al.*, 2007; Egan *et al.*, 2009) ont généré des conditions de surpression même dans les intervalles sédimentaires les moins profonds comme le montre la Figure 3.14. La surpression générée par de forts taux de sédimentation est liée au déséquilibre de compaction (Osborne & Swarbrick, 1997; Swarbrick *et al.*, 2002) qui entraîne une sous-compaction des couches sédimentaires. L'intervalle Miocène-Quaternaire dans le SCB est connu pour être sous-compacté (Smith-Rouch, 2006). Au niveau d'Absheron, la compaction normale devrait se produire dans les 500 premiers mètres qui sont à la pression hydrostatique, alors que l'ensemble de la colonne sédimentaire

sous-jacente doivent être sous-compactée au vu des fortes surpressions enregistrées. Par conséquent, le nouveau système pourrait se limiter à des contraintes de 35-40 MPa, correspondant à un enfouissement compris entre 1500 et 1800m.

L'analyse de la géométrie des fractures a été réalisée au travers du Plexiglas et correspond à la surface visible des échantillons. De ce fait, la géométrie des fractures pourrait être plus complexe que ce qui a été décrit dans le chapitre 4. Des mesures utilisant des rayons X permettraient de visualiser leur structure interne. Un tel système permettrait aussi une quantification plus précise du degré de saturation en gaz grâce à une quantification précise du volume représenté par les fractures. Les appareils conventionnels de mesures aux rayons X ne sont pas adaptés car ils impliqueraient de démonter la cellule de consolidation avant la fin de l'essai. Donc, un système de mesure dédié devrait être développé afin de rendre possible ces mesures sur nos essais. Il faudra de ce fait choisir un matériau laissant passer les rayons X si le choix est fait de développer une cellule plus résistante.

3.3. Modélisation numérique

Les modèles numériques développés lors de cette étude peuvent être améliorés en intégrant les considérations suivantes.

Premièrement, le modèle de diffusion 2D ne considère que les processus diffusifs et ignore les potentiels phénomènes d'advection le long de réservoirs perméables ou le long des fractures. L'advection le long des failles et des fractures a été artificiellement reproduite en augmentant leur diffusivité moléculaire du méthane et en imposant une porosité de fracture arbitraire conduisant à une augmentation localisée de la perméabilité. Il serait mieux de considérer l'apparition locale de circulation de fluides par advection lors de la création de fractures. Avec la façon actuelle de modéliser les fractures, la présence de l'ASF empêche leur propagation verticale. De plus, le calcul de l'endommagement des sédiments lors de l'exsolution est basé sur les résultats des essais en laboratoire et devrait être mis à jour avec les résultats d'essais atteignant des contraintes plus élevées. La géométrie utilisée dans le modèle correspond à la géométrie actuelle et n'a pas été restaurée comme elle était à l'époque de la formation du VBA alors que la source était enfouie sous une colonne sédimentaire moins épaisse de 1000 m. Cette géométrie pourrait être améliorée en interprétant sur les données sismiques régionales l'horizon correspondant à la base des premiers dépôts du volcan de boue.

La simulation de la remobilisation de la boue vers la surface présente plusieurs limites majeures qui ont été en partie discutées dans le chapitre 5. Par exemple, l'expansion du gaz n'affecte pas que la densité de la boue mais aussi sa viscosité. Cette viscosité pourrait ainsi passer de 10^{12} à 10^3 kPa.s en considérant les estimations de Kopf & Behrmann (2000) ce qui augmenterait la vitesse de remontée de la boue. Cette amélioration impliquerait cependant une augmentation significative des temps de calcul qui sont déjà très long. Par conséquent, la méthode de résolution numérique devrait d'abord être optimisée afin de réduire ces temps de calculs. De plus, des études montrent que la remobilisation de la boue est due à une

combinaison d'inversion de densité et de propagation de fractures (Kopf, 2002; Roberts *et al.*, 2010). Donc, une des améliorations possibles du modèle actuel serait de considérer l'impact de cette propagation de fractures. La combinaison de concepts de mécanique des fluides avec des concepts de mécanique des roches dans un modèle numérique est un sujet de recherche complexe, donc une prise en compte artificielle de ces fractures serait un moyen plus simple de simuler leur propagation. Par exemple, en imposant une faible densité et viscosité aux zones de fracture (lorsque la pression de fracturation est dépassée), ce qui implique que les fractures sont instantanément envahies par la boue.

4. Implications scientifiques et perspectives de cette étude

Cette étude du VBA a permis de répondre à des questions scientifiques spécifiques à ce travail de recherche. Des implications et des perspectives plus larges peuvent être déduites de nos conclusions.

Le chapitre 1 a mis en lumière les spécificités de chaque VB qui peuvent être présents dans des contextes géologiques très différents : leur morphologie, leur source et leur activité dépendent de leur contexte géologique et les conditions physiques où ils se situent. Deux volcans localisés dans une même région peuvent être différents. Par exemple, sur l'anticlinal d'Absheron, la morphologie du VB enfoui diffère de celle du VBA et a une source différente. De la même façon Fowler *et al.* (2000) et Dupuis (2017) ont montré que la dizaine de volcans enfouis sous l'anticlinal de Shah Deniz n'ont pas tous la même morphologie ni la même source. Par conséquent, notre étude confirme les observations de Yusifov & Rabinowitz (2004) et le modèle de Deville (2009) qui affirment que les VB n'ont pas nécessairement tous la même source dans une zone géographique proche.

Cependant, des similarités peuvent être notés entre ces structures. Par exemple, la surpression et la présence de gaz semblent être des éléments essentiels accompagnant la présence de VB (chapitre 1). Les enregistrements réalisés pendant l'initiation de Lusi confirment que le mécanisme déclenchant des VB serait l'association de la surpression et de l'endommagement des sédiments par l'exsolution et l'expansion du gaz conduisant à l'hydrofracturation (Tingay *et al.*, 2017). Nos observations, nos mesures et nos simulations mènent aux mêmes conclusions. Au lieu d'une surpression se transmettant verticalement et sur une très courte durée le long d'un forage, elle se transmet latéralement sur une période de temps de plusieurs millions d'années le long de couches sous-compactées et du fait de forts taux de sédimentation.

Par conséquent, au travers de cette étude du VBA, nous suggérons que la formation de la plupart des VB devrait être directement lié à l'augmentation de la surpression jusqu'à la pression de fracturation et à la présence de méthane en profondeur qui sont des conditions nécessaires pour initier la remobilisation de sédiments. La méthodologie appliquée dans l'étude du VBA peut être utilisée dans l'étude d'autres VB. Cette méthodologie repose essentiellement sur la détermination de la source de la boue et de ses liens avec les structures régionales, la détermination des propriétés hydromécaniques de la source de la boue et des

strates avoisinantes et sur l'intégration de ces éléments dans leur contexte géologique au travers de modèle numériques simples. De ce fait, certaines données sont nécessaires pour mener ce type d'étude. Notamment, des données sismiques de bonne qualité, des données sur le champ de pression (par des puits ou des modèles de bassins par exemple), une bonne connaissance du contexte régional et des sédiments. Concernant les sédiments, afin de contourner les limites liées aux sédiments utilisés dans cette étude, nous recommandons d'utiliser des équivalents latéraux de la source stratigraphique de la boue et des autres couches modélisés là où ils sont facilement accessibles plutôt que d'utiliser de la boue du volcan. Il serait bon de voir si ces équivalents latéraux qui sont accessibles à terre dans le cas du SCB, peuvent présenter les mêmes caractéristiques pétro-minéralogiques et les mêmes conditions d'enfouissement que l'ASF à Absheron. Cela permettrait de mesurer directement les propriétés hydromécaniques des couches simulées.

En termes d'implications industrielles, le modèle du VBA montre que le gaz expulsé ne provient pas des réservoirs qui seront produits. De ce fait, le VBA ne représente pas de risque d'exploration. De plus, Javanshir *et al.* (2015) n'ont pas observé de perturbation dans les champs de pression à proximité des VB présents sur les champs de Shah Deniz et d'ACG voisins d'Absheron. Cela confirme que le fait qu'un VB traverse les réservoirs ciblés n'en condamne par la prospectivité. En revanche, l'intervalle-source du volcan de boue a de fortes chances d'être en surpression au voisinage et l'estimation des pressions avant forage doit prendre en compte ce facteur de risque. Notre étude quantifie les critères physiques ayant conduit à la formation du VBA notamment les conditions d'hydrofracturation. Ces critères dépendent de la zone d'étude considérée mais devraient être estimés et considérés avant toute opération de forage proche d'un VB.

A notre connaissance, c'est la première fois qu'un modèle numérique de pression en 2D a été utilisé pour expliquer la génération de boue en profondeur. Cette étude ne considère qu'une source de surpression liée aux forts taux de sédimentation mais d'autres sources peuvent être impliquées. Par exemple, l'activité tectonique régionale peut être, suivant les zones d'étude, une forte source de surpression ainsi que la déshydratation des argiles.

Les volcans de boue représentent un champ de recherche complexe dû à la diversité de ces structures et de leurs contextes géologiques. La formation du VBA a été interprétée à partir d'un jeu de données dense ce qui est rarement disponible au-dessus des volcans de boue mais des améliorations restent possibles tant dans les méthodes utilisées que dans le traitement des données. Cette étude définit et quantifie les processus physiques menant à la formation d'un volcan de boue et développe une approche de modélisation numérique qui pourrait être adaptée et améliorée pour étudier d'autres volcans de boue.

References

A

- Abdelaziz, A. I. (2016) *Well logging - Neutron density and sonic logs*. Available at: <https://www.slideshare.net/AmirGhaly/neutron-density-and-sonic-logs> (Accessed: 3 June 2019).
- Abdullayev, E. and Leroy, S. A. G. (2016) 'Provenance of clay minerals in the sediments from the Pliocene Productive Series, western South Caspian Basin', *Marine and Petroleum Geology*. Elsevier Ltd, 73, pp. 517–527. doi: 10.1016/j.marpetgeo.2016.03.002.
- Abdullayev, N. R. (2000) 'Seismic stratigraphy of the Upper Pliocene and Quaternary deposits in the South Caspian Basin', *Journal of Petroleum Science and Engineering*, 28(4), pp. 207–226. doi: 10.1016/S0920-4105(00)00079-6.
- Abreu, V. and Nummedal, D. (2007) 'Miocene to Quaternary Sequence Stratigraphy of the South and Central Caspian Basins', *AAPG Studies in Geology*, 55, pp. 65–86. doi: 10.1306/1205845St553000.
- Agirrezabala, L. M. *et al.* (2013) 'Outcrop analogues of pockmarks and associated methane-seep carbonates: A case study from the Lower Cretaceous (Albian) of the Basque-Cantabrian Basin, western Pyrenees', *Palaeogeography, Palaeoclimatology, Palaeoecology*. Elsevier B.V., 390, pp. 94–115. doi: 10.1016/j.palaeo.2012.11.020.
- Alfaro, M. C. and Wong, R. C. K. (2001) 'Laboratory studies on fracturing of low-permeability soils', *Canadian Geotechnical Journal*, 38(2), pp. 303–315. doi: 10.1139/cgj-38-2-303.
- Alizadeh, A. A. *et al.* (2017) *Geosciences of Azerbaijan Volume II: Economic Geology and Applied Geophysics*. Basel: Springer International Publishing Switzerland. doi: 10.1007/978-3-319-40493-6.
- Allen, M. B. *et al.* (2002) 'Onset of subduction as the cause of rapid Pliocene-Quaternary subsidence in the South Caspian basin', *Geology*, 30(9), pp. 775–778. doi: 10.1130/0091-7613(2002)030<0775:OOSATC>2.0.CO;2.
- Amaratunga, A. and Grozic, J. L. H. (2001) 'On the undrained unloading behaviour of gassy sands', *Canadian Geotechnical Journal*, 46, pp. 1267–1276. doi: 10.1139/T09-056.
- Anderson, A. L. *et al.* (1998) 'Bubble populations and acoustic interaction with the gassy floor of Eckernförde Bay', 18.
- Anderson, D. L. *et al.* (1974) 'The effect of oriented cracks on seismic velocities', *Journal of Geophysical Research*, 79(26), pp. 4011–4015.
- Antonielli, B. *et al.* (2014) 'Pre-eruptive ground deformation of Azerbaijan mud volcanoes detected through satellite radar interferometry (DInSAR)', *Tectonophysics*. Elsevier B.V., 637, pp. 163–177. doi: 10.1016/j.tecto.2014.10.005.
- Artyushkov, E. V (2007) 'Formation of the superdeep South Caspian basin: subsidence driven by phase change in continental crust', *Russian Geology and Geophysics*, 48, pp. 1002–1014. doi: 10.1016/j.rgg.200.
- ASTM International (1996) 'D 2435 – 96 - Standard test method for one-dimensional consolidation properties of soils', *American Society for Testing and Materials*. West Conshohocken, 04.08, pp. 196–205. doi: 10.1520/D2435-96.

B

- Bahorich, M. S. and Farmer, S. L. (1995) '3-D seismic discontinuity for faults and stratigraphic features: The coherence cube', in *SEG Technical Program Expanded Abstracts 1995*. Society of Exploration Geophysicists, pp. 93–96. doi: 10.1190/1.1887523.
- Barber, A. J. *et al.* (1986) 'Mud Volcanoes, Shale Diapirs, Wrench Faults, and Melanges in Accretionary Complexes, Eastern Indonesia.', *American Association of Petroleum Geologists Bulletin*, 70(11), pp. 1729–1741.
- Barry, M. and Boudreau, B. P. (2010) 'First-order description of the mechanical fracture behavior of fine-grained surficial marine sediments during gas bubble growth', *Journal of Geophysical Research: Atmospheres*, 115, pp. 1–10. doi: 10.1029/2010JF001833.
- Battani, A. *et al.* (2010) 'Trinidad Mud Volcanoes: The Origin of the Gas', *Shale tectonics: AAPG Memoir*, 93, pp. 225–238. doi: 10.1306/13231317M933427.
- Benjamin, U. K. and Huuse, M. (2017) 'Seafloor and buried mounds on the western slope of the Niger Delta', *Marine and Petroleum Geology*. Elsevier Ltd, 83, pp. 158–173. doi: 10.1016/j.marpetgeo.2017.02.023.
- Berberian, M. (1983) 'The southern Caspian: A compressional depression floored by a trapped, modified oceanic crust"', *Canadian Journal of Earth Sciences*, 20, pp. 163–183. doi: 10.1139/e83-015.
- Biot, M. A. (1956) 'Theory of Propagation of Elastic Waves in a Fluid-Saturated Porous Solid. II. Higher Frequency Range', *Journal of the Acoustical Society of America*, 28(2), pp. 179–191.
- Blouin, A. *et al.* (2019) 'Evolution model for the Absheron mud volcano : from in - situ observations to numerical modeling', *Journal of Geophysical Research: Earth Surface*, 124(3), pp. 766–794. doi: 10.1029/2018JF004872.
- Bochud, M. (2011) 'Tectonics of the Eastern Greater Caucasus in Azerbaijan'. University of Fribourg.
- Bogges, R. and Robertson, P. K. (2011) 'CPT for Soft Sediments and Deepwater Investigations', *Offshore Technology Conference*, 21244(May), pp. 2–5.
- Bonini, M. (2009a) 'Reply to comment by G. Etiope and G. Martinelli: "“Pieve Santo Stefano” is not a mud volcano: Comment on Structural controls on a carbon dioxide-driven mud volcano field in the Northern Apennines', *Journal of Structural Geology*, 31, pp. 1272–1274. doi: 10.1016/j.jsg.2009.06.010.
- Bonini, M. (2009b) 'Structural controls on a carbon dioxide-driven mud volcano field in the Northern Apennines (Pieve Santo Stefano, Italy): Relations with pre-existing steep discontinuities and seismicity', *Journal of Structural Geology*. Elsevier Ltd, 31(8), pp. 853–856. doi: 10.1016/j.jsg.2009.02.002.
- Bonini, M. (2012) 'Mud volcanoes: Indicators of stress orientation and tectonic controls', *Earth-Science Reviews*. Elsevier B.V., 115(3), pp. 121–152. doi: 10.1016/j.earscirev.2012.09.002.
- Bouchet, A. *et al.* (2000) *Minéraux argileux: structure cristalline, identification par diffraction de rayons X*. TOTAL FINA. Pau, France.
- Boudreau, B. P. (1996) 'The diffusive tortuosity of fine-grained unlithified sediments', *Geochimica et Cosmochimica Acta*, 60(16), pp. 3139–3142. doi: 10.1016/0016-7037(96)00158-5.
- Boudreau, B. P. *et al.* (2005) 'Bubble growth and rise in soft sediments', *Geology*, 33(6), pp. 517–520. doi: 10.1130/G21259.1.
- Boudreau, B. P. (2012) 'The physics of bubbles in surficial , soft , cohesive sediments', *Marine and Petroleum Geology*. Elsevier Ltd, 38(1), pp. 1–18. doi: 10.1016/j.marpetgeo.2012.07.002.

Breck, D. W. (1974) *Zeolite Molecular Sieves*. John Wiley & Sons.

Bredehoeft, J. D. *et al.* (1988) 'Lateral fluid flow in a compacting sand-shale sequence: South Caspian basin.', *American Association of Petroleum Geologists Bulletin*, 72(4), pp. 416–424. doi: 10.1306/703C9A1E-1707-11D7-8645000102C1865D.

Brown, K. M. and Westbrook, G. K. (1988) 'Mud Diapirism and subcretion in the Barbados Ridge Complex: the role of fluids in accretionary processes', *Tectonics*, 7(3), pp. 613–640.

Brown, K. M. (1990) 'The nature and hydrogeologic significance of mud diapirs and diatremes for accretionary systems', *Journal of Geophysical Research*, 95(B6), p. 8969. doi: 10.1029/JB095iB06p08969.

Brunet, M.-F. *et al.* (2003) 'The South Caspian Basin: a review of its evolution from subsidence modelling', *Sedimentary Geology*, 156, pp. 119–148.

Brunet, M. F. *et al.* (2007) 'Precaspian and south Caspian Basins: Subsidence Evolution of Two Superdeep Basins', in Yilmaz, P. O., and Isaksen, G. H. (eds) *Oil and Gas of the Greater Caspian Area: AAPG Studies in Geology* 55, pp. 151–155. doi: 10.1306/1205830St553247.

C

Caine, J. S. *et al.* (1996) 'Fault zone architecture and permeability structure', *Geology*, 24(11), pp. 1025–1028. doi: [https://doi.org/10.1130/0091-7613\(1996\)024<1025:FZAAPS>2.3.CO;2](https://doi.org/10.1130/0091-7613(1996)024<1025:FZAAPS>2.3.CO;2).

Capaccioni, B. *et al.* (2017) 'Sand volcano generated by a violent degassing from methane-saturated aquifers: The case study of Medolla (Modena, Italy)', *Engineering Geology*. Elsevier B.V., 221, pp. 91–103. doi: 10.1016/j.enggeo.2017.02.027.

Carcione, J. M. and Helle, H. B. (2002) 'ROCK PHYSICS OF GEOPRESSURE AND PREDICTION OF ABNORMAL PORE FLUID PRESSURES USING SEISMIC DATA', *CSEG Recorder*, pp. 34–39.

Carman, P. C. (1937) 'Fluid flow through granular beds', *Transactions, Institution of Chemical Engineers*. London, 15, pp. 150–166.

Cartwright, J. *et al.* (2007) 'Seal bypass systems', *AAPG Bulletin*, 91(8), pp. 1141–1166. doi: 10.1306/04090705181.

Cathles, L. M. (2001) 'Capillary seals as a cause of pressure compartmentation in sedimentary basins', in *Petroleum Systems of Deep-Water Basins: Global and Gulf of Mexico Experience. 21st Annual Bob F. Perkins Research Conference*. Gulf Coast Section of the Society of Economic Paleontologists and Mineralogists, pp. 561–572. doi: 10.5724/gcs.01.21.0549.

Cathles, L. M. *et al.* (2010) 'The physics of gas chimney and pockmark formation, with implications for assessment of seafloor hazards and gas sequestration', *Marine and Petroleum Geology*. Elsevier Ltd, 27(1), pp. 82–91. doi: 10.1016/j.marpetgeo.2009.09.010.

Catuneanu, O. *et al.* (2009) 'Towards the standardization of sequence stratigraphy', *Earth-Science Reviews*. Elsevier B.V., 92(1–2), pp. 1–33. doi: 10.1016/j.earscirev.2008.10.003.

Ceramicola, S. *et al.* (2018) 'Submarine Geomorphology', in. doi: 10.1007/978-3-319-57852-1.

Chan, C. M. (2012) 'On the interpretation of shear wave velocity from bender element tests', *Acta Technica Corviniensis - Bulletin of Engineering*, 5(1), pp. 29–34. Available at: <http://acta.fih.upt.ro/pdf/2012-1/ACTA-2012-1-03.pdf>.

Chenrai, P. and Huuse, M. (2017) 'Pockmark formation by porewater expulsion during rapid progradation in the offshore Taranaki Basin, New Zealand', *Marine and Petroleum Geology*. Elsevier Ltd, 82,

pp. 399–413. doi: 10.1016/j.marpetgeo.2017.02.017.

Choi, K. *et al.* (2011) 'Predicting the impact of sedimentological heterogeneity on gas–oil and water–oil displacements: fluvio-deltaic Pereriv Suite Reservoir, Azeri–Chirag–Gunashli Oilfield, South Caspian Basin', *Petroleum Geoscience*, 17(2), pp. 143–163. doi: 10.1144/1354-079310-013.

Chong, S.-H. and Santamarina, J. C. (2016) 'Soil Compressibility Models for a Wide Stress Range', *Journal of Geotechnical and Geoenvironmental Engineering*, 142(6), pp. 1–7. doi: 10.1061/(ASCE)GT.1943-5606.0001482.

Chu, J. *et al.* (2002) 'Consolidation and Permeability Properties of Singapore Marine Clay', *Journal of Geotechnical and Geoenvironmental Engineering*, (September), pp. 724–732.

Cita, M. B. (1981) 'Prometheus mud breccia: an example of shale diapirism in the western Mediterranean ridge', *Annales géologiques des Pays helléniques*, 30, pp. 543–569.

Clari, P. *et al.* (2007) 'A Miocene Mud Volcano and Its Plumbing System: A Chaotic Complex Revisited (Monferrato, NW Italy)', *Journal of Sedimentary Research*, 74(5), pp. 662–676. doi: 10.1306/022504740662.

Colliat, J.-L. *et al.* (2011) 'Gulf of Guinea deepwater sediments: Geotechnical properties, design issues and installation experiences', in White, D., and Gourvenec, S. (eds) *Frontiers in Offshore Geotechnics II*. London: Taylor & Francis Group, pp. 59–86.

Collignon, M., Mazzini, A. *et al.* (2018a) 'Modelling fluid flow in active clastic piercements: Challenges and approaches', *Marine and Petroleum Geology*. Elsevier Ltd, 90, pp. 157–172. doi: 10.1016/j.marpetgeo.2017.09.033.

Collignon, M., Schmid, D. W. *et al.* (2018b) 'Modelling fluid flow in clastic eruptions: Application to the Lusi mud eruption', *Marine and Petroleum Geology*. Elsevier Ltd, 90, pp. 173–190. doi: 10.1016/j.marpetgeo.2017.08.011.

Compton, A. H. (1923) 'Physical Review a Quantum Theory of the Scattering of X-Rays', *Physical Review*, 2(5).

Contet, J. and Unterseh, S. (2015) 'Multiscale site investigation of a giant mud-volcano offshore Azerbaijan - Impact on subsea field development', *Offshore Technology Conference*, OTC-25864(Mv), pp. 1–10. doi: 10.4043/25864-MS.

Corbet, T. F. and Bethke, C. M. (1992) 'Disequilibrium fluid pressures and groundwater flow in the western Canada sedimentary basin', *Journal of Geophysical Research*, 97(B5), p. 7203. doi: 10.1029/91JB02993.

Courtois Energies Conseil (2010) *Masse Volumique et densité des gaz*. Available at: www.courtoisenergies.fr/data/list/docs/Masse_volumique_et_densite_des_gaz.xls (Accessed: 9 August 2019).

Couzens-Schultz, B. A. and Azbel, K. (2014) 'Predicting pore pressure in active fold-thrust systems: An empirical model for the deepwater Sabah foldbelt', *Journal of Structural Geology*. Elsevier Ltd, 69(PB), pp. 465–480. doi: 10.1016/j.jsg.2014.07.013.

Crain, E. (2018) *Crain's Petrophysical Handbook*. Available at: <https://www.spec2000.net/00-index.htm> (Accessed: 3 June 2019).

Crank, J. (1975) 'the Mathematics of Diffusion'. doi: 10.1016/0306-4549(77)90072-X.

Cuss, R. *et al.* (2014) 'Experimental observations of mechanical dilation at the onset of gas flow in Callovo-Oxfordian claystone', in Norris, N. *et al.* (eds) *Clays in Natural and Engineered Barriers for Radioactive Waste Confinement*. London: Geological Society, pp. 507–519. doi: 10.1144/SP400.26.

D

- Das, B. M. (2013) *Principles of Geotechnical Engineering - 7th edition, Journal of Chemical Information and Modeling*. CENGAGE Learning. doi: 10.1017/CBO9781107415324.004.
- Davies, J. H. (1999) 'The role of hydraulic fractures and intermediate-depth earthquakes in generating subduction-zone magmatism', *letters to nature*, 398(March), pp. 142–145.
- Davies, R. J. *et al.* (2008) 'The East Java mud volcano (2006 to present): An earthquake or drilling trigger?', *Earth and Planetary Science Letters*, 272(3–4), pp. 627–638. doi: 10.1016/j.epsl.2008.05.029.
- Day-Stirrat, R. J. *et al.* (2010) 'Diagenetic and Seismic Concerns Associated with Interpretation of Deeply Buried "Mobile Shales"', *Shale Tectonics: AAPG Memoir 93*, pp. 5–28. doi: 10.1306/13231306M93730.
- DeGroot, D. J. *et al.* (2010) 'Recommended best practise for geotechnical site characterisation of cohesive offshore sediments', in Gourvenec, S., and White, D. (eds) *Frontiers in Offshore Geotechnics II*. Perth, Australia: CRC Press, Taylor & Francis Group, pp. 33–57.
- Deming, D. (2002) 'Abnormal Fluid Pressures', in *An introduction to Hydrogeology*. McGraw-Hill Science/Engineering/Math, pp. 219–239.
- Deville, E. *et al.* (2003) 'The origin and processes of mud volcanism: new insights from Trinidad', *Geological Society, London, Special Publications*, 216(1), pp. 475–490. doi: 10.1144/gsl.sp.2003.216.01.31.
- Deville, E. *et al.* (2006) 'Liquefied vs stratified sediment mobilization processes: Insight from the South of the Barbados accretionary prism', *Tectonophysics*, 428(1–4), pp. 33–47. doi: 10.1016/j.tecto.2006.08.011.
- Deville, E. (2009) 'Mud Volcano Systems', in Lewis, N., and Moretti, A. (eds) *Volcanoes: Formation, Eruptions and Modelling*. Nova Science Publishers, pp. 95-125 (404).
- Deville, E. and Guerlais, S. (2009) 'Cyclic activity of mud volcanoes : Evidences from Trinidad (SE Caribbean)', *Marine and Petroleum Geology*. Elsevier Ltd, 26(9), pp. 1681–1691. doi: 10.1016/j.marpetgeo.2009.03.002.
- Deville, E. *et al.* (2010) 'Fluid dynamics and subsurface sediment mobilization processes: An overview from Southeast Caribbean', *Basin Research*, 22(4), pp. 361–379. doi: 10.1111/j.1365-2117.2010.00474.x.
- Diaconescu, C. C. *et al.* (2001) 'Geophysical evidence for gas hydrates in the deep water of the South Caspian Basin, Azerbaijan', *Marine and Petroleum Geology*, 18(2), pp. 209–221. doi: 10.1016/S0264-8172(00)00061-1.
- Dimitrov, L. I. (2002) 'Mud volcanoes-the most important pathway for degassing deeply buried sediments', *Earth-Science Reviews*, 59(1–4), pp. 49–76. doi: 10.1016/S0012-8252(02)00069-7.
- Doll, H. G. (1949) 'Introduction to Induction Logging and Application to Logging of Wells Drilled With Oil Base Mud', *Journal of Petroleum Technology*. San Francisco, 1(06), pp. 148–162. doi: 10.2118/949148-g.
- Duan, Z. and Mao, S. (2006) 'A thermodynamic model for calculating methane solubility, density and gas phase composition of methane-bearing aqueous fluids from 273 to 523 K and from 1 to 2000 bar', *Geochimica et Cosmochimica Acta*, 70(13), pp. 3369–3386. doi: 10.1016/j.gca.2006.03.018.
- Dubacq, B. (2008) 'THERMODYNAMIQUE DES PHYLLOSILICATES DE BASSE TEMPERATURE : de l'approche macroscopique à la simulation atomistique'. Université Joseph Fourier - Grenoble - France.
- Dubacq, B. *et al.* (2013) 'An activity model for phase equilibria in the H₂O – CO₂ – NaCl system', *Geochimica et Cosmochimica Acta*, 110, pp. 229–252. doi: 10.1016/j.gca.2013.02.008.

Dugan, B. and Flemings, P. (2000) 'Overpressure and fluid flow in the new jersey continental slope: implications for slope failure and cold seeps', *Science (New York, N.Y.)*, 289(July), pp. 288–291. doi: 10.1126/science.289.5477.288.

Dupré, S. *et al.* (2008) 'High-resolution mapping of large gas emitting mud volcanoes on the Egyptian continental margin (Nile Deep Sea Fan) by AUV surveys', *Marine Geophysical Researches*, 29(4), pp. 275–290. doi: 10.1007/s11001-009-9063-3.

Dupré, S. *et al.* (2014) 'Warm brine lakes in craters of active mud volcanoes, Menes caldera off NW Egypt: evidence for deep-rooted thermogenic processes', *Geo-Marine Letters*, 34(2–3), pp. 153–168. doi: <http://dx.doi.org/10.1007/s00367-014-0367-1>.

Dupré, S. *et al.* (2015) 'Tectonic and sedimentary controls on widespread gas emissions in the Sea of Marmara: Results from systematic, shipborne multibeam echo sounder water column imaging', *Journal of Geophysical Research: Solid Earth RESEARCH*, pp. 1–22. doi: 10.1002/2014JB011617.

Dupuis, M. (2017) 'Processus de mise en place et évolution des systèmes de volcans de boue.' Université Lille 1 - Sciences et technologies.

Dupuis, M. *et al.* (2019) 'Mud volcanism by repeated roof collapse : 3D architecture and evolution of a mud volcano cluster off shore Nigeria', *Marine and Petroleum Geology*, 110(July), pp. 368–387. doi: 10.1016/j.marpetgeo.2019.07.033.

Dvorkin, J. *et al.* (1999) 'Elasticity of marine sediments: Rock physics modeling', *Geophysical Research Letters*, 26(12), pp. 1781–1784.

E

Eaton, B. A. (1975) 'The equation for geopressure prediction from well logs', in *50th Annual Fall Meeting of the Society of Petroleum Engineers of AIME*. Dallas, Texas: Society of Petroleum Engineers, p. 5.

Egan, S. S. *et al.* (2009) 'Subsidence and uplift mechanisms within the South Caspian Basin: insights from the onshore and offshore Azerbaijan region', *Geological Society, London, Special Publications*, 312(1), pp. 219–240. doi: 10.1144/SP312.11.

Egermann, P. and Vizika, O. (2000) 'A NEW METHOD TO DETERMINE CRITICAL GAS SATURATION AND RELATIVE PERMEABILITY DURING DEPRESSURIZATION IN THE NEAR-WELLBORE REGION', in *SPE annual technical conference and exhibition*. Society of Petroleum Engineers, pp. 1–12. doi: doi:10.2118/63149-MS.

Engdahl, E. R. *et al.* (2006) 'Relocation and assessment of seismicity in the Iran region', *Geophysical Journal International*, 167(2), pp. 761–778. doi: 10.1111/j.1365-246X.2006.03127.x.

Esrig, M. I. and Kirby, R. C. (1977) 'Implications of gas content for predicting the stability of submarine slopes', *Marine Geotechnology*, 2(1–4), pp. 81–100. doi: 10.1080/10641197709379771.

Etiopie, G. and Milkov, A. V. (2004) 'A new estimate of global methane flux from onshore and shallow submarine mud volcanoes to the atmosphere', *Environmental Geology*, 46(8), pp. 997–1002. doi: 10.1007/s00254-004-1085-1.

Etiopie, G. *et al.* (2009) 'Terrestrial methane seeps and mud volcanoes: A global perspective of gas origin', *Marine and Petroleum Geology*, 26(3), pp. 333–344. doi: 10.1016/j.marpetgeo.2008.03.001.

Etiopie, G. and Martinelli, G. (2009) '““ Pieve Santo Stefano ”” is not a mud volcano : Comment on ““ Structural controls on a carbon dioxide-driven mud volcano field in the Northern Apennines ”” (by Bonini , 2009)', *Journal of Structural Geology*. Elsevier Ltd, 31(10), pp. 1270–1271. doi: 10.1016/j.jsg.2009.06.009.

Evans, J. P. *et al.* (1997) 'Permeability of fault-related rocks, and implications for hydraulic structure of fault zones', *Journal of Structural Geology*, 19(11), pp. 1393–1404. doi: [https://doi.org/10.1016/S0191-8141\(97\)00057-6](https://doi.org/10.1016/S0191-8141(97)00057-6).

Evans, R. J. *et al.* (2007) 'Phase-reversed seabed reflections in seismic data : examples related to mud volcanoes from the South Caspian Sea', *Geo-Marine Letters*, 27, pp. 203–212. doi: [10.1007/s00367-007-0073-3](https://doi.org/10.1007/s00367-007-0073-3).

F

Fader, G. B. J. (1997) 'The Effects of Shallow Gas on Seismic Reflection Profiles', in Davies, T. A. *et al.* (eds) *Glaciated Continental Margins*. Dordrecht: Springer, pp. 29–30. doi: https://doi.org/10.1007/978-94-011-5820-6_4.

Feng, T. W. (2000) 'Fall-cone penetration and water content relationship of clays', *Geotechnique*, 50(2), pp. 181–187. doi: <https://doi.org/10.1680/geot.2000.50.2.181>.

Feng, T. W. (2005) 'Reappraisal of the fall cone test', in *Proceedings of the 16th International Conference on Soil Mechanics and Geotechnical Engineering*. Osaka: Millpress Science Publishers/IOS Press, pp. 357–360. doi: [10.3233/978-1-61499-656-9-357](https://doi.org/10.3233/978-1-61499-656-9-357).

Fialips, C. I. *et al.* (2018) 'Quantitative Mineralogy of Vaca Muerta and Alum Shales From Core Chips and Drill Cuttings by Calibrated SEM-EDS Mineralogical Mapping'. doi: [10.15530/urtec-2018-2902304](https://doi.org/10.15530/urtec-2018-2902304).

Field, M. E. and Barber, J. H. J. (1993) 'A Submarine Landslide Associated with Shallow Sea-Floor Gas and Gas Hydrates off Northern California', in Schwab, W. C., Lee, H. J., and Twichell, D. C. (eds) *Submarine Landslides : Selected Studies in the U.S. Exclusive Economic Zone*. Reston, Virginia (USA): US Geological Survey, pp. 151–157.

Finkbeiner, T. *et al.* (2001) 'Stress, pore pressure, and dynamically constrained hydrocarbon columns in the South Eugene Island 330 field, northern Gulf of Mexico', *AAPG Bulletin*, 85(6), pp. 1007–1031.

Fleischer, P. *et al.* (2001) 'Distribution of free gas in marine sediments : a global overview', *Geo-Marine Letters*, 21, pp. 103–122. doi: [10.1007/s003670100072](https://doi.org/10.1007/s003670100072).

Forte, A. M. *et al.* (2010) 'Late Cenozoic deformation of the Kura fold-thrust belt, southern Greater Caucasus', *Bulletin of the Geological Society of America*, 122(3–4), pp. 465–486. doi: [10.1130/B26464.1](https://doi.org/10.1130/B26464.1).

Forte, A. M. and Cowgill, E. (2013) 'Late Cenozoic base-level variations of the Caspian Sea: A review of its history and proposed driving mechanisms', *Palaeogeography, Palaeoclimatology, Palaeoecology*. Elsevier B.V., 386, pp. 392–407. doi: [10.1016/j.palaeo.2013.05.035](https://doi.org/10.1016/j.palaeo.2013.05.035).

Forte, A. M. *et al.* (2015) 'Late miocene to pliocene stratigraphy of the kura basin, a subbasin of the south caspian basin: Implications for the diachroneity of stage boundaries', *Basin Research*, 27(3), pp. 247–271. doi: [10.1111/bre.12069](https://doi.org/10.1111/bre.12069).

Foucher, J. P. *et al.* (2009) 'Structure and Drivers of Cold Seep Ecosystems', *Oceanography*, 22(1), pp. 92–109. doi: [10.5670/oceanog.2009.11](https://doi.org/10.5670/oceanog.2009.11).

Fowler, S. R. *et al.* (2000) 'Mud volcanoes and structural development on Shah Deniz', *Journal of Petroleum Science and Engineering*, 28(4), pp. 189–206.

Frank, U. and Barkley, N. (1995) 'Remediation of low permeability subsurface formations by fracturing enhancement of soil vapor extraction neering and cost data based on field tests of selected technologies . This paper addresses', *Journal of hazardous materials*, 40, pp. 191–201.

Furbish, D. J. (1997) *Fluid Physics in Geology*. New York: Oxford University Press.

G

Galland, O. *et al.* (2015) 'Laboratory Modelling of Volcano Plumbing Systems : A Review', in Breitzkreuz, C., and Rocchi, S. (eds) *Physical Geology of Shallow Magmatic Systems: Dykes, Sills and Laccoliths*. Cham: Springer International, pp. 147–214. doi: 10.1007/11157.

Gautherot, T. *et al.* (2015) 'Absheron Field – ABX-2 Exploration Drilling Challenges and Realizations Return to Absheron field', (June 2009), pp. 4–6.

Gay, A. *et al.* (2003) 'Sinuous pockmark belt as indicator of a shallow buried turbiditic channel on the lower slope of the Congo basin, West African margin', *Geological Society, London, Special Publications*, 216(1), pp. 173–189. doi: 10.1144/gsl.sp.2003.216.01.12.

Geary, A. (2018) *Resistivity Log, SEG Wiki*. Available at: https://wiki.seg.org/wiki/Resistivity_log.

Ginsburg, G. D. *et al.* (1992) 'Gas hydrates of the southern caspian', *International Geology Review*, 34(8), pp. 765–782. doi: 10.1080/00206819209465635.

Gisler, G. (2009) 'Simulations of the explosive eruption of superheated fluids through deformable media', *Marine and Petroleum Geology*. Elsevier Ltd, 26(9), pp. 1888–1895. doi: 10.1016/j.marpetgeo.2008.12.006.

Golonka, J. (2007) 'Geodynamic Evolution of the South Caspian Basin', *Oil and Gas of the Greater Caspian Area*, 55, pp. 17–41. doi: 10.1306/1205844St551463.

Gordon, D. S. and Flemings, P. B. (1998) 'Generation of overpressure and compaction-driven fluid flow in a Plio-Pleistocene Eugene Island 330 , offshore Louisiana', *Basin Research*, 10, pp. 177–196.

Graue, K. (2000) 'Mud volcanoes in deepwater Nigeria', *Marine and Petroleum Geology*, 17(8), pp. 959–974. doi: 10.1016/S0264-8172(00)00016-7.

Grauls, D. J. and Baleix, J. M. (1994) 'Role of overpressures and in situ stresses in fault-controlled hydrocarbon migration : a case study', *Marine and Petroleum Geology*, 11(6), pp. 734–742.

Green, T. *et al.* (2009) 'Sedimentation and subsidence in the South Caspian Basin, Azerbaijan', *Geological Society, London, Special Publications*, 312(1), pp. 241–260. doi: 10.1144/SP312.12.

Grosjean, Y. *et al.* (2009) 'Burial Hydrodynamics and Subtle Hydrocarbon Trap Evaluation : From the Mahakam Delta to the South Caspian Sea', *International Petroleum Technology Conference held in Doha, Qatar, 7-9 December 2009*, pp. 1–12.

Grozić, J. L. H. *et al.* (2000) 'Cyclic liquefaction of loose gassy sand', *Canadian Geotechnical Journal*, 37, pp. 843–856.

Grozić, J. L. H. *et al.* (2005) 'On the undrained shear strength of gassy clays', *Computer and Geotechnics*, 32, pp. 483–490. doi: 10.1016/j.compgeo.2005.10.002.

Guillon, S. and Keskes, N. (2004) 'Sismage and the 3D Visualization at Total', in *AAPG International Conference*, pp. 1–3.

Guliyev, I. S. *et al.* (2001) 'Isotope Geochemistry of Oils from Fields & Mud Volcanoes in the South Caspian Basin, Azerbaijan', *Petroleum Geoscience*, 7(2), pp. 201–209. doi: 10.1144/petgeo.7.2.201.

Guliyev, I. and Panahi, B. (2004) 'Geodynamics of the deep sedimentary basin of the Caspian Sea region: Paragenetic correlation of seismicity and mud volcanism', *Geo-Marine Letters*, 24(3), pp. 169–176. doi: 10.1007/s00367-004-0174-1.

Guliyev, I. *et al.* (2011) 'Hydrocarbon Potential of Ultra Deep Deposits in the South Caspian Basin', in *AAPG European Region Annual Conference*. Kiev, Ukraine, p. 66.

Gulmammadov, R. *et al.* (2017) 'Geomechanical characterization of mud volcanoes using P-wave velocity datasets', *Geological Society, London, Special Publications*, 458, pp. 273–292. doi: 10.1144/SP458.2.

H

Haines, S. H. *et al.* (2009) 'Clay fabric intensity in natural and artificial fault gouges: Implications for brittle fault zone processes and sedimentary basin clay fabric evolution', *Journal of Geophysical Research: Solid Earth*, 114(5). doi: 10.1029/2008JB005866.

Hao, F. *et al.* (2015) 'Factors controlling petroleum accumulation and leakage in overpressured reservoirs', *AAPG Bulletin*, 99(5), pp. 831–858. doi: 10.1306/01021514145.

Hedberg, H. D. (1974) 'Relation of Methane Generation to Undercompacted Shales, Shale Diapirs, and Mud Volcanoes', *AAPG Bulletin*, 58(4), pp. 661–673. doi: 10.1306/83D91466-16C7-11D7-8645000102C1865D.

Helgerud, M. B. *et al.* (1999) 'Elastic-wave velocity in marine sediments with gas hydrates: Effective medium modeling', *Geophysical Research Letters*, 26(13), pp. 2021–2024.

Henry, P. *et al.* (1996) 'Fluid Flow in and around a mud volcano field of the Barbados accretionary wedge: Results from Manon cruise', *Journal of Geophysical Research*, 101(96), pp. 297–323.

Henry, P. *et al.* (2019) 'Strain and flow pathways in a shale fault zone : An in-situ test of fault seal integrity', in *Fifth International Conference on Fault and Top Seals*. Palermo, Italy: EAGE Publications, pp. 8–12.

Hight, D. W. *et al.* (2002) 'Engineering characterization of the Nile Delta clays', in Nakase, A., and Tsuchida, T. (eds) *Coastal geotechnical engineering in practice*. Lisse, the Netherlands: Swets & Zeitlinger, pp. 149–162.

Hight, D. W. and Leroueil, S. (2003) 'Characterisation of soils for engineering purposes', in Tan, T. S. *et al.* (eds) *Characterisation and engineering properties of natural soils - volume 1*. Lisse, The Netherlands: Swets & Zeitlinger, pp. 255–360.

Hinds, D. J. *et al.* (2004) 'Sedimentation in a discharge dominated fluvial-lacustrine system: The Neogene Productive Series of the South Caspian Basin, Azerbaijan', *Marine and Petroleum Geology*, 21(5), pp. 613–638. doi: 10.1016/j.marpetgeo.2004.01.009.

Hollingsworth, J. *et al.* (2008) 'Extrusion tectonics and subduction in the easter South Caspian region since 10 Ma', *Geology*, 36(10), pp. 763–766. doi: 10.1130/G25008A.1.

Hong, Y. *et al.* (2017) 'Effect of initial pore pressure on undrained shear behaviour of fine-grained gassy soil', *Canadian Geotechnical Journal*, 54(11), pp. 1592–1600.

Horvei, B. and Nilsen, K. E. (2010) 'A new high resolution wideband multibeam echo sounder for inspection work and hydrographic mapping', *MTS/IEEE Seattle, OCEANS 2010*. doi: 10.1109/OCEANS.2010.5664080.

Howell, L. G. and Froscht, A. (1939) 'Gamma-Ray Well-Logging', in *Humble Oil & Refining Co. Annual*

Meeting. Oklahoma City: Humble Oil & Refining Co., pp. 106–114.

Huang, T. H. *et al.* (1995) 'Elastic Moduli for Fractured Rock Mass', *Rock Mechanics and Rock Engineering*, 28(3), pp. 135–144.

Hubbert, M. K. (1937) 'Theory of scale models as applied to the study of geologic structures', *Bulletin of the Geological Society of America*, 48, pp. 1459–1520.

Hubbert, M. K. (1953) 'Entrapment of petroleum under hydrodynamic conditions', *AAPG Bulletin*, 37(8), pp. 1954–2026.

Hubbert, M. K. and Willis, D. G. (1957) 'Mechanics of Hydraulic Fracturing', *Society of Petroleum Engineers*, 210, pp. 153–163. Available at:
<http://archives.datapages.com/data/specpubs/methodo2/data/a075/a075/0001/0200/0239.htm>.

Hudson, S. M. *et al.* (2008) 'Stratigraphy and geochemical characterization of the Oligocene-Miocene Maikop series: Implications for the paleogeography of Eastern Azerbaijan', *Tectonophysics*, 451(1–4), pp. 40–55. doi: 10.1016/j.tecto.2007.11.045.

Huffman, A. R. and Bowers, G. L. (2002) 'Pressure Regimes in Sedimentary Basins and Their Prediction', *AAPG Memoir*. AAPG Memoir, 76, p. 248.

Hustoft, S. *et al.* (2009) 'Effects of rapid sedimentation on developing the Nyegga pockmark field: Constraints from hydrological modeling and 3-D seismic data, offshore mid-Norway', *Geochemistry, Geophysics, Geosystems*, 10(6). doi: 10.1029/2009GC002409.

I

Imbert, P. *et al.* (2014) 'How to evacuate 10 km³ of mud: Saturate with gas and decrease the pressure!', *Geo-Marine Letters*, 34(2–3), pp. 199–213. doi: 10.1007/s00367-014-0357-3.

Inan, S. *et al.* (2002) 'Deep petroleum occurrences in the Lower Kura Depression, South Caspian Basin, Azerbaijan: an organic geochemical and basin modeling study', *Marine and Petroleum Geology*, 14(7–8), pp. 731–762. doi: 10.1016/s0264-8172(97)00058-5.

J

Jackson, J. *et al.* (2002) 'Active Tectonics of the Iran Plateau and South Caspian Basin', *Geophysical Journal International*, 148, pp. 214–245. Available at:
<http://adsabs.harvard.edu/abs/2002AGUFM.S61D..08P%5Cnpapers2://publication/uuid/083D0381-ABF2-42DD-9E79-D4987F09FC37>.

Jain, A. K. and Juanes, R. (2009) 'Preferential Mode of gas invasion in sediments: Grain-scale mechanistic model of coupled multiphase fluid flow and sediment mechanics', 114(1), pp. 1–19. doi: 10.1029/2008JB006002.

Jang, J. and Santamarina, J. C. (2014) 'Evolution of gas saturation and relative permeability during gas production from hydrate-bearing sediments: Gas invasion vs. gas nucleation', *Journal of Geophysical Research: Solid Earth*, 119, pp. 116–126. doi: 10.1002/2013JB010480. Received.

Javanshir, R. J. *et al.* (2015) 'Validation of lateral fluid flow in an overpressured sand-shale sequence during development of Azeri-Chirag-Gunashli oil field and Shah Deniz gas field: South Caspian Basin, Azerbaijan', *Marine and Petroleum Geology*. Elsevier Ltd, 59, pp. 593–610. doi: 10.1016/j.marpetgeo.2014.07.019.

Jeong, S. W. (2013) 'Determining the viscosity and yield surface of marine sediments using modified Bingham models', *Geosciences Journal*, 17(3), pp. 241–247. doi: 10.1007/s12303-013-0038-7.

Jones, R. W. and Simmons, M. D. (1998) 'A review of the stratigraphy of Eastern Paratethys (Oligocene-Holocene), with particular emphasis on the Black Sea.', *AAPG Memoir*, pp. 39–52.

Jónsson, S. *et al.* (2003) 'Post-earthquake ground movements correlated to pore-pressure transients', *letters to nature*, 424(July), pp. 179–183. doi: 10.1038/nature01758.1.

Judd, A. G. (2003) 'The global importance and context of methane escape from the seabed', *Geo-Marine Letters*, 23, pp. 147–154. doi: 10.1007/s00367-003-0136-z.

Judd, A. G. and Hovland, M. (2007) 'Seabed fluid flow: the impact of geology, biology and the marine environment', *Cambridge University Press*, (February), pp. 1–442. doi: 10.1007/s00254-004-1086-0.

K

Kahraman, S. (2002) 'The effects of fracture roughness on P -wave velocity', 63, pp. 347–350.

Katsman, R. (2015) 'Correlation of shape and size of methane bubbles in fine-grained muddy aquatic sediments with sediment fracture toughness', *Journal of Structural Geology*. Elsevier Ltd, 70, pp. 56–64. doi: 10.1016/j.jsg.2014.11.002.

Khain, V. E. *et al.* (2007) 'Tectonic origin of the Apsheron Threshold in the Caspian Sea', *Doklady Earth Sciences*, 414(1), pp. 552–556. doi: 10.1134/s1028334x07040149.

Kieckhefer, R. M. *et al.* (2003) 'Sea-floor properties from the inversion of 3D multichannel seismic data: a submarine mud-volcanic flow in the Absheron block, offshore Azerbaijan', *Oceans 2003. Celebrating the Past ... Teaming Toward the Future (IEEE Cat. No.03CH37492)*, 5, pp. 2727–2734. doi: 10.1109/oceans.2003.178337.

Kirkham, C. B. (2015) 'A 3D seismic interpretation of mud volcanoes within the western slope of the Nile Cone'. Cardiff University.

Kirkham, C. *et al.* (2017a) 'The genesis of mud volcano conduits through thick evaporite sequences', *Basin Research*, pp. 1–20. doi: 10.1111/bre.12250.

Kirkham, C. *et al.* (2017b) 'The spatial, temporal and volumetric analysis of a large mud volcano province within the Eastern Mediterranean', *Marine and Petroleum Geology*. Elsevier Ltd, 81, pp. 1–16. doi: 10.1016/j.marpetgeo.2016.12.026.

Knapp, C. C. *et al.* (2004) 'Crustal-scale structure of the South Caspian Basin revealed by deep seismic reflection profiling', *Marine and Petroleum Geology*, 21(8), pp. 1073–1081. doi: 10.1016/j.marpetgeo.2003.04.002.

Komar, P. D. (1990) 'Mud volcanoes on Mars?', *Reports of Planetary Geology and Geophysics Program*, pp. 539–541. Available at: <https://ntrs.nasa.gov/search.jsp?R=19920001720>.

Kopf, A. and Behrmann, J. H. (2000) *Extrusion dynamics of mud volcanoes on the Mediterranean Ridge accretionary complex*, *Geological Society, London, Special Publications*. doi: 10.1144/gsl.sp.1999.174.01.10.

Kopf, A. *et al.* (2001) 'Extreme efficiency of mud volcanism in dewatering accretionary prisms', *Earth and Planetary Science Letters*, 189(3–4), pp. 295–313. doi: 10.1016/S0012-821X(01)00278-3.

Kopf, A. J. (2002) 'Significance of mud volcanism', *Reviews of Geophysics*, 40(2), p. 1005. doi: 10.1029/2000RG000093.

Kopf, A. *et al.* (2010) 'Long-term in situ monitoring at Dashgil mud volcano, Azerbaijan: A link between seismicity, pore-pressure transients and methane emission', *International Journal of Earth Sciences*, 99(SUPPL. 1), pp. 227–240. doi: 10.1007/s00531-009-0487-4.

Kozeny, J. (1927) 'Über kapillare leitung der wasser in boden', *Royal Academy of Science Proceedings*. Vienna, 136(2a), pp. 271–306.

Krijgsman, W. *et al.* (2010) 'Rise and fall of the Paratethys Sea during the Messinian Salinity Crisis', *Earth and Planetary Science Letters*. Elsevier B.V., 290(1–2), pp. 183–191. doi: 10.1016/j.epsl.2009.12.020.

Kroonenberg, S. B. *et al.* (2005) 'Two Deltas, Two Basins, One River, One Sea: The Modern Volga Delta as an Analogue of the Neogene Productive Series, South Caspian Basin', *SEPM Special Publication - River Deltas—Concepts, Models, and Examples*, 83, pp. 231–256. doi: 10.2110/pec.05.83.0231.

Kullenberg, B. (1947) 'THE PISTON CORE SAMPLER', *Svenska Hydrografisk-Biologiska Kommissionens Skrifter*, 1(2), p. 46.

Kvalstad, T. J. *et al.* (2005) 'The Storegga slide: Evaluation of triggering sources and slide mechanics', *Marine and Petroleum Geology*, 22(1-2 SPEC. ISS.), pp. 245–256. doi: 10.1016/j.marpetgeo.2004.10.019.

L

Lamontagne, R. a *et al.* (1973) 'Methane Concentrations in Various Marine Environments', *Journal of Geophysical Research*, 78(24), pp. 5317–5324. doi: 10.1029/JC078i024p05317.

Landrou, G. *et al.* (2016) 'Procédé innovant pour développement d'un béton d'argile auto-plaçant', *Terra Lyon*, pp. 1–8. Available at: https://f-origin.hypotheses.org/wp-content/blogs.dir/1981/files/2018/05/TERRA-2016_Th-4_Art-267_Landrou.pdf.

Lee, M. W. and Collett, T. S. (2006) 'Gas hydrate and free gas saturations estimated from velocity logs on hydrate ridge, Offshore Oregon, USA', in Tréhu, A. M. *et al.* (eds) *Proceedings of the Ocean Drilling Program, Scientific Results*. College Station, Texas: Ocean Drilling Program, pp. 1–25. doi: 10.2973/odp.proc.sr.204.103.2006.

Leucci, G. and Giorgi, L. De (2006) 'Experimental studies on the effects of fracture on the P and S wave velocity propagation in sedimentary rock (" Calcarene del Salento ")', 84, pp. 130–142. doi: 10.1016/j.enggeo.2005.12.004.

Limonov, A. F. *et al.* (1996) 'The mediterranean ridge and related mud diapirism: A background', *Marine Geology*, 132(1–4), pp. 7–19. doi: 10.1016/0025-3227(96)00150-8.

Lin, W. *et al.* (2008) 'Estimation of minimum principal stress from an extended leak-off test onboard the Chikyu drilling vessel and suggestions for future test procedures', *Scientific Drilling*, (6), pp. 43–47. doi: 10.2204/lodp.sd.6.06.2008.

Liu, K. *et al.* (2016) 'Deformation behaviour of geotechnical materials with gas bubbles and time dependent compressible organic matter', *Engineering Geology*. Elsevier B.V., 213, pp. 98–106. doi: 10.1016/j.enggeo.2016.09.003.

Locat, J. and Demers, D. (2008) 'Viscosity, yield stress, remolded strength, and liquidity index relationships for sensitive clays', *Canadian Geotechnical Journal*, 25(4), pp. 799–806. doi: 10.1139/t88-088.

Loncke, L. *et al.* (2004) 'Mud volcanoes, gas chimneys, pockmarks and mounds in the Nile deep-sea fan (Eastern Mediterranean): geophysical evidences', *Marine and Petroleum Geology*, 21, pp. 669–689. doi: 10.1016/j.marpetgeo.2004.02.004.

Long, J. C. S. and Witherspoon, P. A. (1985) 'The relationship of the degree of interconnection to permeability in fracture networks', *Journal of Geophysical Research*, 90(B4), p. 3087. doi: 10.1029/jb090ib04p03087.

Luhmann, A. J. *et al.* (2013) 'Permeability reduction produced by grain reorganization and accumulation of exsolved CO₂ during geologic carbon sequestration: A new CO₂ trapping mechanism', *Environmental Science and Technology*, 47(1), pp. 242–251. doi: 10.1021/es3031209.

Lunne, T. *et al.* (1997) *Cone Penetration Testing in Geotechnical Practise*. London: Spon Press.

Lunne, T. *et al.* (2001) 'Deepwater sample disturbance due to stress relief', in *Proceedings of the 1st Annual Offshore Technology Conference*. Houston, Texas, pp. 64–85.

Lunne, T. (2010) 'The CPT in offshore soil investigations - a historic perspective', in *2nd International Symposium on Cone Penetration Testing*. Huntington Beach, CA, USA.

M

Mainguy, M. and Longuemare, P. (2002) 'Coupling Fluid Flow and Rock Mechanics : Formulations of the Partial Coupling between Reservoir and Geomechanical Simulators', *Oil & Gas Science and Technology*, 57(4), pp. 355–367.

Maltman, A. J. and Bolton, A. (2003) 'How sediments become mobilized', *Geological Society, London, Special Publications*, 216(1993), pp. 9–20. doi: 10.1144/GSL.SP.2003.216.01.02.

Manzocchi, T. and Childs, C. (2013) 'Quantification of hydrodynamic effects on capillary seal capacity', *Petroleum Geoscience*, 19, pp. 105–121. doi: 10.1144/petgeo2012-005.

Marett, G. *et al.* (1976) 'Shaly sand evaluation using gammara ray spectrometry, applied to the North Sea Jurassic', in *SPWLA 17th Annual Logging Symposium*, p. 21.

Mazzini, A. *et al.* (2007) 'Triggering and dynamic evolution of the LUSI mud volcano, Indonesia', *Earth and Planetary Science Letters*, 261(3–4), pp. 375–388. doi: 10.1016/j.epsl.2007.07.001.

Mazzini, A. *et al.* (2012) 'A new hydrothermal scenario for the 2006 Lusi eruption, Indonesia. Insights from gas geochemistry', *Earth and Planetary Science Letters*. Elsevier B.V., 317–318(May 2006), pp. 305–318. doi: 10.1016/j.epsl.2011.11.016.

Mazzini, A. and Etiope, G. (2017) 'Mud volcanism: An updated review', *Earth-Science Reviews*. Elsevier B.V., 168, pp. 81–112. doi: 10.1016/j.earscirev.2017.03.001.

Menapace, W. *et al.* (2017) 'Long-term in situ observations at the Athina mud volcano, Eastern Mediterranean: Taking the pulse of mud volcanism', *Tectonophysics*. Elsevier, 721(September), pp. 12–27. doi: 10.1016/j.tecto.2017.09.010.

Michel, G. (2017) 'Mise en place et pérennisation d'un vaste système fluide microbien sur le plateau aquitain : caractérisation et facteurs de contrôle'. Paris 6.

Milkov, A. V. (2000) 'Worldwide distribution of submarine mud volcanoes and associated gas hydrates', *Marine Geology*, 167(1–2), pp. 29–42. doi: 10.1016/S0025-3227(00)00022-0.

Miller, S. A. *et al.* (2004) 'Aftershocks driven by a high- pressure CO₂ source at depth', *letters to nature*, 427(February), pp. 2–5.

Modica, C. J. and Lapierre, S. G. (2012) 'Estimation of kerogen porosity in source rocks as a function of thermal transformation: Example from the Mowry Shale in the Powder River Basin of Wyoming', *AAPG Bulletin*, 96(1), pp. 87–108. doi: 10.1306/04111110201.

- Morgan, E. C. *et al.* (2012) 'Estimation of free gas saturation from seismic reflection surveys by the genetic algorithm inversion of a P-wave attenuation model', 77(4).
- Morley, C. K. (2003) 'Mobile shale related deformation in large deltas developed on passive and active margins', *Geological Society, London, Special Publications*, 216(1), pp. 335–357. doi: 10.1144/gsl.sp.2003.216.01.22.
- Morley, C. K. *et al.* (2011) 'Earth-Science Reviews Deepwater fold and thrust belt classification, tectonics, structure and hydrocarbon prospectivity : A review', *Earth Science Reviews*, 104(1–3), pp. 41–91. doi: 10.1016/j.earscirev.2010.09.010.
- Morley, C. K. *et al.* (2017) 'Review of major shale-dominated detachment and thrust characteristics in the diagenetic zone: Part I, meso- and macro-scopic scale', *Earth-Science Reviews*, 172(May). doi: 10.1016/j.earscirev.2017.07.019.
- Morton, A. *et al.* (2003) 'Provenance patterns in a neotectonic basin: Pliocene and quaternary sediment supply to the South Caspian', *Basin Research*, 15(3), pp. 321–337. doi: 10.1046/j.1365-2117.2003.00208.x.
- Mosar, J. *et al.* (2010) 'Cenozoic-Recent tectonics and uplift in the Greater Caucasus: a perspective from Azerbaijan', *Geological Society, London, Special Publications*, 340(1), pp. 261–280. doi: 10.1144/SP340.12.
- Mourgues, R. *et al.* (2012) 'Formation of conical fractures in sedimentary basins: Experiments involving pore fluids and implications for sandstone intrusion mechanisms', *Earth and Planetary Science Letters*. Elsevier B.V., 313–314(1), pp. 67–78. doi: 10.1016/j.epsl.2011.10.029.
- Mukherjee, S. *et al.* (2010) 'Viscosity estimates of salt in the Hormuz and Namakdan salt diapirs , Persian Gulf', *Geology Magazine*, 147(4), pp. 497–507. doi: 10.1017/S001675680999077X.
- Mumma, M. J. *et al.* (2009) 'Strong Release of Methane on Mars in Northern Summer 2003', *Science*, 323, pp. 1041–1045.

N

- Nadirov, R. S. *et al.* (1997) 'Flexural plate subsidence, sedimentation rates, and structural development of the super-deep South Caspian Basin', *Marine and Petroleum Geology*, 14(4), pp. 383–400. doi: 10.1016/S0264-8172(96)00054-2.
- Nageswaran, S. (1983) 'Effect of gas bubbles on sediment behavior'. University of Oxford.
- Naudts, L. *et al.* (2012) 'Stratigraphic and structural control on the distribution of gas hydrates and active gas seeps on the Posolsky Bank , Lake Baikal', *Geo-Marine Letters*, 32, pp. 395–406. doi: 10.1007/s00367-012-0286-y.
- Nava Castro, R. (2010) *Influencia del gas metano en las propiedades mecánicas de la arcilla marina*. Mexico D.F.
- Nava Castro, R. *et al.* (2013) 'Variation of Mechanical Properties of Soft Marine Clay with Methane Gas Content - OMAE2013-10800', in *Proceedings of the ASME 2013 32nd International Conference on Ocean, Offshore and Arctic Engineering - OMAE2013*. Nantes, pp. 1–9.
- Naylor, P. *et al.* (2000) 'Relative permeability measurements for post-waterflood depressurisation of the Miller field, North Sea', in *SPE annual technical conference and exhibition*. Dallas, Texas: Society of Petroleum Engineers, pp. 491–497.

Nely, G. (1986) '8. La méthode de sismique réflexion', in *Méthodes Géophysiques (Vol. 2)*. Editions TECHNIP, pp. 147–244.

Nerموen, A. *et al.* (2010) 'Experimental and analytic modeling of piercement structures', *Journal of Geophysical Research: Solid Earth*, 115(10), pp. 1–15. doi: 10.1029/2010JB007583.

Niemann, H. and Boetius, A. (2014) 'Mud Volcanoes', in Timmis, K. N. (ed.) *Handbook of Hydrocarbon and Lipid Microbiology*. Berlin: Springer-Verlag, pp. 205–214. doi: 10.1007/978-3-642-00810-8.

Nolen-hoeksema, R. (2013) 'Elements of Hydraulic Fracturing', *Oilfield Review*, (2), pp. 51–52.

O

Obradors-Prats, J. *et al.* (2017) 'Assessing the implications of tectonic compaction on pore pressure using a coupled geomechanical approach', *Marine and Petroleum Geology*. Elsevier Ltd, 79, pp. 31–43. doi: 10.1016/j.marpetgeo.2016.10.017.

Odonne, F. *et al.* (1999) 'Abnormal reverse faulting above a depleting reservoir', *Geology*, 27(2), pp. 111–114. doi: 10.1130/0091-7613(1999)027<0111:ARFAAD>2.3.CO;2.

Odonne, F. *et al.* (in press) 'MUD VOLCANO GROWTH BY RADIAL EXPANSION: EXAMPLES FROM ONSHORE AZERBAIJAN', *Marine and Petroleum Geology*. Elsevier Ltd.

Oehler, D. Z. and Allen, C. C. (2010) 'Evidence for pervasive mud volcanism in Acidalia Planitia, Mars', *Icarus*. Elsevier Inc., 208(2), pp. 636–657. doi: 10.1016/j.icarus.2010.03.031.

Olsen, H. W. (1960) 'Hydraulic Flow Through Saturated Clays', *Clays and Clay Minerals*, 9(1), pp. 131–161.

Opara, A. I. (2011) 'ESTIMATION OF MULTIPLE SOURCES OF OVERPRESSURES USING VERTICAL EFFECTIVE STRESS APPROACH : CASE STUDY OF THE NIGER DELTA , NIGERIA', *Petroleum & Coal*, 53(4), pp. 302–314.

Oppo, D. *et al.* (2014) 'Mud volcanism and fluid geochemistry in the Cheleken peninsula, western Turkmenistan', *Marine and Petroleum Geology*. Elsevier Ltd, 57, pp. 122–134. doi: 10.1016/j.marpetgeo.2014.05.009.

Oppo, D. and Capozzi, R. (2016) 'Spatial association of mud volcano and sandstone intrusions, Boyadag anticline, western Turkmenistan', *Basin Research*, 28(6), pp. 827–839. doi: 10.1111/bre.12136.

Osborne, M. J. and Swarbrick, R. E. (1997) 'Mechanisms for Generating Overpressure in Sedimentary Basins : A Reevaluation 1', *AAPG Bulletin*, 6(6), pp. 1023–1041.

P

PCDM (2018) *Calculateur principal, DATARMOR*. Available at: <https://wwz.ifremer.fr/pcdm/Equipement> (Accessed: 27 August 2019).

Perez-García, C. *et al.* (2009) 'The Håkon Mosby mud volcano : 330 000 years of focused fluid flow activity at the SW Barents Sea slope', *Marine Geology*, 262, pp. 105–115. doi: 10.1016/j.margeo.2009.03.022.

Peters, K. E. and Cassa, M. R. (1994) 'Applied Source Rock Geochemistry', in Magoon, L. B., and Dow, W. G. (eds) *The Petroleum System - From Source to Trap*. American Association of Petroleum Geologists, pp. 93–120. doi: <https://doi.org/10.1306/M60585>.

Planke, S. *et al.* (2003) 'Mud and fluid migration in active mud volcanoes in Azerbaijan', *Geo-Marine*

Letters, 23(3–4), pp. 258–267. doi: 10.1007/s00367-003-0152-z.

Pollastro, R. M. (1993) 'Considerations and applications of the illite/smectite geothermometer in hydrocarbon-bearing rocks of miocene to Mississippian age', *Clays and Clay Minerals*, 41(2), pp. 119–133. doi: 10.1346/CCMN.1993.0410202.

Pondrelli, M. *et al.* (2011) 'Mud volcanoes in the geologic record of Mars: The case of Firsoff crater', *Earth and Planetary Science Letters*. Elsevier B.V., 304(3–4), pp. 511–519. doi: 10.1016/j.epsl.2011.02.027.

Popov, S. V. *et al.* (2004) *Lithological-paleogeographic maps of paratethys*, CFS Courier Forschungsinstitut Senckenberg.

Popp, T. and Salzer, K. (2007) 'Anisotropy of seismic and mechanical properties of Opalinus clay during triaxial deformation in a multi-anvil apparatus', *Physics and Chemistry of the Earth*, 32, pp. 879–888. doi: 10.1016/j.pce.2006.04.022.

Posamentier, H. W. and Allen, G. P. (1999) *Siliciclastic Sequence Stratigraphy—Concepts and Applications*. SEPM Society for Sedimentary Geology. doi: <https://doi.org/10.2110/csp.99.07>.

Praeg, D. *et al.* (2009) 'Tectonically-driven mud volcanism since the late Pliocene on the Calabrian accretionary prism, central Mediterranean Sea', *Marine and Petroleum Geology*. Elsevier Ltd, 26(9), pp. 1849–1865. doi: 10.1016/j.marpetgeo.2009.03.008.

Priest, J. A. *et al.* (2014) 'Potential impact of gas hydrate and its dissociation on the strength of host sediment in the Krishna-Godavari Basin', *Marine and Petroleum Geology*. Elsevier Ltd, 58(PA), pp. 187–198. doi: 10.1016/j.marpetgeo.2014.05.008.

Priestley, K. *et al.* (1994) 'Implications of earthquake focal mechanism data for the active tectonics of the South Caspian and surrounding regions', *Geophysical Journal International*, 118, pp. 111–141.

Prinzhofer, A. and Deville, E. (2013) 'Origins of hydrocarbon gas seeping out from offshore mud volcanoes in the Nile delta', *Tectonophysics*, 591, pp. 52–61. doi: 10.1016/j.tecto.2011.06.028.

R

Rebata-landa, V. and Santamarina, J. C. (2006) 'Mechanical limits to microbial activity in deep sediments', *Geochemistry Geophysics Geosystems*, 7(11), pp. 1–12. doi: 10.1029/2006GC001355.

Rebata-Landa, V. *et al.* (2012) 'Mechanical Effects of Biogenic Nitrogen Gas Bubbles in Soils', (February), pp. 128–137. doi: 10.1061/(ASCE)GT.1943-5606.0000571.

Reilinger, R. E. *et al.* (1997) 'Preliminary estimates of plate convergence in the Caucasus collision zone from global positioning system measurements', *Geophysical Research Letters*, 24(14), pp. 1815–1818.

Ren, X. *et al.* (2016) 'A relation of hydraulic conductivity — void ratio for soils based on Kozeny-Carman equation', *Engineering Geology*. Elsevier B.V., 213, pp. 89–97. doi: 10.1016/j.enggeo.2016.08.017.

Revil, A. *et al.* (1998) 'Capillary sealing in sedimentary basins: A clear field example', *Geophysical Research Letters*, 25(3), pp. 389–392.

Revil, A. *et al.* (1999) 'Fluid overpressures in western Mediterranean sediments, Sites 974-979', *Proc. Ocean Drill. Program, 161 Sci. Results*, 161, pp. 117–128. doi: 10.2973/odp.proc.sr.161.274.1999.

Riboulot, V. *et al.* (2013) 'Sea-level change and free gas occurrence influencing a submarine landslide and pockmark formation and distribution in deepwater Nigeria', *Earth and Planetary Science Letters*. Elsevier, 375, pp. 78–91. doi: 10.1016/j.epsl.2013.05.013.

Riboulot, V. *et al.* (2016) 'Initiation of gas-hydrate pockmark in deep-water Nigeria: Geo-mechanical analysis and modelling', *Earth and Planetary Science Letters*. Elsevier B.V., 434, pp. 252–263. doi: 10.1016/j.epsl.2015.11.047.

Ricker, N. (1953) 'The Form and Laws of Propagation of Seismic Wavelets', *Geophysics*, 18(1), pp. 10–40.

Riedel, M. *et al.* (2006) 'PHYSICAL PROPERTIES OF NEAR-SURFACE SEDIMENTS AT SOUTHERN HYDRATE RIDGE : RESULTS FROM ODP LEG 204', 204(April).

Rietveld, H. M. (1969) 'A profile refinement method for nuclear and magnetic structures', *Journal of Applied Crystallography*. International Union of Crystallography, 2(2), pp. 65–71. doi: 10.1107/S0021889869006558.

Robein, E. (2010) *Seismic Imaging. A review of the Techniques, their Principles, Merits and Limitations*. Houten, The Netherlands: EAGE Publications bv.

Roberts, K. S. *et al.* (2010) 'Structure of exhumed mud volcano feeder complexes, Azerbaijan', *Basin Research*, 22(4), pp. 439–451. doi: 10.1111/j.1365-2117.2009.00441.x.

Roberts, K. S. (2011) 'Mud Volcano Systems : Structure , Evolution and Processes'. Durham University. Available at: <http://etheses.dur.ac.uk/752/>.

Ross, D. J. K. and Bustin, R. M. (2009) 'The importance of shale composition and pore structure upon gas storage potential of shale gas reservoirs', *Marine and Petroleum Geology*. Elsevier Ltd, 26(6), pp. 916–927. doi: 10.1016/j.marpetgeo.2008.06.004.

Ross, J. A. *et al.* (2011) 'An integrated model of extrusive sand injectites in cohesionless sediments', *Sedimentology*, 58(7), pp. 1693–1715. doi: 10.1111/j.1365-3091.2011.01230.x.

Ryzak, M. and Bieganski, A. (2011) 'Methodological aspects of determining soil particle-size distribution using the laser diffraction method', *Journal of Plant Nutrition and Soil Science*, 174(4), pp. 624–633. doi: 10.1002/jpln.201000255.

S

Santos Betancor, I. (2015) 'Mud Diapirs and Folds in the South Caspian Basin : Geometry and Syn-Sedimentary Evolution of Structures with Petroleum Interest'. University of Granada. Available at: <http://hdl.handle.net/10481/42148>.

Santos Betancor, I. and Soto, J. I. (2015) '3D geometry of a shale-cored anticline in the western South Caspian Basin (offshore Azerbaijan)', *Marine and Petroleum Geology*. Elsevier Ltd, 67, pp. 829–851. doi: 10.1016/j.marpetgeo.2015.06.012.

Savage, H. M. and Brodsky, E. E. (2011) 'Collateral damage: Evolution with displacement of fracture distribution and secondary fault strands in fault damage zones', *Journal of Geophysical Research: Solid Earth*, 116(3). doi: 10.1029/2010JB007665.

Schlumberger (2019) *StethoScope Formation Pressure-While-Drilling Service*. Available at: https://www.slb.com/services/drilling/mwd_lwd/formation_pressure/stethoscope.aspx.

Schneider, F. *et al.* (2004) 'Basin Modeling in a Complex Area: Example from the Eastern Venezuelan Foothills', in Swennen, R., Roure, F., and Granath, J. W. (eds) *Deformation, fluid flow, and reservoir appraisal in foreland fold and thrust belts*. AAPG Hedberg Series, pp. 357–369. doi: 10.1306/1025700H1504.

Segesman, F. F. (1980) 'Well-logging method', 45(11), pp. 1667–1684.

- Shin, H. and Santamarina, J. C. (2011) 'Open-mode discontinuities in soils', *Géotechnique Letters*, 1, pp. 95–99. doi: <http://dx.doi.org/10.1680/geolett.11.00014>.
- Sibson, R. H. (2003) 'Brittle-failure controls on maximum sustainable overpressure in different tectonic regimes', *American Association of Petroleum Geologists Bulletin*, 87(6), pp. 901–908. doi: 10.1306/01290300181.
- Sills, G. C. *et al.* (1991) 'Behaviour of offshore soils containing gas bubbles', *Géotechnique*, 41(2), pp. 227–241.
- Sills, G. C. and Gonzalez, R. (2001) 'Consolidation of naturally gassy soft soil', *Géotechnique*, 51(7).
- Skempton, A. W. (1944) 'Notes on the compressibility of clays', *Quarterly Journal of the Geological Society of London*, 100, pp. 119–135.
- Skinner, J. A. and Tanaka, K. L. (2007) 'Evidence for and implications of sedimentary diapirism and mud volcanism in the southern Utopia highland – lowland boundary plain, Mars', *Icarus*, 186, pp. 41–59. doi: 10.1016/j.icarus.2006.08.013.
- Skinner, J. A. and Mazzini, A. (2009) 'Martian mud volcanism : Terrestrial analogs and implications for formational scenarios', *Marine and Petroleum Geology*. Elsevier Ltd, 26(9), pp. 1866–1878. doi: 10.1016/j.marpetgeo.2009.02.006.
- Smith-Rouch, L. S. (2006) 'Oligocene-Miocene Maykop/Diatom Total Petroleum System of the South Caspian Basin Province, Azerbaijan, Iran, and Turkmenistan', *U.S. Geological Survey Bulletin*, 2201–I, p. 27.
- Snyder, D. and Fleming, D. B. (1985) 'Well logging-A 25-year perspective', 50(12), pp. 2504–2529.
- Soave, G. (1972) 'Equilibrium constants from a modified Redlich-Kwong equation of state', *Chemical Engineering Science*, 27(6), pp. 1197–1203. doi: 10.1016/0009-2509(72)80096-4.
- Sobkowicz, J. C. (1982) 'The Mechanics of Gassy Sediments'. University of Alberta.
- Sobkowicz, J. C. and Morgenstern, N. R. (1984) 'The undrained equilibrium behaviour of gassy sediments', *Canadian Geotechnical Journal*, 21, pp. 439–448.
- Somoza, L. *et al.* (2003) 'Seabed morphology and hydrocarbon seepage in the Gulf of Cádiz mud volcano area: Acoustic imagery, multibeam and ultra-high resolution seismic data', *Marine Geology*, 195(1–4), pp. 153–176. doi: 10.1016/S0025-3227(02)00686-2.
- Stewart, S. A. and Davies, R. J. (2006) 'Structure and emplacement of mud volcano systems in the South Caspian Basin', *AAPG Bulletin*, 90(5), pp. 771–786. doi: 10.1306/11220505045.
- Stratton, J. A. (1941) *Electromagnetic Theory*. New York: McGraw-Hill.
- Sultan, N. *et al.* (2004) 'Triggering mechanisms of slope instability processes and sediment failures on continental margins: A geotechnical approach', *Marine Geology*, 213(1–4), pp. 291–321. doi: 10.1016/j.margeo.2004.10.011.
- Sultan, N. *et al.* (2007) 'Potential role of compressional structures in generating submarine slope failures in the Niger Delta', *Marine Geology*, 237(3–4), pp. 169–190. doi: 10.1016/j.margeo.2006.11.002.
- Sultan, N. *et al.* (2010) 'Investigation of a possible submarine landslide at the Var delta front (Nice slope - SE France)', *Canadian Geotechnical Journal*, 47(4), pp. 486–496.
- Sultan, N. *et al.* (2010) 'YIELDING AND PLASTIC BEHAVIOUR OF BOOM CLAY', *Géotechnique*, 60(9), pp. 657–666.
- Sultan, N. *et al.* (2012) 'Mechanical behaviour of gas-charged marine plastic sediments', *Géotechnique*,

62(9), pp. 751–766. doi: 10.1680/geot.12.OG.002.

Sultan, N. and Garziglia, S. (2014) 'Mechanical behaviour of gas-charged fine sediments: model formulation and calibration', *Géotechnique*, 64(11), pp. 851–864. doi: 10.1680/geot.13.P.125.

Swarbrick, R. E. *et al.* (2002) 'Comparison of Overpressure Magnitude Resulting from the Main Generating Mechanisms Generating Mechanisms', *AAPG Memoir*, 76, pp. 1–12.

T

Tagiyev, M. F. *et al.* (1997) 'Geohistory, thermal history and hydrocarbon generation history of the north-west South Caspian Basin', *Marine and Petroleum Geology*, 14(4), pp. 363–382. doi: 10.1016/S0264-8172(96)00053-0.

Taleb, F. *et al.* (2018) 'Hydromechanical Properties of Gas Hydrate-Bearing Fine Sediments From In Situ Testing', *Journal of Geophysical Research: Solid Earth*, 123(11), pp. 9615–9634. doi: 10.1029/2018JB015824.

Tang, X. *et al.* (2016) 'A dual-site Langmuir equation for accurate estimation of high pressure deep shale gas resources', *Fuel*, 185(December), pp. 10–17. doi: 10.1016/j.fuel.2016.07.088.

Terzaghi, K. (1943) *THEORETICAL SOIL MECHANICS*. Edited by John Wiley and Sons Incorporated. New York.

Terzaghi, K. and Peck, R. B. (1948) *SOIL MECHANICS IN ENGINEERING PRACTICE*. Edited by Chapman & Hall Limited. London.

Thomas, S. D. (1987) 'The consolidation behaviour of gassy soil'. University of Oxford.

Tingay, M. R. P. *et al.* (2005) 'Present-day stress orientation in Brunei: a snapshot of "prograding tectonics" in a Tertiary delta', *Journal of the Geological Society*, 162(1), pp. 39–49. doi: 10.1144/0016-764904-017.

Tingay, M. R. P. *et al.* (2007) "'Vertically transferred" overpressures in Brunei: Evidence for a new mechanism for the formation of high-magnitude overpressure', *Geology*, 35(11), pp. 1023–1026. doi: 10.1130/G23906A.1.

Tingay, M. *et al.* (2008) 'Triggering of the Lusi mud eruption: Earthquake versus drilling initiation', *Geology*, 36(8), pp. 639–642. doi: 10.1130/G24697A.1.

Tingay, M. R. P. *et al.* (2015) 'Initiation of the Lusi mudflow disaster', *Nature Geoscience*, 8(7), pp. 493–494. doi: 10.1038/ngeo2472.

Tingay, M. *et al.* (2017) 'An alternative review of facts, coincidences and past and future studies of the Lusi eruption', *Marine and Petroleum Geology*, (December). doi: 10.1016/j.marpetgeo.2017.12.031.

Torrance, J. K. (2010) 'Shear resistance of remoulded soils by viscometric and fall-cone methods: a comparison for the Canadian sensitive marine clays', *Canadian Geotechnical Journal*, 24(2), pp. 318–322. doi: 10.1139/t87-037.

Tryggvason, G. *et al.* (2006) 'Direct numerical simulations of gas / liquid multiphase flows Direct numerical simulations of gas / liquid multiphase flows', *Fluid Dynamics Research*, 38, pp. 660–681. doi: 10.1016/j.fluidyn.2005.08.006.

Tryggvason, G. *et al.* (2011) *Direct Numerical Simulations of Gas-Liquid Multiphase Flows*. Cambridge university press.

Tryggvason, G. (2012) *A Front-tracking/Finite-Volume Navier-Stokes Solver for Direct Numerical Simulations of Multiphase Flows*.

U

Unterseh, S. and Contet, J. (2015) 'Integrated geohazards assessments offshore Azerbaijan, Caspian Sea', *Offshore Technology Conference*, OTC-25911(May), pp. 1–8. doi: 10.4043/25911-MS.

V

Vernant, P. *et al.* (2004) 'Deciphering oblique shortening of central Alborz in Iran using geodetic data', *Earth and Planetary Science Letters*, 223(1–2), pp. 177–185. doi: 10.1016/j.epsl.2004.04.017.

Vernik, L. (1994) 'Hydrocarbon-generation-induced microcracking of source rocks', *Geophysics*, 59(4), pp. 555–563.

Vidal, O. and Dubacq, B. (2009) 'Thermodynamic modelling of clay dehydration, stability and compositional evolution with temperature, pressure and H₂O activity', *Geochimica et Cosmochimica Acta*. Elsevier Ltd, 73(21), pp. 6544–6564. doi: 10.1016/j.gca.2009.07.035.

Vincent, S. J. *et al.* (2010) 'Contrasting Pliocene fluvial depositional systems within the rapidly subsiding South Caspian Basin; a case study of the palaeo-Volga and palaeo-Kura river systems in the Surakhany Suite, Upper Productive Series, onshore Azerbaijan', *Marine and Petroleum Geology*. Elsevier Ltd, 27(10), pp. 2079–2106. doi: 10.1016/j.marpetgeo.2010.09.007.

W

Wanzhong, S. (2007) 'Effect of Overpressure on Rock Frame and Its Implications for Overpressure Evolution', *Journal of China University of Geosciences*, 18(3), pp. 232–241.

Wheeler, S. J. (1986) 'THE STRESS-STRAIN BEHAVIOUR OF SOILS CONTAINING GAS BUBBLES'. University of Oxford.

Wheeler, S. J. (1988) 'The undrained shear strength of soils containing large gas bubbles', *Géotechnique*, 38(3), pp. 399–413.

Wibberley, C. A. J. *et al.* (2008) 'Recent advances in the understanding of fault zone internal structure: a review', *Geological Society, London, Special Publications*, 299(1), pp. 5–33. doi: 10.1144/sp299.2.

Wibberley, C. A. J. *et al.* (2017) 'Faults as barriers or channels to production-related flow: insights from case studies', *Petroleum Geoscience*, 23(1), pp. 134–147. doi: 10.1144/petgeo2016-057.

Wikipedia: Absheron gas field (2018). Available at: https://en.wikipedia.org/wiki/Absheron_gas_field (Accessed: 1 June 2019).

Wilkins, R. H. and Richardson, M. D. (1998) 'The influence of gas bubbles on sediment acoustic properties: in situ, laboratory, and theoretical results from Eckernförde Bay, Baltic sea', *Continental Shelf Research*, 18, pp. 1859–1892.

Woolsey, S. *et al.* (1975) 'Modeling of Diatreme Emplacement', pp. 29–42.

Wu, K. and Olson, J. E. (2015) 'Simultaneous Multifracture Treatments: Fully Coupled Fluid Flow and Fracture Mechanics for Horizontal Wells', in *SPE Annual Technical Conference and Exhibition*. New Orleans: Society of Petroleum Engineers, pp. 337–346.

Wyllie, M. R. J. *et al.* (1958) 'An experimental investigation of factors affecting elastic wave velocities in porous media', *Geophysics*, XXIII(3), pp. 459–493. doi: 10.1190/1.1438493.

Y

Yusifov, M. and Rabinowitz, P. D. (2004) 'Classification of mud volcanoes in the South Caspian Basin, offshore Azerbaijan', *Marine and Petroleum Geology*, 21, pp. 965–975. doi: 10.1016/j.marpetgeo.2004.06.002.

Z

Zhang, T. *et al.* (2012) 'Effect of organic-matter type and thermal maturity on methane adsorption in shale-gas systems', *Organic Geochemistry*. Elsevier Ltd, 47, pp. 120–131. doi: 10.1016/j.orggeochem.2012.03.012.

Zhang, X. *et al.* (2013) 'Porosity Formation and Evolution of the Deeply Buried Lower Triassic Feixianguan Formation, Puguang Gas Field, NE Sichuan Basin, China', *Open Journal of Geology*, 3(August), pp. 300–312. doi: 10.4236/ojg.2013.34035.

Zitter, T. (2004) 'Mud volcanism and fluid emissions in Eastern Mediterranean neotectonic zones'. Free University of Amsterdam. doi: 10.1017/S002221510700713X.

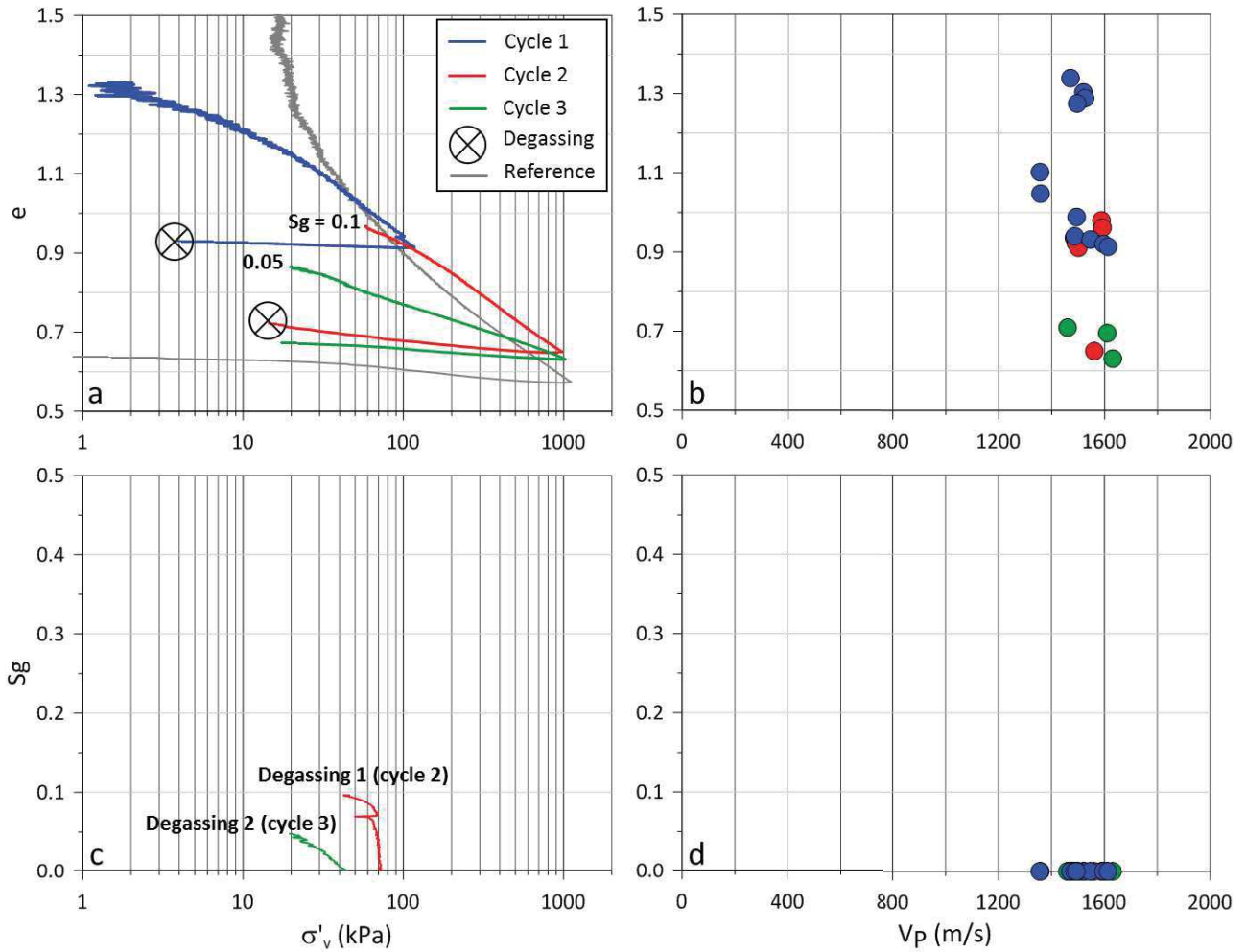
Zonenshain, L. P. and Pichon, X. (1986) 'Deep basins of the Black Sea and Caspian Sea as remnants of Mesozoic back-arc basins', *Tectonophysics*, 123(1–4), pp. 181–211. doi: 10.1016/0040-1951(86)90197-6.

Zoporowski, A. and Miller, S. A. (2009) 'Modelling eruption cycles and decay of mud volcanoes', *Marine and Petroleum Geology*. Elsevier Ltd, 26(9), pp. 1879–1887. doi: 10.1016/j.marpetgeo.2009.03.003.

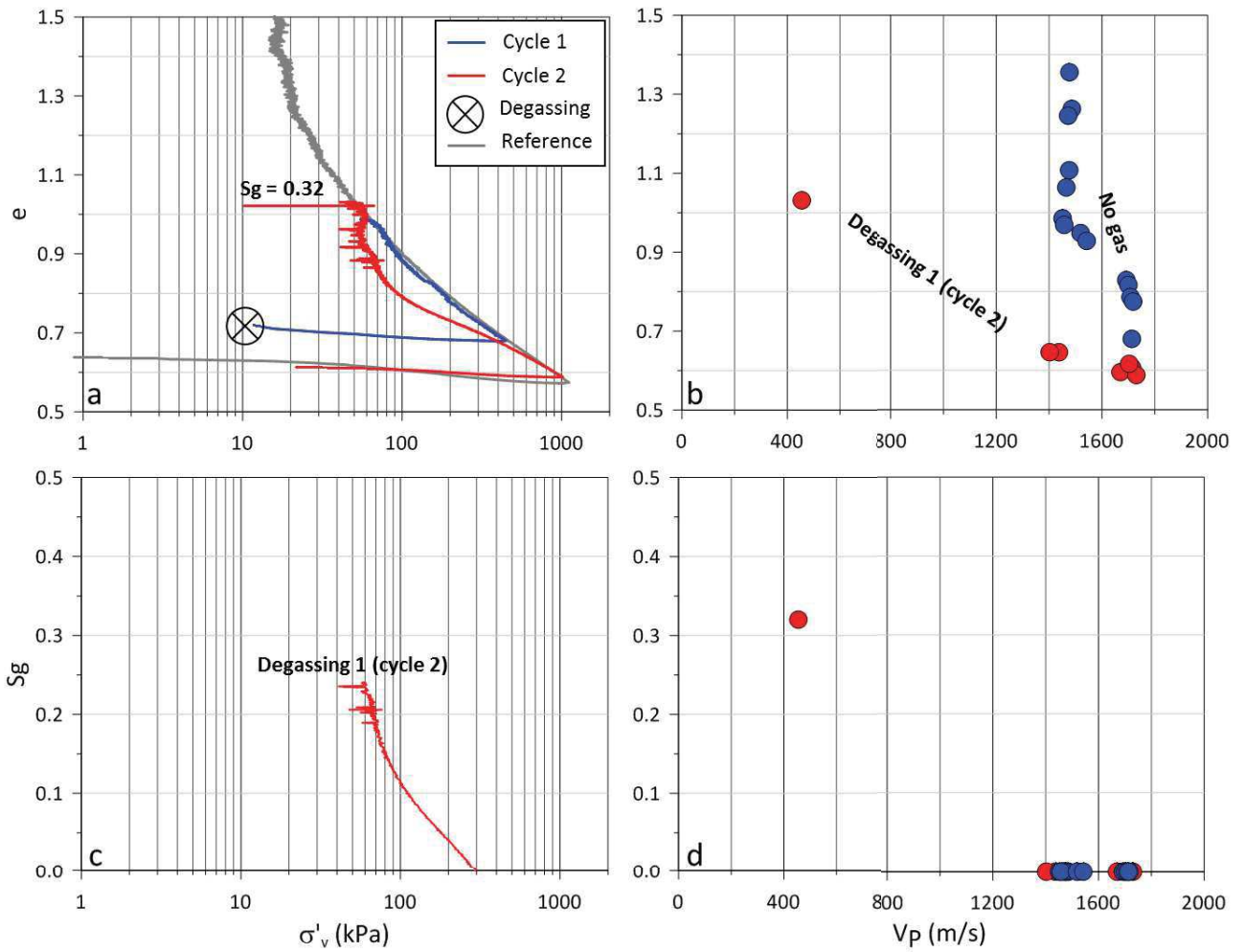
Zuo, L. *et al.* (2012) 'An Experimental Study of CO₂ Exsolution and Relative Permeability Measurements During CO₂ Saturated Water Depressurization', *Transport in Porous Media*, 91(2), pp. 459–478. doi: 10.1007/s11242-011-9854-2.

Appendix 1: Additional testing results

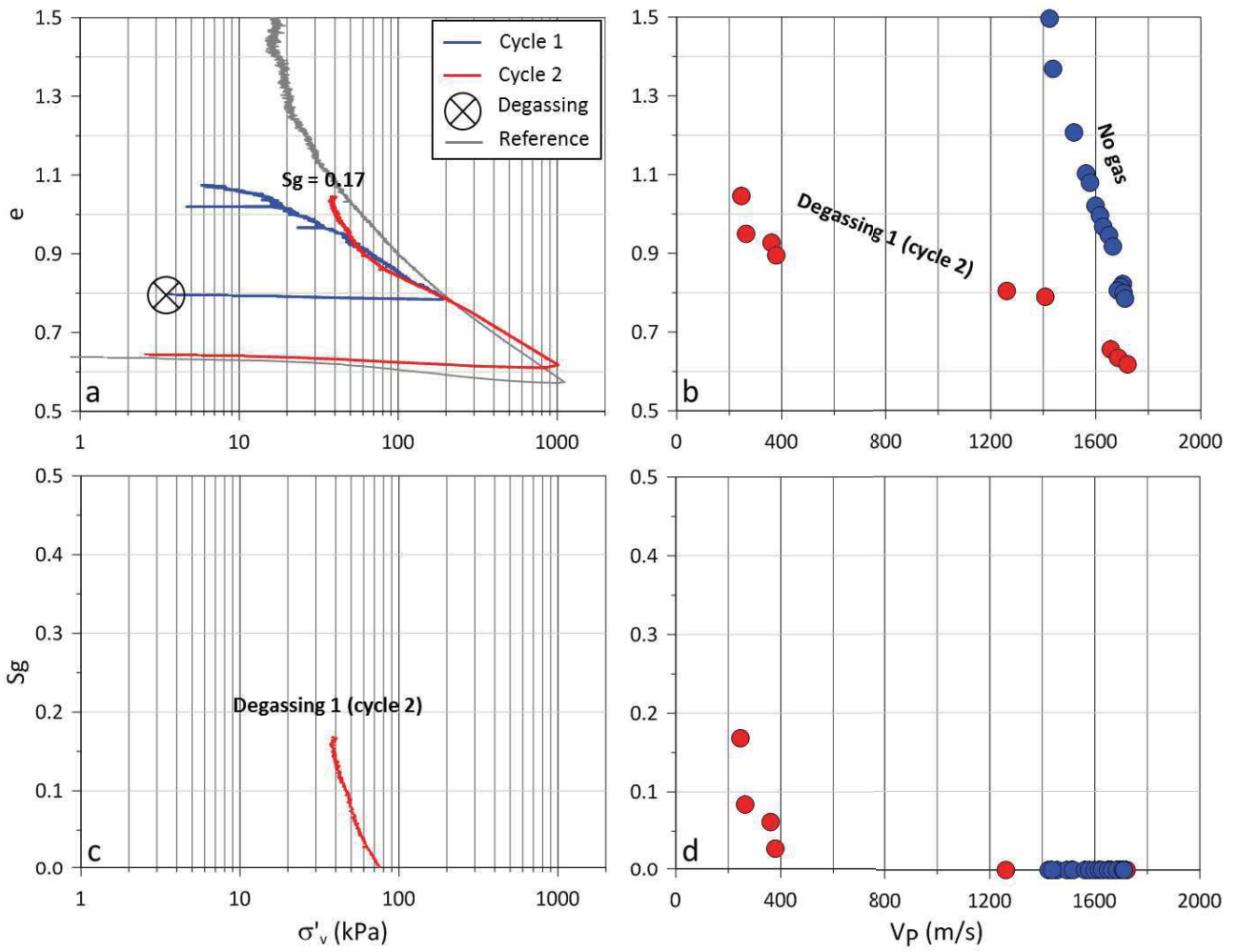
This appendix displays the experimental testing results that were not detailed in Chapter 4. The results are presented in the same fashion as in Figure 4.12, Figure 4.14 and Figure 4.16.



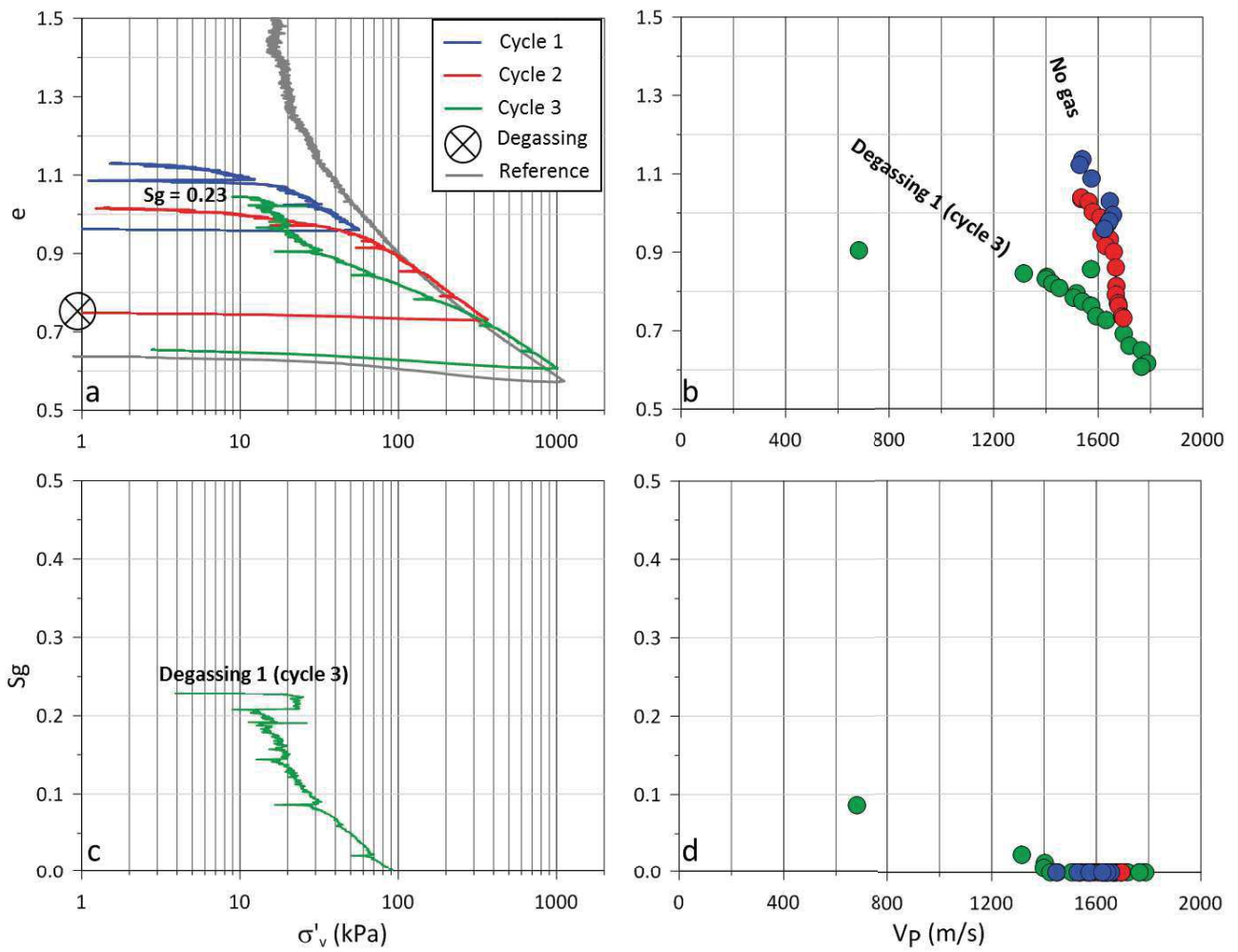
Appendix 1 - Figure 1: Results for test#2 with 3 load/unload cycles. Each color represents a load/unload cycle. a: void ratio (e) versus vertical effective stress (σ'_v); b: void ratio-versus P wave velocity (V_p); c: degree of gas saturation (S_g) versus σ'_v and d: S_g versus V_p . The grey line in (a) represents the reference consolidation test.



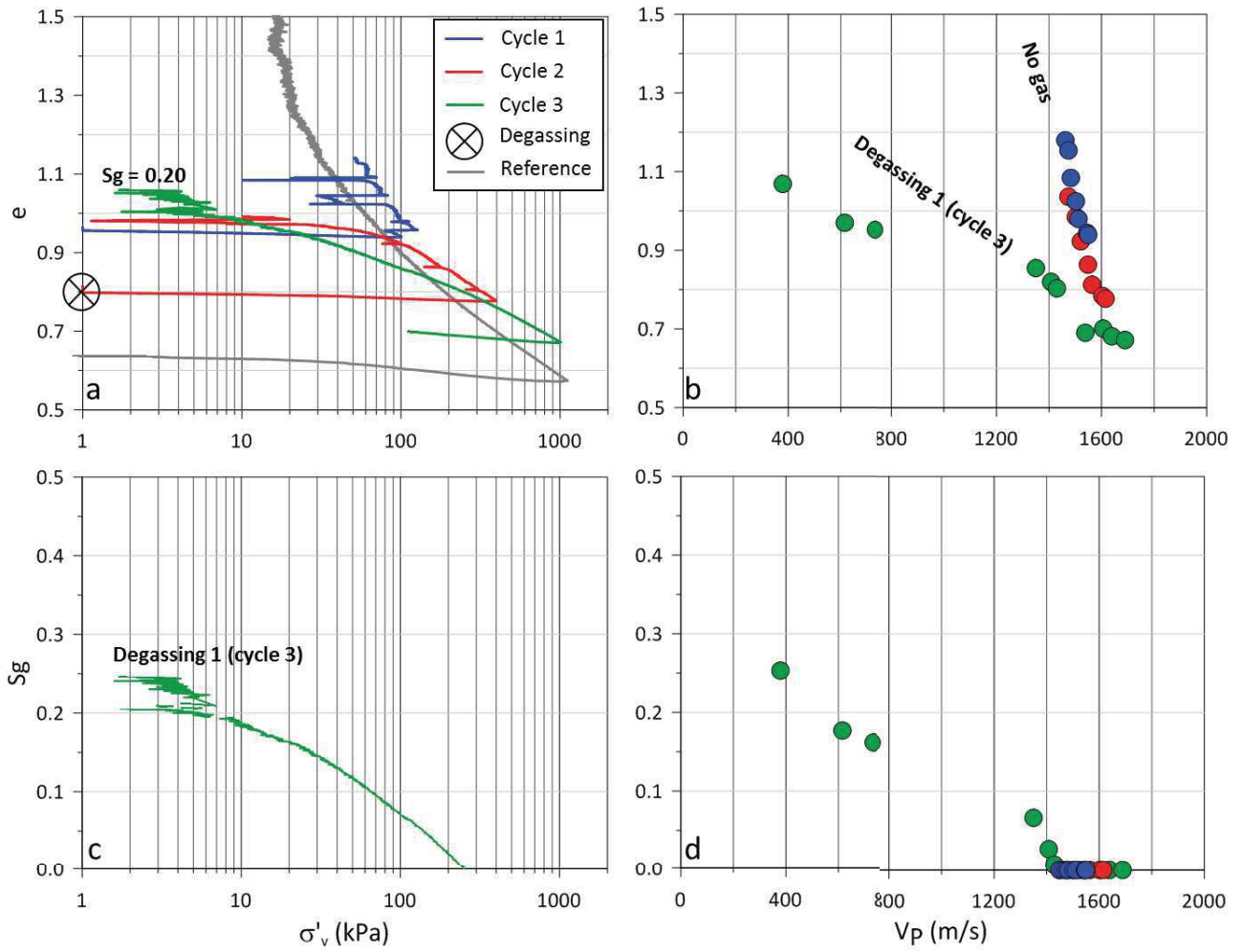
Appendix 1 - Figure 2: Results for test#3 with 2 load/unload cycles. Each color represents a load/unload cycle. a: void ratio (e) versus vertical effective stress (σ'_v); b: void ratio-versus P wave velocity (V_p); c: degree of gas saturation (S_g) versus σ'_v and d: S_g versus V_p . The grey line in (a) represents the reference consolidation test.



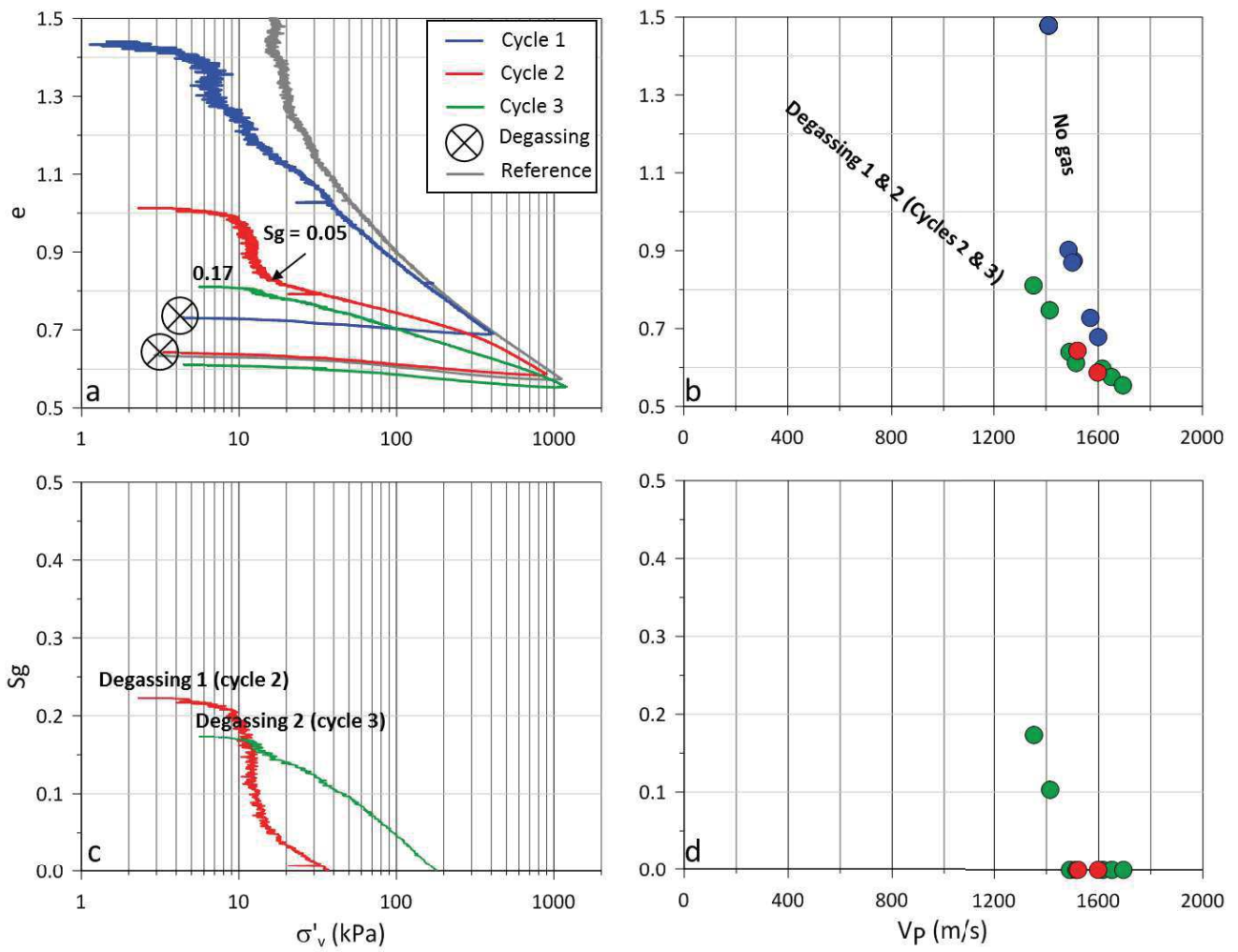
Appendix 1 - Figure 3: Results for test#4 with 2 load/unload cycles. Each color represents a load/unload cycle. a: void ratio (e) versus vertical effective stress (σ'_v); b: void ratio-versus P wave velocity (V_p); c: degree of gas saturation (S_g) versus σ'_v and d: S_g versus V_p . The grey line in (a) represents the reference consolidation test.



Appendix 1 - Figure 4: Results for test#6 with 3 load/unload cycles. Each color represents a load/unload cycle. a: void ratio (e) versus vertical effective stress (σ'_v) b: void ratio-versus P wave velocity (V_p); c: degree of gas saturation (S_g) versus σ'_v and d: S_g versus V_p . The grey line in (a) represents the reference consolidation test.



Appendix 1 - Figure 5: Results for test#7 with 3 load/unload cycles. Each color represents a load/unload cycle. a: void ratio (e) versus vertical effective stress (σ'_v) b: void ratio-versus P wave velocity (V_p); c: degree of gas saturation (S_g) versus σ'_v and d: S_g versus V_p . The grey line in (a) represents the reference consolidation test.



Appendix 1 - Figure 6: Results for test#9 with 3 load/unload cycles. Each color represents a load/unload cycle. a: void ratio (e) versus vertical effective stress (σ'_v); b: void ratio-versus P wave velocity (V_p); c: degree of gas saturation (S_g) versus σ'_v and d: S_g versus V_p . The grey line in (a) represents the reference consolidation test. The fourth load/unload cycle is not displayed as exsolution was completed under a constant vertical stress and the results are not relevant in this study. As the sample broke into two separate parts during the first exsolution, the degree of gas saturation was calculated once the two halves were in contact again (black arrow).

Appendix 2: Published journal articles

This section lists the work presented and/or accepted for publication related to this research.

The first article presents the main results of Chapter 3 and is published in the *Journal of Geophysical Research: Earth Surface* and was accepted for publication in February 2019: Blouin, A. *et al.* (2019) 'Evolution model for the Absheron mud volcano: from in - situ observations to numerical modeling', *Journal of Geophysical Research: Earth Surface*, 124(3), pp. 766–794. doi: 10.1029/2018JF004872. The article is attached below.

A second article is accepted in the *Engineering Geology* journal in May 2019 and awaits for editor's decision after minor revisions. The article is submitted under the title "Sediment damage caused by gas exsolution: a key mechanism for mud volcano formation". It presents the results of Chapter 4.

Results presented in Chapter 5 will be submitted soon as a companion paper of Blouin *et al.* (2019).

Another article presents results from fieldwork realized over several active mud volcanoes located onshore Azerbaijan. I participated in the fieldwork in 2017 and in some of the data acquisition and interpretation and I am therefore co-author of the paper. The purpose of the paper is to understand the growth of flat-topped MVs combining geophysical data and field observations and structural measurements. The paper was successfully submitted and accepted in the *Marine and Petroleum Geology* journal under the title "Mud volcano growth by radial expansion: examples from onshore Azerbaijan" (Odonne, F. *et al.* (in press) 'MUD VOLCANO GROWTH BY RADIAL EXPANSION: EXAMPLES FROM ONSHORE AZERBAIJAN', *Marine and Petroleum Geology*.).

RESEARCH ARTICLE

10.1029/2018JF004872

Evolution Model for the Absheron Mud Volcano: From In Situ Observations to Numerical Modeling

Arthur Blouin^{1,2,3} , Patrice Imbert² , Nabil Sultan¹ , and Jean-Paul Callot³ ¹Ifremer, Géosciences Marines, LAD, Plouzané, France, ²R&D/EP Total S.A., Pau, France, ³E2S-UPPA, Laboratoire des Fluides Complexes et de leurs Réservoirs, IPRA, Université Pau and Pays Adour, Pau CEDEX, France

Key Points:

- The Absheron mud volcano, unlike many mud volcanoes in the South Caspian Basin, is not sourced from the deep Maykop Formation but from the Upper Productive Series
- The developed numerical model shows that an interaction between methane-saturated areas and potential rupture zones allows locating the mud volcano formation
- A formation model is proposed where hydrofracturing is the initial trigger for the subsequent gas exsolution and expansion that disaggregate and remobilize weak sedimentary layers

Correspondence to:

A. Blouin,
arthur.blouin@ifremer.fr

Citation:

Blouin, A., Imbert, P., Sultan, N., & Callot, J.-P. (2019). Evolution model for the Absheron mud volcano: From in situ observations to numerical modeling. *Journal of Geophysical Research: Earth Surface*, 124, 766–794. <https://doi.org/10.1029/2018JF004872>

Received 10 SEP 2018

Accepted 18 JAN 2019

Accepted article online 15 FEB 2019

Published online 19 MAR 2019

Abstract The morphology of mud volcanoes (MVs) has been extensively studied over the last few decades. Although recent research has begun to focus on deep processes and structures, little is known about mud generation mechanisms. This study aims to investigate the feeder system and formation of an active kilometer-scale MV by relying on a 3-D seismic survey and an in situ data set on the Absheron anticline (South Caspian Basin). Seismic data show a depleted area in the Anhydritic Surakhany Formation (ASF), whose mineralogical composition fits with surface mud. Well data show that the ASF is a succession of evaporitic beds and low-temperature shales near its fracture pressure. Biostratigraphic analysis confirms a Pliocene origin for the mud, suggesting that the ASF may be the source. Numerical modeling of sedimentation coupled with laboratory test results and well sonic logs fairly reproduces the observed in situ overpressure trend. Two-dimensional methane diffusion coupled with overpressure caused by rapid sedimentation highlights the superposition of critical fracturing conditions with methane-saturated sediments at the base of the studied MV. The present study demonstrates the predominant role of fluid overpressure due to sedimentation and gas saturation in the formation of the Absheron MV, and this is shown to occur as follows: (1) methane migration through the thrust-related faults reaching the ASF, accompanied by (2) lateral overpressure, caused by rapid sedimentation, diffusing along the ASF leading to (3) hydro-fracturing of overpressured and methane-saturated sediments resulting in an important decrease in overpressure, causing (4) gas exsolution and expansion triggering sediment remobilization.

Plain Language Summary Mud volcanoes have proved to be a real risk for people living near them (e.g., Lusi catastrophe, Indonesia) and for infrastructures. While their surface morphology is well understood and their plumbing system is correctly imaged by high-resolution seismic technology, their formation mechanisms and their trigger is yet to be understood. The South Caspian Basin is known for the presence of a large number of active structures. On the Absheron anticline, a giant active mud volcano is surrounded and covered by a large data set from seismic imaging to sediment cores. From the analysis of the seismic data, and from diverse measurements on sediments, we were able to locate the source of the mud, which is shallower than the source for many mud volcanoes in the region. We developed a numerical model able to reproduce the pore pressure trends recorded at the wells, and it shows that the interaction between methane-saturated areas and potential rupture zones is able to explain the mud volcano location. Finally, based on the different results and observations, a formation model is proposed where hydrofracturing is the initial trigger for the subsequent gas exsolution and expansion that disaggregate and remobilize weak sedimentary layers.

1. Introduction

Although mud volcano (MV) surface morphologies have been described in detail and worldwide, both onshore and offshore, little is known about their evolution and formation processes (e.g., Deville, 2009; Kopf, 2002; Mazzini & Etiope, 2017). On the other hand, earlier extensive work on fluid emissions at the surface has improved understanding of subsurface processes and the multiple sourcing of the different elements forming the material ejected by MVs (Deville, 2009; Kopf, 2002; Mazzini & Etiope, 2017).

Nevertheless, recent technical improvement of geophysical tools, such as high-resolution 3-D seismic imaging, allows for detailed analysis of the MV's rooting system and has opened the way for studying mud generation processes (Dupuis, 2017; Kirkham et al., 2017a; Stewart & Davies, 2006). Understanding these generation mechanisms is a key issue for geohazard assessment (e.g., the Lusi catastrophe near

Sidoarjo, Indonesia, since 2006; Tingay et al., 2015), for environmental impacts on seabed ecosystems (Foucher et al., 2009; Zitter, 2004), targeting drilling areas, and anchoring zones for offshore infrastructures (Contet & Unterseh, 2015; M. Tingay et al., 2008). Furthermore, one characteristic shared by all MV's around the world is the presence of gas in the ejected material (Etiope et al., 2009; Hedberg, 1974). Yet it is not clear at present if the gas is a driver of mud extrusion or a passive actor, captured in the mud during its ascent. If gas has a driving role in mud extrusion, the understanding of mud generation mechanisms could provide elements to quantify the volume of expelled methane and therefore evaluate the natural contribution of MVs to the atmospheric carbon budget (Kopf, 2002).

The South Caspian Basin (SCB), along with its onshore continuation, the Lower Kura Basin, is a prolific hydrocarbon basin and is also known to hold the highest density of MVs (I. Guliyev et al., 2010; A. Mazzini & Etiope, 2017). The Absheron gas field is a challenging exploration and production area due to the presence of a giant active MV. A high-resolution 3-D seismic block was acquired in 1996, two exploration wells were drilled in 1999 and 2011, and a geotechnical campaign with sediment core sampling and in situ measurements was operated in 2014 for geohazard assessment.

Altogether, we have a rare opportunity to study a MV with a complete set of surface and subsurface data. Several issues are assessed in this article regarding the stratigraphic source of the mud, the stratigraphic and lateral location of the mud generation zone, and the physical mechanisms responsible for the MV formation.

We provide within this study a detailed geomorphological description of the structure as well as the extrusion timing based on seismic imaging and other data. Well data and sediment analysis results were integrated into numerical 1-D and 2-D models in order to quantify the lateral pressure transmission and the gas migration effect. Finally, a conceptual evolution model based on these results is proposed.

2. Regional Setting

The SCB is a remnant of the Paratethys Sea that became isolated from the world ocean during the Late Miocene, Early Pliocene, at the end of the compressive phase of the Alpine tectonic cycle (Bochud, 2011; Golonka, 2007; Popov et al., 2004). It is now delimited to the north by the Absheron peninsula and ridge, to the south by the Alborz massif, to the west by the Greater and Lesser Caucasus separated by the Kura depression, and to the east by the Kopet Dagh (Figure 1; Allen et al., 2002; Brunet et al., 2003; Popov et al., 2004; Morley et al., 2011).

Since the Middle Miocene, compression uplifted all these massifs and triggered the high-amplitude folding of the South Caspian sedimentary series (Allen et al., 2002; Egan et al., 2009; Javanshir et al., 2015; Popov et al., 2004). This compression initiated the subduction of the South Caspian basement below the basement of the North Caspian domain, creating the Absheron ridge in-between (Figure 1; Allen et al., 2002; Stewart & Davies, 2006). The subduction allowed the deposition of more than 8 km of sediments over the last 5.5 Myr based on a representative stratigraphic column of the northwestern part of the basin, which is faster than sedimentation rates recorded in typical foreland basins (Allen et al., 2002; Morley et al., 2011; Stewart & Davies, 2006).

The Maykop Formation was deposited from the Late Oligocene to the Early Miocene in a shallow marine anoxic environment (Golonka, 2007; Hudson et al., 2008; Popov et al., 2004). It is the main hydrocarbon source rock for the Caspian and Black Sea areas (Allen et al., 2002; Hudson et al., 2008) and acts as the main décollement level for the high-amplitude folds of the SCB (Allen et al., 2002; Stewart & Davies, 2006). The Maykop sediments are mainly organic-rich clays with a minor fraction of coarser detrital material (Hudson et al., 2008).

Post-Maykop Miocene sediments were deposited in a context of global regression until basin isolation occurred in the Late Miocene. These sediments are shallow marine and lacustrine thick clayey deposits (Allen et al., 2002; Javanshir et al., 2015).

The Pliocene was dominated by deltaic and lacustrine environments during a regression phase, fed from the ancestral Kura, Volga, and Amu-Darya rivers that drained sediments from all the topographic highs surrounding the basin (Abdullayev & Leroy, 2016; Allen et al., 2002). The subduction-related subsidence at

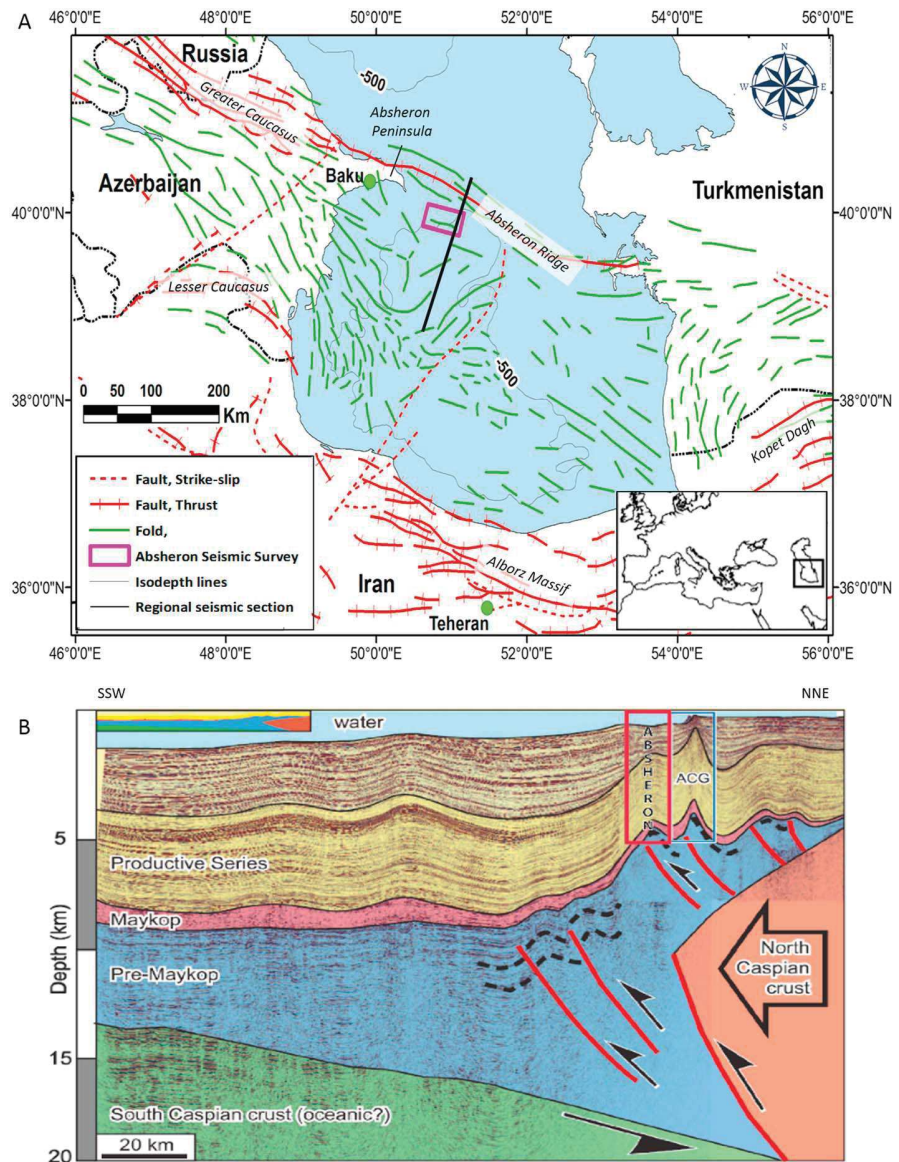


Figure 1. (a) Structural map of the South Caspian region showing the main folds and faults, structural domains, and depocenters (modified from Oppo et al., 2014). (b) Regional interpreted deep seismic section, showing the main subsurface structural elements with the folds above the Maykop detachment level associated in the northern part to deeply rooted thrusts. The location of the line is shown on the left map by a black line. The red box shows the approximate location of the Absheron structure (modified from Stewart & Davies, 2006).

the end of the Miocene accommodated the deposition of thick deltaic deposits containing the regional hydrocarbon reservoirs and forming the Productive Series (PS; Allen et al., 2002; Javanshir et al., 2015). The sedimentation rate was very high, reaching 2.4 km/Myr, allowing the deposition of up to 6 km of PS sediments (Allen et al., 2002; Brunet et al., 2003; Stewart & Davies, 2006). At the top of the Surakhany Formation (Upper PS), the regression was maximal and evaporitic beds are found in the northern part of the basin (Javanshir et al., 2015). This interval will hereafter be called Anhydritic Surakhany.

Above the PS, the Akchagyl Suite consists of open marine mudstones. This transgressive interval records the temporary reconnection of the SCB to the world ocean from 2.4 to 1.6 Ma (Allen et al., 2002; Dupuis, 2017; Javanshir et al., 2015). From 1.6 Ma to present, deepwater lacustrine and brackish conditions have dominated, forming the Absheron Suite and younger units.

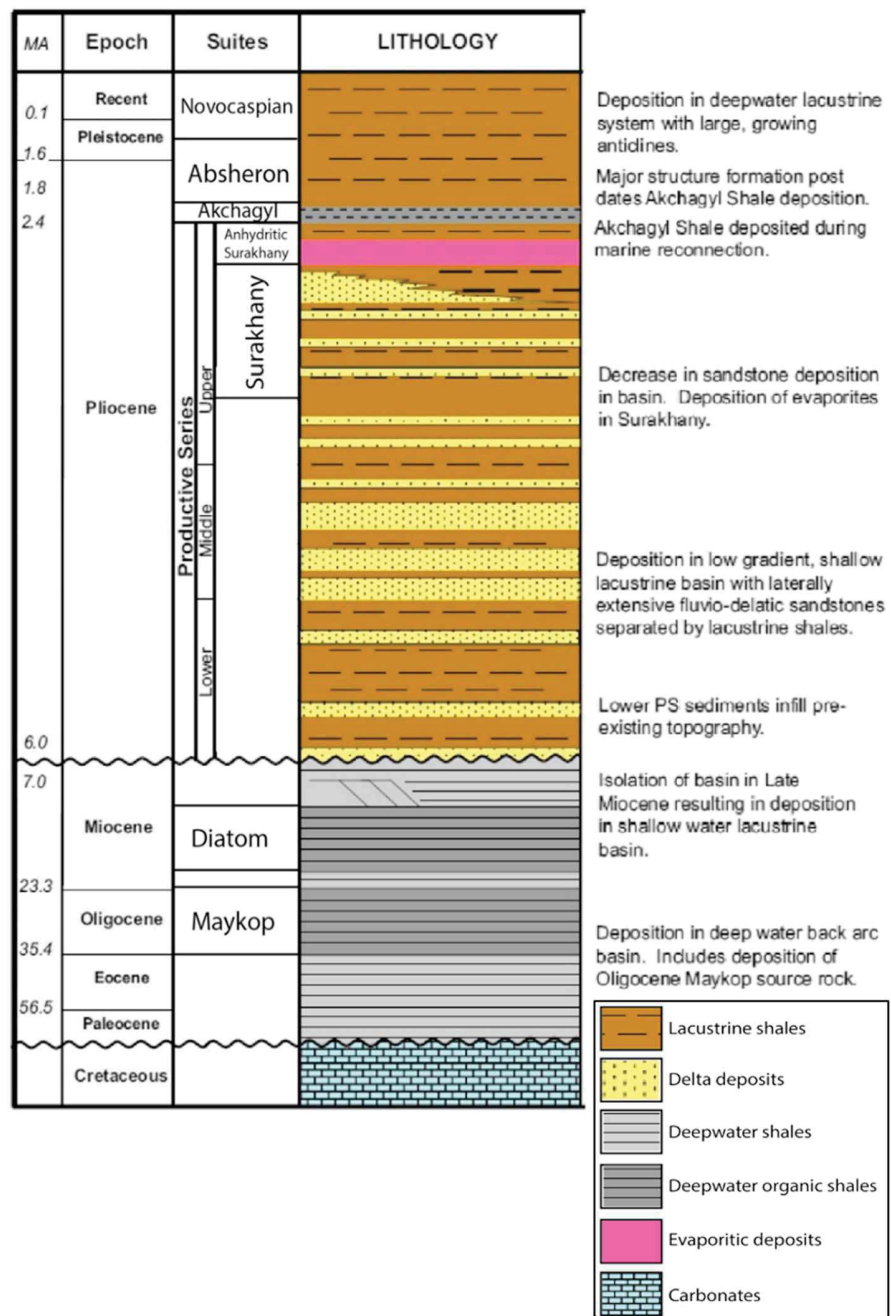


Figure 2. Stratigraphic column for the South Caspian Basin showing the ages, lithology, and main tectonic and paleo-geographical context from Cretaceous to present (modified from Javanshir et al., 2015).

Information on the stratigraphy of the SCB is synthesized in Figure 2.

The presence of the high total organic carbon Maykop Formation and of the well-connected PS reservoirs make the SCB a prolific hydrocarbon basin (Alizadeh et al., 2017; Hudson et al., 2008; Javanshir et al., 2015). The Maykop Formation generates gas in the deeper part of the basin and is still generating oil onshore and in the northern margin of the basin (Javanshir et al., 2015). Large-scale anticlines (50–150 km long), detached over the overpressured and under compacted Maykop formation (Morley et al., 2011), form excellent oil and gas traps as hydrocarbons migrate from the deep basin into the onshore

heights along the regionally continuous reservoirs (Javanshir et al., 2015). The large-scale anticline main growth stage occurred at the end of Pliocene. However, fold-growth is ongoing although slower (Mosar et al., 2010).

One hundred and eighty active MVs are listed onshore, and at least the same amount is estimated in the offshore part of the SCB (I. S. Guliyev et al., 2001; Kopf, 2002; A. Mazzini & Etiope, 2017; Milkov, 2000). These structures are mainly located along the crests of anticlines where oil and gas have accumulated in reservoirs (E. Deville, 2009; Javanshir et al., 2015; A. Mazzini & Etiope, 2017). They are generally considered to be sourced by the Maykop Formation (Kopf, 2002; Roberts et al., 2010; Stewart & Davies, 2006). Additionally, Fowler et al. (2000) noticed on the offshore Shah Deniz anticline a close relationship between the development of folds and MV activity as MVs activated during or after fold initiation and the authors correlate structural growth with MV activity phases.

The Absheron anticline is a NW-SE oriented, 40-km-long fold, located at the northwestern edge of the SCB, 100 km to the south-west of Baku and 50 km south of the ACG gas field (Figure 1a). Methane was recently discovered in the Absheron field, and a giant active MV pierces the crest of the structure at the southwestern limit creating potential hazards for drilling operations (Contet & Unterseh, 2015). Previous studies on the Absheron anticline evidenced the presence of four mass transport deposits in the Post-Absheron interval (Imbert et al., 2014). The most recent mass transport deposit covers the whole anticline with the exception of the MV location where it stumbles on the northern flank of the volcano. Morphology of the MV in the upper 500 m of the sediment pile is described in Dupuis (2017). The poorly imaged central part is surrounded by three stacked wedges affected by multiple thrusts. Recent activity of the MV is confirmed by four mudflows imaged in the first 100 m below seafloor (BSF).

3. Materials and Methods

3.1. Seismic Data

This study focuses on the Absheron anticline, where an active MV is imaged by a 3-D seismic survey (limits and location on Figure 1). The seismic survey covers 650 km², in water depths ranging from 180 to 700 m. The seismic sections presented here are from Kirchhoff prestack depth migration reprocessing (Robein, 2010), which was applied on 550 km² of the seismic survey. The velocity model used in the reprocessing aimed to improve the imaging of the deep structures (thrust and dips), taking into account the lateral velocity variations across the thrust as well as the velocity heterogeneity in the shallow intervals due to the presence of the MV and free gas (F. Adler, 12/12/2018, personal communication). The model parameterization is a vertical transverse isotropy that considers the vertical anisotropy imposed by the sedimentary strata (Robein, 2010). The model was entirely built by tomography inversion (Robein, 2010), and in the deep part, it was corrected using an interpretative method in order to preserve the structural coherency and to fit the well data (F. Adler, 12/12/2018, personal communication). The seismic volume is composed by 2,203 inlines and 2,120 crosslines with 12.5-m spacing inline and 18.5 crossline. The vertical resolution varies with depth as it depends on interval velocity. From visual observations of the sections, we estimate a resolution approximately 20 m in the strata above 2,000 m, progressively decreasing to 150 m at 11 km.

Seismic interpretation was carried out using the Total in-house software Sismage (Guillon & Keskes, 2004). From the 3-D seismic cube, we calculated the seismic coherency attribute, which can be projected on horizontal slices or seismic horizons. Seismic coherency allows to laterally differentiate continuous areas (undisturbed deposits) from low continuity zones (faults or MV deposits for instance; Bahorich & Farmer, 1995).

Each medium has its own acoustic impedance. Therefore, when a seismic signal reaches a limit between two media with different impedances, part of the acoustic signal will be reflected (Nely, 1986). A seismic signal can be decomposed in wavelets, which are characterized by their polarity, their amplitude (peak area), its period, and its phase (Nely, 1986). Normal polarity is given by the seafloor polarity, which in the data presented hereafter are a wavelet with a strong central positive amplitude surrounded by two weak negative amplitudes. Thus, the normal polarity is a strong positive peak enclosed between two weak negative peaks indicating a stepwise increase in impedance. The opposite shows a stepwise decrease in impedance (Nely, 1986; Ricker, 1953).

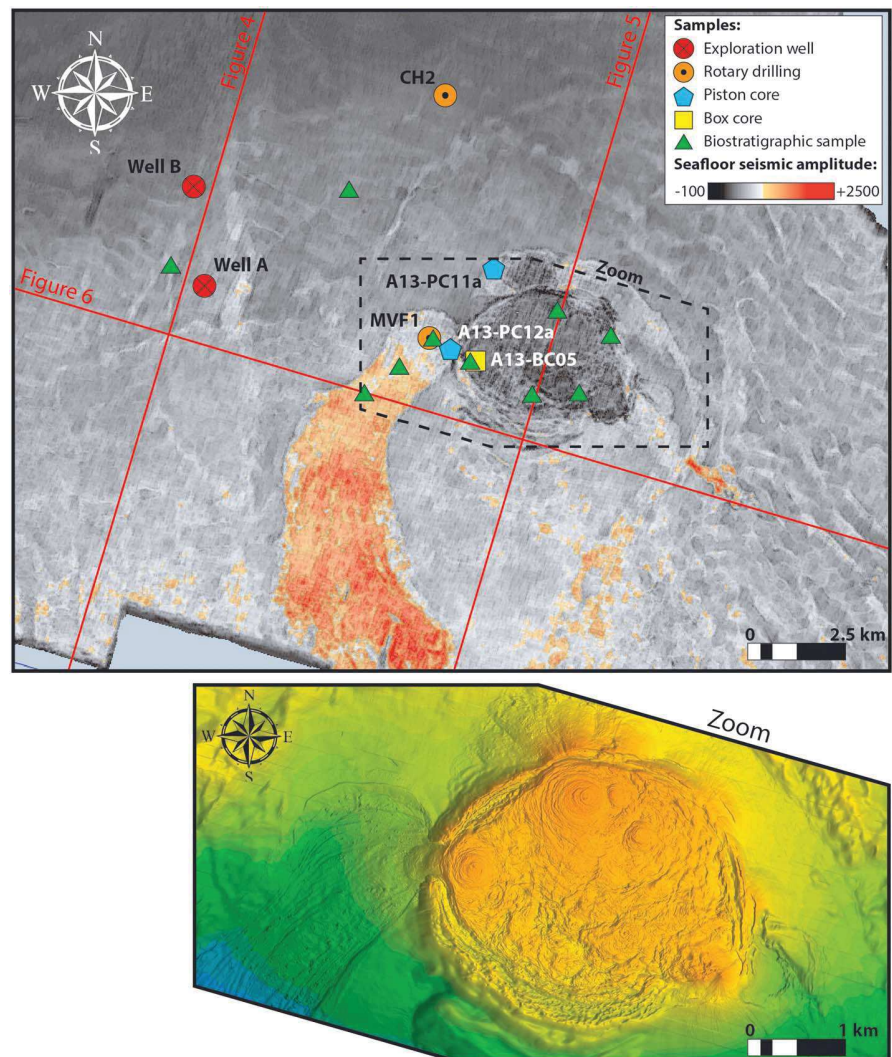


Figure 3. Seismic amplitude map of the seafloor around the Absheron mud volcano. In orange, a high-amplitude mudflow is imaged to the west of the volcano. The dark patch corresponds to the shield composing the mud volcano itself. On the same map, the location of the different coring and drilling sites are shown. Limits and location of the 3-D seismic survey are presented on the regional map of the South Caspian Basin (SCB; Figure 1a). The red lines indicate the location of the seismic lines presented in Figures 4 to 6. The dotted black polygon is the limit of the zoom shown below, presenting a detailed image of the seafloor on and around the mud volcano acquired with a multibeam echo sounder. Orange stands for the shallower areas; green is for the deeper parts.

The presence of free gas is a well-documented cause of attenuation or data wipe-out (Benjamin & Huuse, 2017; Graue, 2000). MVs are known to be accompanied by large emissions of gas (Kopf, 2002; A. Mazzini & Etiope, 2017). Therefore, seismic masking is expected to occur below large structures such as the Absheron MV (AMV; Benjamin & Huuse, 2017; Graue, 2000). Imaging issues that cannot be settled by migration algorithms may arise from steep dips (Day-Stirrat et al., 2010).

Horizons were propagated and named according to stratigraphic limits encountered in the two exploration wells drilled on the Absheron anticline (Figure 3 for location). These stratigraphic limits are interpreted based on cuttings analysis and gamma ray, sonic, and resistivity logs.

In parallel of the seismic imaging, high-resolution bathymetric maps (Figure 3) were acquired using a multibeam echosounder.

3.2. Sediment Cores and Geotechnical Analysis

3.2.1. Sample Collection

A marine geological and geotechnical survey of the seabed above the Absheron gas discovery was carried out in 2014 in order to better constrain and delineate geological hazards associated with the MV (Total proprietary report, G. Dan & S. Po, 12/09/2017, personal communication). The geotechnical/geological survey used rotary drilling, AUV (autonomous underwater vehicle) sampling with box corer and piston corer, and in situ geotechnical testing (Cone Penetration Testing [CPT]). Well logging and CPT were performed on two boreholes: CH2 was located outside the MV area to provide a stratigraphic reference in continuous series, and MVF1 sampled on a MV flow (for location see Figure 3).

To improve the characterization of MV deposits, we selected eight samples from different sediment cores. Table 1 lists the coordinates and depth below seabed of these samples, and Figure 3 shows their location with respect to the MV. The samples were selected to provide information on the spatial and temporal variability of the MV deposit (Total proprietary report, G. Dan & S. Po, 12/09/2017, personal communication). Five samples were selected at three different depths from the same rotary drilling cores MVF1, thus potentially sampling different mud eruption episodes. One sample from A13-PC12a core was taken from the same mudflow as the one drilled by MVF1 but at a different location. A different mudflow was sampled on the A13-PC11a core at the northern edge of the MV. Finally, a sample was taken from the A13-BC05 core directly on the top of the mud shield (see Table 1 for further details and Figure 3 for location).

3.2.2. Mineralogical and Biostratigraphic Analysis of Mud

The MVF1E RAW sample was separated into two different grain size classes, with a limit at 5 μm , in order to compare the composition of the clay-size fraction and the coarser fraction. The >5 μm of the raw sample was extracted by suspension of fine fractions in water followed by centrifugation.

Eight samples were analyzed using a reference quantitative mineralogy method called MinEval QM (Table 1; Fialips et al., 2018). This method is based on the integration of results from various measurements performed on crushed samples, including X-ray diffraction on bulk powders and extracted fine fractions, loss on ignition, X-ray fluorescence, insoluble residue upon HCl 15% treatment, bulk solid density, and cationic exchange capacity (see Fialips et al., 2018 for more details). This method performs an initial semiquantitative mineralogy analysis by Rietveld refinement of the X-ray diffraction patterns (Rietveld, 1969), and quantification is completed applying a dedicated software that uses an iterative approach. The <5- μm fraction of MVF1E-RAW only obtained a semiquantitative mineralogical analysis of clay minerals. The quantity of fine material obtained after separation was insufficient to perform the complete quantitative study.

Furthermore, a biostratigraphic study by Chevron in 2000 was carried out with the aim of dating the oldest material composing the mudflows. A series of samples were recovered in and around the volcano location (green triangles in Figure 3). The samples around the structure were used as age control points. The elements picked and counted on the different samples are diatoms, pollens, foraminifera, nannofossils, and ostracods.

Initial grain size distribution for the natural mud was determined using the Mastersizer 3000 device for laser diffraction granulometry (Ryzak & Bieganski, 2011).

3.2.3. Geotechnical Analysis of Mud

Oedometer tests with permeability measurements were carried out on four samples taken from the GT1-MVF1 core (MECA 6-10-15-22 in Table 1 and tests from 1 to 8 in Table 2). Tests were duplicated in order to check for potential trial mistakes. The samples were selected based on CPT (Das, 2013) data showing at least four mechanically distinct intervals (Total proprietary report, G. Dan & S. Po, 12/09/2017, personal communication). The aim of these oedometer tests was to define compressibility characteristics (void ratio versus effective stress) and to determine the relationship between hydraulic conductivity and void ratio of the considered sediment intervals (ASTM International, 1996).

The void ratio e changes are tied to the vertical effective stress σ'_v , by the following compressibility relation:

$$e = e_0 - \lambda \ln\left(\frac{\sigma'_v}{\sigma'_{v0}}\right) \quad (1)$$

where e_0 is the initial void ratio for a reference vertical effective stress σ'_{v0} and λ is the compression index depending on the sediments. e_0 and λ for the tested samples are shown in Table 2.

Table 1
DRX and Mechanical Sample Names and Details Used in This Study

Core name	Sample name	Type of sample	Type of analysis	Water depth (m)	Depth below seafloor (m)	
					Top	Bottom
MVF1C	DRX1	Core Sample	Mineralogy	521	3.53	3.55
	MECA-6	Core Sample	Granulometry, oedometer		3.71	3.80
	MECA-10	Core Sample	Granulometry, oedometer		5.14	5.22
MVF1D	MECA-15	Core Sample	Granulometry, oedometer	522	10.00	10.08
	MECA-16	Core Sample	Oedometer		10.41	10.48
	MECA-17	Core Sample	Oedometer		10.68	10.75
	DRX2	Core Sample	Mineralogy		19.00	19.06
MVF1E	DRX3	Core Sample	Mineralogy	522	33.04	33.06
	MECA-22	Core Sample	Granulometry, oedometer		33.08	33.15
	RAW>5 μm	fraction >5 μm	Mineralogy		34.00	34.61
	RAW<5 μm	fraction <5 μm	Mineralogy		34.00	34.61
A13-PC11A	DRX4	Core Sample	Mineralogy	467	0.91	1.00
A13-PC12A	DRX5	Core Sample	Mineralogy	505	0.11	0.17
A13-BC05	DRX6	Core Sample	Mineralogy	453	0.32	0.36

Note. Total proprietary report, G. Dan and S. Po (12/09/2017, personal communication).

The permeability relation to void ratio is assumed to be

$$\ln(K) = ae + b \tag{2}$$

with K the Darcy permeability (Das, 2013) or hydraulic conductivity (m/s), a and b are constants characteristic of the tested sediments.

The samples were all reconstituted with an artificial initial water content of around 1.5 wL (wL being the liquid limit). The wL (Table 2) was determined using the fall cone method (Feng, 2005). Oedometer tests were conducted using incremental loading according to the ASTM D-2435 method (ASTM International, 1996). The determination of hydraulic conductivities and permeability coefficients was also possible using the falling head method (Das, 2013). Using an exponential regression on the obtained measurements is necessary to obtain a law of the form of equation (2).

In order to artificially characterize the impact of coarse material on mechanical properties, additional oedometer tests were carried out on combined MECA-16 and MECA-17 samples (Tables 1 and 2) mixed with a known mass of fine sand (80–125 μm); the goal was to obtain their compressibility and permeability in order to integrate these results in the numerical diffusion model. The fractions of coarse material added to the samples were selected based on the net to gross (ratio between sand layer cumulated thickness over total interval thickness) values calculated from well data.

Table 2
Details on Sample Preparation for Oedometer Rests and Results

Test number	Sample	σ'_{vmax} (kPa)	wL	e_0	λ	Sample preparation
1	MECA-6	1765.12	0.42	1.95	0.35	1.5 wL water input
2	MECA-22	1765.12	0.43	1.7	0.34	1.5 wL water input
3	MECA-10	1765.12	0.56	2.11	0.42	1.5 wL water input
4	MECA-15	1765.12	0.44	1.79	0.32	1.5 wL water input
5	MECA-6	1765.12	0.42	2.23	0.36	1.5 wL water input
6	MECA-22	1765.12	0.43	1.9	0.33	1.5 wL water input
7	MECA-10	1765.12	0.56	2.58	0.46	1.5 wL water input
8	MECA-15	1765.12	0.44	2.18	0.34	1.5 wL water input
9	MECA-16 + 17 + 5% sand	1765.12	0.44	1.38	0.25	1.5 wL water input, mixed samples
10	MECA-16 + 17 + 10% sand	1765.12	0.44	1.23	0.23	1.5 wL water input, mixed samples
11	MECA-16 + 17 + 25% sand	1765.12	0.44	1.14	0.20	1.5 wL water input, mixed samples

3.3. In Situ Well Data and Hydraulic Conductivity Calculations

Stratigraphic information was obtained from the two exploration wells drilled on the Absheron anticline (Figure 3). Well A reached 6,506-m TVD/MSL (true vertical depth below mean sea level), while Well B reached 6,823 TVD/MSL.

Lithology is obtained from cuttings analysis. Pore pressures in shales were estimated from sonic data using Eaton's (1975) method. Sonic logs were acquired either with wireline or logging while drilling tools depending on the interval. The StethoScope pressure-while-drilling tool (Schlumberger) was used to measure in situ reservoir pore pressure. Fracturing pressure log is evaluated from leak-off tests or formation integrity tests (Lin et al., 2008), as well as downhole mud losses. Wireline tools measured temperatures at different points either in open hole or cased hole.

The sonic measurements are given as slowness of the acoustic waves, for example, the inverse of acoustic velocity. Wyllie et al. (1958) gave a relationship between measured velocity of a porous media and its porosity ϕ :

$$\frac{1}{V_m} = \frac{\phi}{V_f} + \frac{(1-\phi)}{V_s} \quad (3)$$

with V_m indicating the measured acoustic velocity, V_f indicating the acoustic velocity in pore fluid, and V_s indicating the acoustic velocity in the rock matrix.

As void ratio and porosity are linked through the relation:

$$e = \frac{\phi}{1-\phi} \quad (4)$$

it is possible to calculate hydraulic conductivities K for reservoir layers using the Kozeny-Carman relationship (Ren et al., 2016):

$$K = C_F \frac{1}{S_s^2} \frac{\gamma_f}{\mu \rho_s^2} \frac{e^3}{(1+e)} \quad (5)$$

where C_F is a shape constant around 0.2, S_s is the specific surface area of particles (m^2/g) taken here as equal to $0.5 \text{ m}^2/\text{g}$, γ_f is the unit weight of pore fluid (N/m^3), ρ_s (kg/m^3) is particle density, and μ is fluid viscosity ($\text{N s}/\text{m}^2$).

Therefore, it is possible to estimate the hydraulic conductivity of reservoirs directly from acoustic log data. Oedometer test results on natural mud allowed calculation of permeability in the shales. From the lithological log, the column was split into reservoirs and shale intervals. Using equations (2), (3), and (5), we calculate for each defined interval the hydraulic conductivity K . The net to gross ratio (cumulated sand thickness divided by total interval thickness) was calculated for each drilled formation. The arithmetic average of hydraulic conductivities gives the horizontal hydraulic conductivity for the considered formation, while the harmonic average gives its vertical hydraulic conductivity (Das, 2013).

3.4. Numerical Modeling: Sedimentation, Transient Pore Pressure, and Gas Diffusion

3.4.1. 1-D Sedimentation and Pore Pressure Accumulation

Geological formations remain at hydrostatic pressure after deposition and burial as long as pore fluids are able to escape up through the overburden or laterally toward the seabed or surface. High permeabilities or low sedimentation rates help pore water escaping during consolidation. In contrast, when permeability is low or sedimentation rate is high enough, fluids cannot escape fast enough to keep hydrostatic conditions. As loading increases through sedimentation, pore water starts to support part of the overburden pressure, which prevents pores from closing. Thus, normal consolidation is delayed, sediments become undercompacted, and pore pressure increases above hydrostatic conditions. This excess pore pressure is called overpressure and this mechanism of overpressure buildup is called compaction disequilibrium (Osborne & Swarbrick, 1997; Sultan et al., 2004; Swarbrick et al., 2002).

In this work, we calculate in one dimension the overpressure generated (Δu) only by sedimentation effect in the southern part of the considered section where the sedimentary column is the thickest. The high

sedimentation rates observed in the basin are within the strongest recorded worldwide (Allen et al., 2002; Brunet et al., 2003; Stewart & Davies, 2006). Moreover, high sedimentation rates are considered to be one of the main overpressure generation mechanism (Osborne & Swarbrick, 1997; Swarbrick et al., 2002). Therefore, the modeling work focuses on this sedimentation effect as a first approach. The SeCoV3 proprietary software of IFREMER (Sultan et al., 2004) allows quantification of the evolution of pore pressure using a back analysis based on sedimentation rates, compressibility properties (equation (1)) and permeability evolution with void ratio (equation (2)). In addition to the equations solved by SeCoV3, in the present work we use a mesh-update method considering the compressibility of sediments and the mobile position of the upper boundary (seawater-sediment interface) at each calculation step.

Sedimentation rates and the model geometry used in this study were calculated using present thicknesses and ages from Green et al. (2009). These sedimentation rates have been corrected (decompression) for compaction using Terzaghi compaction equations (Terzaghi, 1943). At the end of sedimentation and compaction modeling, we applied a trial and error method until the model matched present-day observed thicknesses.

Compressibility and permeability properties characterizing each of the defined layers were determined based on oedometer and permeability tests (Table 2) carried out on natural mud mixed with known fractions of very fine sand (ASTM International, 1996). The fractions of added sand were selected thanks to net to gross values calculated from well data (Table 3). The purpose was to model the behavior of layers having different amounts of coarser material.

3.4.2. Two-Dimensional Transient-Diffusion Process: Darcy's and Fick's Laws

The two-dimensional transient dissipation of excess pore pressure generated by the sedimentation process is considered along a 63-km-long and 10-km-thick block of the section presented in Figure 11 of Green et al. (2009). We defined the geometrical model with 300 horizontal and 50 vertical nodes by considering six stratigraphic layers, the fault network around the Absheron fold, and normal faults at the extrados of the fold.

The excess pore pressure generated by sedimentation and calculated using SeCoV3 was considered as a boundary condition for the 2-D Darcy transient flow calculation. The two-dimensional dissipation and transmission of overpressure is calculated using the 2-D diffusion equation given by

$$\frac{\partial \Delta u}{\partial t} = \left(\frac{\partial(D_{hx}\partial\Delta u)}{\partial x^2} + \frac{\partial(D_{hy}\partial\Delta u)}{\partial y^2} \right) \quad (6)$$

with Δu being the overpressure and D_{hx} and D_{hy} , respectively, the horizontal and vertical hydraulic diffusivities that are calculated directly from the horizontal and vertical hydraulic conductivities K_x and K_y (Table 3).

In addition to the transmission/diffusion of pore pressure, we considered in the present work the molecular diffusion of dissolved methane. Methane diffusion is calculated using a two-dimensional diffusion equation referred to as Fick's law (equation (7)), which allows for the description of diffusion of dissolved molecules into a solvent (Crank, 1975):

$$\frac{\partial C}{\partial t} = D_C \left(\frac{\partial(D_C\partial C)}{\partial x^2} + \frac{\partial(D_C\partial C)}{\partial y^2} \right) \quad (7)$$

with C being the dissolved methane concentration and D_C being the methane molecular diffusivity of the porous water. The effect of tortuosity of pores on molecular diffusivity is considered through the porosity of the sediment as described by Boudreau (1996).

To solve numerically the 2-D diffusion equations (equations (6) and (7)), a centered explicit finite difference discretization scheme is used by considering the initial and boundary conditions for pore pressure and methane concentration.

Faults are characterized by their own methane molecular diffusivities creating preferential pathways for methane. Moreover, as the modeled stratigraphic column is formed by a succession of metric-scale sand layers and plurimetric shale intervals, a ratio between horizontal and vertical hydraulic conductivities was integrated based on the results of the hydraulic conductivity calculations at wells (Table 3). This ratio allows modeling of the natural anisotropy of the sedimentary column due to sand-shale successions.

Table 3
Results of Hydraulic Conductivity Calculations Based on Sonic-Log Data and Oedometer Tests on Natural Mud

Layer name	Layer number in model	NTG (%)	Mean void ratio from logs	Kh (m/s)	Kv (m/s)	Kh/Kv	Void ratio ranges from 1-D model	K ranges from oedometer tests (m/s)	Model kx/ky
Novocaspian-Absheron	Layer 5	5	0.33	5.03E-07	2.27E-10	2212	2.73-0.36	5.01E-07 to 3.53E-10	2200
Surakhany	Layer 4	8	0.18	3.18E-09	2.13E-10	15	0.43-0.24	7.50E-10 to 4.17E-10	15
Sabunchy	Layer 3	12	0.14	1.27E-09	1.95E-10	6	0.22-0.21	4.70E-10 to 4.56E-10	6
Balakhany-Fasila	Layer 2	24	0.17	5.16E-10	2.57E-10	2	0.27-0.24	7.78E-10 to 7.05E-10	2
NKG	Layer 1	8	0.17	2.18E-10	2.10E-10	1	0.24-0.22	4.17E-10 to 3.92E-10	1

Note. NTG is the net to gross, being the ratio between total sand thickness over total interval thickness. The mean void ratio is calculated from the sonic log (equation (3)) and Kh (horizontal hydraulic conductivity) and Kv (vertical hydraulic conductivity) result respectively from arithmetic and harmonic average of calculated hydraulic conductivities on individual sand or shale layers using equation (5). The 1-D-sedimentation model gives a range of void ratio for each stratigraphic interval, corresponding to hydraulic conductivity ranges on oedometer test results obtained for different sand fraction content (Table 2). Measured and calculated K 's are in the same ranges of magnitude.

3.4.3. Hydrofracturing

In some cases, excess pore pressure can exceed the effective least principal stress plus the tensile strength of the medium allowing hydrofracturing to occur (Alfaro & Wong, 2001). When sediments are only submitted to the load of the overlying sedimentary cover, the greatest effective stress is vertical (σ'_v), whereas the least effective stress is horizontal (σ'_h ; Sibson, 2003). Fractures then open in the direction of the least principal stress and propagate in the direction of the plane perpendicular to the least principal stress (Hubbert & Willis, 1957). Therefore, in the case of sole loading effects, hydrofractures will propagate vertically.

The vertical effective stress and excess pore pressure are an output of 2-D Darcy's diffusion equation. The ratio between fracturing pressure and overburden pressure (lithostatic stress) observed in the well ranges between 0.83 and 0.99, with an average of 0.9. Consequently, we consider in the present work that hydrofracturing will occur whenever the ratio between excess pore pressure and vertical effective stress ($\Delta u/\sigma'_v$) exceeds 0.9.

4. Results

4.1. Geomorphological Investigation of the AMV

Figures 4 and 5 present two parallel SSW-NNE sections. Figure 4 runs across the axis of the Absheron fold in the vicinity of the two exploration wells drilled on the anticline and Figure 5 cuts through the center of the AMV as located on Figure 3. The ages of five of the seismic horizons that are presented in this study were calibrated from the stratigraphic results of the well (total proprietary data). We were able to map the top of Absheron Suite, the top of the Akchagyl Suite, the top of the PS, the top of the Anhydritic Surakhany Formation (ASF), the Top Diatom Suite, and the top of the Maykop Suite (see Figure 2 for the stratigraphic column). Seven other seismic horizons were interpreted in order to highlight particular structures such as normal faults or the morphology of the fold.

The deep part of the Absheron fold is cut by a deep E-W trending thrust that dies out in the Diatom Suite. This thrust has more than 2 km of throw, and the northern block overrides the southern block. The thickening of the interval between Top Diatom and Top Maykop is interpreted as the result of a backthrust system that would have been inverted later during its history. Another thrust 5 km to the NNW has a throw of only 1 km (Figure 4). The main thrust is responsible for the formation of the Absheron fold, and several folding phases can be distinguished. The PS interval has a rather uniform thickness of 5 km across the anticline with only 10% of total thinning from the flanks to the crest of the anticline, indicating a rapid deposition during a phase of low-activity for the fold (Figure 4). The Akchagyl Suite presents a thickening toward the southern flank of the fold of 300 m, corresponding to 60% of its maximum thickness (Figure 4), thus indicating that growth of the anticline was accelerated during deposition of this interval. Fold activity was still strong during deposition of the Absheron Suite as the thinning at the crest reaches 650 m for this interval, 35% of its maximum thickness. More precisely, the interval between horizons A3 and A2 recorded a thinning of 330 m (45% of maximum thickness), and between A1 and A2, 190 m (40% of maximum thickness; Figure 4). More

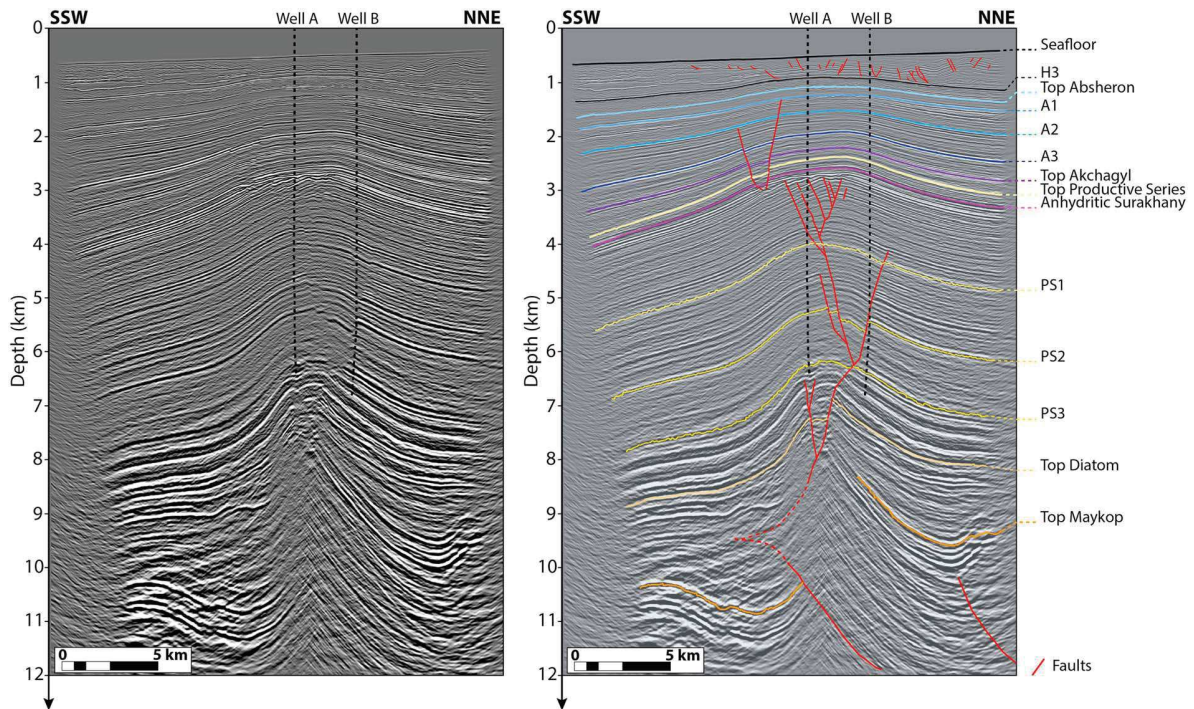


Figure 4. Uninterpreted and interpreted seismic line crossing the anticline near the two exploration wells A and B; it was used as reference for horizon picking for this study. A deep thrust cores the Absheron anticline, and another thrust, smaller, is also visible at the NNE of the section. From the thickness differences between the flanks and the crest of the structure, we note that folding started during the Akchagyl deposition. The main growing phases are during deposition of the Absheron Suite (A3-A1) and later during the Post-Absheron times. See Figure 3 for location.

recently, during Post-Absheron times, the fold reactivated and another 450 m of thinning (45% of maximum thickness) is visible from Top Absheron horizon to the seafloor (Figure 4). Therefore, sediment thinning at the crest of the anticline indicates that fold activity really started at the Akchagyl times, when it reached its climax. During the Absheron Suite deposition, the fold activity was intense for a longer time interval, and recent intense fold activity was also recorded in the Post Absheron interval.

Besides, normal faults on the extrados of the fold form a complex network from the thrust up to the Upper PS (Figure 4). The backthrust was then inverted to form the main observed normal fault.

The AMV is located in the SE part of the 3-D seismic survey. Figure 3 shows the seismic amplitude of the seafloor horizon, with a color-scale set to outline high and low amplitude zones. Orange stands for the highest amplitude and darker areas correspond to lower amplitude zones. The high-resolution bathymetric map (Figure 3) reveals present seafloor morphology related to recent MV activity. Near-surface morphology of the MV was already detailed by Dupuis (2017), with the presence of three main wedges (*Transparent Facies* and *Chaotic Facies* on Figure 5) and at least four recent mudflows evidenced on seismic data.

This MV is a subcircular mud shield, 4 to 5 km in diameter (Figure 3). It is surrounded by a gently dipping apron (average outward slope from 4 to 6°); the relief above the surrounding seafloor does not exceed 70 m (Figure 3). The highest area is a relatively flat plateau, but at a closer look reveals at least four gently mounded circular structures, 0.5- to 1-km diameter (Figure 3); we interpret these as the loci of most recent mud emission. At the western edge of the mud shield, a 12-km-long, 1.5- to 3-km-wide high-amplitude patch extends from the volcano to the west before following the natural slope toward the south of the Absheron seismic survey (Figure 3). This high-amplitude patch was already described as a giant mudflow by Dupuis (2017). This mudflow shows up strongly on seabed amplitude maps, indicating that is closer to seabed than the resolution of the data set.

Interpretation of the section running through the center of the AMV (Figure 3 for location) is given in Figure 5. The first obvious observation is the presence of a large seismically transparent body spreading horizontally in the first 500 m BSF. Four wedges of this feature are imaged at the SSW from the center of the

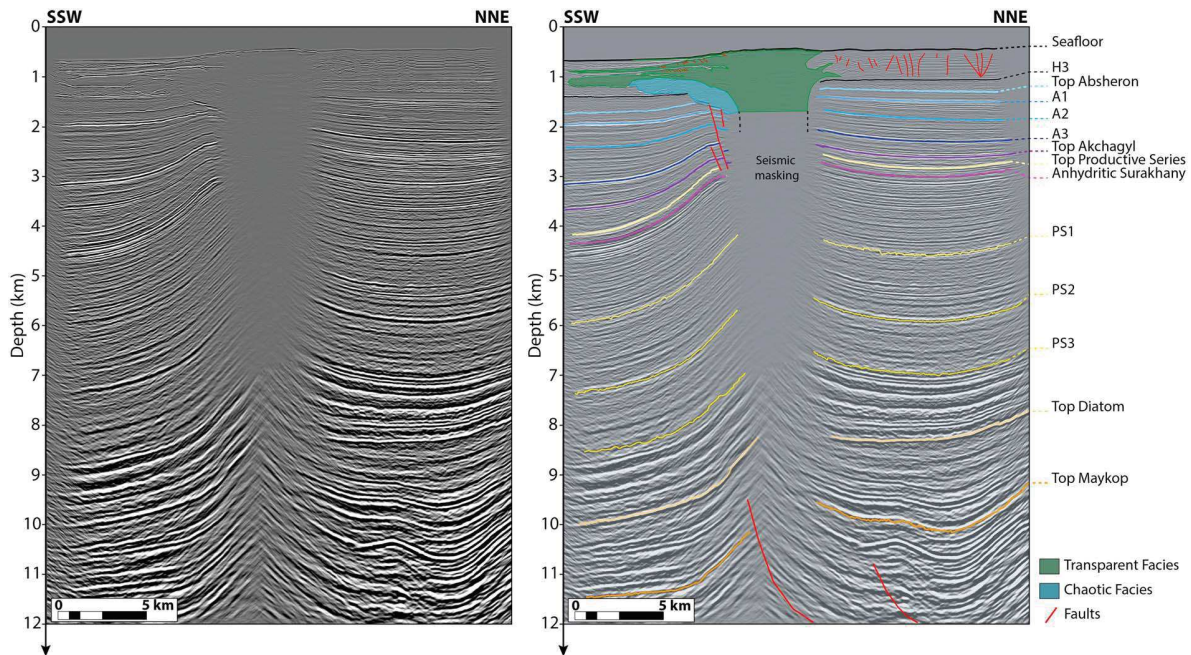


Figure 5. Uninterpreted and interpreted seismic line across the active mud volcano. The first 2 km are clearly imaged and show four seismically transparent wedges, corresponding to mudflows. A chaotic signal below can be discriminated from the blind signal and is interpreted as reworked sediments. The rooting system is blind, maybe due to a masking effect from the low velocity mud deposits. Near the blind area, some normal faults are present between 1.5 and 3 km. A deep thrust is coring the main anticline. The activation of the mud volcano is contemporaneous to the main folding phase (see text and Figure 4 for details and Figure 3 for location).

volcano. These interdigitations reunite at the center of the structure and form one large seismically transparent zone from the seafloor down to 1 km BSF. The shallowest digitation follows exactly the seafloor seismic horizon and is less than 50 m thick. As it was sampled notably with the box core A13-BC05 (Figure 3), this transparent area can directly be interpreted as mudflow deposits forming the MV edifice (green patch on Figure 5). Below 2 km at the center of the structure, a seismically transparent cone goes down to 7 km. This area could reveal the masking effect of the low velocity mass formed by the shallower mud deposits that may also be saturated with gas, preventing the acoustic signal from propagating below. Another seismic facies can be discriminated from the blind signal: the blue patch can be described as a chaotic signal. This area is located between the mudflows and host sediments.

Moreover, the deeply rooted thrusts described on Figure 4, are still imaged, yet not as clearly because of the seismic masking. Nevertheless, the AMV is centered above the exact vertical of the main thrust (Figure 5). The first mudflows imaged were deposited during the post-Absheron interval, between seismic horizons H3 and the Seafloor. No activity is recorded before H3. Consequently, the AMV seems to have been initiated after the end of the Absheron folding phase, during the post-Absheron folding phase.

Normal faults are imaged near the blind cone (Figure 5). They cross the Absheron Suite and end in the Upper PS, near the Anhydritic Surakhany interval.

After the time of extrusion, we addressed the issue of the primary source of the mud by identifying a possible depletion zone (Kirkham et al., 2017b; Stewart & Davies, 2006). In order to alleviate the seismic masking, we looked at lines crossing the volcano away from its center. Figure 6 presents a WNW-ESE seismic section, perpendicular to the section shown in Figure 5 and crossing the volcano 2 km away from its center. The section crosses the distal part of both transparent facies bodies and of the chaotic facies body from 0.5 to 2 km. The mudflow deposits appear 200 m above the H3 seismic horizon. The Top Absheron horizon is truncated by the chaotic mass. Deeper seismic horizons, from Absheron to Top PS, bend downwards, forming a bowl shape particularly visible on tracked horizons A1 and A3. The Anhydritic Surakhany horizon and the 200-m-thick interval below are truncated by downlapping younger intervals. Another truncated interval, 400 m thick, is imaged between 3,400 and 3,800 m and contained approximately the lower interval of the Upper PS, below the ASF. From 3,800 m to deeper, horizons become continuous and flat again.

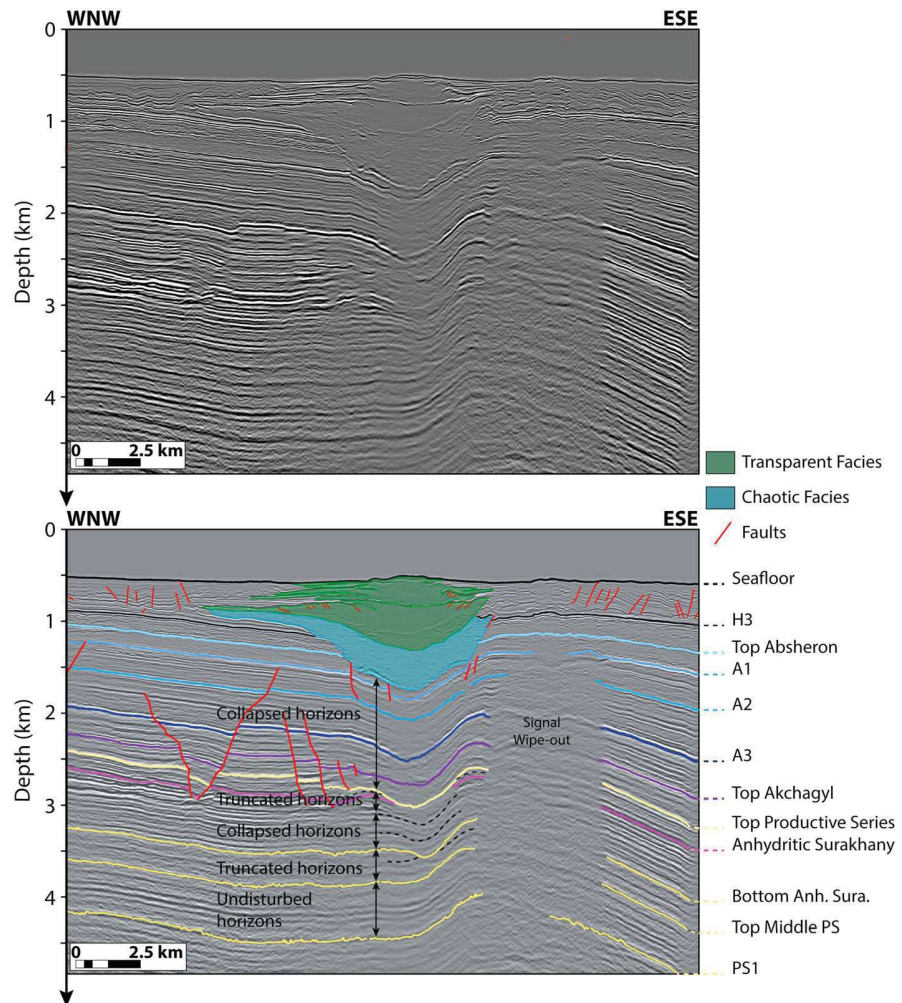


Figure 6. Uninterpreted and interpreted seismic line south of the mud volcano center. The gas blanking effect reduces below the mudflows. The transparent and chaotic signals are still present. A bending of seismic horizons from 1.5 to 3 km is noted forming a bowl-like geometry. Horizons of the upper part of the Anhydritic Surakhany are truncated by younger intervals as well as a 400-m-thick interval in the lower part of the Upper Productive Series. Horizons recover their continuity and their flat geometry below 3,800 m in the Productive Series. See Figure 3 for location.

Two main eruptive events can be distinguished (one seismic phase between the two green blocks in Figure 6). This can be due either to a quiescent phase of the MV activity when normal sedimentation was recorded or to very high sedimentation events, such as mass-flows, that can drap MVs (Deville et al., 2006). The continuity of the seismic horizon separating the two mud masses is in favor of a normal sedimentation and does not seem related to any sediment instability present during the Post-Absheron interval (Imbert et al., 2014). Normal faults flank the bowl-shaped area from 1,500 to 2,000 m and show the motion toward the center of the bowl-shaped geometry.

Thus, the main feature is the presence of a bowl-shaped geometry in the Absheron interval, truncating the upper part Anhydritic Surakhany as well as the lower part of the Upper PS where some of the horizons are discontinuous and downlap on the younger intervals. Seismic continuity then extends into the Middle PS, and some normal faults are imaged around the edges of the bowl-shaped area.

4.2. Physical, Sedimentological, and Geotechnical Properties of the Mud

DRX analysis (Figure 7a) reveals that all the samples contain 42.3 to 53.6 mass% of clays and micas, between 19.8 and 24.9 mass% of quartz, around 8 mass% of albite. Calcite is also a major mineral of the tested mud of which it represents 6.1 to 14.4 mass%. Pyrite is relatively constant for all the samples with around 1.5 mass%.

The clay fraction was analyzed in detail (Figure 7b) and is composed of 38 to 49% interstratified illite/smectite, 29 to 38% Illite and/or micas, and around 15% kaolinite. The rest is composed of around 5% chlorite and less than 2% smectite.

More details are provided by the results of the two fractions of the same samples ($R_{aw} > 5 \mu\text{m}$; $R_{aw} < 5 \mu\text{m}$; see Table 1). Even when separating the clay-size particles from the rest, the coarser fraction is still composed of 31.8 mass% of clay minerals (Figure 7) showing the presence of clay aggregates or claystone clasts larger than $5 \mu\text{m}$ that were not separated during suspension and centrifugation processes (Figure 7). The maximum amount of calcite and the only significant gypsum content are reached on this fraction with respectively 23.6 and 5.4 mass%. Comparatively with the $<5\text{-}\mu\text{m}$ fraction, it also contains a greater part of chlorite with 23% of the clay fraction. Further analysis on the chlorite fraction would be necessary to conclude on its origin and the reasons for this variability as acid treatment destroys chlorite minerals.

In the fraction of particles less than $5 \mu\text{m}$ in diameter (Figure 7b), there is only 20% illite and/or micas but also more kaolinite and chlorite (23% and 13% respectively). Illite is known to form at a higher temperature than interstratified illite/smectite (Pollastro, 1993), which means that the finer fraction is composed of a smaller portion of high-temperature clay minerals than the unseparated samples but is also composed of more kaolinite and chlorite.

Peaks of carbonates have been observed in the coarser fraction of MVF1E as well as the BC05-DRX5 and the PC12a-DRX4. Sample BC05 was recovered from the top of the mud shield, while PC12a comes from the top of the mudflow (Figure 3 and Table 1). This peak could be the result of the formation of authigenic carbonate crusts due to methane bubbling through fresh mud after an eruptive phase or at the top of the structure during a dormant phase (Kopf, 2002; Zitter, 2004).

Thus, the Absheron mud is essentially composed of clay minerals and quartz particles (Figure 7). Clay minerals are not only contained in the matrix as fractions of particles larger than $5 \mu\text{m}$ also contain more than 30% of clays.

Biostratigraphic results on pollens and ostracods show a clear difference between samples collected on the MV or on mudflows and background samples (Figure 3 for location). Samples from the MV shield and the mudflow contain pollens from Miocene to Recent and ostracods from Late Miocene (PS). Conversely, background sediments when not barren contain pollens from the Pleistocene and Holocene ostracods (Post-Absheron). Diatoms were only found in shallow background sediments and mudflows, with Pleistocene to Holocene taxa. The presence of diatoms identical to those of the background in mudflows and their absence from shield samples may indicate that the flows remobilized surface sediments on their way downslope and mixed with them. Nannofossil results are not considered reliable due to the poorness of elements present in the samples. Put together, these biostratigraphic results seem to indicate that the mud expelled at the AMV only comes from the PS.

Samples for oedometer tests were initially selected based on MVF1 CPT data from the Absheron mudflow (Figure 3 for location, Total proprietary report, G. Dan & S. Po, 12/09/2017, personal communication). CPT curves (cone resistance, pore pressure, and friction) present four intervals with distinct evolution of the three measured parameters. We suppose that these distinct tendencies are related to different intrinsic mechanical behavior of the mud intervals and oedometer tests were run on one selected reconstituted sample per interval at water content of around 1.5 wL in order to test this hypothesis (Tables 1 and 2). Details on preparation and results of these oedometer tests are presented in Table 2. Oedometer tests presented in Figure 8a show no distinct behavior except for the MECA 10 sample, which also has a slightly different granulometric curve than the other three selected samples (Figure 8c). Indeed, the MECA 10 sample has a greater fraction of fine material (from 2 to $10 \mu\text{m}$) and less coarse fraction (from 30 to $300 \mu\text{m}$) than the three other samples. This also matches with the high initial void ratio and the high compressibility of the MECA 10 sample with respect to the other samples (Figure 8a). Likewise, natural sediments show similar hydraulic conductivity with void ratio results except for MECA-10 that has a slightly lower permeability trend in accordance with the lower granulometry of this sample (Figures 8b and 8c).

MECA 6-15-22 compressibility curve (equation (8)) was considered as representative of all the other natural mud samples given the very low variability between the three different samples (Figure 8a) taken from different depths of the MVF1 core (Table 1).

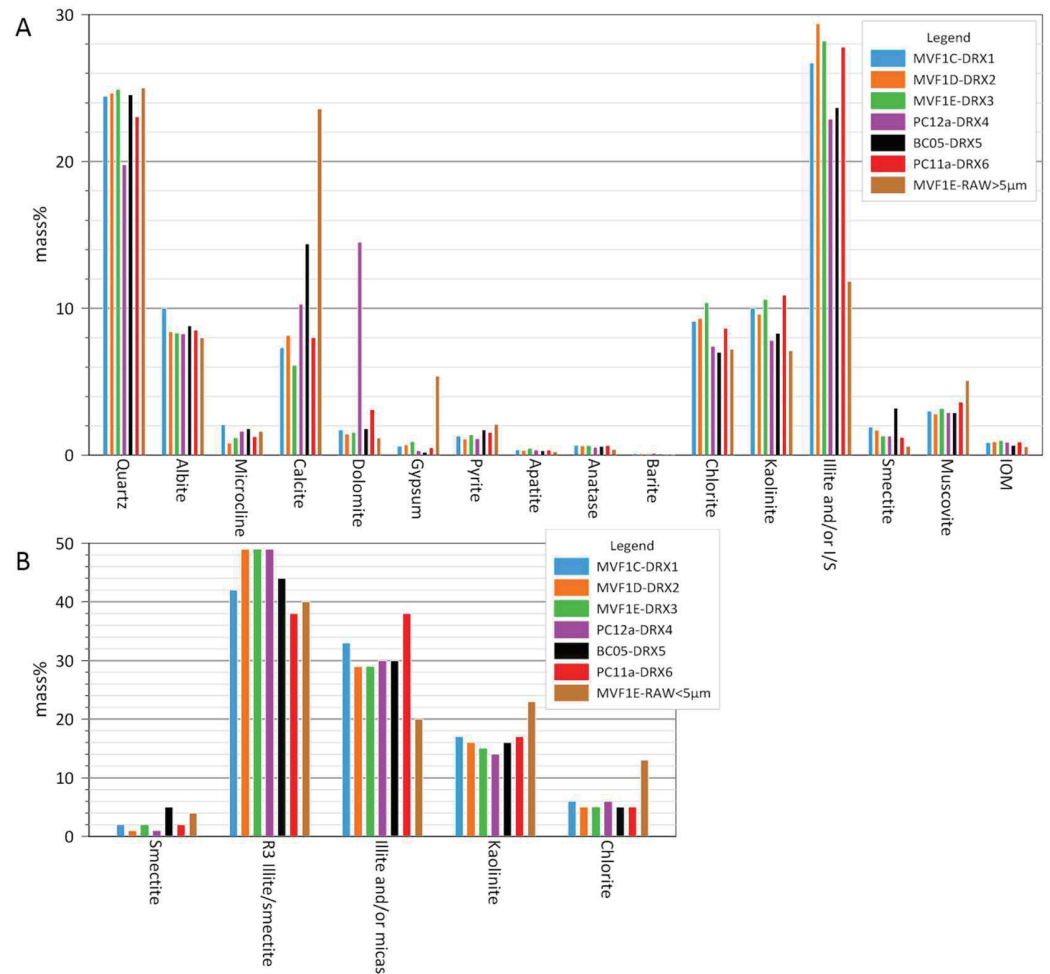


Figure 7. (a) Whole rock mineralogical analysis for all the samples collected except the less than 5- μm fraction of the MVF1E-RAW sample. The main elements composing the mud are clearly clay minerals and quartz particles. (b) Mineralogical composition of clay for all the samples collected except the MVF1E-RAW>5 μm . Globally, clay fraction is mainly composed by up to 50% of interstratified illite/smectite, 30% of Illite and/or micas, 15% of kaolinite, and a minor part of chlorite and smectite. The less than 5- μm fraction of the MVF1E-RAW sample differs from the whole samples as they have less illite and/or micas, and more kaolinite and chlorite. See Figure 3 for location map and Table 1 for details of samples.

$$e = 1.64 - 0.16 \ln \left(\frac{\sigma'_v}{\sigma'_{v0}} \right) \quad (8)$$

Permeability results showed no real differences between the different natural samples except for MECA-10 (Figure 8b), and a global linear regression for the other natural samples between $\ln(K)$ and the void ratio was adopted:

$$\ln(K) = 3.06e - 22.48 \quad (9)$$

Figure 8a shows that oedometer tests carried out on natural mud with a coarser fraction are characterized by a relatively low compressibility with a low initial void ratio (Table 2). At around 1,000 kPa of vertical effective stress, the different compressibility curves converge at the same void ratio (Figure 8a). The permeability globally increases with the fraction of coarser material with the same parallel trend as natural sediments (Figure 8b).

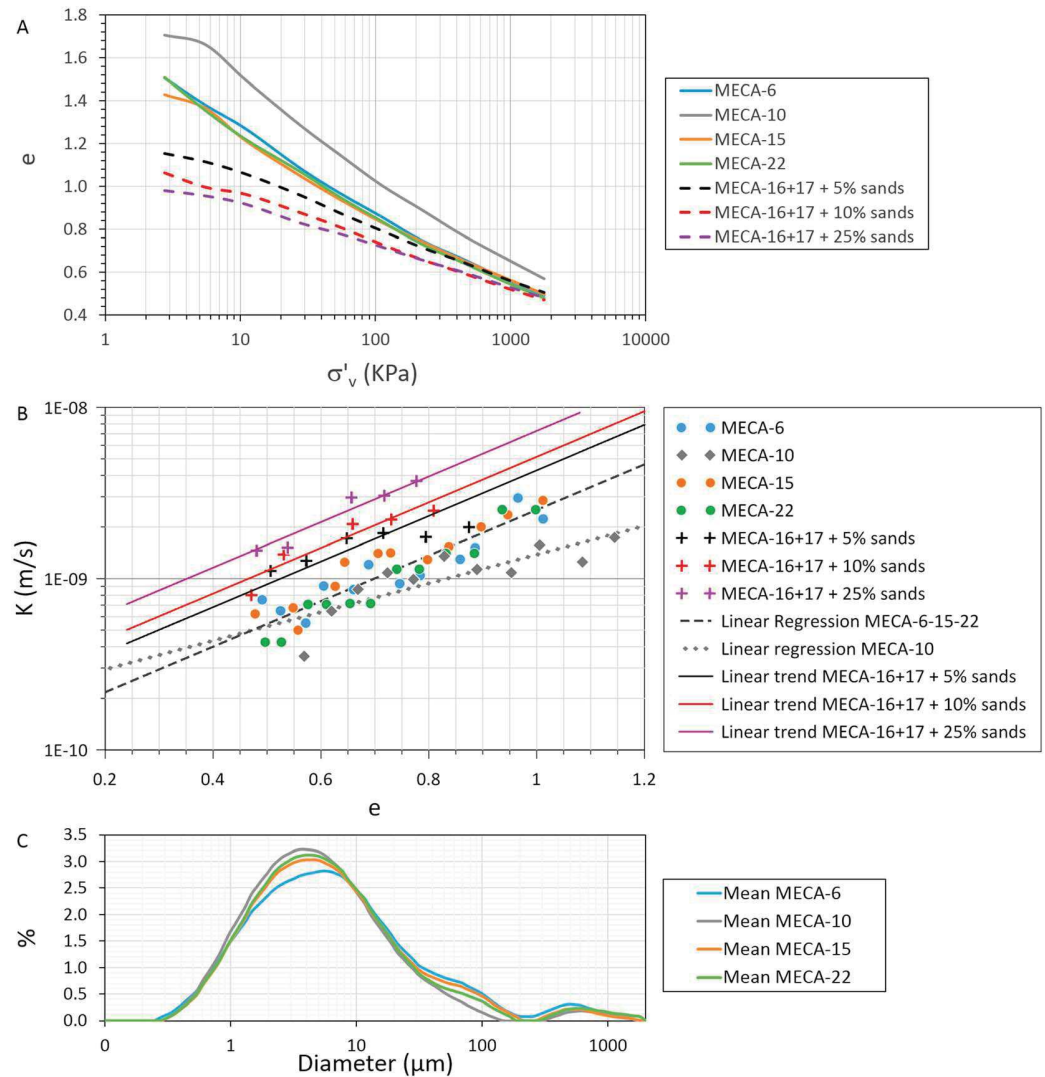


Figure 8. (a) Oedometer tests with void ratio (e) versus vertical effective stress (σ'_v) for the different tested samples. For the natural samples, only the MECA-10 has a higher compressibility and a higher initial void ratio than the other samples. The input of coarser materials reduce the initial void ratio and reduce the compressibility of the samples. (b) Hydraulic conductivity (k) versus void ratio (e) resulting from oedometer test and falling head method results for the different samples analyzed. Again, MECA-10 has a lower permeability than other natural samples, which fit the same trend. The input of coarser material increases the hydraulic conductivity but the general trend stays parallel to natural samples. (c) Cumulative granulometry for the natural samples showing that MECA 10 is finer than the three other samples. See Figure 3 and Table 1 for more details on the samples.

4.3. In Situ Lithology, Temperature, and Excess Pore Pressure Derived From In Situ Well Data

The Post-Absheron interval and the Upper part of the Absheron Suite are composed of claystone. Interstratified claystones and siltstones form the rest of the Absheron Suite and the Akchagyl Suite. The ASF extends from 2,501 to 2,887 m TVD/MSL in well B and 2,522 to 2,905 m TVD/MSL in well A. It is composed of claystone and evaporitic beds (mainly anhydrite and halite) and a minor part of siltstone. Over the 400 m of drilled Anhydritic Surakhany, 30% of evaporitic beds were encountered with individual thicknesses ranging from less than 1 to 8 m. Finally, the rest of the PS varies from claystone with rare pluri-decimetric to metric beds of siltstone to sandstone in the Surakhany (Upper PS) to interstratified claystones, siltstones, and sandstones in the Lower PS. Some of the sandstone beds reach 15 m in thickness.

Table 3 shows the results of NTG calculations based on well B data. The maximum NTG is reached for the Balakhany-Fasila interval (layer 2 in the numerical model), with a 24% NTG. The Surakhany interval has only 8% of NTG, and the Novocaspian-Absheron interval has the smallest NTG with 5%. As the well ends in the NKG interval, the NTG calculation for this particular layer may be inaccurate. From equations (3) and (5), vertical and horizontal hydraulic conductivities were calculated based on sonic logging. The calculated values fall within the measured ranges of oedometer tests on samples having a coarse content selected on the base of the NTG value of each interval.

Moreover, an unstable interval was crossed during the drilling of the ASF in well B. This interval is described as a swelling claystone and is interstratified between two 5-m-thick evaporite layers. A high acoustic velocity and abnormally low electric resistivity characterize it. Cuttings from the interval present a rather similar mineralogical composition to the mud analyzed in this study (Figure 7) with 18.5 mass% of quartz, 34 mass% of clays and micas in which there is 35% illite and/or micas, and 25% kaolinite and no smectite. However, some fractions vary from the mud analyzed: 12.8% of anhydrite were measured in the unstable interval; none was detected in the mud. Similarly, chlorite is present at 30% of the total clay fraction when in the mud, less than 10% was measured as well as calcite, which was present at 20 mass% at the considered interval, when around 10 mass% was measured in the mud.

During drilling, temperatures were also measured at different points of the well allowing to approach a geothermal gradient of 16 °C/km.

Both wells, which are located 9.5 km west of the MV (Figure 9), are overpressured at only 200 to 300 m BSF and remain in an overpressured state down to the well bottom. Overall, shale overpressure increases more or less linearly down to the top PS with a gradient of 3 MPa/km. Deeper down, the increase is linear again, with a higher gradient. In addition, six pressure peaks, that are located all along the PS Interval, can be observed in both wells (Figure 9). On these intervals, shale pressure values nearly reach the fracturing pressure, making the concerned intervals easier to fracture if pressure buildup happens. The concerned formations are the Anhydritic Surakhany (peak 1 in Figure 9) as well as five other intervals of the PS.

We noted potential links between structural features and pressure peaks (Figure 9). For instance, the pressure peak 4 in well A is split into two minor peaks in well B. There is a normal fault cut by well B that matches the pore pressure decrease observed at well B. Moreover, pressure peaks can be transposed below the MV to visualize which intervals are more prone to overpressure below the structure.

Pressures were also recorded in the reservoirs. In well A, reservoirs tested above 5,000 m BSF are in equilibrium with surrounding shales. Below 5,000 meters, in wells A and B, reservoirs are at least 20 MPa below the surrounding shales. In well A, some of these deep reservoirs are as overpressured as the shales. These results show that shallower reservoirs are not able to dissipate overpressure, whereas deeper ones appear drained and their pressure is much lower than surrounding shales. The deeper reservoir intervals are known to be regionally continuous and some even outcrop onshore in Azerbaijan (Javanshir et al., 2015). They act as regional drains for overpressured fluids with a northward hydraulic gradient (Bredhoeft et al., 1988; Javanshir et al., 2015). The sands in the northern area of the SCB are at hydrostatic pressure, while an excess hydraulic head creates deeper in the center of the basin.

4.4. Numerical Calculations of Transient Pore Pressure and Methane Diffusion

4.4.1. 1-D Modeling

The first step of the numerical modeling was a one-dimension calculation of sedimentation-generated overpressure in the deep part of the basin, 25 km south of Absheron. For this purpose, each layer was characterized by a compaction-corrected sedimentation rate based on Green et al. (2009) sediment ages and present thicknesses, compressibility, and permeability laws (Figure 10). Nadirov et al. (1997) gave average sedimentation rates for the SCB also based on present seismic thicknesses. Their estimated rate values span from 1 to 3 km/Myr for the Quaternary and around 0.5 km/Myr for the PS interval. These values are too low considering the results of our compaction-corrected 1-D modeling (Figure 10). However, our sedimentation rates depend on the compressibility laws integrated in the model. In the present paper, we present compressibility behavior of samples artificially created from natural mud and a known fraction of sand. Compressibility laws for natural sediments of each modeled stratigraphic interval might be different from the laws used in this study.

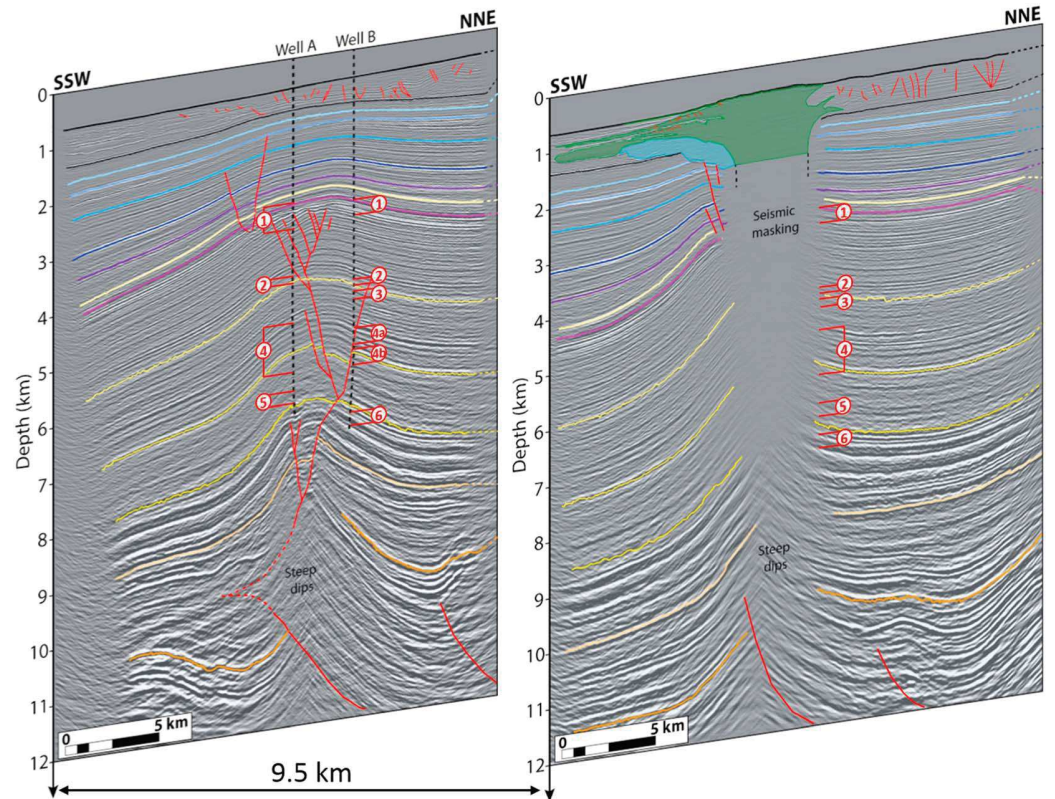


Figure 9. 3-D view of the two parallel seismic lines distant of 9.5 km. The right one is described in Figure 5. The left one in Figure 4. The pressure peaks numbered from 1 to 6 and observed on the pressure logs recorded on the two exploration wells are reported in front of the corresponding interval on seismic.

The calculation runs over 5 Myr, during which 9,600 m of compacted sediments have been deposited. As compression laws for mixed mud and very fine sands were measured for the first 1,800 kPa of vertical effective stress, at higher effective stress, the void ratio may reach negative values in some layers. In order to avoid this type of problem, we set a minimum limit for the void ratio at 0.1 in the software to obtain a compressibility trend similar to the ones presented by Chong and Santamarina (2016). Permeability laws for natural mud and mud mixed with very fine sands obtained from oedometer test results were integrated to characterize each stratigraphic interval (Figures 8a and 8b). The validity of the permeability laws was confirmed by the calculations on sonic logging (Table 3).

Figure 10 shows the porosity profile versus depth at the end of the sedimentation history. It gives a good representation of how sediments have compacted during the sedimentation history. The overpressure plot shown in Figure 10 corresponds to the overpressure generated by high sedimentation rates in the deepest part of the basin. Overpressure rises rapidly with depth in the low permeability layer 5 as overpressure cannot be evacuated and transmitted rapidly to the whole interval. The increase is slower from layer 4 down because of higher permeability. Finally, overpressure increases with a very low gradient from layer 2 below, layer 2 having the highest permeability.

4.4.2. 2-D Modeling

The second part of the modeling consisted of creating a structural model for two-dimensional diffusion of overpressure and methane. The structural model presented in Figure 11 is based on the work of Green et al. (2009) and on the fault network observed on the reference section in Figure 4. The initial section presented by Green et al. (2009) was only reproduced from the deeper part of the basin to the Absheron Ridge, where the seafloor is shallowest. The direction is the same as the section presented in Figure 1b. The total length of the section is 55 km, and its maximum depth 9.6 km. Faults shown in Figure 11 are

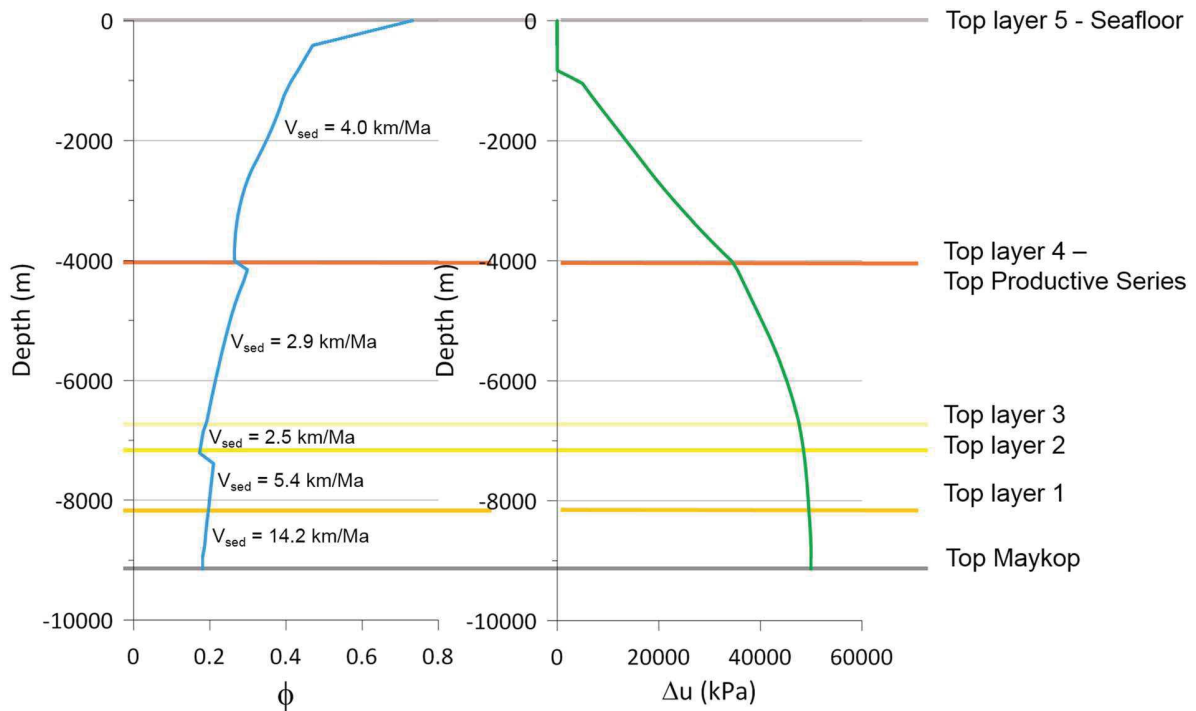


Figure 10. Results of the one-dimensional sedimentation modeling. On the left, porosity versus depth trend at the end of the 5 Myr of sedimentation with corrected sedimentation rates for each layer. On the right, overpressure versus depth trend at the end of the 5 Myr of sedimentation.

meant to represent not only the fault surfaces (localized thin shear zone) but also to the damage zone surrounding them. We estimated the thickness of the damage zone based on the work of Savage and Brodsky (2011), who relate the damaged thickness around a fault to the throw of the fault. With a total throw about 2 kilometers for the main thrust, a damage zone of a few hundred meters is expected. In the present work, a damage zone of 300 m is considered as representative of the fault zones.

Figure 11 shows the boundary conditions used for the numerical calculation of methane and pore pressure diffusions. No lateral or vertical exchange of pore pressure and methane with the outside of the model is permitted through the laterally impermeable southern and northern borders and the vertically impermeable upper and lower borders. The seawater has a fixed pore pressure of 0 kPa and a methane concentration of 10^{-5} mM (millimolar, 1 molar corresponding to a solution of 1 mol/L of concentration), which is a mean oceanic value (Lamontagne et al., 1973). The pore pressure calculated in one dimension from sedimentation with SeCoV3 (Figure 10) is imposed at the southern border of the model, where the sedimentary column is the thickest. Finally, a methane concentration of 10^{-3} mM is fixed at the bottom of the fault network, methane being generated in the Maykop Formation, the regional source rock, the deepest layer represented in the model.

Pressure and methane migration calculation were run over 5 Myr. Results of the diffusion equation resolution (equations (6) and (7)), in terms of overpressure migration, are shown in Figure 12a. Methane concentration and ratio between overpressure and vertical effective stress are shown together in Figure 12b in order to compare possible hydrofractured zones with high dissolved methane saturated areas.

Overpressure (Δu) propagated from south to north of the model at different diffusion rates. Indeed, depending mainly on permeability laws, overpressure will propagate more or less quickly and in different directions. For instance, in layer 5 overpressure did not accumulate (Figure 12a). This layer being the youngest, it maintained a high void ratio and so a higher permeability. The effect is amplified by the ratio between horizontal and vertical permeabilities. Layer 5 having a ratio of 2,200 (Table 3), the horizontal permeability in the model is 2,200 times larger than the permeability defined by oedometer test results. Therefore, in layer 5, pressure diffusion is mainly horizontal and the seawater condition (no overpressure) has significant impact on the overpressure values of this interval. From layer 4

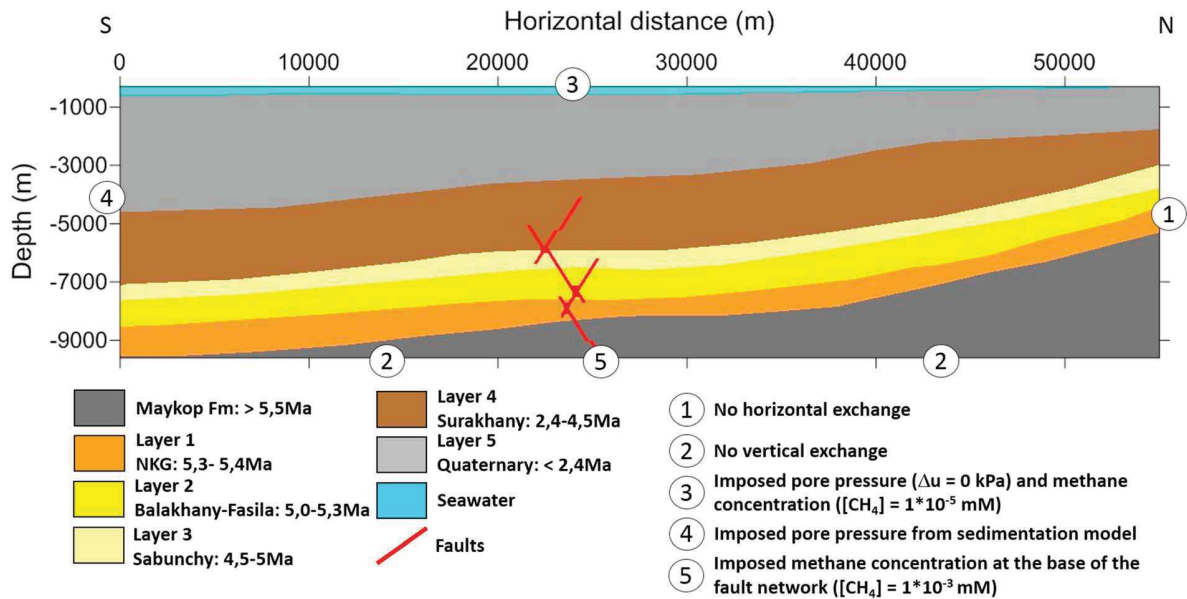


Figure 11. Structural model based on Green et al. (2009) work and on the fault network observed in Figure 4. The line follows the same trend as the seismic section of Figure 1b. Eight layers extend along the section corresponding to different sedimentation rates, compaction laws, and permeability trends (see Figure 10). The layers NKG, Balakhany-Fasila, Sabunchy, Surakhany, and quaternary are named layers 1 to 5, respectively, in other figures. Numbers showed at the limits of the model correspond to limit conditions imposed for the diffusion of pore pressure and methane.

below, the pressure is mainly diffused laterally creating a pressure front. At a given distance from the south of the model, where overpressure was injected from one-dimension sedimentation modeling (Figure 11), overpressure is larger in layer 4 than in other layers reproducing the pressure peaks observed at the wells (Figure 9).

Faults and associated damage zones were designed to rapidly diffuse methane therefore artificially reproducing methane advection through fractured zones. Methane was injected at the base of the fault network with a concentration of 10^{-3} mM (Figure 11). Methane molecular diffusivity in the rest of the model is 3 orders of magnitude lower than in faults. As a result, methane rapidly saturated the area adjoining the faults, and then diffused slowly through the sedimentary column until saturating an area nearly 2 km wide around the fault network (Figure 12b). The ratio of overpressure over vertical effective stress ($\Delta u / \sigma'_v$) is higher in layer 5, particularly in the north of the model. As it is the shallowest interval, σ'_v is the lowest of the model. Besides, little overpressure accumulation was possible in layer 5. Nevertheless, values are high at the top of the layer 4, where the ratio varies between 0.5 and 0.6. So we expect critical values in the area of high methane saturation at the Absheron crest.

5. Discussion

5.1. What Is the Stratigraphic Source of the Mud?

The geomorphological description of the AMV evidenced a bowl-shaped geometry below the mass extruded through the Absheron interval (Figure 6). This feature is formed by the Anhydritic Surakhany horizons that terminate as truncations (Catuneanu et al., 2009) below the younger seismic horizons of the Upper PS. Truncations are also observed 500 m below, in the lower part of the Upper PS. Horizon continuity resumes in the Middle PS. This particular geometry was already described and corresponds to a depleted area forming a potential former mud generation zone (Dupuis, 2017; Kirkham et al., 2017b; Stewart & Davies, 2006). The presence of two truncated intervals (Figure 6) indicates that there may have been several mud generation stages.

The unstable interval drilled in the Anhydritic Surakhany has a mineralogical composition similar to the mud analyzed in this study (Figure 7), with nearly 50% of clay minerals. Mud sampled at the seafloor is poorer in anhydrite, chlorite, and calcite than the unstable interval analyzed in the ASF. The mineralogical differences may be explained by the different paths and histories of the samples. Mud was driven upward

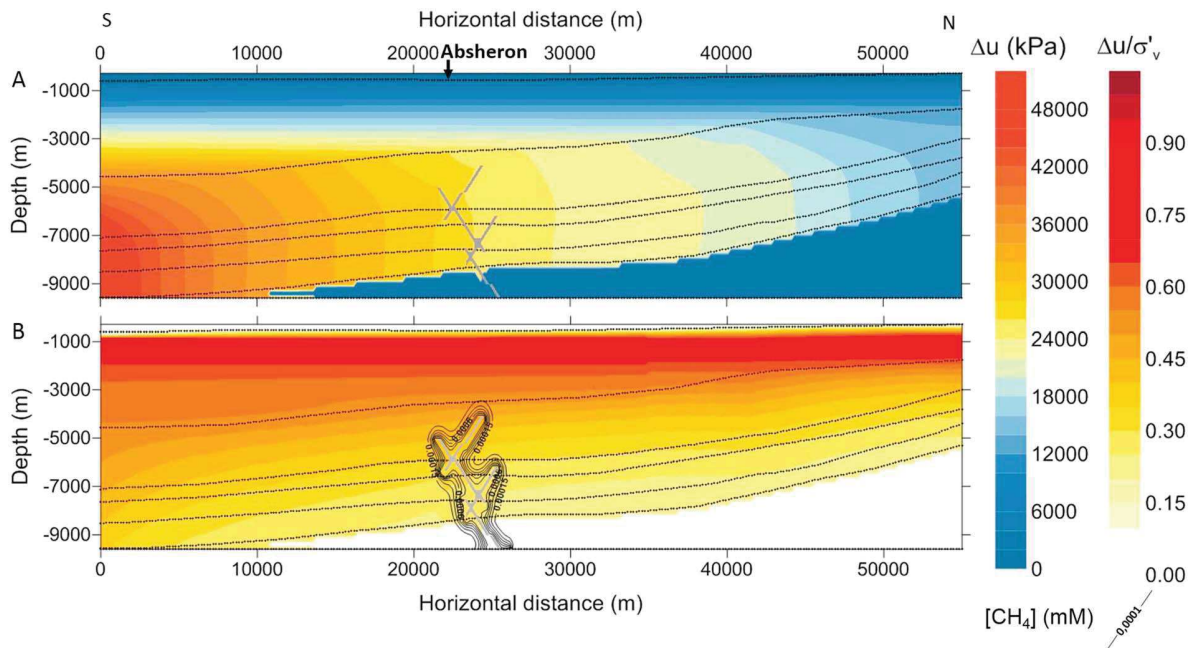


Figure 12. Results of overpressure and methane migration modeling after 5 Myr of calculation. (a) overpressure (Δu) in kPa after 5 Myr of migration through the structural model presented on Figure 11. Overpressure migrated more rapidly through layer 4, which has a higher permeability. (b) $\Delta u/\sigma'_v$ contours with values exceeding 0.75 and potentially reaching the level of hydro-fracturing. High values located in layer 5 are due to the low σ'_v near the seafloor. The black lines correspond to methane concentration contours. The top of the methane-saturated area corresponds to a zone where hydro-fracturing may occur if overpressure was slightly higher. The black dotted lines are for layer limits.

and deposited at the seafloor after a catastrophic event leading to remobilization of deep sediments. Thus, it potentially interacted with seawater but also with deeper fluids and gases forming for instance carbonate crusts at some methane seeping points or during diffuse degassing after a mud eruption (Kopf, 2002; Zitter, 2004). Conversely, the unstable interval cuttings were extracted directly from the formation through the drilling process and were in contact with the drilling mud.

From the biostratigraphic analysis of the mud and recent background sediments deposited at the seafloor, we can infer a Late Miocene to Pliocene (PS) origin for the mud.

Mineralogical analysis showed that fine fraction is poorer in illite and micas than unseparated samples (Figure 7b). These minerals are high-temperature minerals compared to smectite or interstratified illite/smectite (Pollastro, 1993). Unseparated samples are composed of a non-negligible fraction of diverse clasts when the fine fraction extraction is constituted of mud matrix particles. Therefore, clasts and coarse particles may find their source deeper than the mud matrix. However, the presence of a larger percentage of chlorite in the fine fraction (Figure 7b) tends to show a degradation of micas and illite in the mud matrix. The contact of deep fluids and seawater with the mud matrix particles may be responsible for this reaction, while coarser particles and clasts may preserve better illite and micas. Thus, mineral reactions with deep fluids and seawater could explain the different mineralogical compositions between mud matrix and clasts and they might come from the same depth magnitudes.

The Anhydritic Surakhany interval has several particularities. First, it is composed of 30% of evaporitic beds that can reach up to 8 m in thickness. The rest is mainly composed of claystones. An unstable interval was noticed during drilling, but others may exist in the Anhydritic Surakhany. Therefore, this interval may have a specific mechanical behavior. Moreover, the thermal gradient approximated from the temperatures measured at the wells is 16 °C/km, which is in accordance with mean thermal gradients measured at other SCB locations (Ginsburg et al., 1992). Considering that the MV activated after deposition of H3 (Figure 6), and considering that the thermal gradient remained constant during the Quaternary, the Anhydritic Surakhany temperature was around 30 °C when the first eruption occurred. Day-Stirrat et al. (2010) state that above 80 °C, chemical compaction (cementation processes and precipitations) will strengthen the

mudstone fabric and this process is irreversible, so the mudstone can no longer behave in a ductile way. Thus, the ASF would have been well within the temperature range where ductile deformation is conceivable.

Finally, overpressure logs show that the Anhydritic Surakhany forms a pressure peak at both wells (Figure 9). Rupture in this interval would happen earlier than in other formations for a given pressure increase or stress decrease. The fact that highly overpressured mudstones are blocked between meter-thick layers of evaporites may explain the weak behavior of some layers. As compaction water cannot be expelled vertically because of evaporites, these layers are likely to stay undercompacted and overpressured.

From these observations and measurements it seems plausible to conclude that Upper PS, and more precisely the ASF, is the source of the solid fraction of the mud expelled at the AMV.

5.2. How Do the Field Pore Pressure Measurements Compare to the Model?

It is quite clear on pressure logs that pressure regimes are completely different in shales and in reservoirs. Indeed, shales are highly overpressured all along the well, following a trend nearly parallel to the lithostatic pressure from the Top Akchagyl to the Bottom PS. In the bottom part of the wells (from the PS2 seismic horizon downward), overpressure level in shales remains rather constant, while reservoir pressures are nearly hydrostatic. Javanshir et al. (2015) describe similar pressure regime and magnitudes in the neighboring Shah Deniz fold. The Upper PS there have equal sandstone and shale overpressures and as the reservoir facies become more abundant and continuous in the Bottom PS, they become less overpressured. Therefore, in Shah Deniz and Absheron, the deep reservoirs seem to act as permeable drains as they allow overpressure to dissipate. The fact that shale pressure is also affected shows that dewatering might occur in the thinner shale intervals contained in the Bottom PS. Indeed, the abundance of permeable reservoirs would allow compaction water to be drained away from the shales, reducing their pressure. There is lateral pressure transmission from the deep part of the basin to the edges through regional-scale reservoirs (Javanshir et al., 2015), from the south to the north of the sections presented in Figure 9.

However, pressure horns in Absheron shales are not recorded in the data of Javanshir et al. (2015). Some intervals of the PS of Absheron wells are more overpressured than the rest of the stratigraphic interval. These peaks bring the corresponding intervals to pressure values between 5 and 10 MPa below hydrofracturing pressure in wells located 9.5 km from the MV center. The difference between hydrofracturing pressure and shale pressure may be even smaller near the MV, or it may have been smaller in the past, before MV activation. Therefore, they represent weak areas where a local rise in overpressure through clay dehydration or tectonic overpressuring for instance (Osborne & Swarbrick, 1997), or a drop in effective stress (erosion or fold growth and crestal uplift) could generate hydrofractures.

Pressures recorded in the two wells are not exactly the same: in the southern well (Well A), shale pressure decreases more gently within the Bottom PS and reservoir pressures are higher. Moreover, pressure horns are stronger in well B (to the north). Differential sedimentation between the deep basin located at the south of the Absheron anticline and the northern edge of the basin where less sediments accumulate could explain this phenomenon (Grosjean et al., 2009; Javanshir et al., 2015). As pressure transmission is oriented roughly from the south to the north of the anticline, the northern side of the anticline would accumulate more overpressure in the shales, whereas reservoirs would be more drained than in the southern flank. This phenomenon was also noted at the neighboring Shah Deniz anticline (Javanshir et al., 2015).

Two-dimensional model sections reproducing the main features of the pressure plots are shown on Figure 12. The overpressure rises down to 2,000 and 5,000-m deep depending on the location. Then overpressure remains constant at 30 MPa at the Absheron location and even decreases to 25 MPa when reaching the bottom part of the PS where highly continuous and abundant reservoir facies are present. Moreover, the numerical modeling results emulate the Top Surakhany pressure horn. Yet the modeling results underestimate the overpressure at the Absheron location (Figure 12a) as they are not in accordance with overpressure values recorded at the wells. Indeed, from Top Surakhany down, overpressure reaches values between 20 and 50 MPa. The discrepancy between measured and calculated overpressures may be related to the compressibility and permeability laws applied to the model, which were obtained from artificial

(reconstituted) sandy-clayey samples and not from natural samples from the different stratigraphic layers. Besides, the considered source of overpressure is related to fast sedimentation and might not be sufficient to model the natural pressure conditions of the Absheron anticline. Indeed, additional sources of pore pressure may play an important role and are yet to be considered in the modeling work.

However, and as a first approach, the present calculation was able to reproduce the main overpressure trends visible at the wells.

5.3. How Does Methane Diffusion Interact With Excess Pore Pressure Accumulation?

Modeling results shows that high values of $\Delta u / \sigma'_v$ fit with high dissolved methane concentrations and occur around the fault network below the AMV (Figure 12b). The consequence of high $\Delta u / \sigma'_v$ causing hydrofracturing may be an important decrease in pore pressure leading to methane exsolution and expansion (Duan & Mao, 2006) and generation of overpressured mud. Gas exsolution in sediments has proved to be a critical factor controlling sediment damage. Indeed, experience on gassy sediment core recovery in deep water shows important damage and loss of structure during the core ascent to the surface and associated hydrostatic pore reduction (Sultan et al., 2012). Loss of acoustic signal corresponding to the presence of free gas correlates with dramatic decrease of the yield stress ratio illustrating the damage made to the sediments.

Moreover, the presence of normal faults at the anticline crest between the Upper PS and the Top Absheron (Figure 4) shows that the state of stress where the primary source of mud was identified was extensive at the time when the AMV formed. If compressive state was dominating at these time and location, the observed faults must have been thrusts. Therefore, σ_1 (the maximum principal stress) was certainly vertical, so the least principal stress was horizontal. Fractures open in the direction of the least principal stress and then propagate in a plane perpendicular to this direction (Hubbert & Willis, 1957). Thus, hydrofractures generated at the time of the MV formation above the mud generation zone are expected to be vertical.

A present-day studied example of clastic extrusion triggering displays similar results. Indeed, the Lusi disaster, whose 2006 triggering cause is still a matter of debate between an earthquake and drilling issues (A. Mazzini et al., 2007; M. Tingay et al., 2008, 2017), was initiated by the combination of under-compaction/overpressure in the source layer and the presence of dissolved and free gas. According to Davies et al. (2008), fractures generated by drilling activities have caused an important decrease in pore pressure and the consequence was gas exsolution and expansion, overpressured mud generation, and the extrusion of mud to the surface (Davies et al., 2008). However, Mazzini et al. (2012) proposed a hydrothermal source for the gas, and yet Lusi triggering is already explained by gas flowing in undercompacted and overpressured sediments.

Thus, we suggest that the theoretical mechanism we propose for mud generation and extrusion with a combination of potential fracture zones and gas-saturated areas would also be applicable to the Absheron fold, where the studied MV is located.

5.4. What Is the most Plausible Sequence for the Formation of the AMV?

Based on previous observations and conclusions, a qualitative formation model for the AMV is proposed. This model is developed in five main phases:

Phase 1: rapid deposition of the PS (over 3.5 km in 2 Myr) above the gas-mature Maykop Formation that would generate hydrocarbons migrating slowly through the sedimentary column (Figure 13-1). Maykop Formation started generating gas during the Late Miocene in the Shah Deniz region located less than 50 km from Absheron gas discovery (Figure 2.9 in Alizadeh et al., 2017). Moreover, the deposition of the ASF proves that the sea level must have been lower than nowadays at the end of the PS deposition.

Phase 2: folding started during deposition of the Akchagyl Suite. It is linked to the propagation of a deep thrust terminating in the Maykop formation and linked to normal faults related to the fold formation. Methane migration is then focused into the faulted core of the anticline (Figure 13-2). The folding also has the effect of generating preferential rupture zones at its crest (Figure 13-2). Indeed, at the anticline crest, σ'_v is lower than on the flanks. Besides, as more space is available for sediment deposition in the surrounding synclines and in the deeper part of the basin, overpressure is generated and transmitted toward the

Absheron location. Overpressure generation and transmission as well as lower σ'_v at the flanks increases the $\Delta u / \sigma'_v$ ratio thereby increasing pore gas solubility.

Phase 3: $\Delta u / \sigma'_v$ ratio reaches the hydro-fracturing threshold (Figure 13-3), leading to a significant decrease in pore pressure.

Phase 4: hydrofracturing triggers gas exsolution and expansion in gas-saturated and mechanically weak layers such as ASF (Figure 13-4). Exsolution remobilizes the weak interval, generating mud. Overpressured and low-density mud is then transported to the seafloor provoking the first mud extrusion. As gas, mixed with sediments and water, migrates up the hydrofracture network, methane expands amplifying the process and potentially eroding fracture walls (Figure 13-4).

Phase 5: the process goes on with gas exsolution propagating in the Anhydritic Surakhany, depleting this layer continuously. Collapse of the upper strata into the depleted area creates the rather flat and low topography volcano (Figure 13-5). The extruded mud slowly degasses at the seafloor.

Phase 6: quiescent and active phases of the MV alternates, creating a complex interdigitation geometry where normal sedimentation predominates during quiescent phases of the volcano. Further depletion happens in the source, triggering more collapse, while more mud is extruded at the seafloor (Figure 13-6).

The initial trigger of this MV is not related to gas, as hydrofracturing due to overpressure buildup and weakness of the fold-crest initiates the succession of events. However, in this conceptual model, methane would have three essential effects.

Gas needs to saturate the porous network in its dissolved state before hydrofracturing in order to provoke remobilization of sediments. Exsolution of methane weakens and disaggregates host sediments (Sultan et al., 2012; M. R. P. Tingay et al., 2015).

As free gas has very low density (typically about 1/1,000 of that of water in normal conditions), it will flow toward the surface (Brown, 1990), carrying the mud away (solid particles and formation water).

Finally, as gas goes up into the pipe, it expands (Brown, 1990), accelerating the mud ascent, sustaining mud pressure, and eroding fracture walls, creating clasts, to end-up with mud breccia extrusion at the surface.

Thus, methane exsolution is the key to mud formation but also the main driver for mud remobilization toward the surface due to its low density and expansion capacity. Initial rupture is essential in order to start the chain reaction and methane expansion and exsolution will maintain the pipes open and even enlarge them.

5.5. Limits and Perspectives of the Study

This conceptual formation model of MVs closely fits with observations and analysis of the available data set and is partly based on the numerical modeling results presented earlier.

However, Improvements May Be Made at Several Levels:

Data Set: For instance, the seismic masking prevents direct observation of the center of the volcano's plumbing system. Reprocessing of the data was attempted several times and with different methods and approaches, but it remains challenging due to the presence of gas-charged mud and free gas. The available biostratigraphic analyses are not quantitative and for further precision on the mud origin quantitative analyses of the fauna and flora in mud will be necessary. Analysis of the clasts will also help to refine the mud origin.

Numerical modeling: The compressibility laws used in the current model could be improved to consider soil compressibility for the highest stress range (Chong & Santamarina, 2016). In the present work and in order to avoid negative void ratio values, the software limits the minimum void ratio to 0.1. In the present model, pore pressures generated by sedimentation and pressure transmission are not calculated simultaneously. Overpressure due to sedimentation is calculated over 5 Myr of sedimentation history and is integrated as a boundary condition into the 2-D Darcy's and Fick's diffusion equations. The next step would be to integrate both sedimentation and diffusion processes into one unique 2-D model. Finally, the model does not simulate the post-hydrofracturing processes causing gas exsolution and overpressured mud expulsion. Gas exsolution and expansion processes will have to be integrated into this model in order to reproduce MV initiation.

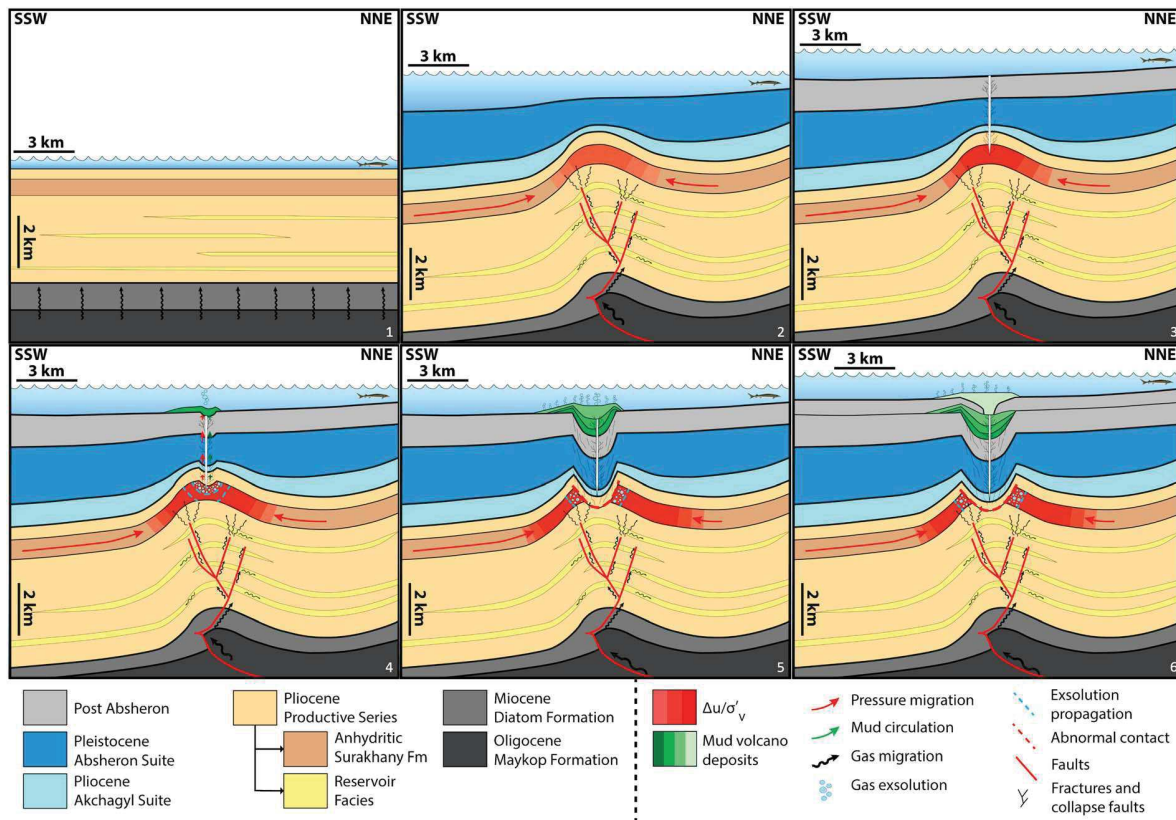


Figure 13. Formation model for the Absheron mud volcano based on in situ observations and measurements, laboratory tests, and analysis and numerical modeling. 1: Rapid deposition of the Productive Series and maturation of the Maykop formation. Slow and extended methane migration. 2: Absheron fold creation. Focusing of the methane migration through fold-related fault network and $\Delta u/\sigma'_v$ increase at the anticline crest. 3: Rupture condition reached and hydrofracturing of the sedimentary column from the seafloor to the Anhydritic Surakhany. 4: Gas exsolution and expansion and remobilization of Anhydritic Surakhany sediments. First extrusion. 5: Propagation of gas exsolution and sediment remobilization. Depletion of the Anhydritic Surakhany and collapse of the overlying strata. 6: Present geometry after alternance of several quiescent and active episodes for the mud volcano. More depletion of the source and collapse of the overlying strata is triggered at each active episodes.

Overpressure Generation Mechanisms: The MV is located at the crest of an active anticline and triggered after one of the main folding phases. Thus, lateral tectonic overpressuring is expected to have happened before the MV formation (Osborne & Swarbrick, 1997; Swarbrick et al., 2002). This tectonic overpressuring has proved to increase the global overpressure up to 16 MPa at 3.5-km deep partly due to porosity decrease (Couzens-Schultz & Azbel, 2014; Obradors-Prats et al., 2017). Moreover, internal sources have not been considered such as clay dehydration and smectite-illite reactions that generate a large volume of water in the pore space, thus generating overpressure (Osborne & Swarbrick, 1997; Swarbrick et al., 2002). Gas generation is also considered as an overpressure generation mechanism and may have implications for this numerical model as gas is generated and diffused through the sedimentary column (Osborne & Swarbrick, 1997; Swarbrick et al., 2002). Considering these new pore pressure input, the $\Delta u/\sigma'_v$ ratio may increase drastically and the model may be able to reproduce the observed in situ pore pressure measurements.

6. Conclusions

Based on 3-D seismic data, mineralogical, geotechnical, and biostratigraphic analyses of the sampled mud together with well data, the morphological observations, we conclude that the ASF is a plausible source for the AMV. Pressures recorded at the wells show, as in Shah Deniz, that deep reservoirs act as drains for pressure provoking a decrease in overall shale pressure logs. Pressure horns were also recorded at specific intervals, as for the ASF, where shale pressure is close to the fracture limit.

Based on these observations, a numerical model with 2-D-diffusion equations was applied on a basin scale section. Sedimentation-related overpressures underestimate by 50% the pressures measured in the wells but reproduce fairly well the observed trends. Additional sources of in situ overpressure generation (i.e., clay dehydration and transformation), which are not included in the current model, may explain the discrepancy between the model prediction and the pore pressure values of wells. The main observation made through the numerical model is the superposition of methane-saturated areas with potential hydrofracturing zones. Indeed, hydrofracturing may produce a drastic decrease in pore pressure, allowing gas exsolution and expansion. Based on the present model results, on experimental results of gassy-sediment behavior in which the gas exsolution damages the sediment and reduces its mechanical strength and on the Lusi disaster studies, we conclude that the superposition of potential hydrofracturing areas and gas-saturated zones can explain that the AMV activated at the crest of the anticline.

As a result, we propose a conceptual evolutionary model for the AMV as follows: initial stages of folding focus methane migration into the anticline crest bringing methane to the upper geological layers and mainly to the Anhydritic Surakhany Fm. Pore pressure accumulation and its lateral migration through the Anhydritic Surakhany Fm. promote hydrofracturing at the location of the AMV, causing a decrease in pore pressure. Those conditions lead to methane exsolution and expansion and to upward remobilization of the already weak Anhydritic Surakhany interval, generating low density and overpressured mud. During mud ascent, gas bubbles expand, splintering fracture walls and incorporating clasts into the mud. Finally, extrusion at the seafloor happens where the mud slowly expels methane. As extrusion goes on, a collapse of the overlying strata into the depleted mud generation zone forms.

Therefore, even though the trigger point for the whole MV formation process in our model is hydrofracturing, clay-rich sediments have to be initially saturated with methane in order to generate mud. The methane is essential and has three main roles: exsolution allows creating the mud from weak layers, its low density decreases the mud one and accelerate its upward flow to the surface, and gas expansion sustains mud overpressure and causes splintering of gas-saturated fracture walls creating clasts.

With the available dense data set, we evidence that in order to form the AMV, a combination of three factors is required: high pore pressure, gas saturation and clay-rich sediments. Recent work on the Lusi eruption also demonstrated the importance of the same factors in a different geological environment. Therefore, detecting the presence of those three factors may help understand the preconditioning conditions of MV's formation.

Acknowledgments

Total S.A. is owner of the seismic and well data used and presented in this paper. Please contact the Research and Development team of Total for information and potential access to this data (SCR/RD, Total CSTJF, Avenue Larribau, 64000 Pau). Sediment analysis results used in this study can be downloaded by following this link: <https://doi.org/10.6084/m9.figshare.7448153>. To access the SeCoV3 software and the input parameters, please directly download it here <https://github.com/ArthurBlouin/SeCoV3.git>. This study was realized in the scope of the PhD of Arthur Blouin under the joint direction of the Pau University (UPPA), Ifremer and Total S.A. The authors would like to thank Claire Fialips for the mud mineralogy analysis, Jérémie Gaillot for the help with biostratigraphy interpretation, and Mickaël Rovere for the help rendered during compressibility/permeability analyses.

References

- Abdullayev, E., & Leroy, S. A. G. (2016). Provenance of clay minerals in the sediments from the Pliocene Productive Series, western South Caspian Basin. *Marine and Petroleum Geology*, 73, 517–527. <https://doi.org/10.1016/j.marpetgeo.2016.03.002>
- Alfaro, M. C., & Wong, R. C. K. (2001). Laboratory studies on fracturing of low-permeability soils. *Canadian Geotechnical Journal*, 38(2), 303–315. <https://doi.org/10.1139/cgj-38-2-303>
- Alizadeh, A. A., Guliyev, I. S., Kadirov, F. A., & Eppelbaum, L. V. (2017). *Geosciences of Azerbaijan Volume II: Economic Geology and Applied Geophysics* (Vol. II). Basel, Switzerland: Springer International Publishing. <https://doi.org/10.1007/978-3-319-40493-6>
- Allen, M. B., Jones, S., Ismail-Zadeh, A., Simmons, M., & Anderson, L. (2002). Onset of subduction as the cause of rapid Pliocene-Quaternary subsidence in the South Caspian basin. *Geology*, 30(9), 775–778. [https://doi.org/10.1130/0091-7613\(2002\)030<0775:OOSATC>2.0.CO;2](https://doi.org/10.1130/0091-7613(2002)030<0775:OOSATC>2.0.CO;2)
- ASTM International. (1996). D 2435-96 - Standard test method for one-dimensional consolidation properties of soils. *American Society for Testing and Materials*, (August), 196–205. doi: <https://doi.org/10.1520/D2435-96>
- Bahorich, M. S., & Farmer, S. L. (1995). 3-D seismic discontinuity for faults and stratigraphic features: The coherence cube. In *SEG Technical Program Expanded Abstracts 1995* (pp. 93–96). Houston, TX: Society of Exploration Geophysicists. <https://doi.org/10.1190/1.1887523>
- Benjamin, U. K., & Huuse, M. (2017). Seafloor and buried mounds on the western slope of the Niger Delta. *Marine and Petroleum Geology*, 83, 158–173. <https://doi.org/10.1016/j.marpetgeo.2017.02.023>
- Bochud, M. (2011). *Tectonics of the Eastern Greater Caucasus in Azerbaijan*, (Vol. 30, p. 207). Fribourg, Switzerland: Université de Fribourg.
- Boudreau, B. P. (1996). The diffusive tortuosity of fine-grained un lithified sediments. *Geochimica et Cosmochimica Acta*, 60(16), 3139–3142. [https://doi.org/10.1016/0016-7037\(96\)00158-5](https://doi.org/10.1016/0016-7037(96)00158-5)
- Bredehoeft, J. D., Djevanshir, R. D., & Belitz, K. R. (1988). Lateral fluid flow in a compacting sand-shale sequence: South Caspian basin. *American Association of Petroleum Geologists Bulletin*, 72(4), 416–424. <https://doi.org/10.1306/703C9A1E-1707-11D7-8645000102C1865D>
- Brown, K. M. (1990). The nature and hydrogeologic significance of mud diapirs and diatremes for accretionary systems. *Journal of Geophysical Research*, 95(B6), 8969. <https://doi.org/10.1029/JB095iB06p08969>
- Brunet, M.-F., Korotaev, M. V., Ershov, A. V., & Nikishin, A. M. (2003). The South Caspian Basin: a review of its evolution from subsidence modelling. *Sedimentary Geology*, 156(1-4), 119–148. [https://doi.org/10.1016/S0037-0738\(02\)00285-3](https://doi.org/10.1016/S0037-0738(02)00285-3)
- Catuneanu, O., Abreu, V., Bhattacharya, J. P., Blum, M. D., Dalrymple, R. W., Eriksson, P. G., et al. (2009). Towards the standardization of sequence stratigraphy. *Earth-Science Reviews*, 92(1–2), 1–33. <https://doi.org/10.1016/j.earscirev.2008.10.003>

- Chong, S.-H., & Santamarina, J. C. (2016). Soil Compressibility Models for a Wide Stress Range. *Journal of Geotechnical and Geoenvironmental Engineering*, *142*(6), 06016003, 1–7. [https://doi.org/10.1061/\(ASCE\)GT.1943-5606.0001482](https://doi.org/10.1061/(ASCE)GT.1943-5606.0001482)
- Contet, J., & Unterseh, S. (2015). Multiscale site investigation of a giant mud-volcano offshore Azerbaijan—Impact on subsea field development. *Offshore Technology Conference, OTC-25864(Mv)*, 1–10. doi: <https://doi.org/10.4043/25864-MS>
- Couzens-Schultz, B. A., & Azbel, K. (2014). Predicting pore pressure in active fold-thrust systems: An empirical model for the deepwater Sabah foldbelt. *Journal of Structural Geology*, *69*(PB), 465–480. <https://doi.org/10.1016/j.jsg.2014.07.013>
- Crank, J. (1975). The mathematics of diffusion. [https://doi.org/10.1016/0306-4549\(77\)90072-X](https://doi.org/10.1016/0306-4549(77)90072-X)
- Das, B. M. (2013). *Principles of geotechnical engineering*, (7th ed.). *Journal of Chemical Information and Modeling* (Vol. 53). Boston, Massachusetts: CENGAGE Learning. <https://doi.org/10.1017/CBO9781107415324.004>
- Davies, R. J., Brumm, M., Manga, M., Rubiandini, R., Swarbrick, R., & Tingay, M. (2008). The East Java mud volcano (2006 to present): An earthquake or drilling trigger? *Earth and Planetary Science Letters*, *272*(3–4), 627–638. <https://doi.org/10.1016/j.epsl.2008.05.029>
- Day-Stirrat, R. J., McDonnell, A., & Wood, L. J. (2010). Diagenetic and seismic concerns associated with interpretation of deeply buried mobile shales. *Shale Tectonics: AAPG Memoir*, *93*, 5–28. <https://doi.org/10.1306/13231306M93730>
- Deville, E. (2009). Mud volcano systems. In N. Lewis, & A. Moretti (Eds.), *Volcanoes: Formation, eruptions and modelling* (pp. 95–125 (404)). Hauppauge, New York: Nova Science Publishers.
- Deville, E., Guerlais, S. H., Callec, Y., Griboulard, R., Huyghe, P., Lallemand, S., et al. (2006). Liquefied vs stratified sediment mobilization processes: Insight from the South of the Barbados accretionary prism. *Tectonophysics*, *428*(1–4), 33–47. <https://doi.org/10.1016/j.tecto.2006.08.011>
- Duan, Z., & Mao, S. (2006). A thermodynamic model for calculating methane solubility, density and gas phase composition of methane-bearing aqueous fluids from 273 to 523 K and from 1 to 2000 bar. *Geochimica et Cosmochimica Acta*, *70*(13), 3369–3386. <https://doi.org/10.1016/j.gca.2006.03.018>
- Dupuis, M. (2017). Processus de mise en place et évolution des systèmes de volcans de boue. Université Lille 1 - Sciences et technologies.
- Eaton, B. A. (1975). The equation for geopressure prediction from well logs. In *Fall meeting of the Society of Petroleum Engineers of AIME* (5 pp.). Dallas, Texas: Society of Petroleum Engineers. <https://doi.org/10.2118/5544-MS>
- Egan, S. S., Mosar, J., Brunet, M.-F., & Kangarli, T. (2009). Subsidence and uplift mechanisms within the South Caspian Basin: Insights from the onshore and offshore Azerbaijan region. *Geological Society, London, Special Publications*, *312*(1), 219–240. <https://doi.org/10.1144/SP312.11>
- Etiopie, G., Feyzullayev, A., & Baci, C. L. (2009). Terrestrial methane seeps and mud volcanoes: A global perspective of gas origin. *Marine and Petroleum Geology*, *26*(3), 333–344. <https://doi.org/10.1016/j.marpetgeo.2008.03.001>
- Feng, T. W. (2005). *Reappraisal of the fall cone test*. In *Proceedings of the 16th International Conference on Soil Mechanics and Geotechnical Engineering*, (Vol. 16, pp. 357–360). Osaka, Millpress Science Publishers/IOS Press. <https://doi.org/10.3233/978-1-61499-656-9-357>
- Fialips, C. I., Labeyrie, B., Burg, V., Mazière, V., Munerel, Y., Haurie, H., et al. (2018). Quantitative mineralogy of Vaca Muerta and alum shales from Core chips and drill cuttings by calibrated SEM-EDS mineralogical mapping. DOI: <https://doi.org/10.15530/urtec-2018-2902304>
- Foucher, J. P., Westbrook, G., Boetius, A., Ceramicola, S., Dupré, S., Mascle, J., et al. (2009). Structure and drivers of cold seep ecosystems. *Oceanography*, *22*(1), 92–109. <https://doi.org/10.5670/oceanog.2009.11>
- Fowler, S. R., Mildenhall, J., Zalova, S., Riley, G., Elsley, G., Desplanques, A., & Guliyev, F. (2000). Mud volcanoes and structural development on Shah Deniz. *Journal of Petroleum Science and Engineering*, *28*(4), 189–206. [https://doi.org/10.1016/S0920-4105\(00\)00078-4](https://doi.org/10.1016/S0920-4105(00)00078-4)
- Ginsburg, G. D., Guseynov, R. A., Dadashev, A. A., Ivanova, G. A., Kazantsev, S. A., Solov'yev, V. A., et al. (1992). Gas hydrates of the southern Caspian. *International Geology Review*, *34*(8), 765–782. <https://doi.org/10.1080/00206819209465635>
- Golonka, J. (2007). Geodynamic evolution of the South Caspian Basin. *Oil and Gas of the Greater Caspian Area*, *55*, 17–41. <https://doi.org/10.1306/1205844St551463>
- Graue, K. (2000). Mud volcanoes in deepwater Nigeria. *Marine and Petroleum Geology*, *17*(8), 959–974. [https://doi.org/10.1016/S0264-8172\(00\)00016-7](https://doi.org/10.1016/S0264-8172(00)00016-7)
- Green, T., Abdullayev, N., Hossack, J., Riley, G., & Roberts, A. M. (2009). Sedimentation and subsidence in the South Caspian Basin, Azerbaijan. *Geological Society, London, Special Publications*, *312*(1), 241–260. <https://doi.org/10.1144/SP312.12>
- Grosjean, Y., Zaugg, P., Gaulier, J.-M., & Total S.A. (2009). Burial hydrodynamics and subtle hydrocarbon trap evaluation: From the Mahakam Delta to the South Caspian Sea. International Petroleum Technology Conference Held in Doha, Qatar, 7-9 December 2009, 1–12.
- Guillon, S., & Keskes, N. (2004). Sismage and the 3D visualization at Total. In *AAPG International Conference* (pp. 1–3).
- Guliyev, I., Aliyeva, E., Huseynov, D., Feyzullayev, A., & Mamedov, P. (2010). Hydrocarbon potential of ultra deep deposits in the South Caspian Basin. In *AAPG European Region Annual Conference* (Vol. 1, p. 66). Kiev, Ukraine.
- Guliyev, I. S., Feizulayev, A. A., & Huseynov, D. A. (2001). Isotope geochemistry of oils from fields & mud volcanoes in the South Caspian Basin, Azerbaijan. *Petroleum Geoscience*, *7*(2), 201–209. <https://doi.org/10.1144/petgeo.7.2.201>
- Hedberg, H. D. (1974). Relation of methane generation to Undercompacted shales, shale diapirs, and mud volcanoes. *AAPG Bulletin*, *58*(4), 661–673. <https://doi.org/10.1306/83D91466-16C7-11D7-8645000102C1865D>
- Hubbert, M. K., & Willis, D. G. (1957). Mechanics of hydraulic fracturing. *Society of Petroleum Engineers*, *210*, 153–163. Retrieved from <http://archives.datapages.com/data/specpubs/methodo2/data/a075/a075/0001/0200/0239.htm>
- Hudson, S. M., Johnson, C. L., Efendiyeva, M. A., Rowe, H. D., Feyzullayev, A. A., & Aliyev, C. S. (2008). Stratigraphy and geochemical characterization of the Oligocene-Miocene Maikop series: Implications for the paleogeography of Eastern Azerbaijan. *Tectonophysics*, *451*(1–4), 40–55. <https://doi.org/10.1016/j.tecto.2007.11.045>
- Imbert, P., Geiss, B., & Fatjó de Martín, N. (2014). How to evacuate 10 km³ of mud: Saturate with gas and decrease the pressure! *Geo-Marine Letters*, *34*(2–3), 199–213. <https://doi.org/10.1007/s00367-014-0357-3>
- Javanshir, R. J., Riley, G. W., Duppenbecker, S. J., & Abdullayev, N. (2015). Validation of lateral fluid flow in an overpressured sand-shale sequence during development of Azeri-Chirag-Gunashli oil field and Shah Deniz gas field: South Caspian Basin, Azerbaijan. *Marine and Petroleum Geology*, *59*, 593–610. <https://doi.org/10.1016/j.marpetgeo.2014.07.019>
- Kirkham, C., Cartwright, J., Hermanrud, C., & Jebsen, C. (2017a). The genesis of mud volcano conduits through thick evaporite sequences. *Basin Research*, *30*(2), 217–236. <https://doi.org/10.1111/bre.12250>
- Kirkham, C., Cartwright, J., Hermanrud, C., & Jebsen, C. (2017b). The spatial, temporal and volumetric analysis of a large mud volcano province within the Eastern Mediterranean. *Marine and Petroleum Geology*, *81*, 1–16. <https://doi.org/10.1016/j.marpetgeo.2016.12.026>
- Kopf, A. J. (2002). Significance of mud volcanism. *Reviews of Geophysics*, *40*(2), 1005. <https://doi.org/10.1029/2000RG000093>

- Lamontagne, R. A., Swinnerton, J. W., Linnenbom, V. J., & Smith, W. D. (1973). Methane concentrations in various marine environments and atmospheric methane concentration of 1.24 ppm for the atmosphere above number of stranded fjords and lakes. Ström, decomposition of organic waters the mechanism of methane production appears to. *Journal of Geophysical Research*, *78*(24), 5317–5324. <https://doi.org/10.1029/JC078i024p05317>
- Lin, W., Yamamoto, K., Ito, H., Masago, H., & Kawamura, Y. (2008). Estimation of minimum principal stress from an extended leak-off test onboard the Chikyu drilling vessel and suggestions for future test procedures. *Scientific Drilling*, *6*, 43–47. <https://doi.org/10.2204/iodp.sd.6.06.2008>
- Mazzini, A., & Etiope, G. (2017). Mud volcanism: An updated review. *Earth-Science Reviews*, *168*, 81–112. <https://doi.org/10.1016/j.earscirev.2017.03.001>
- Mazzini, A., Etiope, G., & Svensen, H. (2012). A new hydrothermal scenario for the 2006 Lusi eruption, Indonesia. Insights from gas geochemistry. *Earth and Planetary Science Letters*, *317–318*(May 2006), 305–318. <https://doi.org/10.1016/j.epsl.2011.11.016>
- Mazzini, A., Svensen, H., Akhmanov, G. G., Aloisi, G., Planke, S., Malthes-Sorensen, A., & Istadi, B. (2007). Triggering and dynamic evolution of the LUSI mud volcano, Indonesia. *Earth and Planetary Science Letters*, *261*(3–4), 375–388. <https://doi.org/10.1016/j.epsl.2007.07.001>
- Milkov, A. V. (2000). Worldwide distribution of submarine mud volcanoes and associated gas hydrates. *Marine Geology*, *167*(1–2), 29–42. [https://doi.org/10.1016/S0025-3227\(00\)00022-0](https://doi.org/10.1016/S0025-3227(00)00022-0)
- Morley, C. K., King, R., Hillis, R., Tingay, M., & Backe, G. (2011). Earth-science reviews deepwater fold and thrust belt classification, tectonics, structure and hydrocarbon prospectivity: A review. *Earth Science Reviews*, *104*(1–3), 41–91. <https://doi.org/10.1016/j.earscirev.2010.09.010>
- Mosar, J., Kangarli, T., Bochud, M., Glasmacher, U. A., Rast, A., Brunet, M.-F., & Sosson, M. (2010). Cenozoic-recent tectonics and uplift in the greater Caucasus: a perspective from Azerbaijan. *Geological Society, London, Special Publications*, *340*(1), 261–280. <https://doi.org/10.1144/SP340.12>
- Nadirov, R. S., Bagirov, E., Tagiyev, M., & Lerche, I. (1997). Flexural plate subsidence, sedimentation rates, and structural development of the super-deep South Caspian Basin. *Marine and Petroleum Geology*, *14*(4), 383–400. [https://doi.org/10.1016/S0264-8172\(96\)00054-2](https://doi.org/10.1016/S0264-8172(96)00054-2)
- Nely, G. (1986). 8. La méthode de sismique réflexion. In *Méthodes Géophysiques (Vol. 2)* (pp. 147–244). Editions TECHNIP.
- Obradors-Prats, J., Rouainia, M., Aplin, A. C., & Crook, A. J. L. (2017). Assessing the implications of tectonic compaction on pore pressure using a coupled geomechanical approach. *Marine and Petroleum Geology*, *79*, 31–43. <https://doi.org/10.1016/j.marpetgeo.2016.10.017>
- Oppo, D., Capozzi, R., Nigarov, A., & Esenov, P. (2014). Mud volcanism and fluid geochemistry in the Cheleken peninsula, western Turkmenistan. *Marine and Petroleum Geology*, *57*, 122–134. <https://doi.org/10.1016/j.marpetgeo.2014.05.009>
- Osborne, M. J., & Swarbrick, R. E. (1997). Mechanisms for generating overpressure in sedimentary basins: A reevaluation 1. *AAPG Bulletin*, *6*(6), 1023–1041.
- Pollastro, R. M. (1993). Considerations and applications of the illite/smectite geothermometer in hydrocarbon-bearing rocks of miocene to Mississippian age. *Clays and Clay Minerals*, *41*(2), 119–133. <https://doi.org/10.1346/CCMN.1993.0410202>
- Popov, S. V., Rögl, F., Rozanov, A. Y., Steininger, F. F., Shcherba, I. G., & Kovac, M. (2004). Lithological-paleogeographic maps of paratethys. CFS Courier Forschungsinstitut Senckenberg.
- Ren, X., Zhao, Y., Deng, Q., Kang, J., Li, D., & Wang, D. (2016). A relation of hydraulic conductivity—Void ratio for soils based on Kozeny-carman equation. *Engineering Geology*, *213*, 89–97. <https://doi.org/10.1016/j.enggeo.2016.08.017>
- Ricker, N. (1953). The form and laws of propagation of seismic wavelets. *Geophysics*, *18*(1), 10–40. <https://doi.org/10.1190/1.1437843>
- Rietveld, H. M. (1969). A profile refinement method for nuclear and magnetic structures. *Journal of Applied Crystallography*, *2*(2), 65–71. <https://doi.org/10.1107/S0021889869006558>
- Robein, E. (2010). *Seismic imaging. A review of the techniques, their principles, merits and limitations*. Houten, The Netherlands: EAGE Publications bv.
- Roberts, K. S., Davies, R. J., & Stewart, S. A. (2010). Structure of exhumed mud volcano feeder complexes, Azerbaijan. *Basin Research*, *22*(4), 439–451. <https://doi.org/10.1111/j.1365-2117.2009.00441.x>
- Ryzak, M., & Bieganski, A. (2011). Methodological aspects of determining soil particle-size distribution using the laser diffraction method. *Journal of Plant Nutrition and Soil Science*, *174*(4), 624–633. <https://doi.org/10.1002/jpln.201000255>
- Savage, H. M., & Brodsky, E. E. (2011). Collateral damage: Evolution with displacement of fracture distribution and secondary fault strands in fault damage zones. *Journal of Geophysical Research*, *116*, B03405. <https://doi.org/10.1029/2010JB007665>
- Sibson, R. H. (2003). Brittle-failure controls on maximum sustainable overpressure in different tectonic regimes. *American Association of Petroleum Geologists Bulletin*, *87*(6), 901–908. <https://doi.org/10.1306/01290300181>
- Stewart, S. A., & Davies, R. J. (2006). Structure and emplacement of mud volcano systems in the South Caspian Basin. *AAPG Bulletin*, *90*(5), 771–786. <https://doi.org/10.1306/11220505045>
- Sultan, N., Cochonat, P., Canals, M., Cattaneo, A., Dennielou, B., Hafliadon, H., et al. (2004). Triggering mechanisms of slope instability processes and sediment failures on continental margins: A geotechnical approach. *Marine Geology*, *213*(1–4), 291–321. <https://doi.org/10.1016/j.margeo.2004.10.011>
- Sultan, N., De Gennaro, V., & Puech, A. (2012). Mechanical behaviour of gas-charged marine plastic sediments. *Géotechnique*, *62*(9), 751–766. <https://doi.org/10.1680/geot.12.OG.002>
- Swarbrick, R. E., Osborne, M. J., & Yardley, G. S. (2002). Comparison of overpressure magnitude resulting from the main generating mechanisms generating mechanisms. *AAPG Memoir*, *76*, 1–12.
- Terzaghi, K. (1943). *Theoretical soil mechanics*. New York: John Wiley and Sons Incorporated, Ed.
- Tingay, M., Heidbach, O., Davies, R., & Swarbrick, R. (2008). Triggering of the Lusi mud eruption: Earthquake versus drilling initiation. *Geology*, *36*(8), 639–642. <https://doi.org/10.1130/G24697A.1>
- Tingay, M., Manga, M., Rudolph, M. L., & Davies, R. (2017). An alternative review of facts, coincidences and past and future studies of the Lusi eruption. *Marine and Petroleum Geology*, *95*, 345–361. (December). <https://doi.org/10.1016/j.marpetgeo.2017.12.031>
- Tingay, M. R. P., Rudolph, M. L., Manga, M., Davies, R. J., & Wang, C.-Y. (2015). Initiation of the Lusi mudflow disaster. *Nature Geoscience*, *8*(7), 493–494. <https://doi.org/10.1038/ngeo2472>
- Wyllie, M. R. J., Gregory, A. R., & Gardner, G. H. F. (1958). An experimental investigation of factors affecting elastic wave velocities in porous media. *Geophysics*, *23*(3), 459–493. <https://doi.org/10.1190/1.1438493>
- Zitter, T. (2004). Mud volcanism and fluid emissions in Eastern Mediterranean neotectonic zones. *Free University of Amsterdam*, *121*(07). <https://doi.org/10.1017/S002221510700713X>



Mud extruded from the bubbling gryphon ending its course (Sare Boga, Azerbaijan)

Abstract

This manuscript assesses the role of gas in the mud generation processes by focusing on a dense and multidisciplinary dataset of the active Absheron mud volcano (AMV), South Caspian Basin. The study is divided in three main parts: definition of the mud source; analysis of the hydro-mechanical behavior of compacted sediments after gas exsolution; numerical modeling of the AMV formation.

First, I identified the source of the AMV as being the Anhydritic Surakhany Fm. (ASF): seismic geomorphology evidences a depletion zone below the AMV and samples from surface mudflows indicate a Pliocene age and the same mineralogy as the ASF. The ASF is composed of interstratified anhydritic beds and low-density overpressured and under-compacted clay-rich layers. The mud source seems located in an interval presenting intrinsic favorable properties to remobilization and at the convergence of overpressure build-up and gas accumulation.

I then tested the impact of gas exsolution on the hydro-mechanical properties of compacted sediments through a novel consolidation apparatus. Results show that sediments are damaged by gas exsolution and do not recover completely after reloading. Gas exsolution leading to a degree of gas saturation higher than 38% generates a critical behavior interpreted as the result of mud generation.

I finally integrated multidisciplinary data and results in simple numerical models to confront the hypothesis on the AMV formation with the geological conditions. A 2D diffusion model confirms that the association of lateral pressure transmission and vertical gas migration along faults leads to mud generation. Fluid mechanics equations show that mud is then able to rise up to the seafloor by density-inversion. Accounting for fracture propagation and dynamic viscosity may improve and accelerate the mud remobilization process. I tested several working hypotheses through this modeling and went from a purely conceptual formation model for the AMV to a semi-quantitative one.

This study identified key parameters for mud volcano formation that are believed to be common to most of these structures and allowed developing a modeling approach that may be adapted and improved to describe mud volcanoes formation in other geological contexts.

Key words: Gassy sediment, mud generation, mud volcano, sediment remobilization, South Caspian Basin.

Résumé

Ce manuscrit étudie le rôle du gaz dans les processus de génération de boue en se concentrant sur un jeu de donnée riche et pluridisciplinaire du volcan de boue actif d'Absheron (VBA) dans le Bassin sud caspien. L'étude est divisée en trois parties principales : la définition de la source de la boue ; l'analyse du comportement hydromécanique des sédiments compactés après exsolution de gaz ; la modélisation numérique de la formation du VBA.

J'ai d'abord identifié la Formation du Surakhany Anhydritique (ASF) comme la source du VBA : les données sismiques montrent une géométrie de zone de déplétion et la boue émise présente une minéralogie et un âge (Pliocène) compatibles avec ceux de l'ASF. L'ASF se compose d'une interstratification de bancs évaporitiques et de sédiments argileux à faible densité, en surpression et sous compactés. La source de la boue semble localisée au niveau d'un intervalle présentant des propriétés intrinsèques favorables à la remobilisation et à la convergence d'une accumulation de surpression et de gaz.

J'ai ensuite testé l'impact de l'exsolution de gaz sur les propriétés hydrodynamiques des sédiments compactés grâce à un nouveau système de consolidation. Les résultats montrent que les sédiments sont endommagés par l'exsolution et qu'ils ne retrouvent pas complètement leurs propriétés initiales après la recompaction. Si l'exsolution de gaz mène à un degré de saturation en gaz supérieur à 38%, j'ai observé un comportement critique que j'interprète comme le résultat de la génération de boue.

Enfin, j'ai intégré tous ces résultats dans des modèles numériques simples afin de confronter les hypothèses sur la formation du VBA aux conditions géologiques. Un modèle de diffusion 2D confirme que l'association d'une transmission latérale de pression et d'une migration verticale de gaz le long des failles mènent à la génération de boue. Des équations de mécanique des fluides montrent que la boue peut alors remonter jusqu'au fond marin par inversion de densité, mais la propagation de fractures et la prise en compte d'une viscosité dynamique pourraient participer et accélérer le processus de remobilisation. Mon travail de modélisation a permis de tester plusieurs hypothèses et de passer d'un modèle de formation du VBA purement conceptuel à un modèle semi-quantitatif.

Cette étude identifie les paramètres clés contrôlant la formation d'un volcan de boue, qui seraient communs à la plupart de ces structures. Une méthode de modélisation a été développée et elle peut être adaptée et améliorée afin de simuler la formation de volcans de boue dans des contextes géologiques différents.

Mots clés : Bassin sud caspien, exsolution de gaz, génération de boue, remobilisation de sédiments, sédiment gazeux, volcan de boue.